

Bangor University

DOCTOR OF PHILOSOPHY

A Lateral Flow Device for the 21st Century

The development of a flexible platform for the PoC detection of genes.

Taaffe, Stephen

Award date:
2024

Awarding institution:
Bangor University

[Link to publication](#)

General rights

Copyright and moral rights for the publications made accessible in the public portal are retained by the authors and/or other copyright owners and it is a condition of accessing publications that users recognise and abide by the legal requirements associated with these rights.

- Users may download and print one copy of any publication from the public portal for the purpose of private study or research.
- You may not further distribute the material or use it for any profit-making activity or commercial gain
- You may freely distribute the URL identifying the publication in the public portal ?

Take down policy

If you believe that this document breaches copyright please contact us providing details, and we will remove access to the work immediately and investigate your claim.

Download date: 25. Jun. 2024

A Lateral Flow Device for the 21st Century:

*The development of a flexible platform for the PoC
detection of genes.*

A thesis submitted for the degree of

Doctor of Philosophy

Prifysgol Bangor • Bangor University



By

Stephen Nicholas Taaffe

Declaration and Consent

Details of the Work

I hereby agree to deposit the following item in the digital repository maintained by Bangor University and/or in any other repository authorized for use by Bangor University.

Author Name: Stephen Taaffe

Title: A Lateral Flow Device for the 21st Century: The development of a flexible platform for the detection of genes by on device amplification and detection.

Supervisor/Department: School of Natural Sciences – Chemistry

Funding body (if any): KESS II

Qualification/Degree obtained: PhD Chemistry

This item is a product of my own research endeavor's and is covered by the agreement below in which the item is referred to as "the Work". It is identical in content to that deposited in the Library, subject to point 4 below.

Non-exclusive Rights

Rights granted to the digital repository through this agreement are entirely non-exclusive. I am free to publish the Work in its present version or future versions elsewhere.

I agree that Bangor University may electronically store, copy or translate the Work to any approved medium or format for the purpose of future preservation and accessibility. Bangor University is not under any obligation to reproduce or display the Work in the same formats or resolutions in which it was originally deposited.

Bangor University Digital Repository

I understand that work deposited in the digital repository will be accessible to a wide variety of people and institutions, including automated agents and search engines via the World Wide Web.

I understand that once the Work is deposited, the item and its metadata may be incorporated into public access catalogues or services, national databases of electronic theses and dissertations such as the British Library's EThOS or any service provided by the National Library of Wales.

I understand that the Work may be made available via the National Library of Wales Online Electronic Theses Service under the declared terms and conditions of use (<http://www.llgc.org.uk/index.php?id=4676>). I agree that as part of this service the National Library of Wales may electronically store, copy or convert the Work to any approved medium or format for the purpose of future preservation and accessibility. The National Library of Wales is not under any obligation to reproduce or display the Work in the same formats or resolutions in which it was originally deposited.

Statement 1:

This work has not previously been accepted in substance for any degree and is not being concurrently submitted in candidature for any degree unless as agreed by the University for approved dual awards.

Signed (candidate)

Date

Statement 2:

This thesis is the result of my own investigations, except where otherwise stated. Where correction services have been used, the extent and nature of the correction is clearly marked in a footnote(s).

All other sources are acknowledged by footnotes and/or a bibliography.

Signed (candidate)

Date

Statement 3:

I hereby give consent for my thesis, if accepted, to be available for photocopying, for inter- library loan and for electronic storage (subject to any constraints as defined in statement 4), and for the title and summary to be made available to outside organisations.

Signed (candidate)

Date

NB: Candidates on whose behalf a bar on access has been approved by the Academic Registry should use the following version of **Statement 3:**

Statement 3 (bar):

I hereby give consent for my thesis, if accepted, to be available for photocopying, for inter- library loans and for electronic storage (subject to any constraints as defined in statement 4), after expiry of a bar on access.

Signed (candidate)

Date

Statement 4:

Choose **one** of the following options

a) I agree to deposit an electronic copy of my thesis (the Work) in the Bangor University (BU) Institutional Digital Repository, the British Library ETHOS system, and/or in any other repository authorized for use by Bangor University and where necessary have gained the required permissions for the use of third party material.	X
b) I agree to deposit an electronic copy of my thesis (the Work) in the Bangor University (BU) Institutional Digital Repository, the British Library ETHOS system, and/or in any other repository authorized for use by Bangor University when the approved bar on access has been lifted.	
c) I agree to submit my thesis (the Work) electronically via Bangor University's e-submission system, however I opt-out of the electronic deposit to the Bangor University (BU) Institutional Digital Repository, the British Library ETHOS system, and/or in any other repository authorized for use by Bangor University, due to lack of permissions for use of third party material.	

Options B should only be used if a bar on access has been approved by the University.

In addition to the above I also agree to the following:

1. That I am the author or have the authority of the author(s) to make this agreement and do hereby give Bangor University the right to make available the Work in the way described above.
2. That the electronic copy of the Work deposited in the digital repository and covered by this agreement, is identical in content to the paper copy of the Work deposited in the Bangor University Library, subject to point 4 below.
3. That I have exercised reasonable care to ensure that the Work is original and, to the best of my knowledge, does not breach any laws – including those relating to defamation, libel and copyright.
4. That I have, in instances where the intellectual property of other authors or copyright holders is included in the Work, and where appropriate, gained explicit permission for the inclusion of that material in the Work, and in the electronic form of the Work as accessed through the open access digital repository, *or* that I have identified and removed that material for which adequate and appropriate permission has not been obtained and which will be inaccessible via the digital repository.
5. That Bangor University does not hold any obligation to take legal action on behalf of the Depositor, or other rights holders, in the event of a breach of intellectual property rights, or any other right, in the material deposited.
6. That I will indemnify and keep indemnified Bangor University and the National Library of Wales from and against any loss, liability, claim or damage, including without limitation any related legal fees and court costs (on a full indemnity bases), related to any breach by myself of any term of this agreement.

Signature: Date :

Signature: Date :

I hereby declare that this thesis is the results of my own investigations, except where otherwise stated. All other sources are acknowledged by bibliographic references. This work has not previously been accepted in substance for any degree and is not being concurrently submitted in candidature for any degree unless, as agreed by the University, for approved dual awards.

Yr wyf drwy hyn yn datgan mai canlyniad fy ymchwil fy hun yw'r thesis hwn, ac eithrio lle nodir ynwahanol. Caiff ffynonellau eraill eu cydnabod gan droednodiadau yn rhoi cyfeiriadau eglur. Nid ywsylwedd y gwaith hwn wedi cael ei dderbyn o'r blaen ar gyfer unrhyw radd, ac nid yw'n cael eigyflwyno ar yr un pryd mewn ymgeisiaeth am unrhyw radd oni bai ei fod, fel y cytunwyd gan yBrifysgol, am gymwysterau deuol cymeradwy.

Declaration and Consent	i
Contents	vi
Abstract	xii
List of Abbreviations	xiii
List of Figures	xvi
List of Tables	xxii
<u>Chapter 1 Introduction</u>	1
1.1 Methicillin Resistant Staphylococcus Aureus (MRSA)	2
1.2 Mechanism of β-lactam antimicrobial resistance in methicillin resistant staphylococcus aureus isolates	4
1.3 Molecular evolution of MRSA AMR factors & genetic functionality of SCCmec	7
1.3.1 Antibiotic resistance factors found on SCCmec	8
1.3.2 Further antimicrobial resistance not encoded by the SCCmec	10
1.3.3 Functional elements of the SCCmec	12
1.3.4 The expression and regulation of <i>mecA</i>	14
1.3.5 The origin of the SCCmec	16
1.4 Conventional Culture Based Detection Methods	16
1.5 State of the art detection methods / Molecular assays	19
1.6 An introduction to Immunoassay and Nucleic Acid Hybridisation Based Lateral Flow Assays	22
1.6.1 Introduction	22
1.6.2 Construction, composition, and working principle of lateral flow devices (LFD's)	
1.6.2a. <i>A schematic overview of construction</i>	23
1.6.2b. <i>The sample pad</i>	24
1.6.2c. <i>The conjugate pad</i>	24
1.6.2d. <i>The lateral flow membrane</i>	25
1.6.2e. <i>The absorbent pad/the wick</i>	26
1.6.3 Analyte detection - A general schematic overview of detection	26
1.6.3a. <i>Competitive and sandwich/direct detection based lateral flow immunoassays.</i>	26
1.6.3b. <i>Nucleic acid lateral flow (immuno)assay</i>	27

1.6.4	Detection Probes	31
	1.6.4a. Colloidal gold nanoparticles	31
	1.6.4b. Silver/gold reduction-based enhancement of colloidal gold nanoparticles	32
	1.6.4c. Amorphous carbon nanoparticles	33
	1.6.4d. Fluorescence probes	33
	1.6.4e. Quantum dots	34
	1.6.4f. Up converting phosphors	35
	1.6.4g. Paramagnetic particles	35
	1.6.4h. Latex particles	36
	1.6.5 Detection Limits	36
1.7	Concluding remarks and aims.	38
 <u>Chapter 2 MRSA Antimicrobial Resistance NALFA Primer Design</u>		40
2.1	Introduction	41
2.2	Methicillin-Resistant Staphylococcus Aureus Antimicrobial Resistance Gene Conservation Analysis	41
2.3	Antimicrobial resistance gene primer and probe sequence selections	47
2.4	Novel NALFA compatible RPA scheme and functional mechanisms	53
2.5	NALFA multiplex capture probe development	58
 <u>Chapter 3 MRSA Reference Materials</u>		66
3.1	Introduction	67
3.2	MRSA Rosenbach ATCC 43300 Reference Culture	67
3.3	MRSA Rosenbach ATCC 43300 Reference gDNA Extraction	69
3.4	Reference mecA gene PCR and purification from ATCC 43300 gDNA	71
3.5	Concluding Remarks	74
 <u>Chapter 4 RT-RPA Kinetic Model</u>		75
4.1	Introduction	76
4.2	Proposed RT-RPA kinetic model	76
	4.2.1 Fitting Function	76
	4.2.2 Regression conditioning issues	78

4.3	Regression preconditioning solver algorithm	81
4.4	First and second derivative fitting functions	82
4.5	Concluding Remarks	84

Chapter 5 Primer Sequence Screening & RT-RPA **85**

5.1	Introduction	86
5.2	PCR screen of unmodified RPA <i>mecA</i> primer sequences	86
5.2.1	Experimental Method	87
5.2.2	Experimental Results	87
5.2.3	Concluding Remarks & Outcomes	88
5.3	RPA screen of PCR pre-screened <i>mecA</i> primer sequences	89
5.3.1	Experimental Method	89
5.3.2	Experimental Results	90
5.3.3	Concluding Remarks & Outcomes	91
5.4	RT-RPA screen of PCR/RPA pre-screened unmodified <i>mecA</i> primer sequences	91
5.4.1	Experimental Method	92
5.4.2	Experimental Results	93
5.4.3	Concluding Remarks & Outcomes	106
5.5	RT-RPA of pre-screened modified variants of the <i>mecA</i> primer sequences	108
5.5.1	Experimental Method	108
5.5.2	C3 Modified RT-RPA Experimental Results	109
5.5.3	C23 Modified RT-RPA Experimental Results	119
5.5.4	Concluding Remarks & Outcomes	129

Chapter 6 Real Time Solid Phase RPA **133**

6.1	Introduction	134
6.2	Solid State Fluorometer	134
6.3	Reaction Matrix Blocking Optimisation	143
6.4	Initial SP-RPA Investigation	147
6.5	SP-RPA Optimisation	150

6.6	Real Time SP-RPA Kinetic Evaluation	152
6.6.1	RT-SP-RPA Set mecA7-C3	153
6.6.2	RT-SP-RPA Set mecA8-C3	154
6.6.3	RT-SP-RPA Set mecA10-C3	155
6.6.4	RT-SP-RPA Set mecA12-C3	156
6.6.5	RT-SP-RPA Set mecA7-C12	157
6.6.6	RT-SP-RPA Set mecA8-C12	158
6.6.7	RT-SP-RPA Set mecA10-C12	159
6.6.8	RT-SP-RPA Set mecA12-C12	160
6.6.9	Discussion and concluding remarks	161
 <u>Chapter 7 Gyromagnetically Enhanced SP-RPA</u>		165
7.1	Introduction	166
7.2	Fe₃O₄ Nanoflower Synthesis	166
7.2.1	Methodology	166
7.2.2	Results and discussion	170
7.3	Fe₃O₄ Nanoflower SiO₂ Coating	173
7.3.1	Methodology	173
7.3.2	Results and discussion	174
7.4	SiO₂ Coated Fe₃O₄ Nanoflower S-H Functionalisation and Protein immobilisation	175
7.4.1	Methodology	175
7.4.2	Results and discussion	175
7.5	Micro-Helmholtz Alternating Magnetic Field Generator	176
7.5.1	Introduction	176
7.5.2	Micro-Helmholtz Coil integration in the RT-SP-RPA Fluorometer	178
7.5.3	Driver Circuitry	179
7.6	Real Time SP-RPA Gyromagnetically Enhanced RPA	181
7.6.1	Introduction	181
7.6.2	Methodology	181
7.6.3	Results w/RT-SP-RPA of mecA12-C3 under magnetic enhancement	182
7.6.4	Discussion and concluding remarks	189

<u>Chapter 8 Nucleic Acid Lateral Flow Assay Development</u>	191
8.1 Introduction	192
8.2 Membrane Blocking optimisation	196
8.2.1 Introduction to membrane blocking solution formulation	196
8.2.2 Blocking solution development: Analyte Adsorptivity Measurement Methodology	197
8.2.3 Experimental Adsorptivity Results	199
8.2.4 Experimental Adsorptivity Velocity Data Ideal Blocking Reagent Concentrations	201
8.2.5 Discussion and outcomes	203
8.3 Membrane Blocking Time Optimisation	205
8.3.1 Introduction	205
8.3.2 Soak time titration procedures	205
8.3.3 Results and discussion	206
8.4 Membrane Blotting Optimisation	207
8.4.1 Introduction	207
8.4.2 Optimisation Methodology	207
8.4.3 Results and discussion	208
8.5 Capture Probe : Amplicon Hybridisation Optimisation	210
8.5.1 Introduction	210
8.5.2 Fluorometric Titration Methodology	211
8.5.3 Results and discussion	212
8.6 Full Membrane Lay-up and AuNP-detection	214
8.6.1 Introduction	214
8.6.2 Methodology	214
8.6.3 Results and discussion	215
8.7 Initial full NALFA layups	218
8.7.1 Introduction and aims:	218
8.7.2 Methodology	218
8.7.3 Results and discussion	219

8.7	Initial full NALFA layups	221
8.8.1	Introduction and Objective:	221
8.8.2	Methodology	221
8.8.3	Results and discussion	222
	<u>References</u>	223
	<u>Appendix</u>	232

The utilisation of point-of-contact diagnostic devices has evolved into a crucial cornerstone within the global public health landscape. Notably, their significance became abundantly clear during the COVID-19 pandemic. This doctoral thesis is dedicated to introducing and perfecting an innovative point-of-contact system designed for the detection of specific genes. This system is rooted in a modified recombinase polymerase DNA amplification method, complemented by an adaptable nucleic acid lateral flow assay.

To showcase the capabilities of this novel system and elucidate the processes involved in its design and optimization for a specific target gene locus, we employed genes linked to methicillin-resistant *Staphylococcus aureus* as our detection targets. The system proved its effectiveness in detecting the antibiotic resistance gene *mecA*, commonly found in methicillin-resistant *Staphylococcus aureus*, even at a single genetic copy, all in less than an hour.

The research in this presentation provides a comprehensive breakdown of the procedures necessary to effectively identify conserved gene loci suitable for our developed system. Additionally, we delve into the methodology for designing compatible primer sets. To make the development of this system possible, we established a kinetic model for real-time recombinase polymerase amplification, which is presented herein. This model enabled us to explore the kinetics of recombinase polymerase amplification reactions in real time, employing a custom-built solid-state fluorometer. Modifications were made to the standard recombinase polymerase amplification procedures to accommodate the altered primer system, with further adjustments detailed to ensure compatibility with the developed nucleic acid lateral flow device. We also address the kinetic implications of these modifications and outline a procedure for further optimising the recombinase polymerase amplification reaction conditions to mitigate any performance losses.

The thesis goes on to discuss the sonochemical synthesis of monodisperse 21nm thiol-functionalised silica-coated superparamagnetic nanoflowers. These nanoflowers were thoroughly characterised using high-resolution transmission electron microscopy, X-ray diffraction, and UV-Vis spectroscopy. Notably, they exhibited the remarkable ability to remain in colloidal solution for extended periods and could endure freeze drying and reconstitution without requiring mechanical redispersion. We also describe how these nanoflowers were to catalyse RPA reactions in solid phase, in the presence of an alternating magnetic field. The magnetic field was generated using a battery-powered field generator developed in-house, compact enough to integrate into a standard lateral flow device, akin to the ones currently available in the market, such as the ClearBlue Digital device.

List of Abbreviations

AC – Alternating Current
aCNP – Amorphous Carbon Nanoparticles
AMR – Antimicrobial Resistance
ASM – American Society for Microbiology
ATCC – American Type Culture Collection
AuNPs – Gold Nanoparticles
BHI – Brain Heart Infusion
BHQ-1 – Black Hole Quencher 1
BLAST – Basic Local Alignment Search Tool
BSA – Bovine Serum Albumin
CAD – Computer-Aided Design
Conc. – Concentration
COVID – Coronavirus Disease 2019
CTAB – Cetrimonium Bromide
D-Ala-D-Ala – D-alanyl-D-alanine
DENV – Dengue Virus
DNA – Deoxyribonucleic Acid
dNTP – Deoxynucleotide Triphosphates
dr-FAM Deoxyribose-Fluorescein Amidite
ds-DNA – Double-Stranded Deoxyribonucleic Acid
E.coli – *Escherichia Coli*
EDTA – Ethylenediaminetetraacetic Acid
EtBr – Ethidium bromide
FAM – Fluorescein Amidite
FPG – Formamidopyrimidine DNA Glycosylase
GC – Guanine: Cytosine
gDNA – Genomic DNA
hCG – Human Chorionic Gonadotropin
HIV – Human Immunodeficiency Virus
HP – High-Performance
HPLC – High-Performance Liquid Chromatography

LC – Inductive Capacitance
LFA – Lateral Flow Assay
LFD – Lateral Flow Device
LFIA – Lateral Flow Immunoassay
LOD – Limit of Detection
MIC – Minimum Inhibitory Concentration
MLST – Multi-Locus Sequence Typing
MPTMS – 3-Mercaptopropyl Trimethoxysilane
MRSA – Methicillin-Resistant *Staphylococcus Aureus*
MSA – Multiple Sequence Alignment
MSSA – Methicillin-Susceptible *Staphylococcus Aureus*
NALF(A) – Nucleic Acid Lateral Flow (Assay)
NALFIA – Nucleic Acid Lateral Flow Immunoassay
NEB – New England Biolabs
NMDEA – N-Methyldiethanolamine
PAGE – Polyacrylamide Gel Electrophoresis
PBD – Protein Data Bank
PBP – Penicillin-Binding Proteins
PBP2 – Penicillin-Binding Protein 2
PBP2a – Penicillin-Binding Protein 2a
PBS – Phosphate Buffered Saline
PCB – Printed Circuit Board
PCR – Polymerase Chain Reaction
PFGE – Pulsed-Field Gel Electrophoresis
PID – Proportional Integral Derivative
PMMA – Poly(methyl methacrylate)
PoC – Point of Contact
PVDF – Polyvinylidene Fluoride
PVP - Polyvinylpyrrolidone
PWM – Pulse Width Modulation
QC – Quality Control
RCF – Relative Centrifugal Force
RPA – Recombinase Polymerase Amplification

rRNA – Ribosomal RNA
RT – Reverse Transcription (Transcriptase)
RT-RPA – Real Time Recombinase Polymerase Amplification
S. epidermidis – *Staphylococcus Epidermidis*
S. fleurette – *Staphylococcus Fleurette*
S. haemolyticus – *Staphylococcus Haemolyticus*
S. aureus – *Staphylococcus Aureus*
S. sciuri – *Staphylococcus Sciuri*
SCCmec – Staphylococcal Cassette Chromosome mec
SD – Standard Deviation
SSBP – Single Stranded DNA Binding Protein
SSC – Saline-Sodium Citrate
ss-DNA – Single Stranded DNA
SSE – Sum of Squared Estimate of Errors
TBE – Tris-Borate-EDTA Buffer
TEC – Thermoelectric Cooler
TEM – Transmission Electron Microscopes
TEMED - Tetramethylethylenediamine
TIA – Transimpedance Amplifier
TEOS - Tetraethyl Orthosilicate
TPSA – Total Prostate-Specific Antigen
TTL – Transistor-Transistor Logic
USA – United States of America
USD – United States Dollar
UV - Ultraviolet
UV-Vis – Ultraviolet-Visible Spectroscopy
VRSA– Vancomycin-Resistant *Staphylococcus Aureus*
WHO – World Health Organisation
XRD – X-ray Diffraction
ZEBOV – Zaire Ebolavirus

Chapter 1

Fig. 1.1 - The molecular structure of penicillin and methicillin.

Fig. 1.2 - Worldwide prevalence of MRSA by country.

Fig. 1.3 - European prevalence of MRSA by country.

Fig. 1.4 - Molecular structure of the staphylococcus aureus peptidoglycan cell wall.

Fig. 1.5 - The structure of the penicillin binding protein PBP2a isolated from a MRSA isolate.

Fig. 1.6 - A schematic arrangement of the SCCmec types I-V.

Fig. 1.7 - Molecular structures of the antibiotic bleomycin (3).

Fig. 1.8 - Molecular structures of antibiotics kanamycin (4) and tobramycin (5).

Fig. 1.9 - Molecular structure of antibiotics ermA transcribes resistance factors against.

Fig. 1.10 - Molecular structure of tetracycline-based antimicrobials.

Fig. 1.11 - The molecular structure of Ciprofloxacin and Amikacin.

Fig. 1.12 - Molecular structure of Vancomycin.

Fig. 1.13 - The 17 main variants of the SCCmec.

Fig. 1.14 - The monomeric crystal structure of Mecl – dsDNA transition state complex.

Fig. 1.15 - Pictorial model of the feature of mecA gene regulation.

Fig. 1.16 - MRSA selective mannitol salt phenol red agar plates.

Fig. 1.17 - Latex agglutination test card.

Fig. 1.18 - MRSA isolates streaked on a MRSASelect II agar plate.

Fig. 1.19 - Pulse field gel electrophoresis of four MRSA isolates.

Fig. 1.20 - PFGE of pairs of isolates with identical allelic profiles.

Fig. 1.21 - Schematic overview for the construction of traditional LFD's.

Fig. 1.22 - The principle working schematic of a traditional lateral flow device.

Fig. 1.23 - Sandwich based detection in Lateral Flow Immuno-Assay (LFIA's).

Fig. 1.24 - Competitive Detection Assay.

Fig. 1.25 - NALFIA Detection Scheme.

Fig. 1.26 - NALFA detection array.

Fig. 1.27 - Three common NALFA capture probe adhesion strategies.

Fig. 1.28 - An example of a hCG pregnancy test.

Fig. 1.29 - Silver/Gold reduction-based enhancement of a colloidal gold based NALF detection array.

Fig. 1.30 - Two commonly used Xanthene (12) and Cyanine Based Fluorophores (13) in LFD's.

Chapter 2

Fig. 2.1 - Multi sequence alignment entropy plot of MecA.

Fig. 2.2 - Multi sequence alignment entropy plot of ant(4').

Fig. 2.3 - Multi sequence alignment entropy plot of bleO.

Fig. 2.4 - Multi sequence alignment entropy plot of ermA.

Fig. 2.5 - Multi sequence alignment entropy plot of TetK.

Fig. 2.6 - Multi sequence alignment entropy plot of TetM.

Fig. 2.7 - Multi sequence alignment entropy plot of VanA.

Fig. 2.8 - Multi sequence alignment entropy plot of NorA.

Fig. 2.9 - Multi sequence alignment entropy plot of NorB.

Fig. 2.10 - Multi sequence alignment entropy plot of ant(9).

Fig. 2.11 - Structural modification to RPA primers and probes.

Fig. 2.12 - Shows the key stages of RPA reactions with modified forward and reverse primers.

Fig. 2.13 - Shows NALFA test line layups.

Fig 2.14 – RT-RPA enzymatic functional mechanism.

Fig. 2.15 - Heatmap of $-\Delta G$ hybridisation between all capture and reverse complement sequences.

Fig. 2.16 - Capture sequences complement $-\Delta G$ hybridisation energy.

Fig. 2.17 - Heatmap of cross $-\Delta G$ hybridisation between primer attached capture sequences.

Fig. 2.18 - Capture sequences specificity ratios with SD's calculated from the $-\Delta G$ cross hybridisation.

Chapter 3

Fig. 3.1 - AMR genes of interest found in ATTC 43300 MRSA isolate, WGS genome ID: 1280.16403.

Fig. 3.2 - Isolated colonies of S. Aureus ATCC 43300 on BHI agar with 50 μ g L-1 kanamycin.

Fig. 3.3 - High-quality gDNA extracted and purified from Isolated colonies of S. Aureus ATCC 43300.

Fig. 3.4 - [gDNA] determined by EtBr fluorometric assay.

Fig. 3.5 - MecA PCR primer screen using S. Aureus ATCC 43300 gDNA. A-C mecA F/Ra-d.

Fig. 3.6 - DNA-Page gel of PCR products, and [mecA] determined by EtBr fluorometric assay.

Fig. 3.7 - Low copy count PCR of MecA reference gene using primers mecA F/Rb.

Chapter 4

Fig. 4.1 - Shows the effect of varying parameters of the proposed logistic function.

Fig. 4.2 - (A)-(C) Shows how f , h and k_m have functional interdependencies.

Fig. 4.3 – Shows the same RT-RPA raw data fitted 4 times using equation x.

Fig. 4.4 - Shows individual residual plots of fits in figure 4.3.

Fig. 4.5 - Shows a single run sample of RT-RPA data fitted using equation 2-4.

Fig. 4.6 - Shows equation 5 and 6 calculated from an RT-RPA fit with equation 1).

Fig. 4.7 - Shows equation 6 and 8 calculated from an RT-RPA fit with equation 1.

Chapter 5

*Fig. 5.1 – DNA-PAGE gel showing PCR products using the original *mecA* RPA primer sequences.*

Fig. 5.2 - DNA migration calibration curve for gels in figure 5.1.

*Fig. 5.3 - Gels showing the results of repeated PCR amplification of primer sets *mecA*₁ and *mecA*₄.*

*Fig. 5.4 – DNA-PAGE gel showing RPA products using the original *mecA* RPA primer sequences.*

Fig. 5.5 - DNA migration calibration curve for gels in figure 5.4.

*Fig. 5.6 - RT-RPA kinetic data using unmodified primer set *mecA*₁₂ w/ *mecA* gene template.*

*Fig. 5.7 - RT-RPA kinetic data using unmodified primer set *mecA*₁₂ w/ MRSA gDNA template.*

*Fig. 5.8 - RT-RPA kinetic data using unmodified primer set *mecA*₁₁w/ *mecA* gene template.*

*Fig. 5.9 - RT-RPA kinetic data using unmodified primer set *mecA*₁₁ w/ MRSA gDNA template.*

*Fig. 5.10 - RT-RPA kinetic data using unmodified primer set *mecA*₁₀w/ *mecA* gene template.*

*Fig. 5.11 - RT-RPA kinetic data using unmodified primer set *mecA*₁₀ w/ MRSA gDNA template.*

*Fig. 5.12 - RT-RPA kinetic data using unmodified primer set *mecA*₉w/ MRSA gDNA template.*

*Fig. 5.13 - RT-RPA kinetic data using unmodified primer set *mecA*₈ w/ *mecA* gene template.*

*Fig. 5.14 - RT-RPA kinetic data using unmodified primer set *mecA*₈ w/ MRSA gDNA template.*

*Fig. 5.15 - RT-RPA kinetic data using unmodified primer set *mecA*₇ w/ *mecA* gene template.*

*Fig. 5.16 - RT-RPA kinetic data using unmodified primer set *mecA*₇ w/ MRSA gDNA template.*

Fig. 5.17 - RT-RPA fluorescence curves of primer sets which failed under RT-RPA conditions.

*Fig. 5.18 - Combined DNA-PAGE gel showing failed RPA w/ unmodified primer sets *mecA*_{2,3,6,9} .*

Fig. 5.19 – Combined processed fits of successful primer sets under RT-RPA conditions.

*Fig. 5.20 - RT-RPA kinetic data using modified primer set *mecA*₁₂-C3 w/ *mecA* gene template.*

*Fig. 5.21 - RT-RPA kinetic data using modified primer set *mecA*₁₂-C3 w/ MRSA gDNA template.*

Fig. 5.22 - RT-RPA kinetic data using modified primer set mecA₁₀-C3 w/ mecA gene template.

Fig. 5.23 - RT-RPA kinetic data using modified primer set mecA₁₀-C3 w/ MRSA gDNA template.

Fig. 5.24 - RT-RPA kinetic data using modified primer set mecA₈-C3 w/ mecA gene template.

Fig. 5.25 - RT-RPA kinetic data using modified primer set mecA₈-C3 w/ MRSA gDNA template.

Fig. 5.26 - RT-RPA kinetic data using modified primer set mecA₇-C3 w/ mecA gene template.

Fig. 5.27 - RT-RPA kinetic data using modified primer set mecA₇-C3 w/ MRSA gDNA template.

Fig. 5.28 - RT-RPA kinetic data of C3 modified primer sets which failed under RT-RPA conditions.

Fig. 5.29 - Combined DNA-PAGE gel showing failed RPA w/ modified primer sets mecA_{2,3,6,,9,11}-C3.

Fig. 5.30 - Combined processed fits of successful primer sets under RT-RPA conditions.

Fig. 5.31 - RT-RPA kinetic data using modified primer set mecA₁₂-C12 w/ mecA gene template.

Fig. 5.32 - RT-RPA kinetic data using modified primer set mecA₁₂-C12 w/ MRSA gDNA template.

Fig. 5.33 - RT-RPA kinetic data using modified primer set mecA₁₀-C12 w/ mecA gene template.

Fig. 5.34 - RT-RPA kinetic data using modified primer set mecA₁₀-C12 w/ MRSA gDNA template.

Fig. 5.35 - RT-RPA kinetic data using modified primer set mecA₈-C12 w/ mecA gene template.

Fig. 5.36 - RT-RPA kinetic data using modified primer set mecA₈-C12 w/ MRSA gDNA template.

Fig. 5.37 - RT-RPA kinetic data using modified primer set mecA₇-C12 w/ mecA gene template.

Fig. 5.38 - RT-RPA kinetic data using modified primer set mecA₇-C12 w/ MRSA gDNA template.

Fig. 5.39 - RT-RPA kinetic data of C12 modified primer sets which failed under RT-RPA conditions.

Fig. 5.40 - Combined DNA-PAGE gel showing failed RPA w/ modified primer sets mecA_{2,3,6,,9,11}-C12.

Fig. 5.41 - Combined processed fits of successful primer sets under RT-RPA conditions.

Fig. 5.42 – Average key kinetic reaction constants highlighting spacer length effect.

Fig. 5.43 - Average key kinetic reaction constants highlighting the effect of template fragment size.

Fig.5.44 - Average key kinetic reaction constants highlighting the effects of primer modifications.

Chapter 6

Fig. 6.1 – Solid state fluorometer.

Fig. 6.2 - Laser driver block diagram.

Fig. 6.3 - Laser control board schematic.

Fig. 6.4 - TEC control board schematic.

Fig. 6.5 - Prototyped Dual-Channel TIA prior to PCB manufacturing.

Fig. 6.6 - TIA board schematic.

Fig. 6.7 - Cross sectional view of real time SP-RPA reaction holder.

Fig. 6.8 - Graph showing the developed solid matrix fluorometer's LoD.

Fig. 6.9 - Shows purified and sonochemical sheared gDNA fragments.

Fig. 6.10 - ss-DNA/protein membrane adsorptivity single reagent blocking titrations.

Fig. 6.11 - DNA/protein RPA matrix blocking efficiency 2nd derivative velocity curves.

Fig. 6.12 - Successful SP-RPA amplicons with spurious amplification products.

Fig. 6.13 - Unsuccessful SP-RPA reaction products.

Fig. 6.14 - Denaturing SDS-PAGE of purified RPA enzymes mixture.

Fig. 6.15 - SP-RPA crowding reagent titrations.

Fig. 6.16 - SP-RPA formamide titrations.

*Fig. 6.17 - RT-SP-RPA kinetic data using modified primer set *mecA*₇-C3 w/ MRSA gDNA template.*

*Fig. 6.18 - RT-SP-RPA kinetic data using modified primer set *mecA*₈-C3 w/ MRSA gDNA template.*

*Fig. 6.19 - RT-SP-RPA kinetic data using modified primer set *mecA*₁₀-C3 w/ MRSA gDNA template.*

*Fig. 6.20 - RT-SP-RPA kinetic data using modified primer set *mecA*₁₂-C3 w/ MRSA gDNA template.*

*Fig. 6.21 - RT-SP-RPA kinetic data using modified primer set *mecA*₇-C12 w/ MRSA gDNA template.*

*Fig. 6.22 - RT-SP-RPA kinetic data using modified primer set *mecA*₈-C12 w/ MRSA gDNA template.*

*Fig. 6.23 - RT-SP-RPA kinetic data using modified primer set *mecA*₁₀-C12 w/ MRSA gDNA template.*

*Fig. 6.24 - RT-SP-RPA kinetic data using modified primer set *mecA*₁₂-C12 w/ MRSA gDNA template.*

Fig. 6.25 - Combined RT-SP-RPA C3 and C12 fits for comparison of primer sets kinetic profiles.

Fig. 6.26 - Combined RT-SP-RPA C3 and C12 measured kinetic profiles parameters.

Fig. 6.27 - SP-RPA Kinetic performance delta between C3 and C12 modified primers.

Chapter 7

Fig. 7.1 – Superparamagnetic iron oxide nanoflower synthesis set up.

Fig. 7.2 - TEM of discarded aggregated Fe₃O₄ crystals.

Fig. 7.3 - Temperature controlled sonochemical reactor.

Fig. 7.4 - Deconvoluted UV-Vis spectra of the colloidal Fe₃O₄ (right) SPR peak = 317.7nm.

Fig. 7.5 - Power XRD diffraction pattern of Fe₃O₄ nanoflowers.

Fig. 7.6 - TEM of monodisperse colloidal Fe₃O₄ nanoflowers.

Fig. 7.7 - TEM of monodisperse superparamagnetic 20±1.9nm Fe₃O₄ nanoflowers.

Fig. 7.8 - TEM of monodisperse superparamagnetic Fe₃O₄ nanoflowers.

Fig. 7.9 - TEM of monodisperse 21nm1.2nm superparamagnetic SiO₂@Fe₃O₄ nanoflowers.

Fig. 7.10 - TEM of monodisperse 21nm1.2nm superparamagnetic BSA-S-S- SiO₂@Fe₃O₄.

Fig. 7.11 - Schematic of a pair of Helmholtz coils Contours.

Fig. 7.12 - Simplified schematic of a pair of LC resonant coils.

Fig. 7.13 - Rendered View of how the coils integrated with the ss-fluorometer sample holder.

Fig. 7.14 - AC Micro-Helmholtz coil high bandwidth class D output amplifier.

Fig. 7.15 - AC Micro-Helmholtz coil tuning and control board.

Fig. 7.16 - RT-SP-RPA magnetically enhanced (500Hz AC magnetic field) kinetic data using modified primer set mecA₁₂-C3 w/ MRSA gDNA template.

Fig. 7.17 - RT-SP-RPA magnetically enhanced (1kHz AC magnetic field) kinetic data using modified primer set mecA₁₂-C3 w/ MRSA gDNA template.

Fig. 7.18 - RT-SP-RPA magnetically enhanced (2.5 kHz AC magnetic field) kinetic data using modified primer set mecA₁₂-C3 w/ MRSA gDNA template.

Fig. 7.19 - RT-SP-RPA magnetically enhanced (8kHz AC magnetic field) kinetic data using modified primer set mecA₁₂-C3 w/ MRSA gDNA template.

Fig. 7.20 - RT-SP-RPA magnetically enhanced (20 kHz AC magnetic field) kinetic data using modified primer set mecA₁₂-C3 w/ MRSA gDNA template.

Fig. 7.21 - RT-SP-RPA magnetically enhanced (90kHz AC magnetic field) kinetic data using modified primer set mecA₁₂-C3 w/ MRSA gDNA template.

Fig. 7.22 - Combined processed fits of successful primer sets under RT-RPA condition.

Fig. 7.23 - Combined processed fits of successful primer sets under RT-RPA condition.

Chapter 8

Fig. 8.1 – Reproduced from Fig. 2.13 showing NALFA test line layups.

Fig. 8.2 -. NALFA construction/probe immobilisation methodology with NC membrane.

Fig. 8.3 - NALFA construction/probe immobilisation methodology with charged nylon membrane.

Fig. 8.4 - NALFA construction/probe immobilisation methodology with PVDF membrane.

Fig. 8.5 – Schematic view of under, optimally and over blocked LF membrane.

Fig 8.6 - ss-DNA/protein membrane adsorptivity single reagent blocking titrations.

Fig. 8.7 - ss-DNA/protein membrane blocking efficiency velocity.

Fig. 8.8 - Membrane blocking time effect on total adsorptivity and capillary flow.

Fig. 8.9 - Probe blotting loading curves showing ideal blotting buffer loading.

Fig. 8.10 – Heatmap of Δ G hybridisation between capture and reverse complement sequences.

Fig. 8.11 - Probe blotting loading curves showing ideal blotting buffer loading.

Fig. 8.12 - Fully optimised membrane only MecA12-C3 amplicons.

Fig. 8.13 - Fully optimised membrane Detection of MecA12-C12 amplicons.

Fig. 8.14 - Fully optimised RPA-NALF coupled assays showing selective detection of the MecA gene.

Fig. 8.15 - Fully optimised RPA-NALF coupled assay showing LoD detection for the MecA gene.

List of Tables

- Table 1.1 - The major classes of mec gene complexes with their structural variation.*
- Table 1.2 - Target housekeeping genes used in MRSA MLST.*
- Table 1.3 - Sequence variation of the seven target loci.*
- Table 1.4 - Lateral flow devices targeted at the detection of small/toxic molecules.*
- Table 1.5 - Comparison of reported Nucleic acid lateral flow (immuno)assays.*
- Table 1.6 - Comparison of report lateral flow devices targeted at protein identification.*
- Table 2.1 - Consensus sequence's locations relate to parent gene.*
- Table 2.2 - Oligonucleotide primer pairs and hybridisation probe sequences for mecA.*
- Table 2.3 - Oligonucleotide primer pairs and hybridisation probe sequences for ant(4').*
- Table 2.4 - Oligonucleotide primer and hybridisation probe sequences for BleO.*
- Table 2.5 - Oligonucleotide primer and hybridisation probe sequences for ermA.*
- Table 2.6 - Oligonucleotide primer and hybridisation probe sequences for TetK.*
- Table 2.7 - Oligonucleotide primer and hybridisation probe sequences for TetM.*
- Table 2.8 - Oligonucleotide primer and hybridisation probe sequences for vanA.*
- Table 2.9 - Oligonucleotide primer and hybridisation probe sequences for norA.*
- Table 2.10 - Oligonucleotide primer and hybridisation probe sequences for norB.*
- Table 2.11 - Oligonucleotide primer and hybridisation probe sequences for ant(9).*
- Table 2.12 - Shows the library of capture sequences for NALFA.*
- Table 2.13 - Most stable capture sequence secondary structures thermodynamically calculated.*
- Table 2.14 - Shows the library RT-RPA primers and probes with NALFA modifications.*
- Table 3.1 - MecA control target PCR primers.*
- Table 5.1 - PCR amplicon properties observed from figure 5.1.*
- Table 5.2 - RPA amplicon properties observed from figure 5.4.*
- Table 5.3 - Average key kinetic reaction constants of unmodified primers.*
- Table 5.4. Key reaction constants from fully functioning primer sets.*
- Table 7.1 – Nanoparticle crystal size estimation using Scherrer equation.*
- Table 7.2 – Key reaction constants.*
- Table 8.1 - Optimal blocking agents' concentration for NC1 from fig. 8.6.*
- Table 8.2 - Optimal blocking agents' concentration for NC2 from fig. 8.6.*
- Table 8.3 - Optimal blocking agents' concentration for NC3 from fig. 8.6.*
- Table 8.4. Optimal blocking agents' concentration for Nylon from fig. 8.6.*

Chapter 1

Introduction.

“Buckle up, Buckaroo”

*Oh, ho ho and a bottle of rum,
I'm stuck in this room for boring PhD scum,
Buckle up Buckaroo, it's going to be a ride,
Listening to this guy talk about his research and his pride.*

*Oh, the PhD introduction, it's such a bore,
I'd rather be in the lab with a flask or four,
Experimenting and testing and making a brew,
Than stuck in this room for this poor fool.*

*He drones on and on with his facts and his figures,
I can't keep my eyes open, I'm getting slumberous rigours,
But alas, I must stay and listen to the end,
Until he's finished, I can't just up and fend.*

*Oh the PhD introduction, it's such a bore,
I'd rather be out on the ocean's shore,
Sailing the seas and singing a tune,
Than stuck in this room listening to this buffoon.*

*Finally, the PhD is done with his spiel,
I can hardly contain my relief and my zeal,
I bolt from the chair and head for the door,
Leaving the PhD and his boring intro no more.*

*Back in the lab, the Bunsens are lit,
I mix and I measure, and I have a fit,
For back to my lectures, students and talks,
Owe to be free to experiment and take on new walks.*

1.1 Methicillin Resistant Staphylococcus Aureus (MRSA):

Introduction:

Staphylococcus aureus is a gram-positive coccus (sphere-shaped) bacterium that is a member of the Firmicutes phylum,¹ frequently found in the nose, respiratory tract, and on the skin.² Since its discovery during the 1880s³ it has been recognised as being responsible for a multitude of infection associated diseases. Ranging from the minor, such as skin infections to the severe,² such as necrotising pneumonia and meningitis.² Preceding the introduction of penicillin such infections had a mortality rate of nearly 80 %.³ Following the continued use and prescription of penicillin to patients presenting suspected *S. aureus* infections,⁴ over 50 % of *S. aureus* isolates were found to be resistant to penicillin by the late 1940s. Such undesired resistance was even documented during its clinical trials earlier that century.⁵ The resistance to penicillin in *S. aureus* was later determined to be caused by the acquisition of a plasmid.³ The plasmid enabled the phenotypic expression of a protein called penicillinase, capable of hydrolysing the β -lactam ring of the naturally occurring antimicrobial agent. Soon after such resistance hit its peak, a particularly virulent and infectious clone of *S. aureus* appeared in Australia and was named strain 80/81.⁶ It spread through the world population causing nearly one third of hospital acquired nasal carriers to develop septicaemia.⁷ Furthermore, control over such an aggressive strain of *S. aureus* was only gained following introduction of the first semi-synthetic penicillin, methicillin (Fig. 1.1).

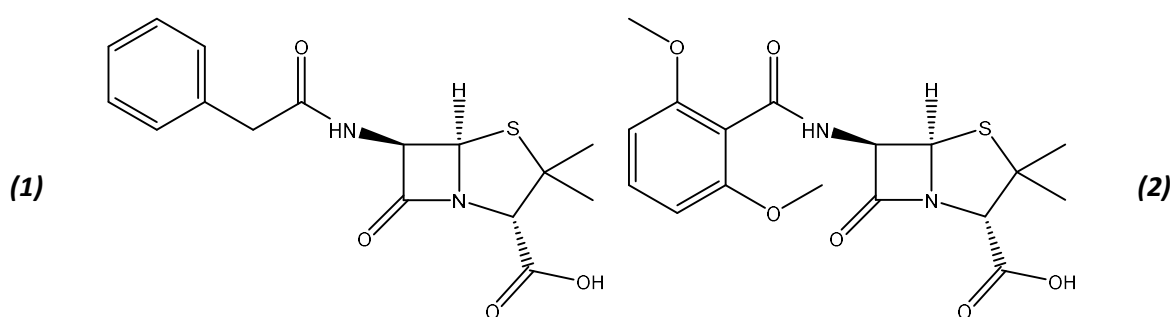


Figure 1.1. The molecular structure of penicillin (1). The molecular structure of methicillin (2). The induced steric hindrance afforded by the addition of two aryl methoxy groups prevented the hydrolysis of the adjacent β -lactam ring by penicillinase.

Methicillin was specifically introduced to resist the hydrolysis by penicillinase, and did so successfully.⁸ However only a few years after its introduction the first case of MRSA was reported.⁹ At the turn of the millennium MRSA was a pathogen at pandemic scale in hospital wards around the

world. *Figure 1.2* shows the worldwide prevalence of MRSA⁶ as of 2007 showing the severity of the global health issue MRSA was causing.

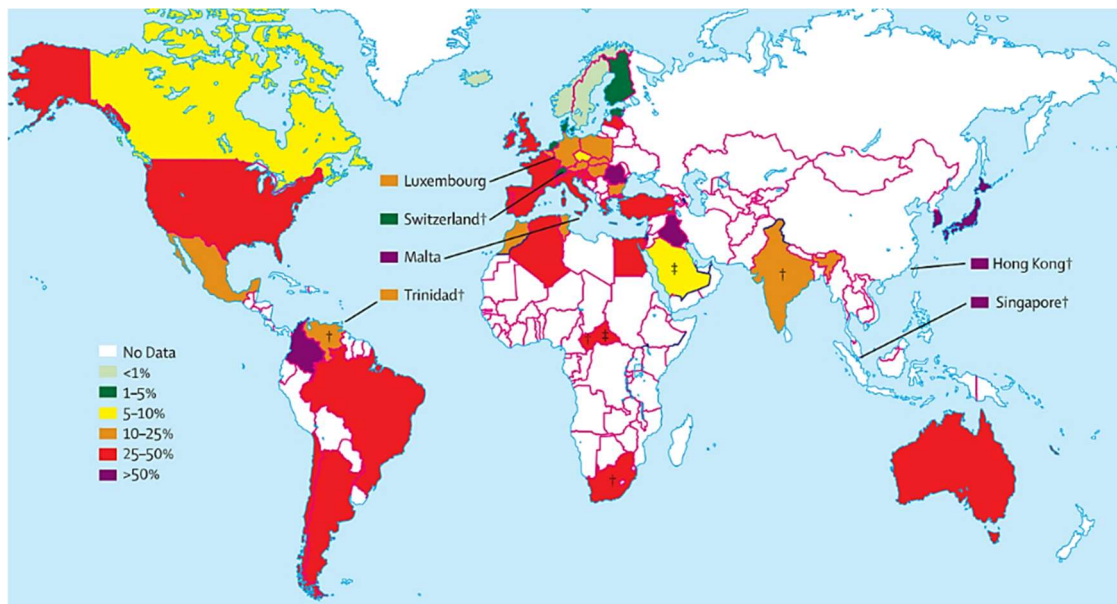


Figure 1.2 Worldwide prevalence of MRSA by country: All presented from studies taken from 1998-2007^{6,10-17}. † Data only available from one hospital ‡ studies between 1993-1997.

A report published by the European Commission for Disease Prevention in 2014 updated the previous 2007 prevalence report of MRSA isolates in exclusively European nations.¹⁸ (*Fig.1.3*).

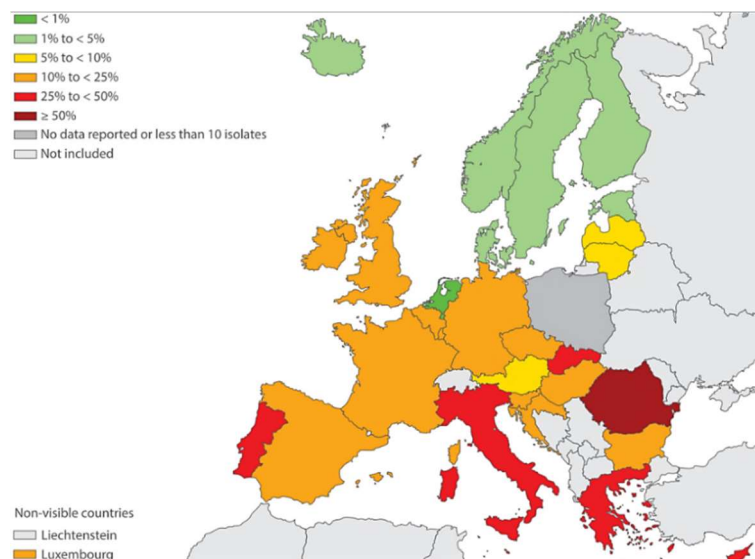


Figure 1.3 European prevalence of MRSA by country¹⁸

A reduction in the prevalence of MRSA isolates in comparison to 2007 report was observed. However, MRSA remains a serious health threat throughout Europe.

1.2 Mechanism of β -lactam antimicrobial resistance in methicillin resistant staphylococcus aureus isolates:

The resistance shown to penicillin in the 1940s by *S. aureus* strains was mechanistically simplistic.⁸ Therefore, overcoming such intrinsic resistance was relatively easy, following minor chemical modifications of penicillin. However, the resistance seen later in MRSA strains was not so simplistic. It was in fact the result of a more sophisticated and robust mechanism providing resistance to not only penicillin and methicillin but all β -lactam antibiotics'. This includes all penicillin's, cephalosporin's and carbapenems based antimicrobials.²

Antimicrobial action of penicillin's:

To appreciate the sophistication of such a resistance mechanism firstly the pharmacodynamic mode of action of penicillin based antimicrobial agent's must be discussed. All β -lactam antimicrobials inhibit a protein that is responsible for the construction and maintenance of bacterial cell walls.¹⁹ Firstly prokaryotic cell walls are composed mostly of peptidoglycans. Such consist of a chain of *N*-acetyl glucosamine and *N*-acetyl muramic acid disaccharides which are repeatedly linked via a β -1,4 glycosidic linkage.²⁰ Furthermore, present in the peptidoglycan are *N*-acetyl muramic acids crosslinked by short oligopeptides.²⁰ (Fig. 1.4) The formation of these 1,4 glycoside linkages (transglycosylation) and oligopeptide cross linkages (transpeptidation) are carried out by the penicillin binding proteins, PBP's; and are structurally what provide the rigidity in the bacterium cell wall.

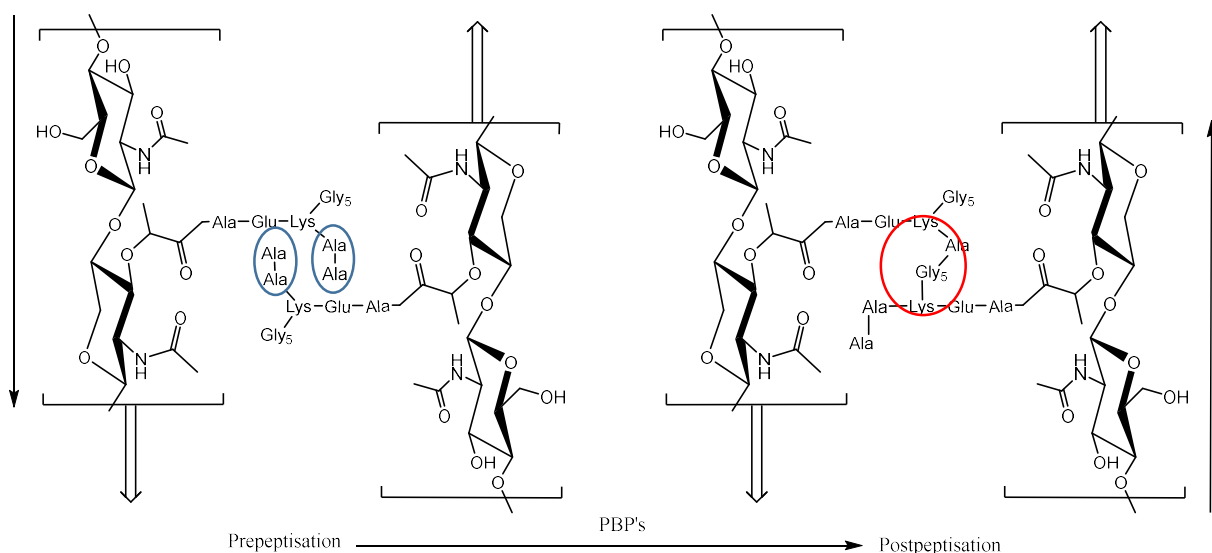


Figure 1.4 Molecular structure of the staphylococcus aureus peptidoglycan cell wall. Blue and red circles indicating the unlinked and linked oligopeptides.

β -lactams specifically inhibit the transpeptidation step of cell wall synthesis by efficiently mimicking the D-Ala-D-Ala side chain of the peptidoglycan (circled in blue Fig 1.4) substrate.²¹ Inhibition of the penicillin binding protein is achieved by the formation of acyl-enzyme complex's (k_2) between the β -lactam and the nucleophilic serine region of the penicillin binding proteins active site.²² (Fig. 1.5). However, de-acylation of this complex would occur with the original peptidoglycan substrate. As the region of the active site which houses the de-acylating acceptor domain and or a potential water molecule for hydrolysis of the acyl complex is occupied by the β -lactam ring it is impeded.¹⁹ Therefore, kinetic regeneration of the non acrylated penicillin binding protein is so slow in comparison to cell division that the enzyme appears to be irreversibly inactivated.^{19,23-25}

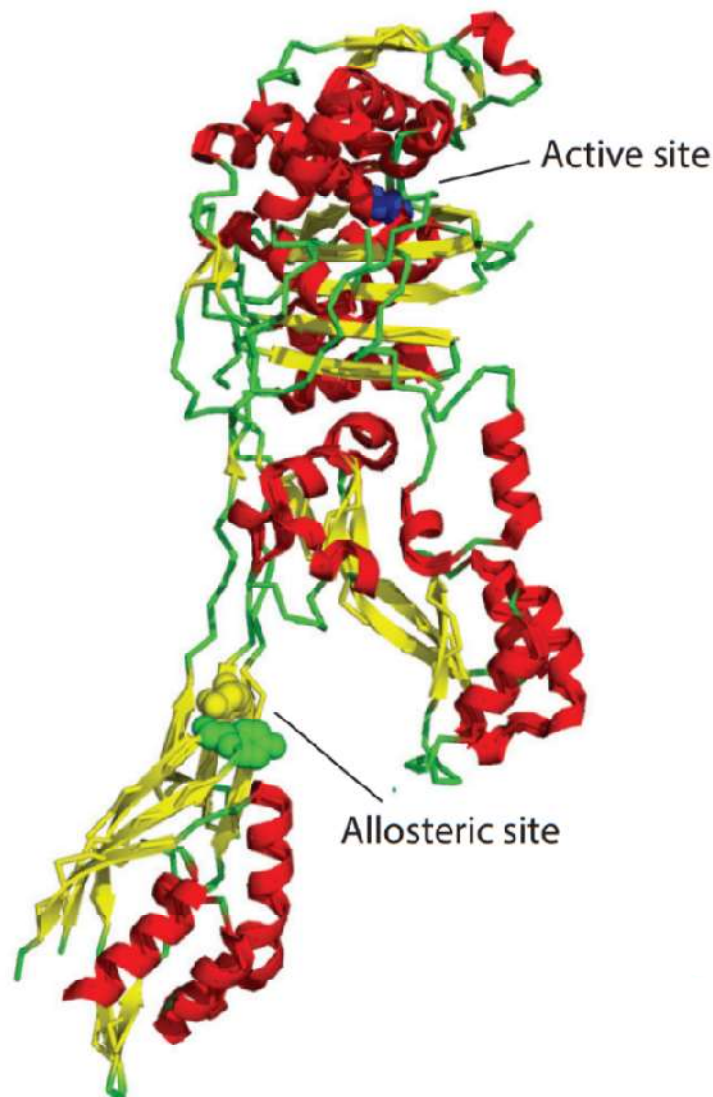
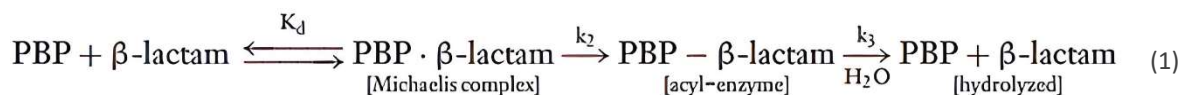


Figure 1.5. The structure of the penicillin binding protein PBP2a isolated from a methicillin resistant *Staphylococcus aureus* isolate. Monomeric unit shown, the active-site serine residue is shown as blue spheres. The allosteric site residues are shown as yellow and green spheres. Structure generated using PYMOL with the PDB code 1VQQ. Figure adapted from Peacock¹⁹

The PBP2a resistance factor:

To combat this inhibition of the native penicillin binding protein (PBP2) methicillin resistant *S. aureus* strains have acquired a gene which transcribes a secondary penicillin binding protein, PBP2a. Such has a reduced binding efficiency to β -lactams.¹⁹ The resistance of PBP2a to β -lactams can be explained by examining the kinetic parameters of the enzymatic reaction of the penicillin binding protein and a β -lactam (1). Primarily, the equilibrium position (K_d) for the formation of the Michaelis complex between PBP2a and the β -lactam is significantly skewed to the non-complexed form. Also, a reduced rate of acylation (k_2) is observed.¹⁹ Conversely once PBP2a is acylated it has a comparable rate of hydrolysis (k_3) to that observed in PBP2.²⁶ Thus meaning the β -lactam is unable to effectively access and bind to the new active site. However, when the site is accessed, it had similar inhibitory effects.



The actual cause for this reduction in the equilibrium constant K_d and rate constant k_2 can be seen in the morphology of the PBP2a (*Fig. 1.5*). Specifically, the region around the serine active site has an obvious narrow and extended cleft. This makes the active site far less accessible to all substrates, including β -lactams. In addition further research suggests that the acylation step of PBP2a requires a conformational change.²⁷ Given that the Michaelis complex for PBP2a does not form at antibiotic concentrations found *in vivo*,^{19,27} these conformational changes are by far the greatest factor defining the resistance.²⁷

When assigning the inhibitory ability of a β -lactam directed at a penicillin binding protein the second order rate constant k_2/K_d is used.^{19,25} This rate ranges depending on the antibiotic, however for PBP2a it is in the region of 1 - 19 M s⁻¹.²²⁻²⁴ Comparatively using the same range of antibiotics β -lactam susceptible PBP's such as the native PBP2 for *S. aureus* is in the range of 10²⁻³ larger.²⁵

The PBP2a resistance factor:

For PBP2a to function correctly it is vital that the uncross linked peptidoglycan substructure can form the Michaelis complex. Due to the cleft around the active site, this too is inhibited, however PBP2a is under allosteric control.²⁸ Located ~60 angstroms from the active site is a non-penicillin binding domain.²⁸ This is the allosteric site which specifically bonds to the D-Ala-D-Ala terminus of the unlinked peptidoglycan strands. (*Fig. 1.4*) This promotes a conformational change at the active site via several salt bridge interactions. Such a conformational change facilitates the efficient transpeptidation of the uncross linked peptidoglycan strands adjacent to the allosterically bound termini.²⁸

1.3 Molecular evolution of MRSA AMR factors & genetic functionality of SCCmec:

Following molecular genotyping of *S. Aureus* genomes the antibiotic resistance associated with MRSA has been attributed to a large mobile genetic element known as the staphylococcal cassette chromosome *mec* (SCC*mec*).^{2,3,5,6,29} Five main types of SCC*mec* have been identified with several subdivisions of I, II, III and IV being reported,^{3,6,11,19,30-32} as of 2012 six more SCC*mec* types had been identified and characterised.¹⁹ However, such are not discussed due to the minority of the genetic variations¹⁹ from the main five. A key point to note here is that Health care acquired MRSA usually carries type I, II or III,^{6,33,34} whereas community acquired MRSA typically carry type IV and sometimes type V.^{6,35,36} Figure 1.6 depicts the most important genetic features found on each of the main divisions of SCC*mec*'s.^{3,37-39}

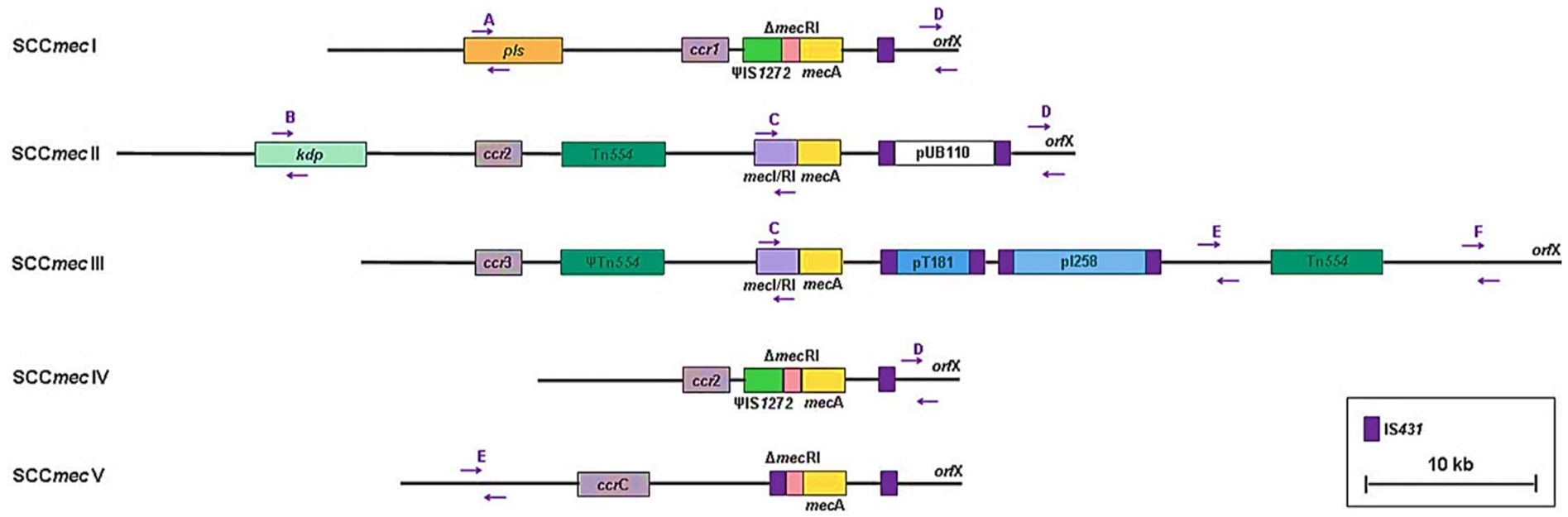


Figure. 1.6 A schematic arrangement of the SCC*mec* types I-V.^{3,37-39} The most significant genetic elements of the SCC*mec* are shown i.e. the *ccr* genes, IS sequences, *mec* complex's, *orfX*, integrated plasmids and transposon. The six loci proposed by Oliveria and de Lencastre⁴⁰ used for SCC*mec* typing are also shown.

1.3.1 Antibiotic resistance factors found on SCCmec:

On the SCCmec is a 2.1 kb gene designated as the *mecA* gene.^{3,6,33} Such a gene is responsible for the synthesis of the aforementioned 78 kDa PBP2a. (Fig 1.4).¹⁹ SCCmec I, SCCmec IV and SCCmec V encode specifically for the resistance to only β -lactam antibiotics via the *mecA* gene. Conversely SCCmec type II and SCCmec type III encode for multiple antimicrobial resistances.

SCCmec II additional resistance genes:

Firstly, SCCmec II carries an additional integrated plasmid sequence called *pUB110*. On the pUB110 plasmid is the gene *ant(4')* and *BleO*, which is responsible for the expression of resistance factors against the antimicrobials kanamycin, tobramycin and bleomycin (Fig. 1.7, Fig 1.8).^{3,33,41}

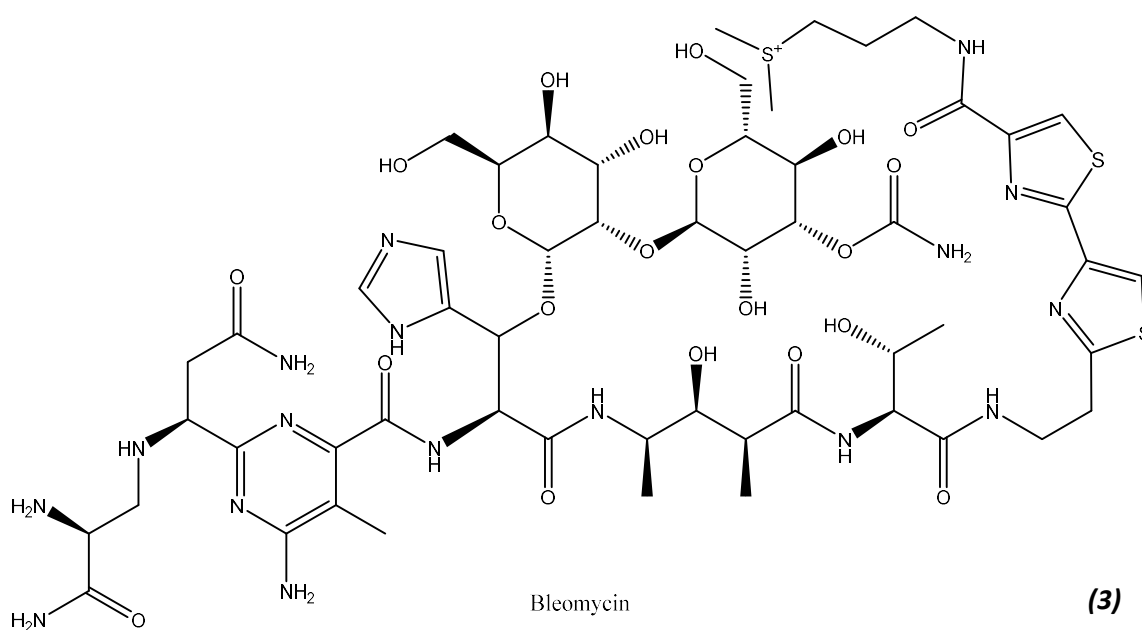


Figure 1.7 Molecular structures of the antibiotic bleomycin (3).

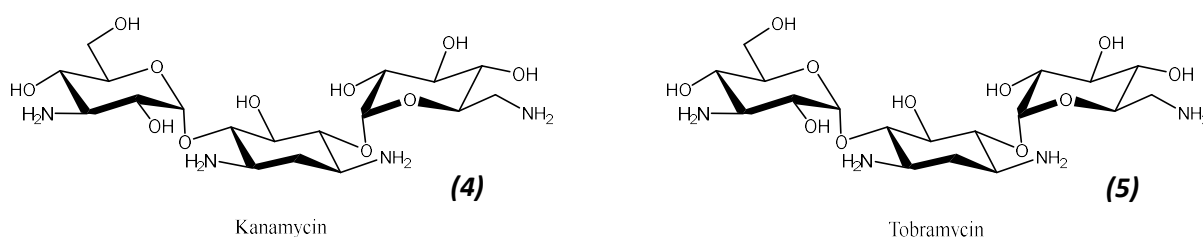


Figure 1.8 Molecular structures of antibiotics kanamycin (4) and tobramycin (5).

Likewise, located on *SCCmec* type II is a transposon called Tn554. Such a region of genetic information possesses the *ermA* gene which is responsible for the inducible production of macrolides, lincosamides and streptogramin (*Fig. 1.9*) resistance factors.^{3,33,41}

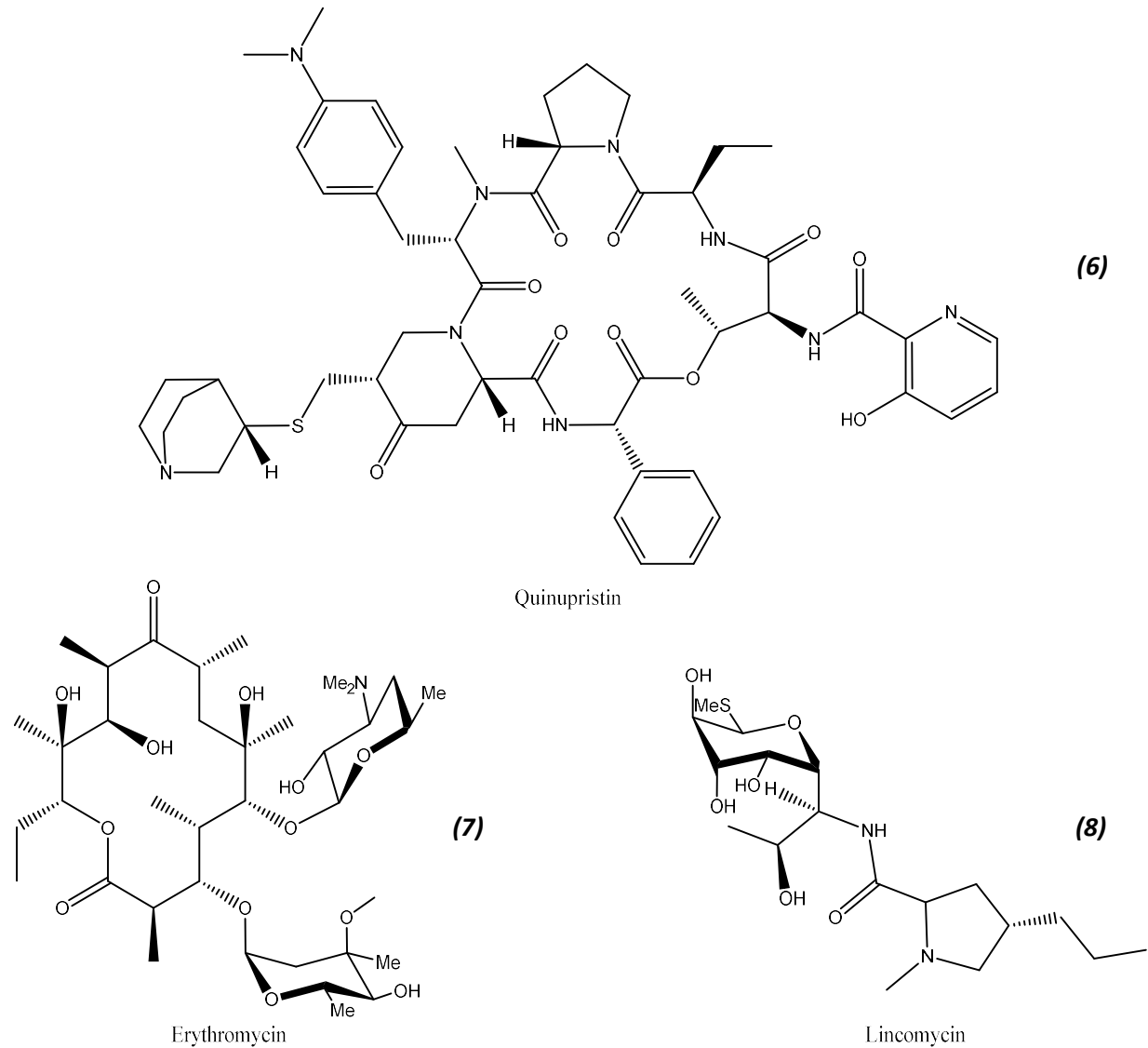


Figure 1.9 Molecular structure of antibiotics ermA transcribes resistance factors against. (streptogramin based antibiotic, Quinupristin).

SCCmec III resistance genes:

SCCmec type III also harbours the previously mentioned *Tn554* transposon responsible for the resistance to macrolides, lincosamides and streptogramin via the *ermA* gene. Additionally, two other plasmidial areas of genetic information are present which transcribe additional resistance factors. Firstly, another integrated plasmid named *pI258* transcribes a P-type ATPase named *CadA*.⁴² This protein is responsible for the resistance to Cd(II), Pb(II) and Zn(II) metal ions.⁴² The second region is

again an integrated plasmid, named *pT181*. It specifically codes for the resistance to tetracycline-based antimicrobials.^{33,41,43} (Fig. 1.10).

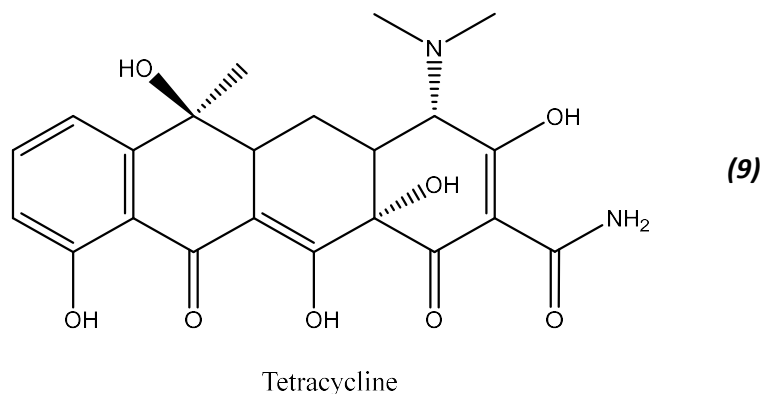


Figure 1.10 Molecular structure of tetracycline-based antimicrobials.

1.3.2 Further antimicrobial resistance not encoded by the SCCmec:

Furthermore, *S. aureus* can also carry further genes relating to antibiotic resistance inserted at other sites of the chromosome and or on plasmids. Such include fluoroquinolone's, aminoglycosides and vancomycin.⁴⁴ (Fig. 1.11)

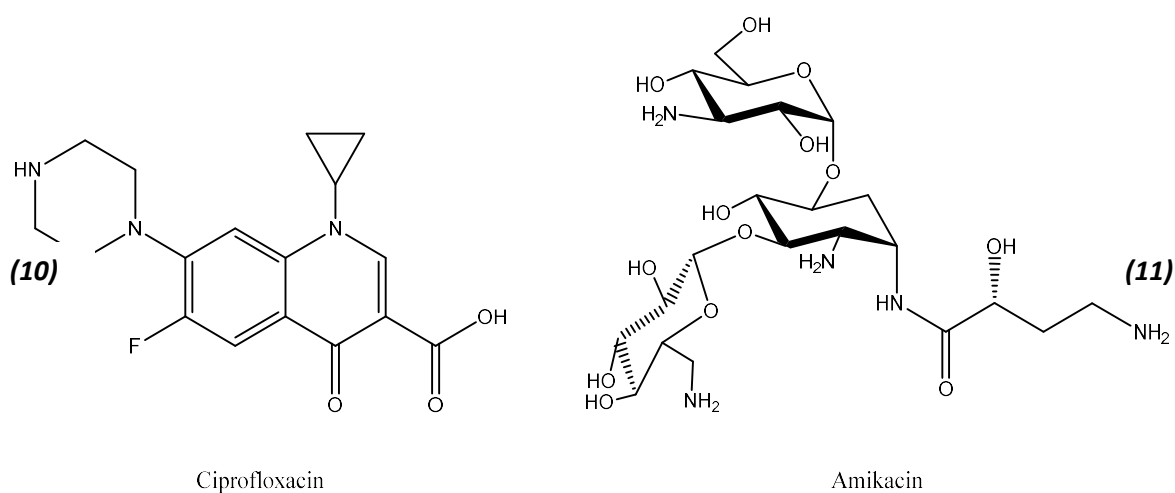


Figure 1.11 Examples of antibiotics methicillin-resistance staphylococcus aureus can express resistance to. Ciprofloxacin (Fluoroquinolone) and Amikacin (Aminoglycoside)

Resistance associated with fluoroquinolones was described to result from environmentally induced point mutations leading to activation of a NorA regulated Influx resistance pump.⁴⁵ A locus identified from whole the genome of *S. aureus* and called *flqB* was shown to regulate the NorA influx response.⁴⁶ Resistance to aminoglycoside-based antimicrobials can result from several loci, usually

differing across *S. aureus* strains. Readers are therefore directed to an excellent paper detailing the mechanisms of resistance to aminoglycosides.⁴⁷

Clinical isolates from Japan were shown to have either intermediate or complete resistance to glycopeptide antimicrobial vancomycin.^{2,48} (Fig. 1.12). The reduced susceptibility to vancomycin was unambiguously linked with the thickening of the cell wall.⁴⁹ Between 2002 and 2004 more isolations of this strain of 3rd line resistant MRSA were recorded,⁶ the patient from which they were isolated were independent. However, a common link was co-infection with vancomycin-resistant enterococci which was key in identifying the origin of vancomycin resistance in *S. aureus*.⁴⁹ The gene found to be responsible was that found on an enterococci plasmid and named *vanA*, readers are again directed to a recent review of such resistance and its mechanisms.⁴⁵

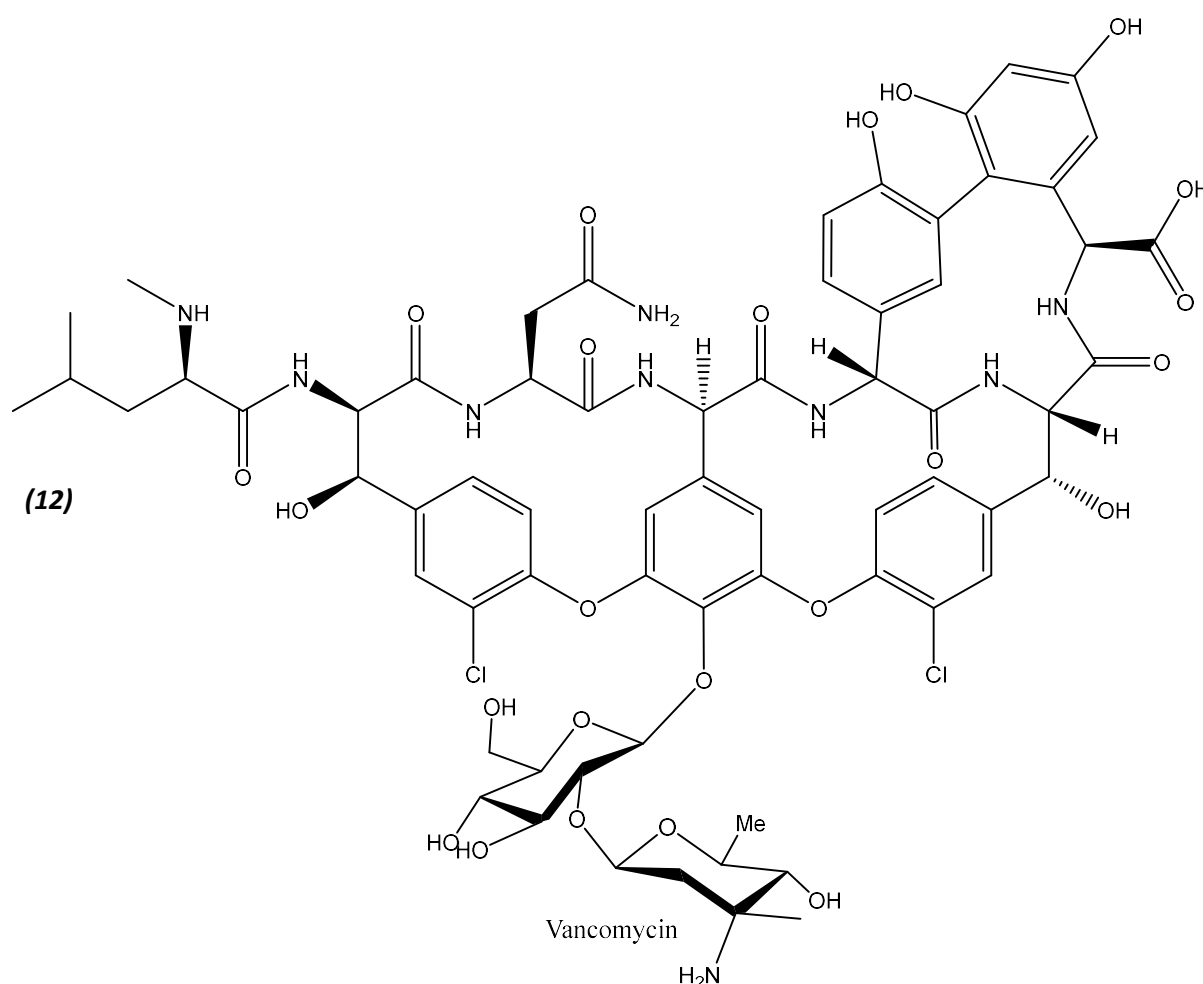


Figure 1.12. Molecular structure of Vancomycin, the third line treatment of methicillin-resistant staphylococcus aureus infections

1.3.3 Functional elements of the SCCmec:

In total, there have been 17 well characterised and distinct SCCmec cassettes.^{33,40,50-55} Shown in figure 1.13 is the structural deviations of each showing all the features of the *ccr* and *mec* gene complexes.

The mec complex:

The *mec* complex found in the SCCmec is the structural element responsible for the transcription regulation of *mecA*. The process of transcription regulation of the *mecA* gene and subsequently the phenotypic expression of PBP2a is detailed later in this chapter. In total main 5 types of *mec* gene complexes have been described A-E (Table. 1.1), however of the 17 characterised cassettes only three are prevalent; A, B and C (Fig. 1.13).^{33,39,56}

Table 1.1. The major classes of *mec* gene complexes with their structural variation.

Class	Mec complex
A	<i>mecI-mec-RI-mecA-IS431</i>
B	<i>IS1272-ΔmecRI-mecA-IS431</i>
C	<i>IS431-ΔmecRI-mecA-IS431</i>
D	<i>ΔmecRI-mecA-IS431</i>
E	<i>ΔmecRI-mecA-IS431'</i>

Crr gene complex and junk regions:

The *ccr* gene complexes (green regions, Fig. 1.13) are the genes responsible for the expression of cassette chromosome recombinase. The function of which is the integration of the SCCmec element into the main chromosome of *S. aureus*, as well as its excision. SCCmec types I and II's *ccr* complexes are designated *ccrA1* and *ccrB1* (shorted to *ccrAB1*). *ccrAB2* is designated to SCCmec types II and IV, *ccrAB3* for type III and *ccrC* for type V.^{37,55-58} The integration and excision of the cassette is site specific to the 3'-end of an open reading frame called *orfX* (Fig. 1.13).^{37,55-58} The function of *orfX* remained a mystery until 2013, when it was subsequently reported to encode for a RlmH type ribosomal methyltransferase.¹⁹ The regions bordering the *mec* and *ccr* regions are designated as the J regions, indicating non-coding DNA. For the main variants of the SCCmec, i.e. type I-V; J_1 is located between the chromosomal junction *attL* and the associated *ccr* genes. J_2 is located between the *ccr* genes and the *mec* complex, J_3 is located after the *mec* complex prior to the *orfX* region.^{37,55-58}

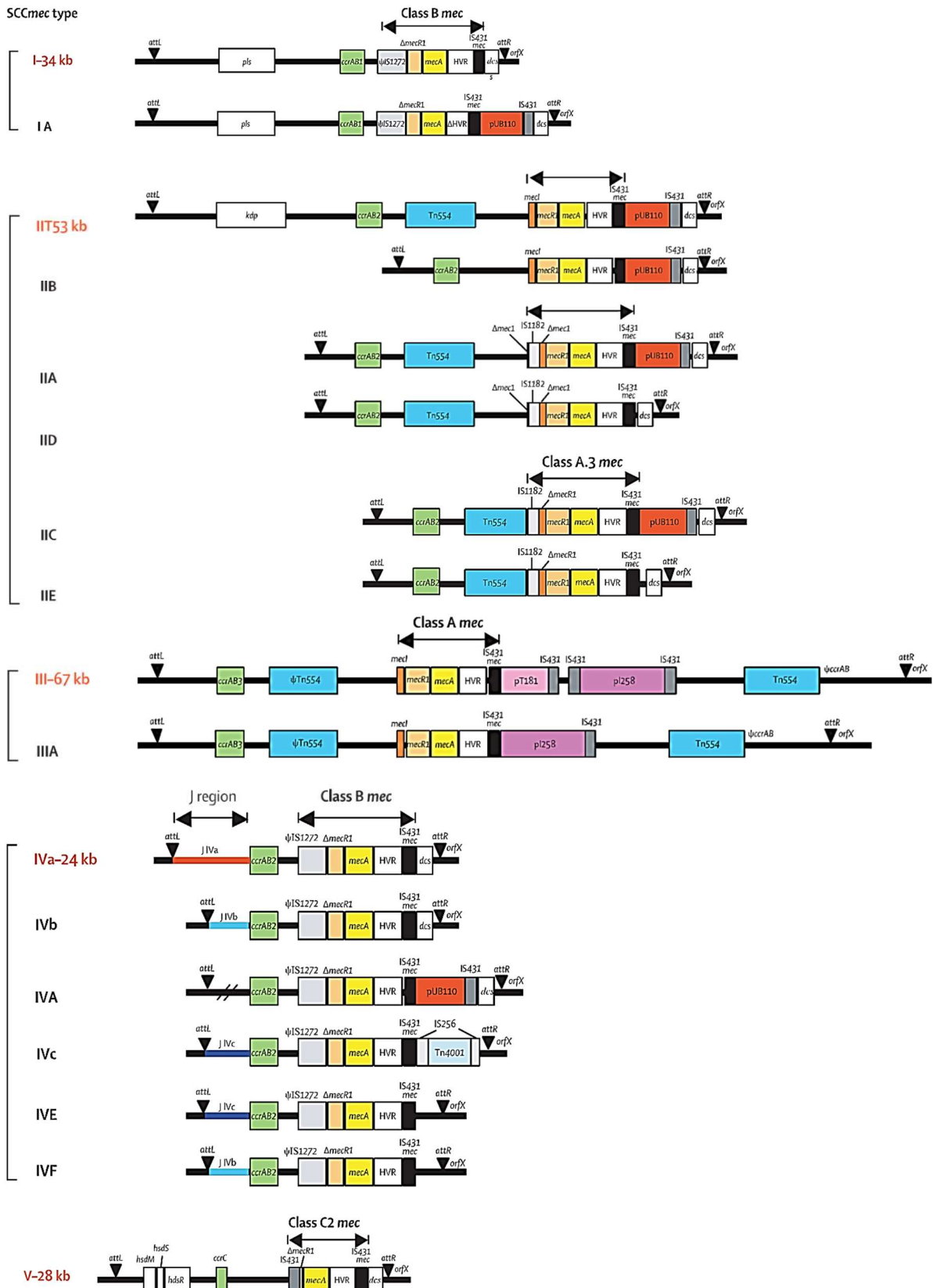


Figure 1.13. The 17 main variants of the SCCmec based upon the work of Oliveria, Okuma, Shore and colleagues.^{33,40,50-55} *Ccr* complexes shown in green, *MecA* shown in yellow. Figure adapted from Grundmann⁶

1.3.4 The expression and regulation of *mecA*:

The mechanisms employed by microorganisms to express for; and regulate their acquired resistances to antimicrobial agents is in general a reactive process.^{19,41,44,47,49} As such this presents key challenges in detecting specific antimicrobial resistance factors clinically without extensive culture. Thus, standard antigen-based protein detections are rendered unreliable without the initial culturing of a suspected pathogen in the clinical setting.⁵⁹ Such detection methods are discussed in *later in this chapter*. The regulation and expression of the *MecA* gene clearly highlights this reactive process. The regulation of *MecA* expression to PBP2a is achieved by the *MecI* repression protein and *MecR1* receptor proteins.³ ⁶⁰In the absence of a β -lactam antimicrobial the *MecI* repressor protein (*Fig. 1.14*) represses the transcription of *mecA* and *MecR1-MecI* gene (*Fig.1.13, Fig 1.15a*)

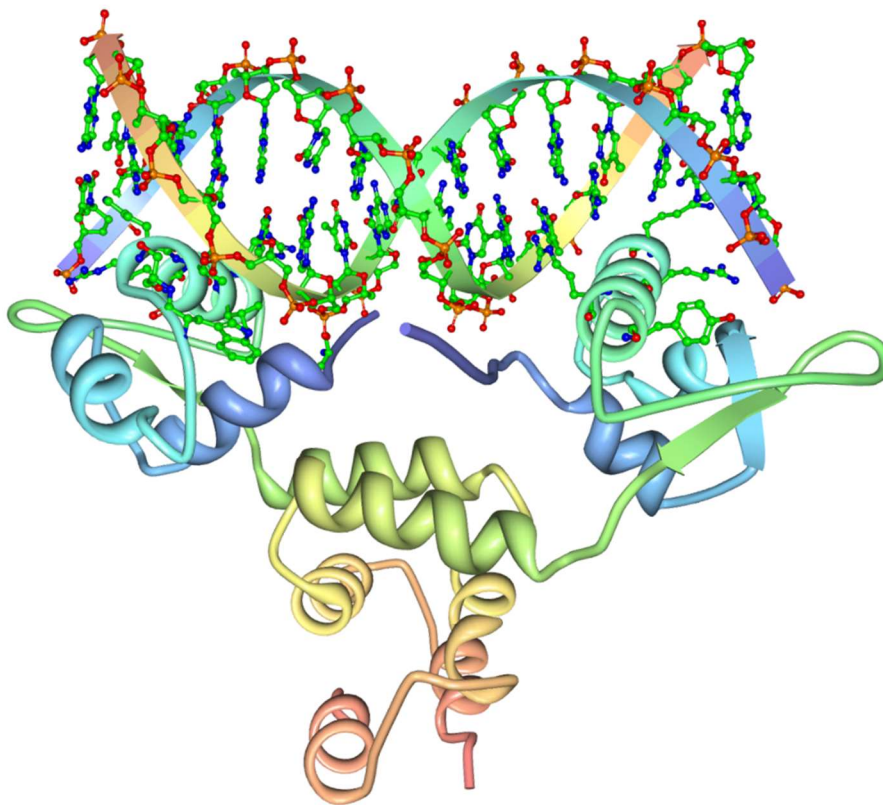
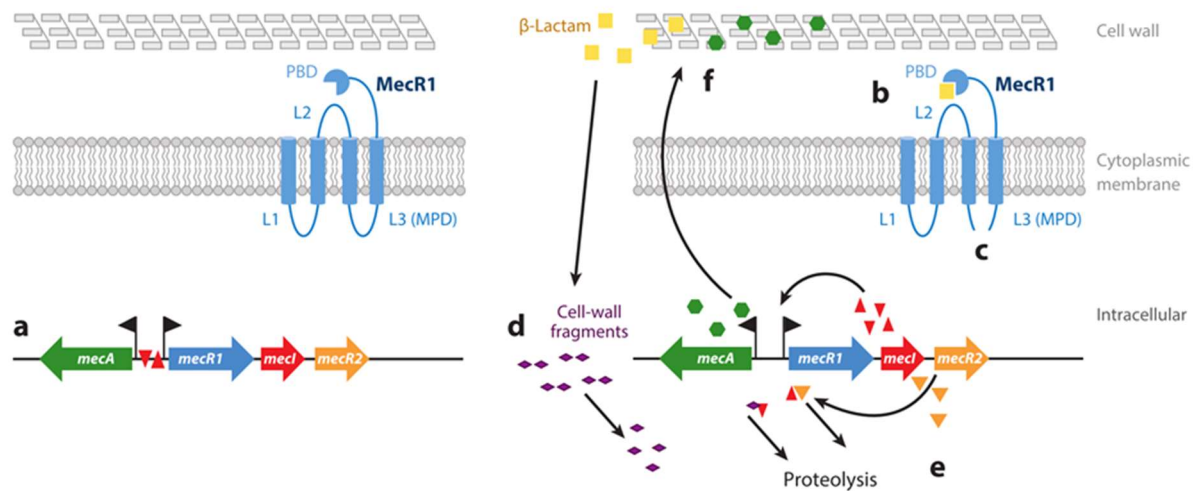


Figure 1.14. The monomeric crystal structure of the Mecl repressor protein complexed with the Mecl DNA binding domain. The side chain structure is shown for the recognition domain of the protein. Produced using data collected and deposited on to Protein Database by Safo and colleagues.⁶¹ PDP code: 2D45

MecI binds to a 30bp palindrome region adjacent to the sequence, it therefore cannot be read and transcribed by an RNA polymerase. *MecR1* is a transmembrane metalloendopeptidase zymogen. Its function is to detect β -lactams in the extracellular penicillin binding domain.¹⁹ (*Fig. 1.15b*) In the

presence of a β -lactam the MecRI protein in the cytoplasmic region of the cell becomes activated by an autocatalytic cleavage of the intracellular sensor domain, induced by a β -lactam itself. Thus, producing an intracellular metalloprotease domain on MecRI. (Fig. 1.15c) The exact role of the now active intracellular metalloprotease domain is not completely clear.¹⁹ However, it is unambiguously linked with the production of dipeptide peptidoglycan cell wall fragments in the cytoplasmic region which directly proteolysis MecI.¹⁹ (Fig. 1.15d) It is also reported that direct proteolysis of MecI by the MecR1 is a possible mechanism. For further discussions of this stage in the mechanism readers are directed to an excellent review by Peacock. A further gene *mecR2* encodes for a protein which transcribes in the presence of β -lactams. (Fig. 1.15e) This protein directly binds to the MecI inhibitor further causing proteolysis allowing *mecA* transcription. (Fig. 1.15f)



*Figure 1.15. Pictorial model of the feature of mecA gene regulation. (a) In the absence of β -lactams, transcription from the mec operator is prevented by the binding of the repressor MecI. (b) β -Lactams are detected by their binding to the penicillin-binding domain of MecR1. (c) Autolytic activation of the intracellular metalloproteinase domain. (d) Cytoplasmic cell-wall fragments act as a coactivator that binds MecI, disrupts its association with the mec operator (e) Anti-repressor, encoded by *mecR2* is transcribed in the presence of β -lactams. (f) The degradation of MecI causes *mecA* transcription.*

It is clearly a complex and ingenious solution that allows the cell to produce only PBP2a when required to maintain the prokaryotic cell wall maintenance in the presence of β -lactams. Conversely both the *mecI* and *mecR1* sequences can be truncated by an insertion sequence, *IS431* or *IS1272* (fig.1.6 and fig. 1.13). The insertion sequence present depends on the type of SCCmec and can depress *mecA* expression, thus reducing its ability to survive in the presence of high antibiotic concentrations.

1.3.5 The origin of the SCCmec:

The origin and mode of gene transfer of the *SCCmec* to *S. aureus* remains in dispute, as no other bacterial isolates of different genera have been found to carry the *SCCmec* element.^{3,6,58} However, an analogue of the *mecA* region of the *SCCmec* can be found in strains of *S. Sciuri* with an 88% sequence similarity.^{6,62-64} A significant amount of evidence suggests that the *ccr* and *mec* gene complexes were brought together in coagulase-negative staphylococci like *S. sciuri*. Following deletion of the regulatory *mec* gene sequences regions were transferred horizontally to *S. aureus* yielding MRSA isolates. The first piece of evidence suggesting such a mechanism is found in the presence of the *IS1272* insertion sequence (*fig 1.6*). Intact and found in mutable locations of *S. haemolyticus* genome, unlike *S. epidermidis* and *S. aureus* which contain usual deletions in the *IS1272* sequence. Thus, suggesting that *S. haemolyticus* was the original host of *IS1272* genetic element found in the *SCCmec* of *S. aureus*. A further study reported the formation of MRSA *in vivo* by horizontal *mecA* transfer from *S. epidermidis* to MSSA during antibiotic treatment.^{6,65,66}

The next element of evidence indicated that recombination between *SCCmec* type I and additional gene sequences from again non-coagulase staphylococci yielded the *SCCmec* type IV *SCCmec* which was subsequently transferred to *S. aureus*.⁶⁷ Additionally, *SCCmec* type IV was only found in *S. epidermidis* isolates prior to 1981 when the first instance of the *SCCmec* IV was detected in *S. aureus*.^{68,69} However more recent data is pointing to *S. fleuretti* the original vesicle for the promotion of the *SCCmec*.⁶⁹

1.4 Conventional Culture Based Detection Methods:

The standard method and most routinely used in microbiology labs for the screening of MRSA is agar culture to identify *S. aureus* colonies.⁷⁰ Swabs of a patient mucous membranes, such as anterior nostrils and throat are taken; perineum swabs are also routinely used in combination for agar based culture.⁷¹ Additional samples may also be taken from the rectum, sputum (ventilated patents), groin and axilla.⁷⁰ The swabs are usually Dacron or cotton and are placed in a buffered medium for storage and transportation for microbiological evaluation.⁷²

The conventional MRSA agar culture relies upon the use of selective culture media to specifically culture suspected MRSA. There are several agars available each with specific properties making them selective for MRSA culture. The most common of culture mediums is the mannitol salt agar. The composition of such agars includes D-mannitol, high NaCl concentration, phenol red, digests

of casein and animal tissue, beef extracts mixed with standard agar.^{70,72} Such a media will specifically grow *staphylococci* due to the presence of high NaCl concentrations.⁷³ Furthermore, the addition of phenol red causes the colour of the medium to change from red to yellow around pathogenic staphylococci that produce acidic metabolites, e.g. colonies such as *S. aureus*.⁷³ (Fig 1.16). Further selectivity for MRSA can be introduced by adding a β -lactam such as oxacillin to the culture media, thus screening out methicillin susceptible *S. aureus* (MSSA) and another β -lactam susceptible bacterium. Alternatively, any colonies grown on the standard mannitol salt agar can be investigated by disk diffusion to ascertain the antimicrobial resistance.^{29,70,72} Plating on to such plates without antibiotics present can be very useful to screen initial swaps taken from clinical settings.

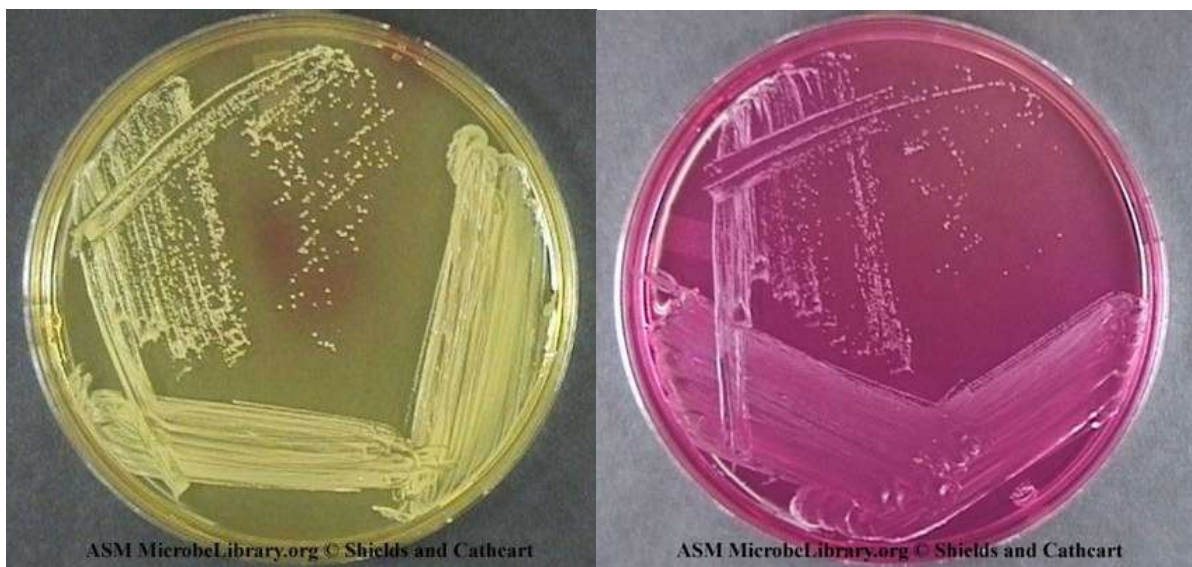


Figure 1.16. MRSA selective mannitol salt phenol red agar plates streaked with an MRSA isolate (Left) and an MSSA isolate (Right). Acidic metabolites produced by MRSA isolates discolour the phenol red allowing for rapid identification of possible pathogenic colonies. Image reproduced from ASM image repository, © Shields and Cathcart.

Another alternative method to disk diffusion or the use of β -lactam inhibiting agar culture is the latex agglutination test.^{59,70} Using anti-PBP2a monoclonal latex sensitised antibodies the presence of PBP2a protein produced by suspected MRSA isolates can be visualised by the coagulation of the blue latex particles.^{59,70} (Fig.1.17) Such tests are in routine use and proved a fast and inexpensive method to quickly identify resistance in suspected isolates. However as discussed in *section 1.3.4* such sensitised latex agglutination tests still require pre-culture in an antibiotic containing mediums. Readers are directed to in-depth performance review of the latex angulation test.⁵⁹

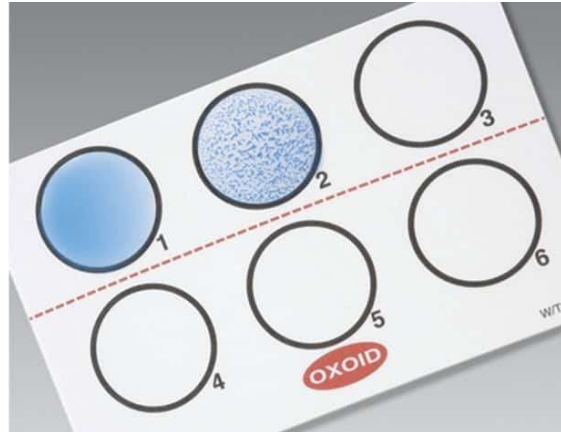


Figure 1.17. Latex agglutination test card. Circle 1 shows a negative result as the latex particles remain colloidal in solution. Circle 2 indicating a positive result as the latex particles have agglomerated out of solution due to the presence of PBP2a protein. Image reproduced from Oxoid Ltd © Fisher Scientific.

Newer methods of MRSA culture-based detection have been developed. New selective media which can identify a target inoculum via a colour change have been readily available from several suppliers. The media used is like that described previously. However chromogenic substances present within the agar matrix specifically mark target enzymes, such as PBP2a.⁷⁴ Consequently, colouring MRSA isolates brightly against the agar medium using primary culture. Therefore, removing the need for subculture. Currently chromogenic media for MRSA detection incorporate chromogens to differentiate *S. aureus* from other pathogens and antibiotics for selective growth of MRSA.⁷⁴ Several are available and differ in chromogenic substrates and antibiotic formulations/concentrations. Readers are directed to a relatively recent review assigning the sensitivity and specificity of such mediums.⁷⁵



Figure 1.18. MRSA isolates streaked are selectively stained on a MRSASelect II agar plate commercially available from Bio-Rad. Image © Bio Rad Laboratories.

1.5 State of the art detection methods - Molecular assays:

In recent times a shift from the traditional culture-based methods to more specific and selective molecular methods have been observed. However, such methods are significantly more expensive and usually require a series of skilled operators. Furthermore, although results are seen as rapid, the dependency on skilled operators induces a reduced throughput of samples.⁷² Such drawbacks have limited the applications of molecular assays to epidemiological studies of MRSA rather than direct screening of patients. Nevertheless, such methods are used routinely in countries that operate under a stringent search and destroy MRSA policy. The benefit of which can be clearly seen from the prevalence rates of MRSA in the Netherlands in the 2014 prevalence study (*Fig. 1.2-1.3*).^{6,10-18}

Pulse field gel electrophoresis:

Gel electrophoresis has been used to distinguish and type biological molecules for many years⁷⁶, however the uses of standard of electrophoresis has its limitations. In the realm of attempting to classify and type bacteriological genomes the limitation is the inability effectively separate large oligonucleotides.⁷⁷ Pulse field gel electrophoresis overcomes this issue by manipulating the direction and timing of the applied electric field across the test gel. The method was originally developed for genome size DNA's isolated from yeasts in 1984.⁷⁷ Today it is still considered the gold standard methodology for typing of MRSA isolates due to its high discriminative power.³ The pulse field gel electrophoresis of MRSA isolates is performed on purified chromosomal DNA digested with the restriction enzyme *Sma*I, followed by the pulse field electrophoresis on agarose gel.⁷⁸

The obtained diagonal patterns are analysed via a Dice co-efficient and unweighted pair-group matching analysis according to the Tenover scheme.⁷⁹ The patterns can then be used to distinguish colonial related MRSA isolates and generate a database based on the unweighted pair-group matching analysis parameters. *Figure 1.19* shows the chromosomal fragments of four MRSA isolates run using pulse filed gel electrophoresis. Issues however arise with this methodology in its repeatability, great efforts have standardised the testing protocols at national levels, however internationally this remains elusive. Thus, meaning the pulse field electrophoretic analysis of two identical isolates carried out in different regions give non-comparable results.⁸⁰⁻⁸²

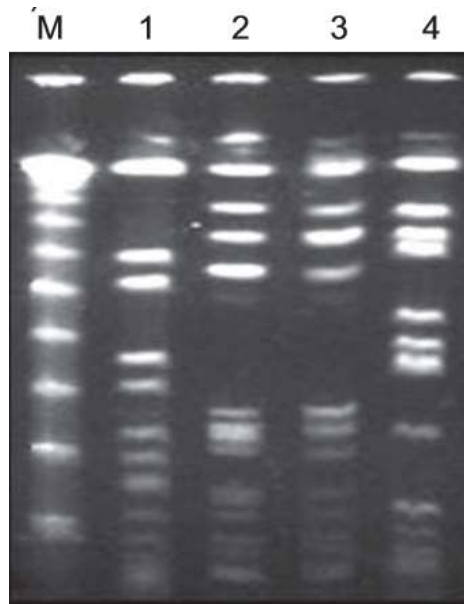


Figure 1.19. Pulse field gel electrophoresis of four methicillin resistant staphylococcus aureus isolates.² For the patterns obtained it is possible even by eye to identify isolates 2 and 3 are from the same clonal complex.

Multi-locus sequence typing (MLST):

Multi-locus sequence typing is a truly molecular based technique, whereby the sequencing of seven essential housekeeping genes of *S. aureus* is performed.⁸³ Automated genetic sequencing is used to build an integer base allelic profile of a particular MRSA strain as well as the *mecA* gene to confirm resistance. Using polymerase chain reaction (PCR), the seven genes are targeted with the primers shown in table 1.2.

Table 1.2. The seven target housekeeping genes used for multi loci sequencing typing of suspected MRSA isolates. Included is the label and sequence of the PCR primers used to amplify the target genes from a chromogenic DNA sample. Table adapted from Enmright⁸³

Gene	Primer	Sequence 5'-3'
Carbamate kinase (<i>arcC</i>)	arcC-Up	TTGATTCACCAGCGCGTATTGTC
	arcC-Dn	AGGTATCTGCTTCAATCAGCG
Shikimate dehydrogenase (<i>aroE</i>)	aroE-Up	ATCGGAAATCCTATTTACATTC
	aroE-Dn	GGTGTGTGATTAATAACGATATC
Glycerol kinase (<i>glpF</i>)	glpF-Up	CTAGGAACTGCAATCTTAATCC
	glpF-Dn	TGGTAAAATCGCATGTCCAATTC
Guanylate kinase (<i>gmk</i>)	gmk-Up	ATCGTTTTATCGGGACCATC
	gmk-Dn	TCATTA ACTACAACGTAATCGTA
Phosphate acetyltransferase (<i>pta</i>)	pta-Up	GTTAAAATCGTATTACCTGAAGG
	pta-Dn	GACCCTTTTGTGAAAAGCTTAA
Triosephosphate isomerase (<i>tpi</i>)	tpi-Up	TCGTTCAATTCTGAACGTCGTGAA
	tpi-Dn	TTTGACCTTCTAACAATTGTAC
Acetyl coenzyme A acetyltransferase (<i>yqiL</i>)	yqiL-Up	CAGCATA CAGGACACCTATTGGC
	yqiL-Dn	CGTTGAGGAATCGATACTGGAAC

Each of these genes have specific known alleles with specifically known polymorphic sites. The PCR products of a suspected MRSA isolate are genetically sequenced to identify the specific alleles based on the sequence and polymorphic sites present (*Table 1.3*).

Table 1.2. Sequence variation of the seven target loci.

Gene	Sequence length	No. of alleles	No. of polymorphic sites
<i>arcC</i>	456	17	19
<i>aroE</i>	456	17	23
<i>glpF</i>	465	11	14
<i>gmk</i>	429	11	13
<i>pta</i>	474	15	18
<i>tpi</i>	402	14	18
<i>ygil</i>	516	16	19

Should five of these MLST genes have identical sequences between two isolates they can be considered clonal complexes. An example of an allelic profile, or sequence type, described by MLST is ST247-MRSA-I; it has a MLST of 3-3-1-12-4-4-16. In total 53 different sequence types were defined by Enright and co-workers, readers are directed to the original paper published for the full allelic profile of each of the 53 sequence types.⁸³ The method was validated by comparison using pulse field gel electrophoresis.³⁰ (*Fig. 1.20*)

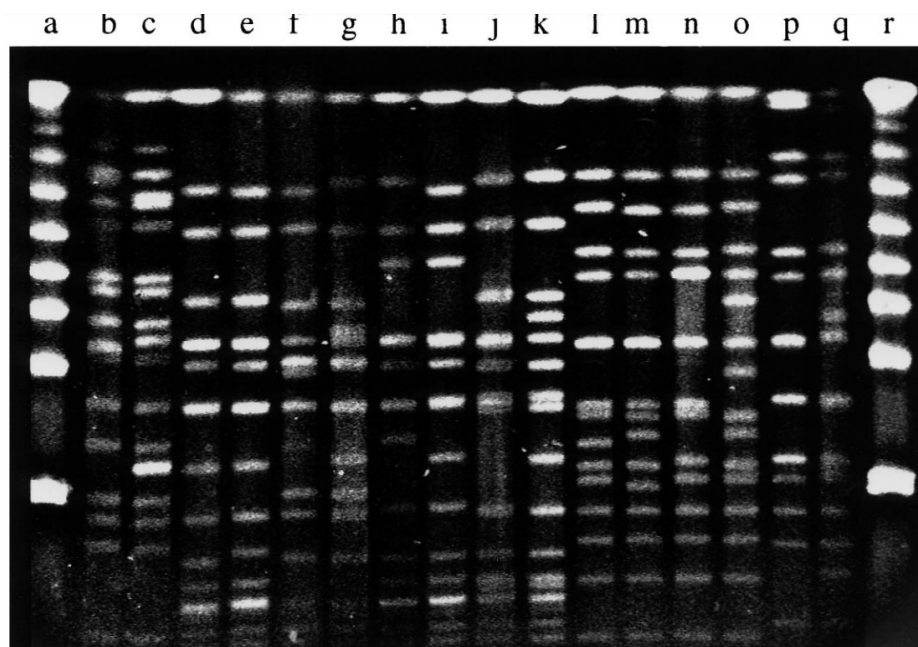


*Figure 1.20 PFGE of pairs of isolates with identical allelic profiles. Chromosomal DNA from pairs of isolates of STs 25 (lanes b and c), 30 (lanes d and e), 34 (lanes f and g), 36 (lanes h and i), 39 (lanes j and k), 45 (lanes l and m), 47 (lanes n and o), and 49 (lanes p and q) were digested with *Sma*I and were separated by PFGE. Concatenated bacteriophage lambda molecular size markers were run in lanes a and r.⁸³*

Isolates which had identical MLST profiles usually had identical SmaI fragmentation patterns or only differed by less than 4 fragment bands. Such where isolates considered the same strain. Those whom differed by only 4-6 are considered to be of the same genetic lineage. The reason for this deviation from pulse field gel electrophoresis was that the rate of gene variation in the house keeping genes was significantly slower than that of the SmaI fragmentation loci. A clear disadvantage of MLST is the requirement to sequence the PCR products. Such a process is not only time consuming but exceptionally expensive when compared to that of conventional culture methods and PFGE. However, clear advantages of such an absolute nomenclature and certainty over the loci genetic sequences makes it highly discriminatory and removes any variation across laboratories. Such that all results gathered using this technique are comparable and repeatable.

1.6 An introduction to Immunoassay and Nucleic Acid Hybridisation Based Lateral Flow Assays

1.6.1 Introduction:

Lateral flow devices are among a small selection of diagnostic and analytical tests to warrant the convergence of the WHO criteria for ASSURED.⁸⁴ Namely: affordable, sensitive, specific, user-friendly, robust, equipment-free and delivered point of care diagnostic devices. The first point of contact diagnostic device becoming commercially available to end users with the advent of the home pregnancy test in the late 1980s.^{85,86} However, the human fascination with point of contact diagnostics spans our history further than one would think. The ancient Egyptians were found to be one of the earliest at attempting such diagnostic tests. The test comprised of a lady in question of being pregnant urinating on to a mixture of barley and wheat seeds over numerous days. The results of the test being determined by if barley grows, it means a male child. If wheat grows, it means a female child. If both do not grow, she will not bear at all.⁸⁷

With the advent of the first pregnancy test showing that the selective and specific detection of the human hCG protein was achievable at an affordable cost. Thanks to the initial work of Judith L. Vaitukaitis and co-workers,⁸⁸ developing the required platforms for such devices.⁸⁹⁻⁹¹ Industry therefore boomed with numerous new point of contact diagnostic devices marketed and sold worldwide by over 200 companies.⁹¹ Such testing formats lead to a global annual market value of \$2.1 billion USD in 2007⁹¹ with a marked increase to \$15.4 billion USD in 2015.⁹² However, such traditional lateral flow devices have distinct disadvantages along with their merits.⁹³ Furthermore, they have

remained relatively conceptually undeveloped preceding their inception; those described by Vaitukaitis are conceptually identical to today's commercially available lateral flow devices⁸⁸ The following sections will dissect the working principles of lateral flow devices in detail. Discussed is their construction, composition, detection mechanisms and probes preceding a discussion on detection limits.

1.6.2 Construction, composition, and working principle of lateral flow devices (LFD's).

1.6.2a. A schematic overview of construction:

Traditional lateral flow devices consist of four main sections comprised of a variety of materials housed within a ridged and robust plastic casing.⁹¹ The four sections overlap to allow the flow of a liquid sample *via* capillary action. From the proximal end to the distal end across the four materials. (Fig. 1.21)

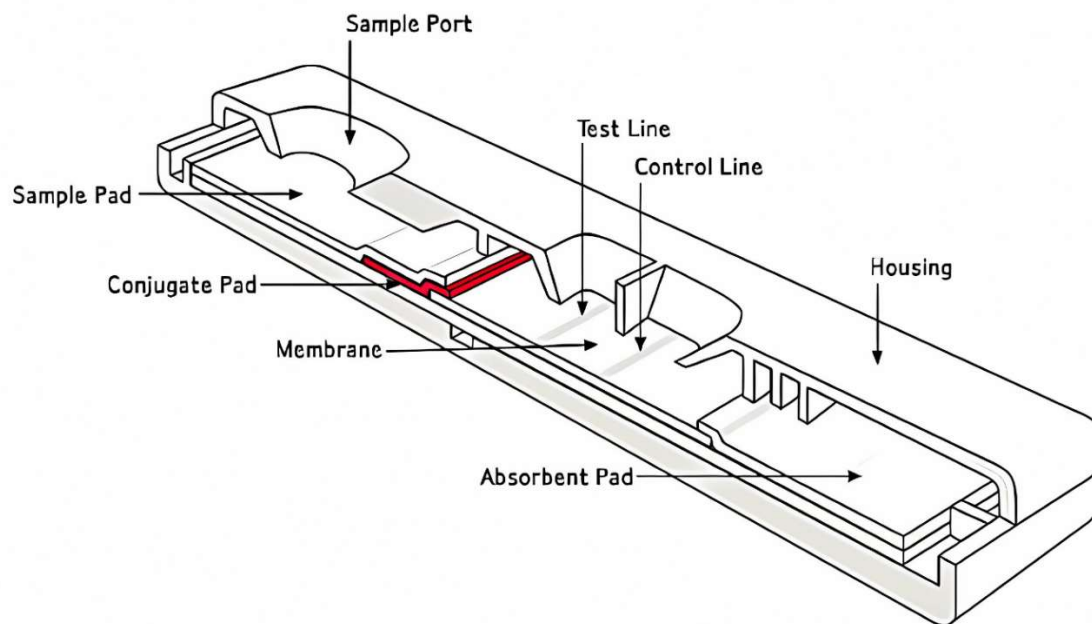


Figure 1.21. Schematic overview for the construction of traditional lateral flow devices (LFD's).⁹⁴

To increase the robustness of the device each section is mounted using a pressure-sensitive adhesive to a non-absorbent backing. Commonly used backing materials include nylon and polystyrene.^{91,93,94}

1.6.2b. The sample pad:

The sample pad is a simple absorbent pad to which the sample is applied. The materials used are not normally reported nor are their optimisation, in general they consist of a cellulose, rayon or crossed linked silica.⁹¹ However, as this area is the devices first point of contact to the sample it has several critical roles. The most important being the initial regulation of even and uniform sample flow through the device.⁹⁰ The other and equally important role is ensuring the sample is processed into a compatible format for the rest of the lateral flow device. To perform this task impregnation of dried chemical reagents to aid in sample preparation into the pad is used. This may aid analyte detection or sample delivery depending on the reagents used. Such as cell lysis and protein denaturing *via* chaotropic reagents. Furthermore, the porous nature of the pad may aid the removal of any remaining sample debris. Thereby preventing any undesired detection interferences. Additionally, the homogeneity of this section of the device is imperative.⁹⁰ For example, any gradients in the concentration of dried reagents across the pad; can significantly affect the devices performance.⁹⁰

1.6.2c. The conjugate pad:

The conjugate pad is the connection between the sample pad and the lateral flow membrane. The pads main function is to capture, immobilise and store the devices analyte/control detection probes.⁹⁴ Following the application of the sample, the probes must be released in the presence of the analyte. Therefore, allowing the formation of the required detection conjugates. Such probes have been specifically modified to specifically bind to the analyte in question, and or the control/test regions of the device. The design, function, materials of such probes is discussed in-depth in section 1.3 and 1.4. pages 8 and 13. The materials of choice for this region can be variable. The most common nevertheless include glass fibres, polyester and again rayon's.⁹³ The flow characteristics of this area of the device are once more critical and materials must possess relatively high flow rates.^{90,91} Achieving this requirement involves the treatment of the previously mentioned materials making them hydrophobic.⁹¹ One example involves the immersion of the pad in protein, polymers and surfactant solutions followed by an intensive high temperature drying process.⁹¹ In similarity to the sample pad, the hydrophobicity profile across the pad must be homogeneous to ensure optimal flow dynamic of the sample to the lateral flow membrane.⁹⁰

1.6.2d. The lateral flow membrane:

The lateral flow membrane is also referred to as the analytical region of the device and is perhaps the most important component found in lateral flow devices. Current literature supports a wealth of lateral flow devices based upon nitrocellulose membranes.^{85,86,95-97} The low cost,⁹⁰ well studied capillary fluid dynamics^{88,90} and substrate binding characteristics⁹⁰ of such membranes are in truth what make them most popular. Nevertheless, such nitrocellulose membranes have characteristics which make them distinctly unsuitable for applications in lateral flow devices. Low reproducibility in performance across batches,⁹⁰ shelf storage degradation issues⁹³ and variable flow characteristics caused by environmental changes^{91,93,94,97} make optimisation of such membranes challenging.⁹⁰ Other polymeric membrane materials have been used but with limited success. Examples include: nylon⁹³, polyether sulfone,^{91,93,97} polyethylene⁹³ and fused silica.⁹¹ However, there is a growing trend in using polyether sulfone⁹³ membranes for lateral flow devices especially those with nucleic acid hybridisation detection methods.

The main function of the lateral flow membrane is to firstly accept the analyte and associated probes from the conjugate pad. Secondly it thereafter transports them to the testing and control regions of the device at a controlled rate. Onto the membrane capture regions are sprayed, i.e. the test and control regions. Such regions selectively capture the analyte-probe conjugates and or the non-conjugated analyte and probes. Hence concentrating them in the test and or the control regions, inciting the result and validity of the test. (Fig 1.22)

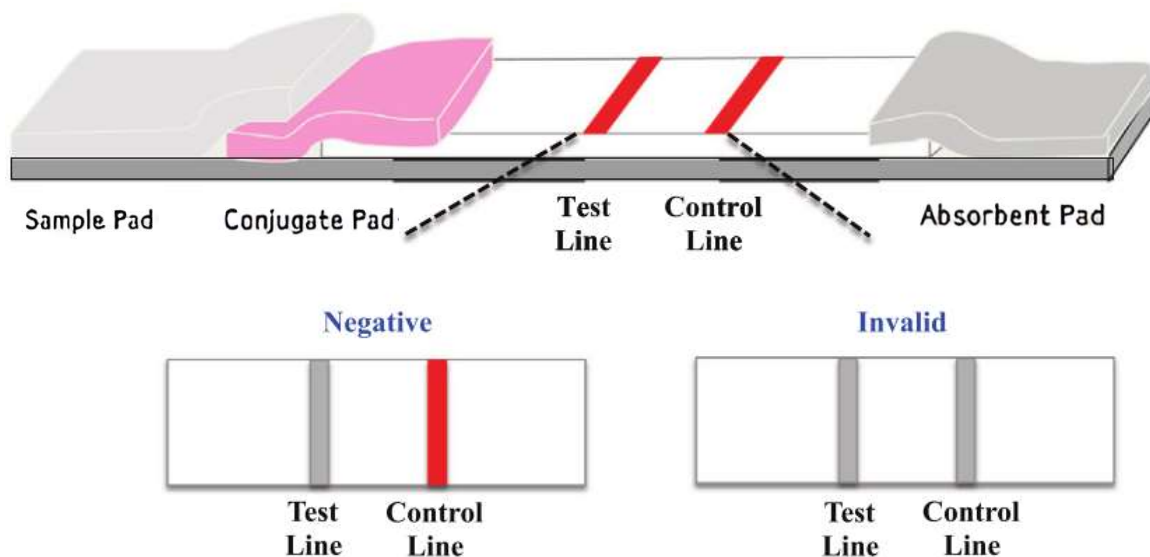


Figure 1.22 The principle working schematic of a traditional lateral flow device showing a negative and invalid test result. Figure adapted from Li and McDonnald⁹⁵

This process of detection is discussed more in depth in section 1.6.2. The selectivity and flow rate of the membrane can be adjusted by optimising the pore size of the membrane.^{90,91,93} Nitrocellulose membranes are available in a variety of pore sizes, 0.05-12 µm; thus, allowing for key optimisations to be made in this area.

1.6.2e. The absorbent pad/the wick:

The purpose of the absorbent pad is to absorb the previously processed sample. However, it plays a vital role in increasing the sensitivity of the device. By increasing the absorption volume, the pad can wick-up more fluid across the membrane. Therefore, increasing the capture efficiency of the test and control regions of the device as more sample is passed over the capture regions. It is also vital that any liquid absorbed into the wick is not released downstream as this can lead to false positive results, in particular on immunoassay lateral flow devices.⁹¹ The material of choice in this area is reportedly high-density cellulose.⁹¹

1.6.3 Analyte detection - A general schematic overview of detection.

1.6.3a. Competitive and sandwich/direct detection based lateral flow immunoassays:

Detection in lateral flow immunoassays operates by detecting target analytes using specifically designed immunological macromolecules such as antibodies. In traditional lateral flow immunoassays, there are two distinct methods to generate a positive or negative result. These are known as sandwich/direct and competitive detection assays. In sandwich/direct assays the conjugate pad contains a labelled antibody, hereby known as the probe; that forms a stable probe-analyte conjugate. These conjugate and excess non-conjugated probes are drawn up the lateral flow membrane *via* capillary action; their flow aided by the wicking effect of the absorbent pad. A specific antibody is adhered to the test line which will explicitly bind to the analyte probe conjugate thus immobilising it. The control line (*Fig 1.23*) will conversely only bind non-conjugated probes.

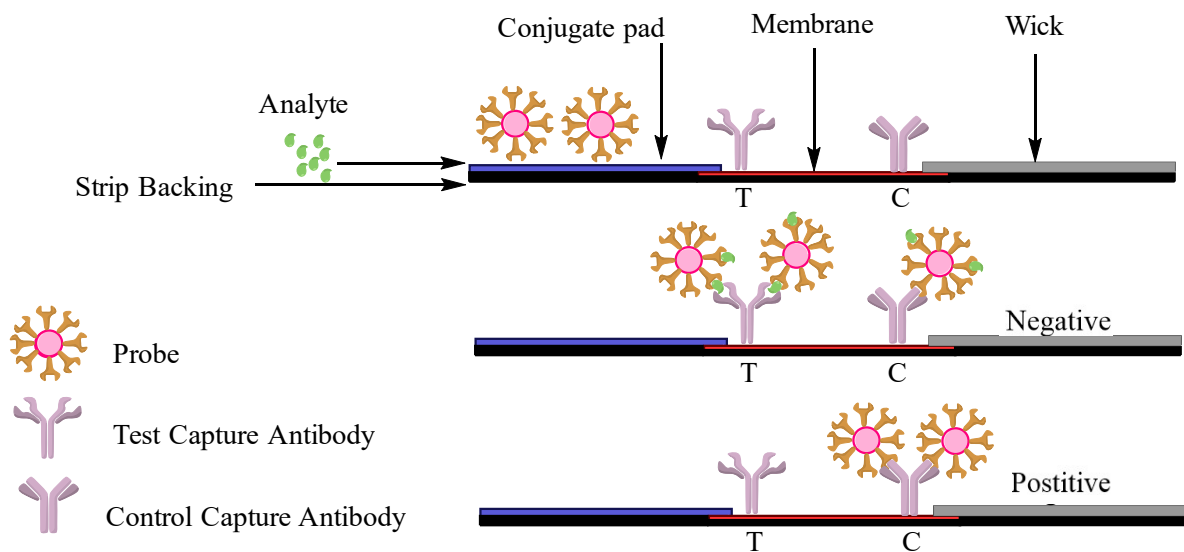


Figure 1.23. Sandwich based detection in Lateral Flow Immuno-Assay (LFIA's)⁹¹

If the analyte is present this will lead to aggregation of probes at the test line and the control line, indicating a positive result. If no analyte is present, then the probe will only aggregate at the control line; indicating a negative result. Such detection arrays are favoured when the target analyte is large and contains multiple antigenic binding sites. Examples of analytes include the hCG protein,^{85,86,88} Dengue antigen⁹⁷⁻¹⁰⁰ and human immunodeficiency deficiency virus (HIV).^{84,97,99,101,102} Noted for such detection methods is the requirement of low to moderate analyte concentrations. If an excess of analyte is present, the lack of non-conjugated probes may invalidate a result as no control line will be developed.

Competitive detection arrays work on a similar but slightly different principle. In this case the detection probe is labelled with an analyte augmented anti-body. This has a binding affinity for both the test capture antibodies and the control capture antibodies. The test zone antibodies are however analyte specific whereas the control is not. Furthermore, binding of the test capture antibodies to the augmented probes is relatively weak; comparatively to the target analyte. Consequently, in the presence of excess target analyte; the test antibody-probe conjugates binding sites will be competitively displaced. In doing so no apparent line in the test region will be visualised. However, a line at the control region subsequently indicates a positive result. The absence of the target analyte will therefore result in two lines (*Fig 1.24*), thus indicating the negative result. Such applications of competitive detection arrays contrast with sandwich-based arrays. Ideally the analyte will be small with only one antigenic determinant, and be present in excessive concentrations.

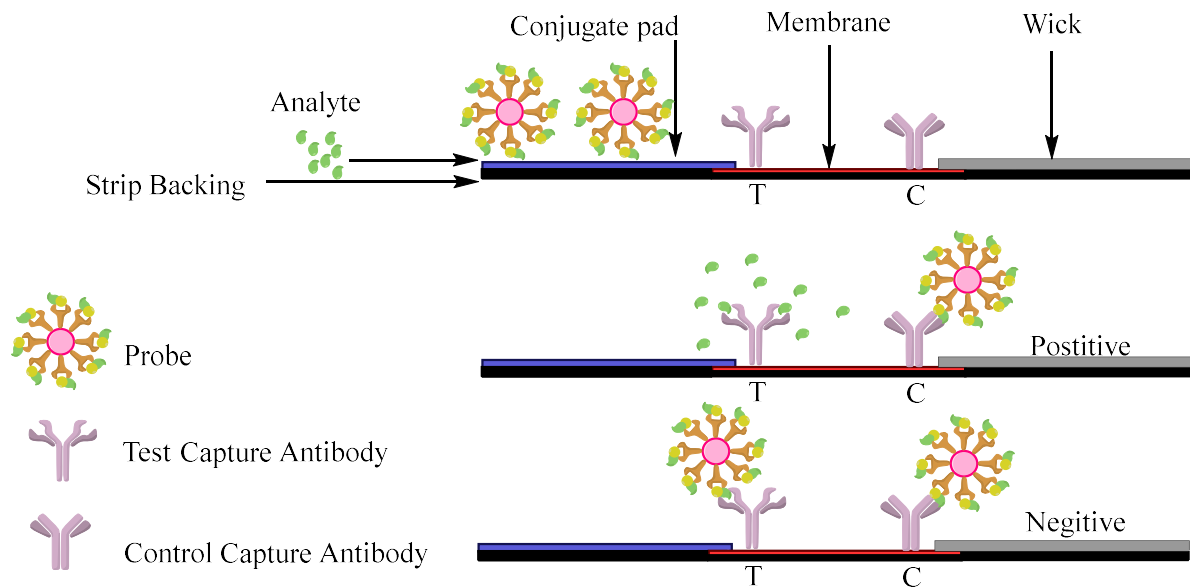


Figure 1.24 Competitive Detection Assay⁹¹

1.6.3b. Nucleic acid lateral flow (immuno)assay:

Nucleic acid lateral flow devices are emerging as one of the most effective ways to easily identify pathogenic microorganisms.^{99,100,103} The main limitations of such methods however are the requirements for sample preparation⁹⁷ and external DNA amplification.¹⁰⁴ In all literature examined^{93-97,99,100,105,106} the DNA amplification steps required for the nucleic acid lateral flow (immuno)assays mentioned were either carried out externally or in lateral flow conjugated microfluidic devices. The detection principles for nucleic acids on lateral flow membranes vary from traditional lateral flow Immunoassays; with the exception of aptamer-based detection methods.¹⁰⁷ Several methods have been reported but the most common/relevant are presented here.

Nucleic acid lateral flow immuno-assay (NALFIA):

In nucleic acid lateral flow immunoassays the analytes are typically double stranded amplicons which are specific to an organism of interest. The amplicon is produced using two or more unique tagged primers, *via* PCR or an isothermal DNA amplification methodology. The primers used are specifically tagged (*Fig 1.25*) at one end so the amplicon can selectively bind to an “anti-tag”, usually an associated antibody. The other side will be selectively bonded to a detection probe. Adhered to the test region of the lateral flow membrane is the anti-tag, which immobilises and aggregates the target double stranded amplicon onto the membrane. The control anti-tag binds to only the probe thus indicating the successful running of the strip. If the target gene is not present in the sample, no ds-amplicon will be formed during the nucleic acid amplification. Consequently, only the tagged ss-

primers will be transferred to the lateral flow strip. which utilised biotin and fluorescein as the tags, antibodies as the anti-tags and avidin coated gold nanoparticles as the probe.

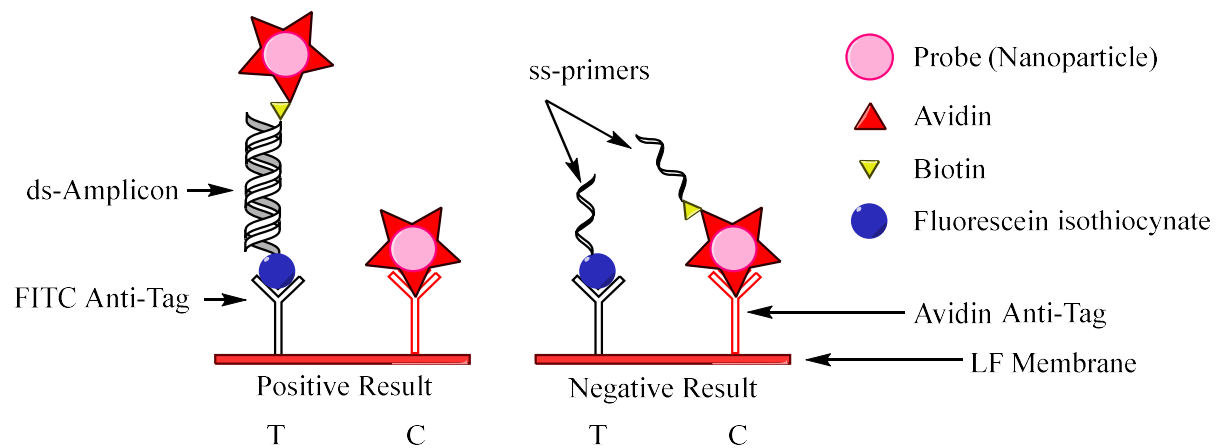


Figure 1.25. NALFIA Detection Scheme⁹⁴

If no target DNA was present prior to DNA amplification using this system, the biotin labelled primer (3' or 5') end will still be captured by the test anti-tag. However, the probe can still independently bind to the control capture anti-tag indicating the test has run successfully.

Nucleic Acid Lateral Flow Assay (NALFA):

In nucleic acid lateral flow assays the analyte is typically a single stranded amplicon which is again specific to an organism of interest, which are generated by an external nucleic acid amplification technique. However, in this methodology (Fig. 1.26) the detection mode is based upon nucleic acid hybridisations rather than antibody-antigen conjugation.^{93,96,103} This is advantageous as there is no requirement for tagged primers in the amplification step, owing to the hybridisation element being encoded at the beginning and end of the amplicon itself. Detection of the relevant single stranded amplicon is achieved by attaching a small oligonucleotide to a detection probe. These detection probes are complementary to the bases at one end of the target amplicon thus allowing hybridisation in the conjugate pad and along the lateral flow membrane. Adhered to the membrane in the test region is again another oligonucleotide which is complementary to the bases at the other end of the target single stranded amplicon. Upon hybridisation, it is immobilised inciting the positive result. The control line has adhered the complementary oligonucleotide to the detection probe thus immobilising only non-hybridised detection probes thus showing the result is valid.

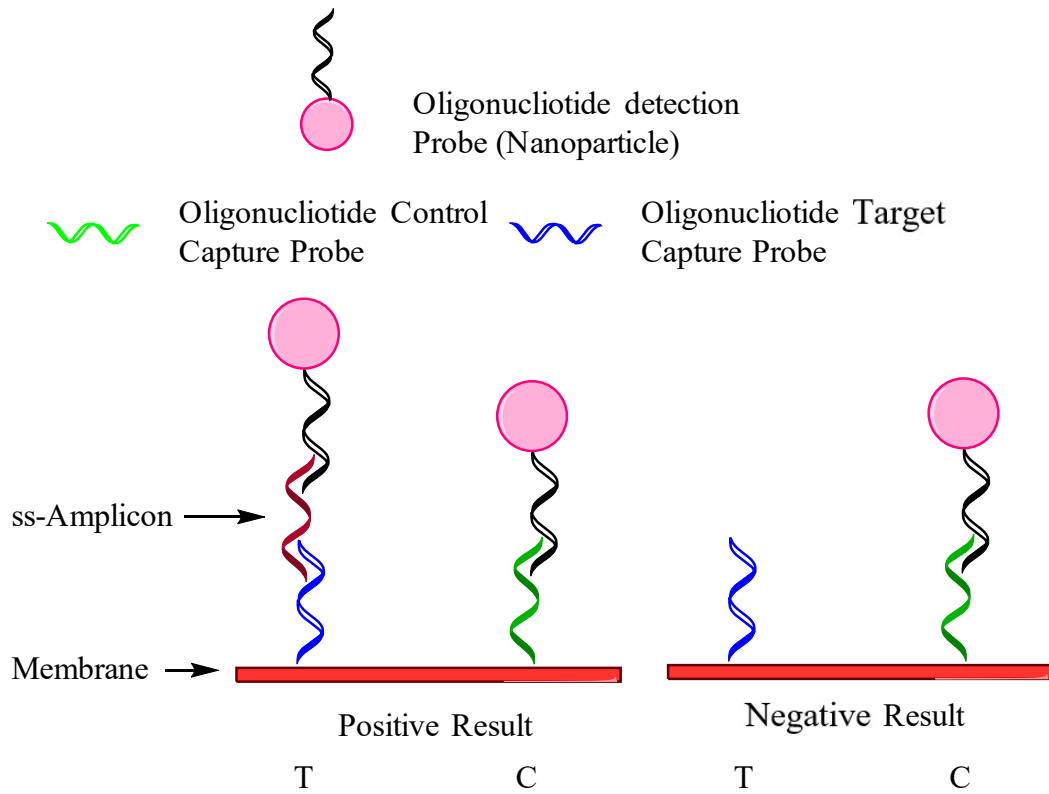


Figure 1.26. NALFA detection array

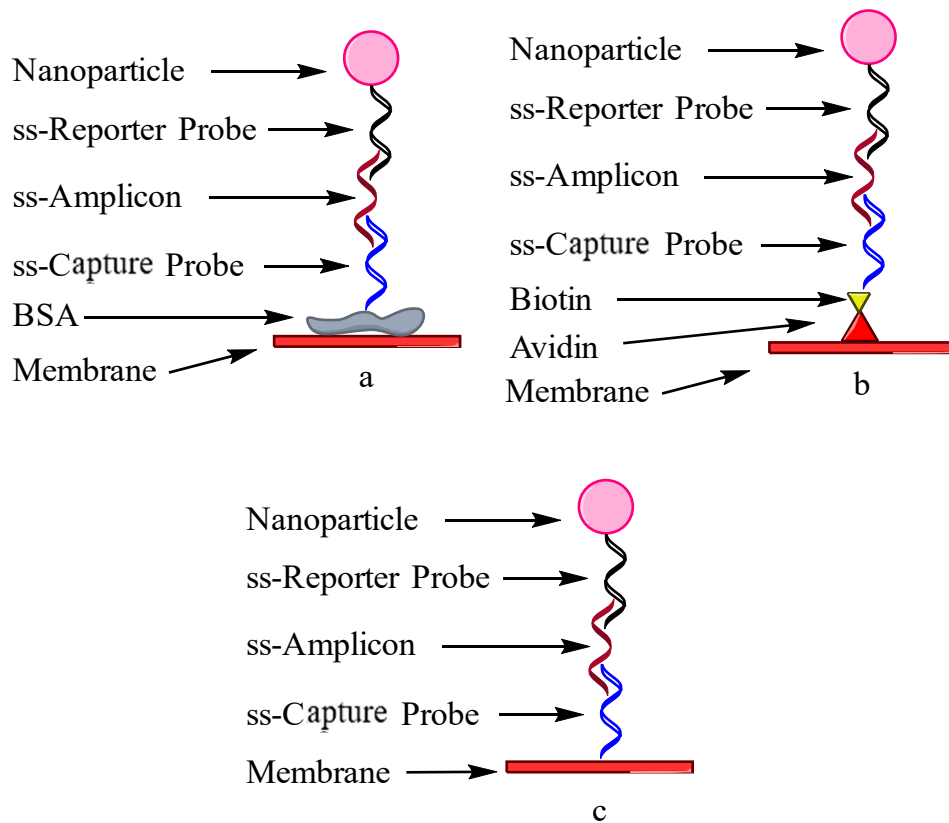


Figure 1.27. Three common NALFA capture probe adhesion strategies.⁹³

The main variant in detection using this approach is the mode of adhering the capture oligonucleotide elements to the lateral flow membrane. Some adsorption strategies include:

- Bovine serum albumin protein linkage (*Fig. 1.27a*);
- Biotin-Avidin adsorption (*Fig. 1.27b*);
- Passive adsorption of the glycoposphate backbone directly to the membrane (*Fig. 1.27c*).

1.6.4 Detection Probes:

One of the most vital components in a lateral flow assay is the visualisation of the result, i.e. the detection probe. It is the single most important element when considering the sensitivity of the device, second only to the lateral flow capture probe/antibody efficiency and selectivity. This section highlights the most reported systems used in lateral flow devices, all are applicable to both lateral flow immunoassay and lateral flow nucleic acid assays.

1.6.4a. Colloidal gold nanoparticles:

Colloidal gold nanoparticles (AuNP's) are by far the most prevalent detection probe used in modern lateral flow devices. The surface plasmonic resonance of such nanoparticles provided very high extinction co-efficient in the red visible region. Thus, providing a very intense colour on aggregation at the relevant regions of the lateral flow membrane. (*Fig. 1.28*) Furthermore, the chemical nature of gold provides effective and well-studied methodologies for the functionalisation of the surface with biological molecules. The first of such functionalisation with an antibody was reported in 1984 by Moeremans¹⁰⁸ and simultaneously by Breda and Roth.¹⁰⁹

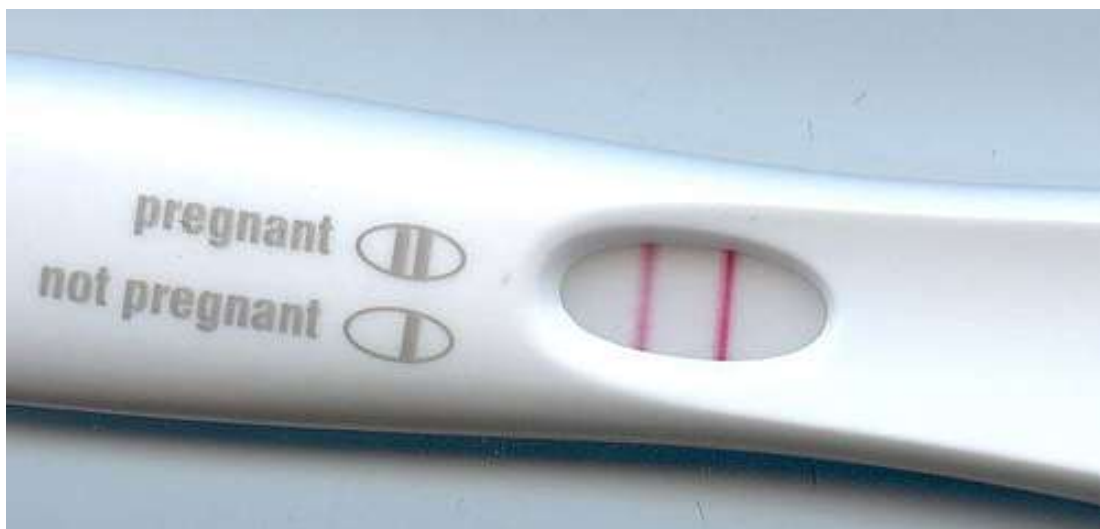


Figure 1.28. An example of a hCG pregnancy test exploiting colloidal gold nanoparticles as the detection probe, seen as bright red lines.

The general methodologies for producing such stable gold nanoparticle colloids involve the reduction of dissolve salt solutions of gold in a controlled manner. Thus, producing uniform nanoparticle in a range of shapes and sizes depending on the reaction conditions. The most common methodology for producing such colloids is that described by Frens in 1973.¹¹⁰ It involves the controlled nucleation of hot tetrachloroauric acid solution by sodium citrate reduction. Such gold colloids produce a strong absorbance between 510-550 nm.¹¹¹ A higher lambda max indicates a larger average particle diameter. Additionally, the uniformity of the particles can be approximated by the width of the maximum absorption line, narrow indicating a uniform colloid; broad conversely indicating a non-uniform colloid.⁸⁹

1.6.4b. Silver/gold reduction-based enhancement of colloidal gold nanoparticles:

Using a further strategy gold nanoparticles sensitivity can be greatly increased. Following initial visualisation with gold nanoparticles, the lateral flow step is immersed in a tank of silver or gold ions. Just as with the production of the original colloids the metal ions are again reduced in a controlled manner. The slow reduction of the silver or gold forms a layer of metal around the conjugated gold nanoparticles (*Fig. 1.29*) increasing their diameter. In doing so the molar extinction coefficient can be enhanced by 1-4 orders of magnitude^{94,89}, without compromising the benefits of using small diameter nanoparticles. The original methodologies for such enhancements were developed on gold colloid stained tissues by Danscher^{112,113} and Holgate.¹¹⁴ The tissue stains were developed using a mixture of silver lactate, hydroquinone and citrate buffer at low pH was used as the developing agent.

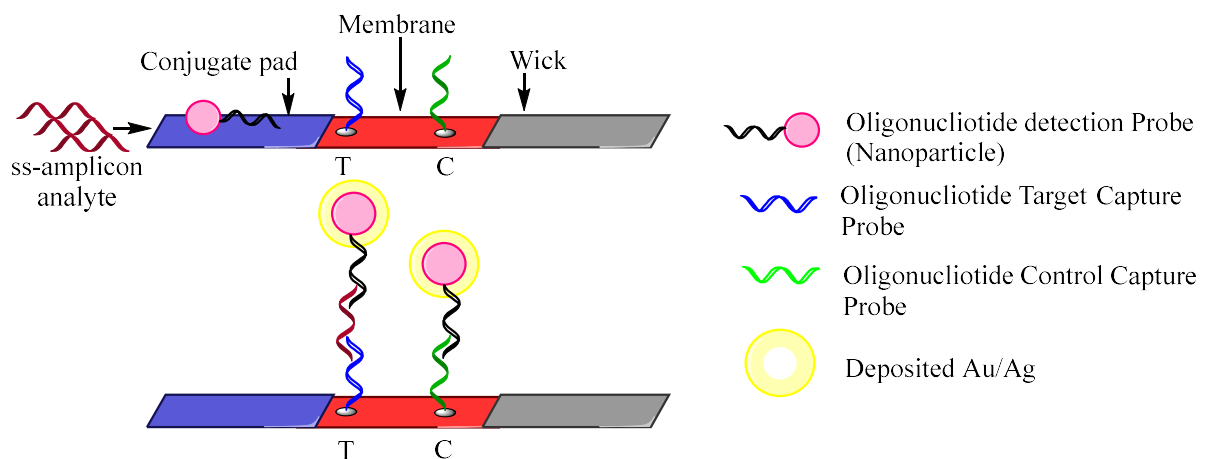


Figure 1.29. Silver/Gold reduction-based enhancement of a colloidal gold based NALF detection array.

1.6.4c. Amorphous carbon nanoparticles :

Amorphous carbon nanoparticles (aCNP's) have been recently reported in several papers as the probe for both lateral flow immuno assays and nucleic acid assays.^{89,91,115} However the availability of such particles is limited and usually their application are proprietary to the manufacturer.⁸⁹ The production in the lab involves the burning of toluene⁸⁹ to produce soot from which the amorphous carbon nanoparticles are isolated; such a procedure is far from ideal.¹¹⁵ Unlike colloidal gold nanoparticles there are no defined methodologies to produce different shaped or sized nanoparticles¹¹⁵ and few methods exist to directly covalently bond to the nanoparticle due to the inert nature of the carbon surface.¹¹⁵ Functionalisation of the surface, i.e. bonding of substrates to the occurs *via* physio-adsorption. This process takes between 1-7 hours to complete. Conversely amorphous carbon nanoparticles do provide benefits, namely they are cheaper than colloidal gold given the relative abundance of material. They have also been shown to provide extended shelf life to that of gold colloids and have similar molar extinction co-efficients.¹¹⁵

1.6.4d. Fluorescence probes:

Fluorescence is a fundamental quantum mechanical behaviour of all matter. The basis of which is the absorption of a specific quantum of electromagnetic radiation, followed by the spontaneous re-emission of the quantum, usually at higher wavelength (Stokes-shift). Fluorescence probes typically have high molar extinction coefficients and the excitation lifetimes are short, in the region of 10 nanoseconds.⁸⁹ One of the main strengths of using this phenomenon as a lateral flow probe is that the intensity of the fluorescence can directly relate to the intensity of an excitation light source.⁸⁹ Thus, by irradiating the probe with an intense light source of a specific wavelength, a response can be detected even if the number of conjugated probes present is small. The size of the Stokes-shift is one of the key optimisations when selecting a fluorescence probe. Larger is generally deemed as better as the distinction between incident light and emitted light is clearer. It is noted that not all photons of the correct energy will excite the probe. The percentage of the photons that do is translated into the quantum efficiency/yield/turnover.⁸⁹ The advantages of such probes are also inherently their weakness because to use such probes an irradiation source and a selective photodiode are needed to measure the fluorescence signal. Such a requirement rises the cost of production and reduces the user friendliness of the device. Reducing their applicability to the WHO "ASSUED" criteria for point of contact diagnostics. Examples the most typically used in lateral flow devices are xanthene and cyanine dyes (Fig. 1.30) owing high extinction coefficients and reactive groups.⁸⁹

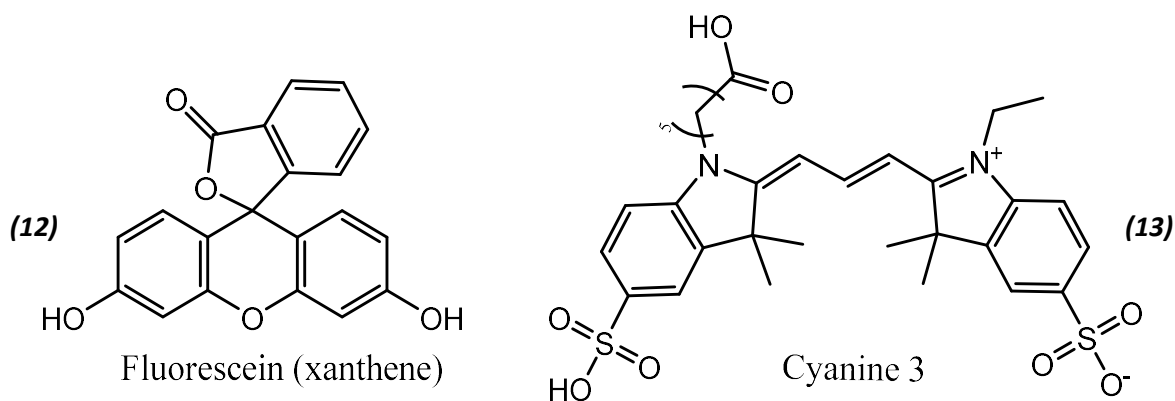


Figure 1.30. Two commonly used Xanthene (12) and Cyanine Based Fluorophores (13) in LFD's

Such reactive groups allow for the easy attachment of a biological molecules; such as proteins, sugars, and nucleic acids. Other probes include lanthanide metal complexes where the electronic transition is a strong charge transfer from outer-sphere metal electrons to the ligand itself. These probes have large Stokes-shifts, but have inconveniently long excitation lifetimes 500-2000 microseconds.⁸⁹ Thus, meaning the signal response is a function of time for quantitative analysis, leading to reduced signal intensity for qualitative evaluations.

1.6.4e. Quantum dots:

Quantum dots are monocrystalline nanoscopic materials, usually based upon semiconducting ceramics and exhibit fluorescence.⁸⁹ Examples include CdSe, CdS, ZnSe, InP, InAs and AnS coated Cd cores.⁸⁹ In comparison to colloidal gold nanoparticles relatively few lateral flow devices have been reported using this detection method.⁸⁹ However, they exhibit desirable characteristics for such applications:⁸⁹

- Quantum efficiencies of ~50%
- Available in colloidal suspensions
- Easy optimisation of emission wavelength and Stokes shifts
- Excitation lifetimes of 30-100 ns
- Emission bandwidths of 10-50 nm

The working principle of quantum dots is based on band theory.¹¹⁶ Upon the absorption of a photon an electron is promoted to the conduction band from the valance band, in doing so leaving behind a positively charge "hole". Such behaviour is true for all semi-conductors. However, when the size of the crystal is like the size of the excitation radii i.e. the radii of the hole and the excited election, the system is therefore constricted to behave in a specific manner.¹¹⁷ The physical nature at this scale

begins to be determined by the exciton-crystal size ratio.¹¹⁸ As the excitation is restricted in motion, owing to the size of the crystal the physicality can be approximated by the particle in box model.^{119,120} In such a model, motion in any direction is forbidden as the potential energy rises immediately to infinity outside the box.^{119,120} Internally this means as the hole and excited electron are recombined the energy cannot be emitted translationally and, in some respects, vibronically.¹²¹ Therefore, the main route of relaxation following absorption is *via* re-emission of the absorbed photon as more photons, giving rise to the observed large quantum efficiencies, this physical behaviour is also termed quantum confinement. Readers wishing to explore the history and physics of quantum dots further are directed to the Nobel prize for chemistry 2023.¹²²

1.6.4f. Up converting phosphors:

These probes are based upon phosphorescence of molecular systems. Such systems are distinct from fluorescence as the emission of spectral light continues even after the excitation beam is removed.¹²³ The length of time of which this emission occurs is known as the decay time, it is typically in the region of 10^{-4} - 10^2 s.⁸⁹ Also, distinct from fluorescence is the mode of emission. Normally fluorescence converts higher-energy photon to lower-energy emitted photons, i.e. Stokes shift. Up conversion phosphorescence is based on the absorption of two or more low-energy typically infrared photons by a nanocrystalline material, followed by the emission of a single higher-energy photon, i.e. anti-Stokes shift. This energy transfer is most often accomplished using a combination of rare-earth lanthanides as dopants on ceramic nanoparticle and yield materials with high quantum efficiency and very large anti-stokes shifts. Some examples include yttrium and erbium oxysulfide's nanocrystalline ceramics.

1.6.4g. Paramagnetic particles:

The majority of paramagnetic nanoparticles reported for the use in lateral flow devices are colloidal particles of iron oxide.⁸⁹ Such particles exhibit magnetism only when in an applied magnetic field thus preventing self-aggregation and destabilisation of the colloidal mixture.⁸⁹ Currently the detection method involves a magnetic flux reader.⁸⁹ Such a device has been specifically designed for lateral flow devices but again rises propriety and cost issues into the mix. In doing so it is diverting any device away from the ASSURED criteria. However, the author suggests that the application of such particles is overlooked. Possible routes of visualisation using combined detection probes could be used for colorimetric assay. By combining the two, the ability for optimising the transport of the probes in the device could be achieved using magnetic fields.

1.6.4h. Latex particles:

Latex particles were one of the first used detection probes on lateral flow immunoassays.⁸⁶ The chemistry for conjugation is vast and can involve direct covalent conjugation or adsorption on to the particle surface.⁸⁹ The composition of such particles can be altered to provide several features such as adding fluorescent dyes into the material or even the aforementioned paramagnetic particles. Furthermore, this route offers distinct advantages in comparison to covalently conjugated fluorescent dyes as they can be conjugated to biological entities by non-chemical means, thus reducing the risk of inadvertent modification of the biological conjugate.⁸⁹

1.6.5 Detection Limits:

The detection limits of lateral flow devices deviate greatly across the literature. This is due to the detection limit of each device being dictated by several factors. Such factors can include the nature of the analyte, detection method, the probe used, sample matrix, strip materials and multiplexed interferences. Therefore, it is advantageous to divide published devices into sections for easier comparison using the tabulated information provided on *table 1.4, 1.5 and 1.6.*

Table 1.4 Lateral flow devices targeted at the detection of small/toxic molecules.

Analyte	Probe	Method	LoD*	Matrix	Ref
Aflatoxin B1	AuNP's	Sandwich	2 µg kg ⁻¹	Pig Feed extracts	106
Botulinum neurotoxin D	AuNP's	Sandwich	50 ng L ⁻¹	Equine faeces	105
Carbaryl	AuNP's	Sandwich	100 µg L ⁻¹	Fruit and cereal extracts	124
Endosulfan	AuNP's	Sandwich	10 µg L ⁻¹	Fruit and cereal extracts	124
Streptomycin	AuNP's	Sandwich	25 µg L ⁻¹	Raw Milk	102
Fumonisin B1	AuNP's	Sandwich	1 µg L ⁻¹	Extracts of cereals	125
Glycyrrhizic acid	AuNP's	Sandwich	50 µg L ⁻¹	Extracts of liquorice plants	126
Medroxy-progesterone	AuNP's	Sandwich	10 mg kg ⁻¹	Swine liver	127
Microcystin-LR	Fluorescence	Sandwich	50-100 ng L ⁻¹	Freshwater	128
Nicarbazin	Latex	Sandwich	2 mg kg ⁻¹	Poultry feed	129

Table 1.5 Comparison of reported Nucleic acid lateral flow (immuno)assays.

Analyte	Probe	Method	LoD*	Matrix	Ref
Bacillus anthracis specific RNA	Polystyrene microspheres	NALFIA	2 <i>B. anthracis</i> cells	Buffer	99
Staphylococcus aureus	AuNP's	NALFA	10 <i>S. aureus</i> cells	Buffer	103
Dengue Serotypes	Liposome	NALFA	50-50000 RNA copies	Serum and buffer	100
Synthetic DNA Targets	AuNP's	NALFA	0.01fM	LAMP product	96

Table 1.6 Comparison of report lateral flow devices targeted at protein identification.

Analyte	Probe	Method	LoD*	Matrix	Ref
Anti-anthrax protective IgG	AuNP's	Competitive	3 mg L ⁻¹ 14 mg L ⁻¹	Serum Whole blood	130
Bovine IgG	AuNP's	Sandwich	0.01% v/v	Serum	131
Cortisol	AuNP's	Sandwich	3.5 µg L ⁻¹	Serum	132
Fungal α- amylase	aCNP's	Sandwich	10 µg L ⁻¹	Buffer	101
hCG	aCNP's	Sandwich	10 mIU mL ⁻¹	Urine	133
Total prostate-specific antigen TPSA	AuNP's	Sandwich	0.2 µL ⁻¹	Serum	134
Oestrone sulphate	Dyed polystyrene	Sandwich	5 µL ⁻¹	Equine urine	135
Progesterone	AuNP's	Competitive	5 µL ⁻¹	Bovine Milk	136
Albumin	Fluorescent dye	Sandwich	12.2 g L ⁻¹	Serum	137
Human C-reactive protein	Fluorescence	Sandwich	0.133 mg L ⁻¹	Serum	138
Human C-reactive protein	AuNP's	Sandwich	2 mg L ⁻¹	Plasma	139
Heart-type fatty acid binding protein	AuNP's	Sandwich	5 µg L ⁻¹	Plasm	139
Lipoprotein A	Selenium labelled antigen	Competitive	40 mg L ⁻¹	Whole Blood	140
Eosinophil protein X	Eu(III) Phosphoresce	Sandwich	0.082 g L ⁻¹	Whole Blood	141
Neutrophil lipoint	Eu(III) Phosphoresce	Sandwich	0.05g L ⁻¹	Whole Blood	141
TPSA	AuNP's	Competitive	1 µg L ⁻¹	Serum	142
Human Serum Albumin	AuNP's	Sandwich	30 mg L ⁻¹	Urine	98
hepatitis B antigen	AuNP's	Sandwich	5 µg L ⁻¹	Serum	143
Antibody to <i>Trichinella</i>	AuNP's	Sandwich	100% Positives	Swine Serum	144
Brucella-specific IgM antibodies	Fluorescence	Sandwich	93% Positives	Serum	145
Mammalian IgG	Fluorescence	Sandwich	10 µg L ⁻¹	Mosquito Bone meal	146
<i>Leptospira</i>-specific IgM	Fluorescence	Sandwich	87% Positives	Serum	147
<i>Rotavirus</i>	AuNP's	Sandwich	70% Positives	Bovine faeces	148
Antibody to <i>Schistosoma japonicum</i> in	Blue colloidal dye	Sandwich	97% Positives	Serum	149
<i>Schistosoma</i> circulating cathodic antigen	aCNP's	Sandwich	0.2 µg L ⁻¹	Urine	150
<i>Foot-and-mouth disease virus serotype O, A and Asia 1 antigens</i>	AuNP's	Sandwich	O 17VP A 3400VP Asia1 7200VP	N/A	97
<i>Hepatitis B virus genotyping A, B, C and D surface antigens</i>	Fluorescence	N/A	A 2.5 IU/mL B 5 IU/mL C 5 IU/mL D 10 IU/mL	N/A	97
<i>Dengue virus (DENV) NS1 protein, Yellow Fever virus (YEV) NS1 protein and Ebola virus, Zaire strain (ZEBOV)</i>	Silver nanoparticles	Sandwich	150ng mL ⁻¹ of each protein	N/A	97

1.7 Concluding remarks and aims:

The landscape of public health has undergone a transformative shift with the emergence of point-of-care diagnostic devices. Their profound significance became especially conspicuous during the COVID-19 pandemic. While it is true that the point-of-care testing solutions used during the pandemic were, to some extent, outperformed by the gold standard PCR testing, the latter remained expensive, time-consuming, and reliant on skilled operators to carry out the tests. They did provide an invaluable first line of defence and information used to guide people's choices as well as clinicians' decisions.

The aim of this research was to enhance traditional lateral flow devices by creating a multiplexed system capable of simultaneously amplifying and detecting genes using a single ASSURED point-of-contact device. To demonstrate the capabilities of this novel system and elucidate the processes involved in its design and optimization for a specific target gene locus, we focused on methicillin-resistant *Staphylococcus aureus* (MRSA) antibiotic resistance genes as our detection targets. The field of antimicrobial resistance was selected to showcase the device's capabilities, as it embodies the primary challenges that have impeded the widespread adoption of traditional lateral flow devices as the gold standard for clinical guidance.

Since the advent of the antibiotic era in 1928, humanity has enjoyed a substantial advantage in the battle against infectious diseases. However, antimicrobial resistance now poses an ever-increasing threat to public health. It is evident that without substantial interventions, it's not beyond the realm of possibility to imagine a return to a public health environment resembling the pre-1928 era, where even simple bacterial infections could once again prove fatal. The world health organisation makes it clear that one of the crucial frontiers in winning the battle against antimicrobial resistance involves extensive surveillance and targeted treatments to curtail the inappropriate use of antibiotics.

As such MRSA was the ideal target for this research due to its numerous genes linked to various antimicrobial resistance properties. As previously discussed, past attempts to tailor treatment for MRSA infections relied heavily on the lengthy process of culturing isolated bacteria and extensive phenotyping to determine the specific subtype of MRSA present. This approach provided clinicians with a general idea of which antibiotics were likely to be ineffective. However, this method is so time-consuming that empirical treatment methods, involving trial and error through multiple antibiotic lines, have remained the gold standard for treating such infections. Unfortunately, this approach often

leads to delayed effective treatment or, in some cases, the patient's demise before finding the appropriate treatment line.

Although MRSA is the primary focus of the presented research, it's worth remembering that this system should be adaptable to any DNA-based target by altering the initial primer sequences discussed in the following chapters. Such versatility aligns with the WHO ASSURED device criteria, a pivotal driving force behind the research endeavours outlined.

Chapter 2

Methicillin-Resistant Staphylococcus Aureus Antimicrobial Resistance Nucleic Lateral Flow Assay Primer Design.

“Are you having a BLAST?”

*Oh ho ho and a bottle of rum!
We're sailing the seas, having some fun.
We've got a mission, a task to complete.
We'll use BLAST, it's the tool we'll repeat.*

*We've got some DNA, it's long and it's tough,
But BLAST can find the match, it's more than
enough. We input the data and hit search with
glee, BLAST comes back with the results, oh so
swiftly!*

*We're having a blast, as clear as can be,
BLAST has found it, as easy as can be.
We raise a glass and a cheer to the sky,
Thank you, BLAST, for making our work fly!*

*So if you're sailing the seas and you need to find,
A match for your DNA, just use BLAST, it's kind.
It'll search through the data and find what you
seek, BLAST is the tool that we all ought to seek!*

*But BLAST can do more than just DNA, you see,
It can find matches in proteins, oh so easily.
We input the data and hit search once more,
BLAST comes back with the answers, oh so sure!*

*We're having a blast, it's clear as can be,
BLAST has found it, as easy as can be.
We raise a glass and a cheer to the sky
Thank you, owe BLAST, for making our work fly!*

*So if you're sailing the seas and you need to find, A
match for your proteins, just use BLAST, it's kind.
It'll search through the data and find what you
seek, BLAST is the tool that we all ought to seek!*

*But we're not done yet, we've got one more task
We need to make primers, it's an easy ask!
We input the data and hit design with glee,
BLAST comes back with the primers, oh so swiftly!*

*But wait, what's this? The primers don't work!
They're not amplifying, it's quite the berk!
We scratch our heads and wonder what to do,
But then we remember, we've still got BLAST, it's
true.*

*We input the data and hit search with glee,
BLAST comes back with the answers, oh so swiftly!*

*We're having a blast, it's clear as can be.
BLAST has found it, as easy as can be.
We raise a glass and a cheer to the sky,
Owe Thank you, Owe BLAST, for making our work
fly!*

*So if you're sailing the seas and you need to fix,
Some primers that just won't amplify in your mix,
Just trust in BLAST, it's quick as can be,
It'll search through the data and find what you
need, BLAST is the tool that we all ought to heed!*

2.1 Introduction:

Chapter two will examine the general methodology used to design oligo-nucleotide libraries for the proposed novel multiplexed isothermal DNA amplification-NALFA (nucleic acid lateral flow assay) coupled gene detection system. Along with the oligo-nucleotides required for optimisation via real-time reaction monitoring. The purported system is universal and can be adapted to any target genes of interest. However, as a proof of concept, AMR genes associated with MRSA were used to demonstrate the scope of the proposed system. Extensive conservation analysis of associated AMR genes found in *S.aureus* was carried out (s2.1), and highly conserved locations were defined for each. Primer sequences optimised for RPA amplification were constructed (s2.2), and novel modifications were made to allow for detection via the coupled NALFA (s2.3).

2.2 Methicillin-Resistant Staphylococcus Aureus Antimicrobial Resistance Gene Conservation Analysis:

An exhaustive library of reference gene sequences (*Appendix 1*) of the target anti-microbial resistance genes found in MRSA subvariants was obtained via the NCBI nr/nt database. Multi sequence alignment (*Appendix 2*) was carried out using BLASTn and ClustalW2 algorithms. Alignment entropy plots and consensus sequences were calculated using BioEdit, and areas with the highest conservation within consensus sequences (*Figs. 2.1-2.10*) were identified.

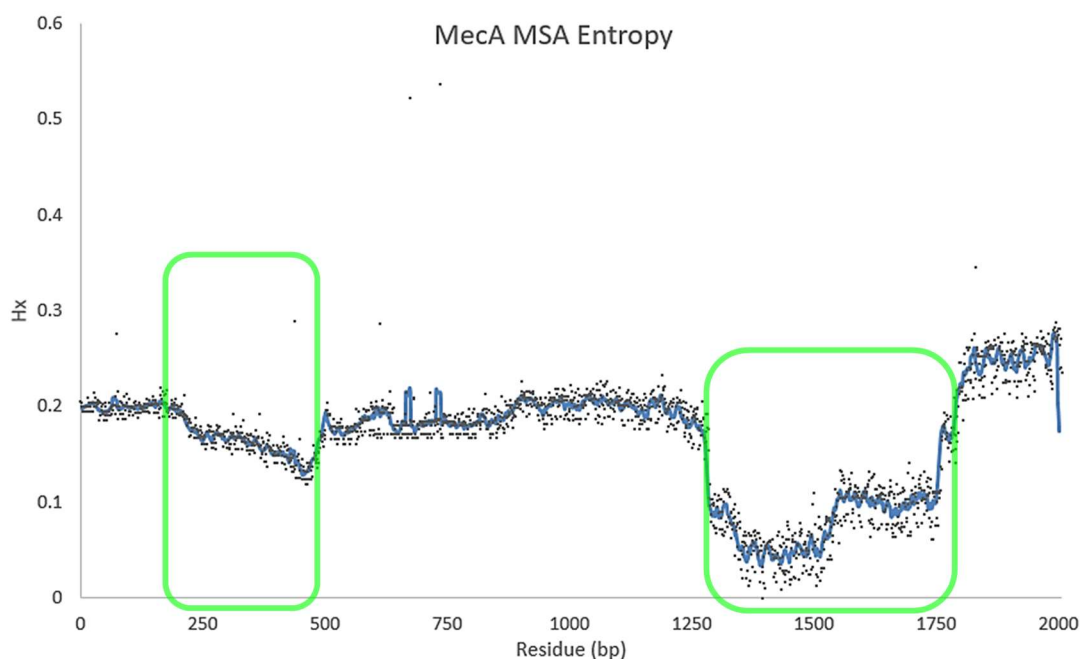


Figure 2.1. Multi sequence alignment entropy plot of MecA (PBP2a, β -lactam resistance factor) consensus sequence, compiled from 1,606 sequences. Black, residue point entropies. Blue, exponential weighted moving average ($p=10bp$, $\alpha=0.1$). Green, areas of high conservation.

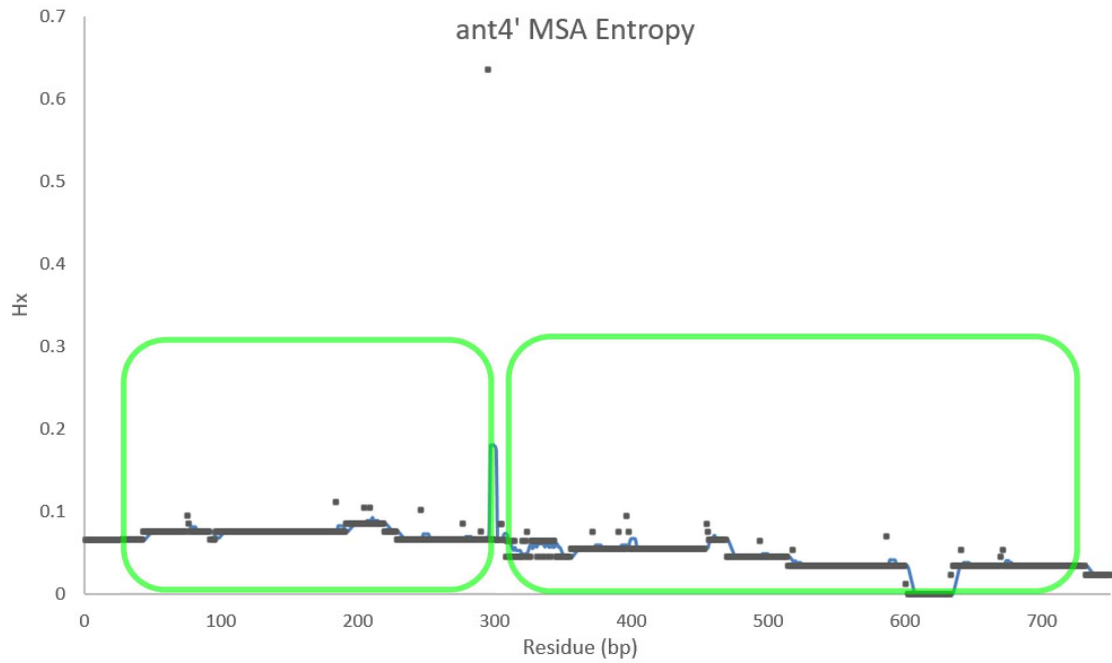


Figure 2.2. Multi sequence alignment entropy plot of *ant(4')* (aminoglycoside 4'-O-adenylyltransferase, aminoglycoside resistance factor) consensus sequence, compiled from 345 sequences. Black, residue point entropies. Blue, exponential weighted moving average ($p=5bp$, $\alpha=0.05$). Green, areas of high conservation

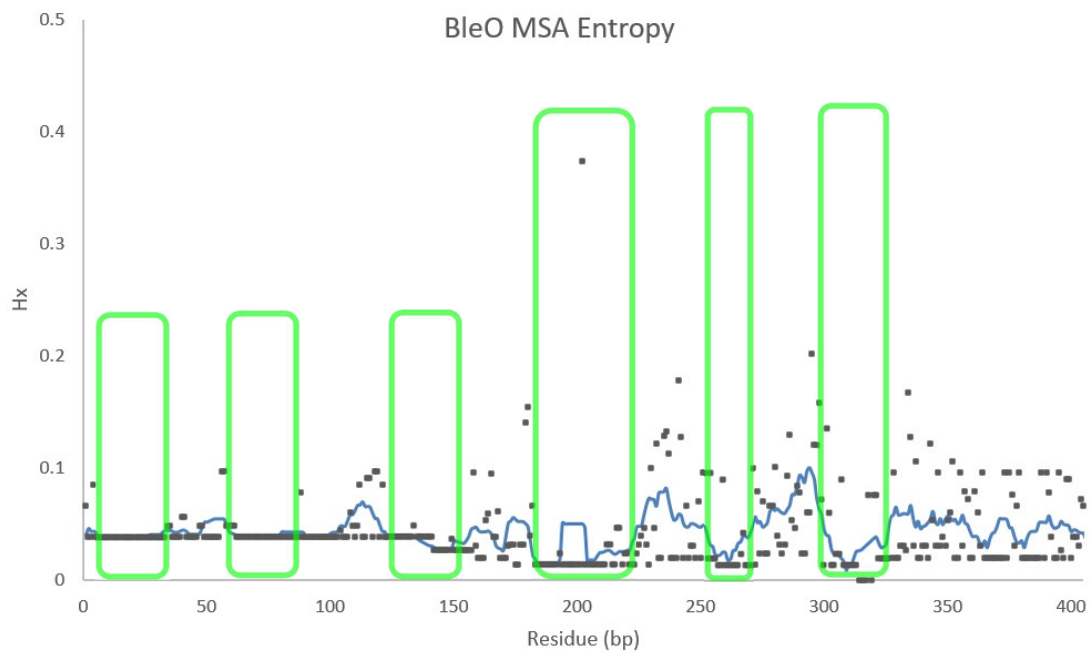


Figure 2.3 Multi sequence alignment entropy plot of *bleO* (Bleomycin resistance factor) consensus sequence, compiled from 206 sequences. Black, residue point entropies. Blue, exponential weighted moving average ($p=10bp$, $\alpha=0.1$). Green, areas of high conservation.

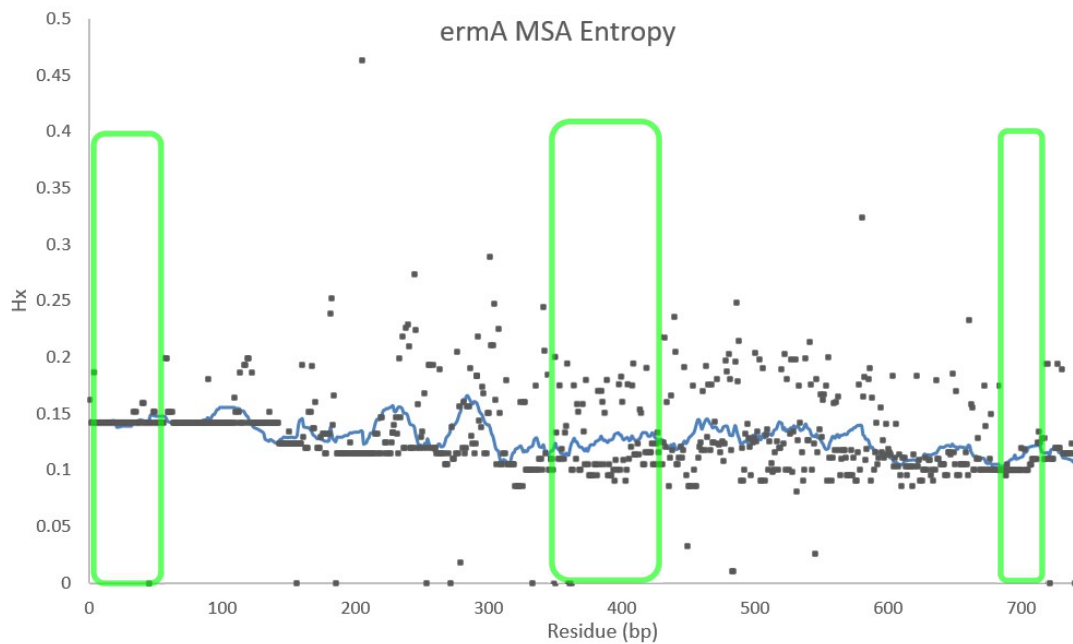


Figure 2.4. Multi sequence alignment entropy plot of *ermA* (rRNA adenine N-6-methyltransferase, macrolide-lincosamide-streptogramin B resistance factor) consensus sequence, compiled from 756 sequences. Black, residue point entropies. Blue, exponential weighted moving average ($p=25bp$, $\alpha=0.1$). Green, areas of high conservation. Green, areas of high conservation.

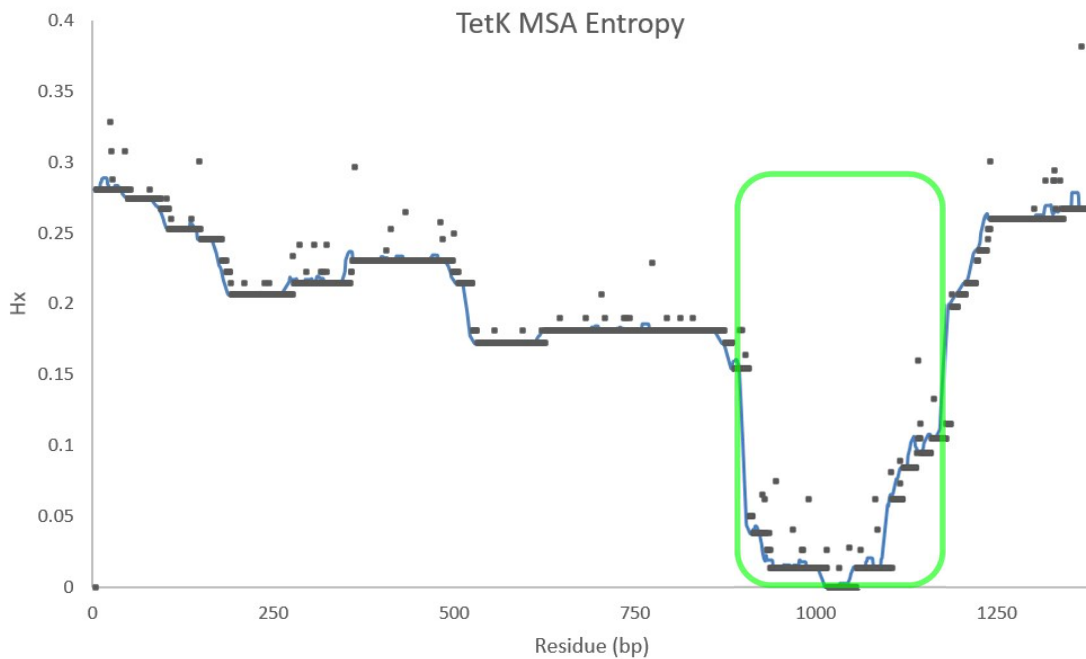


Figure 2.5. Multi sequence alignment entropy plot of *TetK* (Tetracycline resistance efflux protein K, tetracycline resistance factor) consensus sequence, compiled from 234 sequences. Black, residue point entropies. Blue, exponential weighted moving average ($p=10bp$, $\alpha=0.1$). Green, areas of high conservation.

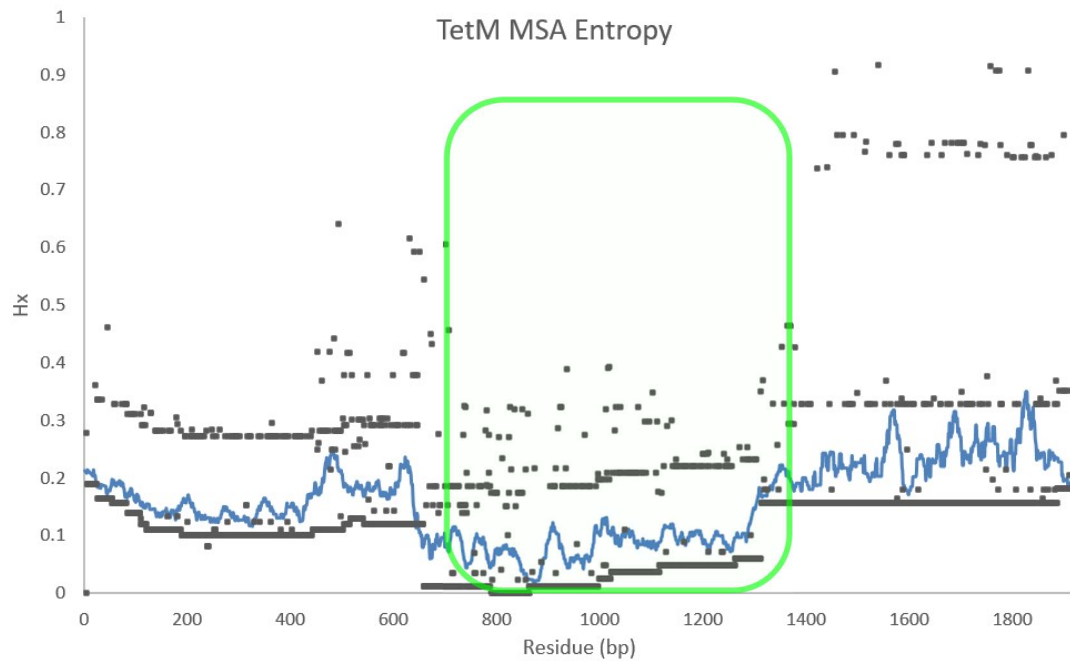


Figure 2.6. Multi sequence alignment entropy plot of TetM (Tetracycline resistance efflux protein M, tetracycline resistance factor) consensus sequence, compiled from 285 sequences. Black, residue point entropies. Blue, exponential weighted moving average ($p=10bp$, $\alpha=0.1$). Green, areas of high conservation.

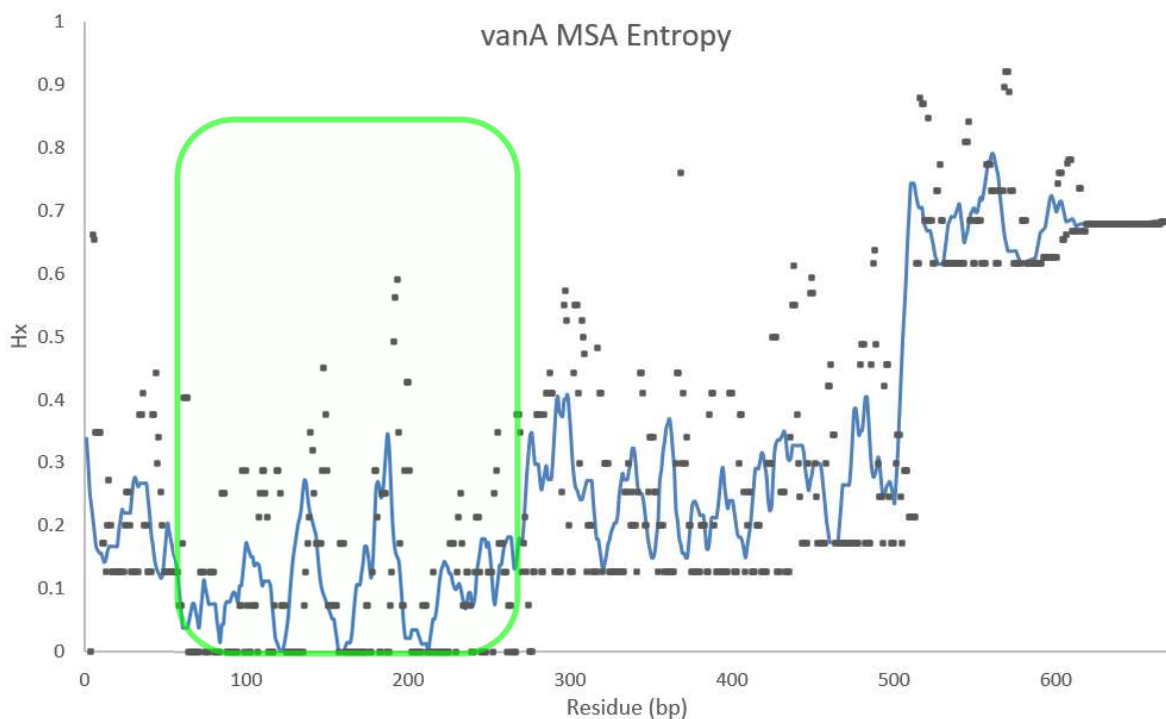


Figure 2.7. Multi sequence alignment entropy plot of VanA (Vancomycin/teicoplanin A-type resistance protein) consensus sequence, compiled from 72 sequences. Black, residue point entropies. Blue, exponential weighted moving average ($p=10bp$, $\alpha=0.1$). Green, areas of high conservation.

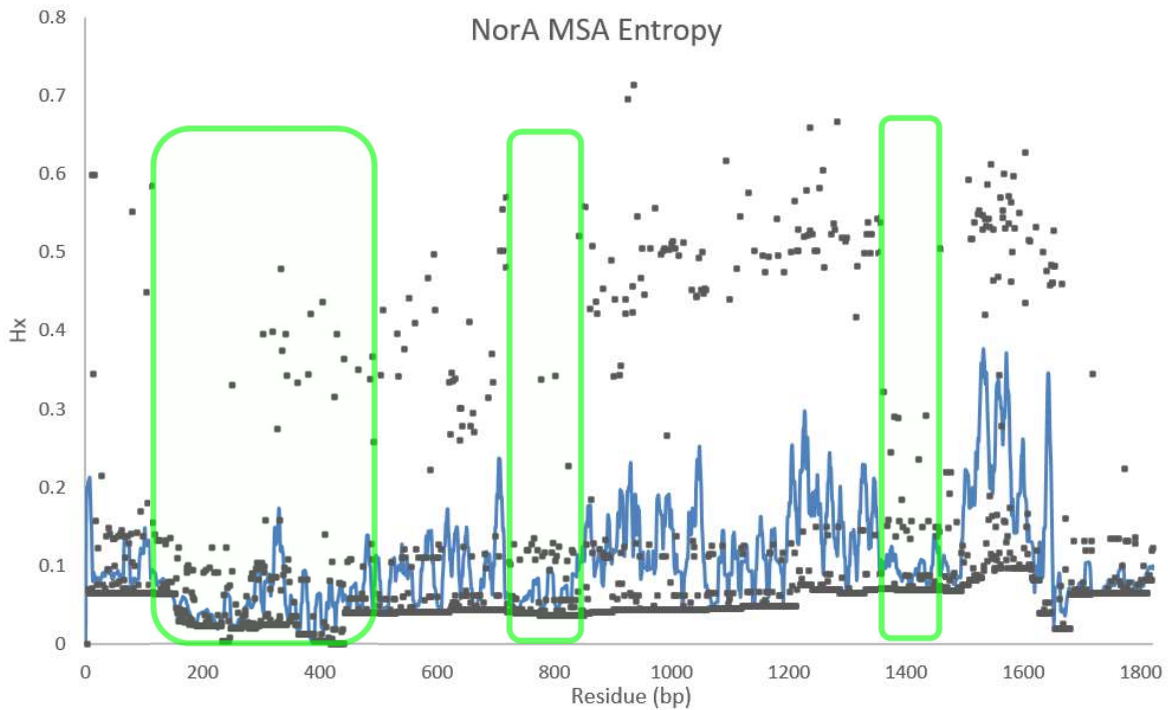


Figure 2.8. Multi sequence alignment entropy plot of NorA (NorA influx pump, quinolone resistance factor) consensus sequence, compiled from 1,459 sequences. Black, residue point entropies. Blue, exponential weighted moving average ($p=10bp$, $\alpha=0.1$). Green, areas of high conservation.

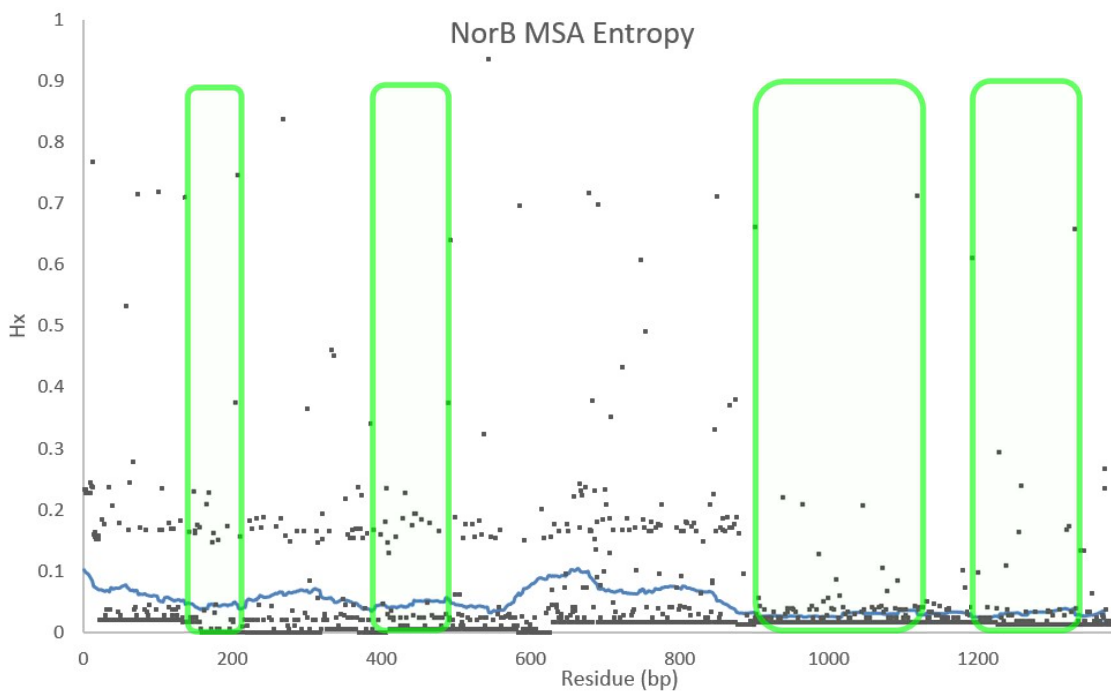


Figure 2.9. Multi sequence alignment entropy plot of NorB (NorB multidrug efflux transporter, fluoroquinolones-tetracycline-biocide resistance factor) consensus sequence, compiled from 1,380 sequences. Black, residue point entropies. Blue, exponential weighted moving average ($p=100bp$, $\alpha=0.25$). Green, areas of high conservation.

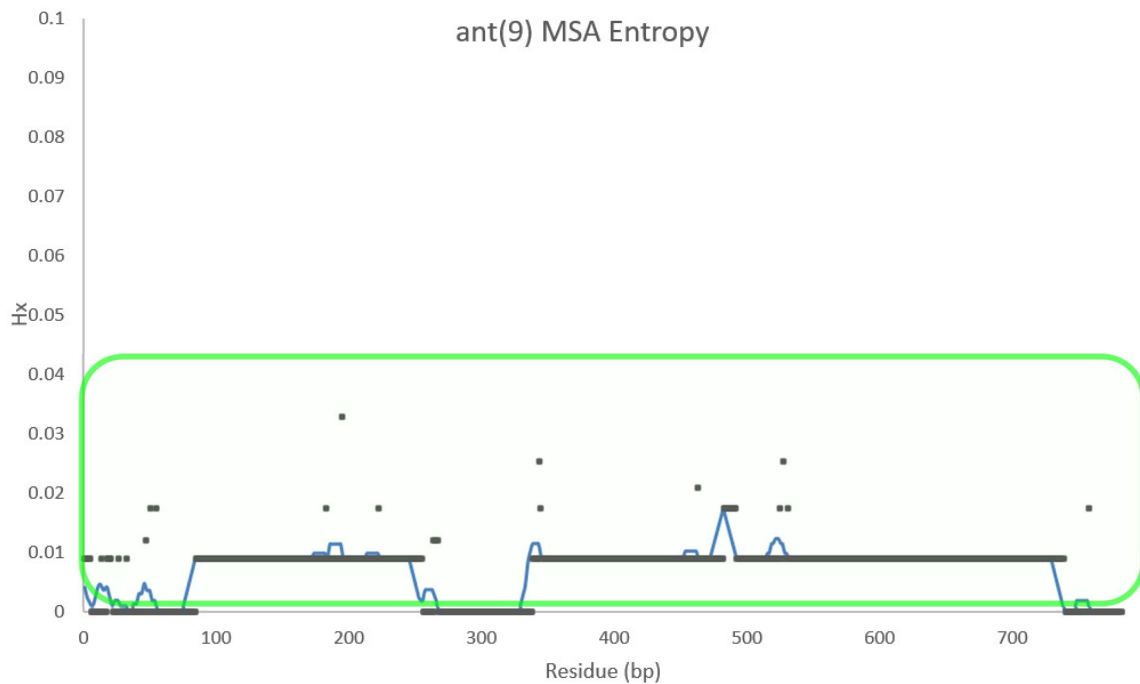


Figure 2.10. Multi sequence alignment entropy plot of *ant(9)* (Spectinomycin 9-adenylyltransferase, aminoglycoside factor) consensus sequence, compiled from 622 sequences. Black, residue point entropies. Blue, exponential weighted moving average ($p=5bp$, $\alpha=0.05$). Green, areas of high conservation.

Discussion:

The presented entropy plots play a critical role in efficiently identifying conserved regions within target genes. In these plots, the areas with the lowest entropies (*highlighted in green fig. 2.1-2.10*) indicate regions with the least variability across the population of aligned DNA sequences related to a specific target gene. These stable regions, often referred to as consensus sequences, serve as the designated targets when generating potential primer sequences. As a result, they provide the most reliable primer sequences capable of working effectively across all known variations of that specific gene.

Traditionally, when creating standard PCR primers, this task is usually automated through tools like the NCBI's BLAST primer design tool. However, in cases involving complex genetic information, large genes of interest, and non-PCR based amplification techniques, relying solely on NCBI's BLAST tool can lead to suboptimal primer sequences. This is due to the limited computational resources allocated for each query. By identifying these conserved regions manually, we significantly streamline the parameters when querying the NCBI. This step is crucial because poorly defined primer sequences can result in unintended amplification artifacts, which do not become apparent until experimentally verified. Consensus areas were selected manually. When identifying conserved areas,

the average entropy is initially used, however it is essential to not allow the consensus sequences to have large areas of high point entropy (*Black points above the moving average fig. 2.1-2.9*).

Table 2.1. Consensus sequence's locations relate to parent gene.

Target gene	Consensus sequence Loci of target gene 5'-3'
MecA	211-503, 1274-1809
Ant4'	0-298, 312-752
BleO	15-37, 55-80, 124-157, 172-222, 255-267, 281-321
ermA	3-57, 312-423, 681-721
TetK	831-1123
TetM	631-1378
VanA	66-279
NorA	168-498, 774-880, 1380-1560
NorB	169-210, 391-532, 749-1164, 1203-1398
ant(9)	Full gene

2.3-Antimicrobial resistance RPA gene primer and probe sequence selections:

Following the identification of the consensus sequences shown in *Table 2.1*. Primer amplification and internal hybridisation sequences for each identified AMR gene found in MRSA were developed. Both sequence functions will become apparent in later sections of this chapter. To do so the Primer3-BLAST algorithm, utilising the NCBI nr and RefSeq databases was used. The algorithmic parameters used were as follows:

Primers required at least three total mismatches to unintended targets, including three mismatches within the last 7 bps at the 3' end. Targets that had six or more mismatches to the primer were ignored. A BLAST stringency factor (E) of 50,000 was used. For primer structural parameters recombinase polymerase amplification (RPA) sequence parameters were used. Product size: 150-250bp. Primer size: 28-30-32 bp. GC%: 25-40%. Internal hybrid size: 34-36 bps.

Primer pair specificity checking was performed, and user guided via the multi sequence alignment entropy data presented in *section 2.1*. Additionally, when designing primers for any DNA amplification system it is essential that a library of potential sequences be produced. It may appear that a single sequence is significantly superior during the *in-silico* design process, but such a sequence may perform poorly experimentally. Furthermore, primer sets that may appear similar *in-silico* can have vastly different kinetic properties which cannot be foreseen due to interactions not modelled by

the Primer3-BLAST algorithm. However, these differences can prove useful later in the development process when matching of primer efficiencies is required in multiplex reactions.

Doing so yielded the following sequence libraries shown in *tables 2.2-2.11* for each MRSA antimicrobial resistance gene.

Table 2.2. Oligonucleotide primer pairs and hybridisation probe sequences for mecA.

Target	Oligo-sequence 5'-3'	Name	Amplicon size
MecA	TTGTAGTTGTCGGGTTTGGTATATATTTTTATG	MecA F1	186bp
	CGCCTAAACTATTATATATTTTTATCGGACGTT	MecA R1	
	TTGTTCCACTTATTTTAATAGTTGTAGTTGTCG	MecA F2	194bp
	ATATATTTTTATCGGACGTTCAGTCATTTCTAC	MecA R2	
	TGTAGTTGTCGGGTTTGGTATATATTTTTATG	MecA F3	173bp
	TATATATTTTTATCGGACGTTCAGTCATTTCT	MecA R3	
	TGTTCCACTTATTTTAATAGTTGTAGTTGTCG	MecA F4	199bp
	ACTATTATATATTTTTATCGGACGTTCAGTCA	MecA R4	
	ATTGTTCCACTTATTTTAATAGTTGTAGTTGT	MecA F5	194bp
	TATATTTTTATCGGACGTTCAGTCATTTCTAC	MecA R5	
	CTTATTTTAATAGTTGTAGTTGTCGGGTTTG	MecA F6	188bp
	TTATATATTTTTATCGGACGTTCAGTCATTTCT	MecA R6	
	ATTGTGCAATTGAAGATAAAAATTTCAAACAAGTT	MecA Int1-6	Probe
	GTATGCAACAAGTCGTAAATAAAACACATAAAG	MecA F7	192bp
	CTTGATACATCTTTAACATTAATAGCCATCATCA	MecA R7	
	TATAGATCTTATGCAAACCTTAATTGGCAAATCC	MecA F8	210bp
	ATATAGCTCATCATACACTTTACCTGAGATTTT	MecA R8	
	AACAAGTCGTAAATAAAACACATAAAGAAGAT	MecA F9	245bp
	ATATAGCTCATCATACACTTTACCTGAGATTT	MecA R9	
	ATAGATCTTATGCAAACCTTAATTGGCAAATCC	MecA F10	225bp
	TTTTATTACCGTTCTCATATAGCTCATCATAC	MecA R10	
	ACAAGTCGTAAATAAAACACATAAAGAAGATA	MecA F11	243bp
	TATAGCTCATCATACACTTTACCTGAGATTTT	MecA R11	
	AAAATATCAATCTATTAAGTATGGTATGCAA	MecA F12	232bp
CTAGCCATTCTTTATCTTGATACATCTTTAAC	MecA R12		
TGGCGACAAATTGGGTGGTTTATATCATATGATAA	MecA Int7-12	Probe	

Table 2.3. Oligonucleotide primer pairs and hybridisation probe sequences for *ant(4')*.

Target	Oligo-sequence	Name	Amplicon size
Ant(4')	TGAAATTAAGGAACGAATATTGGATAAAATATGG CATAATCTAGTAGAATCTCTTCGCTATCAAAAT	Ant(4') F1 Ant(4') R1	215bp
	GAATATTGGATAAAATATGGGGATGATGTTAAGG AATCTAGTAGAATCTCTTCGCTATCAAAATTCA	Ant(4') F2 Ant(4') R2	198bp
	CGAATATTGGATAAAATATGGGGATGATGTTAAG GCATAATCTAGTAGAATCTCTTCGCTATCAAAA	Ant(4') F3 Ant(4') R3	203bp
	CGAATATTGGATAAAATATGGGGATGATGTTAAG GCATAATCTAGTAGAATCTCTTCGCTATCAAAA	Ant(4') F4 Ant(4') R4	193bp
	ATTGGATGATGTGTGTTCATGTCAACAGAGGAAGCA	Ant(4') Int 1-4	Probe
	TAAAGCAATCAGATCTTCCTTCAGGTTATGA TCAAAATGGTATGCGTTTTGACACATCCACTA	Ant(4') F5 Ant(4') R5:7	176bp
	AGTTAAGCAATCAGATCTTCCTTCAGGTTAT TCAAAATGGTATGCGTTTTGACACATCCACTA	Ant(4') F6 Ant(4') R5:7	178bp
	AATCAGATCTTCCTTCAGGTTATGACCATC TCAAAATGGTATGCGTTTTGACACATCCACTA	Ant(4') F7 Ant(4') R7-5:7	170bp
	GTCTGTCAACTTTCCGACTCTGAGAAACTTCTGGA	Ant(4') Int 5-7	Probe

Table 2.4. Oligonucleotide primer and hybridisation probe sequences for *BleO*.

Target	Oligo-sequence	Name	Amplicon size
BleO	TTATTGCGATAAACTAGGTTTCACFTTTGGTTC GTTGATATAATTCATCAATCCCTCTACTTCA	bleO F1 bleO R1	215bp
	TTATTGCGATAAACTAGGTTTCACFTTTGGTT TGTGATATAATTCATCAATCCCTCTACTTTC	bleO F2 bleO R2	216bp
	TCTAATGTGTAATGAGGTTCCGATTCATCTAT ATGCCCAAAGGC TTAATATGTTGATATAATTC	bleO F3 bleO R3	180bp
	TATTGCGATAAACTAGGTTTCACFTTTGGTTC TTGATATAATTCATCAATCCCTCTACTTCAA	bleO F4 bleO R4	213bp
	CTAATGTGTAATGAGGTTCCGATTCATCTAT TGCCCAAAGGC TTAATATGTTGATATAATTC	bleO F5 bleO R5	178bp
	CTAATGTGTAATGAGGTTCCGATTCATCTAT TGCCCAAAGGC TTAATATGTTGATATAATTC	bleO F6 bleO R6	212bp
	TTATTGCGATAAACTAGGTTTCACFTTTGGT ATATAATTCATCAATCCCTCTACTTCAATGC	bleO F7 bleO R7	211bp
	TAAATGTGTAATGAGGTTCCGATTCATCTAT GCCCAAAGGC TTAATATGTTGATATAATTC	bleO F8 bleO R8	176bp
	GATGAGGCTGGCGCTCTCGTAGTAATGATTCACCGG	bleO Int 1-8	Probe

Table 2.5. Oligonucleotide primer and hybridisation probe sequences for *ermA*.

Target	Oligo-sequence	Name	Amplicon size
ermA	TATATTTAGCCTGACTTTCAAAGGTAATTCCTT	ermA F1	153bp
	GTTGATATAAATTCATCAATTC CCTCTACTTCA	ermA R1	
	TAGCTATATTTAGCCTGACTTTCAAAGGTAAT	ermA F2	150bp
	CTCTGAGAATATAAAAAGTGATTCAAACGGATA	ermA R2	
	ATATTTAGCCTGACTTTCAAAGGTAATTCCTT	ermA F3	153bp
	GTAACCCCTCTGAGAATATAAAAAGTGATTCT	ermA R3	
	GCTATATTTAGCCTGACTTTCAAAGGTAATTC	ermA F4	154bp
	AAACCCCTCTGAGAATATAAAAAGTGATTCAA	ermA R4	
	CTATATTTAGCCTGACTTTCAAAGGTAATTCCTT	ermA F5	156bp
	GGTAAACCCCTCTGAGAATATAAAAAGTGATTCT	ermA R5	
	ATAGCTATATTTAGCCTGACTTTCAAAGGTAAT	ermA F6	150bp
	TCTGAGAATATAAAAAGTGATTCAAACGGATA	ermA R6	
	CTATATTTAGCCTGACTTTCAAAGGTAATTC	ermA F7	152bp
	AACCCCTCTGAGAATATAAAAAGTGATTCAAAC	ermA R7	
AGGATATTACCATATATCTTATAGTTTATATGTTT	ermA Int 1-7	Internal	

Table 2.6. Oligonucleotide primer and hybridisation probe sequences for *TetK*.

Target	Oligo-sequence	Name	Amplicon size
TetK	TATTTAAAGTAAATGGTACCTGGTAAATCAACAA	TetK F1 C12	210bp
	TTTTCCCTAGTTTAGGATTAATAAAAAGGGTT	TetK R1	
	TTATTTAAAGTAAATGGTACCTGGTAAATCAACA	TetK F2 C12	206bp
	CCCTAGTTTAGGATTAATAAAAAGGGTTAGAAA	TetK R2	
	GGTCTTACCTACTTATACCTTCCATGATTACA	TetK F3 C12	250bp
	TTAGGATTAATAAAAAGGGTTAGAAACTCTTGA	TetK R3	
	GCTATATTTAGCCTGACTTTCAAAGGTAATTC	TetK F4 C12	211bp
	AAACCCCTCTGAGAATATAAAAAGTGATTCAA	TetK R4	
	ATTTAAAGTAAATGGTACCTGGTAAATCAACAAA	TetK F5 C12	205bp
	TCCCTAGTTTAGGATTAATAAAAAGGGTTAGAA	TetK R5	
	TTATTTAAAGTAAATGGTACCTGGTAAATCAAC	TetK F6 C12	209bp
	TTCCCTAGTTTAGGATTAATAAAAAGGGTTAGA	TetK R6	
ATGTTATAAGTATTTATATGTTTTATGTTATTTACGA	TetK Int 1-6	Internal	

Table 2.7. Oligonucleotide primer and hybridisation probe sequences for TetM.

Target	Oligo-sequence	Name	Amplicon size
TetM	ATTTGTATGGACAAATCGTTGACATACATCG	TetM F1	140bp
	GCTTAACAAAAAACAGGATAGGTAAACGTAG	TetM R1	
	ATATTCAAAGCTCAGCAATTTGTATGGACA	TetM F2	199bp
	GGCTTAACAAAAAACAGGATAGGTAAACGTAG	TetM R2	
	ACAAGAAAAACGGATAATACGCTTTTAGAACGTCAGA	TetM Int 1-2	

Table 2.8. Oligonucleotide primer and hybridisation probe sequences for vanA.

Target	Oligo-sequence	Name	Amplicon size
vanA	TATTATATAACAGTGGAGCGATTACAGAATTA	VanA F1	130bp
	CTTAGTATTTTTCCACTGAAAAGAGGTTATCG	VanA R1	
	TTATTAATATTGGAGTTTTAGCTCATGTTGATG	VanA F2	199bp
	TTAGTATTTTTCCACTGAAAAGAGGTTATCG	VanA R2	
	CTACTCCGCCTTTTGGGTTATTAATAAAGATGATA	VanA Int 1-2	

Table 2.10. Oligonucleotide primer and hybridisation probe sequences for norA.

Target	Oligo-sequence	Name	Amplicon size
norA	CTAGTATGGGTAAATTTTCATAGGTCCTTTAATC	NorA F1	238bp
	AAATTCATAAGAAAAACGATGCTAAATCATTCAT	NorA R1	
	AAATTAATTTTTCTAATAATTGCTGGAGAAAGGC	NorA F2	230bp
	TATGCTACATATTTTGTTCCTTCAATTTTGCT	NorA R2	
	ATAATGTTAATCAGTTTTGTTGTCCTTCATAGG	NorA F3	243bp
	AAATAAAACAATAACAACACCTGCTAATGAAA	NorA R3	
	TAAATGTTAATCAGTTTTGTTGTCCTTCATAGGT	NorA F4	246bp
	TTTCAATTAAAACAATAACAACACCTGCTAAT	NorA R4	
	ACTAGTATGGGTAAATTTTCATAGGTCCTTTAAT	NorA F5	125bp
	TTTTCAATTAAAACAATAACAACACCTGCTAA	NorA R5	
	GCCATTACAAATTAATTTTTCTAATAATTGCTGG	NorA F6	239bp
	TTATGCTACATATTTTGTTCCTTCAATTTTGCT	NorA R6	
	ATTTATGTACACATTGAAGCACCAATTTATATGGCT	NorA Int 1-6	Internal

Table 2.10. Oligonucleotide primer and hybridisation probe sequences for *norB*.

Target	Oligo-sequence	Name	Amplicon size
norB	ACTAAAAGATCCAAATTGCAATAGCTAATAAAG TCTCTAAATAAATTTGACATTAAAGGTC TGGT	NorB F1 NorB R1	147bp
	GCACGCTTTTCAAGAACTATAAAATAAATAAA TCTAAATAAATTTGACATTAAAGGTC TGGTTC	NorB F2 NorB R2	171bp
	TAGCACGCTTTTCAAGAACTATAAAATAAATA CTAAATAAATTTGACATTAAAGGTC TGGTTC	NorB F3 NorB R3	172bp
	AAAAGATCCAAATTGCAATAGCTAATAAAGTAA TAAATTTGACATTAAAGGTC TGGTCTTTTAG	NorB F4 NorB R4	136bp
	AAACTAAAAGATCCAAATTGCAATAGCTAATAA TTATTAAGGCACACCTGAAACTAAATCTAAA	NorB F5 NorB R5	187bp
	TTTGTAGCACGCTTTTCAAGAACTATAAAATAA TCTTTTAGTCATTATGCTCCTCAGTTTAAATA	NorB F6 NorB R6	239bp
	AAGTAGGTTACACCTAATTC TGTATCC TTTAGTAAT	NorB Int 1-6	Internal

Table 2.11. Oligonucleotide primer and hybridisation probe sequences for *ant(9)*.

Target	Oligo-sequence	Name	Amplicon size
Ant(9)	AGATTTATTTGGAAGTTC AATAGTTGGAGTAT ATTTCCAATCTTTCC TGATATAGTCATTAGTC	Ant(9) F1 Ant(9) R1	175bp
	GTTCAATAGTTGGAGTATATCTATTTGGTTCA TATATAAATTC TCTTTTGGAGGATATTGCCA	Ant(9) F2 Ant(9) R2	250bp
	AAAAGATTTATTTGGAAGTTC AATAGTTGGAG CAATCTTTCC TGATATAGTCATTAGTC TTTCT	Ant(9) F3 Ant(9) R3	173bp
	CAATTTGATTAACGGAAAAATACCAAA TCAAG ATCTTTCC TGATATAGTCATTAGTC TTTCTGT	Ant(9) F4 Ant(9) R4	225bp
	TTCAATAGTTGGAGTATATCTATTTGGTT CAG GTATATAAATTC TCTTTTGGAGGATATTGCC	Ant(9) F5 Ant(9) R5	250bp
	AAGATTTATTTGGAAGTTC AATAGTTGGAGTA TTTCC TGATATAGTCATTAGTC TTTCTGTTAG	Ant(9) F6 Ant(9) R6	166bp
	AGTTCAATAGTTGGAGTATATCTATTTGG TTC CTTTCC TGATATAGTCATTAGTC TTTCTGTTA	Ant(9) F7 Ant(9) R7	153bp
	GAAGTTCAATAGTTGGAGTATATCTATTTGG T TCTTTCC TGATATAGTCATTAGTC TTTCTGTT	Ant(9) F8 Ant(9) R8	156bp
	GGAAGTTCAATAGTTGGAGTATATCTATTTGG TCCAATCTTTCC TGATATAGTCATTAGCTTT	Ant(9) F9 Ant(9) R9	162bp
	AAGTTCAATAGTTGGAGTATATCTATTTGG TT TTCCAATCTTTCC TGATATAGTCATTAGCTTT	Ant(9) F10 Ant(9) R10	161bp
	ATACCAAA TCAAGCGATTC AAACATTA AAAAAT TTTCCAATCTTTCC TGATATAGTCATTAGCTCT	Ant(9) F11 Ant(9) R11	212bp
	TGTAATGTTCTAGTCGTCG TGAATCATAGTTTACC	Ant(9) Int 1-11	Internal

2.4-Novel NALFA compatible RPA scheme and functional mechanisms:

To the sequences produced in *section 2.2*, modifications were made to the forward, reverse primers, and hybridisation probes. The modifications made to the primers allow for the detection produced amplicons on the novel NALFA. Whereas the modifications made to the internal probes, are to allow for the monitoring of the RPA reaction amplification kinetics. Importantly, these probes are not required or used in the final device's amplification stage. However, they used to study each primer sets reaction kinetics during assay development. The modifications made to each are shown in *Figure 2.11*.

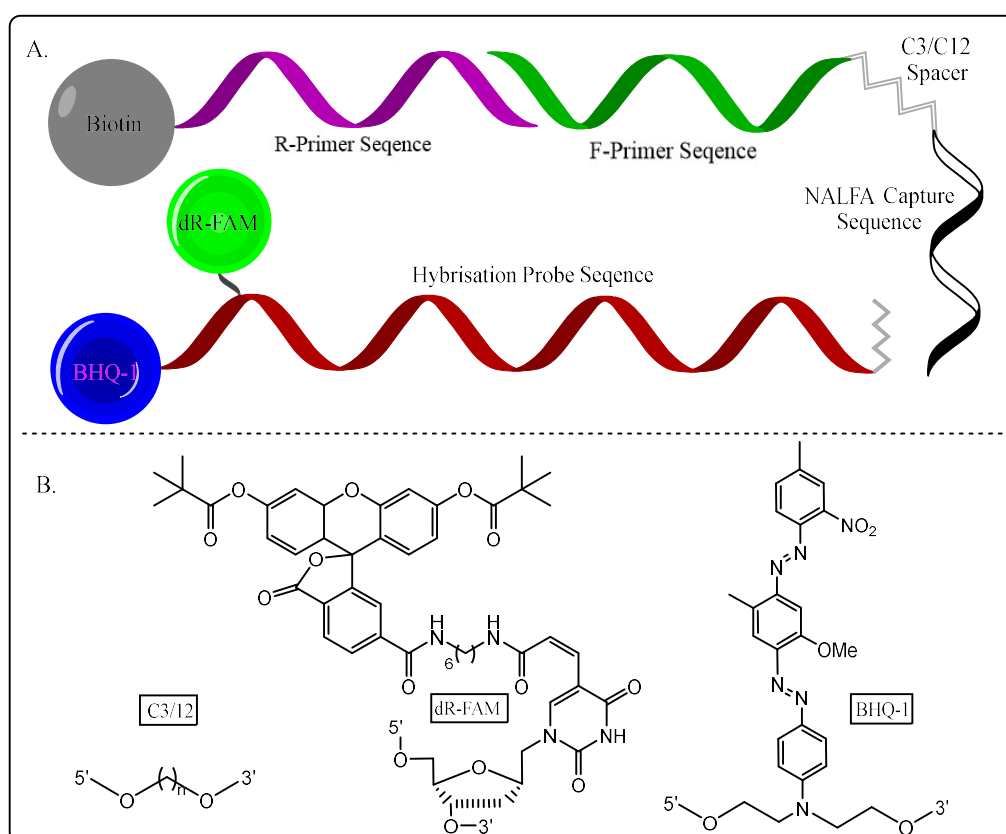


Figure 2.11. A. Structural modification to RPA primers and probes for real-time amplification and NALFA detection. B. Chemical structures of attached/inserted modifications.

A series of unique NALFA capture sequences were developed to facilitate selective capture of each gene on a multiplex NALFA and attached to the reverse primer of each set via a carboxyl spacer. The development of these sequence is discussed further in the proceeding section, to follow is how they function schematically in the present NALFA. Each AMR gene has a unique capture sequence to immobilise its corresponding amplicon in specific locations. If genes encoded for resistance to the same class of anti-microbial agents, they were assigned identical capture sequences. Once added to primers, capture sequences remain single-stranded following RPA amplification due to the C3/12

carboxyl spacer blocking any polymerase activity and do not have a functional role in the RPA reaction (fig. 2.12a).

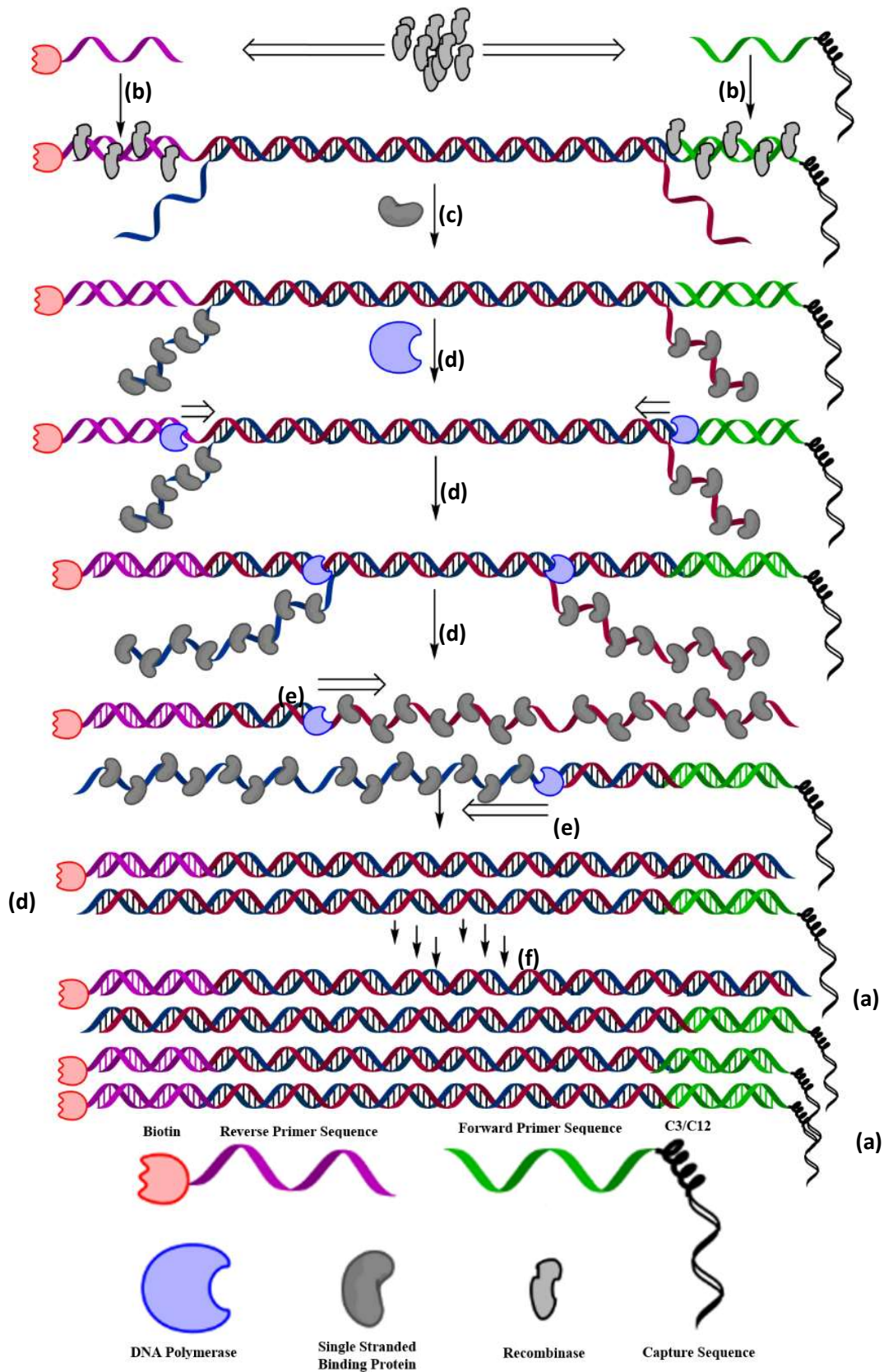


Figure 2.12. Shows the key stages of RPA reactions with modified forward and reverse primers.

During the RPA reactions RecA recombinases form large macromolecular complexes, holding a short ss-DNA strand (primers). This complex entropically denatures the ds-DNA. Unzipped areas of ds-DNA around the complex are stabilised with single-stranded binding protein (SSBP). The RecA(6)-ssDNA complex scans for an area of homology between ss-DNA in complex and the bound ds-DNA. (Fig. 2.12b). Hybridisation between the primer and homologous area of ds-DNA denatures the RecA complex, allowing the protein units to bind to a new piece of ss-DNA. (Fig. 2.12c). With the hybridisation area stabilised with SSBP, DNA polymerase can begin ds-DNA construction as in PCR. (Fig. 2.12d) After this cycle, two types of ds-DNA amplicons are produced, one with a capture probe modified end and the other with a reporter probe modified end. (Fig. 2.12e) Chain reaction of these first amplicons then produces amplicons with capture and reporter probe attached at each end of the amplicon ready for downstream detection. (Fig. 2.12f).

As shown above modifying the forward and reverse primers in this way allows for the attached short oligonucleotide sequence to remain single-stranded. This short single stranded oligonucleotide, attached to the amplicon, is therefore ready for downstream capture and detection on the novel NALFA. The physical construction of which is explored in chapter 7. Figure 2.13 shows how the novel NALFA test line can only be reported if both the forward and reverse primers have been successfully “stitched” together, by an RPA reaction.

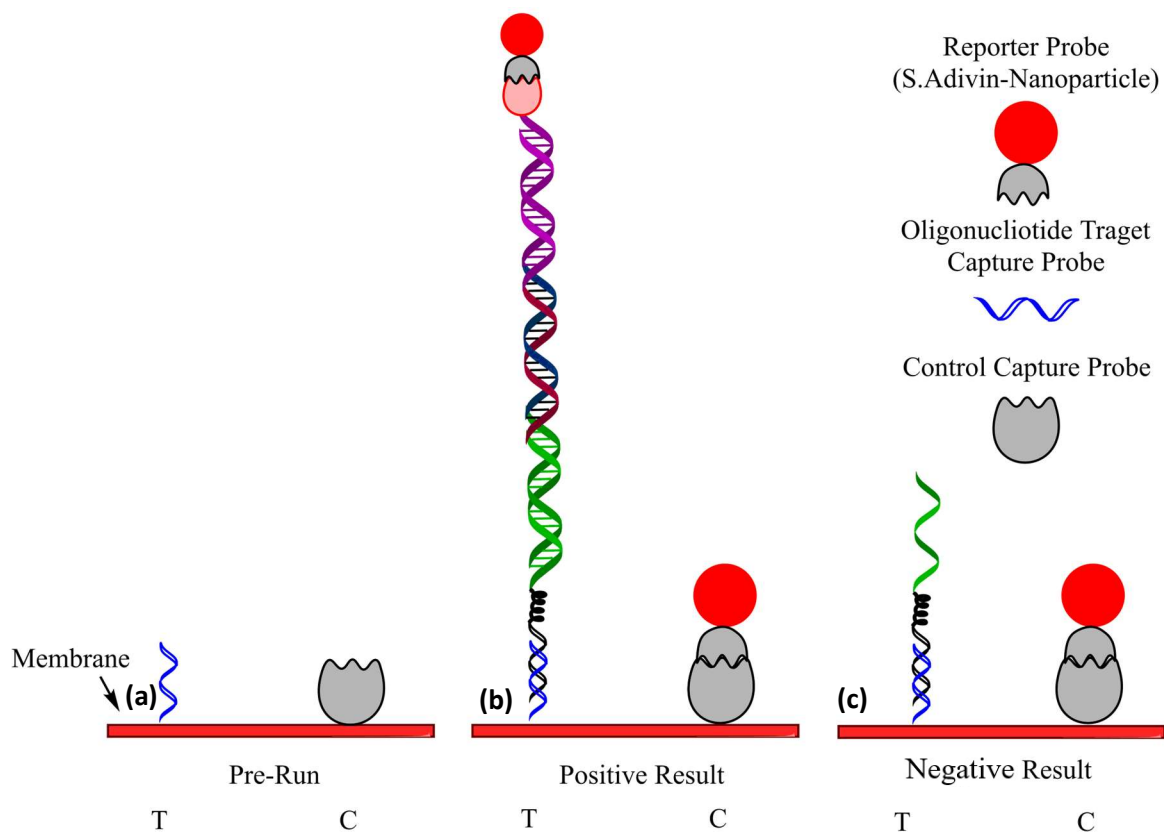


Figure 2.13. Shows NALFA test line layouts.

Pre-run test and control areas of the NALFA are shown, the reverse complement of the unique capture probe sequence; to be added to the amplicon, is presented on the membrane ready to capture the amplicon or unreacted reverse primers. (*Fig. 2.13a*). A positively reported novel NALFA assay test line layout is shown run with a successful RPA reaction sample in *Figure 2.13b*. Here it is clear to see the reporter probes are captured at both the test and control areas of the membrane, due to the successful “stitching” of the two primers by the RPA reaction. A negatively reported novel NALFA assay test line layout is shown run with an unsuccessful RPA reaction sample in *Figure 2.13c*. Here reporter probes can only be captured at the control line of the membrane, thus indicating a negative result where the RPA reaction fails.

Real time monitoring mechanism:

The addition of the dR-FAM and BHQ-1 to the internal probe sequences, in combination with the addition of formamidopyrimidine DNA glycosylase (fpg) to the RPA reactions allows for real-time monitoring of amplicon production akin to real time PCR. The overall schematic for this process is demonstrated in *Figure 2.14*. This is possible as just as shown in *Figure 2.13*, recA recombinases will form large macromolecular complexes with any free ss-DNA in solution. In this case the complex is formed with modified hybridisation probe. Following this the recA-oligonucleotide complexes entropically denature the ds-DNA, and unzipped areas of ds-DNA around the complex are stabilised with single-stranded binding protein (SSBP), the SSBP is not shown in *figure 2.14* for clarity. The complex “scans” for areas of homology along the amplicon sequence. (*Fig 2.14a*). Hybridisation between the probe and a homologous area of ds-DNA denatures the RecA complex, releasing and allowing the protein units to bind to a new piece of ss-DNA. (*Fig 2.14b*). With the hybridised area stabilised with SSBP, formamidopyrimidine DNA glycosylase (fpg) scans the DNA-protein complex and “recognises” the attached dR-FAM. Fpg enzymes are naturally found in *E. Coli*, its role is to repair DNA where point mutations cause mismatched base pairs to “stick out” i.e., denature the secondary structure of ds-DNA. In nature, fpg type enzymes repair these errors by cleaving only the base of the nucleotide; leaving the glycosphosphate backbone intact. In this configuration the fpg enzyme recognises the attached dR-FAM as a “damaged” purine sticking out of the ds-DNA complex. This is achieved via the reverse complement strand misalignment and thus forms a transition complex between the hybridised amplicon probe complex and the fpg enzyme. (*Fig 2.14c*). Following this the dR-FAM is catalytically cleaved by the N-glycosylase activity of fpg, leaving an aprotic site within the probe and FAM free in solution. (*Fig 2.14d*). No longer chemically bound to the BHQ-1 quencher, the FAM molecules can fluoresce, the intensity of which can be measured to monitor the RPA reaction. (*Fig 2.14e*). To work correctly, dR-FAM must be substituted for an adenine or guanine residue with a

four-residue gap to the 5' attached quencher, this ensures fpg activity and also effective coupling between the fluorophore and quencher. When the FAM molecule is excited by excitations photons it is able to relax via covalent electron coupling to the BHQ molecule in lieu of releasing an emission photon. As a result, we have an enzymatically regulated process whereby a proportional amount of fluorescent probe can be selectively de-coupled from the quencher, as the reaction products concentration increases. However, much like RT-PCR this system has its issues. Different entropies of hybridisation between different probes and different amplicons alter the rate of hybridisation of the transition complexes. Thus, making direct comparison between primer sets kinetics difficult.

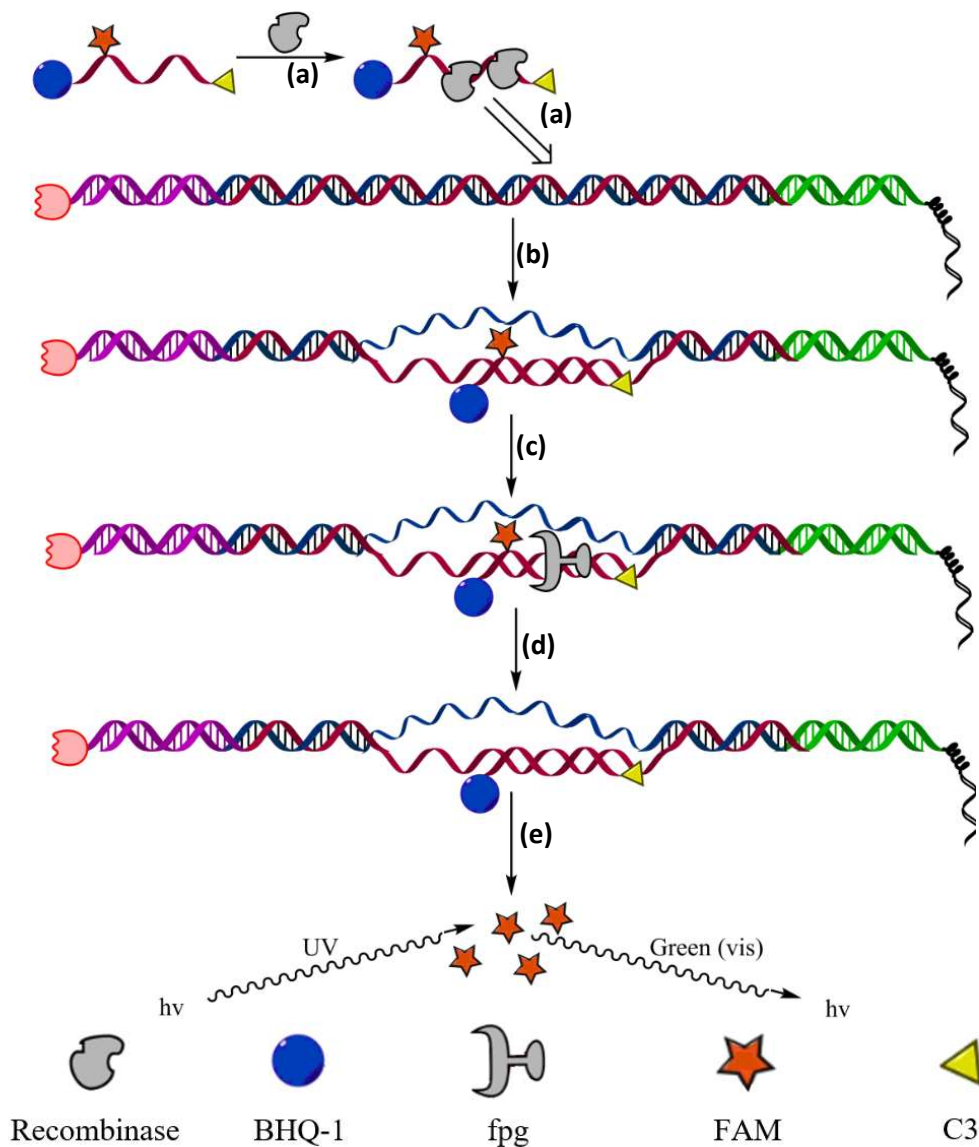


Figure 2.14. Illustrates the process of FAM release from an amplicon that has formed a hybrid with an RPA black hole quenched fluorescent probe. This release occurs within the context of an RPA reaction combined with modified hybridization probe and the addition of fpg enzyme to the reaction mixture.

2.5 - NALFA multiplex capture probe development:

The sequences derived in this chapter are key to the flexibility of the reported system. To accommodate any primer sequence required to target a desired gene, it is vital the proposed nucleic acid capture sequences do not interact in any significant way with possible target nucleic acid sequences. Furthermore, it is most important that the capture sequences perform their main function of selectively capturing the attached amplicon. Therefore, they must interact strongly with their reverse complements and ideally repel the other capture sequence that are not complementary. To achieve this the capture sequences were iteratively designed to 5 main requirements; these were, in order of priority:

- Capture sequences must have minimal cross-reactivity, $\Delta G_{\text{hybridisation}} < -10 \text{ kcal mol}^{-1}$ at 0.5 μM .
- Capture and non-complementary reverse sequences must have minimal cross-reactivity, $\Delta G_{\text{hybridisation}} < -15 \text{ kcal mol}^{-1}$ at 0.5 μM .
- Capture and reverse complement sequences must have similar and high $\Delta G_{\text{hybridisation}} > -30 \text{ kcal mol}^{-1}$ at 0.5 μM
- Capture and reverse complement sequences must have low $\Delta G_{\text{loop}} < -1 \text{ kcal mol}^{-1}$ at 0.5 μM 20 °C
- Capture sequences must not complement any likely sample matrix or target genetic material.

Design requirements were achieved by manually generating initial sequences and calculating all $-\Delta G_{\text{hybridisation}}$. The theoretical performance (P) was assessed using a specificity ratio described by equation 1.

$$P = \frac{\sum \Delta G_i}{\Delta G_{\text{CS-R}}} \quad \mathbf{1}$$

$$\Delta G_i = \textit{intermolecular interaction}$$
$$\Delta G_{\text{CS-RC}} = \textit{Free energy of capture probe and reverse complement interaction}$$

The undesired cross-reactivities of the poorest performing sequences were manually assessed, and point modifications were made. The impact on specificity ratios was assessed by recalculation of the $-\Delta G_{\text{hybridisation}}$. Point modifications were repeated until little to no gain in the specificity ratios of the sequence set was observed. Before accepting a capture sequence BLASTn analysis was used to identify matches to targets or likely contaminated genetic material. If significant interactions were found, a new sequence formulated, assessed, modified and reassessed. BLASTn trees of the final presented capture sequences are available in *appendix 3*, listing known possible interactions with other genetic materials of the final derived capture sequence which are presented in *table 2.12*.

Table 2.12. shows the library of capture sequences for NALFA

Name	Capture sequence 5'-3'
MecA CP	GGTTAATTGGCCTTCC
Ant(4') CP	TAGCCGTTTTTAGCAA
BleO CP	CCCCAAGTGGTTCAC
ermA CP	TGGTCCATCGCTAGGTC
tetK/M CP	CGCGCATGACTAGAGC
vanA CP	TTATATAACGGCGATT
NorA/B CP	CCTACTATGGAGCATAAGC
Ant(9) CP	GCGTTATGCTATGCGT

For the final derived capture sequences, the Gibbs free energy of cross reactivity between capture probe sequences and non-complement reverse complement was -5.12 ± 0.13 kcal mol⁻¹. (Fig. 2.15, Green areas)

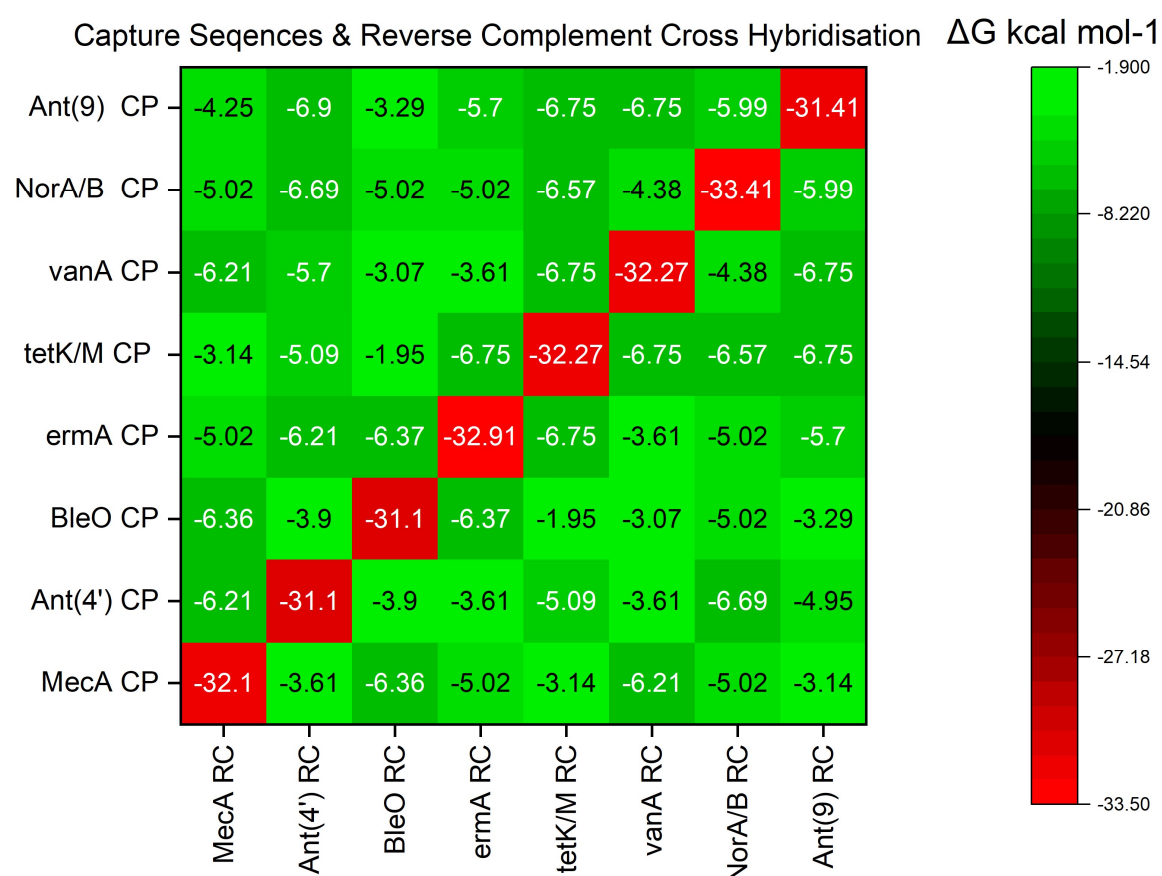


Figure 2.15. Heatmap showing calculated $-\Delta G_{\text{hybridisation}}$ between all capture and reverse complement sequences.

In comparison the average Gibbs free energy of cross reactivity between capture probe sequences and their reverse complements was $-32.07 \pm 0.28 \text{ kcal mol}^{-1}$. (Fig 2.15, red areas & Fig 2.16).

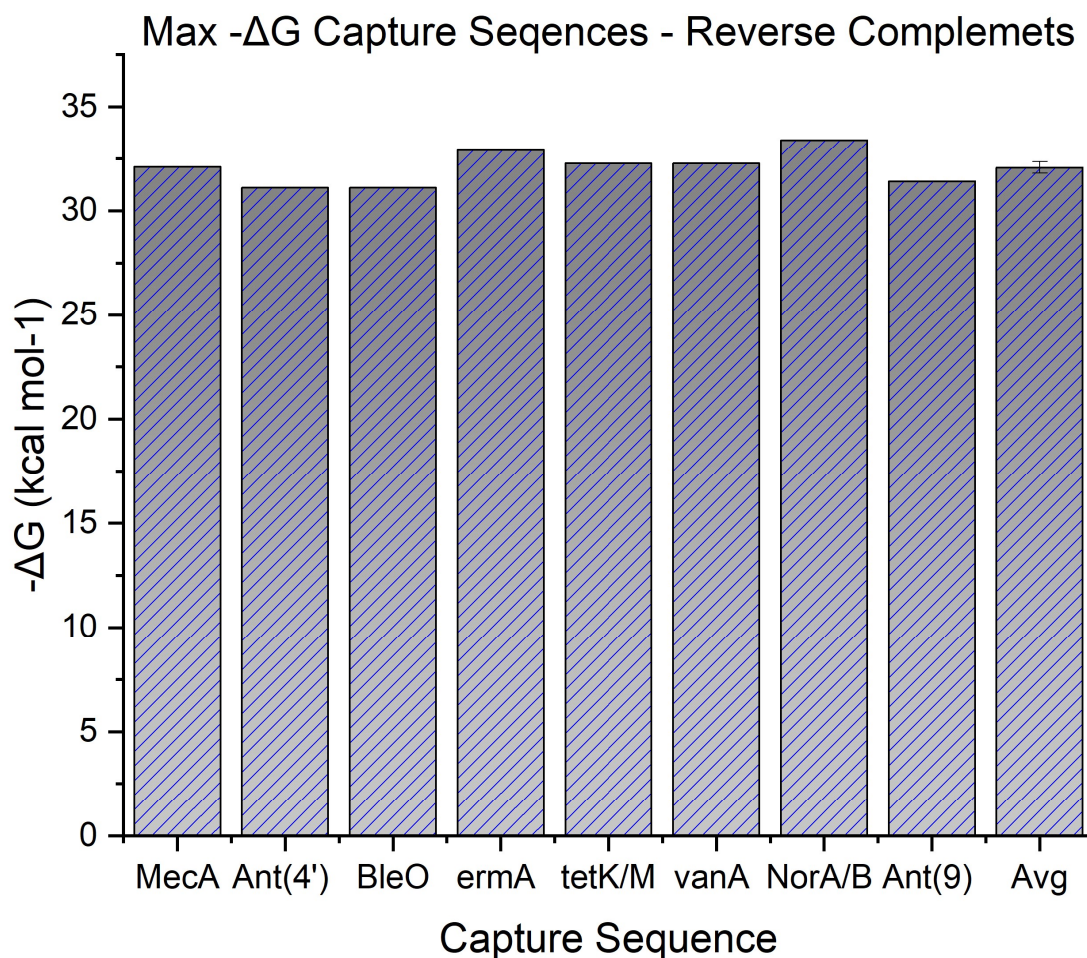


Figure 2.16. Capture sequences complement $-\Delta G_{\text{hybridisation}}$ energy.

It is also essential that that capture sequences do not have highly negative Gibbs free energy of hybridisation to other capture sequences, and conversely that their reverse complements do not either. Consider two primers in solution with two different capture probe sequences. If the two capture probes have highly negative Gibbs free energy of hybridisation to each other; they are likely to form dimerised amplicons when the attached primers are used in a multiplex amplification reaction. As such when run on the proposed NALFA the product will not be captured on the test line, thus producing a false negative result. Furthermore, this holds true if a single capture sequence is complementary to itself in reverse. As such these vital interactions were calculated and are shown in figure 2.17.

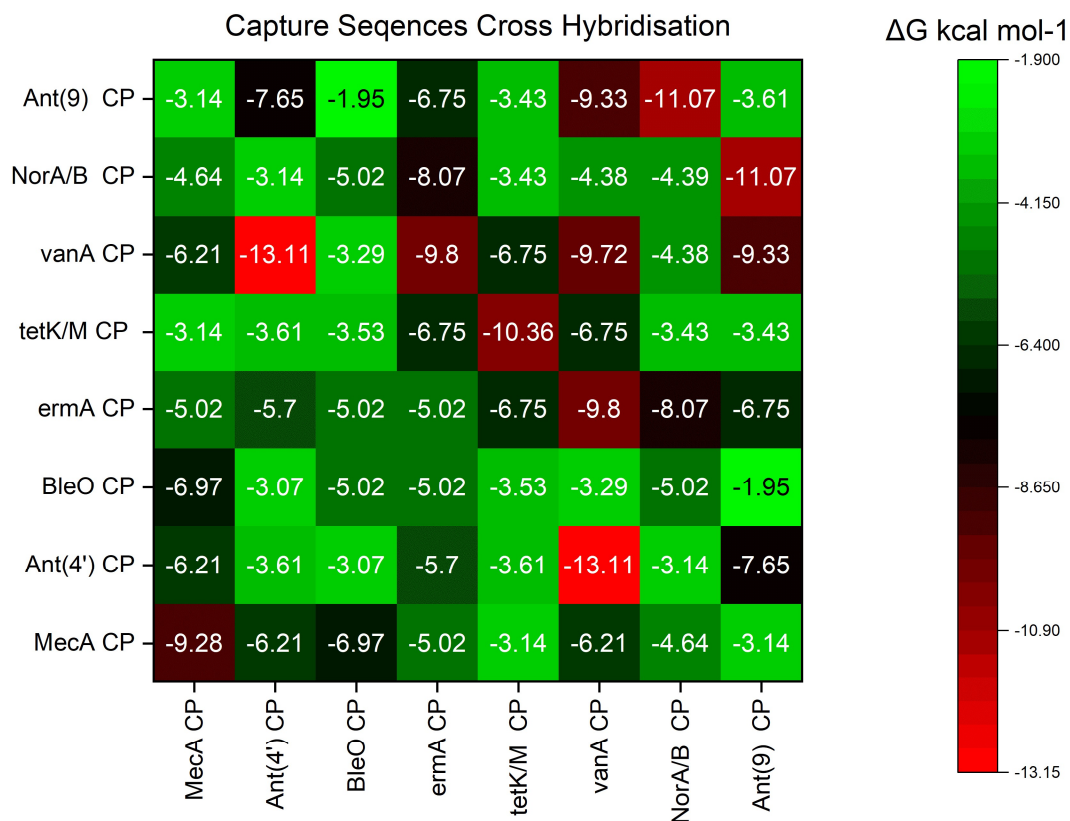


Figure 2.17. Heatmap showing calculated cross $-\Delta G_{\text{hybridisation}}$ between primer attached capture sequences.

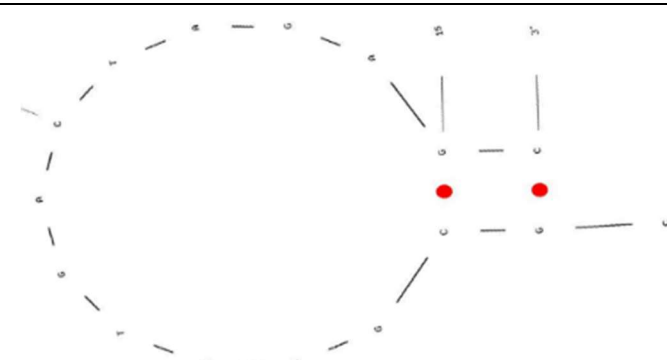
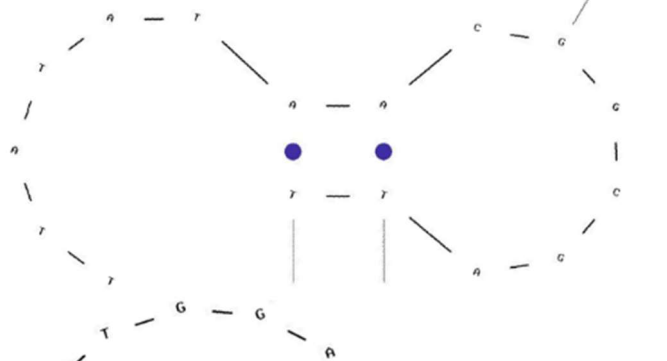
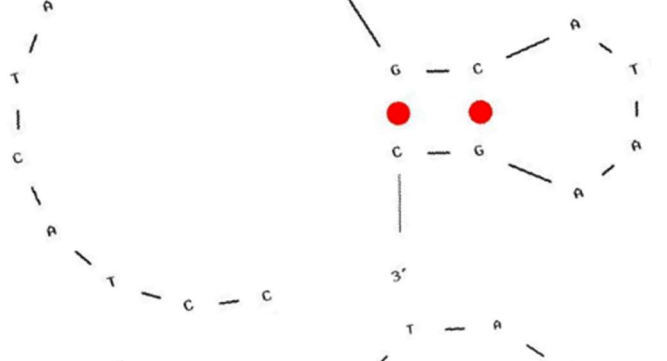
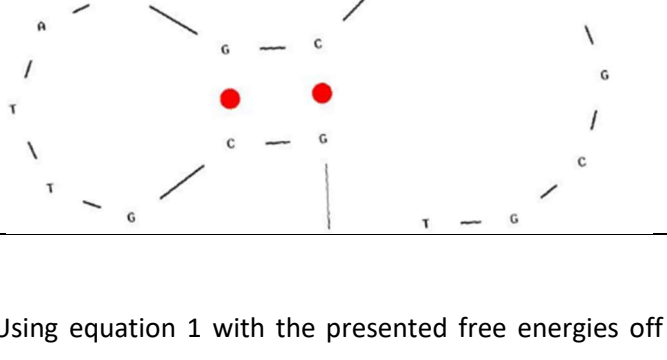
More negative results indicate that the capture sequence may produce unwanted dimerised amplicons if multiplexed in that given pairing. For example pairing the capture sequence allocated to NorA/B and Ant(9). However, it is important to note that these free energy values are calculated without taking into consideration the steric hindrance afforded by significantly larger amplicon linked to the probe. Therefore, when considering three-dimensional structure containing the approximately 200bp amplicon attached to the capture sequence these values are likely significant overestimates. To test this hypothesis the capture sequence which exhibited the largest self-complementary was assigned to the MecA gene. This was done to assess this effect in later experiments which demonstrated it did not cause a significant issue.

Further non-desired intramolecular interactions were considered and calculated using the *UNAFold* algorithm. These interactions are when within the capture sequence itself, and its reverse complements. Secondary structures may form by looping or folding thus stopping the capture sequence from being captured effectively. As such these vital interactions were calculated and are shown in *table 2.13*.

Table 2.13. Most stable capture sequence secondary structures thermodynamically calculated via UNAFold.

Name	2° Structure	ΔG kcal mol ⁻¹	T_m °C	ΔH kcal mol ⁻¹	ΔS kcal K ⁻¹ mol ⁻¹
Meca		0.07	21.3	-16.2	-55
Ant(4')		-0.68	29.5	-21.5	-72.0
Bleo		-0.80	30.7	-22.8	-75.1
ermA		0.09	18.6	-19.2	-47.3

Table 2.13. Cont. Most stable capture sequence secondary structures thermodynamically calculated via UNAFold.

Name	2° Structure	ΔG kcal mol ⁻¹	T_m °C	ΔH kcal mol ⁻¹	ΔS kcal K ⁻¹ mol ⁻¹
tetK/M		0.22	16.6	-18.9	-65.1
vana		1.32	-4.0	-14.8	-54.0
NorA/B		-0.71	33.4	-16.3	-53.0
Ant(9)		-0.93	36.1	-17.9	-57.8

Using equation 1 with the presented free energies off all the possible interactions the specific ratio of each capture sequence was defined. (Fig. 2.18). It is important that this ratio be as close as possible across the set of capture sequences. If there were large variations in these ratios

effectively optimising primer concentrations in multiplexed RPA reactions; as well as blotting concentrations for the coupled NALFA would prove difficult.

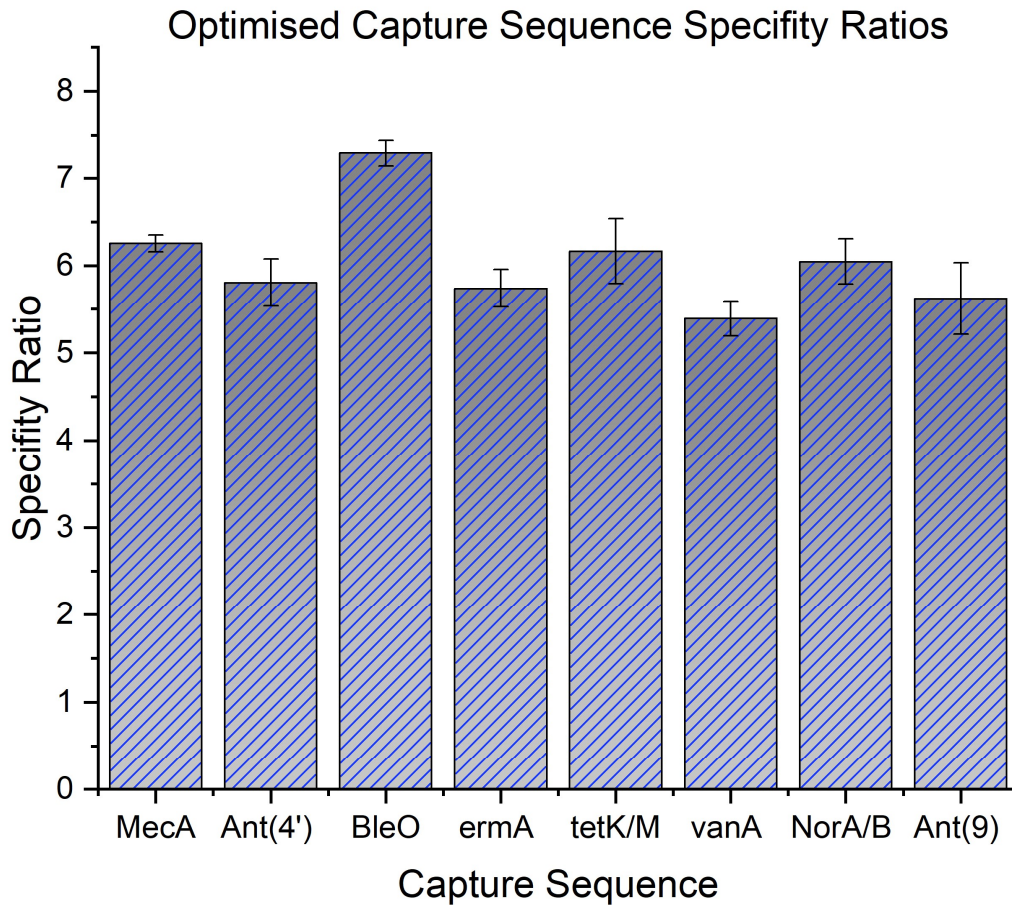


Figure 2.18. Capture sequences specificity ratios with SD's calculated from the $-\Delta G_{\text{cross hybridisation}}$.

In conclusion, the capture sequences presented here have demonstrated their robustness *in silico*, suggesting their potential for strong performance in multiplexed reactions. These sequences closely align with one another across all parameters, and it's essential to note that the process of designing, iterating, and optimizing sequences for this purpose becomes increasingly complex with the addition of each new sequence. This complexity arises from the need for close alignment in performance, and as each sequence is added, the number of possible interactions grows exponentially, following a function of $4n^2$. It may also be possible to discover more compatible better performing sets by utilising HP-compute but as present the limit is 8 using the presented method. Shown in *table 2.14* is the capture sequences and modifications integrated into the primers sequences derived in *section 2.2* that will be used to further develop the proposed system.

Table 2.14. Shows the library RT-RPA primers and probes with NALFA modifications for the development of amplification and NALFA detection of the *mecA* gene. A complete table of all modified primers and probes is available in appendix 4.

Name	Sequence 5'-3'
MecA F1 C12	GGAAGGCCAATTAACC- (C12) - TTGTAGTTGTCGGGTTTGGTATATATTTTTATG
MecA F1 C3	GGAAGGCCAATTAACC- (C3) - TTGTAGTTGTCGGGTTTGGTATATATTTTTATG
MecA R1 Bio	(Biotin) - CGCCTAAACTATTATATATTTTTATCGGACGTT
MecA F2 C12	GGAAGGCCAATTAACC- (C12) - TTGTTCCACTTATTTTAATAGTTGTAGTTGTCG
MecA F2 C3	GGAAGGCCAATTAACC- (C3) - TTGTTCCACTTATTTTAATAGTTGTAGTTGTCG
MecA R2 Bio	(Biotin) - ATATATTTTTATCGGACGTTCACTCATTCTAC
MecA F3 C12	GGAAGGCCAATTAACC- (C12) - TGTTAGTTGTCGGGTTTGGTATATATTTTTATG
MecA F3 C3	GGAAGGCCAATTAACC- (C3) - TGTTAGTTGTCGGGTTTGGTATATATTTTTATG
MecA R3	(Biotin) - TATATATTTTTATCGGACGTTCACTCATTCT
MecA F4 C12	GGAAGGCCAATTAACC- (C12) - TGTTCCACTTATTTTAATAGTTGTAGTTGTCG
MecA F4 C3	GGAAGGCCAATTAACC- (C3) - TGTTCCACTTATTTTAATAGTTGTAGTTGTCG
MecA R4	(Biotin) - ACTATTATATATTTTTATCGGACGTTCACTCA
MecA F5 C12	GGAAGGCCAATTAACC- (C12) - ATTGTTCCACTTATTTTAATAGTTGTAGTTGT
MecA F5 C3	GGAAGGCCAATTAACC- (C3) - ATTGTTCCACTTATTTTAATAGTTGTAGTTGT
MecA R5	(Biotin) - TATATTTTTATCGGACGTTCACTCATTCTAC
MecA F6 C12	GGAAGGCCAATTAACC- (C12) - CTTATTTTAATAGTTGTAGTTGTCGGGTTG
MecA F6 C3	GGAAGGCCAATTAACC- (C3) - CTTATTTTAATAGTTGTAGTTGTCGGGTTG
MecA R6	(Biotin) - TTATATATTTTTATCGGACGTTCACTCATTTC
MecA F7 C12	GGAAGGCCAATTAACC- (C12) - GTATGCAACAAGTCGTAATAAAAACACATAAAG
MecA F7 C3	GGAAGGCCAATTAACC- (C3) - GTATGCAACAAGTCGTAATAAAAACACATAAAG
MecA R7	(Biotin) - CTTGTACATCTTTAACTTAATAGCCATCATCA
MecA F8 C12	GGAAGGCCAATTAACC- (C12) - TATAGATCTTATGCAAACTTAATTGGCAAATCC
MecA F8 C3	GGAAGGCCAATTAACC- (C3) - TATAGATCTTATGCAAACTTAATTGGCAAATCC
MecA R8	(Biotin) - ATATAGCTCATCATACCTTTACCTGAGATTTT
MecA F9 C12	GGAAGGCCAATTAACC- (C12) - AACAAAGTCGTAATAAAAACACATAAAGAAGAT
MecA F9 C3	GGAAGGCCAATTAACC- (C3) - AACAAAGTCGTAATAAAAACACATAAAGAAGAT
MecA R9	(Biotin) - ATATAGCTCATCATACCTTTACCTGAGATTTT
MecA F10 C12	GGAAGGCCAATTAACC- (C12) - ATAGATCTTATGCAAACTTAATTGGCAAATCC
MecA F10 C3	GGAAGGCCAATTAACC- (C3) - ATAGATCTTATGCAAACTTAATTGGCAAATCC
MecA R10	Biotin- TTTTATTACCGTTCTCATATAGCTCATCATAC
MecA F11 C12	GGAAGGCCAATTAACC- (C12) - ACAAGTCGTAATAAAAACACATAAAGAAGATA
MecA F11 C3	GGAAGGCCAATTAACC- (C3) - ACAAGTCGTAATAAAAACACATAAAGAAGATA
MecA R11	(Biotin) - TATAGCTCATCATACCTTTACCTGAGATTTT
MecA F12 C12	GGAAGGCCAATTAACC- (C12) - AAAATATCAATCTATTAACCTGATGGTATGCAA
MecA F12 C3	GGAAGGCCAATTAACC- (C3) - AAAATATCAATCTATTAACCTGATGGTATGCAA
MecA R12	(Biotin) - CTAGCCATTCTTTATCTTTGTACATCTTTAAC
MecA Int1-6 FAM	(BHQ1) - ATTG- (dRFAM) - TGCAAATTGAAGATAAAAAATTCAAACAAGTT- (C3)
MecA Int7-12 FAM	(BHQ1) - TGGC- (dRFAM) - GACAAAATGGGTGGTTTATATCATATGATAA- (C3)

Chapter 3

Methicillin-Resistant Staphylococcus Aureus Reference Materials.

I always look after my bacteria, It's the only culture I know about:

*Cat 2 Biological culture can be a hot and smelly mess,
We work in the heat, we can barely confess,
The stench can be vile, it can be hard to take,
But we must endure, for goodness sake.*

*We toil and sweat, our pipetting nerves fray,
As we try to get our cultures to grow and stay.
We measure and mix, we pipette and pour,
We sterilize, but somehow everything ends up on the floor?*

*The double glove squelch is a sound we know well,
It's a sign of the work, it's a sign of the strain,
But we soldier on, through the heat and the pain.
Our hands are raw, our backs are sore,
But still we must carry on, 'cause that's what we're here for.*

*We work through the day, we work through the night,
We're barely getting by, it's not a pleasant sight,
We're always tired, we're always stressed,
But somehow the results are never the best.*

*So if you think you can handle the heat,
And you're willing to put in the time in the seat,
Then come join us, don't be a fool,
We'll make sure you're a Cat 2 Biological culture mule."*

3.1 Introduction:

A reference MRSA isolate was obtained from the American Type Culture Collection, *Staphylococcus Aureus* Rosenbach ATCC 43300. Collected from a clinical sample in Kansas (USA), this reference isolate is well characterised by Ridom and Kreiswirth¹⁵¹ *spa* typing and has several high-quality annotated whole-genome sequences available. ATCC 43300 is a *pvl* negative, SCCmec type II latent colonising strain and carries target genes of interest. *Figure 3.1*.

tetK	vanA	norA	NorB	ant(9)
✓	✗	✗	✓	✗
mecA	Ant(4')	BleO	ermA	tetM
✓	✓	✓	✓	✗

Figure 3.1. AMR genes of interest found in ATCC 43300 MRSA isolate, WGS genome ID: 1280.16403

3.2 MRSA Rosenbach ATCC 43300 Reference Culture:

A reference *Staphylococcus Aureus* Rosenbach ATCC 43300 freeze-dried pellet was reconstituted in 5mL of brain heart infusion (BHI) broth with 50 µg L⁻¹ kanamycin (250 mL ddH₂O, 9.25 g BHI, 250 µL 50 mg L⁻¹ kanamycin sulphate). The dormant inoculant was activated by temperature gradient incubation over 30 min at 1°C per minute, shaking at 50 rpm. The contents of the vial were removed using a sterile needle and syringe. 675 µl of sterile DMSO was added to 4.5 mL of inoculant and stored at -80 °C. A BHI agar plate with 50 µg L⁻¹ kanamycin (250 mL ddH₂O, 13 g BHI agar, 250 µL 50 mg L⁻¹ kanamycin sulphate) was inoculated with 100 µl of activated *S. Aureus* ATCC 43300 by spreading and incubated at 37 °C for 16 Hr. Shiny gold pigmented colonies were obtained, and several colonies were streaked on a BHI agar plate with 50 µg L⁻¹ kanamycin for isolation. *Figure 3.2*.

Methicillin resistance of the isolated colonies was then confirmed; several were collected by loop and dispersed into 1mL phosphate-buffered saline (PBS) (900mL ddH₂O, 100mL 10X PBS) by 3 min vigorous vortexing. Inoculant was diluted to match a 0.5 McFarland standard (5 µl 1%_{w/v} BaCl₂, 995 µl 1%_{w/v} H₂O₄) with PBS. 10 µl of inoculant was transferred onto the surface of a Mueller-Hinton Agar plate with 2 % NaCl (MHA-salt) (1 L ddH₂O, 38 g MHA, 20 g NaCl), an MHA-salt plate with 2 µg mL⁻¹ oxacillin (1 L ddH₂O, 38 g MHA, 20 g NaCl, 500 µl 4 mg µl⁻¹ sodium oxacillin) and an MHA-salt plate with 4 µg mL⁻¹ oxacillin (1 L ddH₂O, 38 g MHA, 20 g NaCl, 1000 µl 4 mg µl⁻¹ sodium oxacillin) and incubated for 24 hr at 35 °C. Shiny gold pigmented colonies were obtained on all three plates,

indicating the isolates likely desired were pure ATCC 43300 MRSA colonies and not contamination. Colonies were re-plated from the MHA-salt plate with 4 µg/mL oxacillin to a BHI agar plate with 50 µg L⁻¹ kanamycin by streaking.

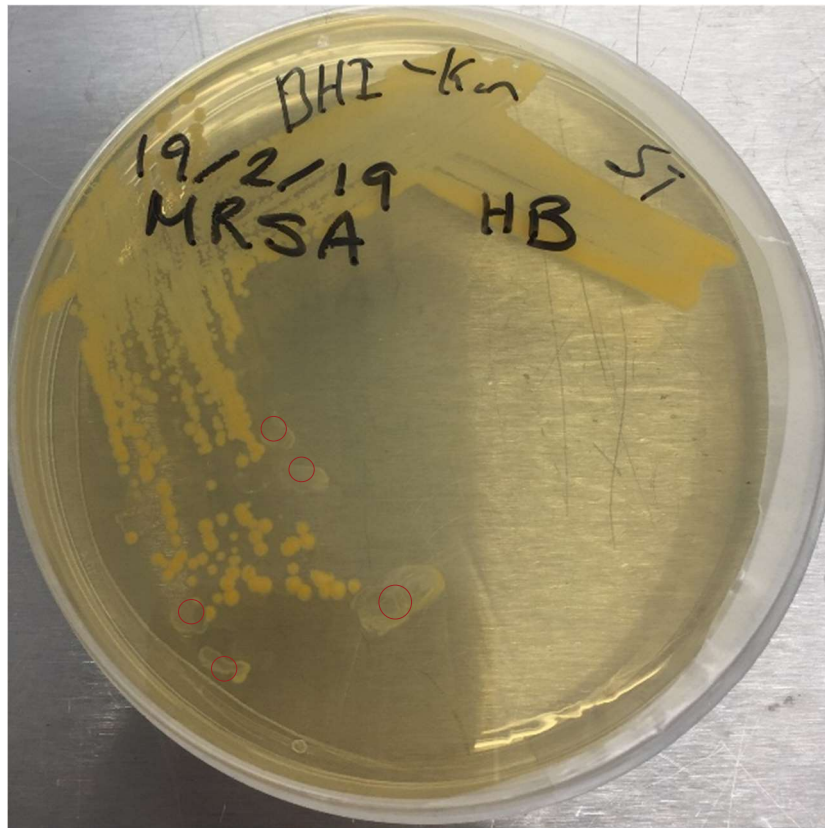


Figure 3.2. Isolated colonies of *S. Aureus* ATCC 43300 on BHI agar with 50µg L⁻¹ kanamycin. Red areas of collected colonies for susceptibility testing.

Methicillin minimum inhibitory concentration (MIC) of the isolated colonies was then confirmed; colonies were collected by loop and dispersed into 1 mL PBS by 3 min vigorous vortexing. Inoculant was diluted to match the optical density of a 0.5 McFarland standard with PBS. The emulsion was allowed to settle for 3 mins, and excess PBS was removed using a sterile cotton bud. The remaining emulsion was spread onto three quantitative MHA-salt plates (4 mm ± 0.5 mm, 26 cm³ medium at 70 °C on 90 mm plates) using a cotton bud in 4 layers, each streaking at a 90° angle to the previous, ensuring complete coverage of the agar surface, with each layer drying under a sterile filtered airstream for 3 mins. An Oxoid oxacillin minimum inhibitory concentration evaluator strip was applied to each plate and incubated for 24 hrs at 35 °C. All three plates displayed a typical MIC pattern, and an oxacillin MIC of 64-48 µg mL⁻¹ was determined.

3.3 MRSA Rosenbach ATCC 43300 Reference gDNA Extraction:

25 mL of BHI broth with 50 $\mu\text{g L}^{-1}$ kanamycin (250 mL ddH₂O, 9.25 g BHI, 250 μL 50 mg L⁻¹ kanamycin sulphate) was inoculated with a single colony of MIC confirmed ATCC 43300 MRSA from a BHI agar plate with 50 $\mu\text{g L}^{-1}$ kanamycin (250 mL ddH₂O, 13 g BHI agar, 250 μL 50 mg L⁻¹ kanamycin sulphate). The inoculated broth was grown in aerobic conditions, at 36 °C for 32 hrs, with vigorous shaking at 250 rpm in a dimpled 50 mL conical flask capped with a gas diffusion membrane. The culture medium was chilled on ice for 10mins, and cultured ATCC 43300 cells were collected by centrifugation at 1000 RCF for 15 mins. The cellular pellet was washed thrice with 15 mL PBS with 0.025%w/v sodium azide (900 mL ddH₂O, 10 0mL 10X PBS, 38.5 μL 10mM NaN₃) by vortexing for 3 mins and centrifugation at 1000 RCF for 15 mins. The cellular pellet was reconstituted in 3.75 mL of PBS with 0.025%w/v sodium azide at pH 7.5. 100 μL 5mg L⁻¹ MetaPolyzyme multilytic enzyme mix (5 mg enzyme mix, 1 mL PBS, pH 7.5) was added and incubated for 6 hr at 35 °C with shaking at 75 rpm. 1.8 mL of cellular lysis solution (60 g guanidium thiocyanate, 20 mL 0.5 M EDTA, 80 mL ddH₂O, 0.5 g of sodium lauryl sarcosinate) was added, and the solution was incubated for 10 mins at 30 °C, then cooled on ice for 10 mins. 1 mL of 7.5 M ammonium acetate (5.78 g ammonium acetate, 10 mL ddH₂O) was added and held on ice for 10 mins. The mixture was washed thrice using 1.8 mL chloroform:pentan-2-ol (24:1) with vigorous mixing for 3 mins, followed by centrifugation at 19000 RCF for 10 mins; subsequently, the aqueous supernatant was removed using a wide bore pipette.

The solution was chilled on ice for 10 mins, 3 mL -18 °C propan-2-ol was added, and the mixture was inverted for 60 s. The precipitated gDNA was collected by centrifugation at 6500 RCF for 60 s. The supernatant was then removed, and the gDNA pellet was washed with -18 °C 70 % ethanol and dried under sterile air for 2 mins. The gDNA pellet was reconstituted in 1 mL of tris-EDTA (TE) buffer (0.8 g tris hydrochloride, 145 mg of EDTA, 500 mL nuclease-free ddH₂O, pH 8) and reprecipitated thrice with 500 μL -18 °C propan-2-ol and 250 μL 7.5M ammonium acetate, with centrifugation at 6500 RCF for 60 s and washed with 70 % ethanol. gDNA was dissolved in 200 μL TE buffer and incubated at 30 °C for 30 mins; 5 μL ribonuclease A 5 mg μL^{-1} was added, vortexed and incubated for 30 mins at 37 °C. gDNA was reprecipitated thrice with 500 μL -18 °C propan-2-ol and 250 μL 7.5 M ammonium acetate, with centrifugation at 6500 RCF for 60 s and washed with 70 % ethanol. The gDNA was dissolved in 500 μL TE buffer, and purity and quality were assessed via UV-vis spectroscopy and agarose gel electrophoresis *figure 3.3*. Pre-stained ethidium bromide (EtBr) 0.6 % agarose gels (0.6 g agarose, 100 mL 1X TBE, 5 μL 5 mg mL⁻¹ ethidium bromide) were run at 3 °C, 1V cm⁻¹, in 1X Tris-borate-EDTA (TBE) buffer (5.4 g Tris base, 2.75 g boric acid 2 mL of 0.5 pH 8.0 EDTA) for 4 hrs. UV-vis spectra indicated an Abs_{260 nm}: Abs_{280 nm} ratio of 1.9 with no impurities visible passed 300 nm.

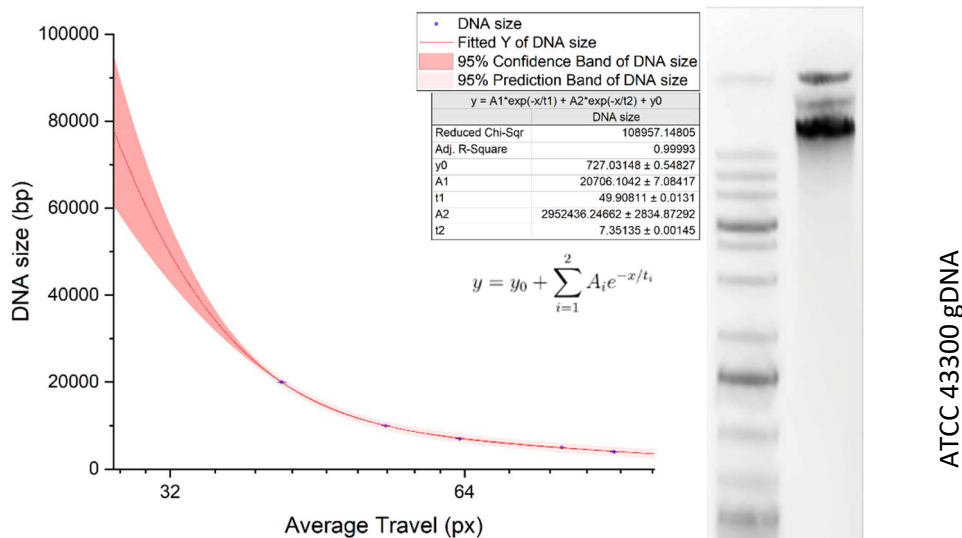


Figure 3.3. High-quality gDNA extracted and purified from Isolated colonies of *S. Aureus* ATCC 43300. gDNA fragments with an average minimum length of approx. 69 kbp.

gDNA concentration was determined via an EtBr fluorometric assay. A serial dilution of salmon sperm DNA ($0.1 \mu\text{g } \mu\text{L}^{-1}$) was made using nuclease-free ddH₂O in triplicate. 1 μL of DNA standards and 1 μL 1000x dilution of ATCC 43300 gDNA were added to 5 μL EtBr-fluorometric solution (15 μL 5 mg mL⁻¹ ethidium bromide, 50 mL 1X saline sodium citrate buffer (SCC) (4.41 g sodium citrate, 8.77 g sodium, 100 mL nuclease-free ddH₂O, pH 7.2)) in a 96 dimpled well plate. The solution was excited with 360 nm light, and emission was measured at 610 nm, figure 3.4. The 1000 x dilution of ATCC 43300 [gDNA] was calculated as $3.3 \pm 0.04 \text{ ng } \mu\text{L}^{-1}$, giving a total yield of 1.65 mg gDNA extracted and a working concentration of $3.3 \mu\text{g } \mu\text{L}^{-1}$.

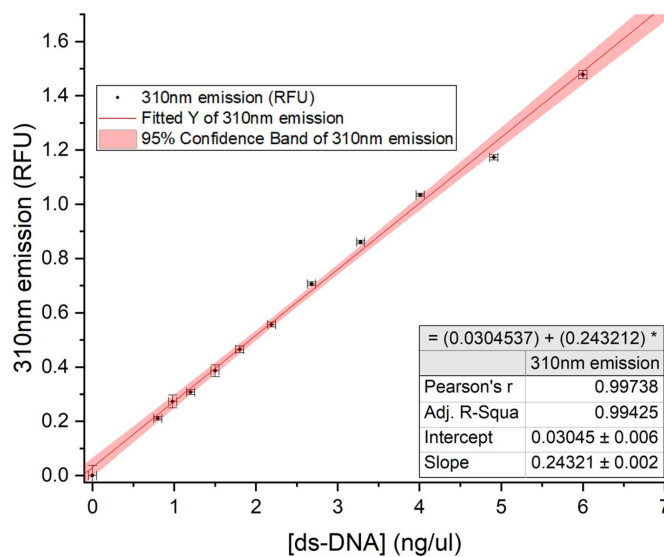


Figure 3.4 [gDNA] determined by EtBr fluorometric assay.

3.4 Reference mecA gene PCR and purification from ATCC 43300 gDNA

Whole gene mecA template primers were generated to create a control target for RPA amplification (*table. 3.1*) using the BLASTprimer search tool. Standard PCR primer design parameters were used unless stated. The mecA consensus sequence was used as a target, GC % was bracketed to 40% +/- 10%, and a minimum product size of 1900 was set. Ensuring the amplicon was large enough to be compatible with the RPA amplification sequences in presented in *table 2.14 (Page 65)*.

Table 3.1. MecA control target PCR primers.

Primer Name	5' - 3' Sequence	Template strand	Amplicon Length	Tm °C	GC%
MecA Fa	ATAGTTGTAGTTGTCGGGTTTGGT	+	1950	60.2	41.67
MecA Ra	ATTACCGTTCATATAGCTCATCA	-		57.53	36
MecA Fb	AATAGTTGTAGTTGTCGGGTTTGG	+	1950	59.24	41.67
MecA Rb	TTACCGTTCATATAGCTCATCA	-		57.11	37.5
MecA Fc	TAAATAGTTGTAGTTGTCGGGTTTGG	+	1951	59.07	40
MecA Rc	TTACCGTTCATATAGCTCATCAT	-		57.53	36
MecA Fd	TTAATAGTTGTAGTTGTCGGGTTTGG	+	1950	57.58	36
MecA Rd	ACCGTTCATATAGCTCATCAT	-		57.01	39.13

A low molecular weight mecA reference gene was produced using an ultra-high-fidelity PCR system (>100X *Tag*) from purified ATCC 43300 gDNA using primers described in section 2.2.3. PCR was carried out at 50 µL total volume with 105°C heated lids. Reaction mixtures composed of 2.5 µL 10 µM forward and reverse primers, 10 µL 5X SuperFi buffer (Invitrogen), 1 µL 10 mM free dNTPs, 0.5 µL Platinum SuperFi DNA polymerase (2 U µL⁻¹ Invitrogen), 1µL 3.3 ng µL⁻¹ gDNA and 32.5 µL nuclease-free ddH₂O were heated to 98°C for 120 s. Thermocycling was performed 35 times at 95 °C for 10 s, 68.3 °C for 10 s, 68 °C for 60 s, then held for a final extension at 72 °C for 5 mins and then held at 5 °C. According to the manufacturer's instructions, mixtures were purified using Monarch® 5 µg PCR & DNA clean-up columns. Cleaned PCR samples were run on pre-stained ethidium bromide (EtBr) 1% agarose gels (1 g agarose, 100 mL 1X TBE, 5 µl 5 mg mL⁻¹ ethidium bromide) run at 3 °C, 3.5V cm⁻¹, in 1X TBE buffer for 2 hrs and visualised using transmissive UV light. (*Fig. 3.5*) Primer set mecA F/Rb produced excellent results with an observed amplicon length of 1949±2 bp vs its theoretical 1950 bp product size. PCR using primers B was repeated at 150 µL total volume using identical reaction conditions. According to the manufacturer's instructions, Reaction mixtures were first purified using Monarch® 5 µg PCR & DNA clean-up columns.

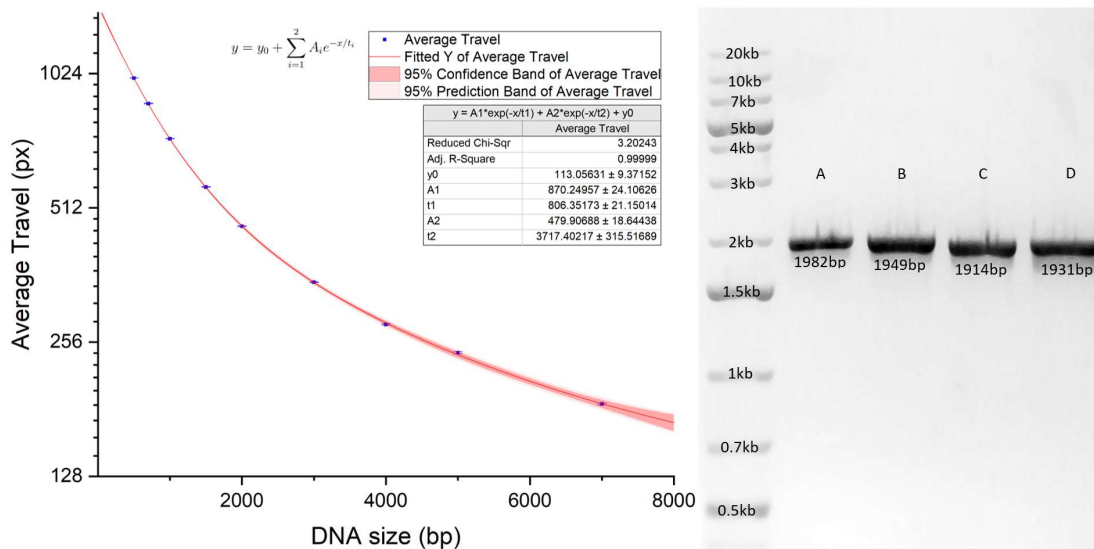


Figure 3.5 *MecA* PCR primer screen using *S. Aureus* ATCC 43300 gDNA. A-C *mecA* F/R_{a-d}

The resulting products were purified by 1 % agarose gel electrophoresis using ultra-low melting temperature agarose (1 g LMT-agarose, 100 mL 1X TBE, 1 µl 5 mg mL⁻¹ ethidium bromide) and a monarch® DNA gel extraction kit according to the manufacturer’s instructions. Purification was done thrice to ensure the purity of the assembled *mecA* gene and eluted into a final volume of 500 µL TE buffer. Products were reassessed by 1 % agarose gel electrophoresis (fig. 3.6). UV-vis indicated an Abs260 nm: Abs280 nm ratio of 1.78 with no impurities visible passed 300 nm. Product concentration was quantified by EtBr fluorometric assay via an identical procedure as [gDNA] quantification using a serial dilution of 2 kb concentration standards (0.1 µg µl⁻¹). A concentration of 100x dilution purified PCR product was measured as 1.27±0.04 ng µL⁻¹, giving a total yield of 63.6 µg *mecA* at a working concentration of 127 ng µL⁻¹. (Fig 3.6).

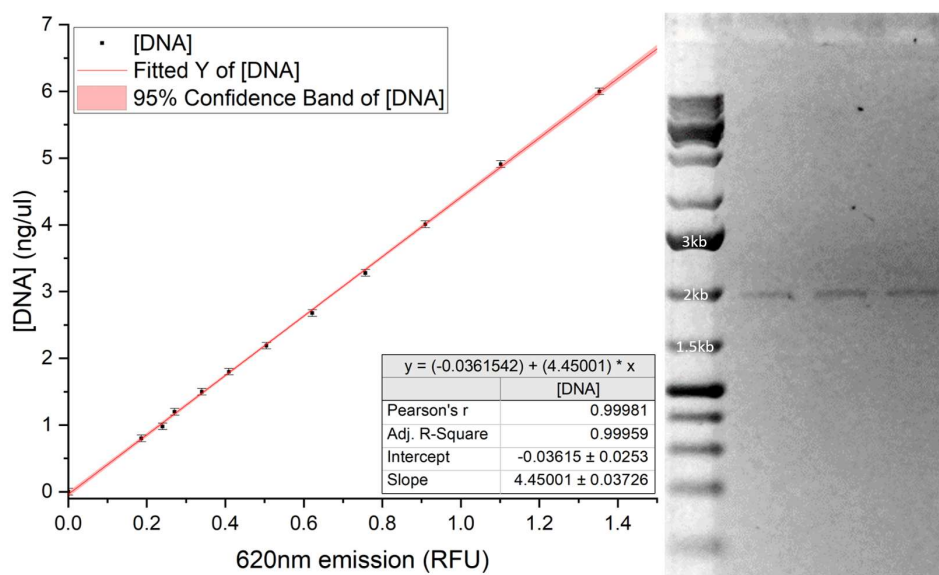


Figure 3.6. DNA-Page gel of PCR products, and [*mecA*] determined by EtBr fluorometric assay.

Low copy count PCR was used to assess the quality of the reference *mecA* gene. A serial dilution of *mecA* gene standards from 500 million (approx. 1.05 ng) to 50 genetic copies was made in TE buffer. PCR was carried out at 50 μ L total volume with 105 $^{\circ}$ C heated lids. Reaction mixtures composed of 7.5 μ L 10 μ M *MecA* F/R_b primers, 10 μ L 5X SuperFi buffer (Invitrogen), 1 μ L 10 mM free dNTP's, 0.5 μ L Platinum SuperFi DNA polymerase (2 U μ L⁻¹ Invitrogen), 1 μ L each *MecA* reference template and 22.5 μ L nuclease-free ddH₂O were heated to 98 $^{\circ}$ C for 120s. Thermocycling was carried out 15 times at 95 $^{\circ}$ C for 10 s, 68.3 $^{\circ}$ C for 10 s, 68 $^{\circ}$ C for 60 s, then held for a final extension at 72 $^{\circ}$ C for 2 mins and then held at 5 $^{\circ}$ C. According to the manufacturer's instructions, mixtures were purified using Monarch[®] 5 μ g PCR & DNA clean-up columns. Cleaned PCR samples were eluted onto pre-stained ethidium bromide (EtBr) 1% agarose gels (1 g agarose, 100 mL 1X TBE, 5 μ l 5 mg mL⁻¹ ethidium bromide) run at 3 $^{\circ}$ C, 3.5V cm⁻¹, in 1X TBE buffer for 2 hrs and visualised using transmissive UV light. (Fig. 3.7).

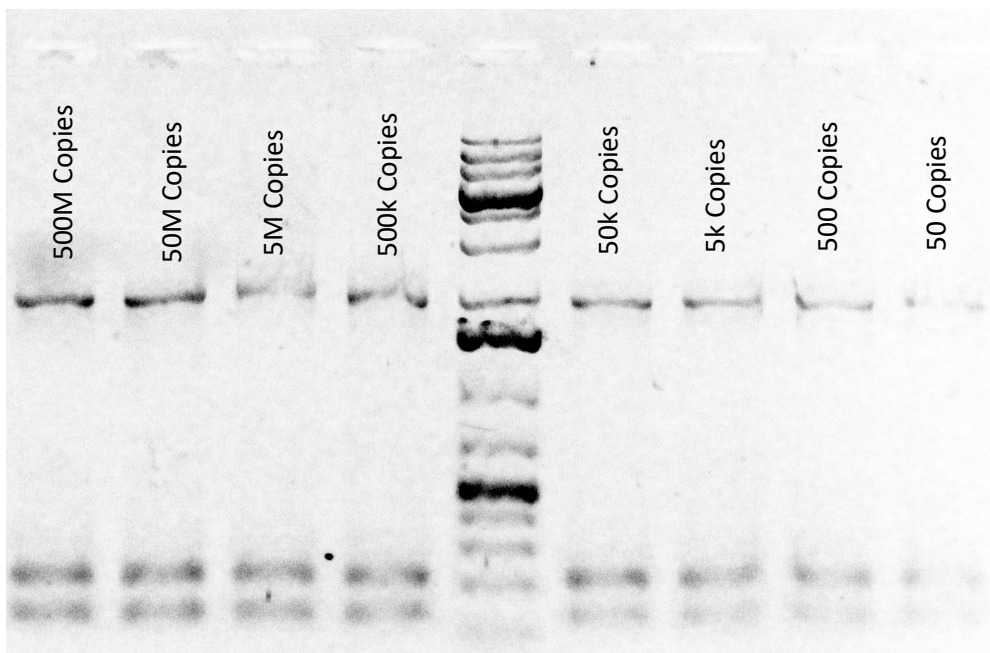


Figure 3.7. Low copy count PCR of *MecA* reference gene using primers *mecA* F/R_b.

The serial diluted *mecA* reference gene templates amplified under PCR conditions resulted in the expected bands on agarose gels. The reactions yielded clearly defined bands at the expected 1950 bp weight down to 50 copies of *mecA* reference template. Importantly, no spurious high molecular weight products were observed. Thus highlighting the stringent fidelity of the produced template and well optimised PCR conditions.

3.5 Concluding remarks:

The above work resulted in three different levels of sample targets for RPA-coupled NALFA testing and the optimisation work discussed in later chapters. This ranged from working with the most complex and "contaminated" raw bacterial cells to the simplest targets, which were purified target genes produced via PCR.

Additionally, reported is a DNA quantification method that is not only quick and cost-effective but also highly efficient. While it may not be as sensitive as some commercially available solutions, the required reagents are readily available in any molecular biology laboratory. Moreover, the stained products can be easily recovered from the EtBr intercalating agent, if necessary, using standard spin column purification.

Furthermore, the presented methods resulted in exceptionally high-quality genomic DNA (gDNA) with minimal shearing demonstrated during the extraction and purification processes. This is particularly crucial for simulating *in-situ* lysed bacterial cells in when dealing with very low template copy RPA counts in later chapters.

Chapter 4

RT-RPA Kinetic Model.

“This was deriving me mad.”

*Deriving these complex equations had derivin' me completely mad,
I just couldn't seem to get them right, it was so very sad.
I spent weeks in matlab, trying to decipher,
But all I got was a headache and called a no-lifer.*

*The derivatives and integrals had derivin' me to despair,
I couldn't seem to find the right solutions anywhere.
My head was constantly spinning, my brain felt completely fried,
All I wanted was to be done and lay down on my backside.*

*But I knew I had to persevere and push on through,
For showing my workings was the key to success, that much I knew was true.
So I kept on trying and trying, and tried not to bluff,
Until I think I almost mastered this rather complex stuff.*

*But oh how I still long for the day I can say,
"I've finally mastered derivation and integrals, hurray!"*

4.1-Introduction:

In order to select the best performing primer sets, end point analysis alone via electrophoresis is not most appropriate for producing the device sought. One of the key elements of an ASSURED PoC device is the speed at which a result is presented to the user. Therefore, the amount of amplicon produced at a defined 40 min endpoint is significantly less important than the speed at which a detectable amount of amplicon can be produced. Presented in the proceeding chapters the initial RPA primers with and without modifications are kinetically assessed to eliminate the worst performers. With the best performing primers taken forward, attempts to optimise and catalyse the modified RPA reactions to meet the ASSURED criteria for the final device were made. To evaluate the performance of the initial RPA primer sequences, the impact of modifications to the RPA reaction conditions, and the catalysis of the reactions, a kinetic model must be established. While the raw data from RT-RPA appears similar to that of qPCR there are key differences that make the already well establish qPCR kinetic models unsuitable.

4.2 – Proposed RT-RPA kinetic model:

As RT-RPA is a continuous, isothermal reaction, conventional profile fitting, and analysis methods used in the analogous process of qPCR are not applicable. Typically, a four-parameter logistic function is used to fit such data. However, reliance on cycle number dependencies and the high degree of asymmetry in curves found in RT-RPA reactions significantly reduces the goodness of fit for such a four-parameter logistic function. Consequently, novel fitting and analysis models for real-time RPA reactions are proposed.

4.2.1: Fitting Function:

A modified five-parameter logistic function, *equation 2*, was selected as the most appropriate fitting function for the obtained RT-RPA data explored in *chapter 5*.

$$\varphi(t) = \frac{\varphi_m - \varphi_i}{f \left(\frac{1}{\left(\frac{t}{t_0}\right)^h} + 1 \right)} + \varphi_i \quad (2)$$

$\varphi(t)$ = Fluorescence \equiv [DNA] φ_i = Fluorescence $_{t=0}$ φ_m = Max Fluorescence t = Time
 f = Asymmetry Factor K_m = Time of Max Rate h = hill slope

To demonstrate how this function works, *Figure 4.1(a)-(e)* shows the effects of varying each parameter in equation 2, while other parameters remain constant as a function of time.

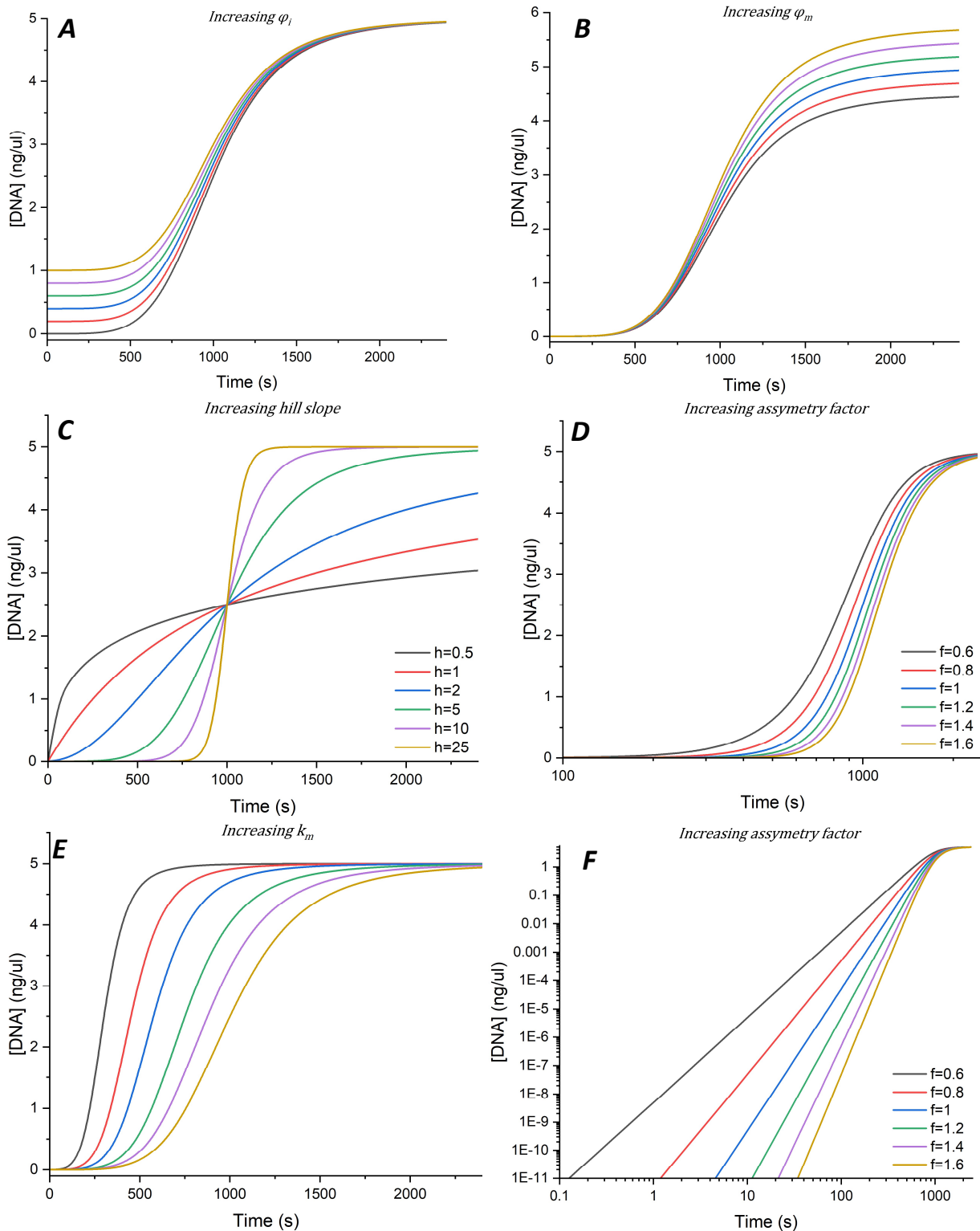


Figure 4.1. (A)-(F) Shows the effect of varying parameters of the proposed logistic function.

A) $\phi_i = 0, 0.2, 0.4, 0.6, 0.8, 1$. $\phi_m = 5$. $h = 5$. $f = 1$. $k_m = 1000$. B) $\phi_i = 0$. $\phi_m = 4.5, 4.75, 5, 5.25, 5.5, 5.75$. $h = 5$. $f = 1$. $k_m = 1000$. C) $\phi_i = 0$. $\phi_m = 5$. $h = 0.5, 1, 2, 5, 10, 25$. $f = 1$. $k_m = 1000$. D) $\phi_i = 0$. $\phi_m = 5$. $h = 5$. $f = 0.6, 0.8, 1, 1.2, 1.4, 1.8$. $k_m = 1000$. E) $\phi_i = 0$. $\phi_m = 5$. $h = 5$. $f = 1$. $k_m = 300, 450, 575, 750, 875, 1000$. F) Log₁₀ $\phi(t)$. $\phi_i = 0$. $\phi_m = 5$. $h = 5$. $f = 0.6, 0.8, 1, 1.2, 1.4, 1.8$. $k_m = 1000$.

4.2.2: Regression conditioning issues:

Although five-parameter logistic functions provide superior accuracy in representing the fitted data, they are significantly more challenging to fit than the four-parameter counterparts, mainly due to the high likelihood of the regression problem becoming ill-conditioned. With five-parameter functions such as this, ill-conditioning at starting integrations is likely due to interdependencies between reaction constants', namely f , h and k_m . In *figure 4.2a*, the relationship between f and k_m can be clearly seen to mimic that of a changing hill slope, while the hill slope remained constant ($h=5$). In *figure 4.2b*, the relationship between f and h can be seen to mimic a changing k_m , despite k_m remaining constant ($k_m=1000$ s). In *figure 4.2c*, the relationship between k_m and h can be clearly seen to nullify the implicit rate increase expected from and increasing hill slope; while also introducing an asymmetry inversely proportional to that of a changing value of f , despite f remaining constant ($f=1$).

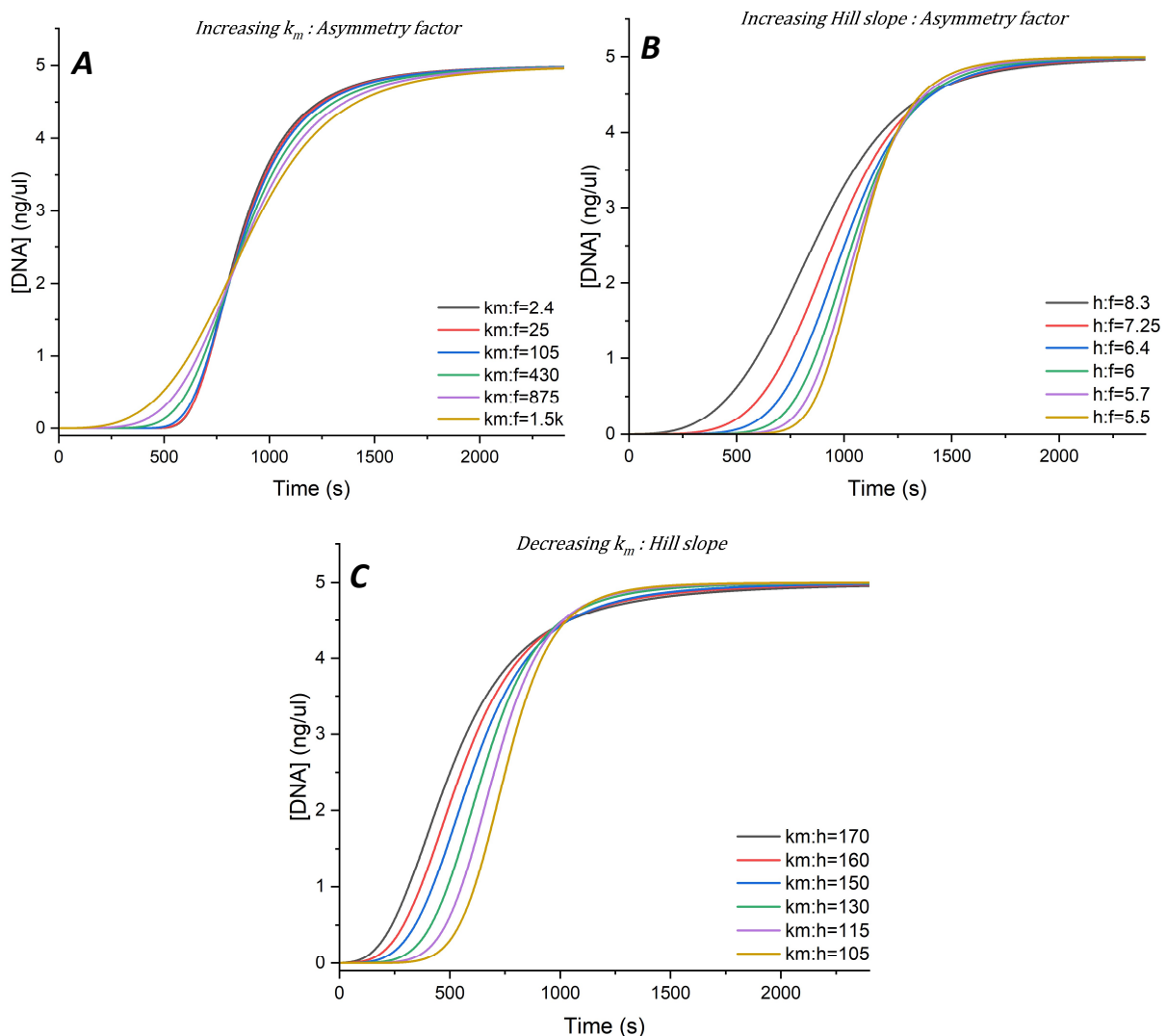


Figure 5.2. (A)-(C) Shows how f , h and k_m have functional interdependencies.

A) $\varphi_i = 0$. $\varphi_m = 5$. $h = 5$. $f = 125, 17.5, 5.5, 1.75, 0.65$. $k_m = 300, 450, 575, 750, 875, 1000$. B) $\varphi_i = 0$. $\varphi_m = 5$. $h = 5, 5.8, 6.4, 7.2, 8, 8.8$. $f = 0.6, 0.8, 1, 1.2, 1.4, 1.8$. $k_m = 1000$. C) $\varphi_i = 0$. $\varphi_m = 5$. $h = 3, 3.5, 4, 5, 6, 7$. $f = 1$. $k_m = 300, 450, 575, 750, 875, 1000$.

Consequently, a five-parameter regression problem of equation 1 can have an almost infinite number of local minima when solved to reduce the sum of squares due to error (SSE). Unlike a four-parameter regression with an order of magnitude less, and single parameter linear regressions only have one global minimum. Therefore, fitting data with equation 1 by solving an ill-conditioned regression problem with standard numerical fitting algorithms; which have limited precision; can result in vastly different function plots that fit the data equally well. (Fig 4.3)

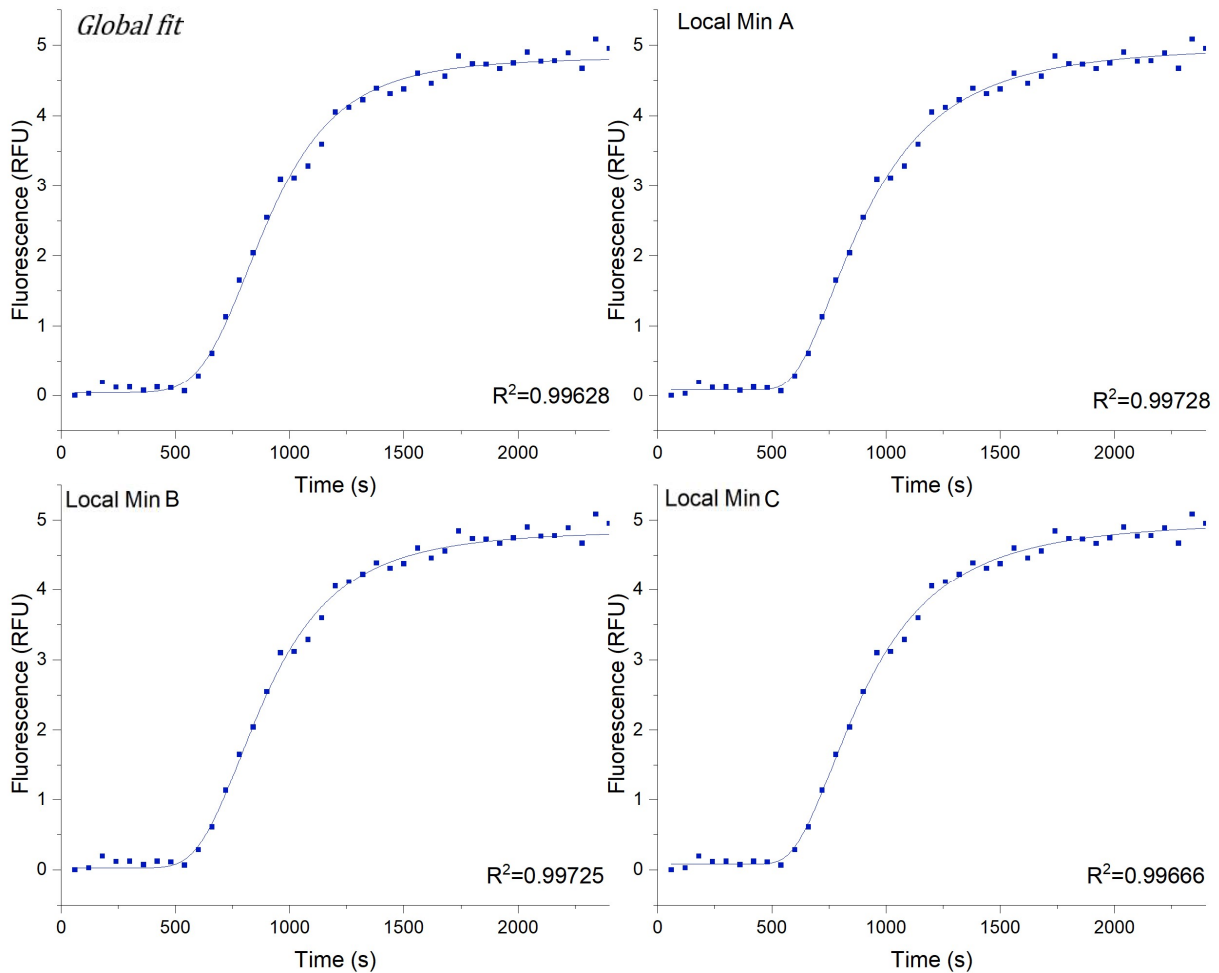


Figure 4.3. Shows the same RT-RPA raw data fitted 4 times using equation 1. Fit has been manually conditioned whereas fits b-d have been automatically solved. Global fit $\varphi_i = 0.043$. $\varphi_m = 4.829$. $h = 4.955$. $f = 1.774$. $k_m = 773$ s. Local min A. $\varphi_i = 0.083$. $\varphi_m = 4.986$. $h = 3.595$. $f = 1503$ $k_m = 107$ s. Local min B. $\varphi_i = 0.026$ $\varphi_m = 4.86$ $h = 4.233$. $f = 3.916$. $k_m = 612$ s. Local min C. $\varphi_i = 0.083$. $\varphi_m = 4.99$ $h = 3.596$. $f = 940$. $k_m = 122$ s.

In figure 4.3, the global fit used pre-calculated approximate function parameters and shows a fit using the global minimum solution. Fits A-C however were solved with no initially approximated function parameters, leading to a fit using local minima solutions. As a result, fits A-C are ill-conditioned solutions and lead to almost identical functions with excellent R^2 within the fit time range but incorrect

numerical reaction constants. Furthermore, the ill fitted functions are only approximately identical within the given data's time range; such solutions sit in local minima and may be drastically far from the desired global minima of the regression. Nevertheless, as each solution fits the data set well within the given time range, it is impossible to distinguish between these and the desired global minimum using numerical fitting algorithms. (fig. 4.4).

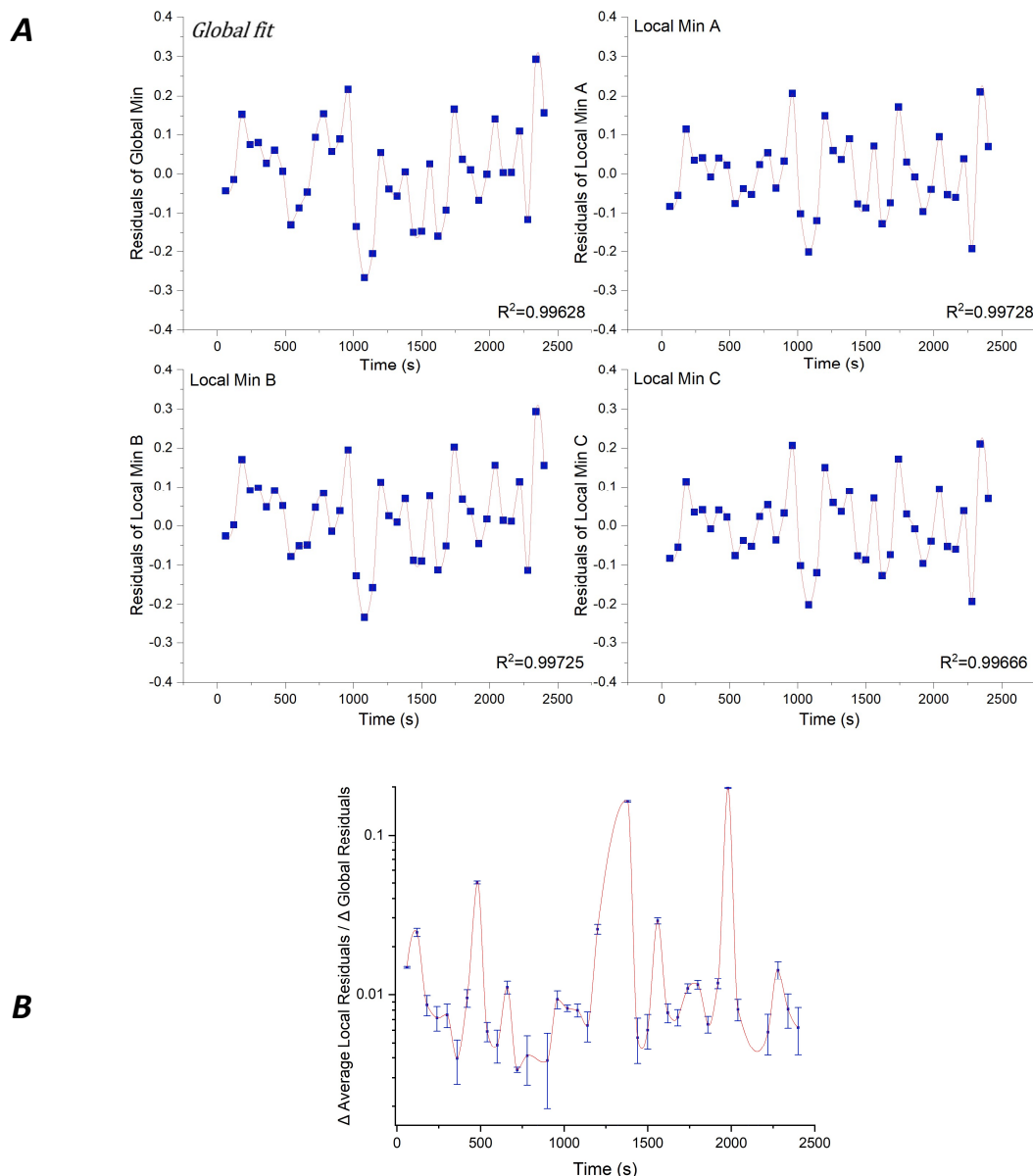


Figure 4.4. A) Shows individual residual plots of fits in figure 4.3. B) Shows the percentage difference between average residuals of local minima vs the global minimum solution. Despite the vast difference in the fit parameters, the % difference between the fits SSE is < 0.1%. Highlighting the high probability of direct fitting using equation 1 to become ill-conditioned.

4.3: Regression preconditioning solver algorithm:

It is crucial when fitting RT-RPA data using *equation 1* that the global minimum solution is used to obtain accurate numerical data from the fit. Therefore, to ensure the accuracy of numerical kinetic data obtained from RT-RPA reactions, curves and reaction constants were first approximated by *equations 2-4*.

$$\varphi(t) \approx \begin{cases} \varphi_i + k_i t & t < t_i \\ \varphi_{ia} + k_a(t - t_i) & t_i \leq t < t_d \\ \varphi_{ad} + k_d(t - t_d) & t \geq t_d \end{cases}, \text{ where } \begin{cases} \varphi_{ia} = \varphi_i + k_i t_i \\ \varphi_{ad} = \varphi_{ia} + k_a(t_d - t_i) \\ \varphi_m = \varphi_{ad} + k_d(t_m - t_d) \end{cases} \quad (2)$$

$$k_m \approx t_i + \frac{t_d - t_i}{2} \approx t_0 \quad (3)$$

$$v_{max} \approx k_a \approx \frac{10^{h^{-1}+f^{-1}}}{t_0} \therefore h^{-1} + f^{-1} = \log k_a t_0 \quad (4)$$

$\varphi(t)$ = Fluorescence \equiv [DNA] φ_i = Fluorescence $t=0$ φ_m = Max Fluorescence t = Time
 k_m = Time of Max Rate k_i = Initiation Rate k_a = Amplification Rate k_d = Depletion Rate
 t_i = Initiation Time t_d = Depletion Time φ_{ad} = Fluorescence at t_d
 φ_{ai} = Fluorescence at t_i f = Asymmetry Factor h = hill slope

Fitting RT-RPA data using *equations 2-4* provides a surprisingly good closeness of fit., it is possible to obtain close estimates of parameters used to fit *equation 1* from these approximations. Thus, by introducing solver constraints via bracketing parameters around these estimated values, the probability of the regression problem becoming ill-conditioned is significantly reduced. Furthermore, to reduce the probability of the regression problem becoming ill-conditioned, the solving of *equation 1* was performed stepwise. By doing so, the degrees of freedom of the regression problem are reduced significantly for each step, and the fit can be iteratively converged following a simple method to prioritise the non-unitless parameters φ and k_m . However, it cannot accurately represent the areas of exponential growth or depletion, i.e., the areas crucial for accurately defining the kinetics of the reactions. *Figure 4.5* shows the same experimental data used in *figure 4.3* fitted using the approximation functions shown in *equations 2-4*.

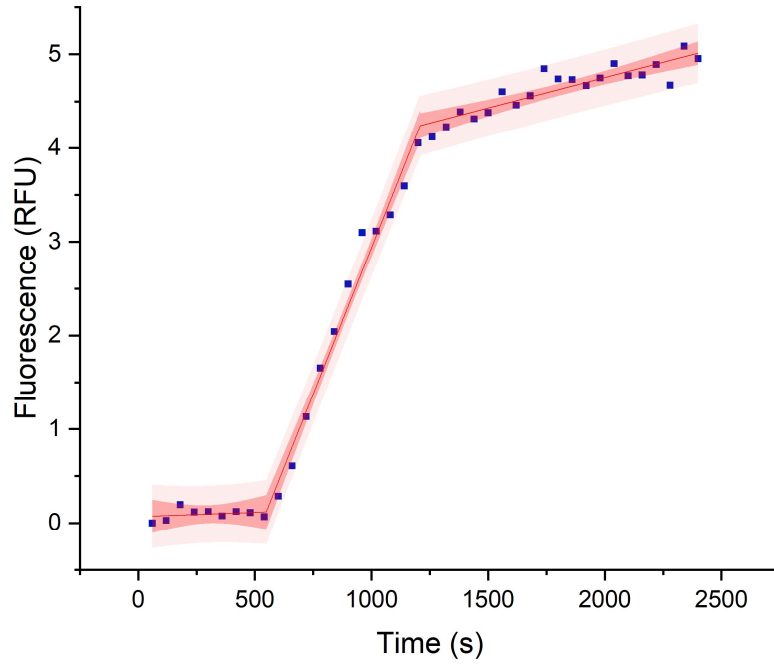


Figure 4.5. Shows a single run sample of RT-RPA data fitted using equation 2-4. Inner red band represents the 95% interval range. Outer red band represents the 95% prediction range. The confidence band encloses the area that its 95% likely to contain the true curve, whereas the outer prediction range shows the area that 95% of the expected future data points will fall.

4.4: First and second derivative fitting functions:

Once the experimental data is successfully fitted to *equation 1*, the rate of reaction at any time can be defined by the first derivate of the fit, *equation 5*. The maximum achieved rate and Km can be obtained by determining the maxima's time and amplitude of *equation 5* through fitting with an asymmetric double sigmoidal peak function, *equation 6*. Figure 4.6.

$$v = \frac{d\varphi}{dt} \left[\frac{\varphi_m - \varphi_i}{\left(\left(\frac{t}{t_0} \right)^h + 1 \right)^f} + \varphi_i \right] = \frac{fh \cdot (\varphi_m - \varphi_i)}{t \cdot \left(\left(\frac{t}{t_0} \right)^h + 1 \right)^f \left(\left(\frac{t}{t_0} \right)^h + 1 \right)} \quad (5)$$

$$v = v_o + \left[\frac{v_{max}}{1 + e^{-\frac{t-k_m + \frac{w_1}{2}}{w_2}}} \cdot 1 - \frac{1}{1 + e^{-\frac{t-k_m + \frac{w_1}{2}}{w_3}}} \right] \quad (6)$$

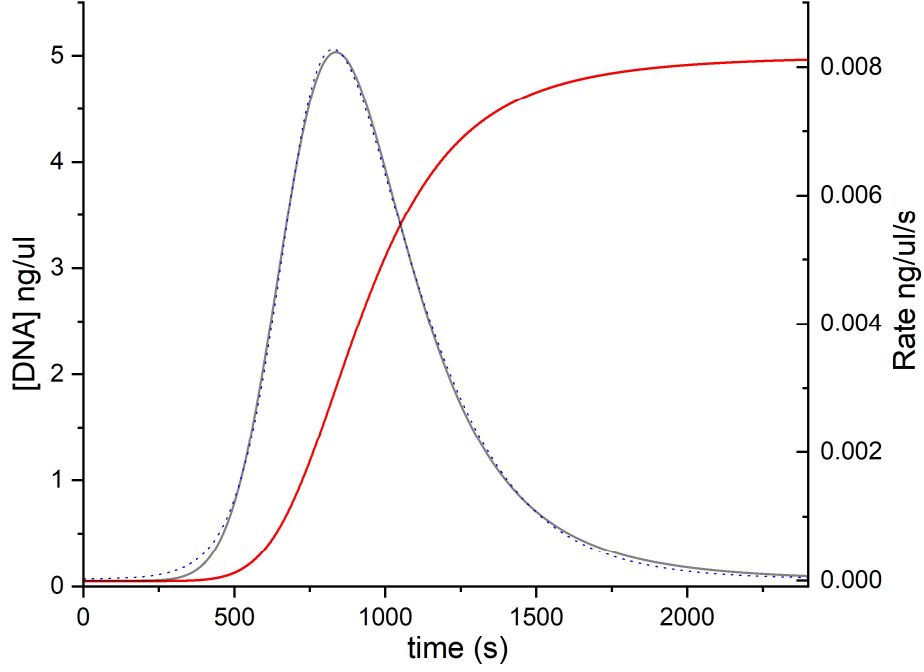


Figure 4.6. Shows equation 5 (solid grey line) and 6 (dotted blue line) calculated from an RT-RPA fit with equation 1 (solid red line).

By taking the second derivate of equation 1, we can then clearly define the acceleration of the rate at any time, *equation 7*. The time to initiation and time to depletion can then be defined as the time of maximum / minimum rate acceleration/deceleration, *equation 8*. A Gaussian amplitude deconvolution function is used to accurately define these parameters, *equation 9*, *figure 4.7*. The derivations for *equations 5* and *8* can be found in *appendix 5*.

$$v_{(t)}^{\vec{}} = \frac{d^2\varphi}{dt^2} \left[\frac{\varphi_m - \varphi_i}{\left(\left(\frac{1}{\left(\frac{t}{k_m}\right)^h} + 1\right)^f + \varphi_i\right)} \right] = - \frac{fh \cdot (\varphi_m - \varphi_i) \left((h+1) \cdot \left(\frac{t}{k_m}\right)^h - fh + 1 \right)}{t^2 \cdot \left(\left(\frac{1}{\left(\frac{t}{k_m}\right)^h} + 1\right)^f \left(\left(\frac{t}{k_m}\right)^h + 1\right)^2\right)} \quad (7)$$

$t_i = \text{time where } v_{(t)}^{\vec{}} \rightarrow \text{maximum}$

$t_d = \text{time where } v_{(t)}^{\vec{}} \rightarrow \text{minimum}$

$$v_{(t)}^{\vec{}} \sim \vec{v}_0 + \left[\vec{v}_{max} \cdot e^{-\frac{(t-t_i)^2}{2w_i^2}} \right] + \left[\vec{v}_{min} \cdot e^{-\frac{(t-t_d)^2}{2w_d^2}} \right] \quad (8)$$

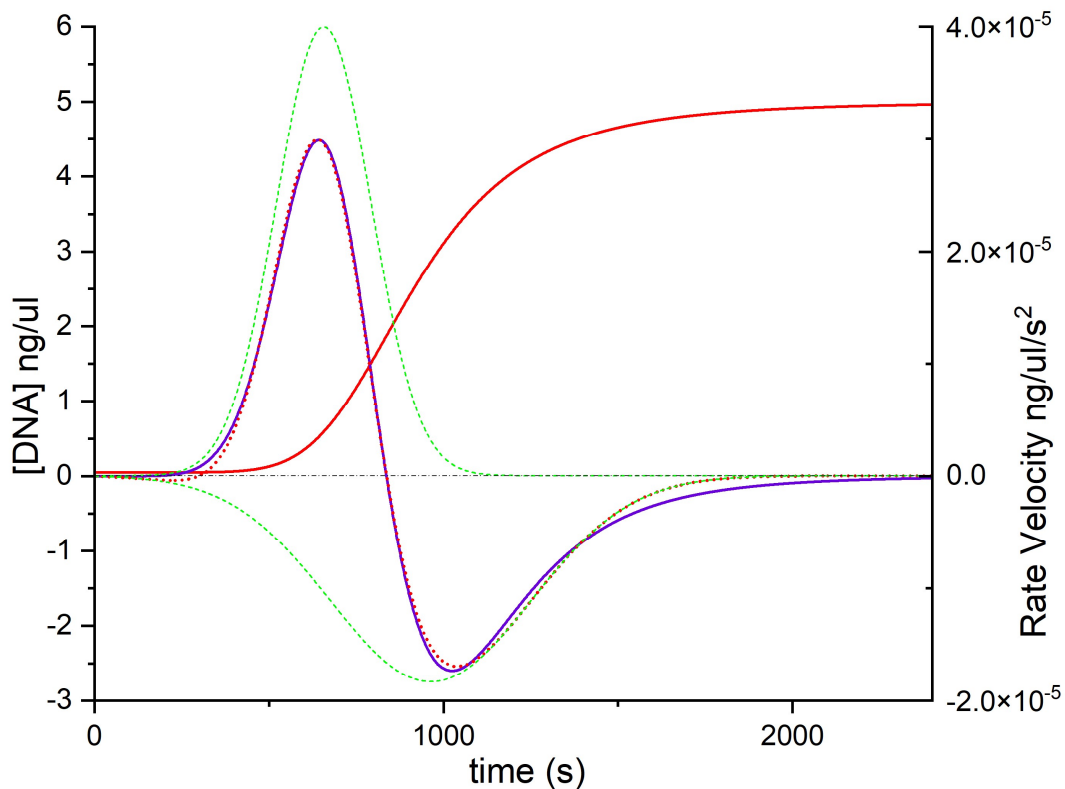


Figure 4.7. Shows equation 6 (Purple solid line) and 8 (dotted red line) calculated from an RT-RPA fit with equation 1 (solid red line). Green dashed lines show each exponent of the de-convolution, equation 8.

4.5: Concluding Remarks:

By applying the discussed functions to the raw kinetic data from RPA reactions, we can extract essential insights into the performance of the amplification reaction. It's important to note that while this experimental method doesn't allow for the deconvolution of full kinetic parameters, such as true rates, due to the lack of calibrated fluorescence output and its variability across primer and probe sets, we can still derive valuable information. In the context of the ASSURED criteria mentioned earlier, it's crucial to emphasize that the speed at which a detectable amplicon becomes present holds greater significance than the total amplicon yield. Therefore, the times of initiation, depletion, and the time of maximum rate – as defined by the first and second derivatives – provide adequate information for effectively optimizing RPA reactions for the intended system. This becomes especially pertinent when considering that the total amplicon yield can be managed by adjusting the total concentration of primers in the reaction mixtures.

Chapter 5

Primer Sequence Screening (RT-RPA).

"The Pipette Tip Chronicles"



*We pipette and pipette, from morning till night,
Our hands are so tired, we could use a good fright,
But we keep on going, for the science we strive
We'll use every last pipette tip, till we're practically not alive.*

*But oh, the distractions, they never seemed to end,
There's always someone talking to you, that annoying colleague friend."
You lose your count and where you are, which solution did you squirt out last?
Well shit, looks like that time again, time to restart the task!*

*But hold your tongue, do not even grimace,
Or tell your postdoc, to mind his own F'n business.
For tho his mouth is as massive, as a horses rear,
saying so to their face, will ruin the rest of your academic year.*

*Just keep on pipetting, with a smile on your lap,
Just mutter inside your head, please shut your trap.
Just keep using those pipette tips, and leave for them the tip-bin brimming.
and hopefully your collected data, will leave you grinning.*

*So here's to the pipette tips, the bane of my life.
We'll wash and we'll dry them, then rack, stack and sterilise them.
But soon enough, it's back to work we'll go,
We'll pipette and pipette, till our hands have no feeling, owe dear, owe no.*

5.1 Introduction:

In this chapter, we delve into the methodology employed to assess primer sets for their compatibility with the proposed NALFA-coupled amplification system. To illustrate this process, we focus on the *mecA* gene as our target of interest. While it would have been advantageous to screen multiple primer sets for various targets, practical constraints dictated that under single persons efforts that was not feasible. Therefore, we turn our attention to the MecA primer sets introduced in Chapter Two. The subsequent chapters lay out the best practices for experimentally screening primer sequences tailored to our system. Within each section of this chapter, a hierarchy of validation steps for the primer sequence library is outlined. This hierarchy progresses from rapid, cost-effective, and easily interpretable evaluations to more intricate and resource-intensive analyses.

The overarching objective here is to narrow down the extensive pool of primer sequences to a select few, the "golden sequences." Any primer sequences that do not yield satisfactory results during the screening phase are excluded from further testing. This decision is driven by the constraints of time and resources, ensuring our efforts are focused on the most promising candidates.

Simultaneously, this chapter delves into an additional line of investigation, exploring the impact of two key variables within the modified RPA amplification system. The first variable under scrutiny is the size of the sample material's DNA molecules. To assess this, we conduct parallel RPA screening tests using the MecA reference template (2 kbp) and gDNA (with an average fragment size of <69 kbp) as templates. Our second area of investigation pertains to the influence of spacer size inserted between the capture probe sequence and the active amplification sequence of the modified primer sets. In order to evaluate this, we perform screening tests using two different spacer lengths, C3 and C12, positioned between the capture probe sequence and the active amplification sequence of the modified primer sets. This approach allows us to make comparisons between the reaction endpoint purities and kinetic parameters across reactions with the different template sizes and internal probes.

5.2 PCR screen of unmodified RPA *mecA* primer sequences:

The performance of the *mecA* primer sequences was first assessed by standard PCR using the unmodified primer sequences described *in table 2.2, page 48*. Standard PCR serves as a valuable tool for uncovering fundamental issues with primer sequences that may not have been apparent during the in-silico design process. When dealing with longer primer sequences, as advised for RPA, the likelihood of missing intra and intermolecular interactions during in silico analysis increases. Hence, if

the initial sequences fail to yield any viable amplicon product under optimized PCR conditions, it is not advisable to invest further time in that specific sequence.

5.2.1: Experimental Method:

Five million (approx. 10 pg) copies of the *mecA* reference gene were used as the PCR template. PCR was carried out at 25 μL total volume with 105°C heated lids. Reaction mixtures composed of 2.5 μL 10 μM forward and reverse primers, 5 μL 5X SuperFi buffer (Invitrogen), 1 μL 10mM free dNTPs, 0.25 μL Platinum SuperFi DNA polymerase (2 U μL^{-1} Invitrogen), 0.5 μL 10M copies μL^{-1} *mecA* reference gene template and 16.25 μL nuclease-free ddH₂O were heated to 98°C for 120 s. Thermocycling was performed 35 times at 95 °C for 10s, melting temperature for 10s, 68 °C for 60s, then held for a final extension at 72 °C for 5mins and then held at 5 °C. Melting temperatures were adjusted for each primer set. Sets with similar T_m were grouped to an average T_m . Sets three-six, nine and ten used 63.9 °C; sets two, seven and eight used 65.2 °C; sets 11 and 12 used 63.4 °C. According to the manufacturer's instructions, mixtures were purified using Monarch® 5 μg PCR & DNA clean-up columns. Cleaned PCR samples were evaluated using 20 % non-denaturing TBE-DNA polyacrylamide gels (1.6 ml 10X TBE, 56 μL 10%_{w/v} ammonium persulphate, 6.5 ml 40%_{w/v} bis-acrylamide, 4.75 ml nuclease-free ddH₂O, set with 2.8 μL Tetramethylethylenediamine (TEMED)) run at 3 °C, 5 V cm^{-1} , in 1.25X TBE buffer for 2 hrs. Gels were stained by soaking in EtBr stain (0.5 $\mu\text{g ml}^{-1}$ EtBr in 1X TBE) for 5mins, rinsed and visualised using transmissive UV light. (Fig. 5.1). Product yield and concentration was determined via an EtBr fluorometric assay described on page 70. (Fig. 5.2).

5.2.2: Experimental Results:

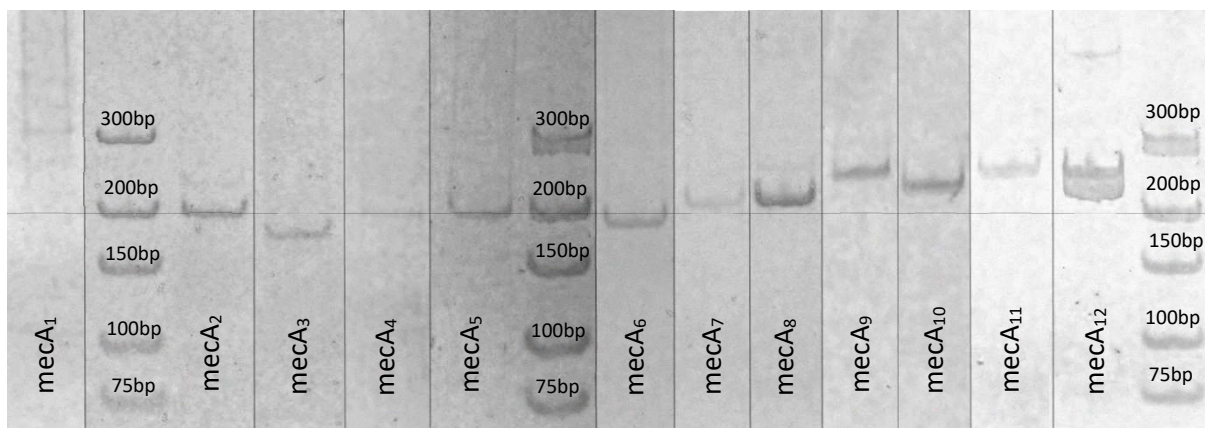


Figure 5.1. PCR products using the original *mecA* primer sequences. Black vertical lines indicate a join between gel images, and a black horizontal line indicates gel alignment reference position. Gels were collated for clarity, post-processed holistically, and background variation is due to post-run staining.

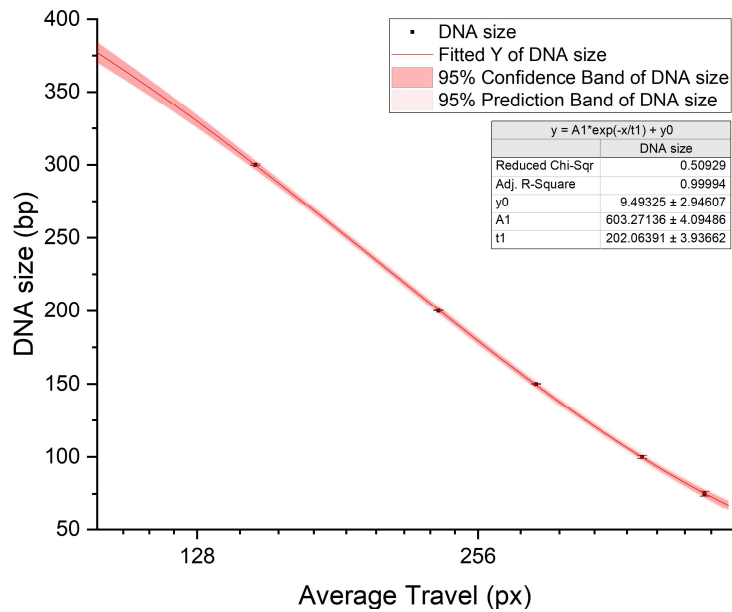


Figure 5.2. DNA migration calibration curve for gels in figure 5.1.

Table 5.1. PCR amplicon properties derived from figure 5.1.

Primer set	Upper Band (bp)	Observed average amplicon weight (bp)	Lower Band (bp)	Amplicon Band SD	Expected Size (bp)	Difference (bp)	Approx. yield (ng)
mecA ₁	452	385	327	29.50	186	141	N/A
mecA ₂	201	200	200	0.16	194	6	97
mecA ₃	180	179	178	0.28	173	5	60
mecA ₄	203	201	198	1.18	199	-1	20
mecA ₅	201	200	199	0.48	194	5	107
mecA ₆	192	191	190	0.46	188	2	90
mecA ₇	202	198	195	1.66	192	3	59
mecA ₈	212	212	212	0.17	210	2	282
mecA ₉	250	249	248	0.60	245	3	154
mecA ₁₀	235	234	232	0.65	225	7	186
mecA ₁₁	254	252	250	0.90	243	7	81
mecA ₁₂	246	240	233	3.13	232	1	389

5.2.3: Concluding Remarks & Outcomes:

In general, the *mecA* primer sequences performed well directly from *in silico*, showing little to no spurious amplification material with acceptable yields. Of particular note was primer sets 8, 9, 10 and 12 which produced exceptional amplicons yields, in the expected bp weight and exhibited little to no spurious materials. However, there was the exception of primer sets one and four. (table 5.1).

Before excluding from further screening, the PCR procedure was repeated to verify the poor performance of these sets. (Fig. 5.3).

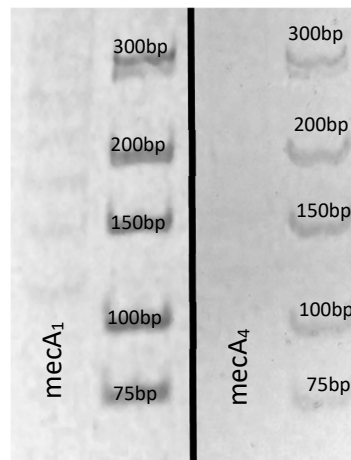


Figure 5.3. Gels showing the results of repeated PCR amplification of primer sets $mecA_1$ and $mecA_4$.

Failure of $mecA_1$ and $mecA_4$ highlighted the importance of producing a library of primer sequences. $mecA_1$ was the top theoretical primer sequence generated by the Primer3-BLAST algorithm and yet failed under ideal conditions. These primer sequences were therefore excluded from further screening or development.

5.3 RPA screen of PCR pre-screened $mecA$ primer sequences:

The performance of the remaining unmodified $mecA$ RPA primer sequences described in table 2.2, page 48 was further investigated by standard RPA. This time however the previously excluded primer sequences $mecA_1$ and $mecA_4$ were excluded from the screening. Again, as previously state should sequences fail yield any viable amplicon product under optimized PCR conditions, it is not advisable to invest further time in that specific sequence.

5.3.1: Experimental Method:

Standard RPA for the remaining unmodified primer sequences was performed under the following conditions. Five million (approx. 10pg) copies of the $mecA$ reference gene were used as the RPA template. According to the manufacturer's instructions, standard RPA reactions were carried out at 25 μ L total volume at 37 $^{\circ}$ C for 20 mins using a Twistdx RPA basic liquid kit. According to the manufacturer's instructions, mixtures were purified using Monarch[®] 5 μ g PCR & DNA clean-up columns. Cleaned RPA amplicons were evaluated using 20% non-denaturing TBE-DNA polyacrylamide

gels run at 3 °C, 5 V cm⁻¹, in 1.25X TBE buffer for 2 hrs. Gels were stained by soaking in EtBr stain for 5mins, rinsed and visualised using transmissive UV light. (Fig. 5.4). Product yield and concentration was determined via an EtBr fluorometric assay described on page 70. (Fig. 5.5).

5.3.2: Experimental Results:

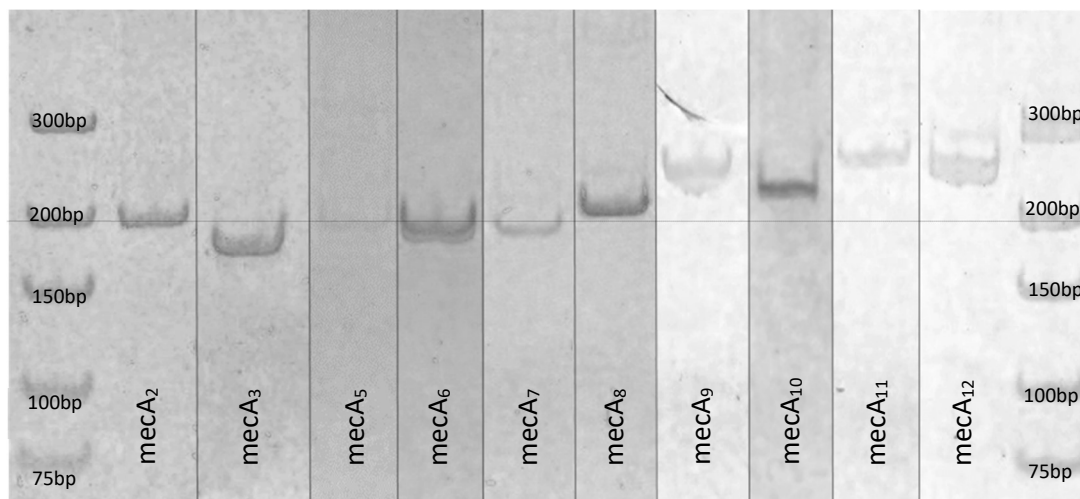


Figure 5.4. RPA products using the original *mecA* primer sequences. Black vertical lines indicate a join between gel images, and a black horizontal line indicates gel alignment reference position. Gels were collated for clarity, post-processed holistically, and background variation is due to post-run staining.

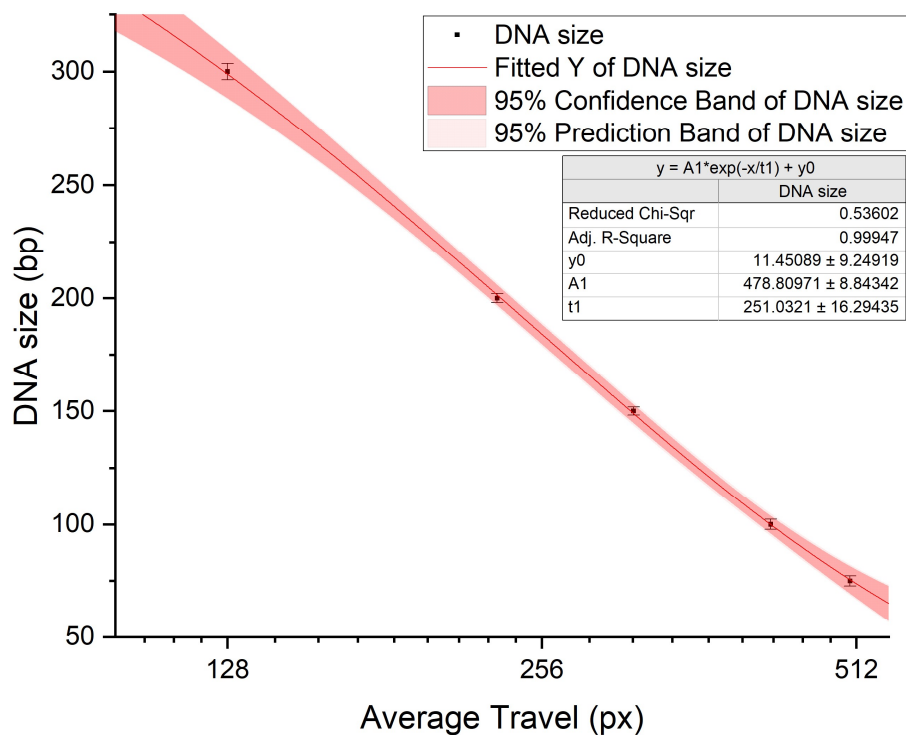


Figure 5.5. DNA migration calibration curve for gels in figure 5.4.

Table 5.2. RPA amplicon properties observed from figure 5.4.

Primer Set	Upper Band (bp)	Observed average amplicon weight (bp)	Lower Band (bp)	Amplicon Band SD	Expected Size (bp)	Difference (bp)	Approx. yield (ng)
mecA ₂	202	201	200	0.58	194	6	99
mecA ₃	183	181	179	0.85	173	6	104
mecA ₅	199	197	196	0.57	194	2	12
mecA ₆	195	192	189	1.20	188	1	130
mecA ₇	194	193	192	0.42	192	0	70
mecA ₈	212	211	209	0.80	210	-1	117
mecA ₉	250	248	246	0.87	245	1	105
mecA ₁₀	233	230	228	1.02	225	3	110
mecA ₁₁	252	251	250	0.66	243	7	77
mecA ₁₂	240	239	238	0.40	232	6	130

5.3.3: Concluding Remarks & Outcomes:

In general, the MecA primer sequences performed well directly from *in silico* to RPA, and most showed little to no spurious amplification material with acceptable yields. Of particular note was primer sets 3, 8, 9, 10 and 12 which produced excellent amplicon yields. However, primer set five produced low amplicon yields repeatably using the RPA basic kit. (Table 5.2). As a result, mecA₅ was excluded from further screening or development.

5.4 RT-RPA screen of PCR/RPA pre-screened unmodified mecA primer sequences:

The real-time amplification performance of the remaining unmodified primer sets was then evaluated. The data to be collected and scrutinized here is firstly a kinetic base line to compare how the addition of the modifications to the primer's structures effect their performance. Secondly if any observed performance difference between large and small targets was visible by comparing the reaction run using the MecA Reference template versus the MRSA gDNA reference template. Thirdly which primers are compatible with RT-RPA under ideal unmodified conditions. Although not essential for the end use of the primers in the PoC diagnostic, the primer sets must be functional with their designed internal hybridisation probes; to ensure the RPA reaction kinetics can be evaluated for objectives 1 and 2 above. Furthermore, allowing for the impact of modifications made to the amplification system in later chapters to be appraised. If sequences fail yield any viable amplicon product under these test conditions, or if the internal hybridisation probe is unable to report the production in the, it is not advisable to invest further time in that specific sequence. Unless all of the

primer sets do not report effectively. In that case modifications internal hybridisation probe should be made by moving the sequence ± 3 bp in each direction and re-evaluation to ensure that the internal probe is functional.

5.4.1: High Throughput RT-RPA Experimental Method:

Real-time amplification reactions were run in triplicate using negative controls, constituting an identical mixture with no target DNA. Negative control curves were used to baseline background kinetic curves and verify no primer-probe interactions. Triplicates were averaged and denoised using a 3-point moving average; standard deviations for the triplicate populations were used in curve fitting as per the scheme set out in *chapter 4*. (Fig. 5.6-5.16)

Real-time liquid RPA reactions were carried out using TwistAmp® fpg freeze-dried enzyme pellets on black-walled PMMA; spheroidal clear bottomed 96 well plates at total reaction volumes of 12.5 μL . Reaction mixtures composed of 0.5 μL 10 μM forward and reverse primers, 0.5 μL 2.5 μM modified internal hybridisation probe, 7.5 μL fpg RPA master mix (10 reaction pellets dissolved in 295 μL fpg rehydration buffer), 1 μL 1M copies μL^{-1} *mecA* reference gene template or 1M copies μL^{-1} ATCC 43300 MRSA gDNA. Mixtures were prepared in advance on a -80°C chilled sponge soaked in 70% isopropyl alcohol. Prepared plates were wrapped in aluminium foil and frozen at -80°C between two 70% isopropyl alcohol-soaked sponges in a sealed container. Plates were then defrosted between the soaked sponges and removed when a control well filled with 100 μL ddH₂O, monitored with a glass-coated micro-K-type thermocouple, reached 3°C . The mixtures were incubated at 45°C until 39°C was reached in the control well. Reaction constituents were mixed five times via drawing through a multi-channel pipette with wide bore 15 μL tips. Reactions were then initiated with the addition of 2.5 μL 70 mM magnesium acetate and further mixed five more times. Bubbles were removed from the reaction mixtures by bath sonication at 38°C for 10s; mixtures were covered using a round slide of 0.2mm acrylic by floating on the liquid surface. Mixtures were sonicated for a further 10 s to level the covers to reduce reflections during fluorescence measurement. Plates were immediately transferred to a 38°C pre-heated ThermoScientific™ Varioskan™ LUX multimode microplate reader. Fluorescence measurements were taken every 60 s using a 1 s integral measuring time, 515 ± 2 nm excitation light was used, and fluorescence was measured at 485 ± 5 nm.

A representative sample for each reaction was taken following RT-RPA and immediately purified using Monarch® 5 μg PCR & DNA clean-up columns. The effect of hybridisation probe integration on amplicon quality was evaluated using 20% non-denaturing TBE-DNA polyacrylamide gels run at 3°C , 5 V cm^{-1} , in 1.25X TBE buffer for 2hrs. Gels were stained by soaking in EtBr stain for 5 mins, rinsed and then visualised using transmissive UV light. (Fig. 5.6b-5.16b & Fig. 5.17).

5.4.2: Experimental Results:

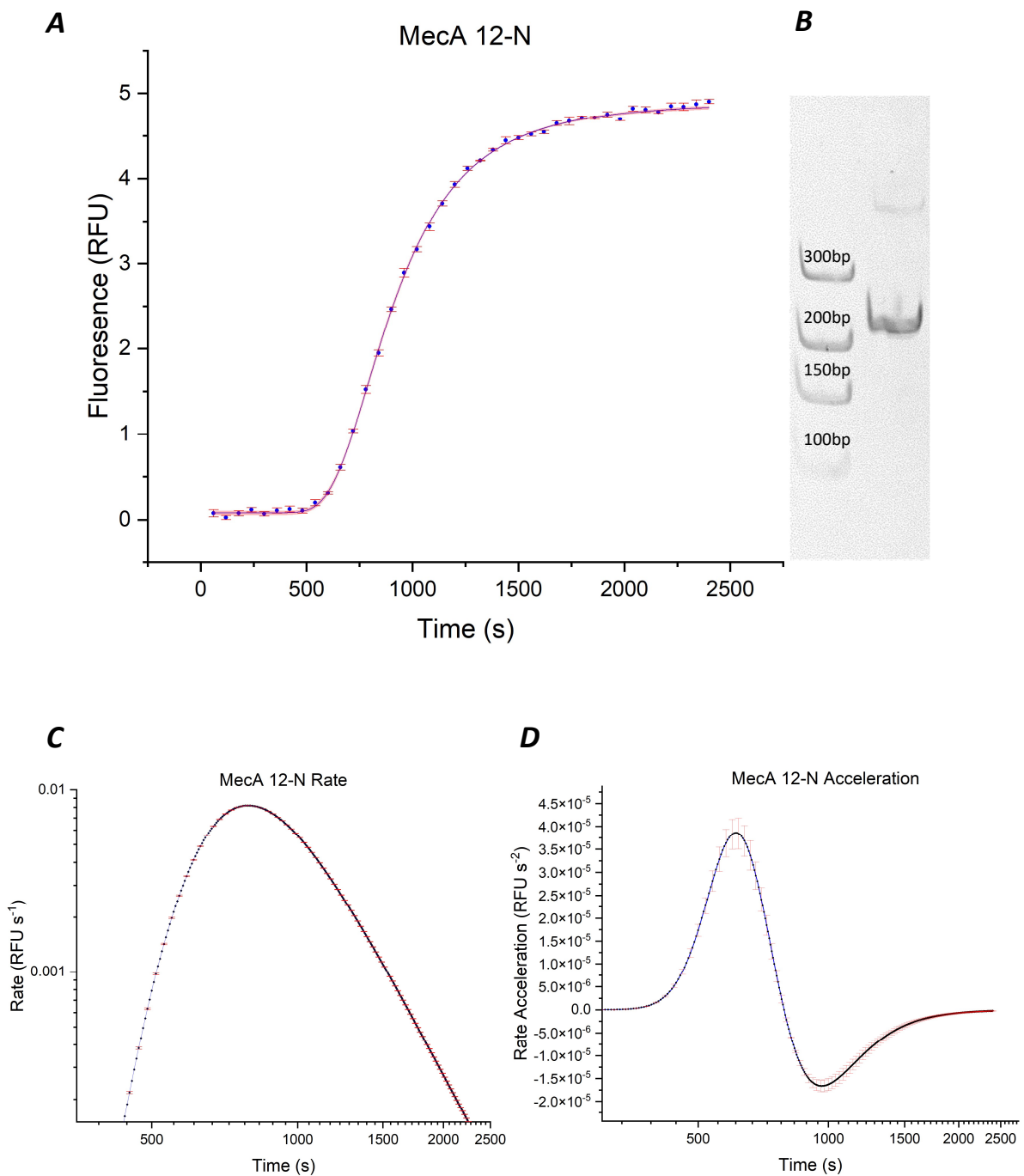


Figure 5.6. A) Processed RT-RPA fluorescence curve of primer set *mecA*₁₂ with 10M copies *mecA* reference gene template fitted using equation 1. $R^2 = 0.998$, $\Phi_i = 0.08 \pm 0.01$, $\varphi_m = 4.89 \pm 0.012$, $h = 4.13 \pm 0.078$, $f = 5.22$, $x_0 = 564.45 \pm 3.75s$. B) TBE-DNA polyacrylamide gel of combined replicates primer set *mecA*₁₂. C) First derivate rate curve for primer set *mecA*₁₂. $v_{max} = 8.2 \times 10^{-3} \pm 1.4 \times 10^{-6}$ RFU s⁻¹, $k_m = 770 \pm 5s$. D) Second derivate rate acceleration curve for primer set *mecA*₁₂. $\vec{v}_{max} = 3.86 \times 10^{-5} \pm 1.38 \times 10^{-6}$, $\vec{v}_{min} = -1.66 \times 10^{-5} \pm 5.96 \times 10^{-7}$, $t_i = 610 \pm 5s$, $t_d = 965 \pm 5s$.

Unmodified primer set MecA₁₂ with gDNA template:

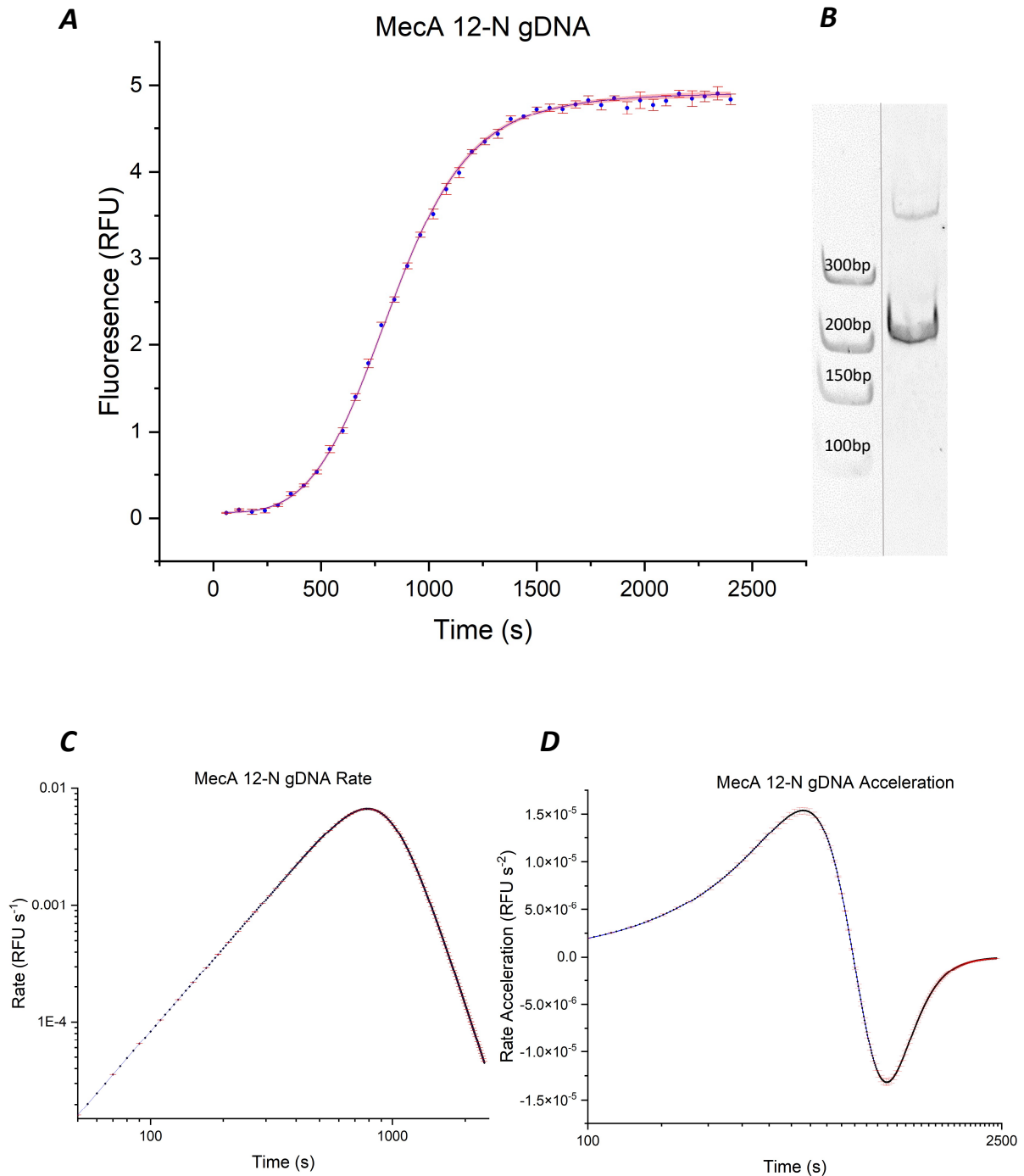


Figure 5.7. A) Processed RT-RPA fluorescence curve of primer set *mecA*₁₂ with 10M ATCC 43300 MRSA gDNA template fitted using equation 1. $R^2 = 0.999$, $\Phi_i = 0.065 \pm 0.006$, $\varphi_m = 4.92 \pm 0.019$, $h = 5.40 \pm 0.185$, $f = 0.625 \pm 0.036$, $x_o = 947.5 \pm 7.6s$. B) TBE-DNA polyacrylamide gel of combined replicates primer set *mecA*₁₂. C) First derivate rate curve for primer set *mecA*₁₂. $v_{max} = 6.6 \times 10^{-3} \pm 1.07 \times 10^{-7} \text{ RFU s}^{-1}$, $k_m = 790 \pm 5s$. D) Second derivate rate acceleration curve for primer set *mecA*₁₂. $\vec{v}_{max} = 1.54 \times 10^{-5} \pm 3.5 \times 10^{-7}$, $\vec{v}_{min} = -1.32 \times 10^{-5} \pm 3.24 \times 10^{-7}$, $t_i = 535 \pm 5s$, $t_d = 1025 \pm 5s$.

Unmodified primer MecA 11 with synthetic template:

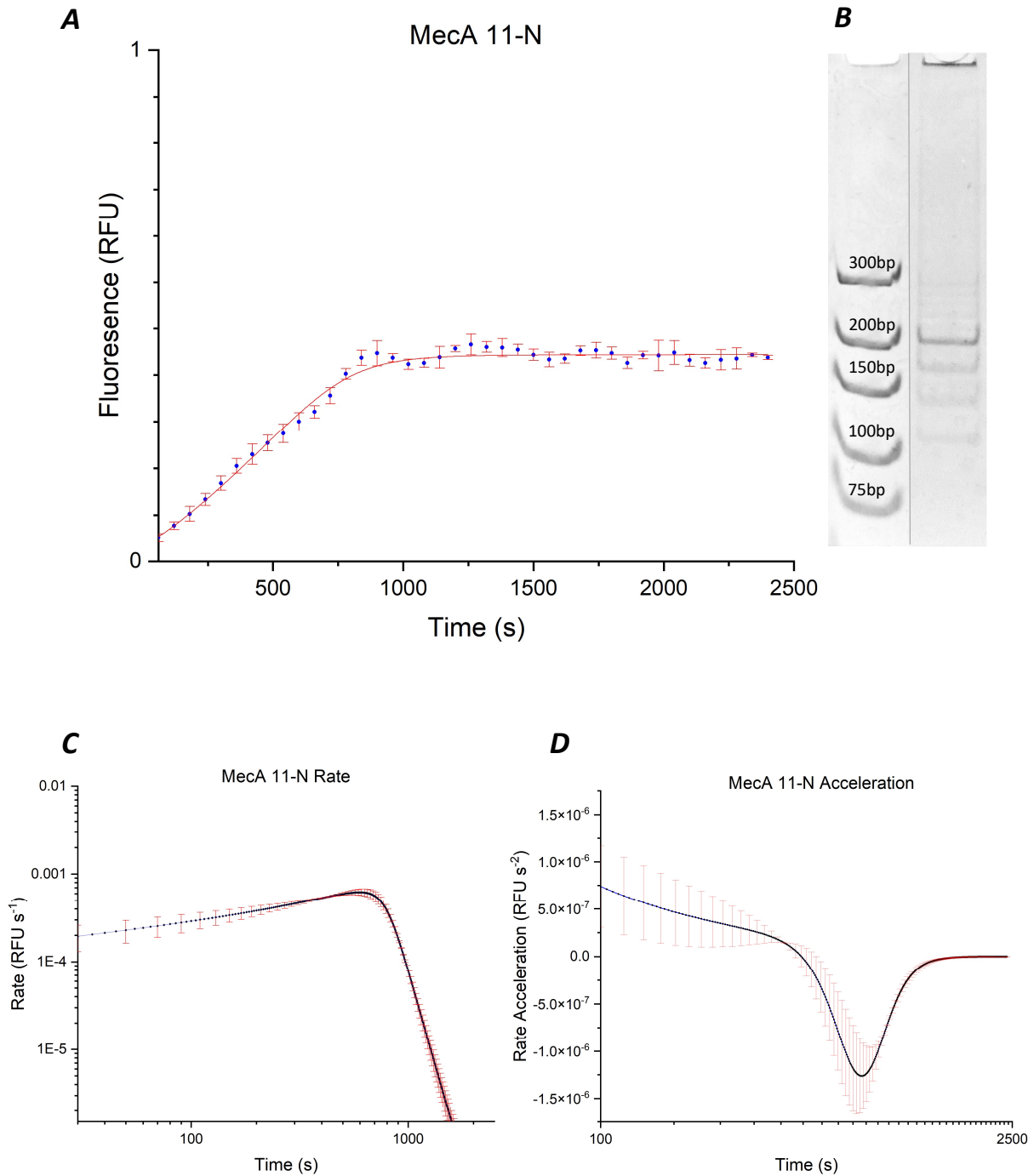


Figure 5.8. Failed RT-RPA reaction. A) Processed RT-RPA fluorescence curve of primer set $mecA_{11}$ with 10M copies $mecA$ reference gene template fitted using equation 1. $R^2 = 0.992$, $\Phi_i = 0.03 \pm 0.012$, $\varphi_m = 0.40 \pm 0.097$, $h = 7.21 \pm 0.785$, $f = 0.167 \pm 0.036$, $x_0 = 803 \pm 27.6s$. B) TBE-DNA polyacrylamide gel of combined replicates of primer set $mecA_{11}$. C) First derivate rate curve for primer set $mecA_{11}$. $v_{max} = 6.22 \times 10^4 \pm 5.16 \times 10^5 RFU s^{-1}$, $k_m = 600 \pm 5s$. D) Second derivate rate acceleration curve for primer set $mecA_{11}$. $\vec{v}_{max} = 7.7 \times 10^{-6} \pm 4.4 \times 10^{-7}$, $\vec{v}_{min} = -1.26 \times 10^{-6} \pm 3.74 \times 10^{-7}$, $t_i = 100 \pm 5s$, $t_d = 770 \pm 5s$.

Unmodified primer MecA 11 with gDNA template:

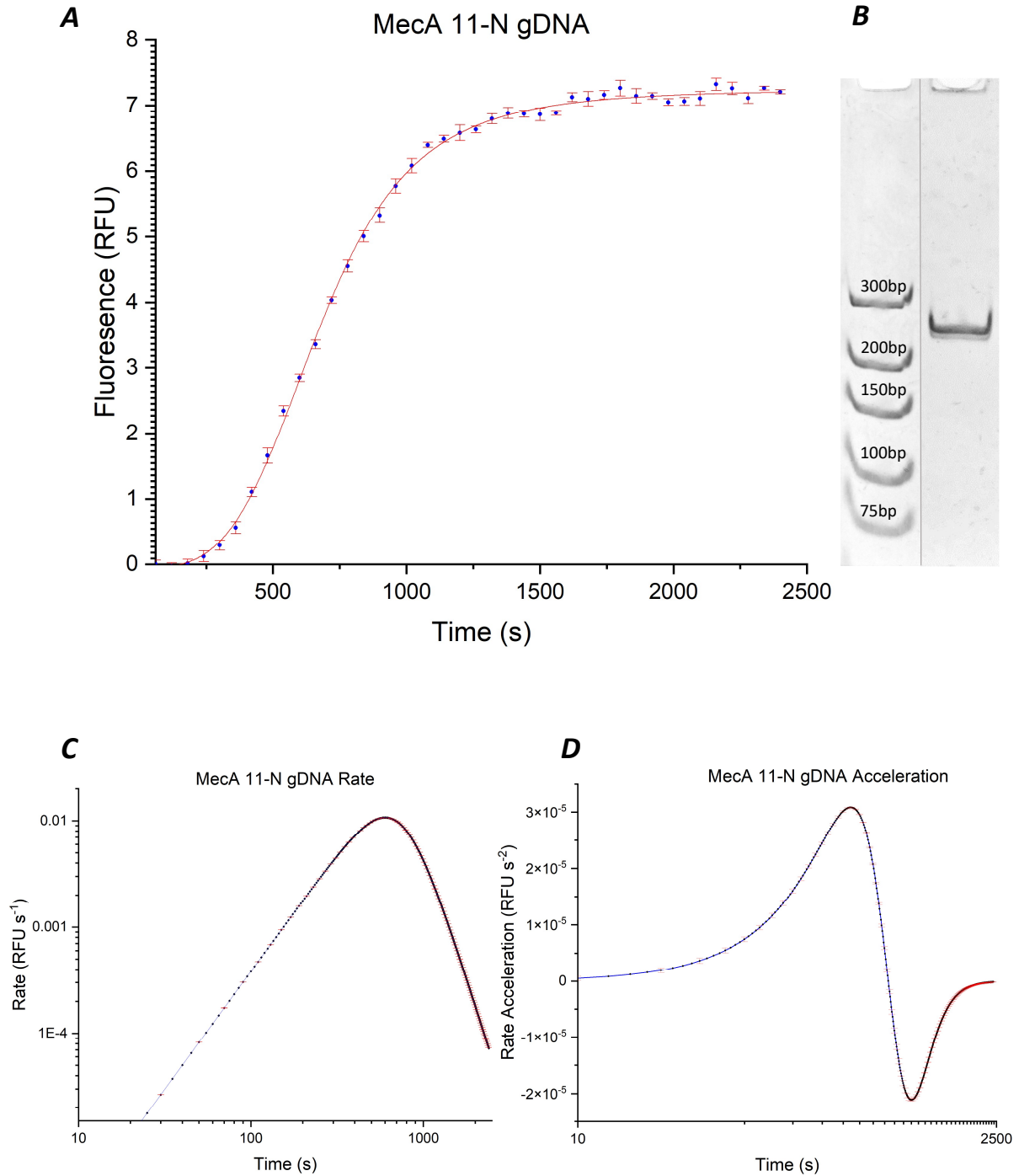


Figure 5.9. A) Processed RT-RPA fluorescence curve of primer set *mecA₁₁* with 10M copies ATCC 43300 MRSA gDNA template fitted using equation 1. $R^2 = 0.997$, $\Phi_i = -0.05 \pm 0.035$, $\varphi_m = 7.24 \pm 0.021$, $h = 4.14 \pm 0.016$, $f = 0.777 \pm 0.086$, $x_o = 735 \pm 2.6s$. B) TBE-DNA polyacrylamide gel of combined replicates of primer set *mecA₁₁*. C) First derivate rate curve for primer set *mecA₁₁*. $v_{max} = 1.08 \times 10^{-2} \pm 4 \times 10^{-7} \text{ RFU s}^{-1}$, $k_m = 600 \pm 5s$. D) Second derivate rate acceleration curve for primer set *mecA₁₁*. $\vec{v}_{max} = 1.54 \times 10^{-5} \pm 2.2 \times 10^{-8}$, $\vec{v}_{min} = -1.32 \times 10^{-5} \pm 2.83 \times 10^{-8}$, $t_i = 535 \pm 5s$, $t_d = 1025 \pm 5s$.

Unmodified primer MecA 10 with synthetic template:

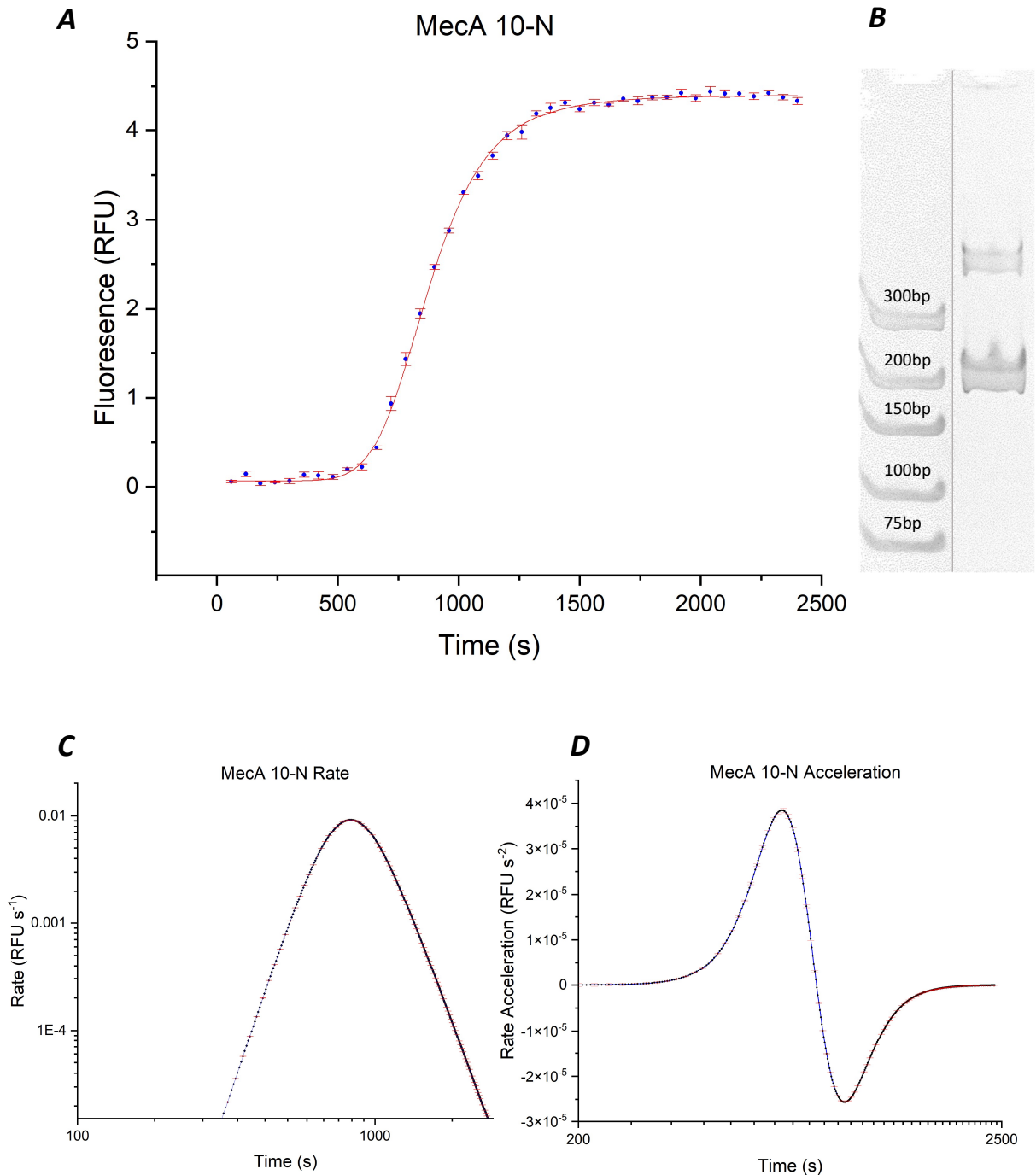


Figure 5.10. A) Processed RT-RPA fluorescence curve of primer set $mecA_{10}$ with 10M copies $mecA$ reference gene template fitted using equation 1. $R^2 = 0.998$, $\Phi_i = 0.074 \pm 0.005$, $\varphi_m = 4.42 \pm 0.011$, $h = 5.72 \pm 0.09$, $f = 2.77 \pm 0.052$, $x_0 = 696 \pm 5s$. B) TBE-DNA polyacrylamide gel of combined replicates of primer set $mecA_{11}$. C) First derivate rate curve for primer set $mecA_{10}$. $v_{max} = 9.20 \times 10^{-3} \pm 1.2 \times 10^{-7}$ RFU s^{-1} , $k_m = 830 \pm 5s$. D) Second derivate rate acceleration curve for primer set $mecA_{10}$. $\vec{v}_{max} = 3.85 \times 10^{-5} \pm 4.54 \times 10^{-7}$, $\vec{v}_{min} = -2.56 \times 10^{-5} \pm 5.3 \times 10^{-7}$, $t_i = 675 \pm 5s$, $t_d = 980 \pm 5s$

Unmodified primer MecA 10 with gDNA template:

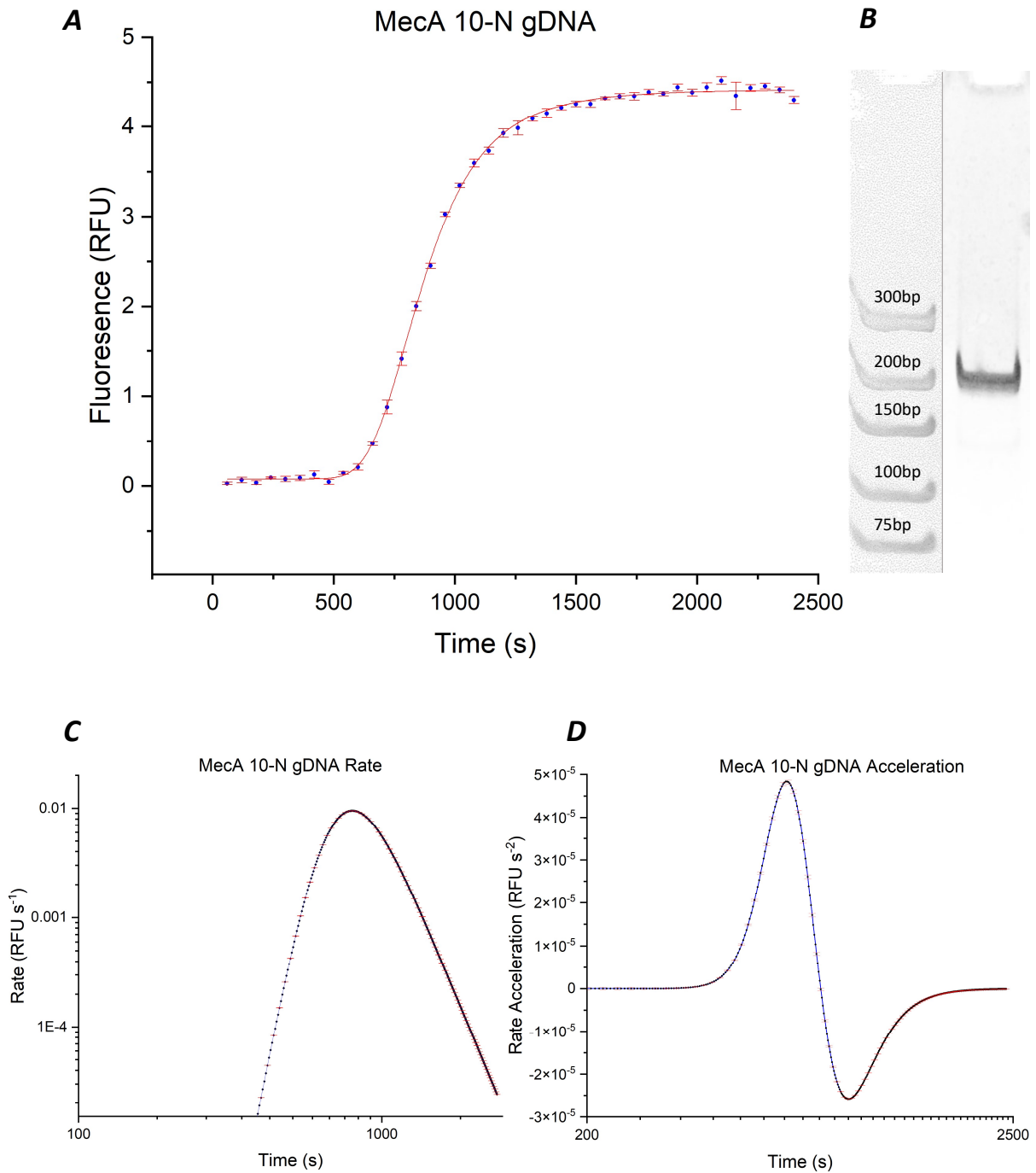


Figure 5.11. A) Processed RT-RPA fluorescence curve of primer set $mecA_{10}$ with 10M copies ATCC 43300 MRSA gDNA template fitted using equation 1. $R^2 = 0.998$, $\Phi_i = 0.063 \pm 0.006$, $\varphi_m = 4.40 \pm 0.01$, $h = 6.52 \pm 0.22$, $f = 1.416 \pm 0.095$, $x_0 = 817 \pm 1.96s$. B) TBE-DNA polyacrylamide gel of combined replicates of primer set $mecA_{10}$. C) First derivate rate curve for primer set $mecA_{10}$. $v_{max} = 9.53 \times 10^{-3} \pm 4 \times 10^{-7} RFU s^{-1}$, $k_m = 800 \pm 5s$. D) Second derivate rate acceleration curve for primer set $mecA_{10}$. $\vec{v}_{max} = 4.84 \times 10^{-5} \pm 4.35 \times 10^{-7}$, $\vec{v}_{min} = -2.58 \times 10^{-5} \pm 6.3 \times 10^{-8}$, $t_i = 655 \pm 5s$, $t_d = 945 \pm 5s$

Unmodified primer MecA 9 with gDNA template:

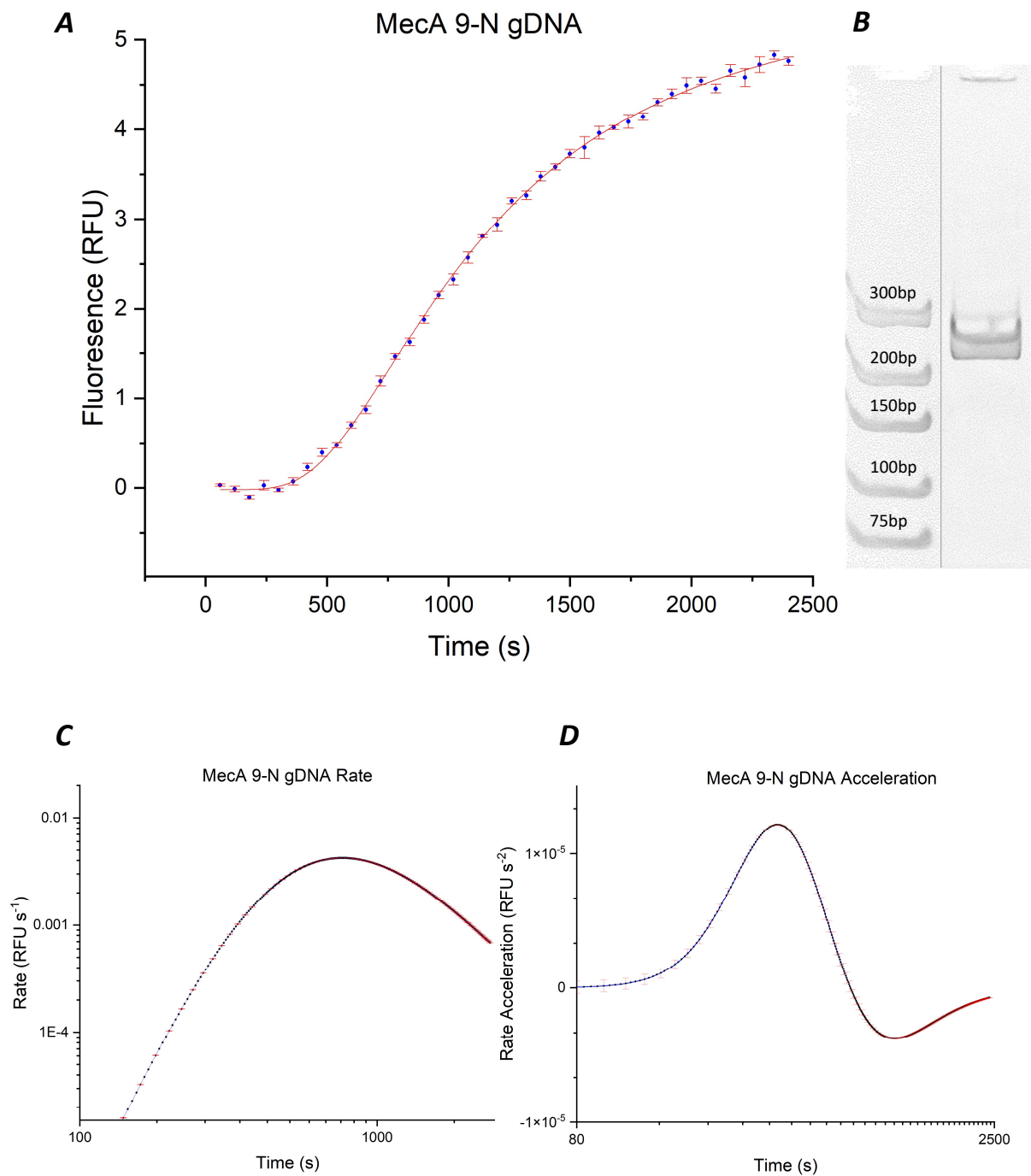


Figure 5.12. A) Processed RT-RPA fluorescence curve of primer set *mecA₉* with 10M copies ATCC 43300 MRSA gDNA template fitted using equation 1. $R^2 = 0.997$, $\Phi_i = -0.02 \pm 0.011$, $\varphi_m = 5.72 \pm 0.13$, $h = 1.98 \pm 0.14$, $f = 3.59 \pm 1.25$, $x_0 = 531 \pm 12.615s$. B) TBE-DNA polyacrylamide gel of combined replicates of primer set *mecA₉*. C) First derivate rate curve for primer set *mecA₉*. $v_{max} = 4.23 \times 10^{-3} \pm 6.12 \times 10^{-7} RFU s^{-1}$, $k_m = 765 \pm 5s$. D) Second derivate rate acceleration curve for primer set *mecA₉*. $\vec{v}_{max} = 1.22 \times 10^{-5} \pm 4.04 \times 10^{-8}$, $\vec{v}_{min} = -3.76 \times 10^{-6} \pm 3.63 \times 10^{-8}$, $t_i = 420 \pm 5s$, $t_d = 1100 \pm 5s$

Unmodified primer MecA 8 with synthetic template:

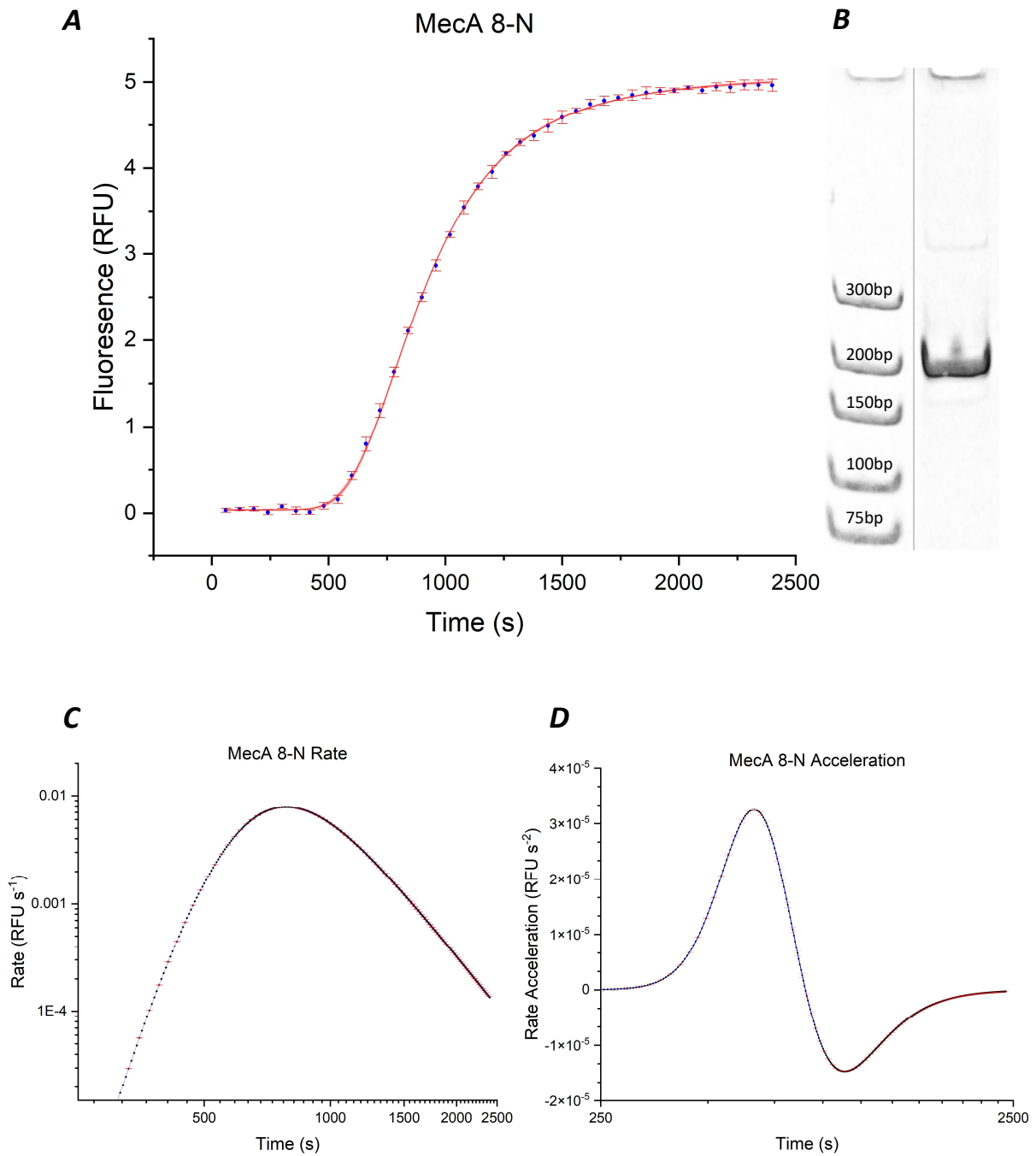


Figure 5.13. A) Processed RT-RPA fluorescence curve of primer set $mecA_8$ with 10M copies $mecA$ reference gene template fitted using equation 1. $R^2 = 0.998$, $\Phi_i = 0.037 \pm 0.009$, $\varphi_m = 5.08 \pm 0.013$, $h = 3.93 \pm 0.15$, $f = 3.43 \pm 0.52$, $x_o = 619 \pm 5.8s$. B) TBE-DNA polyacrylamide gel of combined replicates of primer set $mecA_8$. C) First derivate rate curve for primer set $mecA_8$. $v_{max} = 7.85 \times 10^{-3} \pm 3.6 \times 10^{-7}$ $RFU s^{-1}$, $k_m = 785 \pm 5s$. D) Second derivate rate acceleration curve for primer set $mecA_8$. $\vec{v}_{max} = 3.25 \times 10^{-5} \pm 3.24 \times 10^{-7}$, $\vec{v}_{min} = -1.47 \times 10^{-5} \pm 2.6 \times 10^{-8}$, $t_i = 590 \pm 5s$, $t_d = 975 \pm 5s$

Unmodified primer MecA 8 with gDNA template:

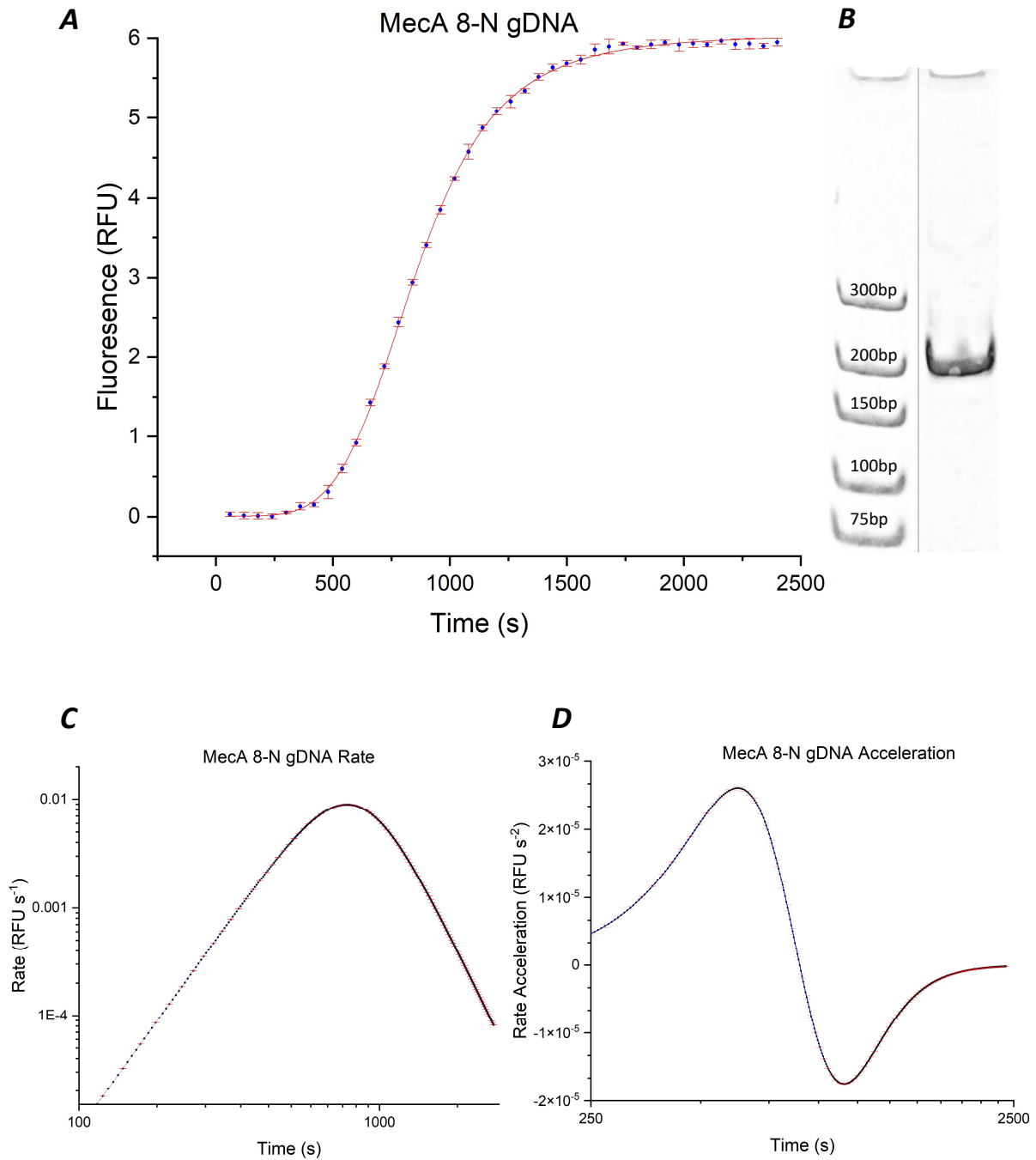


Figure 5.14. A) Processed RT-RPA fluorescence curve of primer set $mecA_8$ with 10M ATCC 43300 MRSA gDNA template fitted using equation 1. $R^2 = 0.997$, $\Phi_i = 0.007 \pm 0.013$, $\varphi_m = 6.04 \pm 0.016$, $h = 4.81 \pm 0.14$, $f = 1.03 \pm 0.09$, $x_o = 848 \pm 2.1s$. B) TBE-DNA polyacrylamide gel of combined replicates of primer set $mecA_8$. C) First derivate rate curve for primer set $mecA_8$. $v_{max} = 8.94 \times 10^{-3} \pm 8.3 \times 10^{-8} RFU s^{-1}$, $k_m = 780 \pm 5s$. D) Second derivate rate acceleration curve for primer set $mecA_8$. $\vec{v}_{max} = 2.6 \times 10^{-5} \pm 2.54 \times 10^{-7}$, $\vec{v}_{min} = -1.75 \times 10^{-5} \pm 3.34 \times 10^{-8}$, $t_i = 555 \pm 5s$, $t_d = 995 \pm 5s$

Unmodified primer MecA 7 with synthetic template:

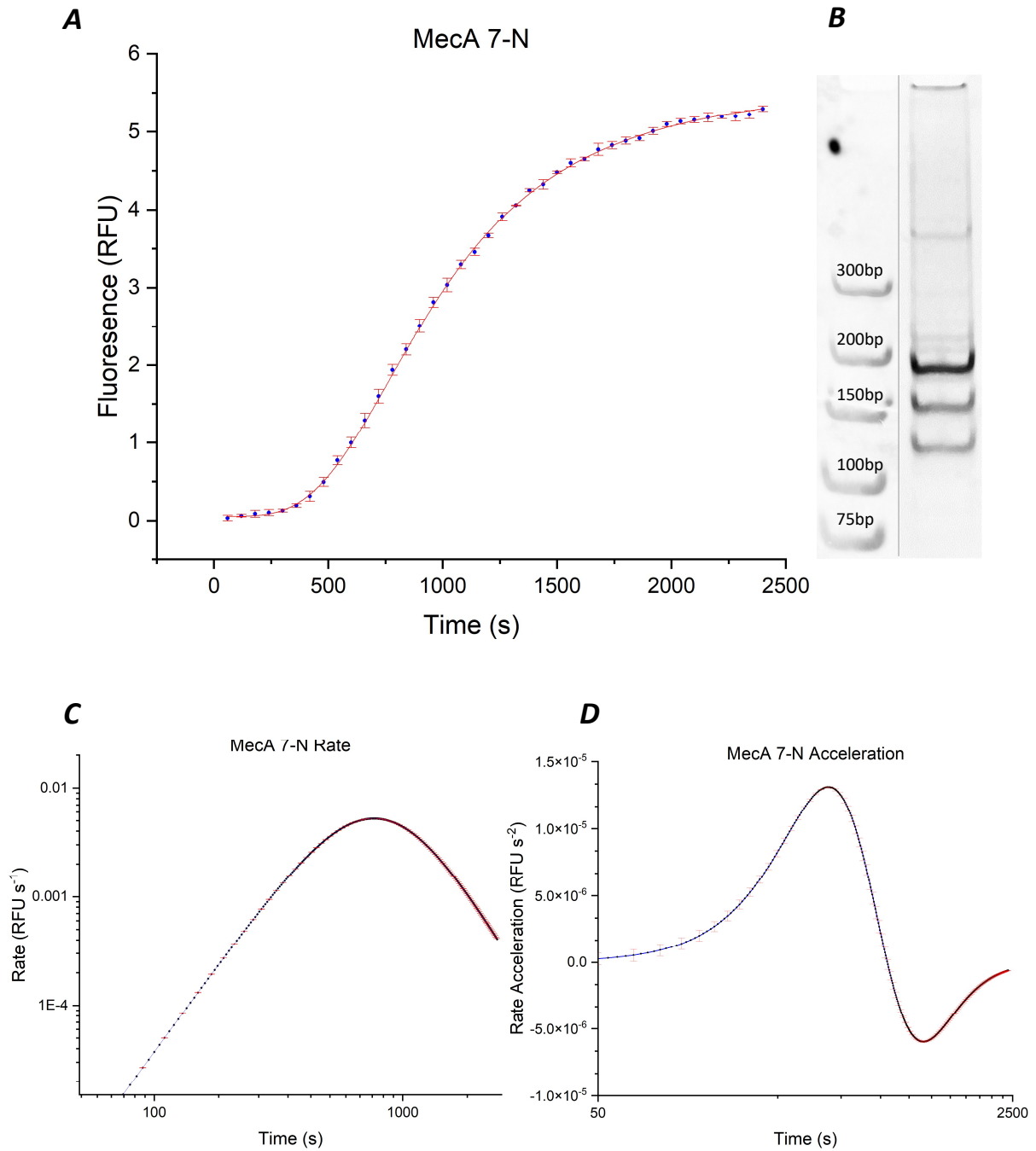


Figure 5.15. A) Processed RT-RPA fluorescence curve of primer set $mecA_7$ with 10M copies $mecA$ reference gene template fitted using equation 1. $R^2 = 0.999$, $\Phi_i = 0.05 \pm 0.014$, $\varphi_m = 5.66 \pm 0.049$, $h = 2.84 \pm 0.13$, $f = 1.45 \pm 0.21$, $x_0 = 823 \pm 5.7s$. B) TBE-DNA polyacrylamide gel of combined replicates of primer set $mecA_7$. C) First derivate rate curve for primer set $mecA_7$. $v_{max} = 5.22 \times 10^{-3} \pm 2.28 \times 10^{-7}$ $RFU s^{-1}$, $k_m = 765 \pm 5s$. D) Second derivate rate acceleration curve for primer set $mecA_7$. $\vec{v}_{max} = 1.31 \times 10^{-5} \pm 3.78 \times 10^{-7}$, $\vec{v}_{min} = -5.97 \times 10^{-6} \pm 3.82 \times 10^{-8}$, $t_i = 440 \pm 5s$, $t_d = 1080 \pm 5s$

Unmodified primer MecA 7 with gDNA template:

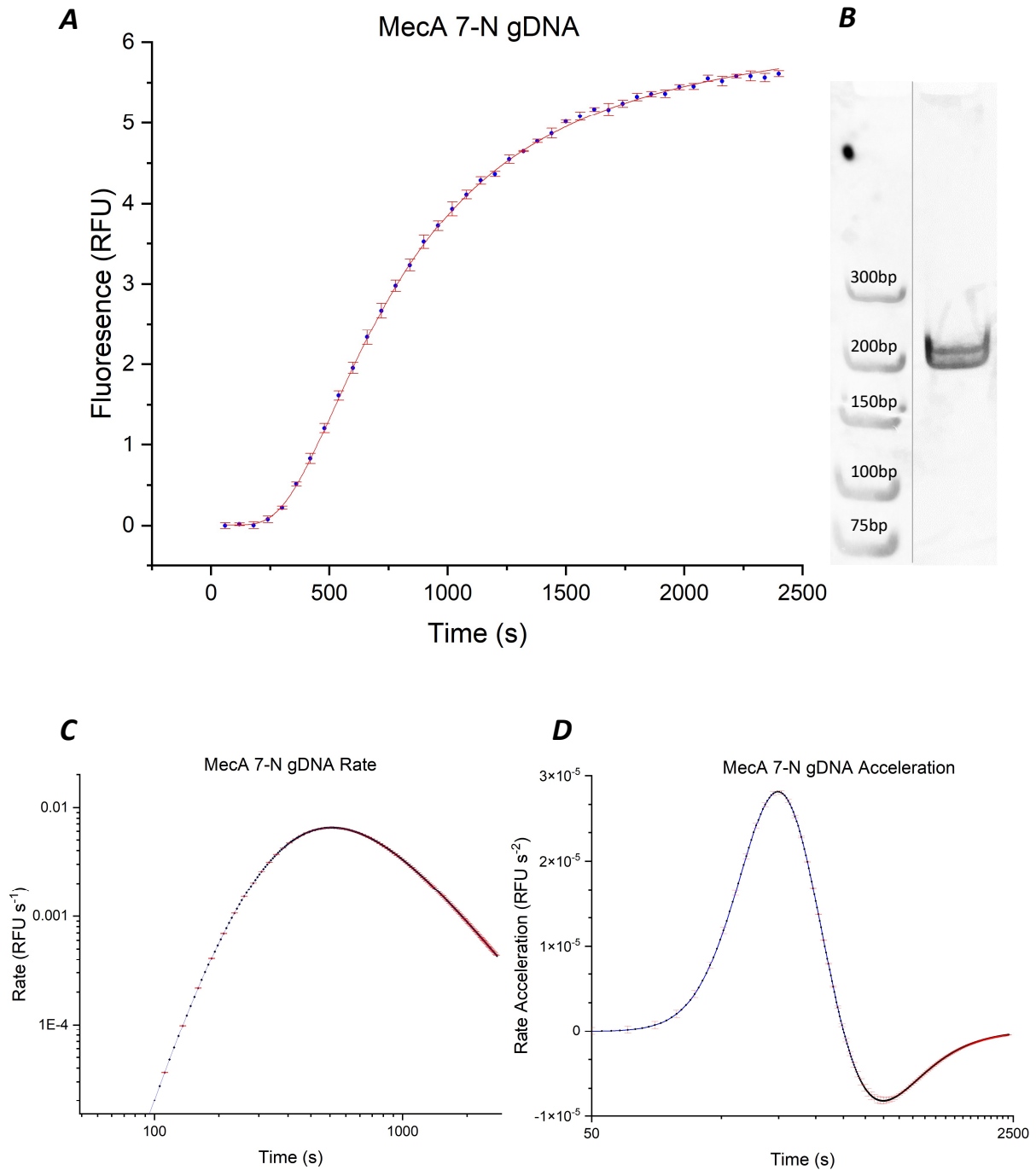


Figure 5.16. A) Processed RT-RPA fluorescence curve of primer set $mecA_7$ with 10M ATCC 43300 MRSA gDNA template fitted using equation 1. $R^2 = 0.998$, $\Phi_i = 0.05 \pm 0.015$, $\varphi_m = 6.27 \pm 0.057$, $h = 1.86 \pm 0.078$, $f = 4.55 \pm 0.55$, $x_0 = 308 \pm 7.6s$. B) TBE-DNA polyacrylamide gel of combined replicates of primer set $mecA_7$. C) First derivate rate curve for primer set $mecA_7$. $v_{max} = 6.47 \times 10^{-3} \pm 1.79 \times 10^{-6}$ RFU s^{-1} , $k_m = 520 \pm 5s$. D) Second derivate rate acceleration curve for primer set $mecA_7$. $\vec{v}_{max} = 2.81 \times 10^{-5} \pm 2.11 \times 10^{-7}$, $\vec{v}_{min} = -8.13 \times 10^{-6} \pm 3.82 \times 10^{-8}$, $t_i = 280 \pm 5s$, $t_d = 750 \pm 5s$.

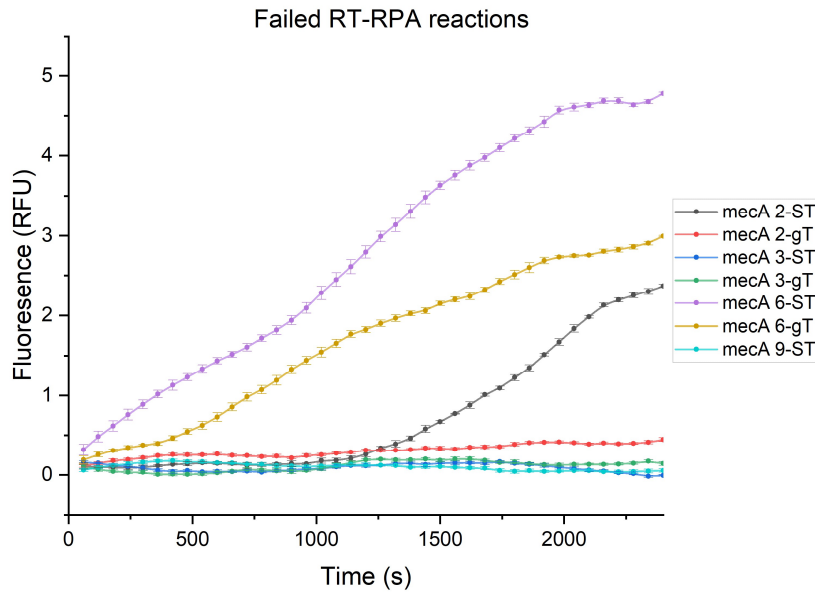


Figure 5.17. Unprocessed RT-RPA fluorescence curves of primer sets which failed under RT-RPA conditions.

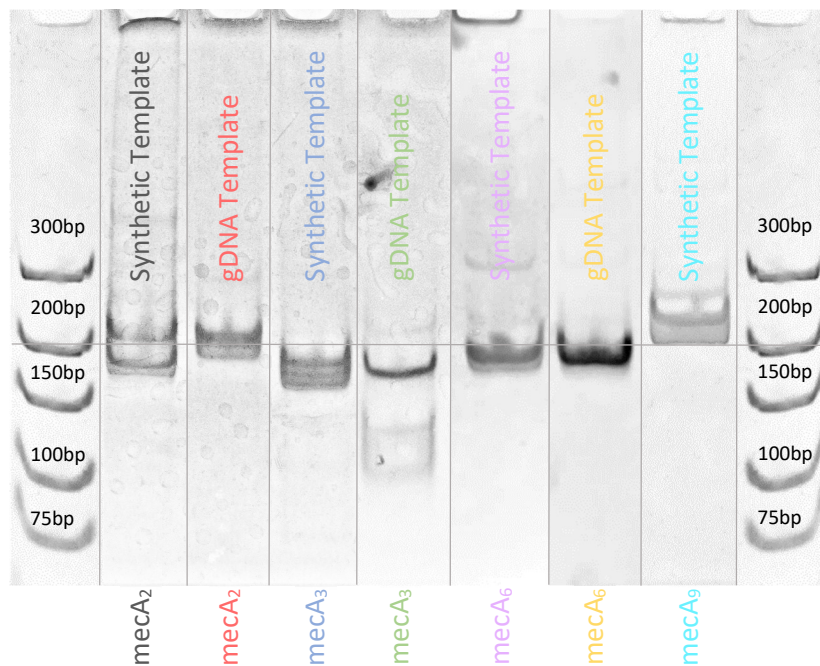


Figure 5.18. Combined TBE-DNA polyacrylamide gels of combined replicates of primer sets which failed under RT-RPA conditions. Black vertical lines indicate a join between gel images, and a black horizontal line indicates gel alignment reference position. Gels were collated for clarity, post-processed holistically, background variation is due to post-run staining.

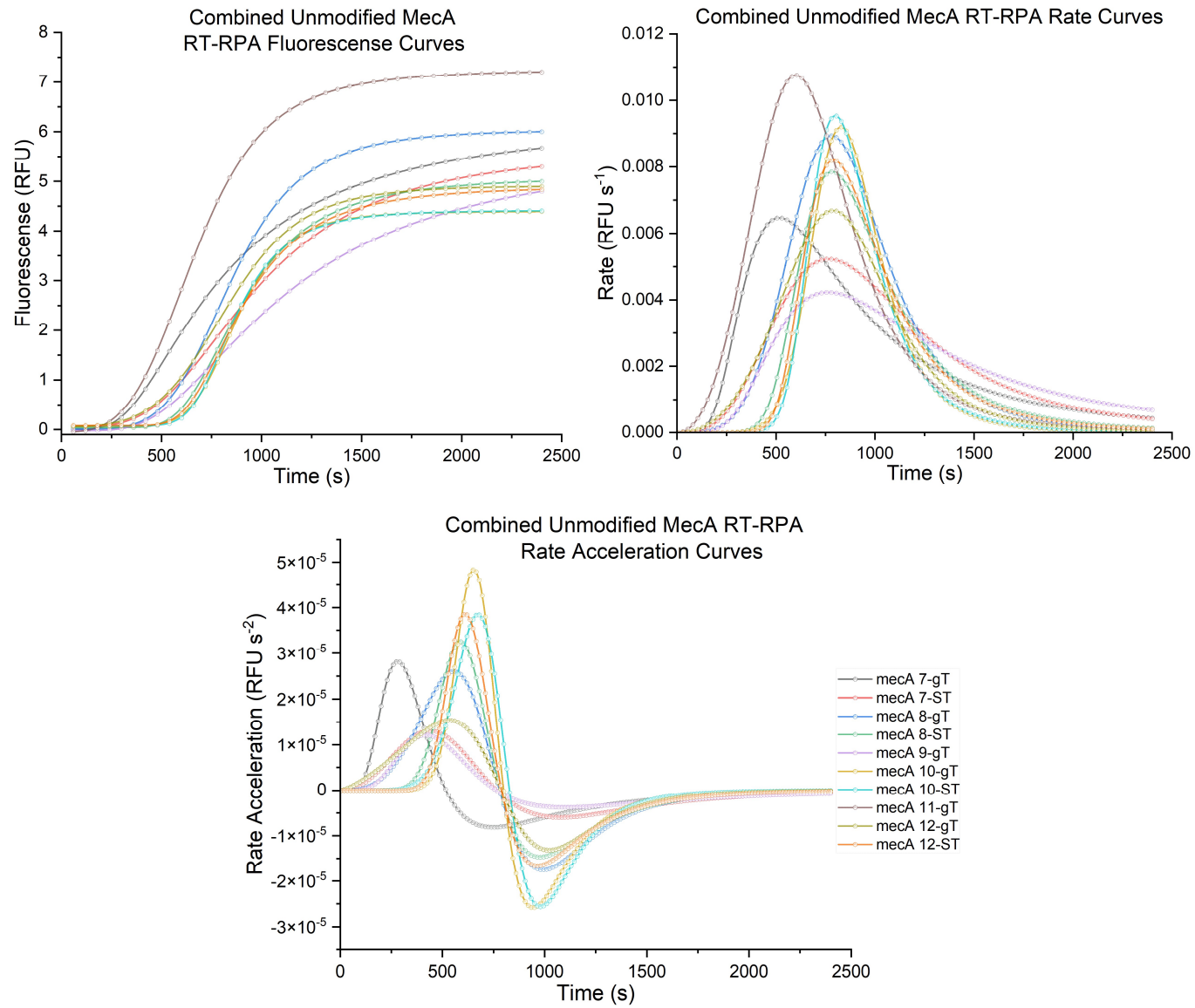


Figure 5.19. Combined processed fits of successful primer sets under RT-RPA conditions.

5.4.3: Concluding Remarks & Outcomes:

In general, the initial RT-RPA screening experiments with the unmodified *mecA* primer sequences produced mixed results. (Fig. 5.19). To begin with only 3 primer sequence sets produced the expected RT-RPA kinetic curves with both templates while maintaining relatively clean endpoint DNA-PAGE gels. (Fig. 5.6-5.7, Fig. 5.10-5.11 & Fig. 5.13-5.14).

Of note, successful primer sets exhibited some spurious endpoint material when amplified under RT-RPA conditions. The spurious bands were typically higher in molecular weight by approximately 150-200bp. It appeared this band was more prevalent in amplification mixtures where the short *MecA* reference gene was used as a template. It is likely given this band is present in the successful reactions that this is amplicon probe complex following fluorophore release remaining hybridised. While this was unexpected it is also showing the probe is working as intended. Furthermore, this should be considered a desired effect as it prevents probes with cleaved fluorophores being rehybridized with amplicons. If it was possible to prove and ensure each amplicon when hybridised with a probe remained hybridised throughout the measurement, then the kinetic curves could be considered quantitative by standardising against known FAM concentrations. This could prove an interesting project to investigate in itself.

Another observation to be made was RT-monitoring was significantly more likely to function when ran using gDNA template. Take primer sets 11 and 7, in both cases a successful RT-RPA curve was obtained accompanied by clean endpoint DNA-PAGE gels, with no unexpected bands; but only when ran using the MRSA gDNA template. However, when ran using the *MecA* reference gene set 11 produced no product where as set 9 produced fantastically clean amplicons but they were not functional with the hybridisation probe. The reasons behind this remain unclear.

From the data presented in *figure 5.18*, it is clear to see that the designed hybridisation probe for sequences 1-6 was not functioning correctly. *Figure 5.19* clearly shows the end point DNA-Page gels for the primer sequence 2, 3 and 6. Each of which produced acceptable amplicons in terms of purity and expected molecular weight, this was especially the case for *mecA*₆. However, no RT RPA curve could be obtained for any of these primer sets. Fortunately sets within the sequence library produced the desired results, saving redefining new probe sequences and repeating this experiment.

As stated previously these results provide a first glimpse into how the system behaves with templates of varying size. *Table 5.3* highlights the key reaction parameters obtained from the 1st and 2nd derivative plots of the RT-RPA fits of the 3 successful primer sets. In general, a small but measurable difference was observed in the time to initiation of the reactions. Were by the gDNA template

reactions were on average 6.9 % faster to initiate versus the MecA reference gene reactions. Initially result was counter intuitive, however it points to an interesting observation about the kinetics. Referring back to *figure 2.12, page 54*; whereby the initial rate limiting step is formation of RecA-primer-template complex's rather than location of the complementary zone of the template. Given the gDNA has significantly more total mass of DNA per MecA copy this formation of initial complex's is accelerated.

Table 5.3 Average key kinetic reaction constants of unmodified primers.

Primer Name	Template	Initiation Time (s)	Time to Max Sudo-Rate (s)	Time to Depletion (s)
MecA ₁₂	MecA Ref	610	770	965
	MRSA gDNA	535	790	1025
	<i>% Diff</i>	<i>12.3</i>	<i>-2.6</i>	<i>-6.2</i>
MecA ₁₀	MecA	675	830	980
	gDNA	655	800	945
	<i>% Diff</i>	<i>3.0</i>	<i>3.6</i>	<i>3.6</i>
MecA ₈	MecA	590	785	975
	gDNA	555	780	995
	<i>% Diff</i>	<i>5.9</i>	<i>0.6</i>	<i>-2.1</i>
Average	MecA Avg	625	795	973
	gDNA Avg	582	790	988
	<i>% Diff</i>	<i>6.9</i>	<i>0.6</i>	<i>-1.5</i>

Taken forward for full analysis onto the next line of primer screening was MecA₁₂, MecA₁₀, MecA₈ and MecA₇. While MecA₇ did not function well using the MecA template it did have desirable kinetic characteristics and work with gDNA which will be the actual target of interest. Primer sets 2, 3, 6, 9, and 11 advanced to the subsequent phase of primer screening to confirm their unsuitability shown thus far. However, they were not subjected to triplicate analysis without enabling fluorescence normalization. For sets 2 to 6, a fresh internal probe was synthesized by a different supplier to eliminate any potential manufacturing errors associated with the initial probe.

5.5 RT-RPA of pre-screened modified variants of the *mecA* primer sequences:

The real-time amplification performance of the 4 selected primer sequences was then evaluated with their incorporated modifications described in *chapter 2*. As in *section 5.4* the data to be collected and scrutinized here is firstly how the addition of the modifications has altered and compares to the base line kinetic performance. Secondly further observed any performance difference between large and small targets now the primers have been modified. Thirdly which modified primers are compatible with RT-RPA reaction conditions to allow for reaction development in later chapters. And lastly to assess the difference if any the varying spacer length has upon the reaction product quality and kinetics of the amplification reactions.

5.5.1: High Throughput RT-RPA Experimental Method:

Real-time amplification reactions were run in triplicate using negative controls, constituting an identical mixture with no target DNA. Negative control curves were used to baseline background kinetic curves and verify no primer-probe interactions. Triplicates were averaged and denoised using a 3-point moving average; standard deviations for the triplicate populations were used in curve fitting as per the scheme set out in *chapter 4*.

Real-time liquid RPA reactions were carried out the same procedure outlined in *section 5.4.2* however using the C3 and C12 fully modified variants of the modified primer sequences shown in *table 2.14, page 65*. Again, both templates were used to assess the primer sequences performance across target size. Processed kinetic curves for successfully amplified C3 variants of the modified primers are shown in *Figures 5.20-5.27*, followed by C12 variants in *Figures 5.31-5.38*. Failed RT-RPA raw data curves for the C3 and C12 modified variants are shown collated on in *Figures 5.28 and 5.39* respectively.

A representative sample for each reaction was taken following RT-RPA and immediately purified using Monarch® 5 µg PCR & DNA clean-up columns. The effect of hybridisation probe integration on amplicon quality was evaluated using 20 % non-denaturing TBE-DNA polyacrylamide gels run at 3 °C, 5 V cm⁻¹, in 1.25X TBE buffer for 2 hrs. Gels were stained by soaking in EtBr stain for 5mins, rinsed and then visualised using transmissive UV light. Gels showing C3 variant of the modified primers are shown in *Figures 5.20b-5.27b & Figure 5.29*. Gels showing C12 variant of the modified primers are shown in *Figures 5.31b-5.38b & Figure 5.40*.

5.5.2: C3 Modified RT-RPA Experimental Results

Modified primer MecA₁₂-C3 with synthetic template:

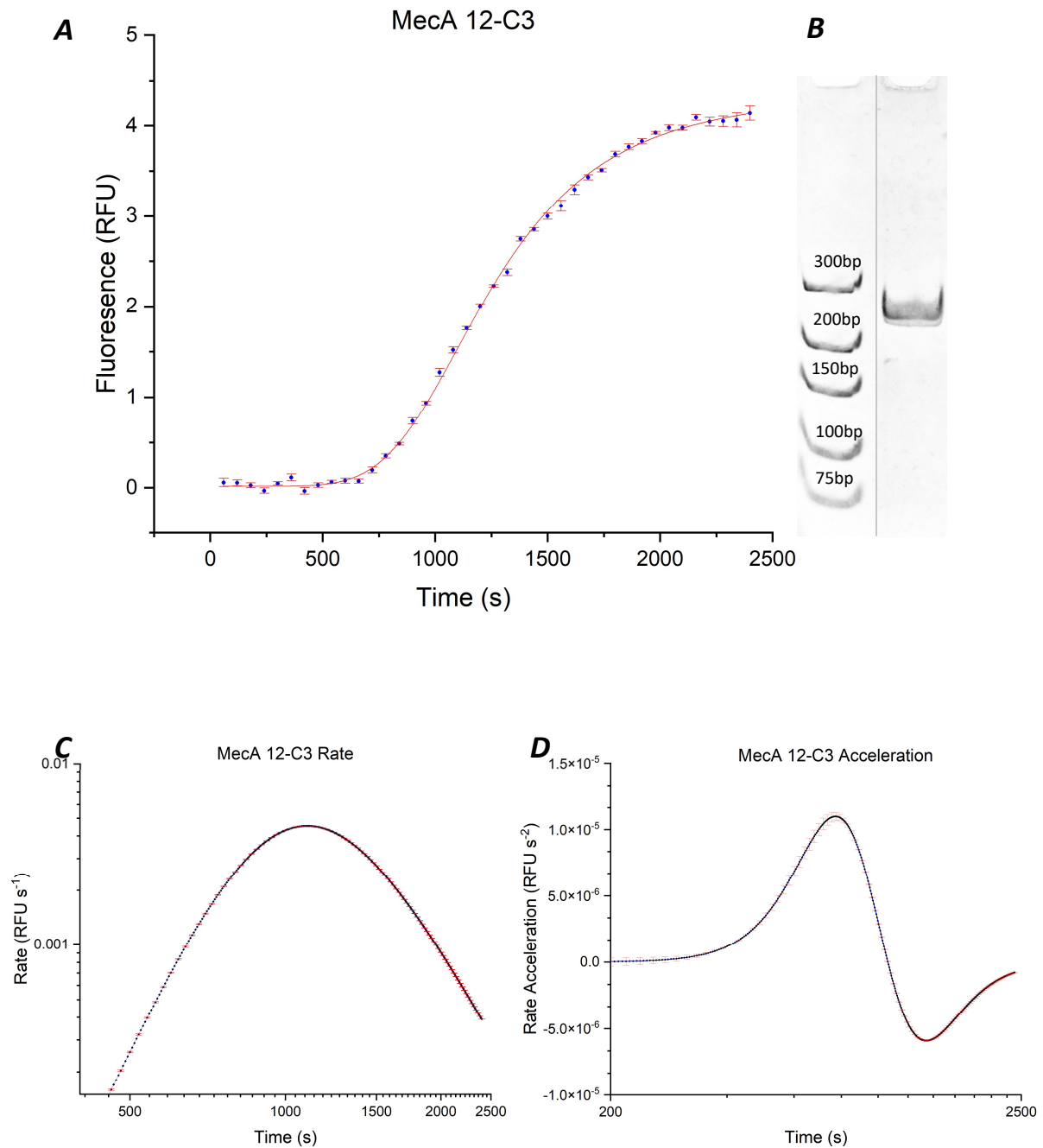


Figure 5.20. A) Processed RT-RPA fluorescence curve of primer set *mecA*₁₂ with 10M copies *mecA* reference gene template fitted using equation 1. $R^2 = 0.999$, $\Phi_i = 0.015 \pm 0.009$, $\varphi_m = 4.37 \pm 0.005$, $h = 4.16 \pm 0.18$, $f = 1.73 \pm 0.33$, $x_0 = 1053 \pm 5.7s$. B) TBE-DNA polyacrylamide gel of combined replicates primer set *mecA*₁₂. C) First derivate rate curve for primer set *mecA*₁₂. $v_{max} = 4.4 \times 10^{-3} \pm 6.6 \times 10^{-6} \text{ RFU s}^{-1}$, $k_m = 1100 \pm 5s$. D) Second derivate rate acceleration curve for primer set *mecA*₁₂. $\vec{v}_{max} = 1.1 \times 10^{-5} \pm 2.94 \times 10^{-7}$, $\vec{v}_{min} = -5.9 \times 10^{-6} \pm 9.06 \times 10^{-9}$, $t_i = 800 \pm 5s$, $t_d = 1395 \pm 5s$.

Modified primer set MecA₁₂-C3 with gDNA template:

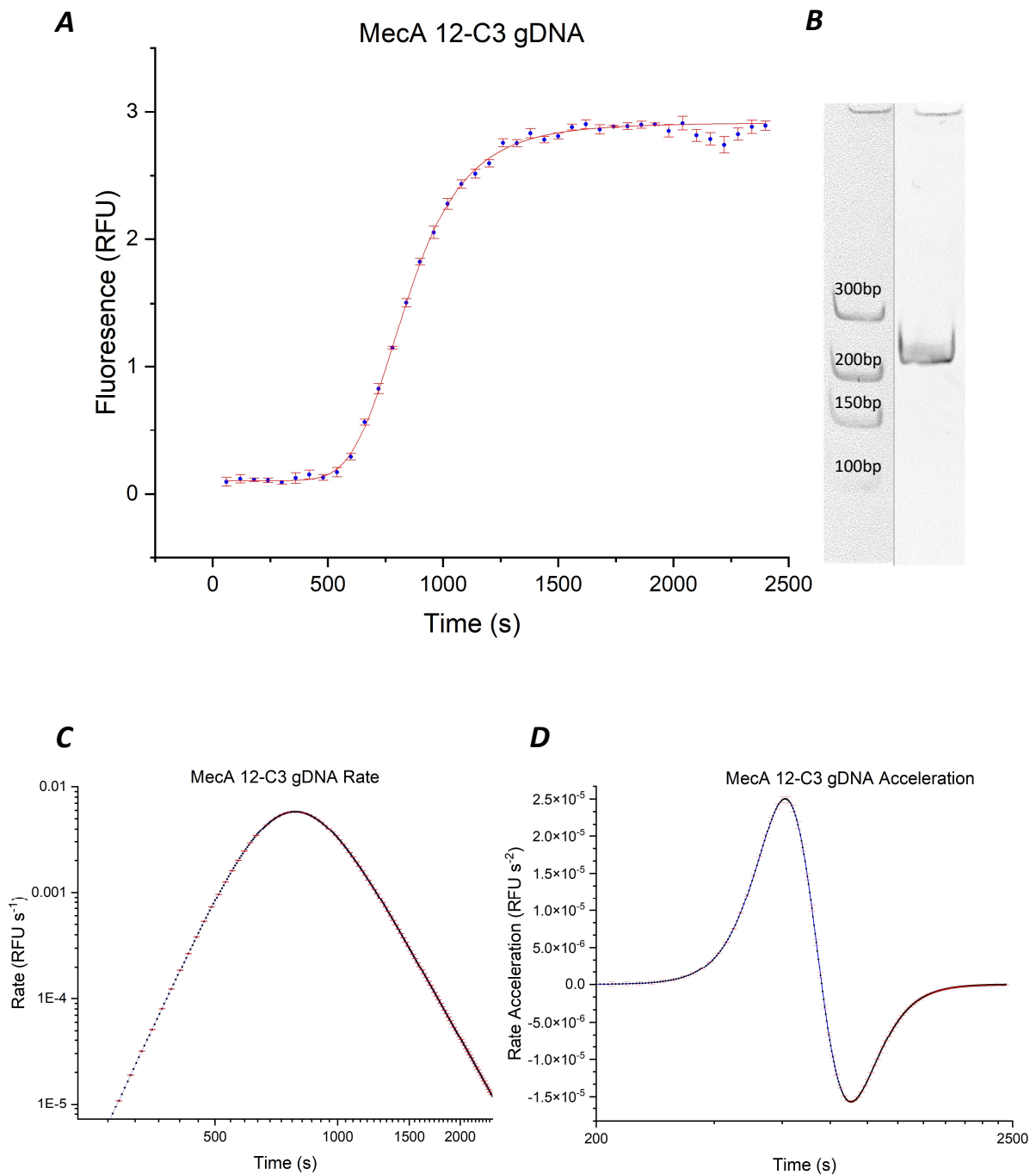


Figure 5.21. A) Processed RT-RPA fluorescence curve of primer set *mecA*₁₂ with 10M ATCC 43300 MRSA gDNA template fitted using equation 1. $R^2 = 0.998$, $\Phi_i = 0.1 \pm 0.007$, $\varphi_m = 2.91 \pm 0.007$, $h = 5.938 \pm 0.24$, $f = 1.57 \pm 0.25$, $x_0 = 762 \pm 2.8s$. B) TBE-DNA polyacrylamide gel of combined replicates primer set *mecA*₁₂. C) First derivate rate curve for primer set *mecA*₁₂. $v_{max} = 5.8 \times 10^{-3} \pm 3.5 \times 10^{-7}$ RFU s^{-1} , $k_m = 785 \pm 5s$. D) Second derivate rate acceleration curve for primer set *mecA*₁₂. $\vec{v}_{max} = 2.26 \times 10^{-5} \pm 3.5 \times 10^{-7}$, $\vec{v}_{min} = -1.46 \times 10^{-5} \pm 3.24 \times 10^{-7}$, $t_i = 620 \pm 5s$, $t_d = 945 \pm 5s$.

Modified primer set MecA₁₀-C3 with synthetic template:

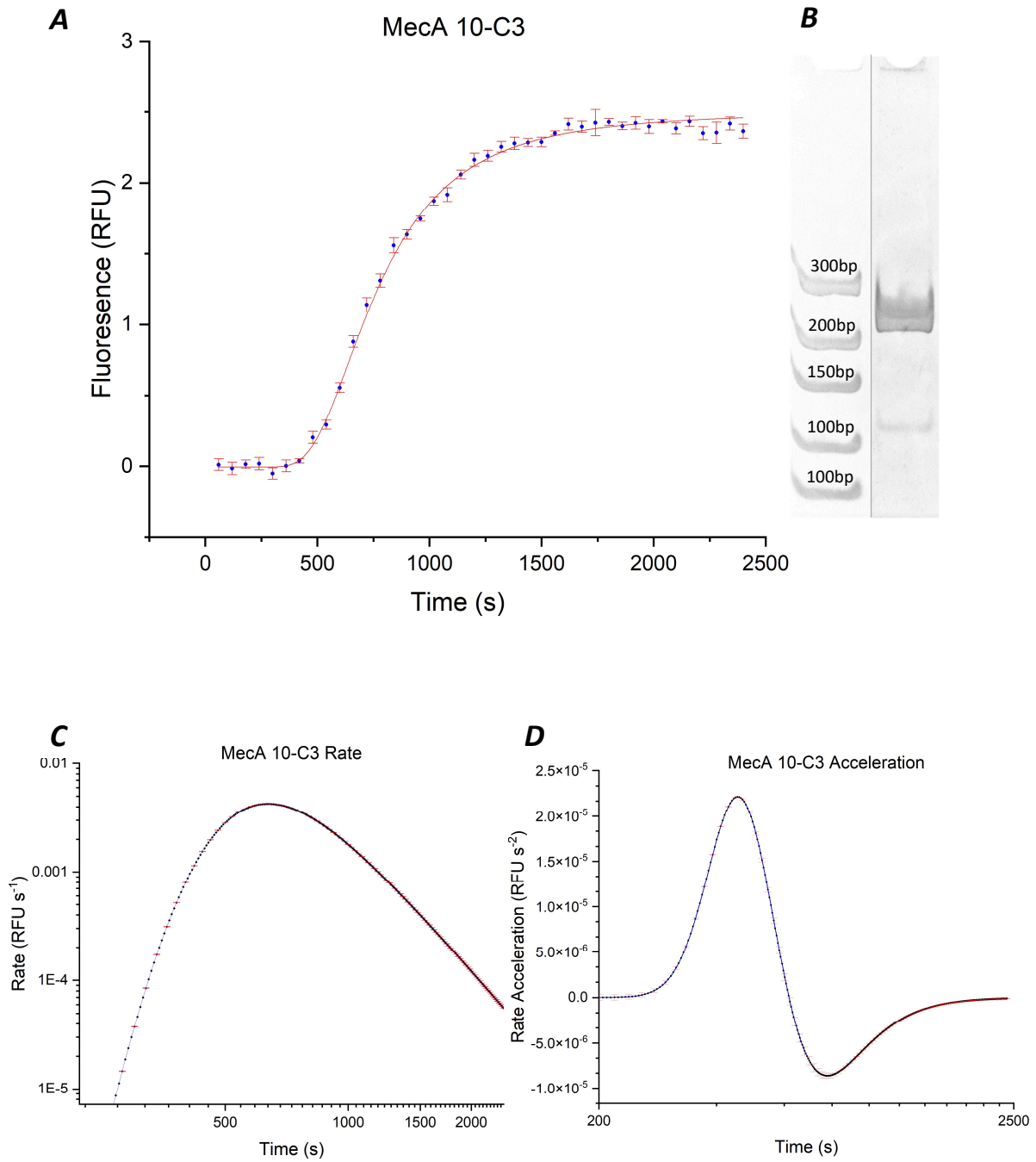


Figure 5.22. A) Processed RT-RPA fluorescence curve of primer set *mecA*₁₀-C3 with 10M copies *mecA* reference gene template fitted using equation 1. $R^2 = 0.994$, $\Phi_i = -0.006 \pm 0.016$, $\varphi_m = 2.5 \pm 0.016$, $h = 3.34 \pm 0.19$, $f = 6.612 \pm 0.43$, $x_0 = 405 \pm 11.7s$. B) TBE-DNA polyacrylamide gel of combined replicates primer set *mecA*₁₀-C3. C) First derivate rate curve for primer set *mecA*₁₀-C3. $v_{max} = 4.26 \times 10^{-3} \pm 9.24 \times 10^{-7} \text{ RFU s}^{-1}$, $k_m = 635 \pm 5s$. D) Second derivate rate acceleration curve for primer set *mecA*₁₀-C3. $\vec{v}_{max} = 2.21 \times 10^{-5} \pm 8.8 \times 10^{-8}$, $\vec{v}_{min} = -8.61 \times 10^{-6} \pm 2.8 \times 10^{-7}$, $t_i = 465 \pm 5s$, $t_d = 800 \pm 5s$.

Modified primer set MecA₁₀-C3 with gDNA template:

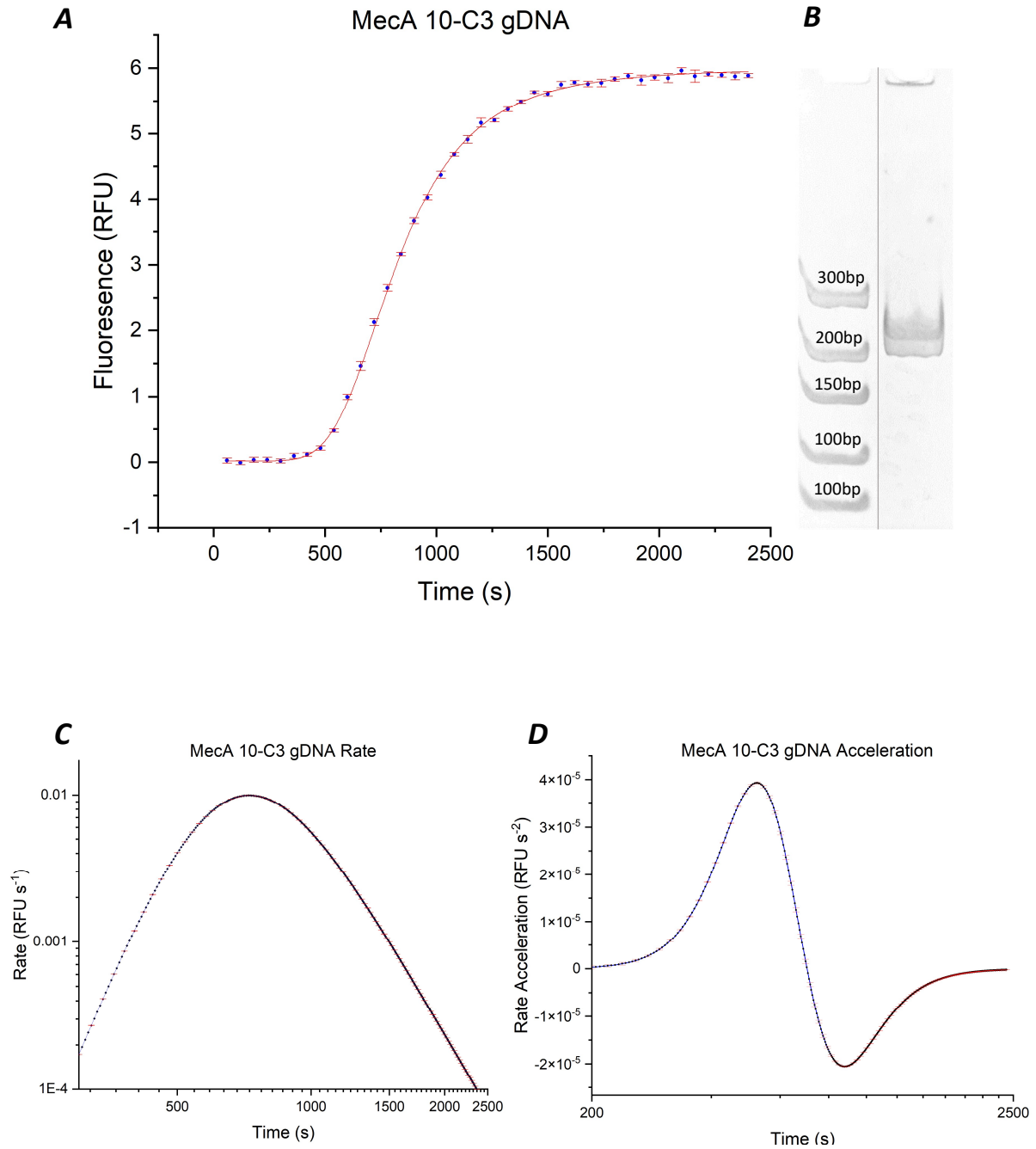


Figure 5.23. A) Processed RT-RPA fluorescence curve of primer set *mecA*₁₀-C3 with 10M ATCC 43300 MRSA gDNA template fitted using equation 1. $R^2 = 0.994$, $\Phi_i = -0.006 \pm 0.016$, $\varphi_m = 2.5 \pm 0.016$, $h = 3.34 \pm 0.19$, $f = 6.612 \pm 0.43$, $x_o = 405 \pm 11.7s$. B) TBE-DNA polyacrylamide gel of combined replicates primer set *mecA*₁₀-C3. C) First derivate rate curve for primer set *mecA*₁₀-C3. $v_{max} = 4.26 \times 10^{-3} \pm 9.24 \times 10^{-7} \text{ RFU s}^{-1}$, $k_m = 635 \pm 5s$. D) Second derivate rate acceleration curve for primer set *mecA*₁₀-C3.

$$\vec{v}_{max} = 2.21 \times 10^{-5} \pm 8.8 \times 10^{-8}, \vec{v}_{min} = -8.61 \times 10^{-6} \pm 2.8 \times 10^{-7}, t_i = 465 \pm 5s, t_d = 800 \pm 5s.$$

Modified primer set MecA₈-C3 with synthetic template:

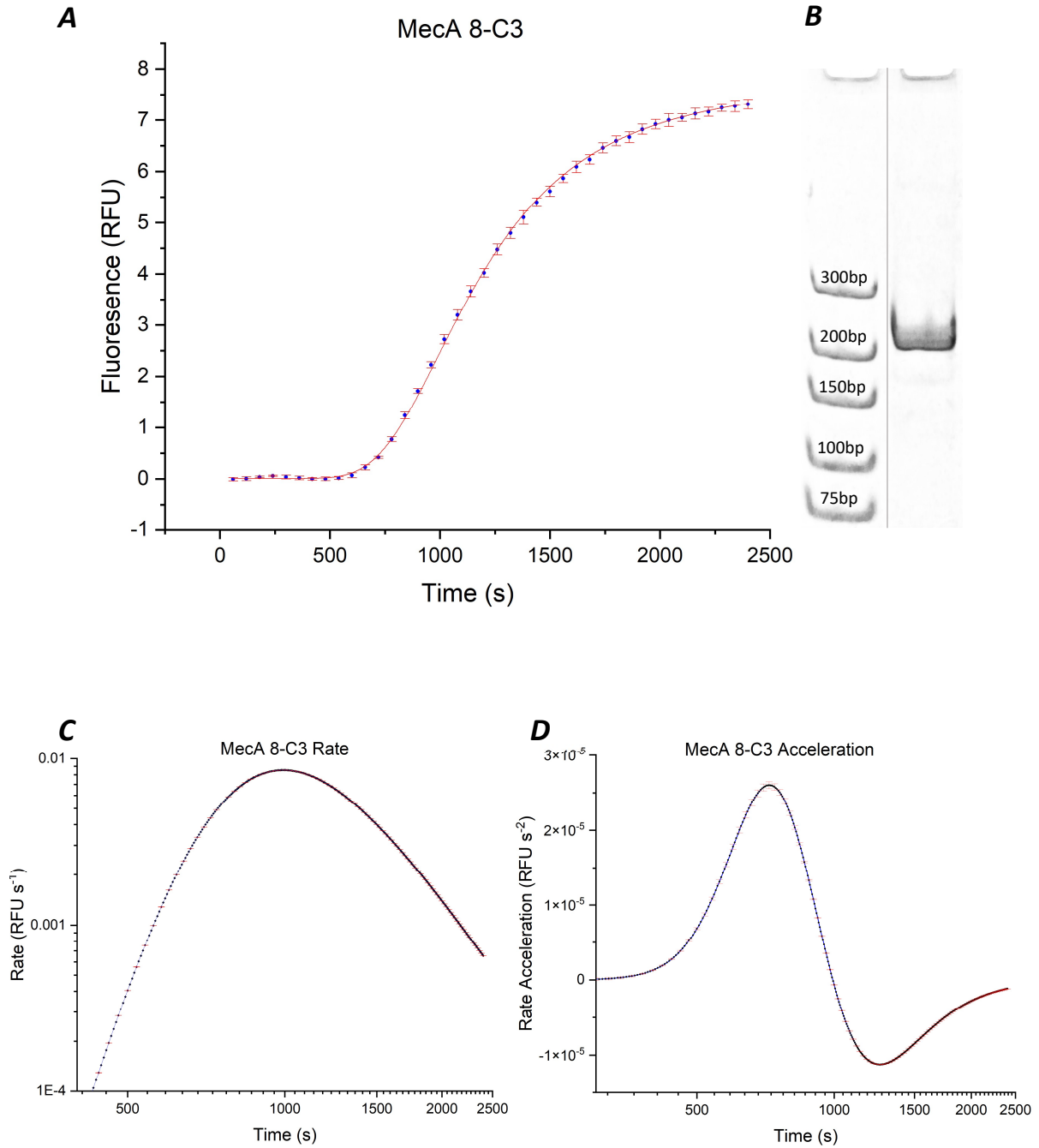


Figure 5.24. A) Processed RT-RPA fluorescence curve of primer set *mecA*₈-C3 with 10M copies *mecA* reference gene template fitted using equation 1. $R^2 = 0.994$, $\Phi_i = 0.005 \pm 0.009$, $\varphi_m = 7.78 \pm 0.036$, $h = 3.53 \pm 0.12$, $f = 3.47 \pm 0.23$, $x_o = 767 \pm 3.1s$. B) TBE-DNA polyacrylamide gel of combined replicates primer set *mecA*₈-C3. C) First derivate rate curve for primer set *mecA*₈-C3. $v_{max} = 8.5 \times 10^{-3} \pm 1.9 \times 10^{-8}$ RFU s⁻¹, $k_m = 995 \pm 5s$. D) Second derivate rate acceleration curve for primer set *mecA*₈-C3. $\vec{v}_{max} = 2.6 \times 10^{-5} \pm 4.55 \times 10^{-7}$, $\vec{v}_{min} = -1.12 \times 10^{-5} \pm 1.8 \times 10^{-8}$, $t_i = 720 \pm 5s$, $t_d = 1260 \pm 5s$.

Modified primer set MecA₈-C3 with gDNA template:

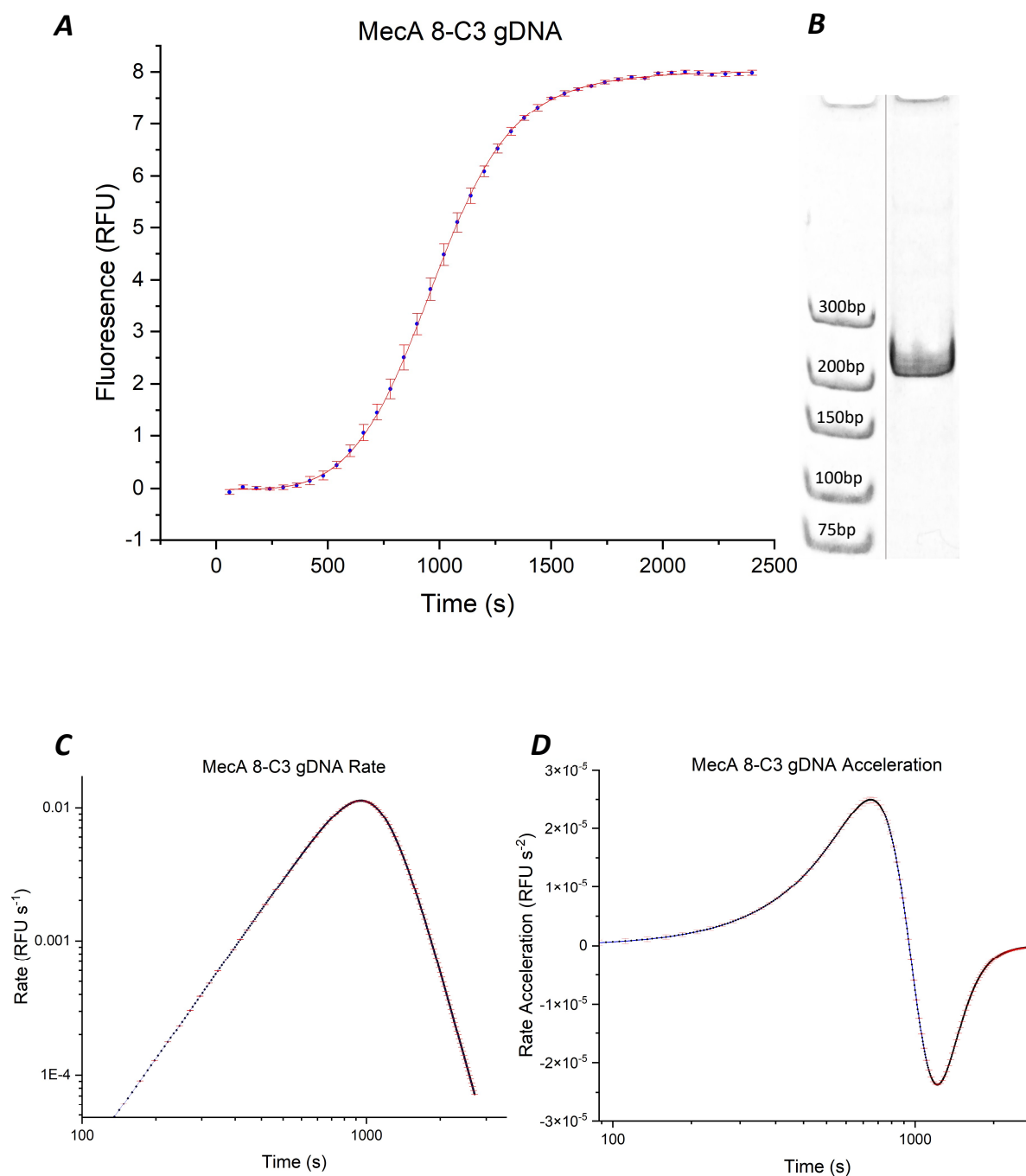


Figure 5.25. A) Processed RT-RPA fluorescence curve of primer set *mecA*₈-C3 with 10M ATCC 43300 MRSA gDNA template fitted using equation 1. $R^2 = 0.994$, $\Phi_i = -0.002 \pm 0.0012$, $\varphi_m = 8.02 \pm 0.015$, $h = 6.69 \pm 0.27$, $f = 0.59 \pm 0.27$, $x_0 = 1101 \pm 2.4s$. B) TBE-DNA polyacrylamide gel of combined replicates primer set *mecA*₈-C3. C) First derivate rate curve for primer set *mecA*₈-C3. $v_{max} = 1.13 \times 10^{-2} \pm 1.9 \times 10^{-8} \text{ RFU s}^{-1}$, $k_m = 995 \pm 5s$. D) Second derivate rate acceleration curve for primer set *mecA*₈-C3. $\vec{v}_{max} = 2.5 \times 10^{-5} \pm 4.58 \times 10^{-7}$, $\vec{v}_{min} = -1.12 \times 10^{-5} \pm 1.8 \times 10^{-8}$, $t_i = 715 \pm 10s$, $t_d = 1185 \pm 5s$.

Modified primer set MecA₇-C3 with synthetic template:

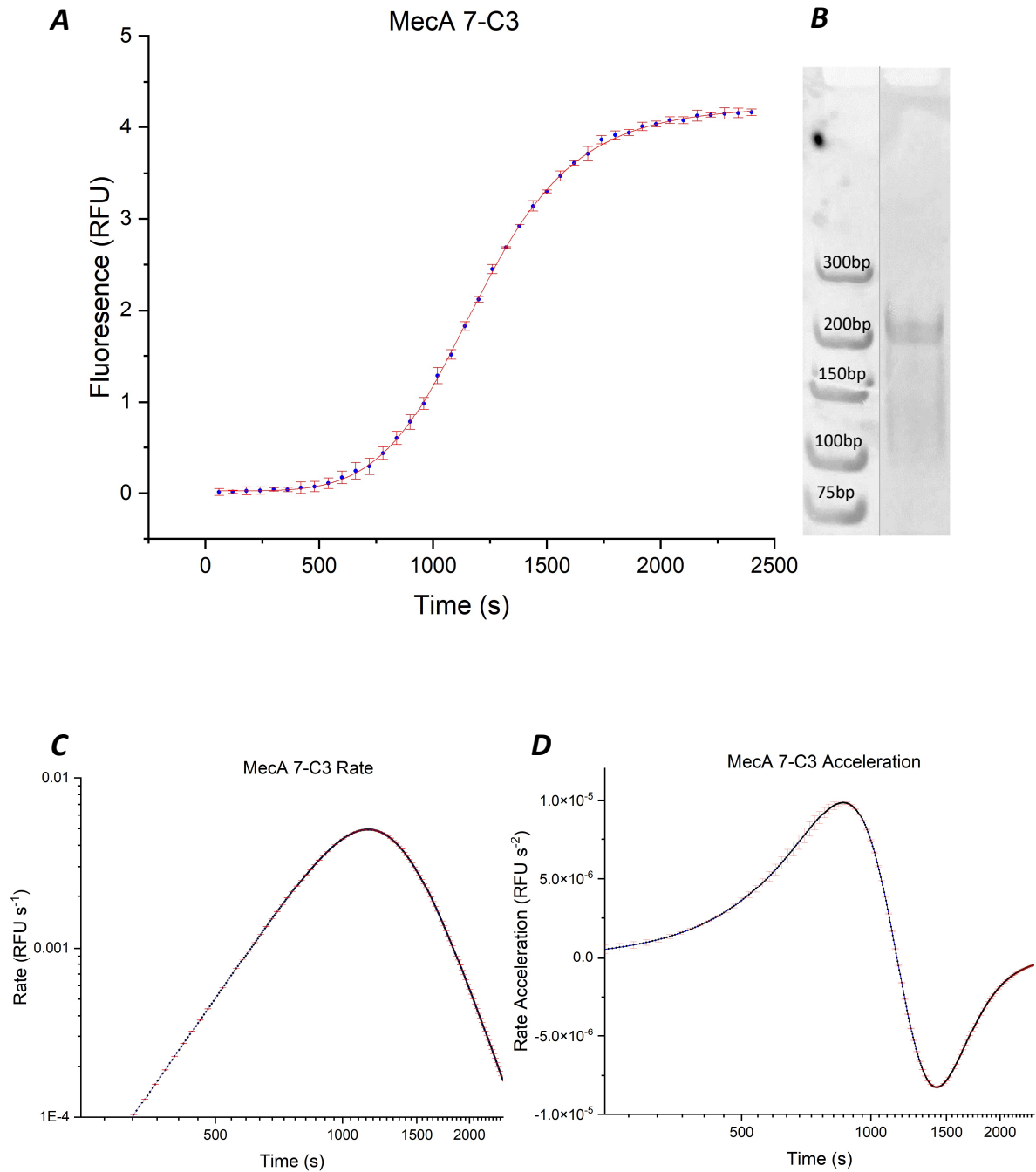


Figure 5.26. A) Processed RT-RPA fluorescence curve of primer set *mecA*₇-C3 with 10M copies *mecA* reference gene template fitted using equation 1. $R^2 = 0.999$, $\Phi_i = 0.025 \pm 0.01$, $\varphi_m = 4.24 \pm 0.025$, $h = 6.17 \pm 0.32$, $f = 0.74 \pm 0.09$, $x_o = 1287 \pm 3.2s$. B) TBE-DNA polyacrylamide gel of combined replicates primer set *mecA*₇-C3. C) First derivate rate curve for primer set *mecA*₇-C3. $v_{max} = 4.9 \times 10^{-4} \pm 2.18 \times 10^{-7} \text{ RFU s}^{-1}$, $k_m = 1150 \pm 5s$. D) Second derivate rate acceleration curve for primer set *mecA*₇-C3. $\vec{v}_{max} = 9.84 \times 10^{-5} \pm 1.53 \times 10^{-6}$, $\vec{v}_{min} = -8.24 \times 10^{-6} \pm 7.8 \times 10^{-9}$, $t_i = 865 \pm 5s$, $t_d = 1425 \pm 5s$.

Modified primer set MecA₇-C3 with gDNA template:

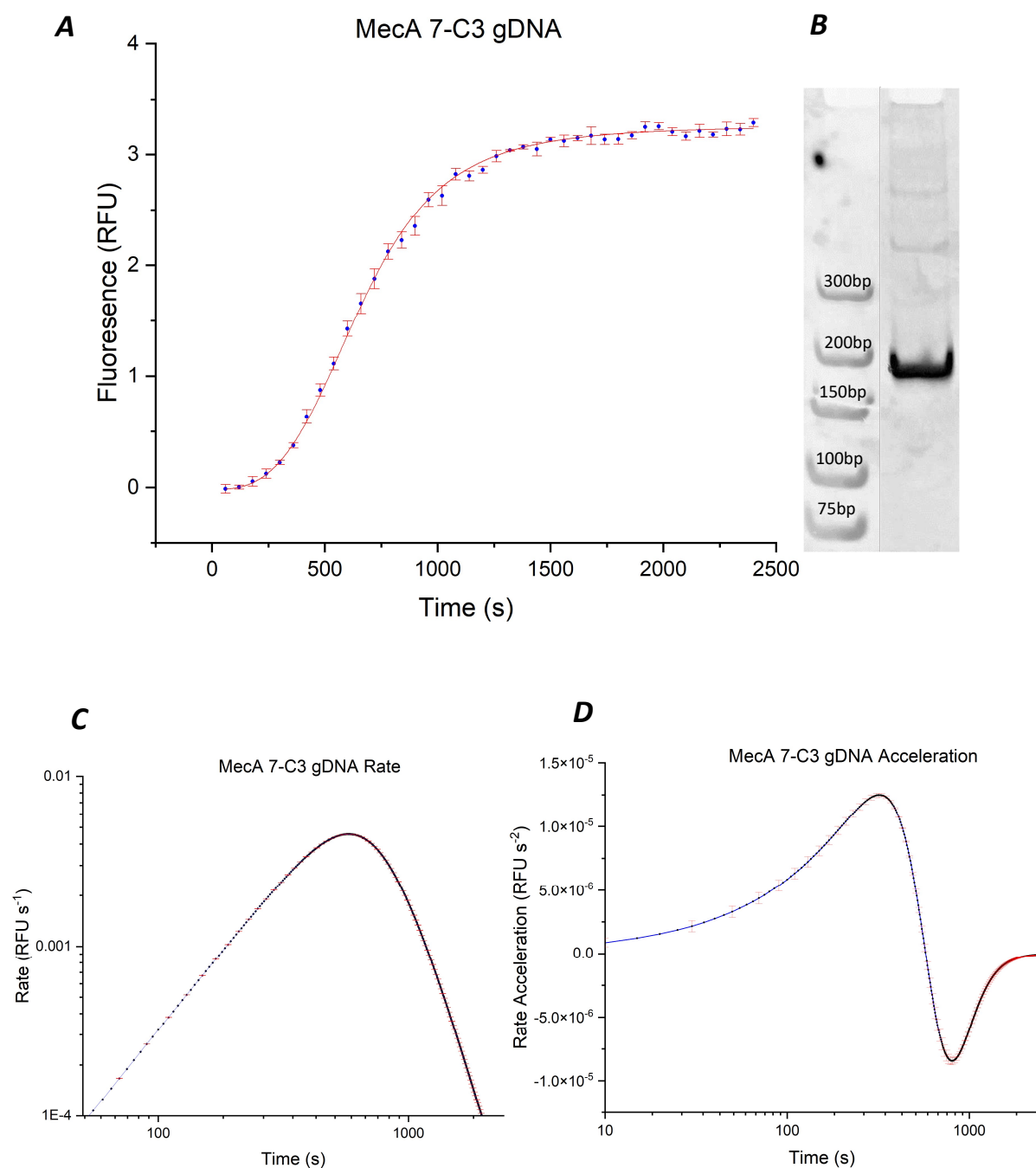


Figure 5.27. A) Processed RT-RPA fluorescence curve of primer set *mecA*₇-C3 with 10M ATCC 43300 MRSA gDNA template fitted using equation 1. $R^2 = 0.999$, $\Phi_i = -0.017 \pm 0.017$, $\varphi_m = 3.26 \pm 0.016$, $h = 3.92 \pm 0.21$, $f = 0.72 \pm 0.09$, $x_o = 742 \pm 3.2s$. B) TBE-DNA polyacrylamide gel of combined replicates primer set *mecA*₇-C3. C) First derivate rate curve for primer set *mecA*₇-C3. $v_{max} = 4.7 \times 10^{-4} \pm 1.78 \times 10^{-8}$ RFU s⁻¹, $k_m = 575 \pm 5s$. D) Second derivate rate acceleration curve for primer set *mecA*₇-C3. $\vec{v}_{max} = 1.25 \times 10^{-5} \pm 1.53 \times 10^{-7}$, $\vec{v}_{min} = -8.44 \times 10^{-6} \pm 2.8 \times 10^{-7}$, $t_i = 320 \pm 5s$, $t_d = 805 \pm 5s$.

Failed C3 Modified Primer Sets:

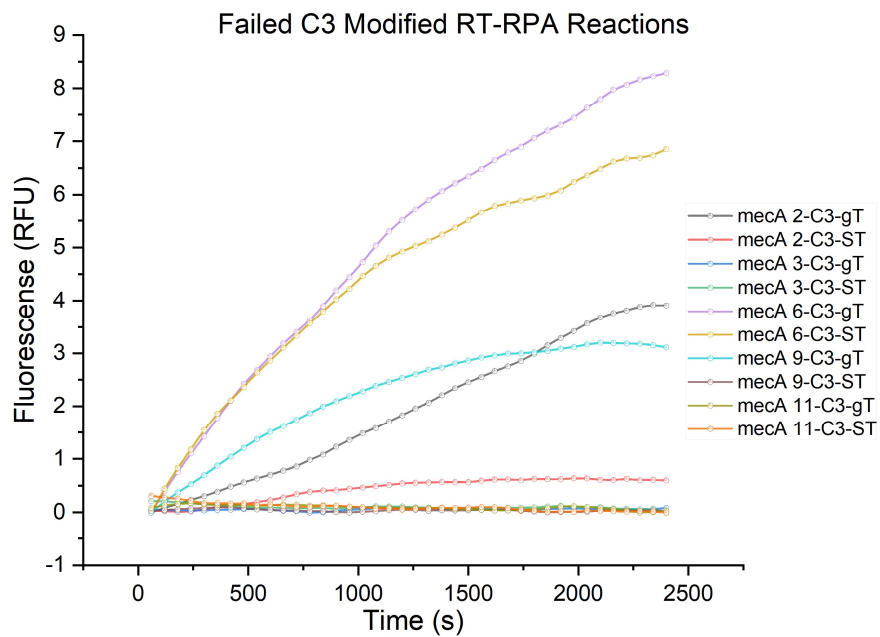


Figure 5.28. Unprocessed RT-RPA fluorescence curves of C3 modified primer sets which failed under RT-RPA conditions.

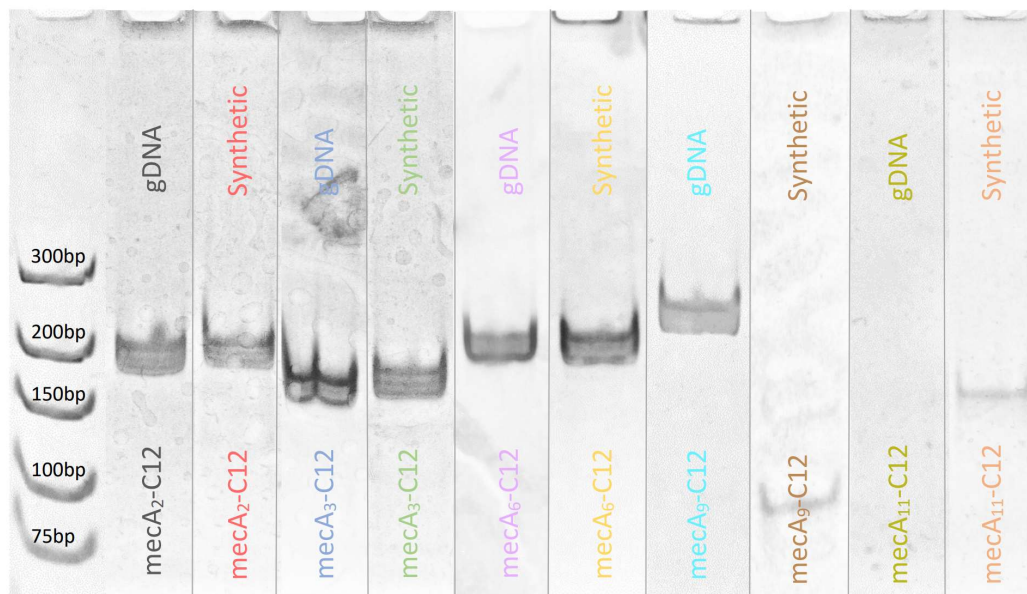


Figure 5.29. Combined TBE-DNA polyacrylamide gels of combined replicates of C3 modified primer sets which failed under RT-RPA conditions. Black vertical lines indicate a join between gel images, black horizontal line indicates gel alignment reference position. Gels were collated for clarity, post-processed holistically, background variation is due to post-run stainin.

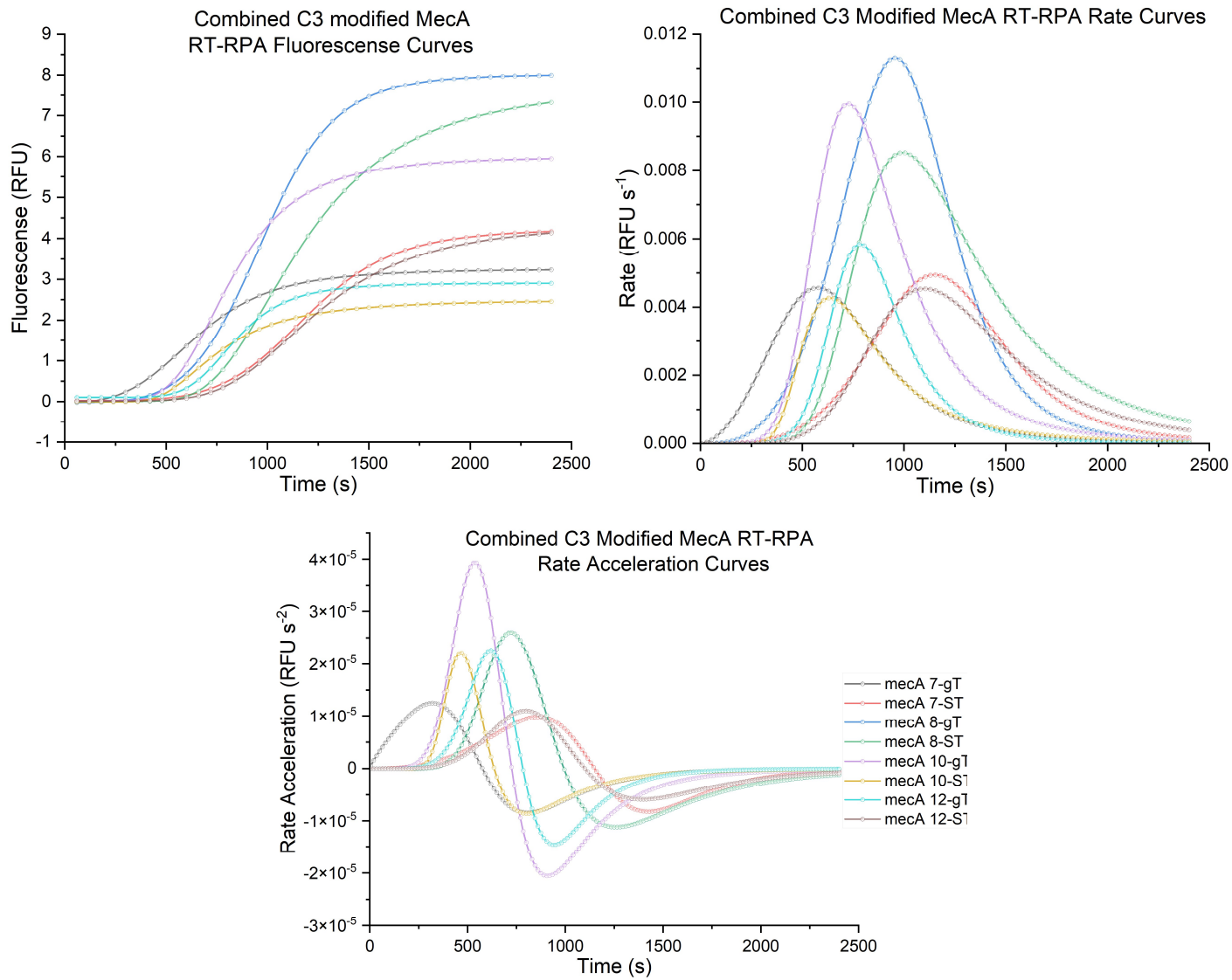


Figure 5.30. Combined processed fits of successful C3 primer sets under RT-RPA conditions.

5.5.3: C12 Modified RT-RPA Experimental Results:

Modified primer $mecA_{12}$ -C12 with synthetic template:

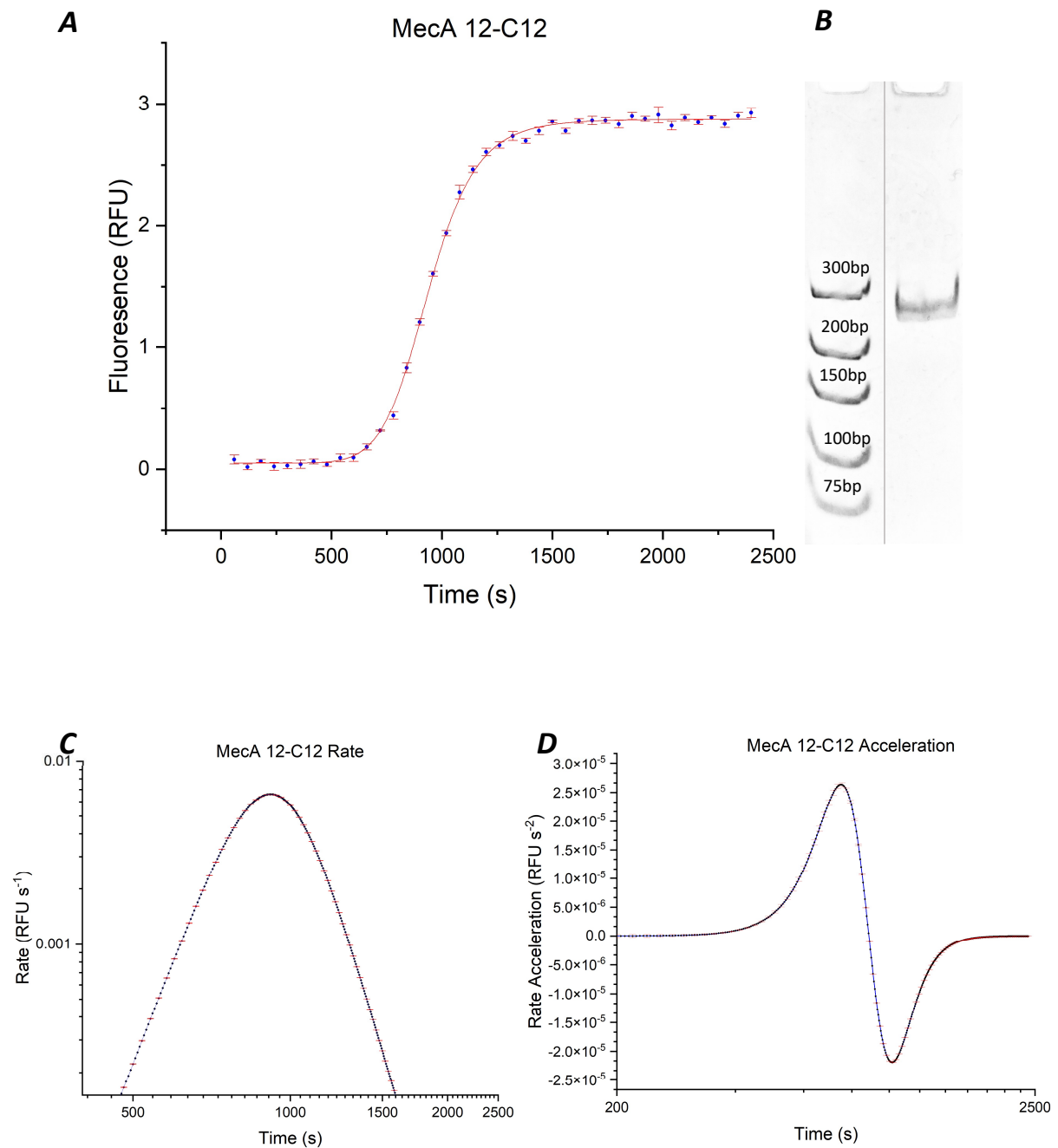


Figure 5.31. A) Processed RT-RPA fluorescence curve of primer set $mecA_{12}$ -C12 with 10M copies $mecA$ reference gene template fitted using equation 1. $R^2 = 0.999$, $\Phi_i = 0.05 \pm 0.007$, $\varphi_m = 2.87 \pm 0.006$, $h = 8.84 \pm 0.35$, $f = 0.95 \pm 0.08$, $x_o = 947 \pm 1.3s$. B) TBE-DNA polyacrylamide gel of combined replicates primer set $mecA_{12}$ -C12. C) First derivate rate curve for primer set $mecA_{12}$ -C12. $v_{max} = 6.6 \times 10^{-3} \pm 1.7 \times 10^{-6} RFU s^{-1}$, $k_m = 915 \pm 5s$. D) Second derivate rate acceleration curve for primer set $mecA_{12}$ -C12.

$$\vec{v}_{max} = 2.64 \times 10^{-5} \pm 3.62 \times 10^{-7}, \vec{v}_{min} = -2.19 \times 10^{-5} \pm 3.9 \times 10^{-8}, t_i = 775 \pm 5s, t_d = 1055 \pm 5s.$$

Modified primer set mecA₁₂-C12 with gDNA template:

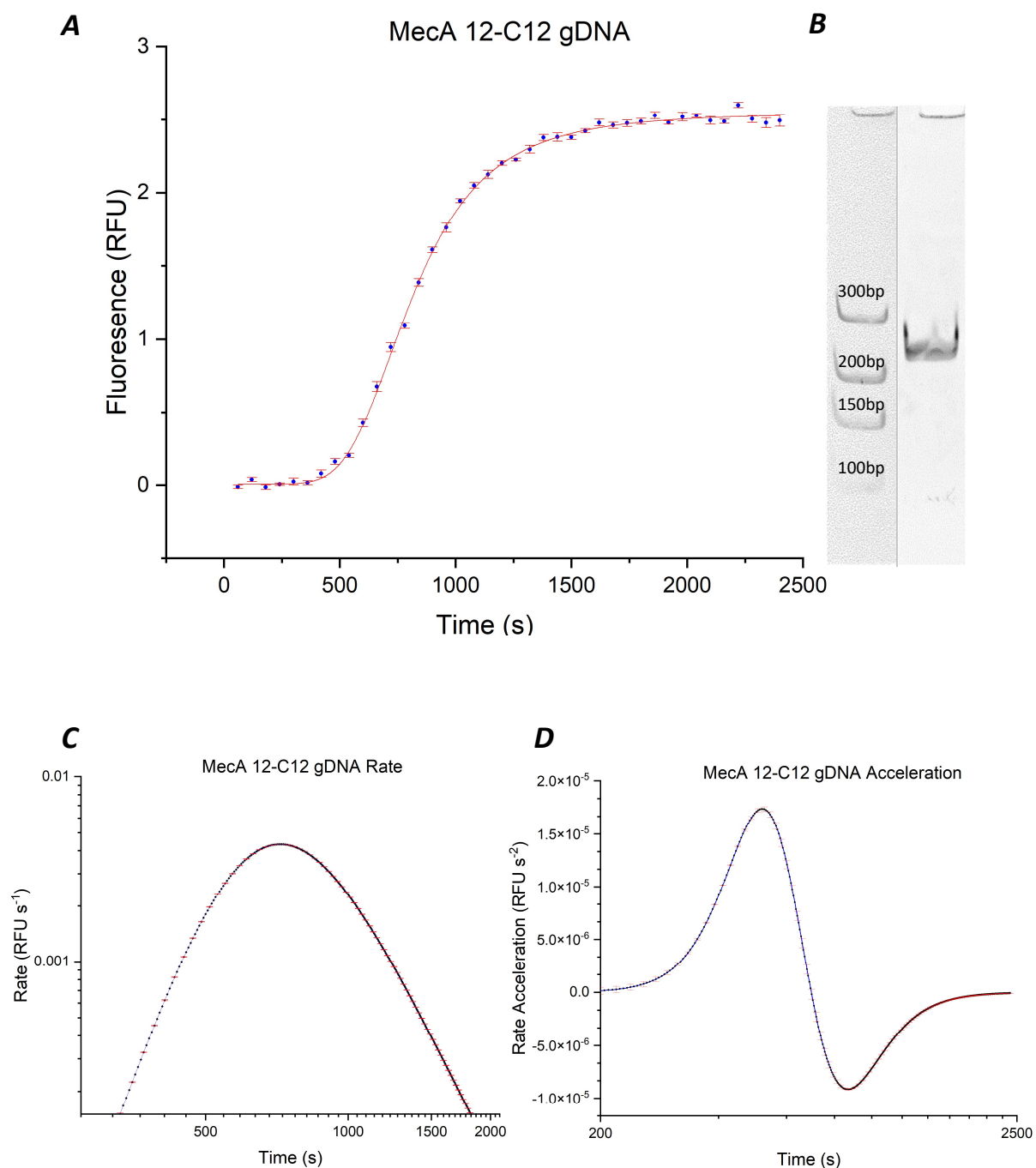


Figure 5.32. A) Processed RT-RPA fluorescence curve of primer set mecA₁₂-C12 with 10M ATCC 43300 MRSA gDNA template fitted using equation 1. $R^2 = 0.999$, $\Phi_i = 0.007 \pm 0.005$, $\varphi_m = 2.55 \pm 0.008$, $h = 4.3 \pm 0.23$, $f = 1.97 \pm 0.29$, $x_0 = 663 \pm 3.2s$. B) TBE-DNA polyacrylamide gel of combined replicates primer set mecA₁₂-C12. C) First derivate rate curve for primer set mecA₁₂-C12. $v_{max} = 4.33 \times 10^{-3} \pm 4 \times 10^{-6} \text{ RFU s}^{-1}$, $k_m = 720 \pm 5s$. D) Second derivate rate acceleration curve for primer set mecA₁₂-C12. $\vec{v}_{max} = 1.74 \times 10^{-5} \pm 2.1 \times 10^{-7}$, $\vec{v}_{min} = -9.15 \times 10^{-6} \pm 4.77 \times 10^{-8}$, $t_i = 535 \pm 5s$, $t_d = 900 \pm 5s$.

Modified primer set $mecA_{10}$ -C12 with synthetic template:

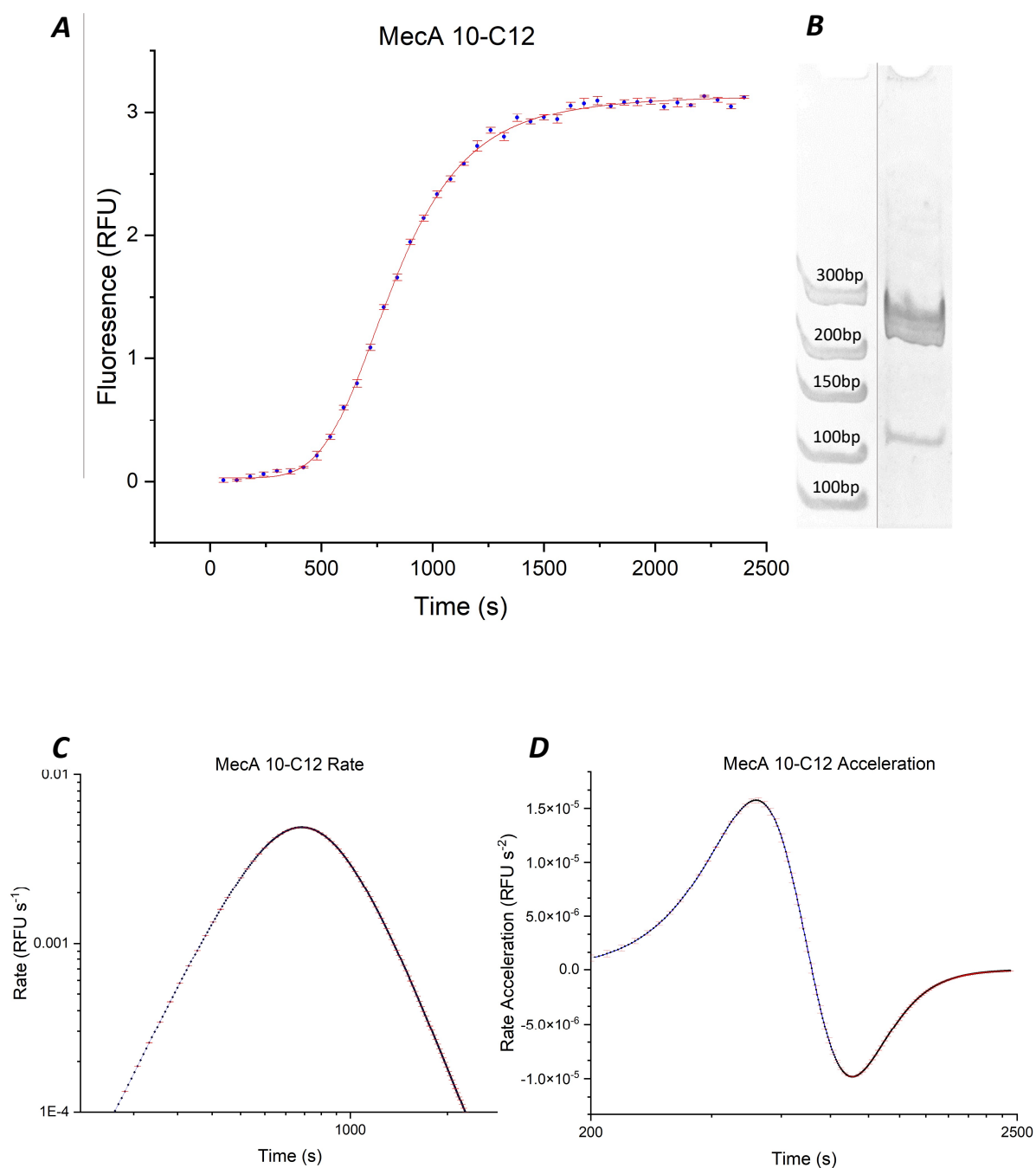


Figure 5.33. A) Processed RT-RPA fluorescence curve of primer set $mecA_{10}$ -C12 with 10M copies $mecA$ reference gene template fitted using equation 1. $R^2 = 0.994$, $\Phi_i = 0.028 \pm 0.005$, $\varphi_m = 3.13 \pm 0.005$, $h = 4.6 \pm 0.12$, $f = 1.19 \pm 0.09$, $x_0 = 778 \pm 1.9s$. B) TBE-DNA polyacrylamide gel of combined replicates primer set $mecA_{10}$ -C12. C) First derivate rate curve for primer set $mecA_{10}$ -C12. $v_{max} = 4.85 \times 10^{-3} \pm 4.8 \times 10^{-9} RFU s^{-1}$, $k_m = 740 \pm 5s$. D) Second derivate rate acceleration curve for primer set $mecA_{10}$ -C12.

$$\vec{v}_{max} = 2.21 \times 10^{-5} \pm 8.8 \times 10^{-8}, \vec{v}_{min} = -8.61 \times 10^{-6} \pm 2.8 \times 10^{-7}, t_i = 465 \pm 5s, t_d = 800 \pm 5s.$$

Modified primer set $mecA_{10}$ -C12 with gDNA template:

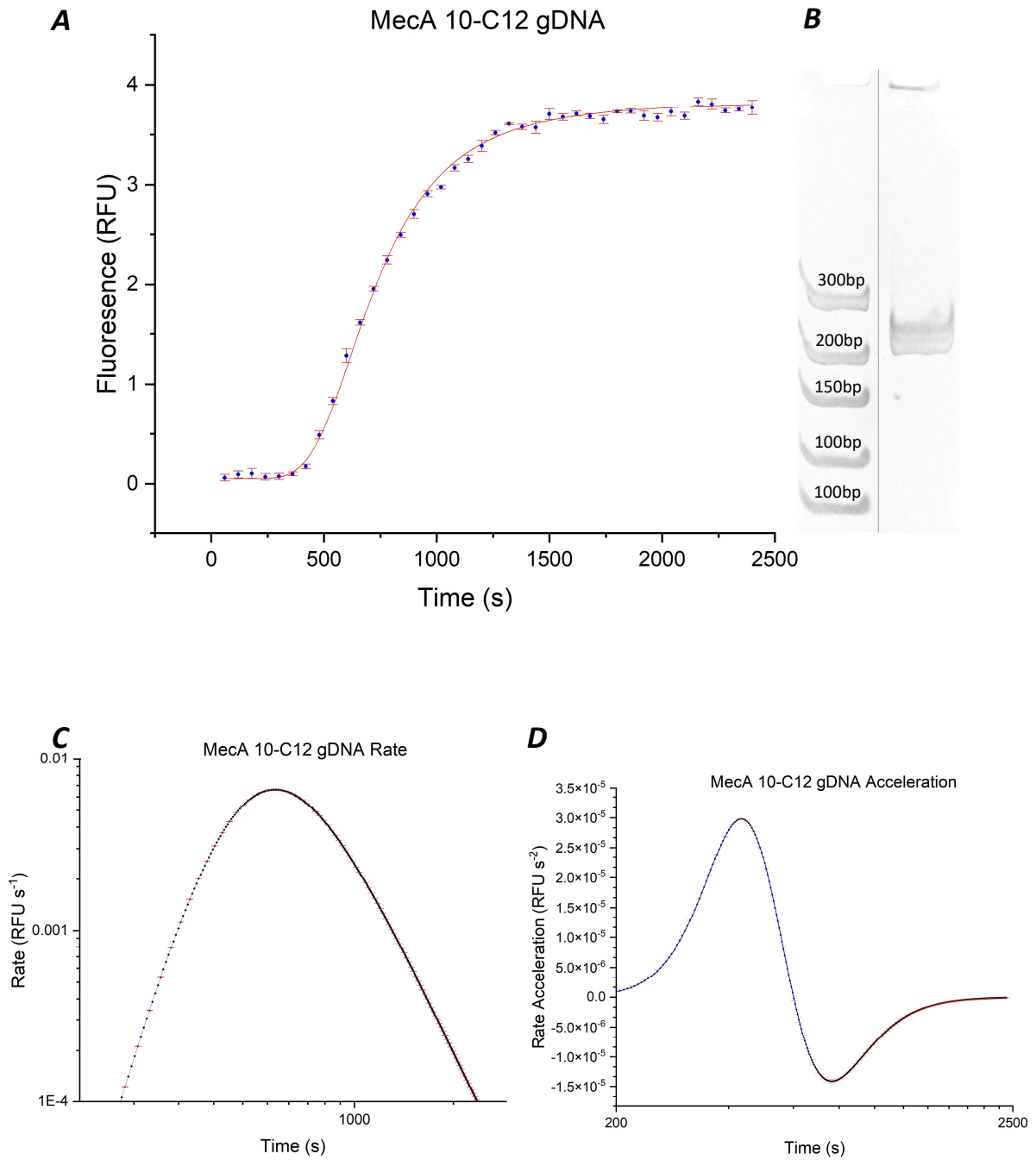


Figure 5.34. A) Processed RT-RPA fluorescence curve of primer set $mecA_{10}$ -C12 with 10M ATCC 43300 MRSA gDNA template fitted using equation 1. $R^2 = 0.996$, $\Phi_i = 0.005 \pm 0.015$, $\varphi_m = 3.8 \pm 0.012$, $h = 3.72 \pm 0.11$, $f = 2.38 \pm 0.44$, $x_0 = 539 \pm 3.5s$. B) TBE-DNA polyacrylamide gel of combined replicates primer set $mecA_{10}$ -C12. C) First derivate rate curve for primer set $mecA_{10}$ -C12. $v_{max} = 6.62 \times 10^{-3} \pm 1.93 \times 10^{-7} RFU s^{-1}$, $k_m = 620 \pm 5s$. D) Second derivate rate acceleration curve for primer set $mecA_{10}$ -C12.

$$\vec{v}_{max} = 2.98 \times 10^{-5} \pm 4.6 \times 10^{-8}, \vec{v}_{min} = -1.41 \times 10^{-5} \pm 3.2 \times 10^{-7}, t_i = 445 \pm 5s, t_d = 790 \pm 5s.$$

Modified primer set $mecA_8$ -C12 with synthetic template:

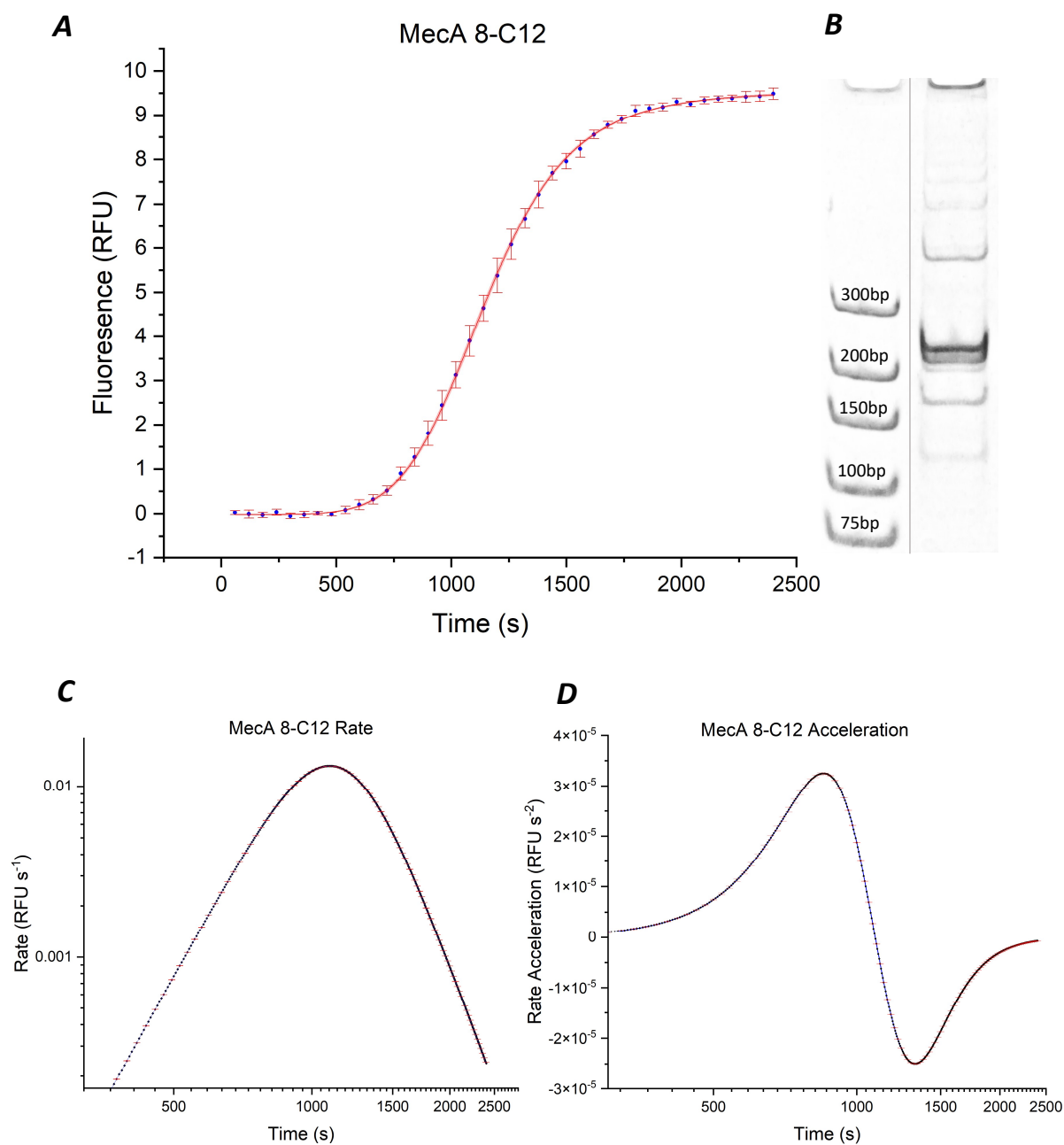


Figure 5.35. A) Processed RT-RPA fluorescence curve of primer set $mecA_8$ -C12 with 10M copies $mecA$ reference gene template fitted using equation 1. $R^2 = 0.999$, $\Phi_i = -0.017 \pm 0.02$, $\varphi_m = 9.55 \pm 0.05$, $h = 6.33 \pm 0.34$, $f = 0.93 \pm 0.16$, $x_o = 1166 \pm 4.9s$. B) TBE-DNA polyacrylamide gel of combined replicates primer set $mecA_8$ -C12. C) First derivate rate curve for primer set $mecA_8$ -C12. $v_{max} = 1.32 \times 10^{-2} \pm 4.3 \times 10^{-7} RFU s^{-1}$, $k_m = 1095 \pm 5s$. D) Second derivate rate acceleration curve for primer set $mecA_8$ -C12. $\vec{v}_{max} = 3.25 \times 10^{-5} \pm 1.54 \times 10^{-7}$, $\vec{v}_{min} = -2.5 \times 10^{-5} \pm 1.3 \times 10^{-8}$, $t_i = 850 \pm 5s$, $t_d = 1325 \pm 5s$.

Modified primer set mecA₈-C12 with gDNA template:

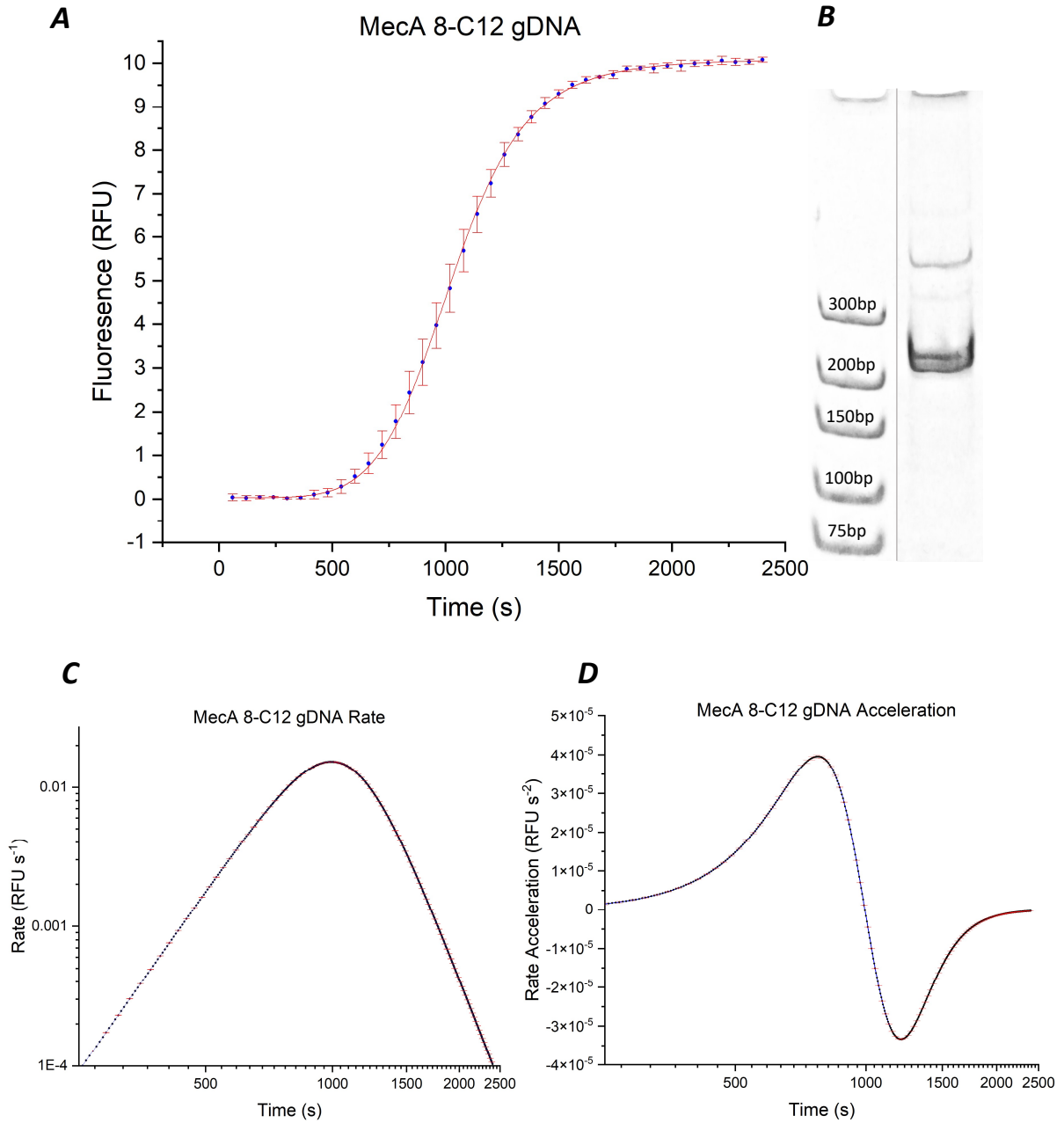


Figure 5.36. A) Processed RT-RPA fluorescence curve of primer set mecA₈-C12 10M ATCC 43300 MRSA gDNA template fitted using equation 1. $R^2 = 0.999$, $\Phi_i = 0.03 \pm 0.001$, $\varphi_m = 10.08 \pm 0.0034$, $h = 6.79 \pm 0.43$, $f = 0.779 \pm 0.12$ $x_o = 1086 \pm 4.2s$. B) TBE-DNA polyacrylamide gel of combined replicates primer set mecA₈-C12. C) First derivate rate curve for primer set mecA₈-C12. $v_{max} = 1.53 \times 10^{-2} \pm 4.76 \times 10^{-7} RFU s^{-1}$, $k_m = 995 \pm 5s$. D) Second derivate rate acceleration curve for primer set mecA₈-C12. $\vec{v}_{max} = 3.95 \times 10^{-5} \pm 3.62 \times 10^{-7}$, $\vec{v}_{min} = -3.34 \times 10^{-5} \pm 2.38 \times 10^{-8}$, $t_i = 775 \pm 10s$, $t_d = 1205 \pm 5s$.

Modified primer set *mecA*₇-C12 with synthetic template:

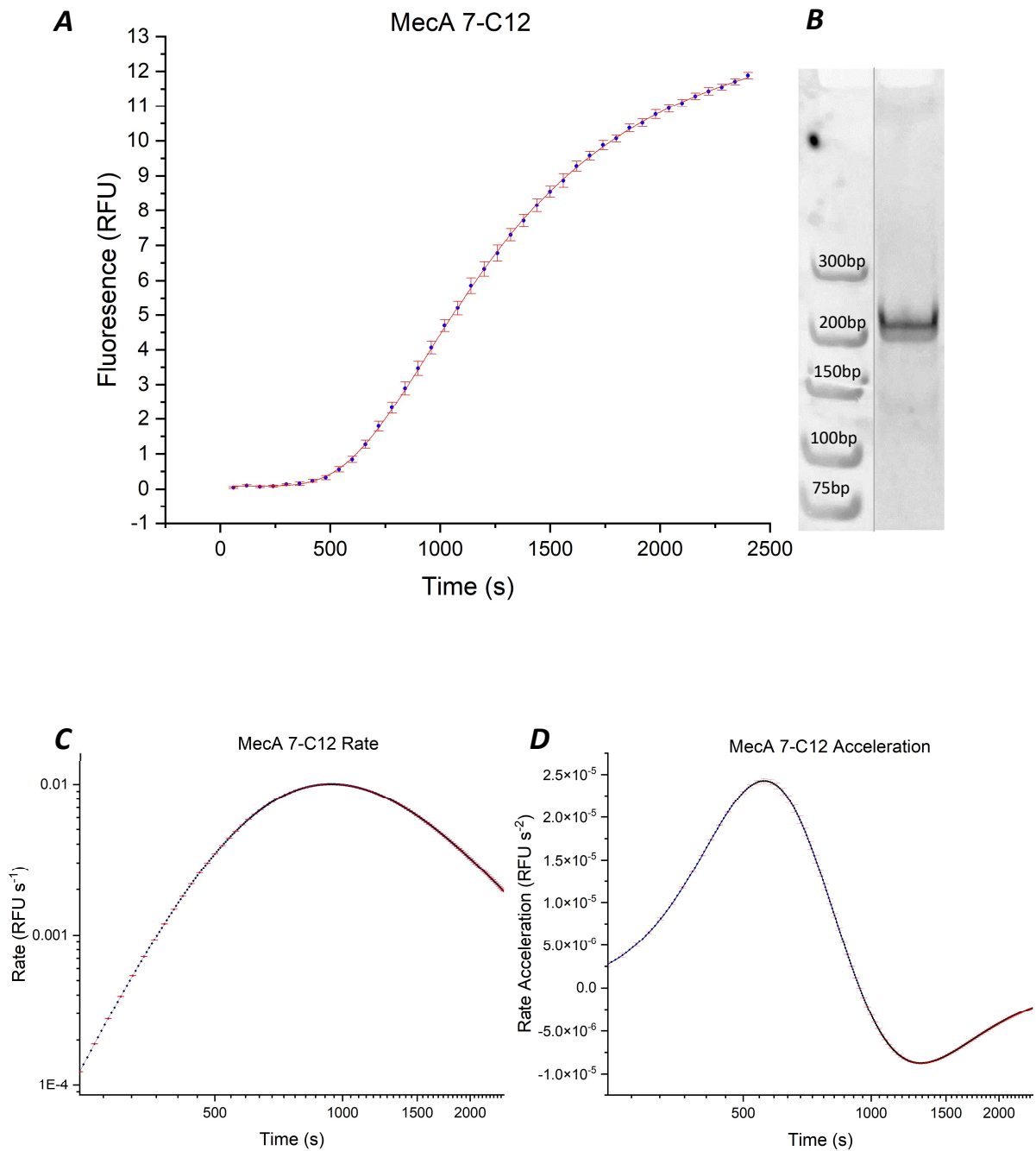


Figure 5.37. A) Processed RT-RPA fluorescence curve of primer set *mecA*₇-C3 with 10M copies *mecA* reference gene template fitted using equation 1. $R^2 = 0.999$, $\Phi_i = 0.085 \pm 0.01$, $\varphi_m = 14.02 \pm 0.33$, $h = 2.39 \pm 0.18$, $f = 2.9 \pm 0.7$, $x_0 = 743 \pm 11.9s$. B) TBE-DNA polyacrylamide gel of combined replicates primer set *mecA*₇-C3. C) First derivate rate curve for primer set *mecA*₇-C3. $v_{max} = 1.0 \times 10^{-2} \pm 1.16 \times 10^{-6}$ RFU s⁻¹, $k_m = 940 \pm 5s$. D) Second derivate rate acceleration curve for primer set *mecA*₇-C3. $\vec{v}_{max} = 2.34 \times 10^{-5} \pm 2.64 \times 10^{-7}$, $\vec{v}_{min} = -8.74 \times 10^{-6} \pm 1.4 \times 10^{-8}$, $t_i = 560 \pm 5s$, $t_d = 1310 \pm 5s$.

Modified primer set mecA₇-C12 with gDNA template:

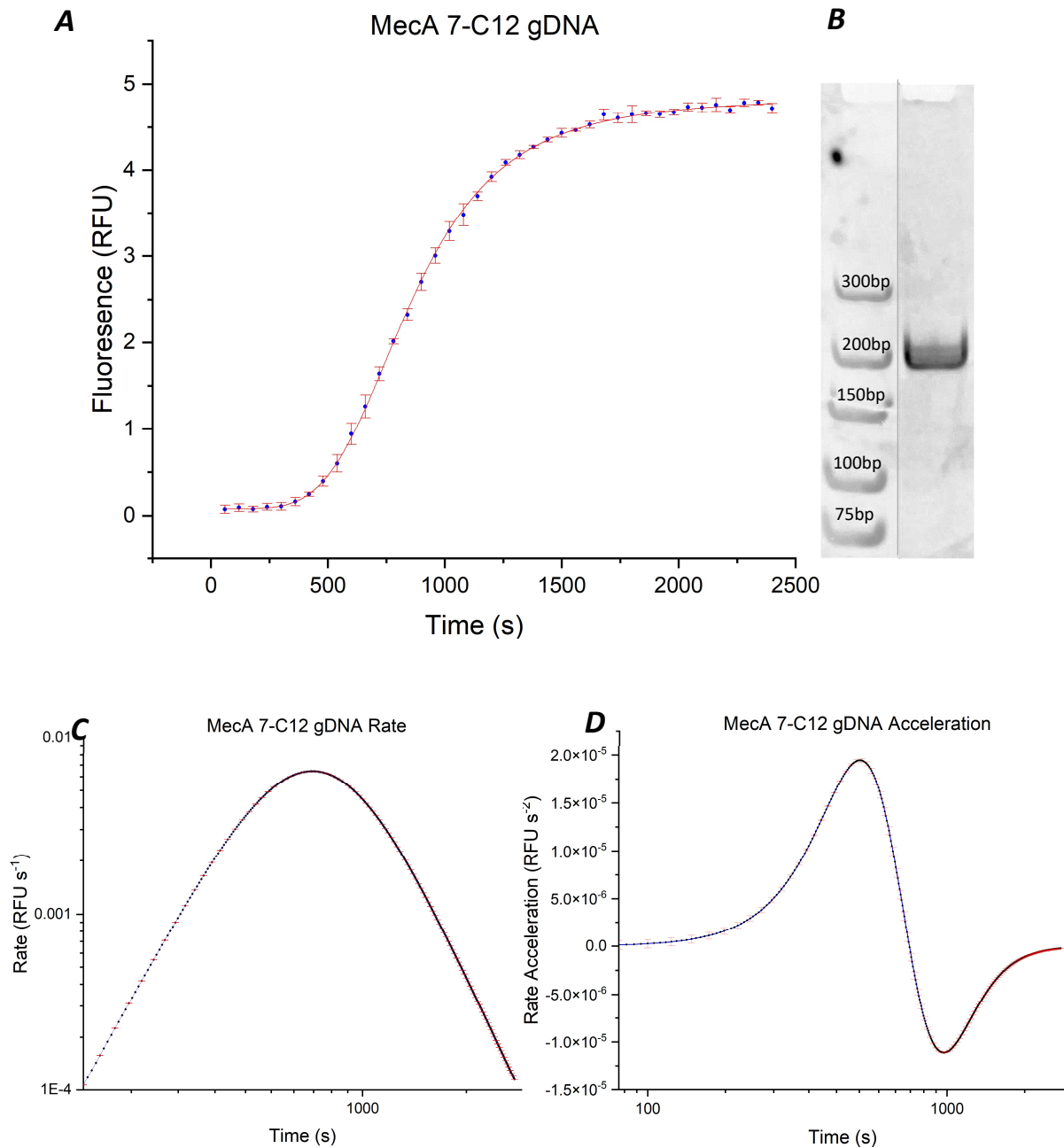


Figure 5.38. A) Processed RT-RPA fluorescence curve of primer set mecA₇-C12 with 10M ATCC 43300 MRSA gDNA template fitted using equation 1. . $R^2 = 0.999$, $\Phi_i = 0.078 \pm 0.019$, $\varphi_m = 4.84 \pm 0.022$, $h = 3.99 \pm 0.015$, $f = 1.29 \pm 0.18$, $x_0 = 784 \pm 3.8s$ B) TBE-DNA polyacrylamide gel of combined replicates primer set mecA₇-C12. C) First derivate rate curve for primer set mecA₇-C12. $v_{max} = 6.46 \times 10^{-3} \pm 8.87 \times 10^{-8} \text{ RFU s}^{-1}$, $k_m = 750 \pm 5s$. D) Second derivate rate acceleration curve for primer set mecA₇-C12. $\vec{v}_{max} = 1.94 \times 10^{-5} \pm 1.65 \times 10^{-7}$, $\vec{v}_{min} = -1.11 \times 10^{-5} \pm 2.6 \times 10^{-8}$, $t_i = 510 \pm 5s$, $t_d = 975 \pm 5s$.

Failed C12 Modified Primer Sets:

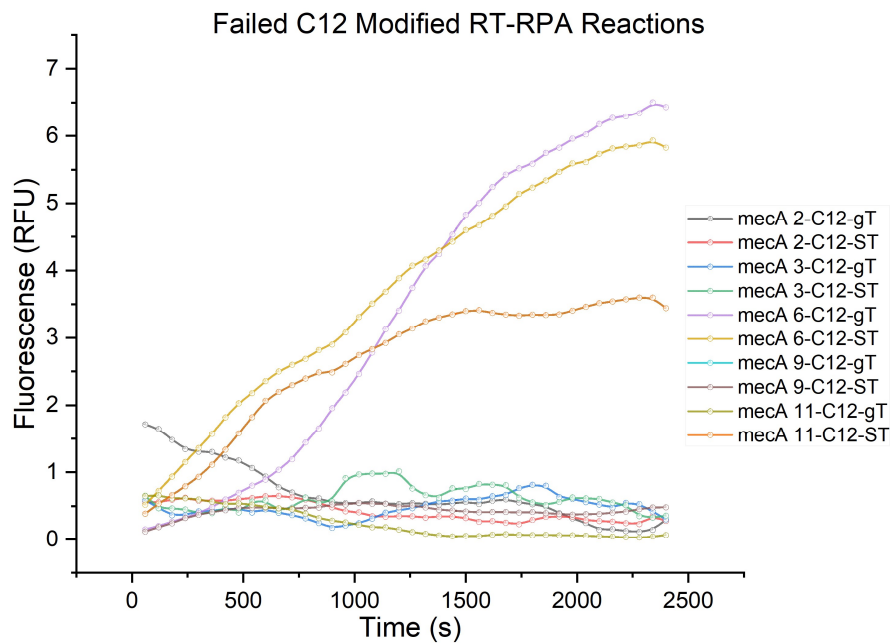


Figure 5.39. Unprocessed RT-RPA fluorescence curves of C12 modified primer sets, which failed under RT-RPA conditions.

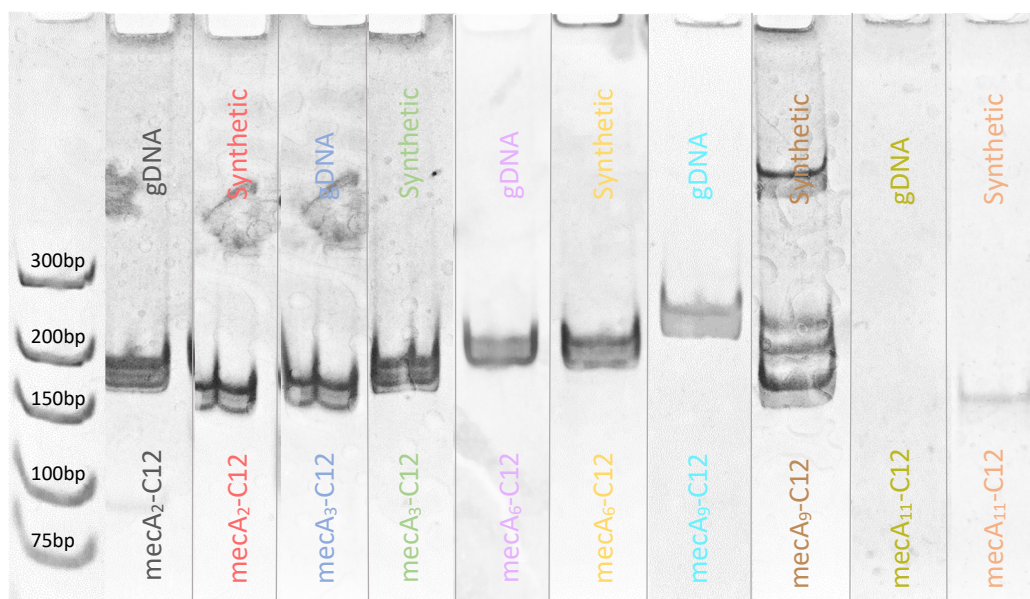


Figure 5.40. Combined TBE-DNA polyacrylamide gels with combined replicates of modified primer sets which failed under RT-RPA conditions. Black vertical lines indicate a join between gel images, black horizontal line indicates gel alignment reference position. Gels were collated for clarity, post-processed holistically, background variation is due to post-run staining.

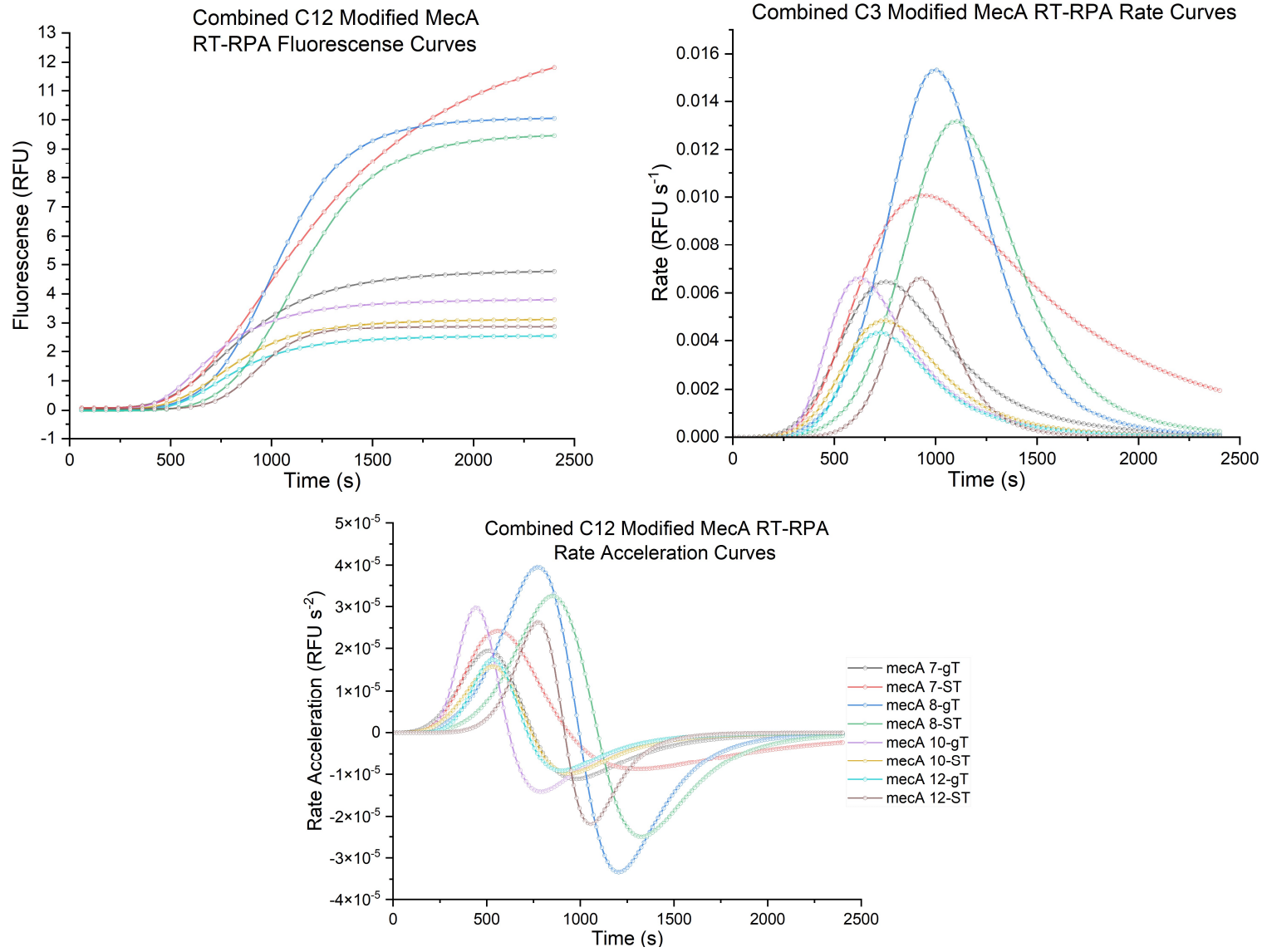


Figure 5.41. Combined processed fits of successful C12 primer sets under RT-RPA condition.

5.5.4: Final Concluding Remarks & Outcomes:

In general, the RT-RPA screening experiments with the pre-screened fully modified mecA primer sequences produced excellent results. (Fig. 5.20-5.27, Fig. 5.30-5.38 & Fig. 5.41). Each primer set produced the expected curves that fitted the kinetic model enabling the extraction of the reaction's key kinetic constants. (Table. 5.4).

Table 5.4. Key reaction constants from fully functioning primer sets. MecA₇ unmodified using the mecA template is exclude from average calculations due to poor endpoint performance.

Primer Name	Template	Modification type	Initiation Time (s)	Time to Max Sudo-Rate (s)	Time to Depletion (s)
MecA ₁₂	gDNA	None	535	790	1025
		C3	620	785	945
		C12	535	720	900
	mecA	None	610	770	965
		C3	800	1100	1395
		C12	775	915	1055
MecA ₁₀	gDNA	None	655	800	945
		C3	540	725	910
		C12	445	620	790
	mecA	None	675	830	980
		C3	465	635	800
		C12	465	740	800
MecA ₈	gDNA	None	555	780	995
		C3	715	995	1185
		C12	775	995	1205
	mecA	None	590	785	975
		C3	720	995	1260
		C12	850	1095	1325
MecA ₇	gDNA	None	280	520	750
		C3	320	575	805
		C12	510	750	975
	mecA	None	440	765	1080
		C3	865	1150	1425
		C12	560	940	1310
Average (s) w/(SD)			596 (31)	824 (33)	1033 (40)

As expected, the previously excluded primer sequences failed in a variety of ways under RT-RPA conditions with modifications in place but are included for completeness. (Fig. 5.28 & Fig. 5.39). Unfortunately, sequence sets MecA 2, 3, and 6 still failed to produce kinetic curves using new internal hybridisation probes despite producing excellent modified endpoint products. (Fig. 5.29 & Fig. 5. 40).

A general observation to be made when comparing the endpoint analysis of the modified primers was the higher likelihood the spurious amplification material being produced in the C12 modified primers. Of particular note in this regard was MecA₈-C12 which produced large amounts of spurious material regardless of template used versus MecA₈-C3 did not. There was a measurable performance deficit when using the C3 spacer versus the C12 spacer. However, this difference was only 3.3 % in the C12 spacers favour. (Fig. 5.42) Therefore at this point was not possible to determine which spacer length was best, consequently both spacers' lengths were included in further investigations.

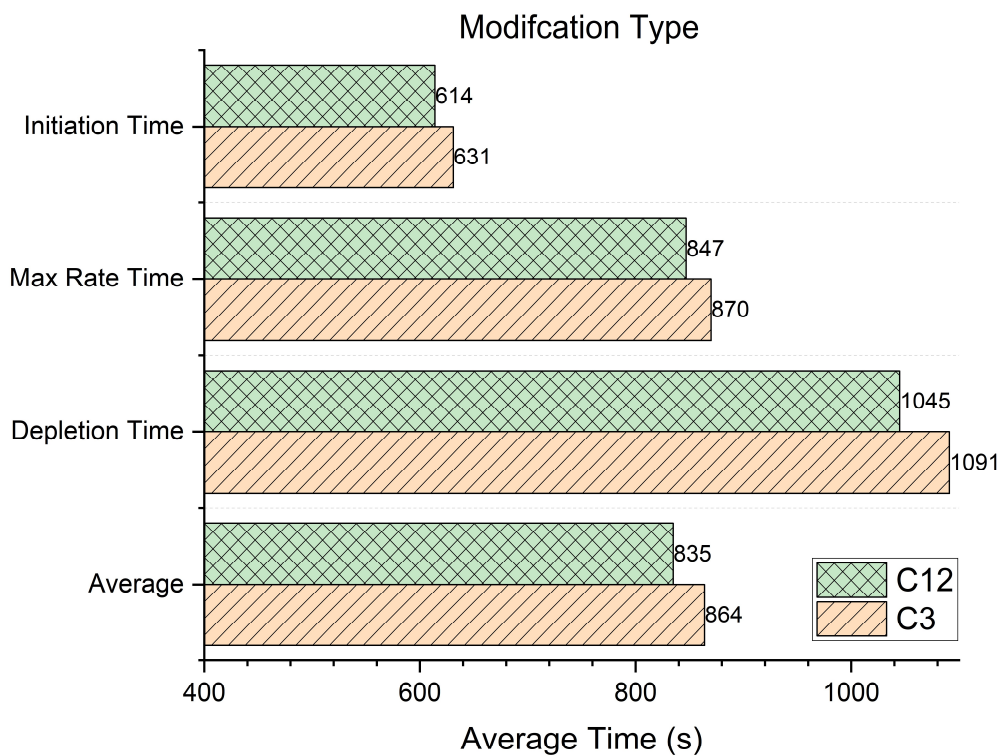


Figure 5.42. Average key kinetic reaction constants derived modified RT-RPA of the modified primer sequence MecA 12, 10, 8 and 7's. Highlighting the overall effect spacer length on reaction efficiency.

Again, in these experiments it was noted that the smaller *mecA* reference template used in reactions was more likely to produce spurious material at endpoint analysis using the modified primer sequences. This is something to note if a target gene of interest is carried on small plasmids¹⁵² or the method of DNA extraction results in small fragment sizes. When comparing the kinetic performance between target material fragment length only a small difference in kinetic performance was observed. When assessed across the entire population set of modified and unmodified RT-RPA reactions this equated to a 3% difference in favour of MRSA gDNA. (Fig. 5.43).

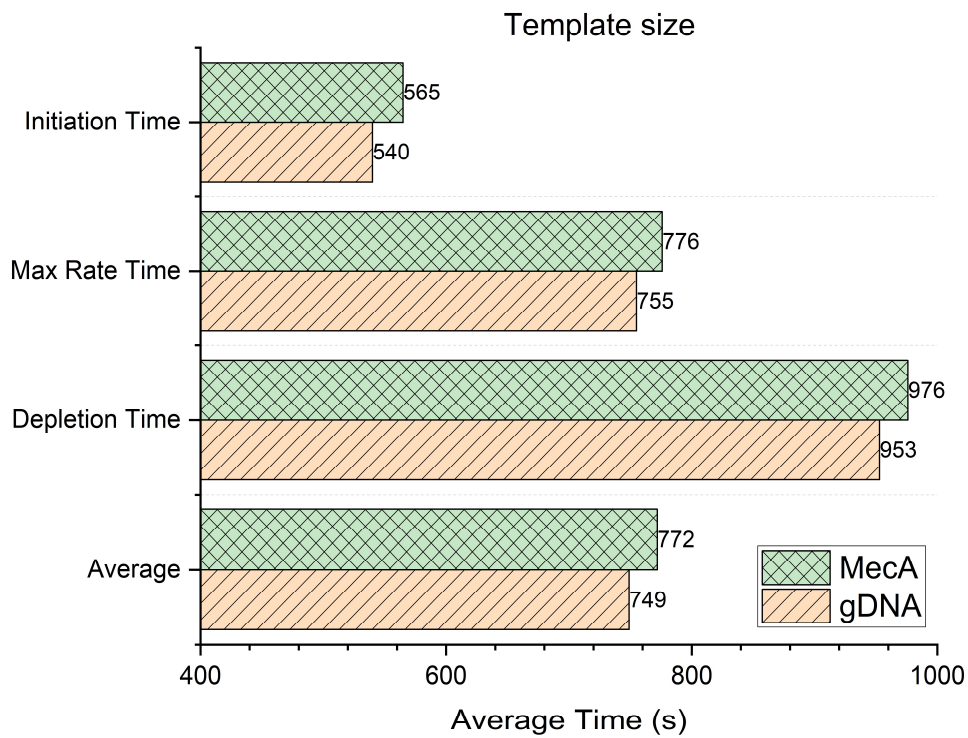


Figure 5.43. Average key kinetic reaction constants derived modified RT-RPA of the modified and unmodified primer sequence MecA 12, 10, 8 and 7's. Highlighting the overall effect template fragment size had on reaction efficiency.

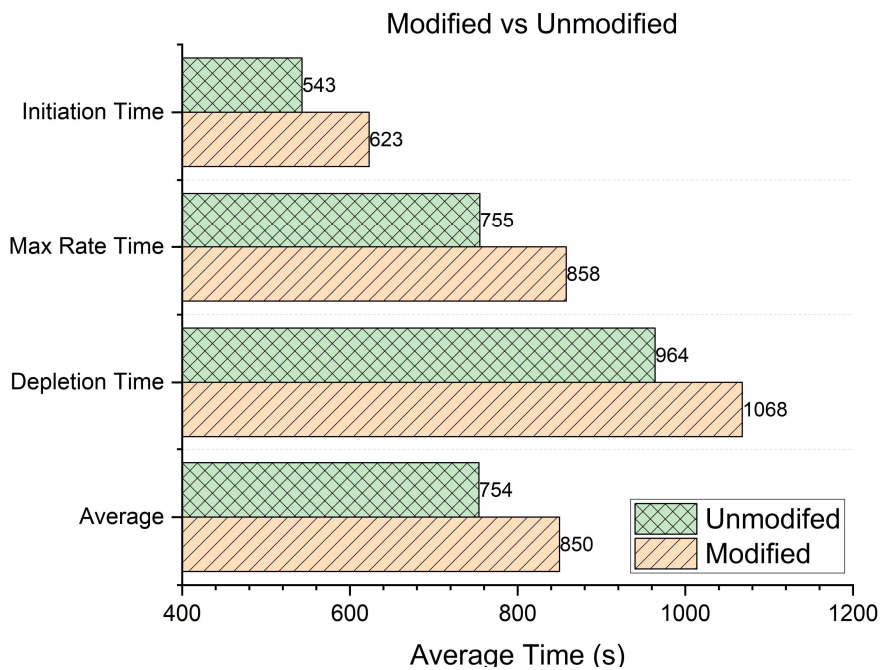


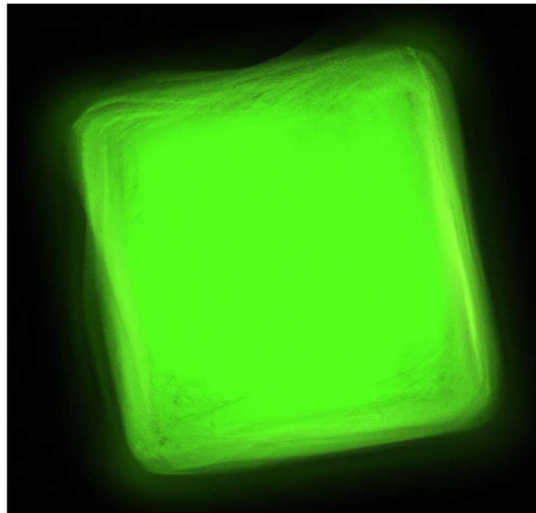
Figure 5.44. Average key kinetic reaction constants derived modified RT-RPA of the modified and unmodified primer sequence MecA 12, 10, 8 and 7's. Highlighting the overall effect the NALFA modification had on reaction efficiency.

To conclude, as expected the addition of the modification to the primer sequences produced a significant drop in amplification efficiency when compared to the performance using the same unmodified primer sequences. Given the level of medication however this was not as severe as originally thought it would be. On average when comparing the key reaction constants from the unmodified primer sequences to the modified ones an 11.3 % reduction in performance was observed. (*Fig. 5.44*). It's worth noting MecA₁₂, regardless of the reaction conditions, consistently demonstrated commendable performance. While it may not have been the fastest in producing amplicons in any particular evaluation, its remarkable consistency across different conditions makes it the leading candidate for integration with the lateral flow assay (LFA) at this stage.

Chapter 6

Real Time Solid Phase RPA.

“DIY Doctor: A Chemistry PhD's Unplanned Adventures in Engineering”



*There once was a chemistry PhD,
Whose work never went as planned you see,
He needed some vital equipment, no doubt,
But procurement was watching, there was no way out.*

*He thinks and he thinks, what can he do?
His research is strained, his hopes are askew,
Then he has a terrible idea, oh so clever,
and says, "screw it I'll build it myself whatever!",
Then foolishly Sets out to learn electronics,
Dabbles his hand in photonics and robotics!*

*He jumps to the googler, studied day and night,
He worked and he worked, with all his might,
He learns about circuits, MOSFETS and wires,
He investigates the photonics and starts a small fire!*

*He struggles and struggles, it's not easy, no sir,
But he won't give up, not until he's a blur,*

*Of hard work and determination, he'll see it through,
Our hero the chemistry PhD, he'll make it true,*

*And when it comes to CAD, he becomes a pro,
He will try and design anything with folly, don't you
know, With his new skills, he tackles his work,
But alas, it's still not going as planned, it's quite a
quirk.*

*He solders micropackages, with the fumes in his eyes!
Codes microcontrollers, it's quite a surprise,
He 3D prints parts, but nothing seems to work,
But he won't give up, even if he goes berserk!*

*So if you're stuck and feeling blue, Just remember, it
means there's something new for you to do.*

*Don't give up, no matter what others say,
You never know what you're capable of, not until you
try and play*

6.1 Introduction:

In chapter six, we will investigate the use of "solid phase" RPA reactions as a means of directly integrating RPA reactions into the proposed NALFA in order to meet the WHO ASSURED criteria for the PoC diagnostics. A lab-made, ultra-low noise, high dynamic range solid state fluorometer was developed and built to study the effect on amplification kinetics caused by moving the reaction within a solid matrix, where reagent diffusion will be significantly affected. Our experiments also sought to modify RPA conditions to enhance the amplification performance within a solid matrix and facilitate detection on the proposed NALFA without further processing.

6.2 Solid State Fluorometer:

A solid state fluorometer was designed using a similar principle to a fluorescence microscope. Filtering of the excitation and emitted light was performed using MF475-35 & MF530-43 band pass filters with a MD499 Dichroic filter to reject passed IR and UV light to designated beam dumps. A Bi-convex condenser objective was used to both disperse the collimated polarised excitation light and focus the emitted fluorescence onto the detector. (*Fig. 6.1*).

To achieve the desired performance, it was vital incident light intensity was highly regulated. Firstly, the laser used, L462P (Thorlabs), which had excellent output characteristics (*appendix 6*), was very powerful. A good thing for increasing the sensitivity of the device, however it was also capable of photobleaching most fluorophores over an extended exposure period. To negate this the laser was driven in PWM mode at 250kHz using a custom-made driving circuit. By altering the on time of the laser it was possible to reduce the optical output power to a more balanced level, without impacting the optical output characteristics; as the excitation voltage remains constant across the diode at all power levels.

To further reduce this bleaching effect, it was desired to only irradiate the samples for a short period of time at specific intervals, for example 10-50ms every 1-5 seconds. This could be done by simply disabling the laser, however as the laser is turned off for a significant amount of time it will thermally cycle, effecting the optical output characteristics and putting undue thermal strain on the expensive laser diode. Therefore, to achieve this an electromechanically actuated diaphragm optical beam shutter was used (SHB025T, Thorlabs). (*Fig. 6.1*). This was used to break the beam when measurements are not being taken, then open for a precisely controlled short amount of time via TTL signalling.

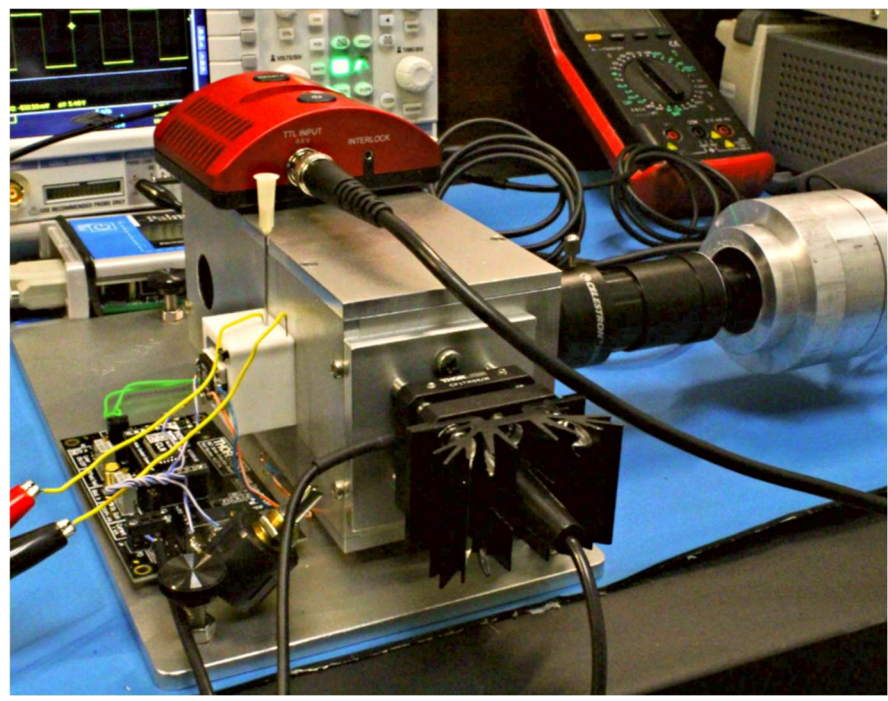
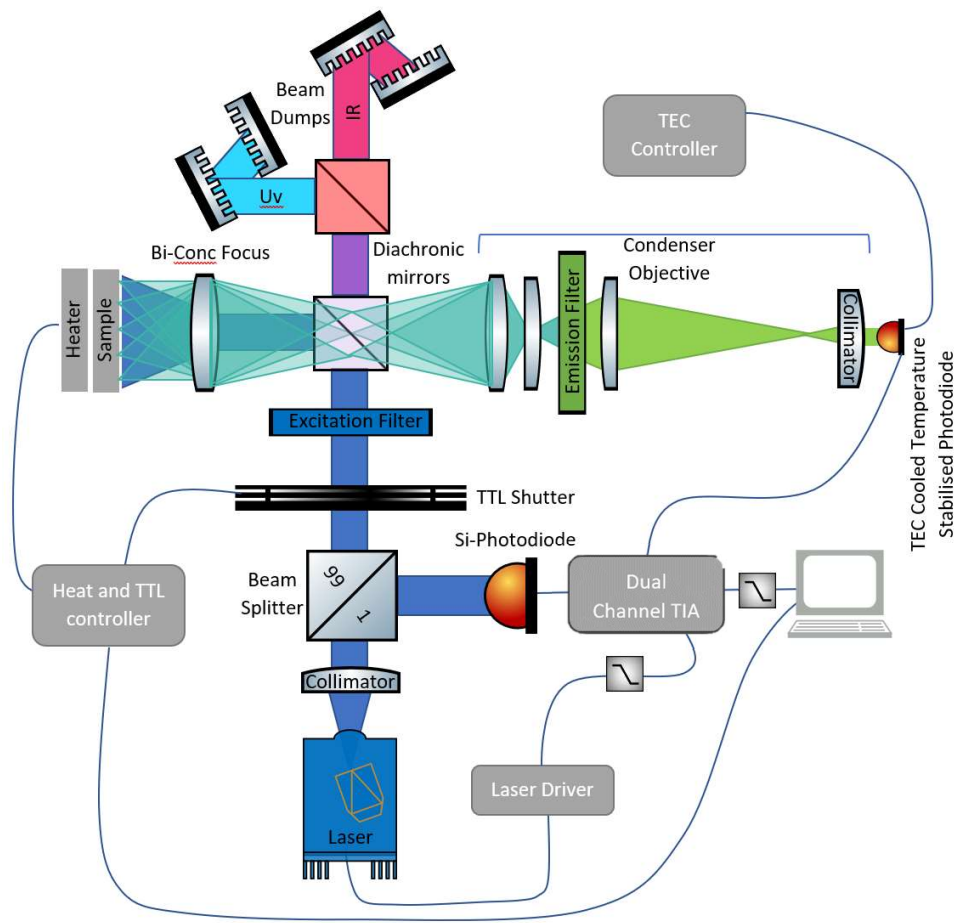


Figure 6.1. A) Functional diagram of the built fluorometer. B) Image of Fluorometer during development.

Secondly, the optical power must remain consistent over a prolonged period of time, as it is not possible to use a reference light path to compare the fluorescence measurement. It is possible to achieve this by running the laser in a constant input power mode using a constant current is less consistent as the efficiency of the laser changes with temperature and less than ideal for pulsed lasers. This was achieved by running the laser in constant out power mode, a compact beam splitter arrangement composing of two non-polarizing beam splitter cubes (BS034, Thorlabs) in V configuration were used to tap a control beam. This was then sent to a photodetector connected to a custom-made trans-impedance amplifier to measure the actual optical power. This signal was filtered then injected into the feedback loop of the laser driver circuit to modulate the on time of the PWM signal driving the laser thus compensating for any in fluctuations optical power output. *Figure 6.2* shows the functional block diagram of the laser regulation and driver circuitry. Following from this *figure 6.3* then shows the full schematic of the control board used to modulate the laser output.

Laser Driving Circuit and Block Diagram:

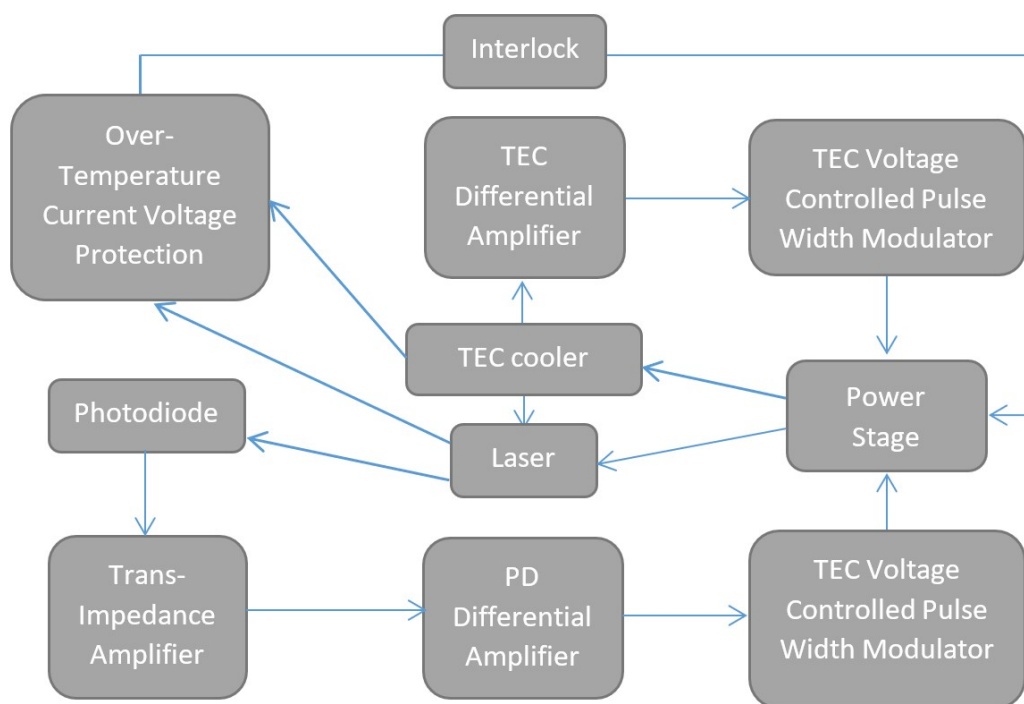


Figure 6.2. Laser driver block diagram.

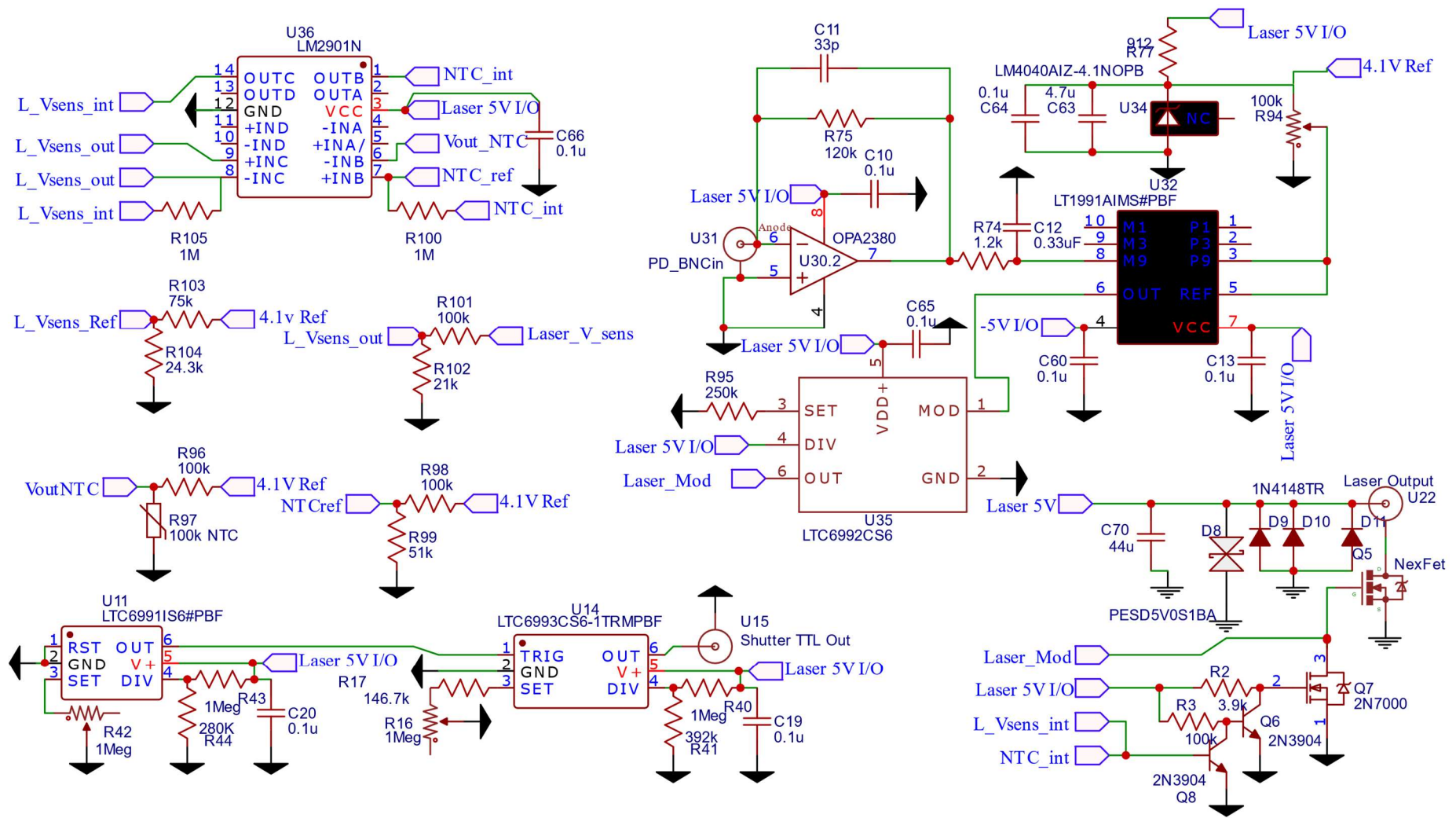


Figure 6.3. Laser control board schematic

Both the laser diode and detector photodiode were cooled, and temperature controlled using thermoelectric coolers (TECs), also known as Peltier coolers. These operate on the Peltier effect, which states that when a current is passed through two conductive materials with different electromotive forces, a temperature difference is created at the junction of the materials. This temperature difference can be used to transfer heat from one side of the TEC to the other. TECs consist of multiple thermocouple junctions connected in parallel and sandwiched between two ceramic plates. When a current is passed through the junctions, it creates an induced temperature gradient across the junctions, resulting in a hot side and a cold side of the TEC. The hot side can be used to dissipate heat, while the cold side can be used to cool an object or environment. In order to achieve the desired cooling effect, TECs must be carefully designed to effectively dissipate the heat generated on the hot side. For the laser cooler two 2x2x0.3 cm TEC elements were used to cool the laser and maintain 20°C during operation, this was achieved in combination with a 20W °C⁻¹ heat sink with a 50mm fan and the TEC elements controlled using a custom-made driver board. (Fig. 6.4).

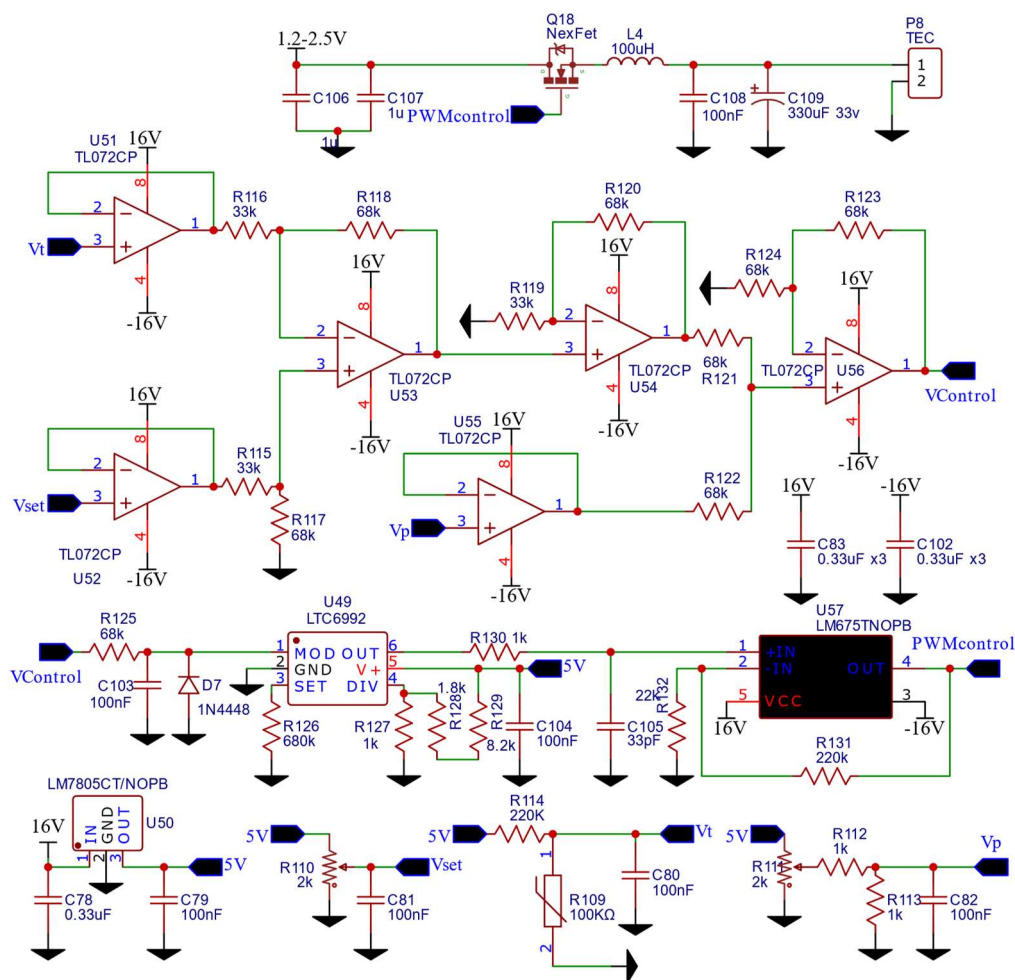


Figure 6.4. TEC control board schematic.

The custom-made photodetector featured a Hamamatsu S3477-03 Si photodiode with an integrated 2 stage thermoelectric cooler. The detector diode housing was water cooled using milled single channel aluminium water block used in conjunction with a sub-ambient chiller to cool the hot side of the TEC. The detector temperature was then controlled using the same TEC control circuit as the laser. The TEC was current limited to 1.5A as per the manufacturer's recommendation. Cooling performance was assessed using the maximum cooler current at -18°C coolant temperature, the detector substrate reached and equilibrium of -68.2 °C. Detector noise and temperature stability was assessed by measuring the temperature and dark current with a Rhode & Schwarz HMO1002 100MHz oscilloscope and a Metrohm Autolab PGSTAT 30 potentiometer. Temperature stability -50 °C was ± 0.04 °C over a 20 min period after reaching thermal equilibrium. Dark current was measured at 116 ± 1.26 fA with no long-term drift evident. The detector was paired with custom made dual channel, ultra-low offset, high bandwidth transimpedance amplifier in a cascade arrangement. The TIA was designed using 4 best-in-class femtoampere input bias current electrometer amplifiers, ADA4530's for Analogue Devices (*Appendix 7*), in a two-stage configuration. Channels were matched by manual trim calibration in low gain mode using a DC-20kHz square wave at 10fA using a dual channel function generator and an oscilloscope. (*Fig. 6.5-6.6*)

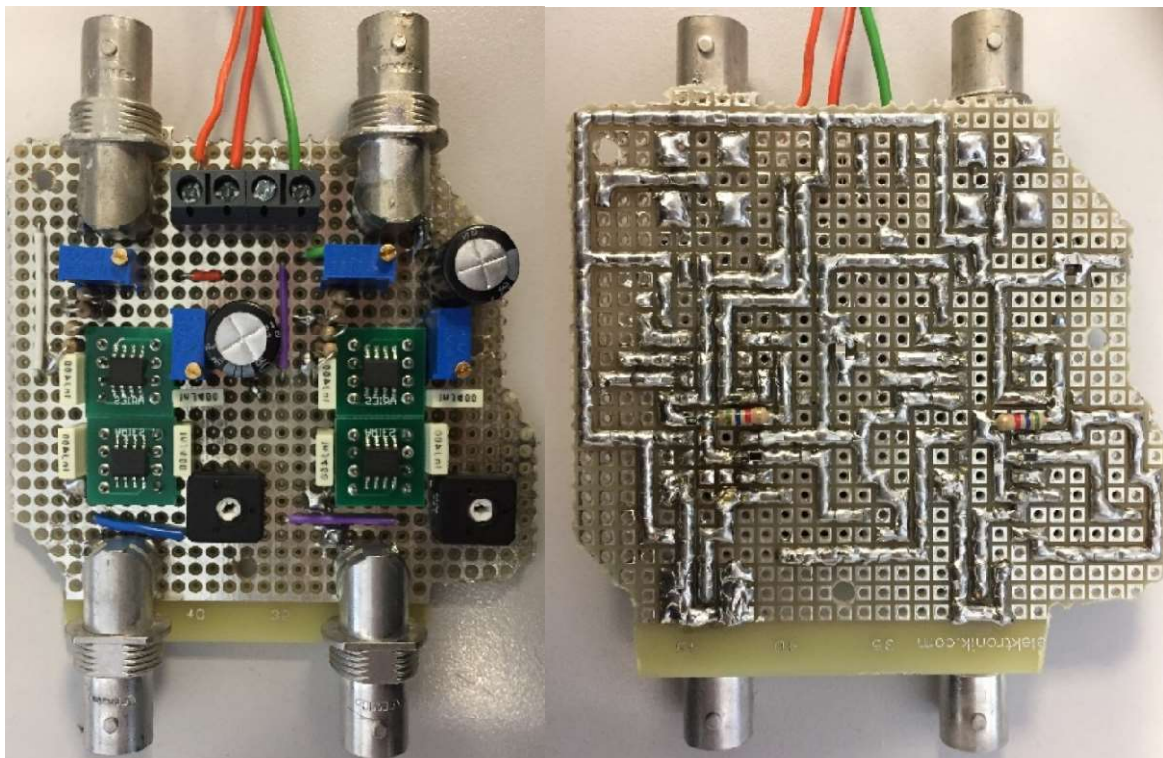


Figure 6.5. Prototyped Dual-Channel TIA prior to PCB manufacturing.

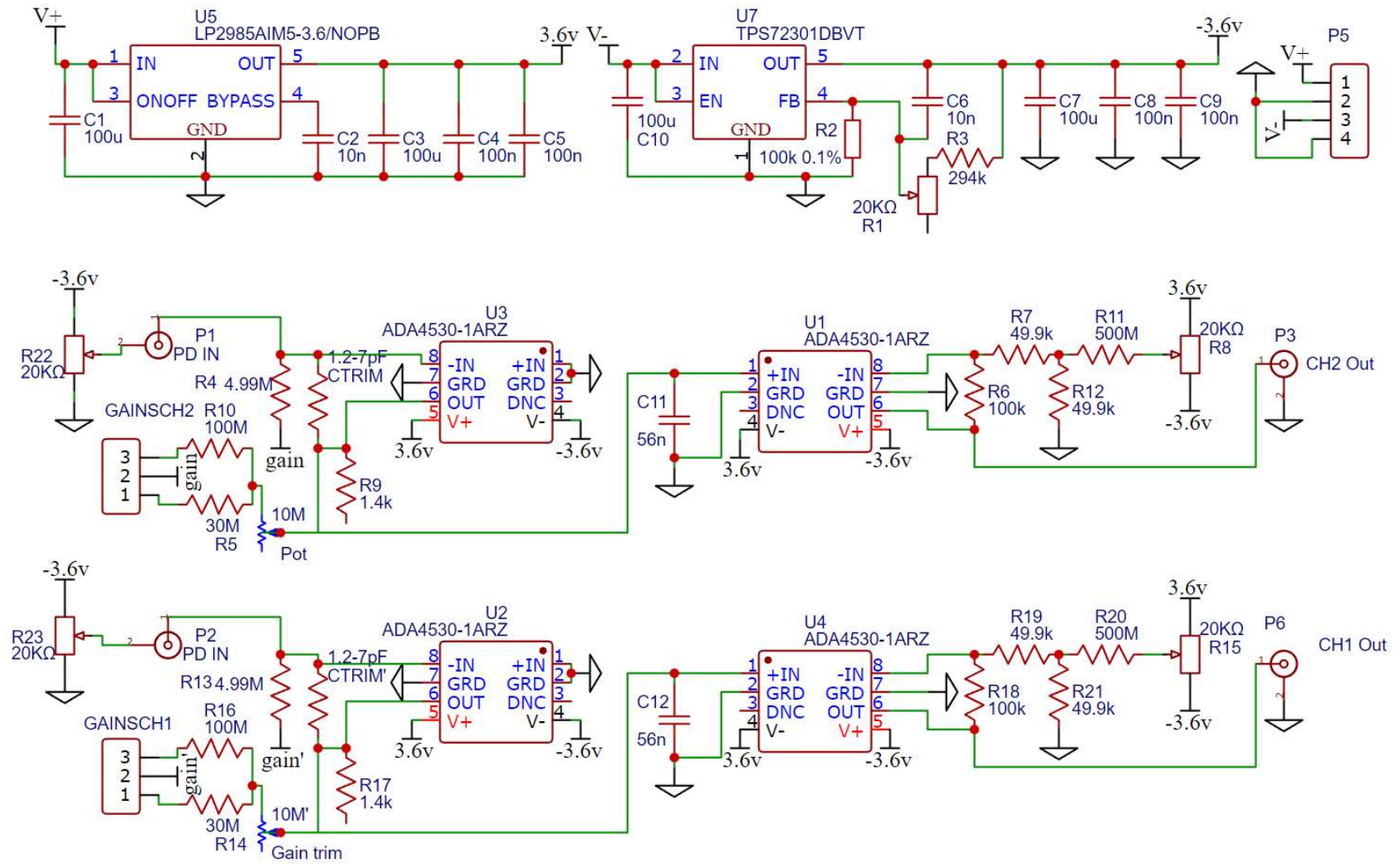


Figure 6.6. TIA board schematic

To hold RPA reaction matrix during measurements a heated sample holder was machined out of Delrin-POM and copper. (Fig. 6.7).

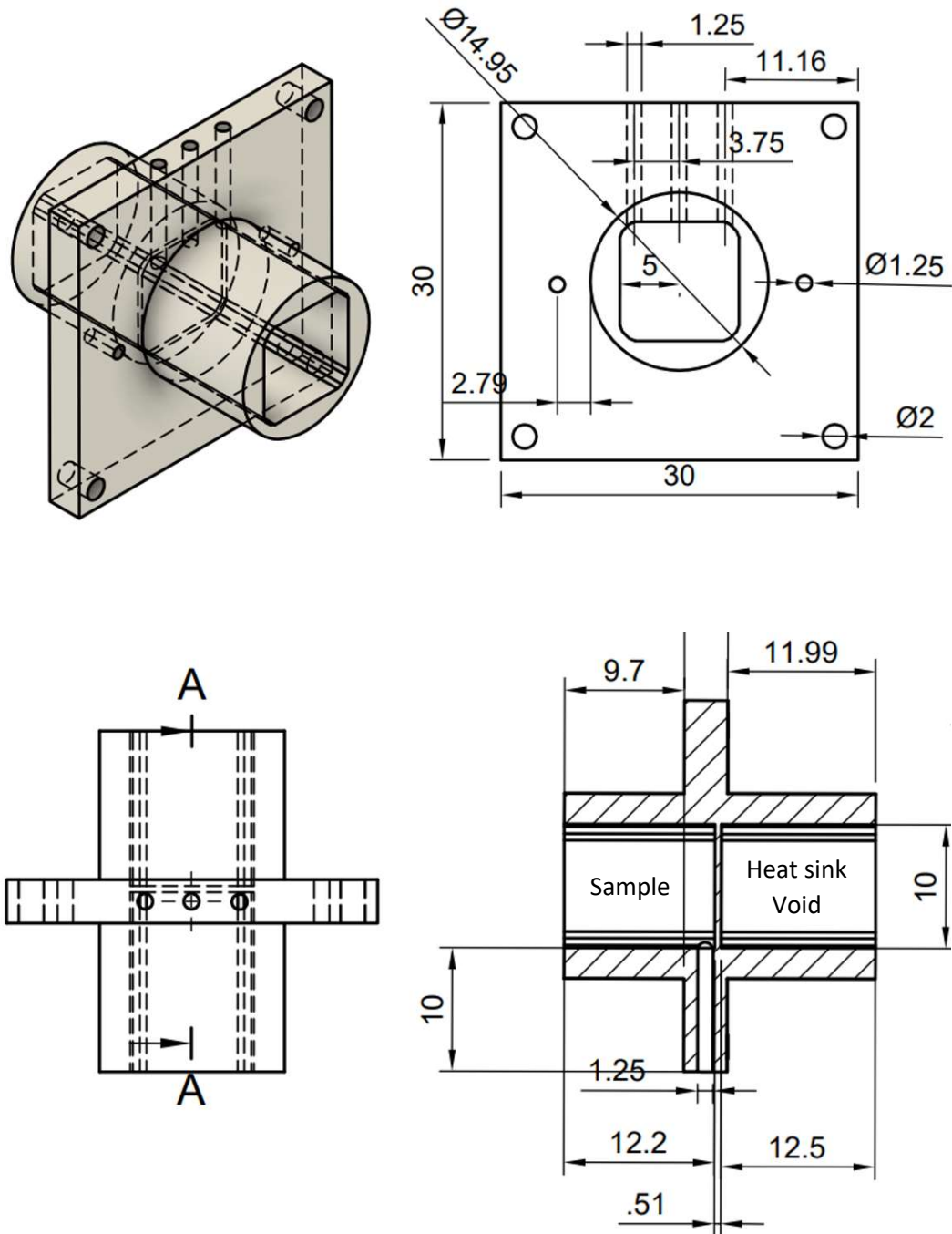


Figure 6.7. CAD drawing of the SP-RPA reaction holder. (Top) Cross sectional view of real time SP-RPA reaction holder showing sample access ports and internal dimensions. (Bottom) All units are in mm scale.

To heat the RPA reactions during real time solid phase RPA monolithic proportionally controlled heater was used (DN515-1228, Themoptics). Unlike a PID controlled heaters these proportionally controlled heaters have virtually no hysteresis once thermal equilibrium is achieved. Setting the desired temperature can be done via a microcontroller using a voltage controlled linear voltage regulator or a simple potentiometer.

The LoD of the fluorometer was assessed using serial dilutions of fluorescein prepared in 0.01M NaOH. Samples were prepared using a glass fibre conjugate material by punching a 1cm² squares from stock sheets and adhering the bottom of the reheated (37 °C) sample cell. 20 µL fluorescein dilution was added by pipette onto the centre of the pad and covered with a 1x1 cm glass cover slip. Samples were held for 30 s then irradiated with excitation light for 20 ms. Signal integration was taken 5ms after shutter opening and stopped 1ms before shutter closed to ensure the shutter was full open during signal integration. Dilutions were run in triplicate at 50 % stabilised excitation power. (Fig 6.8).

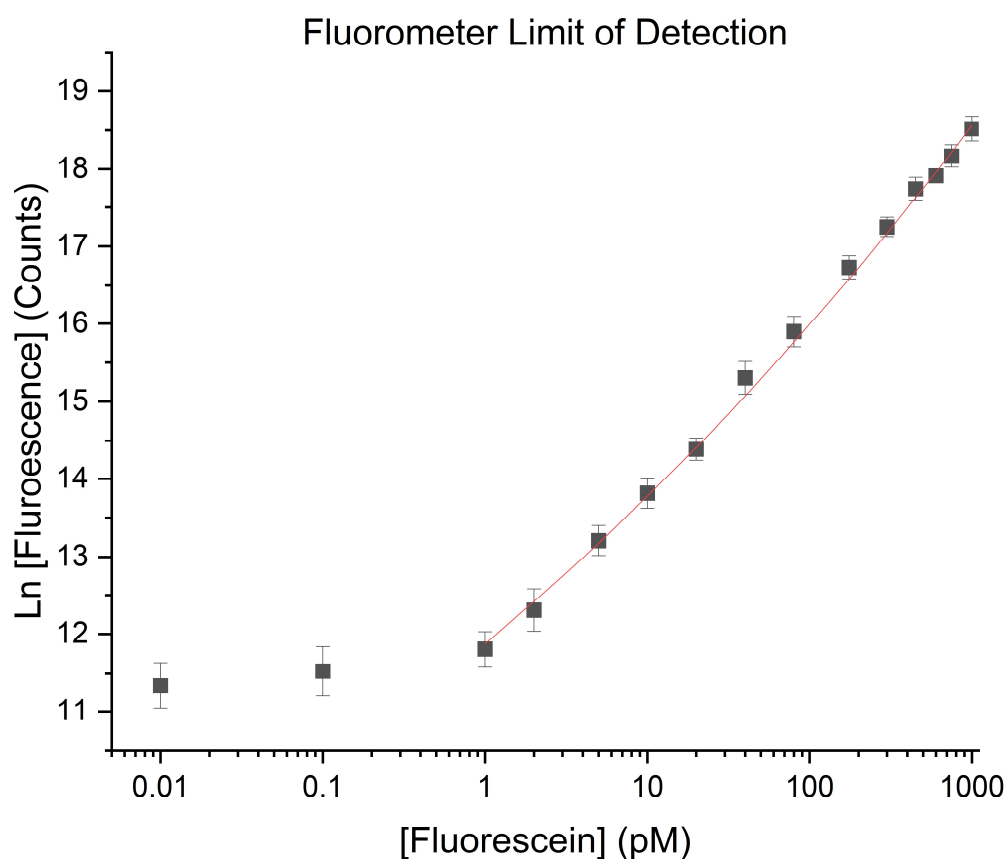


Figure 6.8. Graph showing the developed solid matrix fluorometer's LoD for fluorescein bases fluorescent molecules, and background Raman scattering of incident light on sample matrix.

6.3 Reaction Matrix Blocking Optimisation:

Blocking titrations using each blocking system were carried out with varying concentrations of blocking agents to determine optimum conditions to block RPA reaction matrixes. Blocking performance was assessed by quantitative fluorometric measurements to determine the DNA and protein adsorptivity of treated matrix. DNA and protein adsorptivity measurements were run in triplicate and conducted at the bottom of 96 well plates.

gDNA solution for adsorptivity measurements was prepared using freshly extracted MRSA reference gDNA. Reference DNA was sonochemical sheered by sonicating 500 μL 10 ng μL^{-1} solution at 10 W $\text{cm}^2 \text{cm}^{-3}$ using a 0.4mm titanium probe for 60 seconds. Fragment distribution was assessed by agarose gel electrophoresis using pre-stained 0.6 % agarose gel run at 3 $^{\circ}\text{C}$, 1 V cm^{-1} , in 1X TBE for 4hrs. (Fig. 6.9).

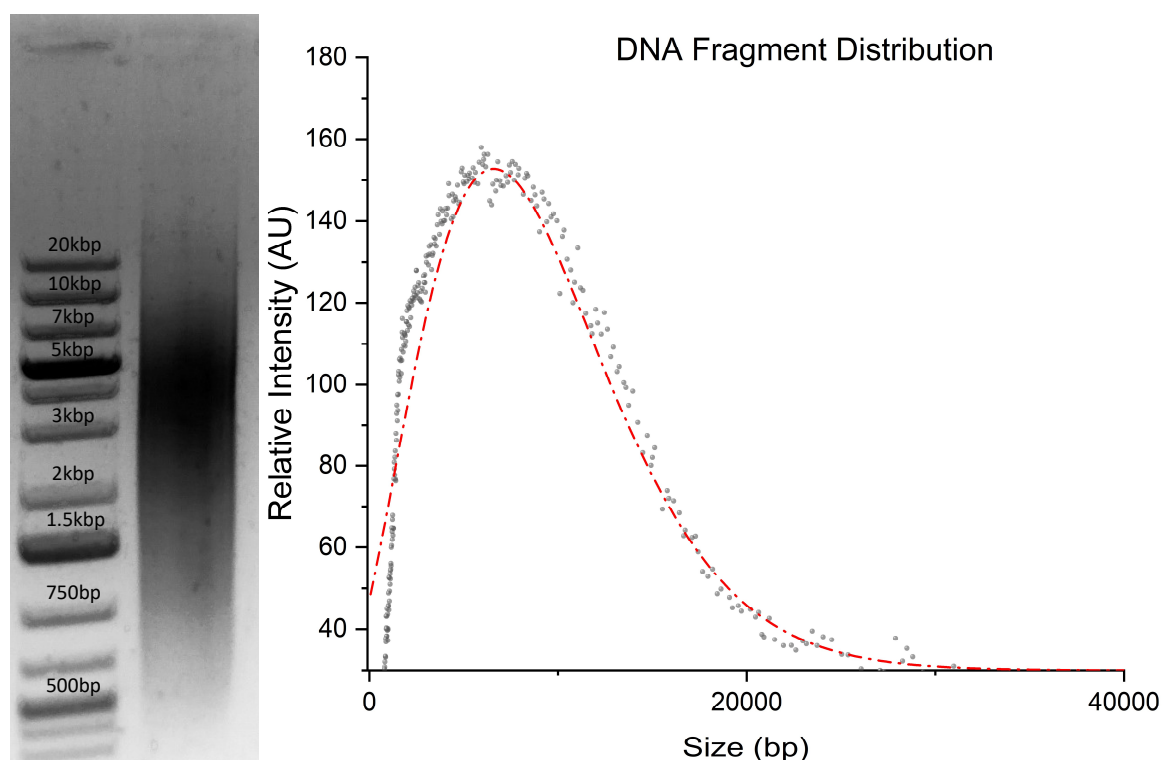


Figure 6.9. Shows purified and sonochemical sheared gDNA fragments.

Fluorescent labelled BSA was made by first dissolving 400 mg lyophilised BSA powder in 5 ml sterile 6X SSC buffer, pH adjusted to 7.2, then filtered using a 0.8 μm cellulose acetate membrane. 1 ml 1mM FITC was added, and the solution pH was adjusted to 8.2 with 0.05 M NaOH, then sonicated at 37 $^{\circ}\text{C}$ for 6 hours. The solution was loaded onto a PD10 desalting column and eluted in 500 μl

aliquots of protease-free HPLC grade H₂O. Fluorescence using 515±20 nm excitation light and fluorescence measured at 485±5 nm was used to identify the aliquots containing the FTIC-BSA. These aliquots were combined into a pre-weighed centrifuge tube, flash frozen in LN₂ and freeze-dried for 24 hr in a light-free chamber. 1 µM FTIC-BSA solution, was made by dissolving 335 mg lyophilised FTIC-BSA in 15 ml 6X SCC buffer.

Blocking solutions were made by diluting stock solutions to the appropriate concentration. BSA stock blocking solution was made by dissolving 0.4 g lyophilised BSA powder in 20 ml sterile 1X PBS, pH adjusted to 7.2, then filtered using a 0.8 µm cellulose acetate membrane. Casein stock blocking solution was made by adding 0.4 g to 8 ml ddH₂O and 500 µL 0.1M NaOH and sonicated for 1 hour at 50 degrees. 10 ml 2X PBS buffer was added, the solution pH adjusted to 7.8 and made up to 20 ml with ddH₂O, then filtered using a 0.8 µm cellulose acetate membrane.

Glass fibre reaction matrix's were first crosslinked and functionalised using of 5 ml 5 mM MPTMS:TEOS solution in EtOH : 10 % w/v NH₄OH 10:1. Reaction pads were heated to 30 °C and incubated for 6 hrs then irradiated with UV light for 60 s using a gel transilluminator. Pads were then washed thrice with ddH₂O and dried at 30 °C. 200 µL of blocking solution was added to the respective well using 20-2 mg mL⁻¹ dilutions. Plates were sealed and incubated with gentle shaking for 4 hr at 40 °C then washed 3x with 200 µL ddH₂O. DNA adsorptivity measurements were obtained by adding 15 µL 1 ng µL⁻¹ sonochemical sheered g-DNA fragments, incubating for 1hr at 37 °C. Each well was washed 3x with 200µL 6X SCC buffer, 25 µl EtBr-fluorometric assay solution was added, plates incubate for 120 s and washes with 200 µL ddH₂O. Plates were immediately transferred to a ThermoScientific™ Varioskan™ LUX multimode microplate reader. Fluorescence measurements were taken using a 1 s integral measuring time, with 620±2 nm excitation light and fluorescence measured at 360±5 nm. Ss-DNA adsorptivity fluorescence was calibrated using internal standards for each membrane. Protein adsorptivity measurements were then obtained by adding 15 µL fluorescent labelled BSA stain to each well, incubating for 1 hr at 37°C. Each well was washed 3x with 200 µL 6X SCC buffer and then refilled with 50 µL fresh 6X SCC buffer. Plates were immediately transferred to a 38 °C pre-heated ThermoScientific™ Varioskan™ LUX multimode microplate reader. Fluorescence measurements were taken using a 1 s integral measuring time, with 515±2 nm excitation light and fluorescence measured at 485±5 nm. Protein adsorptivity fluorescence was calibrated using internal standards for each membrane. Yielding DNA absorptivity plots shown in *figure 6.10*.

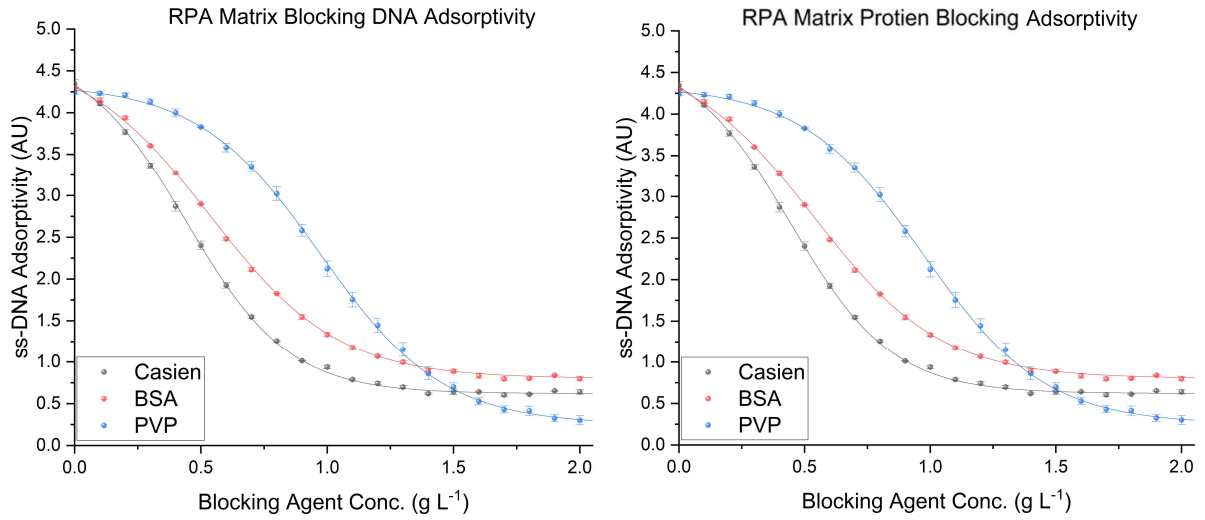


Figure 6.10. ss-DNA/protein membrane adsorptivity single reagent blocking titrations

The SS-DNA and protein adsorptivity curves were fitted using a standard 4-parameter Boltzmann regression function, Equation 9.

$$\varphi(\rho_i) = \frac{\varphi_{\max} - \varphi_{\min}}{1 + e^{\frac{\rho_i - k_m}{\gamma}}} + \varphi_{\min} \quad (9)$$

$$\frac{\partial}{\partial \rho_i} \left[\frac{\varphi_{\max} - \varphi_{\min}}{1 + e^{\frac{\rho_i - k_m}{\gamma}}} + \varphi_{\min} \right] = \frac{(\varphi_{\min} - \varphi_{\max}) e^{\frac{\rho_i - k_m}{\gamma}}}{\gamma \cdot \left(e^{\frac{\rho_i - k_m}{\gamma}} + 1 \right)^2} \quad (10)$$

$$\frac{\partial^2}{\partial \rho_i^2} \left[\frac{\varphi_{\max} - \varphi_{\min}}{1 + e^{\frac{\rho_i - k_m}{\gamma}}} + \varphi_{\min} \right] = -\frac{(\varphi_{\min} - \varphi_{\max}) \left(e^{\frac{\rho_i - k_m}{\gamma}} - 1 \right) e^{\frac{\rho_i - k_m}{\gamma}}}{\gamma^2 \cdot \left(e^{\frac{\rho_i - k_m}{\gamma}} + 1 \right)^3} \quad (11)$$

$\varphi(\rho_i)$ = Fluorescence \equiv Adsorptivity φ_{\min} = Fluorescence φ_{\max} = Max Fluorescence
 ρ_i = Reagent Concentration k_m = Centre Point γ = hill slope

Therefore, the ideal concentration of each blocking reagent for a given material can be determined by finding the maxima of the second derivate of the adsorptivity curve, *equation 10-11*. The concentration of blocking reagent at the given maxima of the second derivative of this function is where the vector rate of negative change in adsorptivity slows relative to the increase in reagent concentration. (*Fig. 6.11*) This is due to the reduced number of blocked sites available and can therefore be considered the most effective blocking concentration.

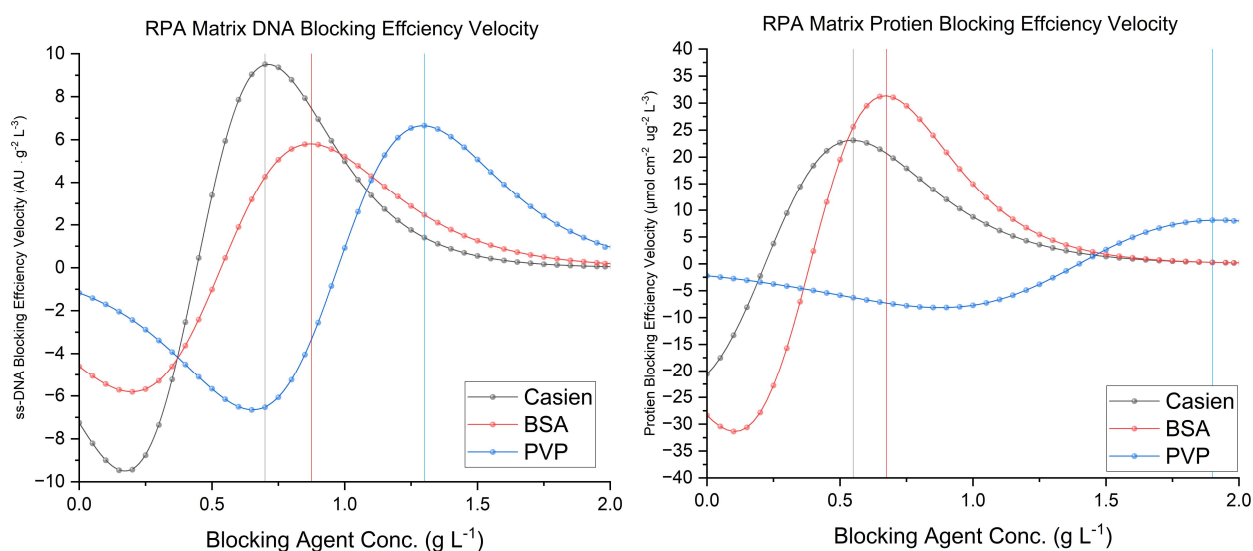


Figure 6.11. DNA/protein RPA matrix blocking efficiency velocity showing the ideal concentration of each blocking reagent.

Using the determined reagent concentrations shown in *table 6.1*, blocking solution can be formulated which can effectively block unwanted molecules from adhering to the material surface, while reducing the probability of aggregation of the blocking materials within the membrane pore structure. This is especially true for membranes with the smallest pore sizes with the largest blocking molecules, which is discussed further in *Chapter 8*.

Table 6.1. Optimal determine blocking agents' concentration from fig. 6.11.

Rejected molecule	Blocking reagent	Optimal concentration (g L ⁻¹)
DNA	Casien	0.73
	BSA	0.82
	PVP-10	1.29
Protein	Casien	0.51
	BSA	0.63
	PVP-10	1.87
Average	Casien	0.62
	BSA	0.72
	PVP-10	1.58

6.4- Initial SP-RPA Investigation:

Solid phase RPA was first investigated using the standard reaction conditions and validated primers sets. Reactions were run using fresh reagents added to the reaction matrix and also by freeze drying the RPA reagents in situ ready for then rehydration, as would be the case in the coupled NALFA.

1 mm thick glass fibre conjugate strips were activated and prepared by submersion in 5mM MPTMS:TEOS solution prepared in EtOH : H₂O : NH₃ 10:1:0.1. Strips were sealed in an airtight container and heated to 30 °C for 6 hrs, removed and irradiated with UV light for 60 s using a gel transilluminator. Strips were then washed thrice with ddH₂O and dried using a fine jet of N₂.

Strips were then submersed in RPA matrix blocking solution formulated in section 6.2, (0.6 g L⁻¹ Casein, 0.7 g L⁻¹ BSA, 1.5 g L⁻¹ PVP-10, in 1X PBS/SCC) and incubated with gentle shaking for 4 hr at 40°C, washed thrice with ddH₂O then dried using a fine jet of N₂. 0.5x3 cm strips were cut using a razor blade and a glass edge, strips were rolled lengthwise and inserted into a retaining ring. Rings were made using 200 µL pipette tips cut 1cm above the tip taper with a 3D printed 4x4 mm polypropylene retaining cross pressed into the taper and top to hold the rolled matrix.

For in situ reactions, 45µL RPA liquid master mix (250 µL Reaction buffer, 92 µL 10 mM dNTP's, 50 µL E-Mix, 25 µL Core enzyme mix) was pipetted on to the reaction matrix. These were then placed in a zip-lock bag and flash frozen in liquid N₂. The bag was the pierced in several location with a wide bore needle, the prepared reaction matrixes were then freeze dried for 16 hrs. In situ initiation solutions were prepared using 10 µL of each 10 µM forward and reverse primers, 4µL 210 pg / 1M copies µL⁻¹ reference MRSA gDNA, 10 µL MgOAc and 166 µL ddH₂O. Standard initiation solutions prepared using 10 µL of 10µM forward and reverse primers, 4 µL 2.1 pg/10k copies µL⁻¹ reference MRSA gDNA, 10 µL MgOAc and 10 µL ddH₂O.

All reaction materials and constituents were equilibrated to 38 °C inside an aluminium heat block, in a 40°C incubator for 15 mins. Standard reactions were initiated by mixing 45 µL of RPA liquid master and 5 µL dry initiation solutions in a separate Eppendorf then added to the blank blocked matrixes directly. In situ initiation was performed by adding 50 µL initiation solutions to the pre-loaded reaction matrices. Reactions were run for 40mins; liquor removed by centrifugation at 1000 RCF for 60 s and immediately purified using Monarch® 5 µg PCR & DNA clean-up columns and analysed by non-denaturing TBE-DNA 20 % polyacrylamide gels run at 3 °C, 5 V cm⁻¹, in 1.25X TBE buffer for 2 hrs. (*Fig. 6.12-6.13*).

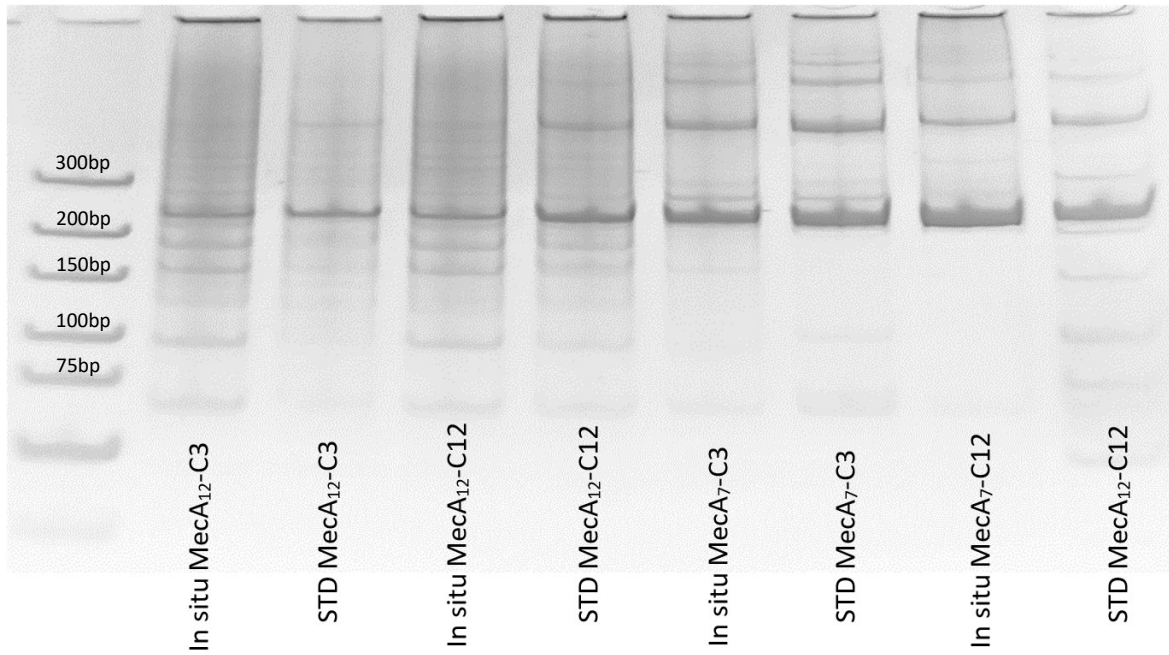


Figure 6.12. Successful SP-RPA amplicons with spurious amplification products.

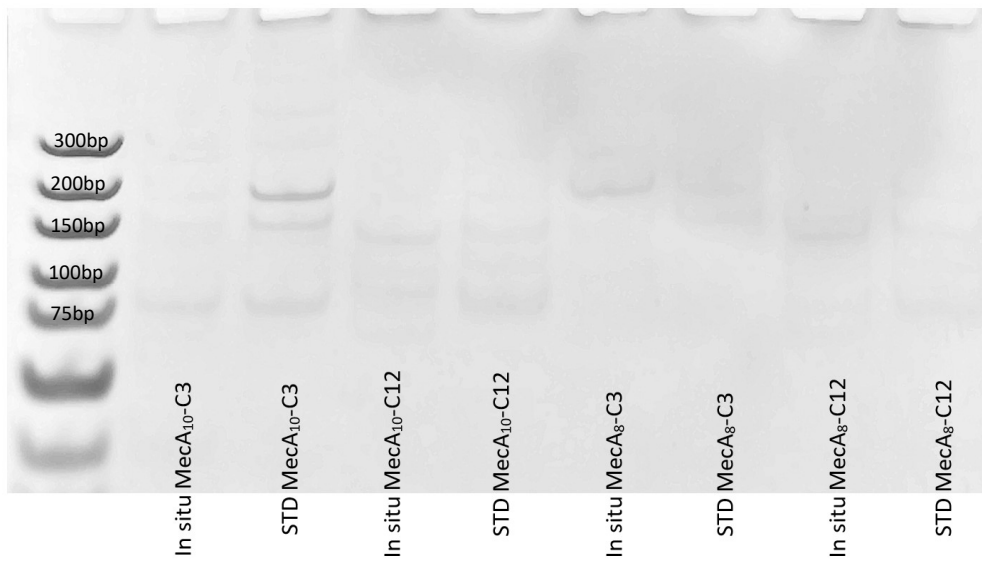


Figure 6.13. Unsuccessful SP-RPA reaction products

The use of standard RPA reaction mixtures within a solid matrix resulted in variable outcomes, with only half of the validated primer sets yielding the desired amplicon. Moreover, the reactions that did proceed exhibited poor quality. The lyophilization of the reaction components onto the matrix seemed to negatively affect the amplification quality in comparison to identical reactions which were

not lyophilised. It was hypothesized that the cause of the poor performance was due to changes in intramolecular interactions between the reaction components, the matrix, and the crowding reagent.

A key element in the process of RPA, and often neglected, is the vital role the crowding reagent plays in the amplification process. RPA at its most basic functional principle is using a series of recombinases that original functions were in reading, altering, and repairing nucleic acids freely distributed within prokaryotic cells. Within the cell the reaction environment consists of a plethora of intramolecular interactions between large macromolecules, the recombinases, and the nucleic acids. This has the effect of reducing the amount of “free space” within the reaction matrix. This in turn helps to keep the enzymes and nucleic acids in close proximity. Therefore, in a lab setting, to mimic this phenomenon a crowding reagent is used. In the case of the standard RPA reaction mixture this is achieved using approximately 5 % PEG-40.

When developing an RPA reaction, a balance is required when choosing crowding reagents and their concentration. It is possible to totally inhibit amplification if intermolecular interactions are too strong and or frequent. In such cases DNA-recombinase complexes may be unable to dissociate, as thermodynamic conditions make the complexes more stable than their dissociated or transition states. Additionally, the probability of finding new substrates such as primers, templates, and cofactors may be significantly reduced under such conditions. In the context of amplification products, moderately over-crowded reaction conditions will likely result in spurious amplification material being produced. As amplicons become increasingly crowded around high concentrations of primers, for example during the initial phase of exponential amplification (T_i); and recombinases, the probability of dimer products forming and unwanted run-away amplification occurring becomes markedly increased.

By constraining the reaction mixtures within the internal structure of the matrix, which is already coated with large macromolecules for blocking; and stock RPA reaction mixtures having been optimised for bulk solution, the reaction mixture is likely highly overcrowded. These conditions coupled with the reduced bulk diffusion of reagents, due to increased surface tension between the liquid and the solid matrix, has a highly detrimental effect on amplification efficacy and efficiency. The manufactures of RPA kits do not allow for the easy optimisation of crowding reagents as they are always mixed with protein master mixes. Additionally, 5 % PEG-40M solutions are not compatible with most lateral flow membranes, as the large linear polymer blocks the internal pore structure; significantly reducing the flow of larger molecules i.e., amplicons and nanoparticle-based reporter probes.

6.5 SP-RPA Optimisation:

Reagent titrations using MecA₁₂-C3 were performed to optimise the RPA reaction mixtures to be compatible with the solid matrix and its blocking system. To achieve this liquid RPA enzyme master mix was purified using salt-induced phase separation to allow for more controlled RPA conditions. 125 μ L 3M K₂HPO₄ and 125 μ L 3M KH₂PO₄ was added 250 μ L core reaction mix (Liquid RPA Basic Kit, Abbott Twistdx) heated to 35 °C and vortexed for 3 mins. The mixture was then centrifuges at 50 kRCF at 3°C for 20 mins. The top PEG containing layer was discarded and the protein mixture desalted using a PD-10 column, fractions were eluted using 50 mM tris and 100 M KOAc buffer at pH 8. Protein containing fractions were combined and 100 mg trehalose added then diluted to 1 mL in 50 mM tris and 100 M KOAc buffer at pH 8.4 to give a 5X enzyme mix and the mixture analysed by SDS-PAGE. (Fig 6.14).

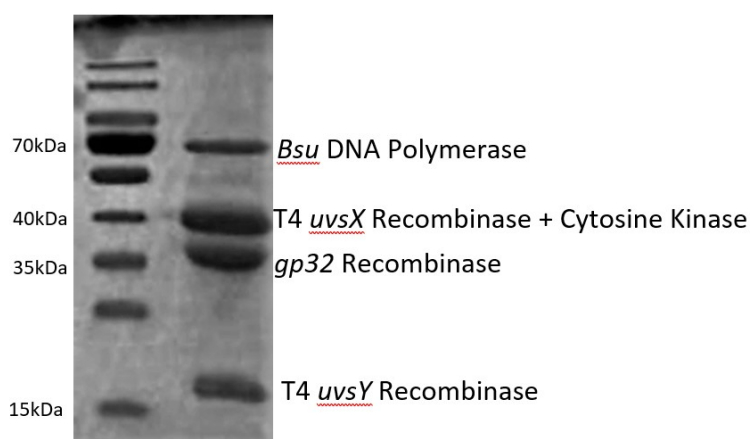


Figure 6.14. Denaturing SDS-PAGE of purified RPA enzymes mixture.

A crowding system more compatible with the proposed NALFA developed in chapter 6 was made using 5 %_{w/v} PVP-10, 10 %_{w/v} HSA, and 20 %_{w/v} and Ficoll 400 yielding a 1000X crowding mix stock solution. Titrations using 0-160X final crowding reagent were made to optimise the crowding reagent working concentration. Crowding reagent concentrations higher than 200X had negative effect on membrane flow rates.

Reaction matrices were activated, blocked, and prepared as before. A 5X reaction buffer was, 2.5 mg DTT, 10 mg ATP, 18 mg phosphocreatine and 50 mg potassium acetate were dissolved in 1000 μ L 1M Tris. 45 μ L SP-RPA master mix (100 μ L modified reaction buffer, 100 μ L 9.2 mM dNTP's, 100 μ L purified enzyme mix, 200 μ L ddH₂O) was pipetted on to the reaction matrix. These were then placed in a zip-lock bag and flash frozen in liquid N₂. The bag was the pierced in several location with a wide bore needle, the prepared reaction matrixes were then freeze dried for 16 hrs. Initiation solutions were

prepared using 10 μL of each 10 μM forward and reverse primers, 8 μL 21 $\text{pg}/100\text{k copies } \mu\text{L}^{-1}$ reference MRSA gDNA, 10 μL MgOAc and 166 μL diluted crowding reagent solution. All reaction materials and constituents were equilibrated to 38 $^{\circ}\text{C}$ inside an aluminium heat block, in a 40 $^{\circ}\text{C}$ incubator for 15 mins. 50 μL Initiation solutions were added to the pre-loaded reaction matrices. Reactions were run for 40 mins; liquor removed by centrifugation at 1000RCF for 60 s and immediately purified using Monarch[®] 5 μg PCR & DNA clean-up columns and analysed by non-denaturing TBE-DNA 20 % polyacrylamide gels run at 3 $^{\circ}\text{C}$, 5 V cm^{-1} , in 1.25X TBE buffer for 2 hrs. (Fig. 6.15).

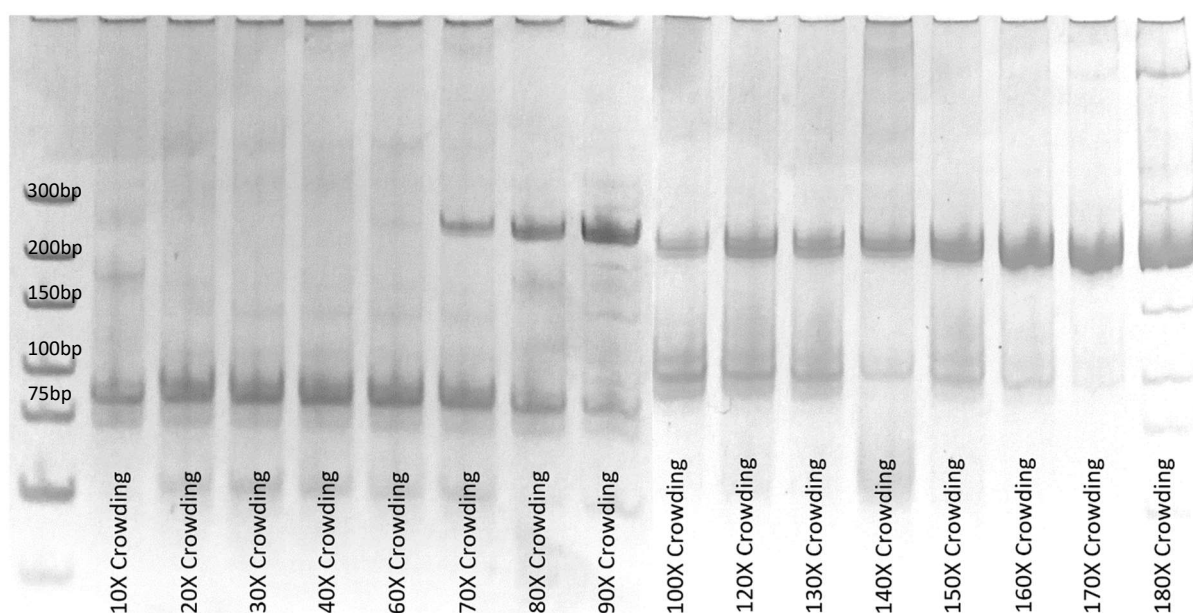


Figure 6.15. SP-RPA crowding reagent titrations clearly showing under-crowded though to moderately over-crowded beginning to cause spurious high molecular weight avalanche amplicons.

Crowding reagents' concentrations of between 150X-170X appeared to be most ideal for this reaction medium. It was not possible to eliminate all spurious amplification product, but it was significantly improved, especially given the high template concentrations used.

To further improve the amplification quality further titrations using varying amounts of formamide were performed using an identical procedure. SP-RPA master mix comprised of 100 μL modified reaction buffer, 100 μL 9.2 mM dNTP's, 100 μL purified enzyme mix, 200 μL 320X crowding solution. Initiation solutions were prepared using 10 μL of each 10 μM forward and reverse primers, 8 μL 0.21 $\text{pg}/1\text{k copies } \mu\text{L}^{-1}$ reference MRSA gDNA, 10 μL MgOAc and 166 μL formamide : ddH₂O solution. (Fig 6.16).

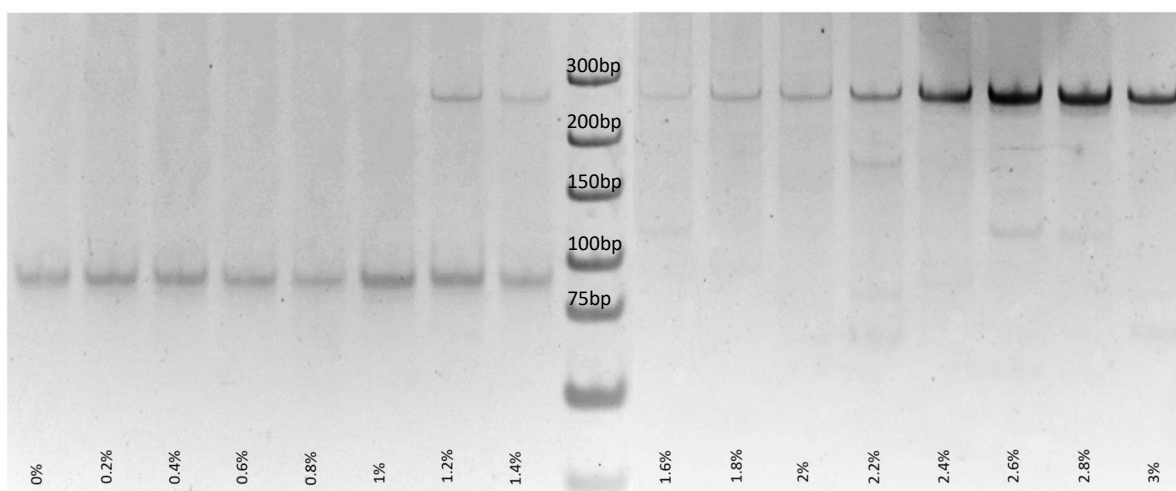


Figure 6.16. SP-RPA formamide titrations showing the increasing the limit of detection by reducing unwanted primer interactions with low template conditions. The yield tapers off as the highest formamide concentration begins to denature the amplification enzymes.

Formamide addition between 2.4-2.8 % to SP-RPA reaction mixture significantly improved both the amplification quality and efficiency. The low template concentration used clearly demonstrates that limit of detection before the addition of higher concentration of formamide was well above the 1k due unwanted primer interactions. In combination the reformulations of the RPA reaction mixtures significantly Improved the amplification stringency and efficiency.

6.6 Real Time SP-RPA Kinetic Evaluation:

To assess the effect of running the reactions within the solid matrix RT-SP-RPA was carried out using the custom made fluorometer and the addition formamidopyrimidine DNA glycosylase (*fpg*, NEB Labs) to the purified protein master mix at $570 \text{ ng } \mu\text{L}^{-1}$. Reaction pads were prepared by cutting 1 cm^2 from activated and blocked glass conjugate strips using a die and punch. RT-SP-RPA master mix comprised of $100 \text{ } \mu\text{L}$ modified reaction buffer, $100 \text{ } \mu\text{L}$ 9.2 mM dNTP's, $100 \text{ } \mu\text{L}$ RT-SP-enzyme mix and $200 \text{ } \mu\text{L}$ 320X crowding solution in $2.5\%_{\text{v/v}}$ formamide. $25 \text{ } \mu\text{L}$ ice cold RT-SP-RPA master mix was pipetted on to the reaction pads. Pads were flash frozen on liquid N_2 and freeze dried for 16 hrs. Initiation solutions were prepared using $10 \text{ } \mu\text{L}$ of each $10 \text{ } \mu\text{M}$ forward and reverse primers, $2 \text{ } \mu\text{L}$ $10 \text{ } \mu\text{M}$ internal probe, $4 \text{ } \mu\text{L}$ $210 \text{ pg}/1\text{M}$ copies μL^{-1} reference MRSA gDNA, $10 \text{ } \mu\text{L}$ MgOAc and $166 \text{ } \mu\text{L}$ ddH₂O. The reaction pad was placed into the sample holder and pre-heated to $37 \text{ } ^\circ\text{C}$. Reactions were started by adding $25 \text{ } \mu\text{L}$ the initiation solution via the sample access point. Reactions were run in triplicate. Incident light power was set at 50 %, with stabilised laser temperature of $35 \text{ } ^\circ\text{C}$ maintained, incident light irradiation time was 20 ms and a detector temperature of $-50 \text{ } ^\circ\text{C}$. Measurements were taken every 90 s over 2 hours giving a total exposure time of 1.6 s.

6.6.1 RT-SP-RPA Set mecA₇-C3:

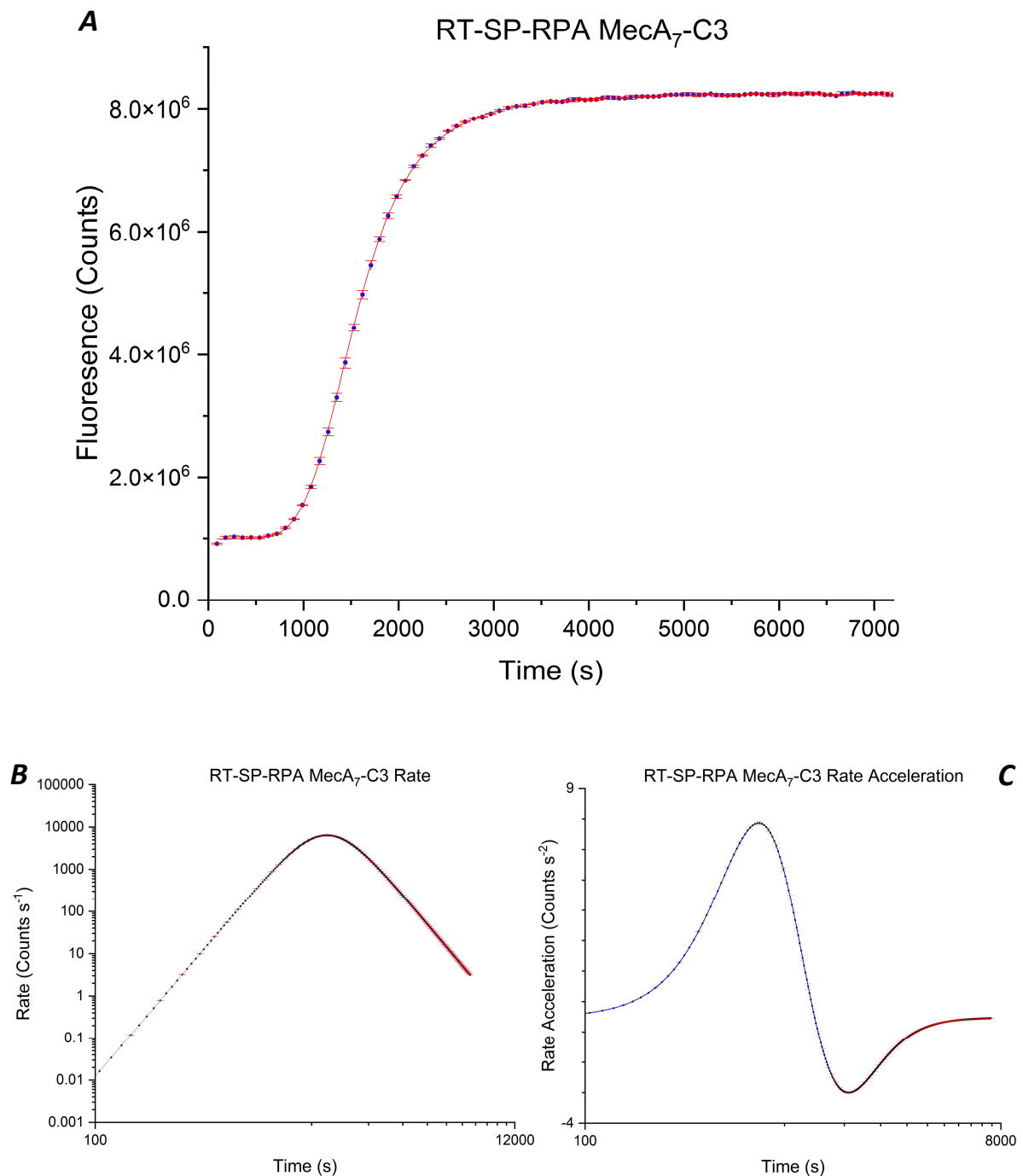


Figure 6.17. A) Processed RT-SP-RPA fluorescence curve of primer set mecA₇-C3 with 1M 43300 MRSA gDNA. $R^2 = 0.999$, $\Phi_i = 9.9 \times 10^5 \pm 0.82 \times 10^4$, $\varphi_m = 9.9 \times 10^6 \pm 0.8 \times 10^4$, $h = 47 \pm 0.03$, $f = 1.4 \pm 0.11 \times_o = 1411 \pm 37s$. C) First derivate rate curve for primer set mecA₇-C3. $v_{max} = 6392 \pm 0.06 \text{ counts s}^{-1}$, $k_m = 1410 \pm 5s$. D) Second derivate rate acceleration curve for primer set mecA₇-C3. $\vec{v}_{max} = 7.36 \pm 0.06 \text{ counts s}^{-2}$, $\vec{v}_{min} = -2.86 \pm 0.0115 \text{ counts s}^{-2}$, $t_i = 630 \pm 5s$, $t_d = 1605 \pm 5s$.

6.6.2 RT-SP-RPA Set mecA₈-C3:

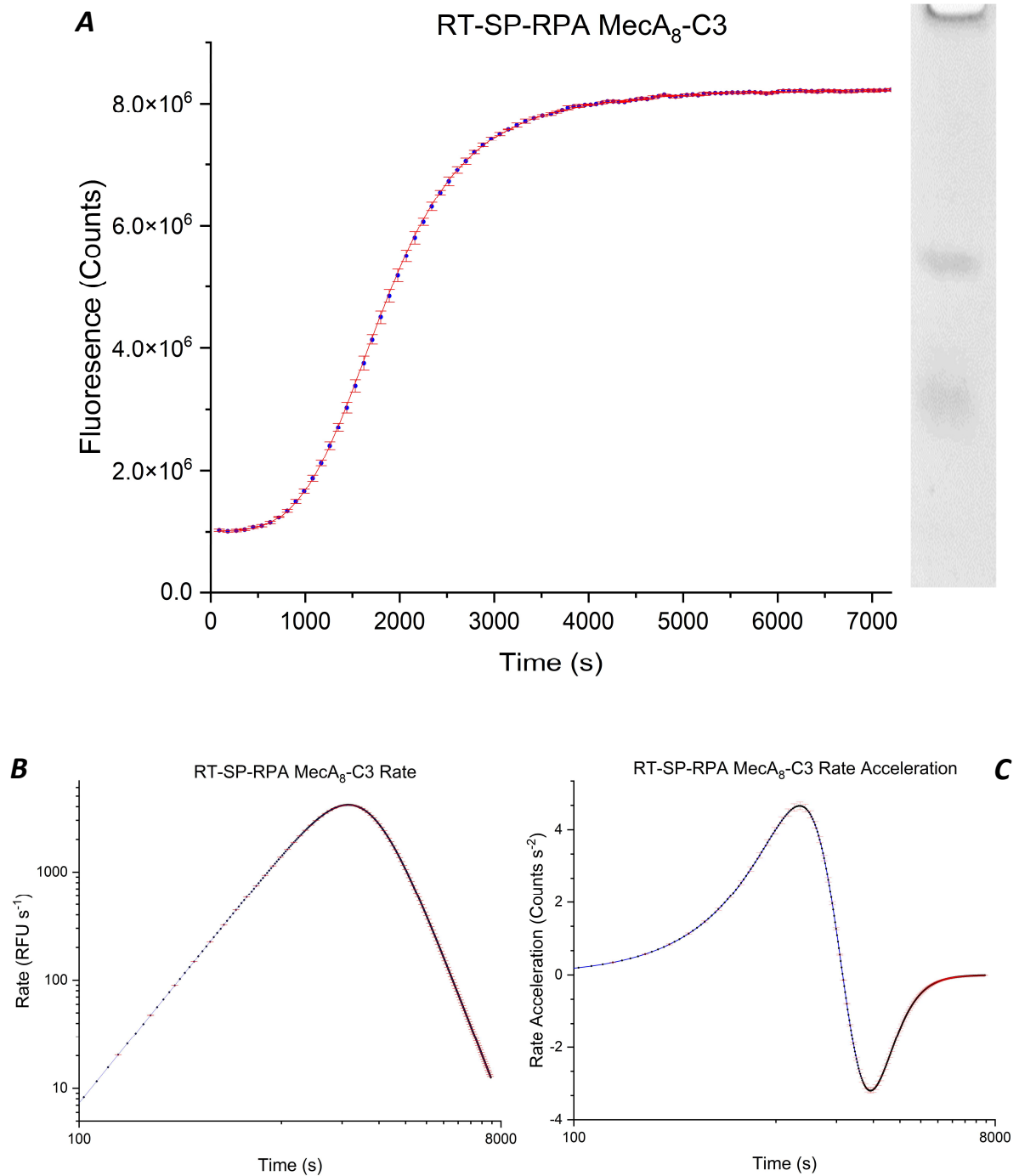


Figure 6.18. A) Processed RT-SP-RPA fluorescence curve of primer set mecA₈-C3 with 1M 43300 MRSA gDNA. $R^2 = 0.999$, $\Phi_i = 10.2 \times 10^6 \pm 7.6 \times 10^4$, $\varphi_m = 8.23 \times 10^6 \pm 2.8 \times 10^4$, $h = 4.3 \pm 0.04$, $f = 0.81 \pm 0.02$, $x_o = 1946 \pm 21$ s. C) First derivate rate curve for primer set mecA₈-C3. $v_{max} = 4162 \pm 0.004$ counts s⁻¹, $k_m = 1635 \pm 5$ s. D) Second derivate rate acceleration curve for primer set mecA₈-C3. $\vec{v}_{max} = 4.65 \pm 0.01$ counts s⁻², $\vec{v}_{min} = -3.2 \pm 0.06$ counts s⁻², $t_i = 1050 \pm 5$ s, $t_d = 2190 \pm 5$ s.

6.6.3 RT-SP-RPA Set $mecA_{10}$ -C3:

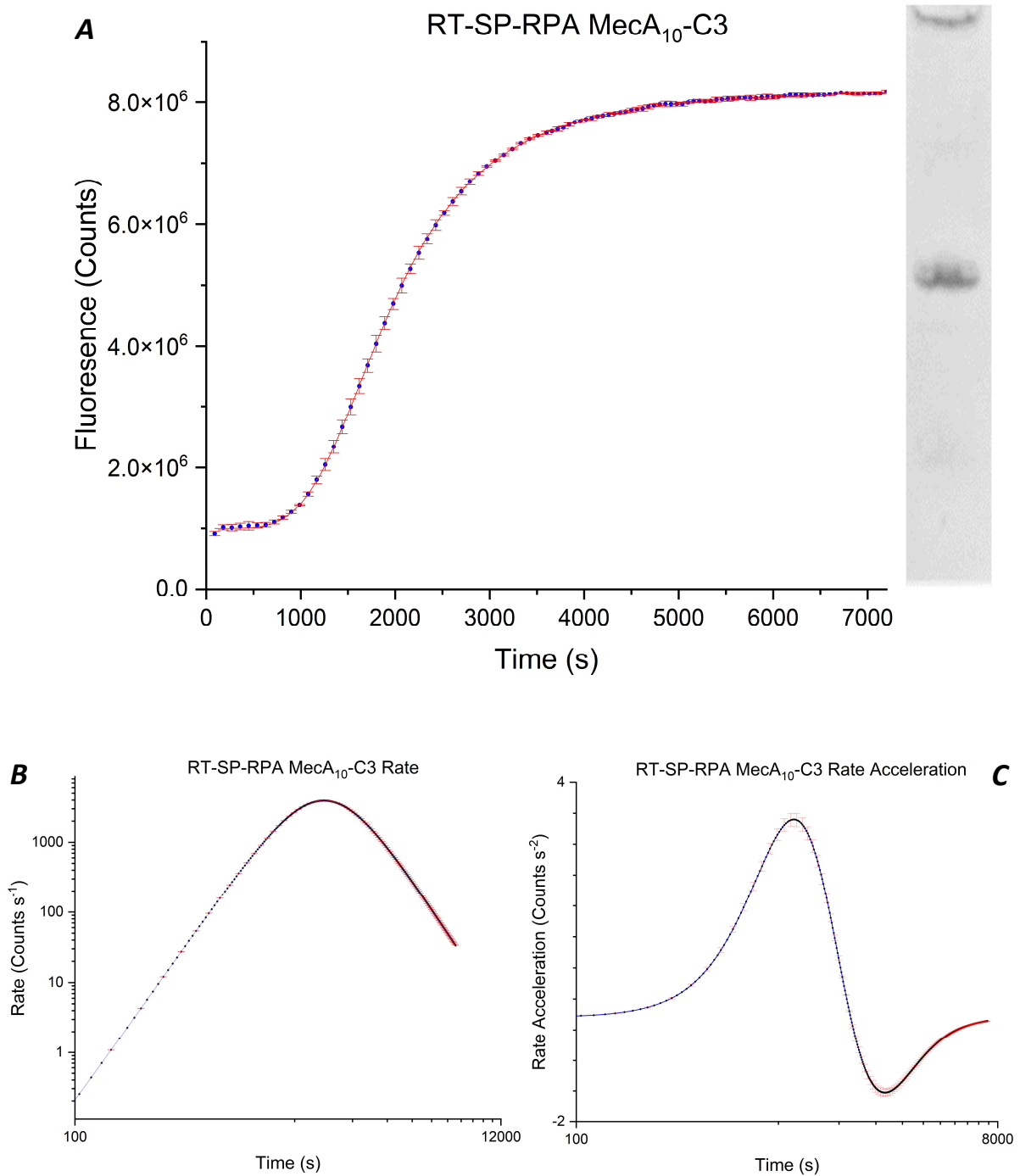


Figure 6.19. A) Processed RT-SP-RPA fluorescence curve of primer set $mecA_{10}$ -C3 with 1M 43300 MRSA gDNA. $R^2 = 0.999$, $\Phi_i = 9.99 \times 10^5 \pm 1.6 \times 10^3$, $\varphi_m = 8.2 \times 10^6 \pm 3.2 \times 10^4$, $h = 3.4 \pm 0.04$, $f = 1.48 \pm 0.08$, $x_o = 1680 \pm 38s$. B) First derivate rate curve for primer set $mecA_{10}$ -C3. $v_{max} = 3931 \pm 0.05$ counts s^{-1} , $k_m = 1635 \pm 5s$. C) Second derivate rate acceleration curve for primer set $mecA_{10}$ -C3. $\vec{v}_{max} = 3.06 \pm 0.12$ counts s^{-2} , $\vec{v}_{min} = -1.2 \pm 0.15$ counts s^{-2} , $t_i = 960 \pm 5s$, $t_d = 2475 \pm 5s$.

6.6.4 RT-SP-RPA Set $mecA_{12}$ -C3:

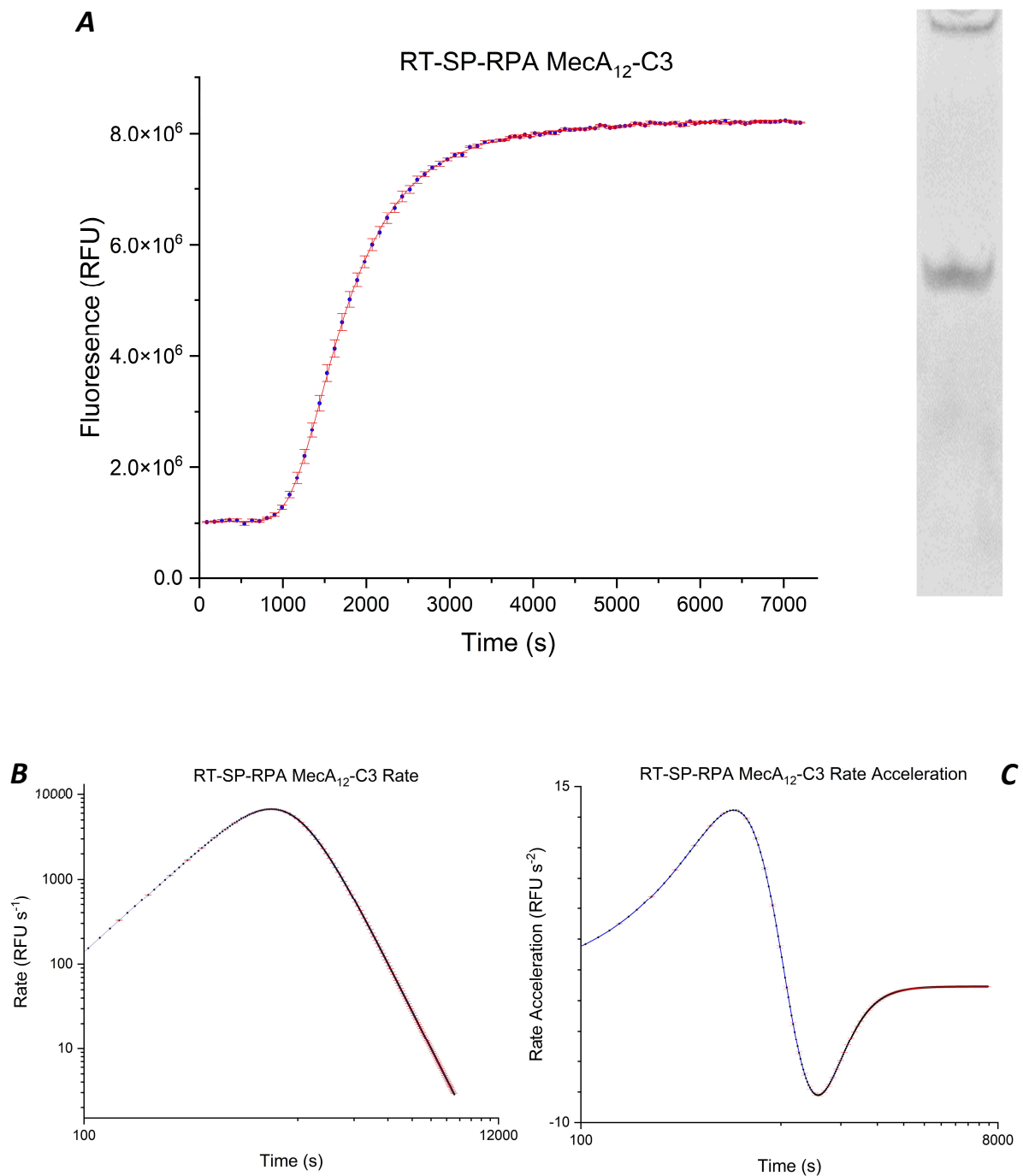


Figure 6.20. A) Processed RT-SP-RPA fluorescence curve of primer set $mecA_{12}$ -C3 with 1M 43300 MRSA gDNA. $R^2 = 0.999$, $\Phi_i = 8.2 \times 10^5 \pm 0.23 \times 10^5$, $\varphi_m = 10.5 \times 10^6 \pm 0.155 \times 10^5$, $h = 3.86 \pm 0.11$, $f = 1.10 \pm 0.04$, $x_0 = 1076 \pm 23.9s$. C) First derivate rate curve for primer set $mecA_7$ -C3. $v_{max} = 6698 \pm 0.09$ counts s⁻¹, $k_m = 870 \pm 5s$. D) Second derivate rate acceleration curve for primer set $mecA_7$ -C3. $\vec{v}_{max} = 12.9 \pm 6.35 \times 10^{-2}$ counts s⁻², $\vec{v}_{min} = -7.99 \pm 9.45 \times 10^{-2}$ counts s⁻², $t_i = 495 \pm 5s$, $t_d = 1215 \pm 5s$.

6.6.5 RT-SP-RPA Set mecA₇-C12:

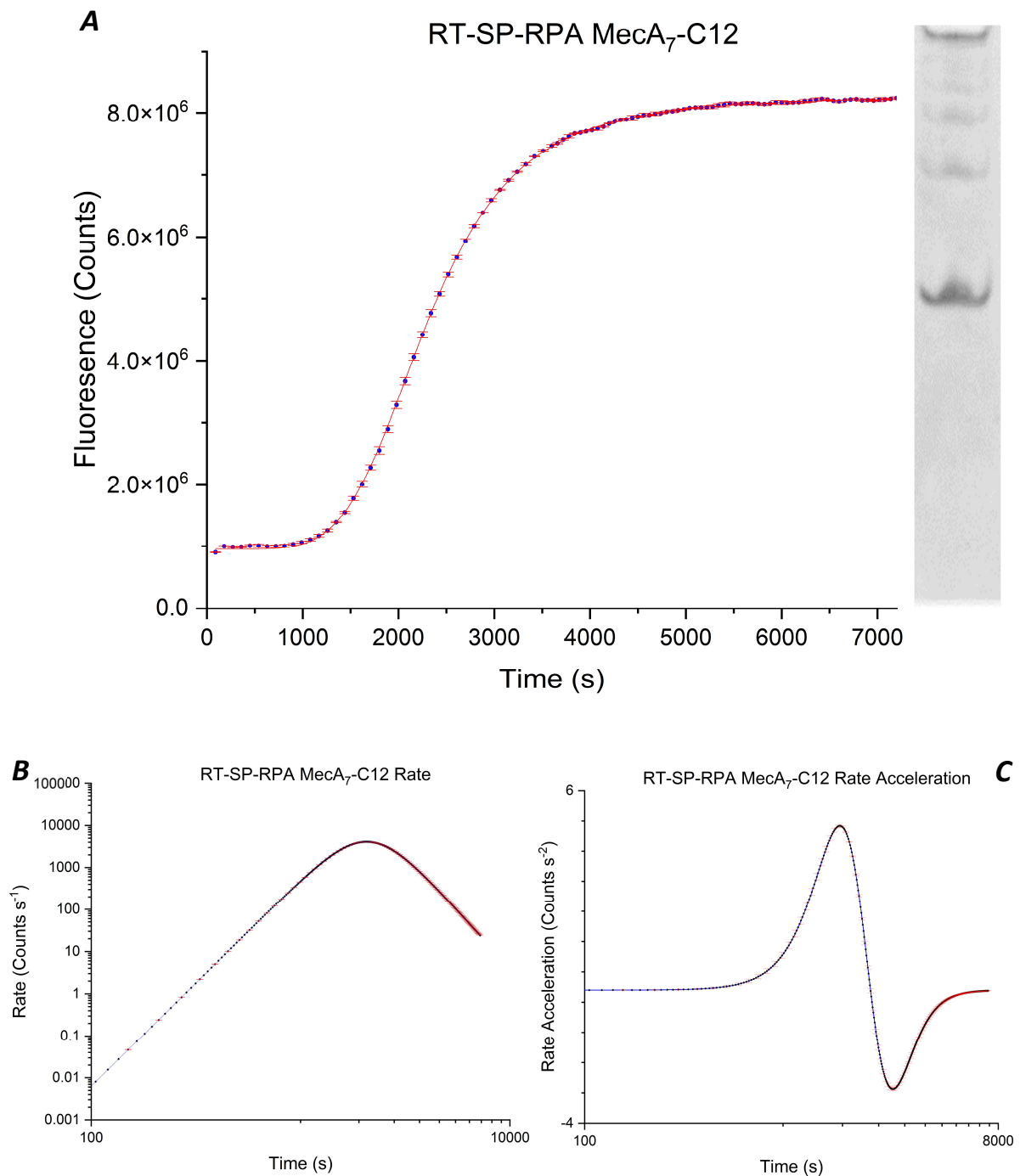


Figure 6.21. A) Processed RT-SP-RPA fluorescence curve of primer set mecA₇-C12 with 1M 43300 MRSA gDNA. $R^2 = 0.999$, $\Phi_i = 9.5 \times 10^5 \pm 0.81 \times 10^4$, $\varphi_m = 8.25 \times 10^6 \pm 0.8 \times 10^4$, $h = 4.51 \pm 0.04$, $f = 1.31 \pm 0.12$, $x_o = 2122 \pm 24s$. B) First derivate rate curve for primer set mecA₇-C12. $v_{max} = 4114 \pm 1.2$ counts s⁻¹, $k_m = 2070 \pm 5s$. C) Second derivate rate acceleration curve for primer set mecA₇-C12. $\vec{v}_{max} = 4.94 \pm 0.03$ counts s⁻², $\vec{v}_{min} = -2.98 \pm 0.0115$ counts s⁻², $t_i = 1500 \pm 5s$, $t_d = 2625 \pm 5s$.

6.6.6 RT-SP-RPA Set mecA₈-C12:

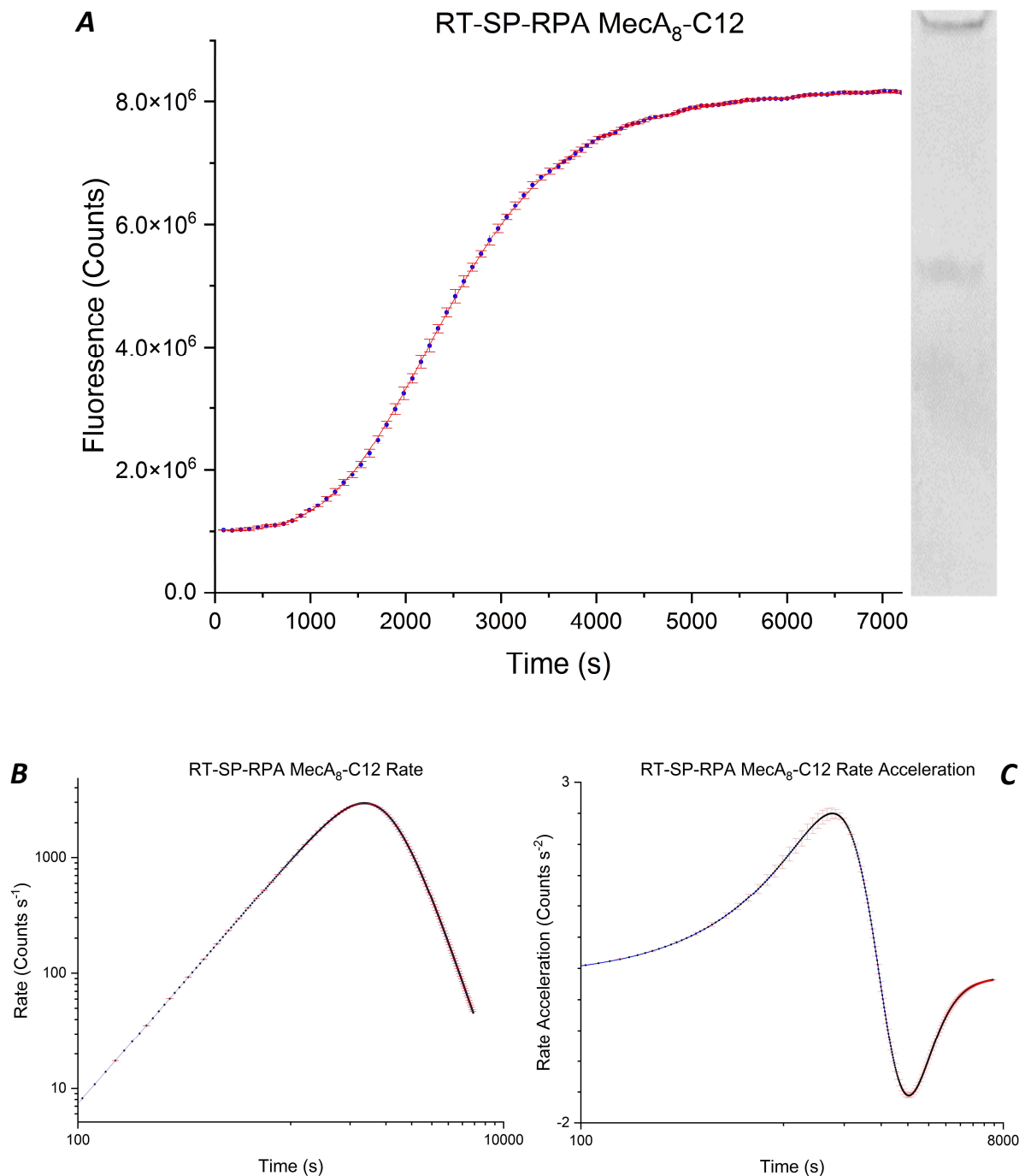


Figure 6.22. A) Processed RT-SP-RPA fluorescence curve of primer set mecA₈-C12 with 1M 43300 MRSA gDNA. $R^2 = 0.999$, $\Phi_i = 1.02 \times 10^6 \pm 0.76 \times 10^4$, $\varphi_m = 8.23 \times 10^6 \pm 0.28 \times 10^4$, $h = 4.35 \pm 0.06$, $f = 0.72 \pm 0.02$, $x_0 = 2745 \pm 24$ s. B) First derivate rate curve for primer set mecA₈-C12. $v_{max} = 2942 \pm 1.2$ counts s⁻¹, $k_m = 2220 \pm 5$ s. C) Second derivate rate acceleration curve for primer set mecA₈-C12. $\vec{v}_{max} = 2.24 \pm 0.06$ counts s⁻², $\vec{v}_{min} = -1.62 \pm 0.032$ counts s⁻², $t_i = 1365 \pm 5$ s, $t_d = 3000 \pm 5$ s.

6.6.7 RT-SP-RPA Set mecA₁₀-C12:

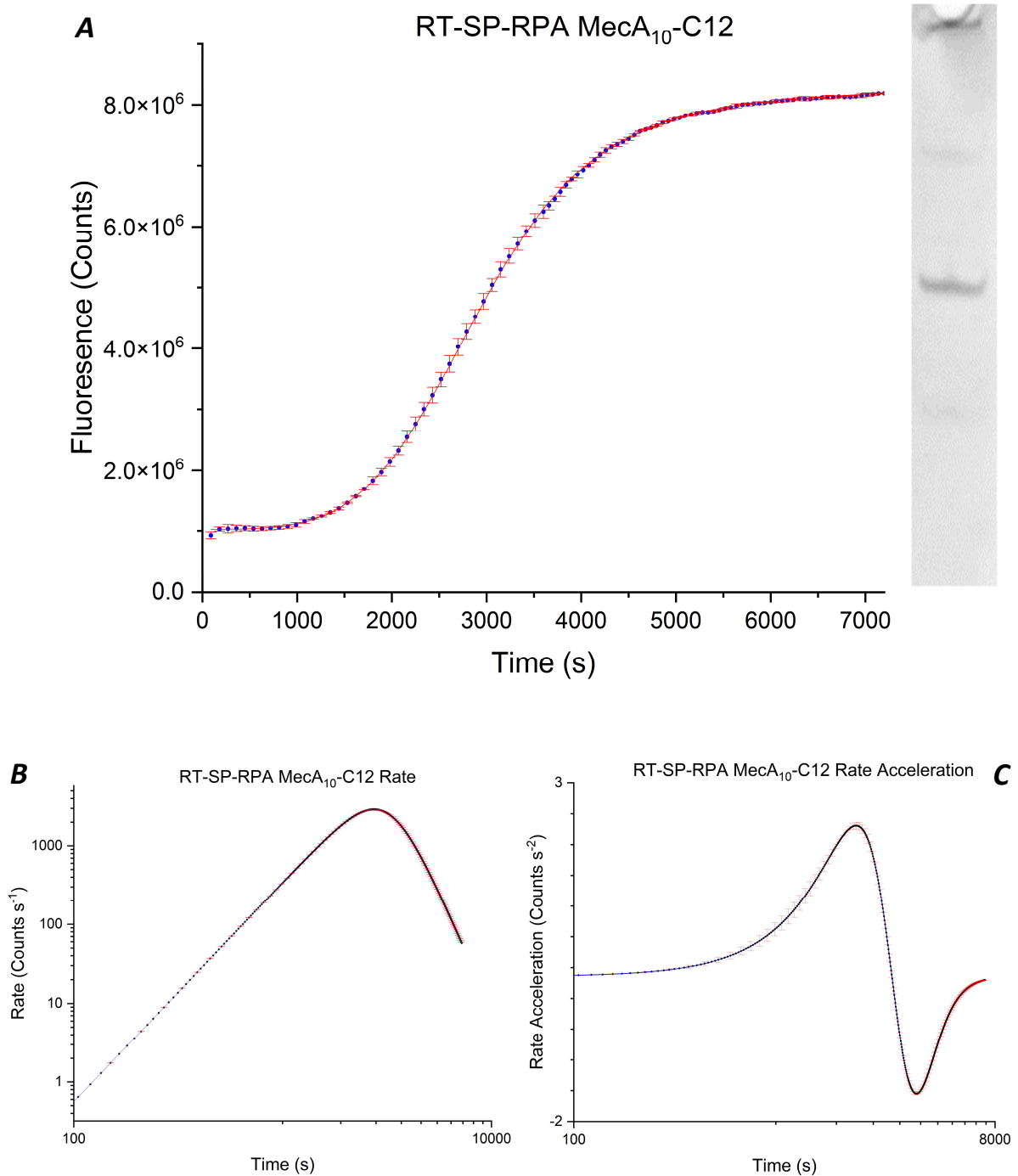


Figure 6.23. A) Processed RT-SP-RPA fluorescence curve of primer set mecA₁₀-C12 with 1M 43300 MRSA gDNA. $R^2 = 0.999$, $\Phi_i = 1.02 \times 10^6 \pm 1.59 \times 10^4$, $\varphi_m = 8.26 \times 10^6 \pm 0.03 \times 10^4$, $h = 5.11 \pm 0.042$, $f = 0.74 \pm 0.11$, $x_0 = 3193 \pm 36$ s. B) First derivate rate curve for primer set mecA₁₀-C12. $v_{max} = 2909 \pm 0.02$ counts s⁻¹, $k_m = 2730 \pm 5$ s. C) Second derivate rate acceleration curve for primer set mecA₁₀-C12. $\vec{v}_{max} = 2.08 \pm 0.046$ counts s⁻², $\vec{v}_{min} = -1.64 \pm 0.014$ counts s⁻², $t_i = 1890 \pm 5$ s, $t_d = 3540 \pm 5$ s.

6.6.8 RT-SP-RPA Set *mecA*₁₂-C12:

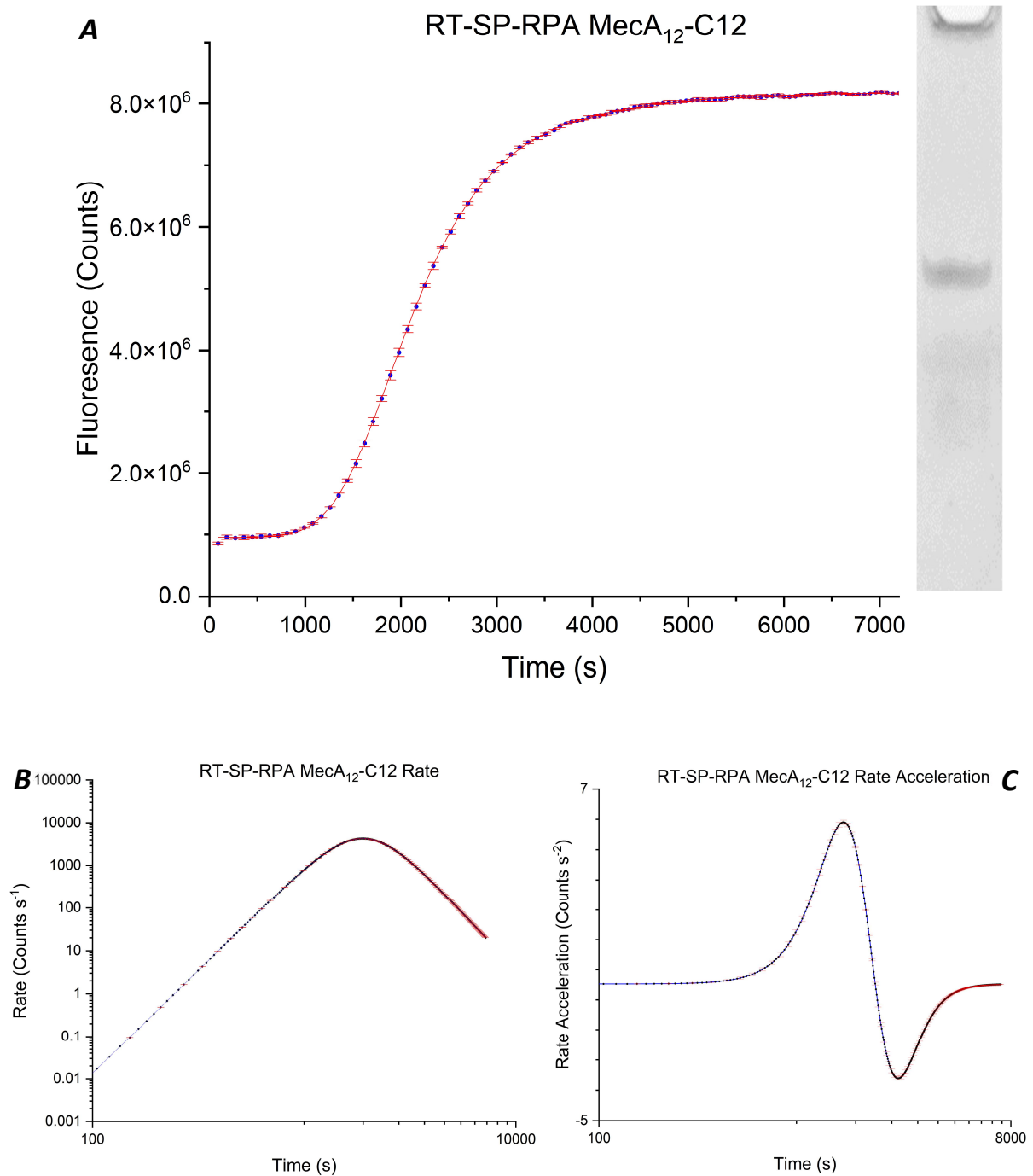


Figure 6.24. A) Processed RT-SP-RPA fluorescence curve of primer set *mecA*₁₂-C12 with 1M 43300 *MRSA gDNA*. $R^2 = 0.999$, $\Phi_i = 9.5 \times 10^5 \pm 8.59 \times 10^3$, $\varphi_m = 8.19 \times 10^6 \pm 8.1 \times 10^3$, $h = 4.31 \pm 0.031$, $f = 1.34 \pm 0.13$, $x_0 = 1933 \pm 38$ s. B) First derivate rate curve for primer set *mecA*₁₂-C12. $v_{\max} = 4289 \pm 0.02$ counts s⁻¹, $k_m = 1890 \pm 5$ s. C) Second derivate rate acceleration curve for primer set *mecA*₁₂-C12. $\vec{v}_{\max} = 5.54 \pm 0.075$ counts s⁻², $\vec{v}_{\min} = -3.24 \pm 0.064$ counts s⁻², $t_i = 1350 \pm 5$ s, $t_d = 2415 \pm 5$ s.

6.6.9 Discussion and concluding remarks:

The presented results clearly illustrate the impact of customising reaction mixtures for a given set of primers and conditions. Even when conducted in solid-phase format, each of the modified primer sets exhibited outstanding performance, yielding the anticipated kinetic curves and almost pristine endpoint products. (Fig. 6.17-6.24). However, it's important to note that, while the performance significantly improved compared to the use of modified primers in standard reaction mixtures, there was still some evidence of sporadic material production when employing the C12 modified primers. Evaluation of the combined kinetic curves reveals a significant variation in performance among the different primer sequences under these conditions. (Fig. 6.25). In contrast to the liquid-phase amplification, where the efficiencies remained relatively consistent across primer sets. (Table. 6.1).

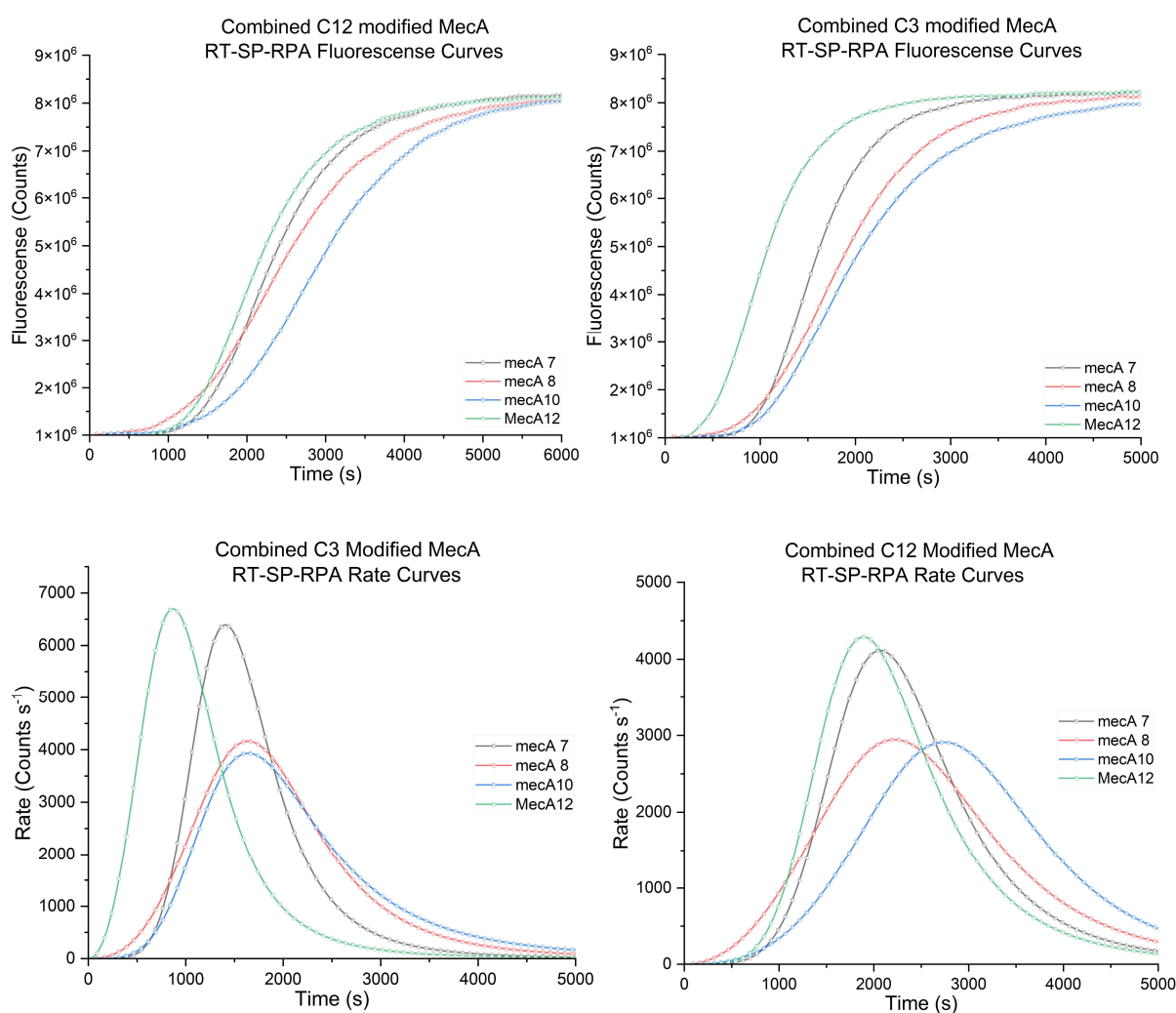


Figure 6.25. cont. Combined RT-SP-RPA C3 and C12 fits for comparison of primer sets kinetic profiles.

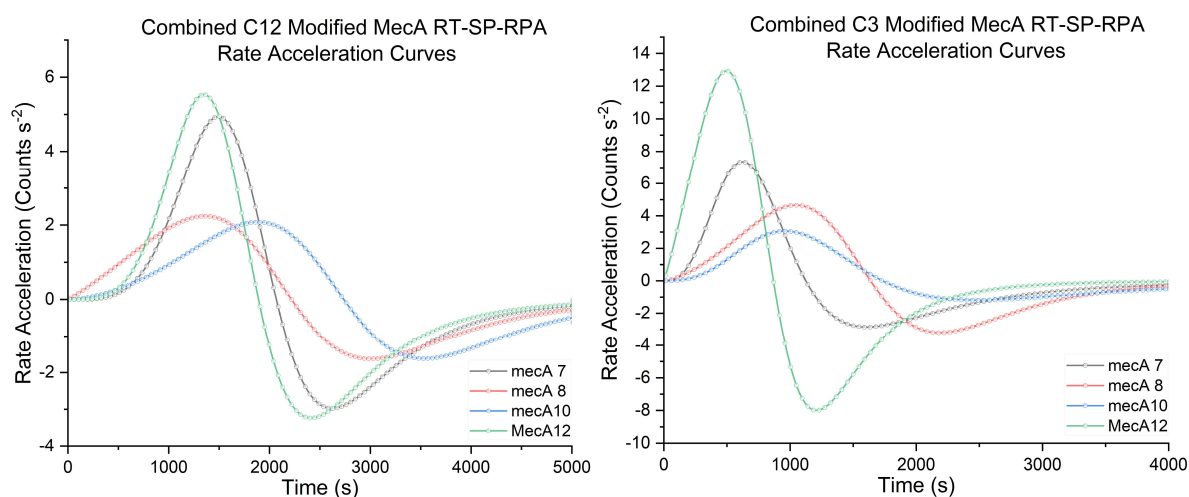


Figure 6.25. cont. Combined RT-SP-RPA C3 and C12 fits for comparison of primer sets kinetic profiles.

Table 6.1. Key reaction constants from fully functioning primer sets.

Primer Name	Phase	Modification type	Initiation Time (s)	Time to Max Sudo-Rate (s)	Time to Depletion (s)
MecA ₁₂	Liquid	C3	620	785	945
		C12	535	720	900
MecA ₁₀	Solid	C3	595	870	1215
		C12	1350	1890	2415
MecA ₁₀	Liquid	C3	540	725	910
		C12	445	620	790
MecA ₈	Solid	C3	960	1635	2475
		C12	1365	2220	3000
MecA ₈	Liquid	C3	715	995	1185
		C12	775	995	1205
MecA ₇	Solid	C3	1050	1635	2190
		C12	1500	2070	2625
MecA ₇	Liquid	C3	320	575	805
		C12	510	750	975
Average performance loss			48.3%	42.6%	40.5%

The data presented above reveals several discernible patterns. Firstly, there is a clear and, on average, significant drop in performance when transitioning from liquid phase to solid phase, with an average reduction in amplification efficiency of 56.2 %. However, it's worth noting that MecA₁₂-C3 stands as an exceptional outlier in this overall trend. Although there was some reduction in performance, it was relatively marginal at 16 %, and its initiation performance remained on par with the liquid-phase reaction. Unlike when the modified primers were assessed in liquid phase, from these

experiments there a large performance discrepancy between the C3 and C12 modified primer sets under solid phase optimised conditions. Secondly unlike in the liquid phase reaction with the standard reaction conditions there was a significant difference in performance between C3 and C12 modifications used. (Fig. 6.26).

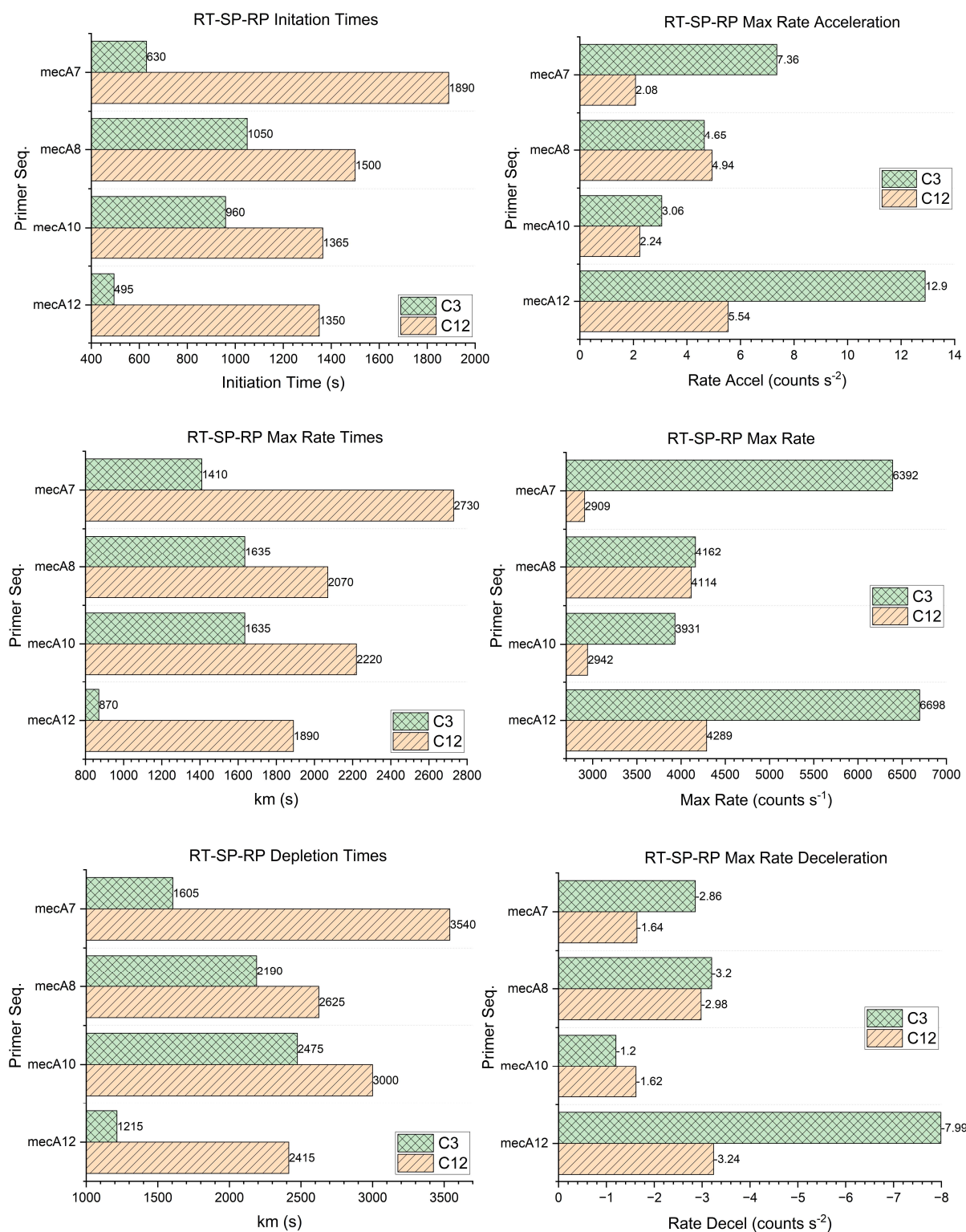


Figure 6.26. Cont. Combined RT-SP-RPA C3 and C12 measured kinetic profiles parameters.

On average the amplification efficiencies were reduced by 66 % when comparing the C12 modified primer sequence to the C3 modified primer sequence. (Fig. 6.27).

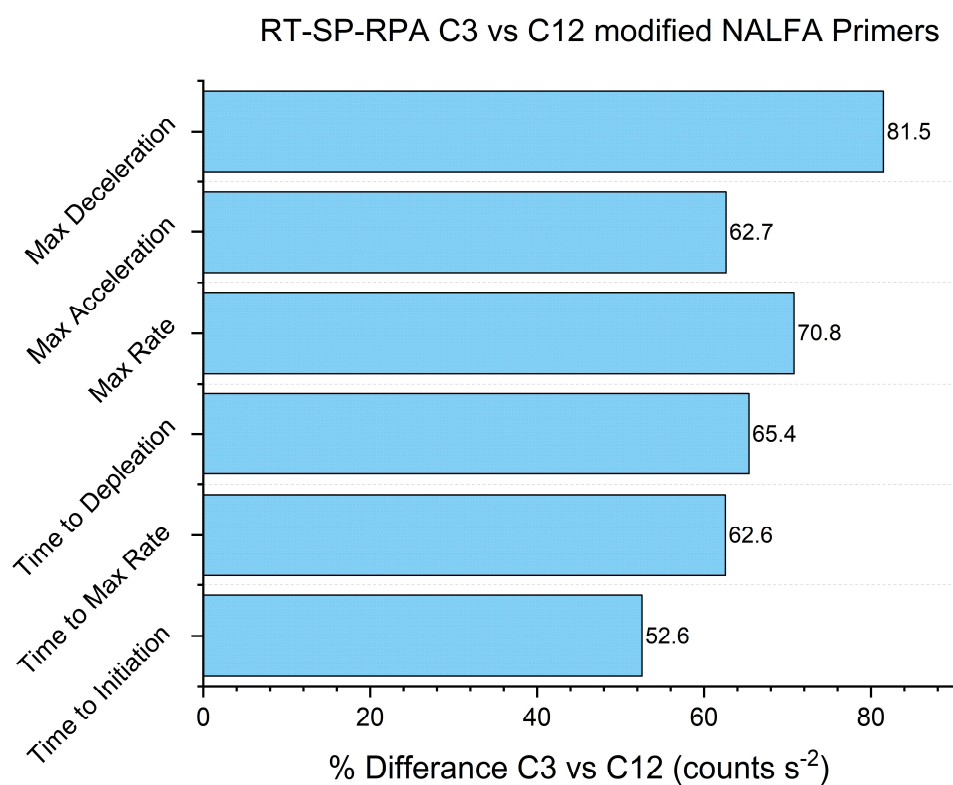


Figure 6.27. SP-RPA Kinetic performance delta between C3 and C12 modified primers.

This result was quite unexpected, but it can be partially explained by the methodology used to optimize the solid-phase reaction conditions. During the optimisation process, the best-performing primer from the liquid-phase screening was selected, as it offered the highest likelihood of achieving a successful amplification reaction in the solid phase. This decision was warranted, considering the initial poor performance of the primers in the solid phase matrix with standard reaction mixtures and conditions. However, this choice might indicate that the SP-RT-RPA screening is highly tailored to that specific primer and modification, and given the exceptional performance observed with that specific primer it may be the case. Therefore, it might be advantageous to revisit the optimization procedures and individually fine-tune the conditions for each primer set, striving to find a middle ground that works more consistently with the entire range of available primers. Nevertheless, for detecting the *mecA* gene from MRSA isolates primer set MecA₁₂-C3 provides the best choice of primer to take forward onto the LFA development.

Chapter 7

Gyromagnetically Enhanced SP-RPA.

“You spin me right round baby, right round!”

7.1 Introduction:

Chapter seven will examine the synthesis and magnetic excitation of iron oxide nanoparticles as a kinetic enhancement to SP-RPA. As seen in *chapter 6* it was possible to get RPA functioning with our available primers for MecA detection within a solid matrix. However, it was at the cost of meaningful reduction in the amplification efficiency versus liquid reactions. Thus, increasing the total time to detection when using the proposed SP-RPA NALF assay. It was hypothesised that the main cause for the reduction in amplification efficiency was due to the constrained, fluid dynamic conditions of the system, thus reducing the reagent diffusion rate within the reaction. This has the effect of significantly delaying the initial amplification cycles from progressing. This is especially true for very low copy count amplifications. In liquid phase when using low copy counts, it is often necessary to homogenize the reaction mixture after a few minutes of incubation. This is to avoid "hot spotting," where the initial template is amplified disproportionately based on template distribution. As the template may only be present as a single molecule and therefore the solution cannot be initially homogeneous. The poor flow characteristics of the high viscosity crowding reagent, which is needed to promote strand displacement between the recombinase enzymes, impedes produced amplicons from reaching areas of the reaction liquor where no initial template was available. This is why adding overcrowding reactions can in effect completely inhibit low copy count amplifications, while promoting excellent rates of amplification with higher template amounts. Therefore, to overcome this problem, "mixing" of the solution within the solid matrix is required. It was proposed that magnetic nanoparticles excited using an external alternating magnetic field could achieve this. Excitation within a rotational resonance frequency range (1-50 kHz) could locally homogenate reactions via the large shearing forces induced by the particle rotation and the surrounding crowding reagents. Furthermore, it may also be possible to promote mass diffusion using low frequency fields to macro-migrate particles through solution. Such a system could be cheap and efficient and could be on an in-ear headphone driver with no core, driven by a Blob-Onboard class D amplifier and tone generator, ubiquitous with cheap children's toys. Such a system would be relatively simple and therefore inexpensive when compared other LFA's on the market, such as Clearblue's digital readout system for example.

7.2 - Fe₃O₄ Nanoflower Synthesis:

7.2.1 - Methodology:

Extra dry degassed NMDEA was prepared in a round bottom flask using 1/8 flask volume of super active 4A super active molecular sieves and 2/3 flask volume of fresh NMDEA. This was stirred under ultra-high vacuum for 1hr, exchanged with argon 5 times followed by vigorous stirring 1hr on

ultra-high vacuum. The mixture was heated to 85 °C using an oil bath and stirred with normal vacuum applied overnight and left for 6 hrs before use to allow molecular sieves to settle.

Fe₃O₄ nanoflowers were synthesised using an adapted method described by Caruntu et al¹⁵³ and further by Hemery et al¹⁵⁴ via NMDEA mediated hydrolysis. 200 mg (0.1 mmol) FeCl₂·4H₂O and 540 mg FeCl₃·6H₂O (0.2 mmol) were weighed into an oven dried 100 ml Schlenk flask and protected under argon. 40 g extra dry N-methyl diethanolamine was transferred onto the metal chlorides using Schleck technique and stirred with gentle convection heating until dissolved yielding a light brown solution. In a separate round bottom flask 320 mg (1.6 mmol) ultra-pure dry NaOH was protected under argon and dissolved in 40 g extra dry N-methyl diethanolamine with 100 µL HPLC water under argon using Schleck technique. The metal chloride solution was transferred into the refluxing flask of the reaction vessel and the NaOH solution transferred to the separator funnel using a double-sided needle. (Fig. 7.1).

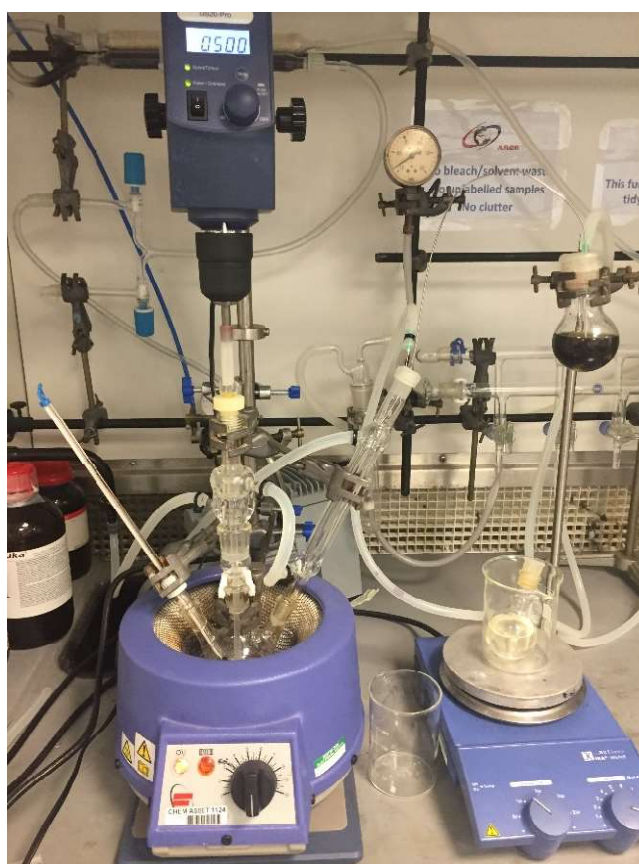


Figure 7.1. Metal chloride solution being transferred into the high temperature mechanically stirred argon protected reflux set up.

Then heated to 150 °C at 6.7 °C per minute with mechanical stirring at 350 RPM. The NaOH solution was added dropwise while the temperature was increase to 225 °C. The mixture turned dark emerald green and was refluxed for 14 hrs then cooled to RT period yielding a black solution.

Once cooled the reaction liquor was diluted 1:1 in MeOH and probe sonicated at 0.1 W ml^{-1} for 10 mins then centrifuged at 1 kRCF for 10 mins and the pellet discarded. (Fig. 7.2).

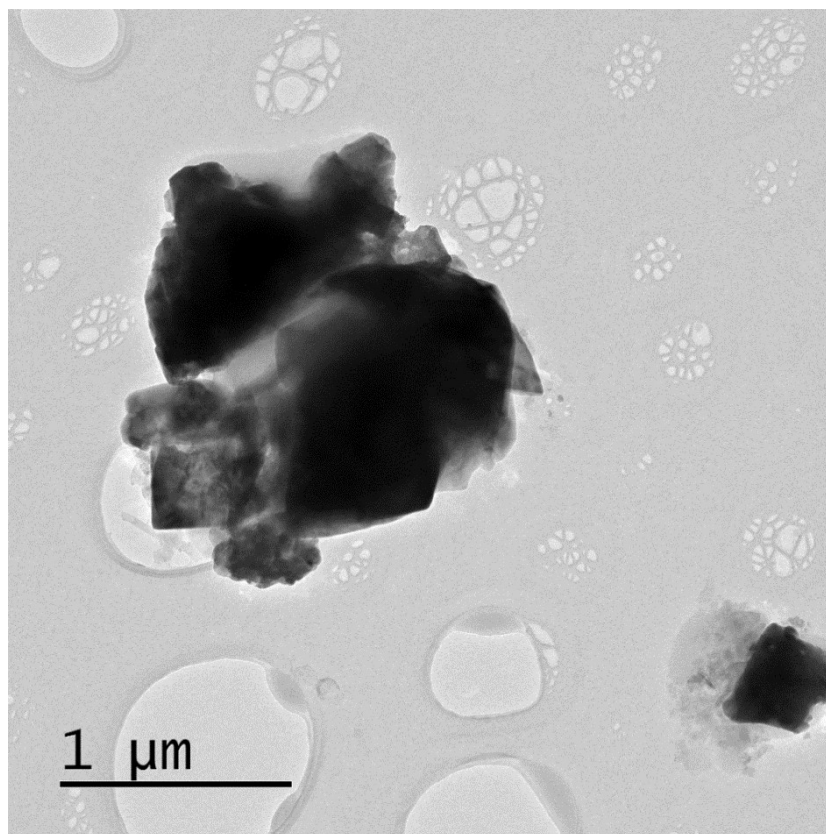


Figure 7.2. TEM of discarded aggregated Fe_3O_4 crystals separated by initial centrifugation at 1k RCF.

The liquor was then centrifuged at 37 kRCF for 1hr and the pellet was washed 3x with MeOH and centrifuging at 50 kRCF at 3°C . The collected pellet was redispersed in 40ml EtOAc then vigorously shook for 16 hrs at 40°C . The solution was then sonicated at 0.1 W ml^{-1} for 15mins, magnetic nanoparticles were then collected by magnetic separation and wash 3x with hexane. Solids were then redispersed in 20ml ddH₂O by probe sonication at 0.2 W ml^{-1} at 12°C for 30 mins. 35 ml 20 % HNO₃ was added into the cavitation zone under probe rapidly. The solution was sonicated for a further 90 mins at 0.2 W ml^{-1} at 12°C . Magnetic nanoparticles were then collected by magnetic separation and wash 3x EtOH and 3x with hexane. Solids were then redispersed in 49ml ddH₂O by probe sonication at 0.2 W ml^{-1} at 12°C for 30 mins. 1ml conc. NH₃ solution was then added into the cavitation zone under probe rapidly at 0.73 W ml^{-1} . The solution was sonicated for 1 hr at 70°C yielding an ultra-stable black colloidal suspension of NMDEA coated Fe_3O_4 nano-particles at 1.64 mg ml^{-1} . (Fig. 7.3).

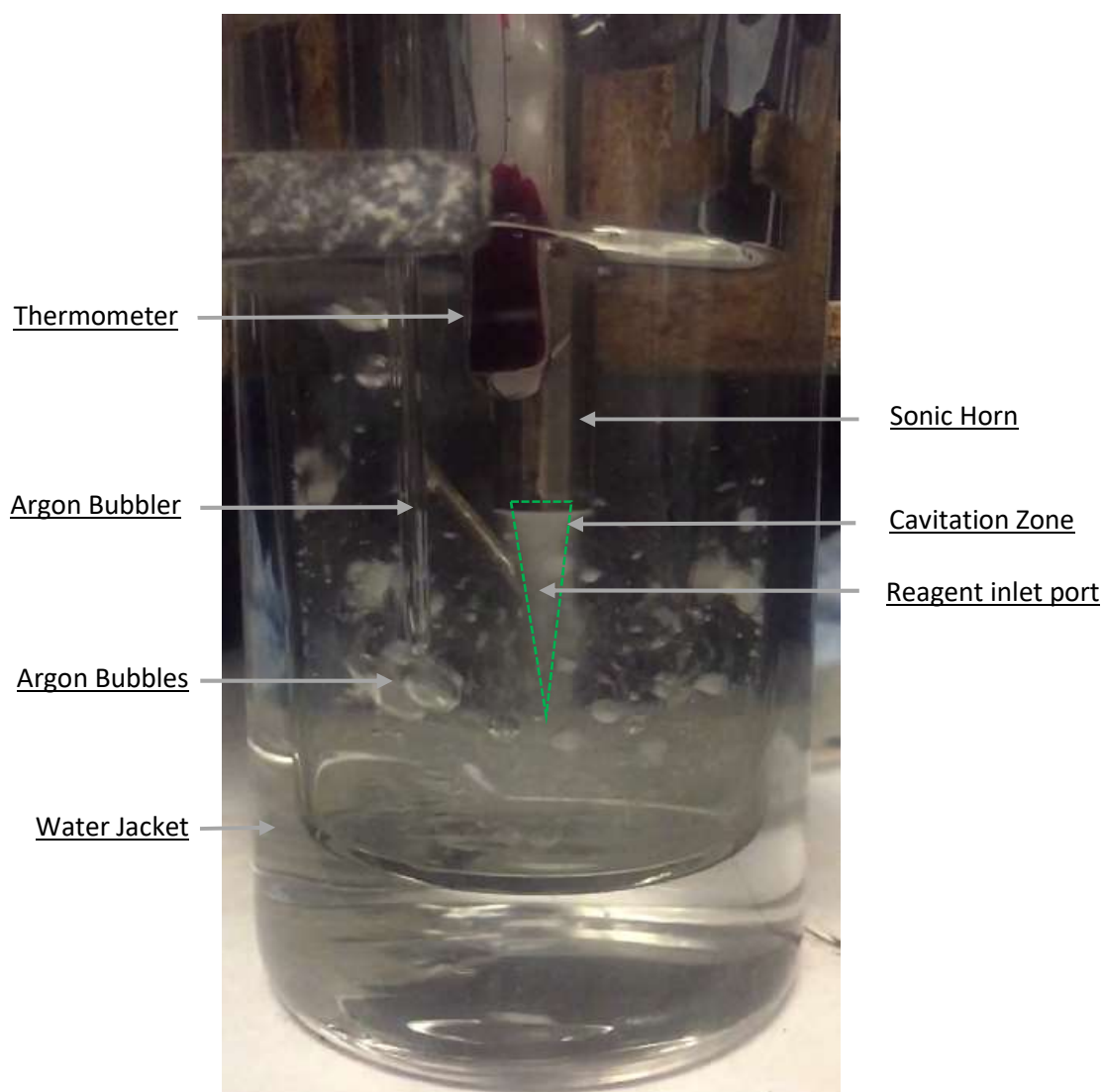


Figure 7.3. Temperature controlled sonochemical reactor showing the argon bubbler, injection needle, sonic horn, and the cavitation zone.

The colloidal solution was then diluted to 1mg ml^{-1} and further purified by gradient centrifugation by adding 1.5 g PVP-10 to the solution and sonicating at 0.1 W ml^{-1} . The solution was then centrifuged at 100 RCF 4 hr, 500 RCF 2 hr, 1 kRCF 20 mins, 5 kRCF 20 mins, 10 kRCF 20 mins, 20 kRCF 5 mins, 40 kRCF 5mins, 50 kRCF 1min. Between each centrifugation any sediment was removed gently using a needle without disturbing the forming density gradient. The purified nanoparticle solution was then diluted with 50ml EtOH and centrifuged at 100 kRCF for 10mins at $50\text{ }^{\circ}\text{C}$, washed 3 times with EtOH and redistributed in 49 ml ddH₂O by probe sonication at 0.2W ml^{-1} at $12\text{ }^{\circ}\text{C}$ for 30 mins. 1 ml conc. NH₃ solution was then added into the cavitation zone under probe rapidly at 0.73W ml^{-1} . The solution was sonicated for 1 hr at 70°C yielding a yellow colloidal solution, *figure 7.4*; with a concentration of 0.78mg ml^{-1} .

7.2.2 – Results and discussion:

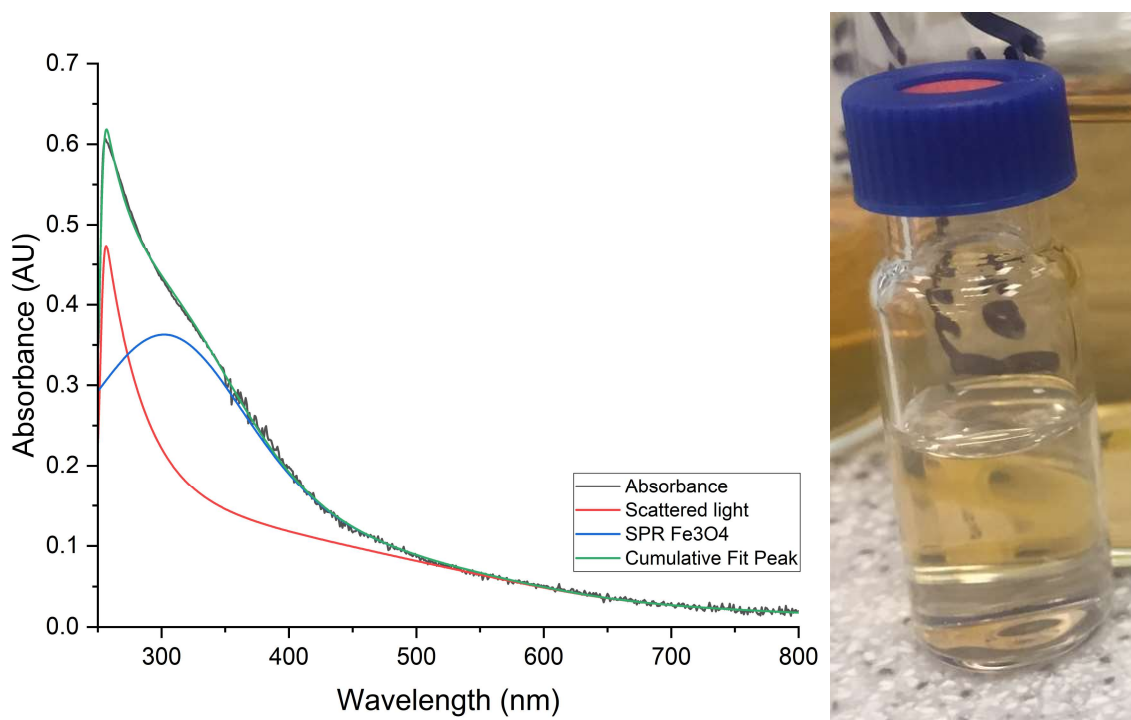


Figure 7.4. Deconvoluted UV-Vis spectra of the colloidal Fe_3O_4 (right) SPR peak = 317.7nm

Particle crystal domain size was estimated using the Scherrer equation via powder XRD on a Si (111) single crystal. This the powder diffractogram was achieved by dispersing concentrated colloidal solution on to the surface of a Si (111) single crystal until a powder layer was formed. (Fig. 7.5, Table 7.1). Particles were analysed by High resolution TEM. (Fig.7.6 - 7.8).

Table 7.1. Fe_3O_4 XRD peak and Sherrer crystal size estimation data.

Crystal plane	d-Spacing (Å)	Measured Peak Pos (2Theta)	Crystalline size
3 1 1	0.263	35.467	16.1 nm
4 4 0	0.148	62.624	30.6 nm
5 1 1	0.161	57.014	22.6 nm
4 0 0	0.209	47.295	18.9 nm
2 2 0	0.296	30.119	16.4 nm
5 1 1	0.161	53.48	26.1 nm
Average			21.7±2.2 nm

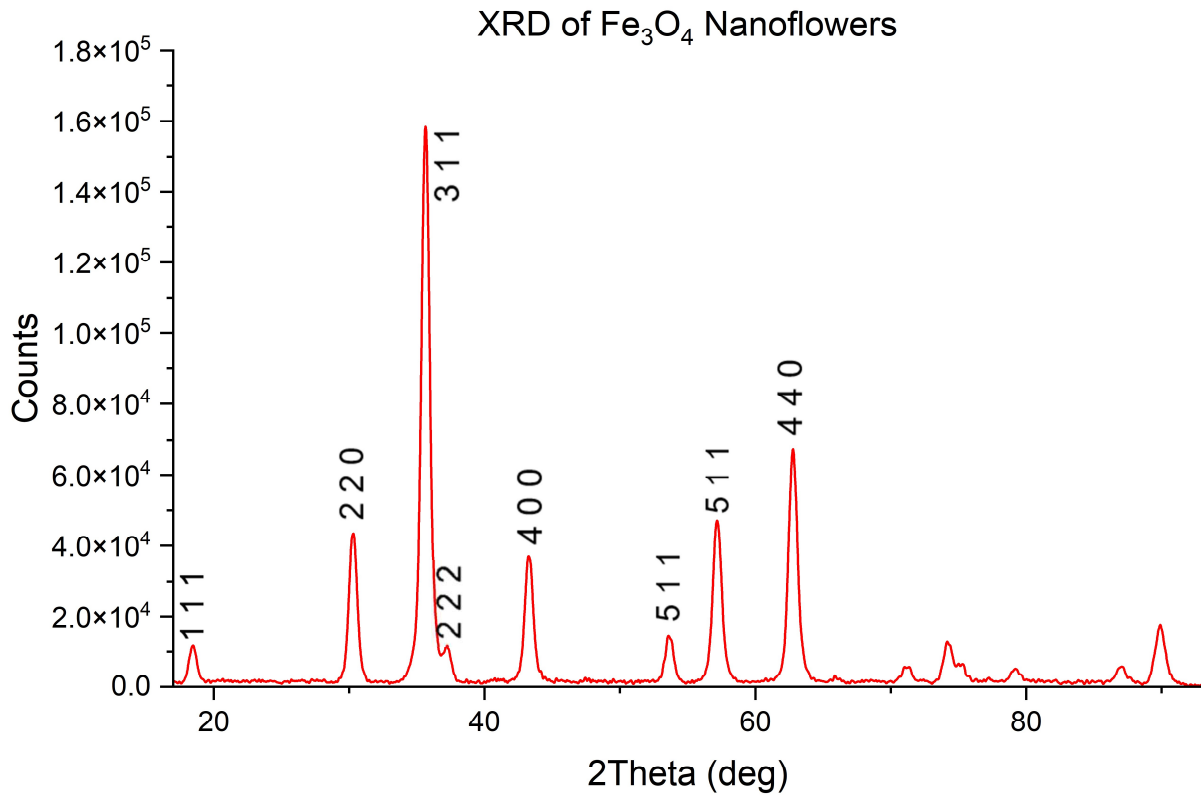


Figure 7.5. Power XRD diffraction pattern of Fe₃O₄ nanoflowers.

The XRD diffraction pattern of the obtained nanoparticle powder demonstrated extremely sharp peaks consistent with a highly crystalline material. Furthermore, the diffraction pattern also confirmed the nanoparticles to be of pure oxidation state. There were no traces of Fe₂O₃ peaks in the diffractogram, as there is no visible [1 0 4] expected from Fe₂O₃ at approximately 27 degrees 2 θ .

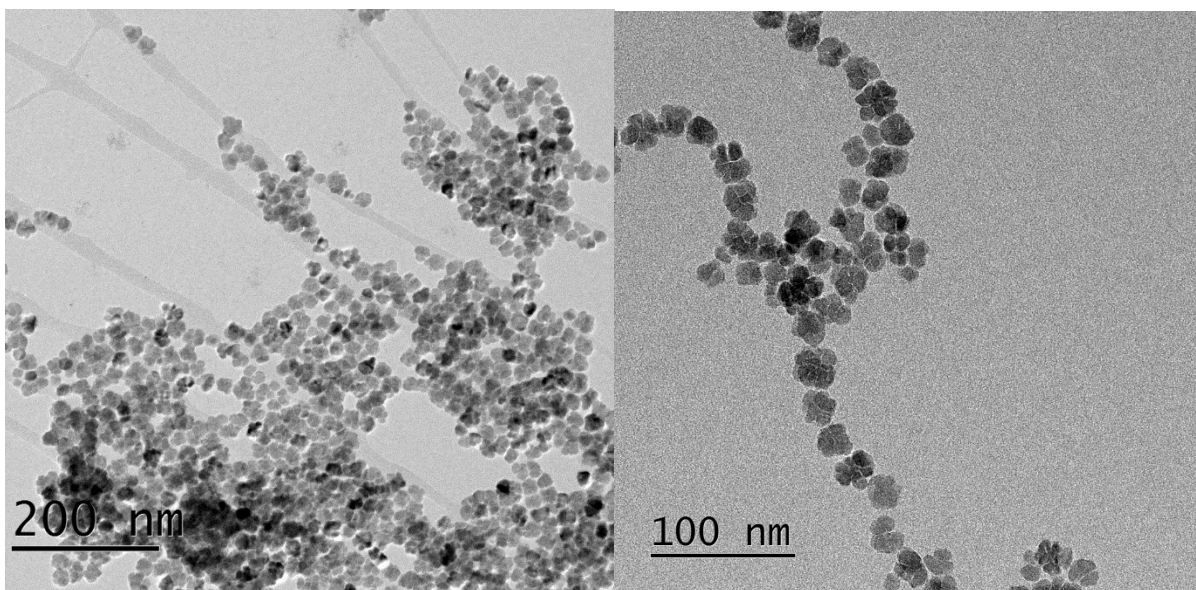


Figure 7.6. TEM of monodisperse colloidal Fe₃O₄ nanoflowers.

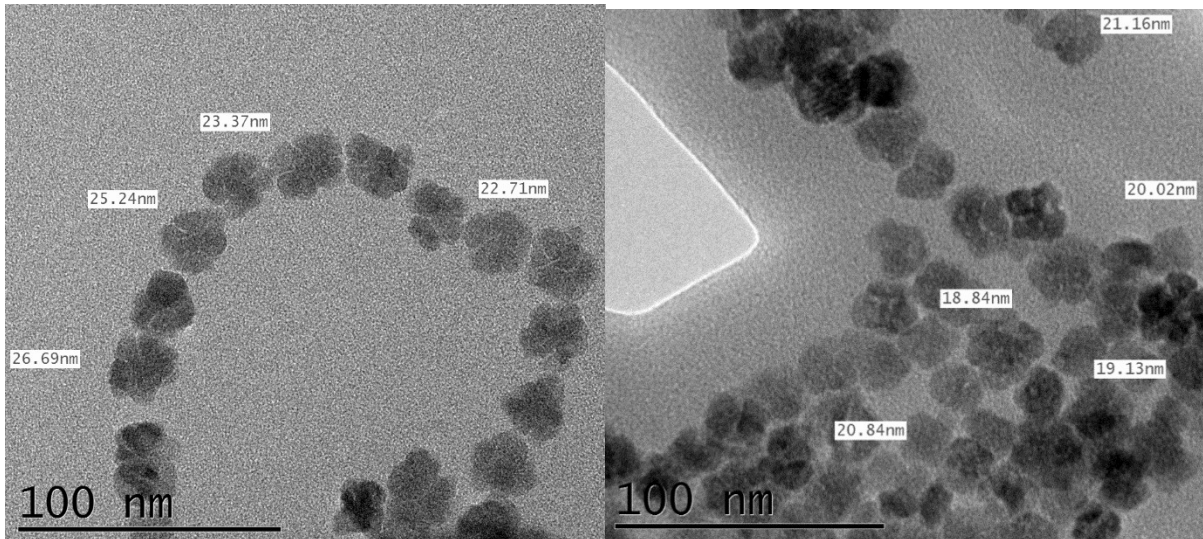


Figure 7.7. TEM of monodisperse superparamagnetic 20 ± 1.9 nm Fe_3O_4 nanoflowers.

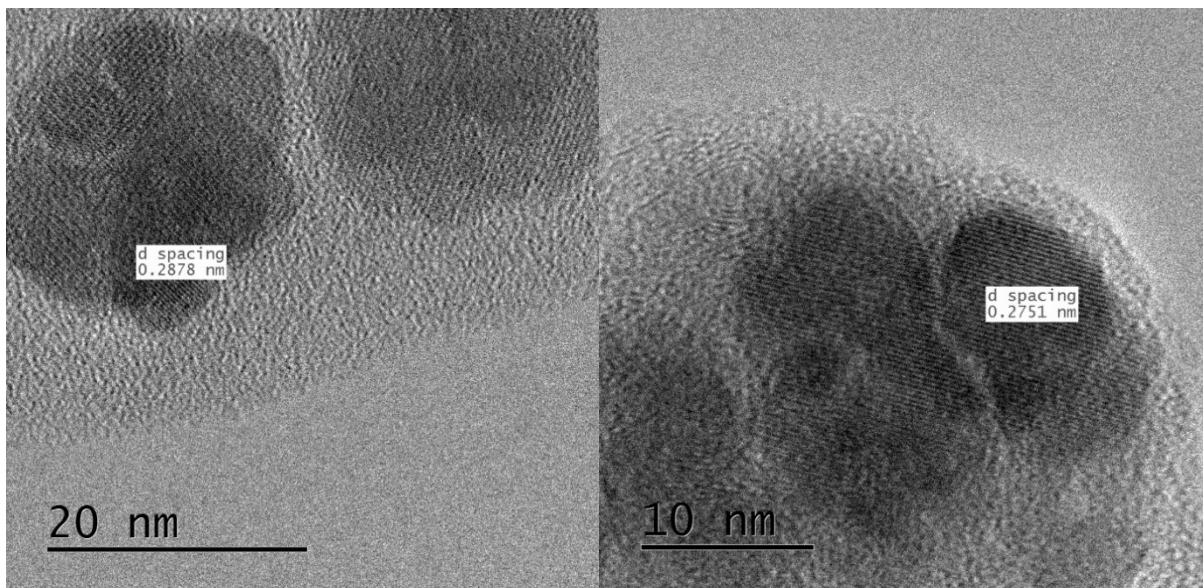


Figure 7.8. TEM of monodisperse superparamagnetic Fe_3O_4 nanoflowers highlighting d-spacing of highly crystalline nanoparticles L image showing [220] R showing [311].

The TEM analysis revealed the synthesised nanoparticles exhibited the desired nanoflower morphology. Particles had generally symmetrical spherical shapes with nobbled surfaces. This morphology was desired for later coating modifications to the nanoparticles as the rutted surface provides extra surface area for the coatings to adhere too. (Fig 7.6). Additionally, when examined under high magnification the particles were highly crystalline. The atomic Miller planes were clearly visible running end to end of the particles. Particles exhibited primarily [220] and [311] crystal habits desired for the later magnetic properties explored.

Upon examination, the average particle diameter was measured at $19.71 \text{ nm} \pm 2.82 \text{ nm}$ (see Fig. 7.7). These produced particles displayed remarkable monodispersity, with minimal aggregated impurities remaining following centrifugal separation. Achieving such uniformity is notably challenging with sub-100 nm superparamagnetic nanocrystals. This challenge arises from the fact that these nanocrystals can align their crystal lattices when exposed to magnetic fields, leading to bonding at elevated temperatures, akin to the annealing process in bulk metals. This effect is particularly pronounced during synthesis and when subjecting the particles to high static magnetic fields for purification.

A practical approach to assess this effect before conducting TEM analysis involves using a strong static magnet. When dispersed particles encounter an exceptionally strong magnetic field, they quickly separate from the colloidal solution and often form needle-like spikes adjacent to the magnetic source. In this state, they effectively exhibit ferromagnetic behaviour. While it is possible to redisperse the particles from this state through vigorous horn sonication, if left undispersed, they will tend to anneal by merging their crystal lattices into larger particles, even at room temperature forming aggregated particles. This is one of the key advantages to using this synthetic approach at high temperatures the solvent is catalytically polymerised around the formed nanoparticles protecting them from crystalline aggregations. The required sonicated in strong ammonia solution yielding a colloid in an aqueous solution removed this protective layer of polymerised solvent. It is also possible to remove this layer without cavitation refluxing in 30% nitric acid, but it is difficult to perform without over oxidising though to the particles changing them to Fe_2O_3 .

7.3 - Fe_3O_4 Nanoflower SiO_2 Coating:

7.3.1 - Methodology:

The synthesised nanoparticles were first sonochemically coated in a SiO_2 using the same sonochemical reactor shown in *figure7.3*. 20 ml (0.33 mg ml^{-1}) Fe_3O_4 nanoflower colloidal solution was pH adjusted with ammonia to pH 11 then transferred to a sonochemical reactor. The solution was sonicated at 15 W and 10 ml EtOH was added into the cavitation zone at 0.3 ml min^{-1} . Next, 8.3 mg PVP-10 ($3.3 \text{ } \mu\text{mols}$) in 5 ml EtOH was added into the cavitation zone at $0.083 \text{ ml min}^{-1}$ at 30 W, followed by 15 mg CTAB in 5 ml EtOH in 1 aliquot and sonicated for a further 15 mins. $30 \text{ } \mu\text{L}$ TEOS in 5 ml EtOH was the injected into the cavitation zone at 0.05 ml min^{-1} . The reaction liquor was then centrifuged at 12.5 kRCF then washed 3X with EtOH at 2 kRCF. The pellet was then redispersed in 20 ml MeOH by sonicating for 30 mins at 1.75 W ml^{-1} , then magnetically separated for 16 hrs and washed 3X with MeOH pH adjusted with ammonia and redispersed at 2 W ml^{-1} for 60 s yielding a yellow colloidal with

mild of white turbidity in direct light. The colloidal nanoparticle solution was purified by gradient centrifugation using the same method as previously in MeOH. (Fig. 7.9)

7.3.2 – Results and discussion:

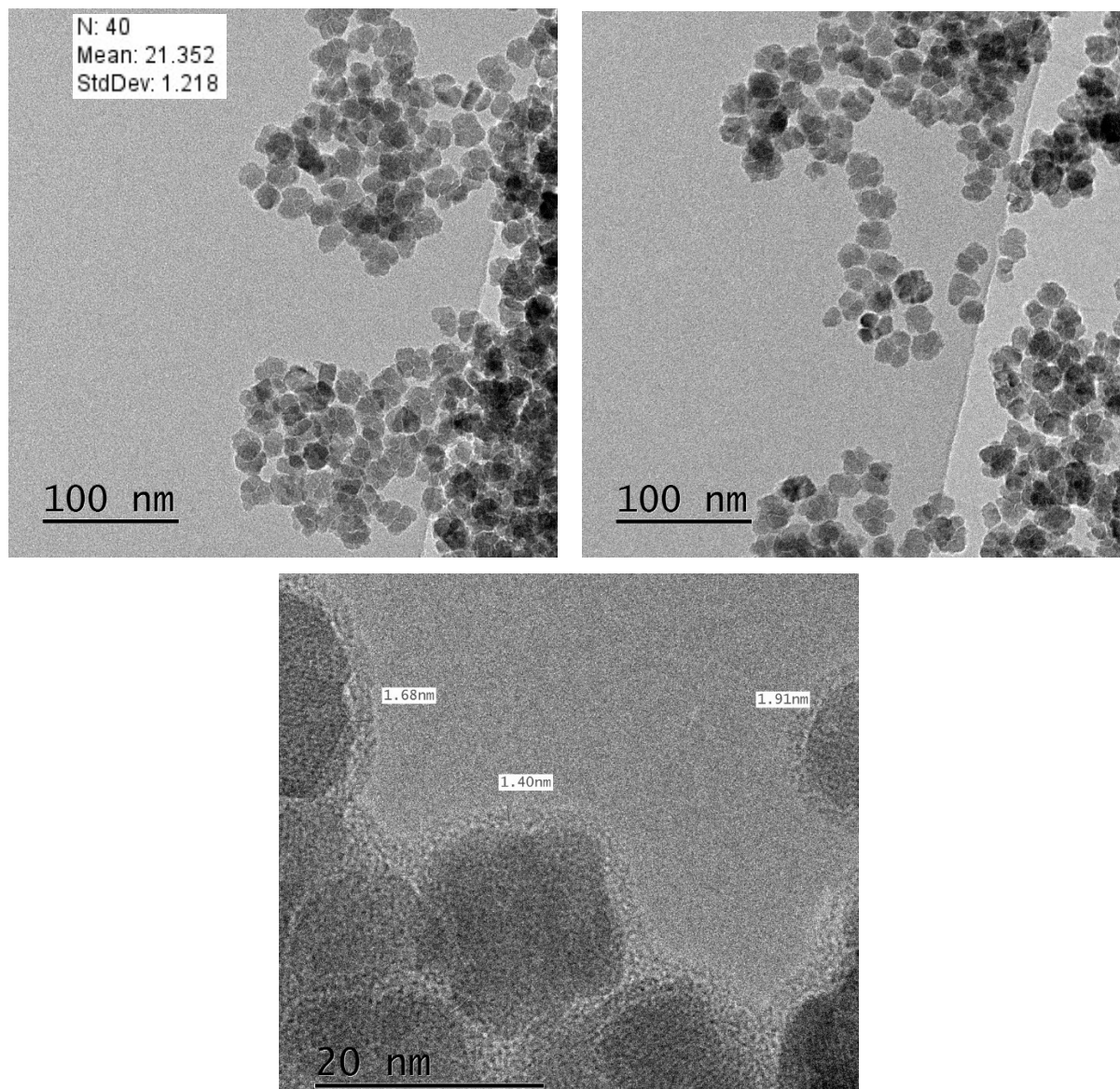


Figure 7.9. TEM of monodisperse 21 nm \pm 1.2 nm superparamagnetic SiO₂ coated Fe₃O₄ nanoflowers. Bottom image clearly shows the approx. 1.6 nm layer of deposited SiO₂.

TEM analysis unveiled that the synthesized nanoparticles were effectively coated with SiO₂. The TEM images consistently demonstrated that the particles maintained their monodisperse nature without aggregation. On average, a 1.6 nm layer of SiO₂ was successfully deposited on the surface of the iron oxide nanoflowers, resulting in monodisperse particles with an average diameter of 21.3 nm \pm 1.21 nm. The SiO₂ coating not only provided a chemically modifiable layer but also substantially enhanced the sphericity of the particle surface, further refining the size distribution of the particles.

7.4 – SiO₂ Coated Fe₃O₄ Nanoflower S-H Functionalisation and Protein immobilisation.

7.4.1 - Methodology:

The nanoparticle solution was returned to the sonochemical reaction chamber sonicated for 90 mins at 0.5 W ml⁻¹ with 8.3 μl MPTMS. The reaction liquor was then centrifuged at 12.5 kRCF then washed 3X with EtOH at 2 kRCF. The pellet was then redispersed in 20 ml MeOH by sonicating for 30 mins at 1.75 W ml⁻¹, then magnetically separated for 16 hrs and washed 3X with 10 mM NaCit with 0.01 % PVP-10 and redispersed in 20 ml 10 mM NaCit with 0.01 % PVP-10 with a particle concentration of 0.19 mg ml⁻¹. To this solution 5eq HSA protein was added with 100 μl tetraethyl amine, the solution was bath sonicated at 30 °C for 4 hrs to conjugate the protein to the nanoparticle surface. Solutions was then then magnetically separated for 36 hrs at 3 °C and 1X SP-RPA crowding reagent to a final concentration 300 μg μL⁻¹.

7.4.2 – Results and discussion:

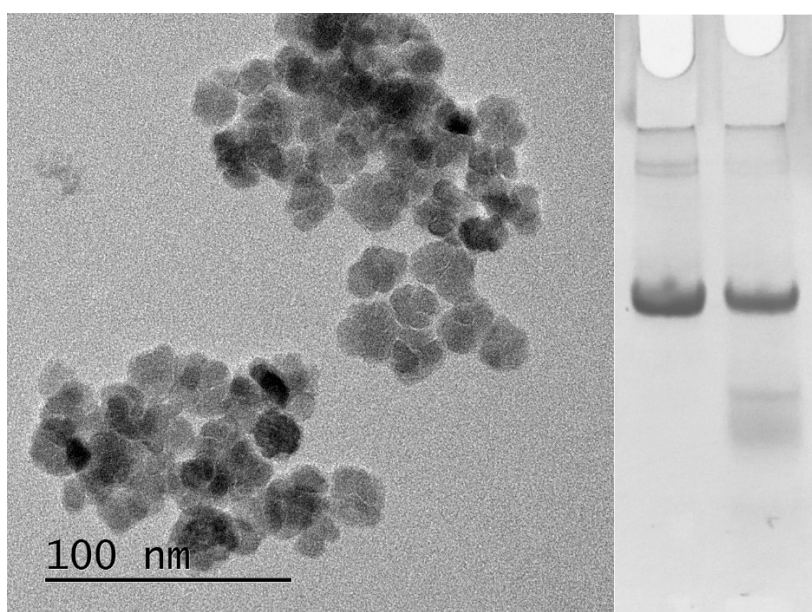


Figure 7.10. TEM of monodisperse 21nm±1.2nm superparamagnetic BSA-S-S- SiO₂ coated Fe₃O₄ (right). Non-denaturing PAGE gel of BSA coating nanoparticles after synthesis then 4 weeks later. (left).

TEM confirmed particles remained monodisperse after MPTMS functionalisation and protein conjugation. The colloid remained stable in solution for up to 4 weeks at 3 °C, after 4 weeks the colloid was able to be recovered by gentle bath sonication, non-denaturing PAGE showed only mild protein degradation after 4 weeks. (Fig. 7.10).

7.5 Micro-Helmholtz Alternating Magnetic Field Generator:

7.5.1 - Introduction

To generate a controlled and uniform magnetic field to assess the effect the synthesised functionalized nanoflower a pair of miniature Helmholtz coils were designed and built into the RT-SP-Fluorometer to monitor the effect using real time amplification data. Helmholtz coils are solenoid devices which when positioned correctly relative to each other can produce a region of almost uniform magnetic field. They are typically used to cancel out the earth's magnetic field or to generate large static fields for experiments. They consist of pairs of two identical solenoidal coils spaced by exactly the radius of the coils, in doing so they produce a field of almost uniform strength within the central space between the coils. (Fig. 7.11).

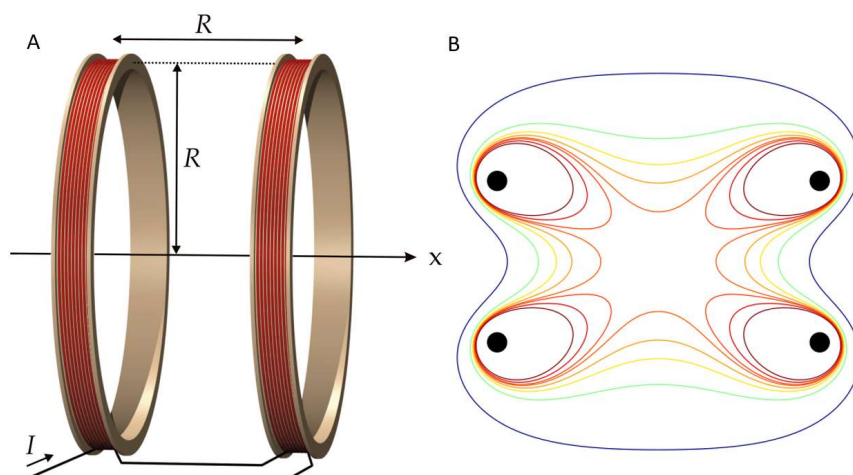


Figure 7.11. a) Schematic of a pair of Helmholtz coils Contours showing the magnitude of the magnetic field near a coil pair, with one coil at top and the other at bottom. Inside the central "octopus", the field is within 1% of its central value B_0 . The eight contours are for field magnitudes of $0.5 B_0$, $0.8 B_0$, $0.9 B_0$, $0.95 B_0$, $0.99 B_0$, $1.01 B_0$, $1.05 B_0$, and $1.1 B_0$.¹⁵⁵

The amplitude of the magnetic field generated by the pair of coils in the central region B_0 can be accurately calculated by equation 12, obtained via a Taylor series expansion of the Biot-Savart law.¹⁵⁵

$$H_{(x=0)} = \left(\frac{4}{5}\right)^{\frac{3}{2}} \frac{\mu_0 n I}{R} \quad (12)$$

μ_0 = Magnetic Permeability ($m A^{-1}$) n = number of turns

I = Current (A) R = Radius (m)

Such coils can also be modelled relatively simply and can be considered as an inductor and a resistor in series, for static fields the voltage required to drive such coils at $I=x$ can be derived from ohms' law by considering the overall inductance and parasitic resistance of the coils, *equation 13*.

$$V_x = I \ 2(l + r) \quad (13)$$

However, when generating high frequency alternating magnetic fields the inductance of the coils becomes a function of the input AC frequency. This is known as reactive inductance; the effect occurs due to the proportionally increasing self-induced electromagnetic field within the coil. The expression for the overall reactive impedance of the coils is given by *equation 14*.

$$V_x = I \left[\sqrt{\omega(l_1 + l_2)^2 + (R_1 + R_2)^2} \right] \quad (14)$$

$$\omega = 2 \pi v$$

$v = AC \text{ input frequency (Hz)}$

$l_{1,2} = DC \text{ coil inductance } (v = 0) \text{ (Henres)}$

$R_{1,2} = \text{Coils parasitic resistance}$

$\omega = \text{angular frequency (radians)}$

This therefore creates issues driving coils at high frequencies with meaningful currents as for even relatively small inductance coils, at high kHz frequencies kV driver are required to drive 1 A of current. This is possible in the laboratory but not practical but is almost impossible on a portable handheld device. To overcome this issue Helmholtz coils can be run in series resonant mode. (*Fig. 7.12*).

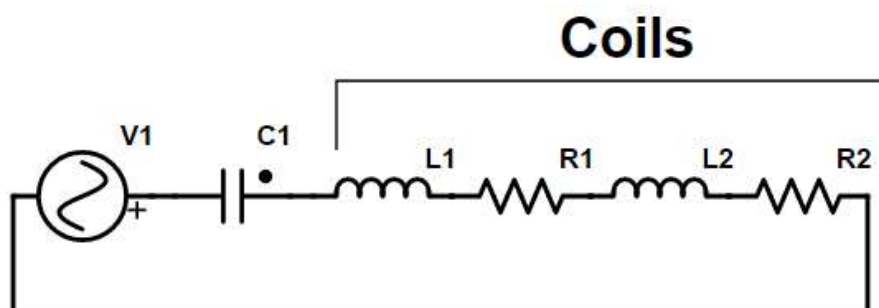


Figure 7.12. Simplified schematic of a pair of LC resonant coils.

In this configuration, when the capacitance matches the coils inductance the overall effect is the reactive impedance is reduced to only the parasitic resistance of the coils as the current across the capacitors and coils are exactly 180° out of phase. Enabling meaningful current to be driven at reasonable voltage ranges, however the bandwidth of the resonant frequency is small. The capacitance required to resonate the coils at a specific frequency is given by *equation 15*.

$$C_s = \frac{1}{\omega^2 (l_1 + l_2)} \quad (15)$$

The voltage across the resonant element of the circuit is given by *equation 16*.

$$V_s = \frac{1}{2\pi \sqrt{(l_1 + l_2) C_s}} \quad (16)$$

7.5.2 - Micro-Helmholtz Coil integration in the RT-SP-RPA Fluorometer:

To test the hypothesis, that the amplification reactions could be enhanced by magnetically exciting the synthesised particles, a pair of Helmholtz coils were integrated into the sample holder of the ss-fluorometer. Coils were wound using Type 1 34 AWG 5/40AWG Litz (*OSCO defence division*), were wound by hand and stabilised using epoxy resin and had approx. 5000 turns each. (*Fig. 7.13*).

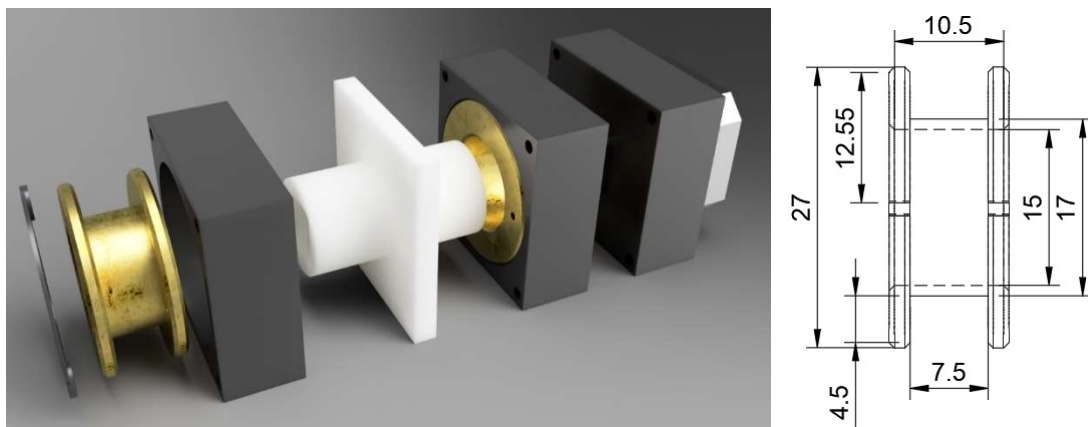


Figure 7.13. Rendered view of how the coils integrated with the ss-fluorometer sample holder with a dimensional sketch of the machined unwound coil body. All units in mm.

Coils were characterised as having an ohmic resistance of 47.6 ohms using a 4-wire measurement. Coil inductance was measured using an excitation square wave of 10kHz with 0.1nF (0.01%) resonance capacitor and coupling capacitors. A resonance frequency was measured at 359.126 kHz giving a coil inductance of 1.962 mH per coil in air.

7.5.3 Driver Circuitry:

To drive the coils a custom make driver board was made, the board was designed to allow over the air feedback of the coils resonance frequency via an antenna. Thus, allowing for the excitation/driving frequency to be continually adjusted, as small variations in temperature and the magnetic permeability of the surroundings of the coil can drastically alter resonance frequency of the coils. (Fig. 7.15). The top signal path shown is the coil exciter and the bottom in the receiver and output driver. Each excitation cycles the coils are initially excited using a frequency sweep via the top signal path to allow the bottom signal path to detect the current resonance frequency of the coils, once detected a microcontroller switches the feedback driver outputs to the power output stage all with in this all happens within 1 μ s. (Fig. 7.14-7.15).

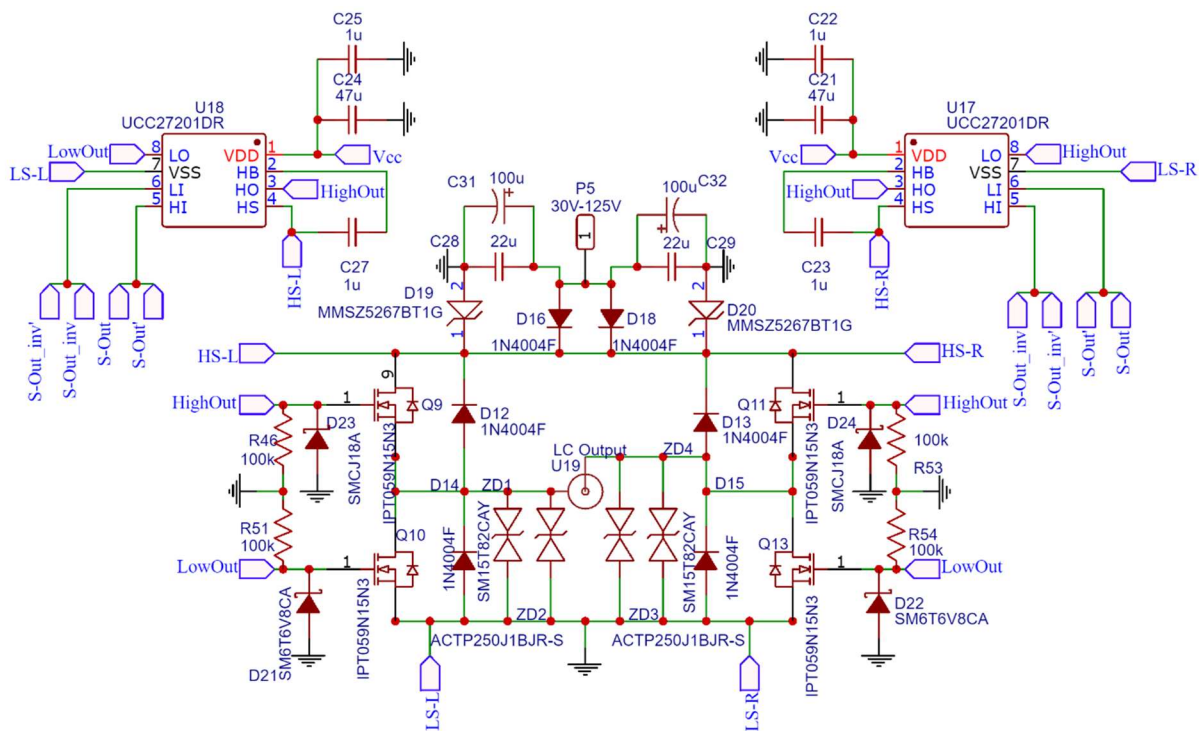


Figure 7.14. AC Micro-Helmholtz coil high bandwidth class D output amplifier

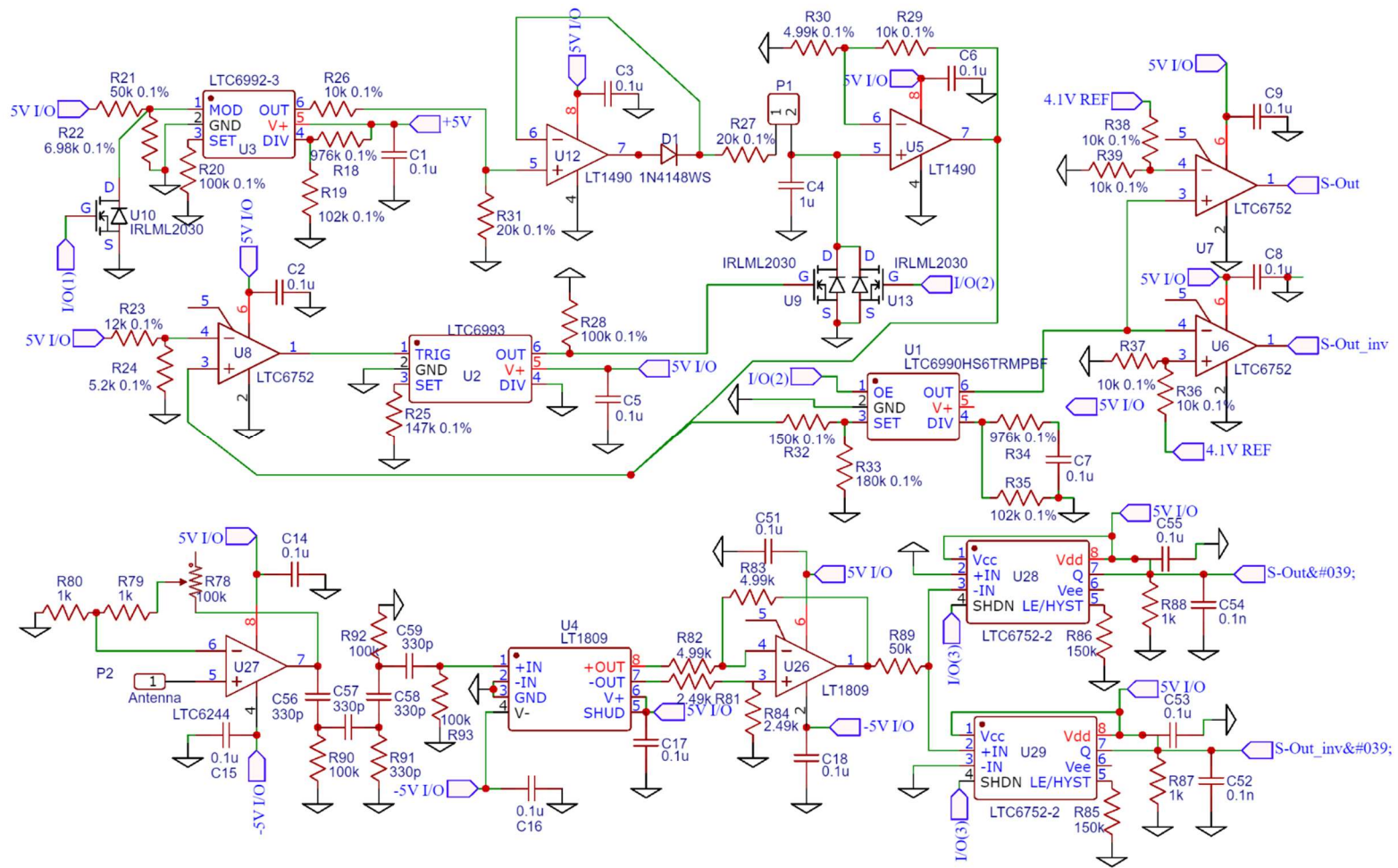


Figure 7.15. AC Micro-Helmholtz coil tuning and control board.

7.6 Real Time SP-RPA Gyromagnetically Enhanced Kinetic Evaluation:

7.6.1 - Introduction

To assess the effect of the excited BSA-S-SiO₂ coated Fe₃O₄ nanoparticles on the kinetics of RPA reactions, RT-SP-RPA was carried out using the most performant primer set, MecA₁₂-C3 and altering the magnetic excitation frequency. Resonant series capacitors were used for frequencies 1 kHz and up, series capacitors were not required as the real ohmic is the largest contributors to the impedance of the coils below 1 kHz. Coils were initially energised with a 30 V_{p-p} square wave, then ran at the true coil resonance frequency using the compositor signal path. Frequency's tested were dictated by the availability of capacitors with low ESR having corresponding capacitance to resonate the coils at a frequency of interest, 100 kHz and below. Namely 1 nF, 10 nF, 100 nF, 1 μF and 10 μF; for approximately 80 kHz, 20 kHz, 8 kHz, 2.5 kHz resonance frequencies. Coils produced approximately 18 W peak reactive power at resonance frequencies.

7.6.2 – Methodology:

Formamidopyrimidine DNA glycosylase (*fpg*, NEB Labs) was added to the purified protein master mix at 570 ng μL⁻¹ allowing the reaction to be monitored in real time on the solid state fluorometer. Reaction pads were prepared by cutting 1 cm² from activated and blocked glass conjugate strips using a die and punch. RT-SP-RPA master mix comprised of 100 μL modified reaction buffer, 100 μL 9.2 mM dNTP's, 100 μL RT-SP-enzyme mix and 200 μL 320X crowding solution in 2.5 %_{v/v} formamide. 25 μL ice cold RT-SP-RPA master mix was pipetted on to the reaction pads. Pads were flash frozen on liquid N₂ and freeze dried for 16hrs. 25 μL freshly prepared 22nm Fe₃O₄@SiO₂@BSA nanoflowers at 330 μg μL⁻¹ was pipetted on to the reaction pads. Pads flash frozen on liquid N₂ and freeze dried for 16hrs. Initiation solutions were prepared using 10 μL of each 10 μM MecA₁₂-C3 F/R primers, 2 μL 10 μM internal probe, 4 μL 210pg/1M copies μL⁻¹ reference MRSA gDNA, 10 μL MgOAc and 166 μL ddH₂O.

The reaction pad was placed into the sample holder and pre-heated to 37 °C. Reactions were started by adding 25 μL the initiation solution via the sample access point. Reactions were run in triplicate. Incident light power was set at 50 %, with stabilised laser temperature of 35 °C maintained, incident light irradiation time was 20 ms and a detector temperature of -50 °C. Measurements were taken every 90 s over 2 hours giving a total exposure time of 1.6 s. Magnetic excitation was performed every 5 seconds with a total excitation time of 100 ms and interlocked when fluorescence measurement were taken to avoid interference with the optical regulators and TIA's. (Fig. 7.16-7.21)

7.6.3 Results w/RT-SP-RPA of $mecA_{12}$ -C3 under magnetic enhancement:

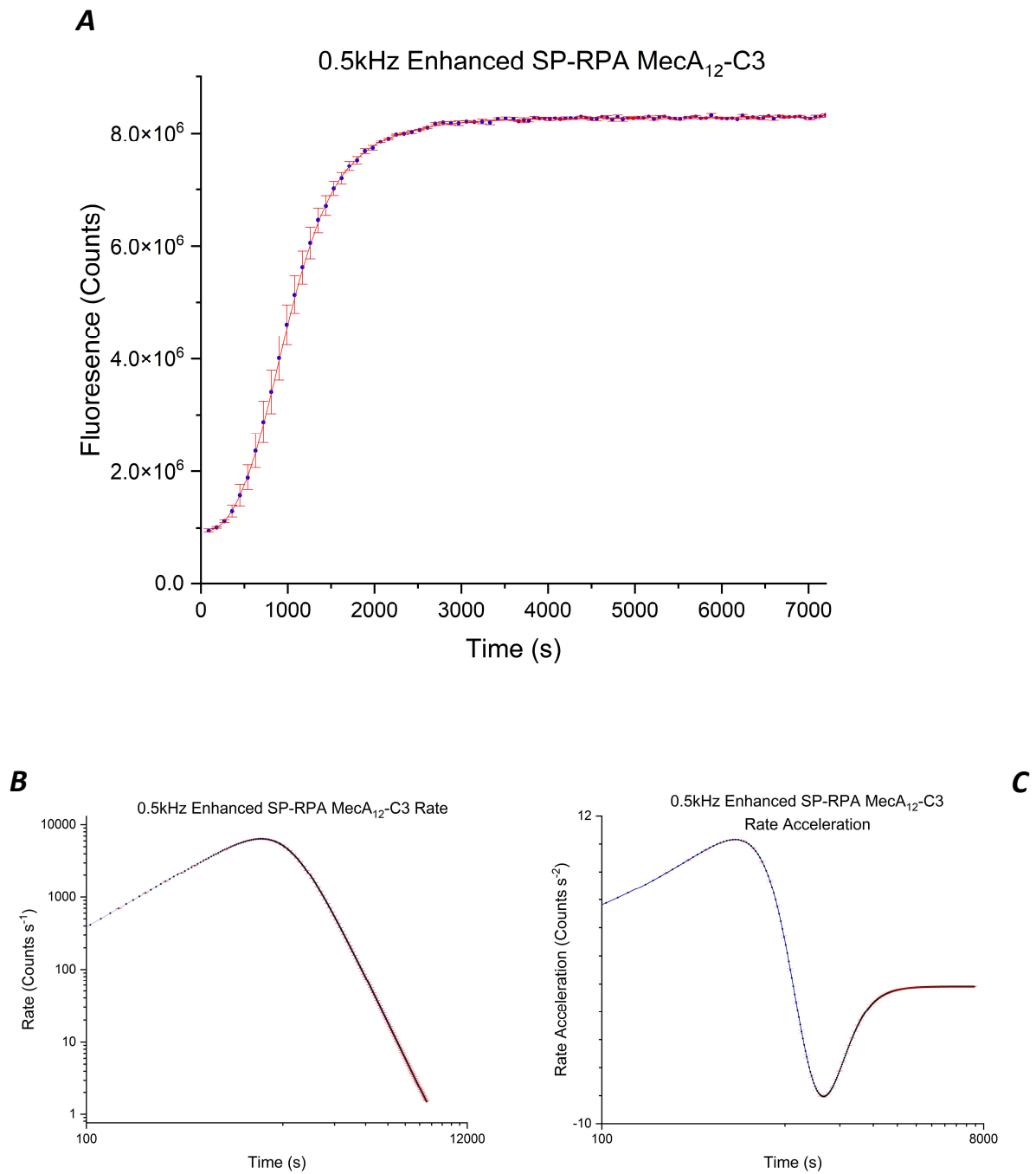


Figure 7.16 A) Processed gyromagnetically enhanced RT-SP-RPA fluorescence curve of primer set $mecA_{12}$ -C3 with 10M copies gDNA and a 500Hz alternating magnetic field fitted using equation 1. $R^2 = 0.996$, $\Phi_i = 9.2 \times 10^5 \pm 0.23 \times 10^5$, $\varphi_m = 0.94 \times 10^6 \pm 0.2 \times 10^5$, $h = 4.14 \pm 0.16$, $f = 0.59 \pm 0.11 \times 1219 \pm 3.9s$. C) First derivate rate curve for primer set $mecA_7$ -C3. $v_{max} = 6414 \pm 0.09 \text{ counts s}^{-1}$, $k_m = 900 \pm 5s$. D) Second derivate rate acceleration curve for primer set $mecA_7$ -C3. $\vec{v}_{max} = 10.18 \pm 6.95 \times 10^{-2} \text{ counts s}^{-2}$, $\vec{v}_{min} = -7.66 \pm 10.45 \times 10^{-2} \text{ counts s}^{-2}$, $t_i = 465 \pm 5s$, $t_d = 1275 \pm 5s$.

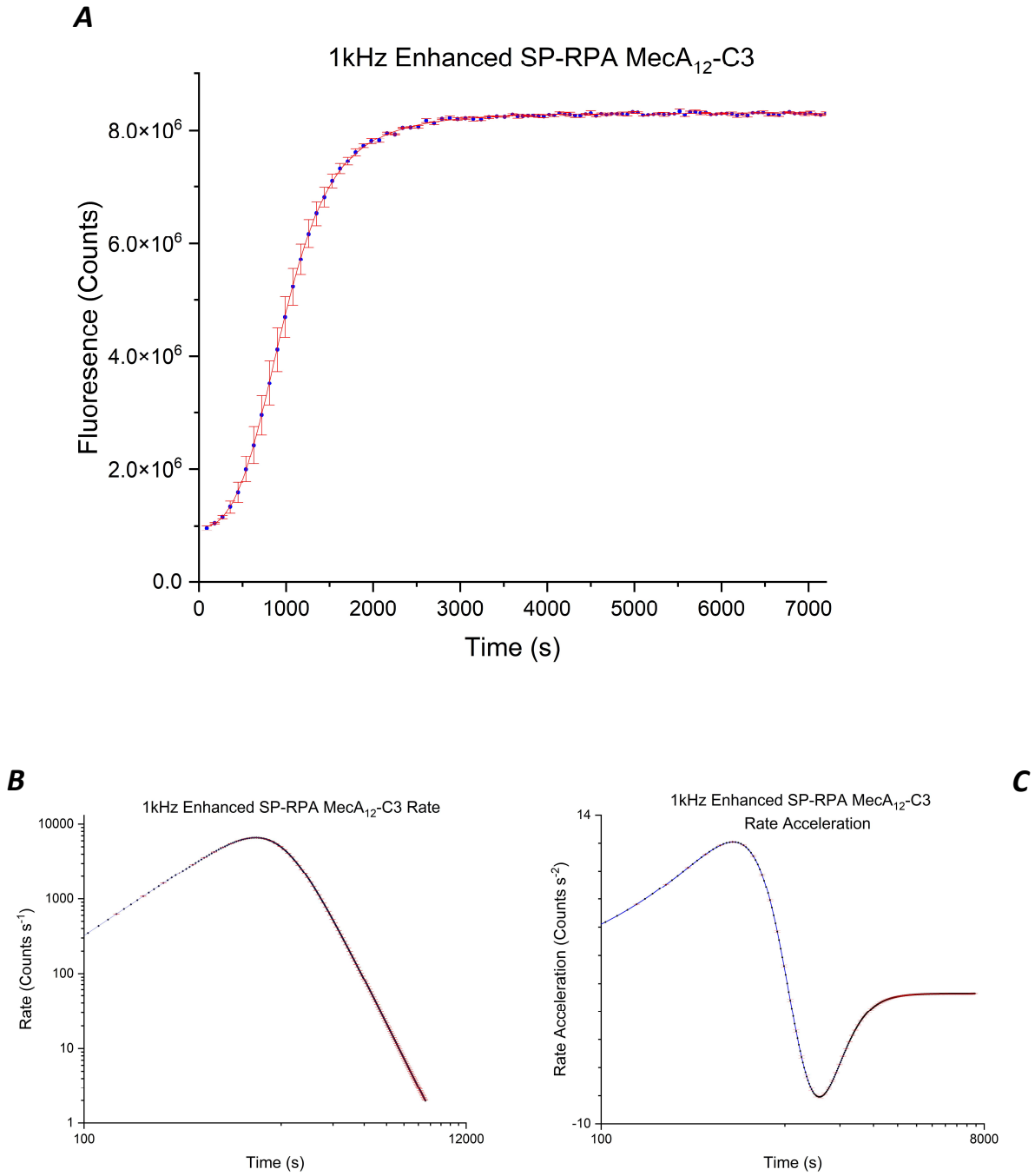


Figure 7.17. A) Processed gyromagnetically enhanced RT-SP-RPA fluorescence curve of primer set *mecA*₁₂-C3 with 10M copies gDNA and a 1kHz alternating magnetic field fitted using equation 1. $R^2 = 0.997$, $\Phi_i = 9.23 \times 10^5 \pm 0.25 \times 10^5$, $\varphi_m = 0.92 \times 10^6 \pm 0.17 \times 10^5$, $h = 3.94 \pm 0.07$, $f = 0.63 \pm 0.05 \times \omega = 1117 \pm 3.5s$. C) First derivate rate curve for primer set *mecA*₇-C3. $v_{max} = 6414 \pm 0.4 \text{ counts s}^{-1}$, $k_m = 855 \pm 5s$. D) Second derivate rate acceleration curve for primer set *mecA*₇-C3. $\vec{v}_{max} = 11.58 \pm 1.95 \times 10^{-2} \text{ counts s}^{-2}$, $\vec{v}_{min} = -7.95 \pm 9.25 \times 10^{-2} \text{ counts s}^{-2}$, $t_i = 450 \pm 5s$, $t_d = 1215 \pm 5s$.

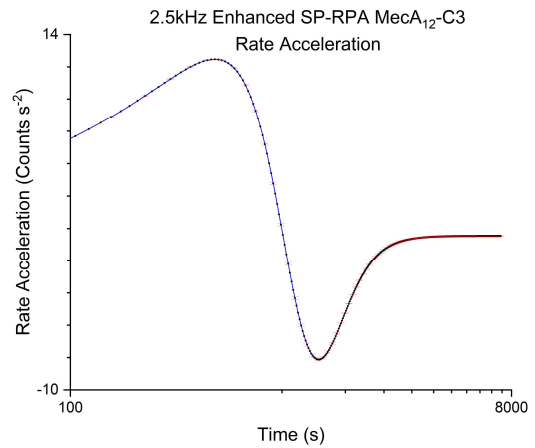
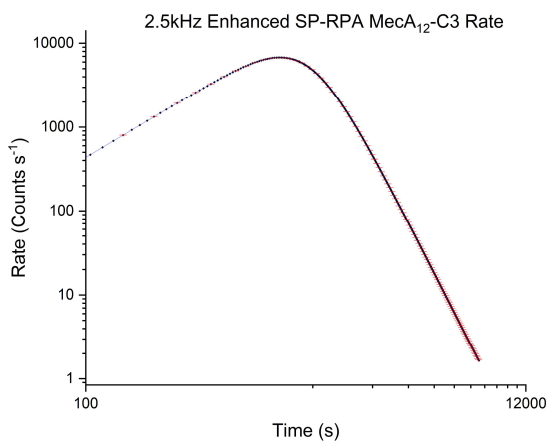
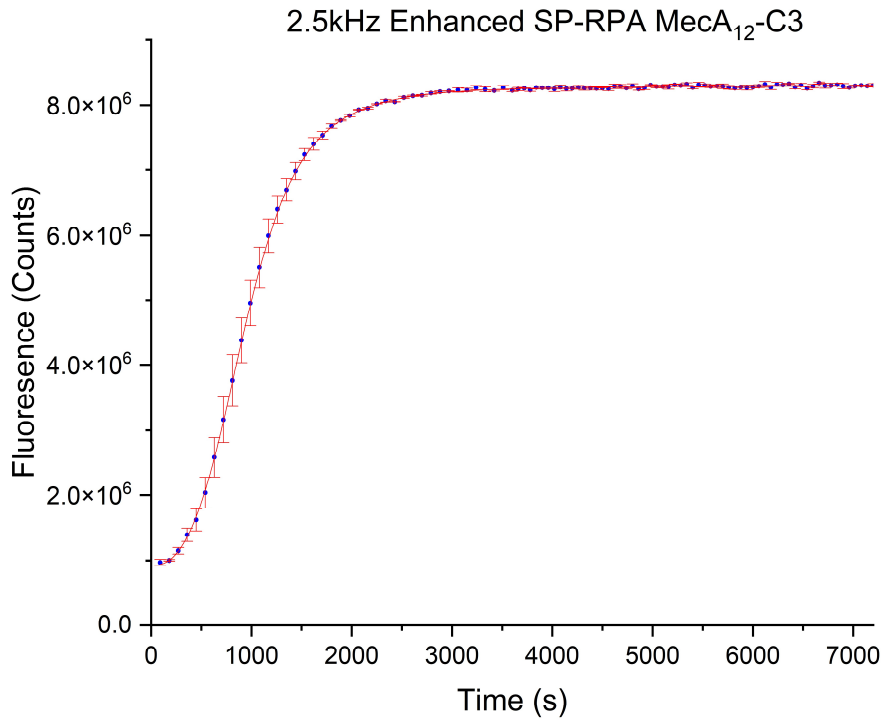


Figure 7.18. A) Processed gyromagnetically enhanced RT-SP-RPA fluorescence curve of primer set $mecA_{12}$ -C3 with 10M copies gDNA and a 2.5kHz alternating magnetic field fitted using equation 1. $R^2 = 0.996$, $\Phi_i = 9.28 \times 10^5 \pm 0.15 \times 10^5$, $\varphi_m = 0.93 \times 10^6 \pm 0.18 \times 10^5$, $h = 3.94 \pm 0.072$, $f = 0.63 \pm 0.062$, $x_0 = 1114 \pm 3.1s$. C) First derivate rate curve for primer set $mecA_{12}$ -C3. $v_{max} = 6796 \pm 0.23 \text{ counts s}^{-1}$, $k_m = 825 \pm 5s$. D) Second derivate rate acceleration curve for primer set $mecA_{12}$ -C3. $\vec{v}_{max} = 11.96 \pm 1.15 \times 10^{-2} \text{ counts s}^{-2}$, $\vec{v}_{min} = -8.4 \pm 6.15 \times 10^{-2} \text{ counts s}^{-2}$, $t_i = 420 \pm 5s$, $t_d = 1185 \pm 5s$.

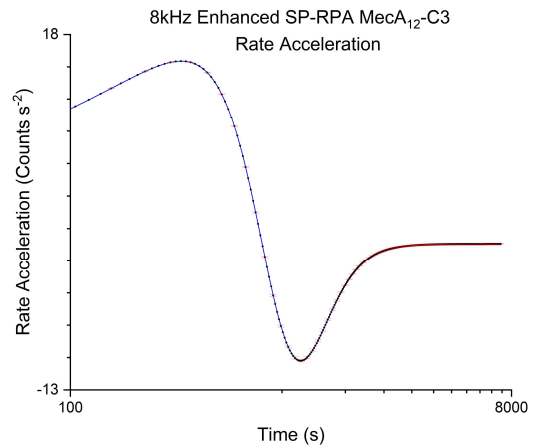
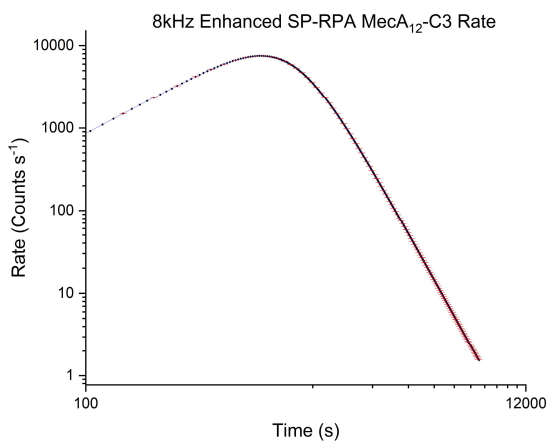
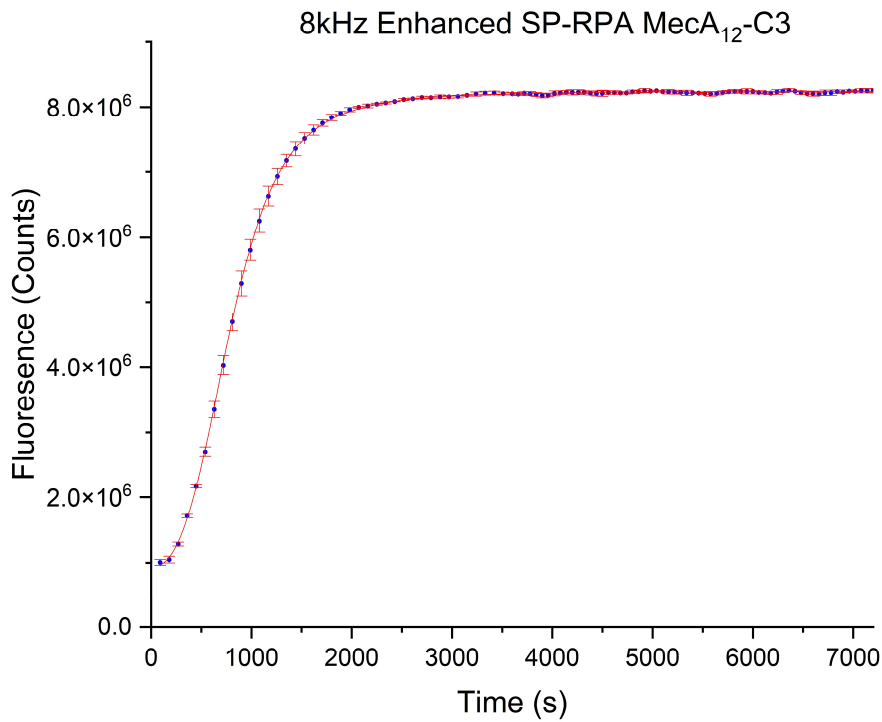


Figure 7.19. A) Processed gyromagnetically enhanced RT-SP-RPA fluorescence curve of primer set *mecA*₁₂-C3 with 10M copies gDNA and a 8kHz alternating magnetic field fitted using equation 1. $R^2 = 0.998$, $\Phi_i = 9.76 \times 10^5 \pm 0.3 \times 10^5$, $\varphi_m = 0.83 \times 10^6 \pm 0.15 \times 10^5$, $h = 3.06 \pm 0.062$, $f = 1.93 \pm 0.262 \times 0 = 637 \pm 3.1s$. C) First derivate rate curve for primer set *mecA*₁₂-C3. $v_{max} = 8979 \pm 0.33 \text{ counts s}^{-1}$, $k_m = 690 \pm 5s$. D) Second derivate rate acceleration curve for primer set *mecA*₁₂-C3. $\vec{v}_{max} = 30.96 \pm 4.65 \times 10^{-2} \text{ counts s}^{-2}$, $\vec{v}_{min} = -13.5 \pm 6.15 \times 10^{-2} \text{ counts s}^{-2}$, $t_i = 360 \pm 5s$, $t_d = 915 \pm 5s$.

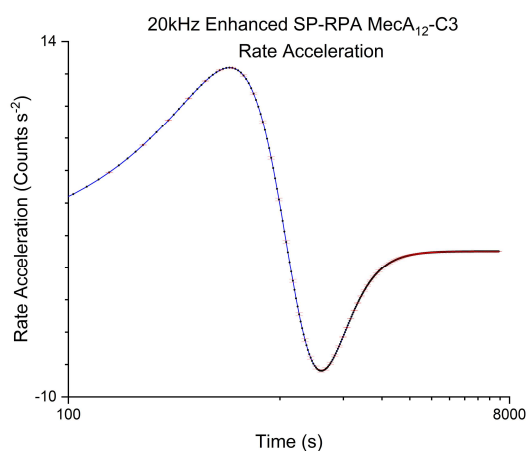
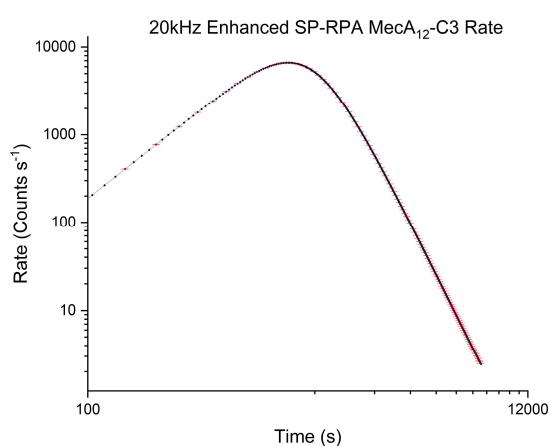
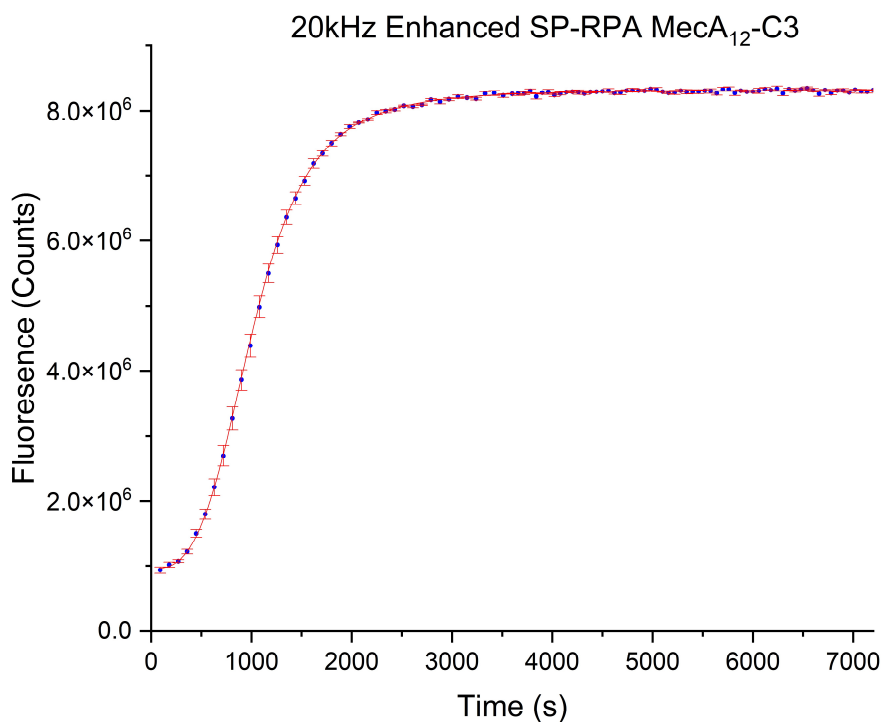


Figure 7.20. A) Processed gyromagnetically enhanced RT-SP-RPA fluorescence curve of primer set $mecA_{12}$ -C3 with 10M copies gDNA and a 20kHz alternating magnetic field fitted using equation 1. $R^2 = 0.997$, $\Phi_i = 9.57 \times 10^5 \pm 0.56 \times 10^5$, $\varphi_m = 0.82 \times 10^6 \pm 0.24 \times 10^5$, $h = 3.83 \pm 0.072$, $f = 0.75 \pm 0.162$, $x_0 = 1126 \pm 3.1s$. C) First derivate rate curve for primer set $mecA_{12}$ -C3. $v_{max} = 6655 \pm 0.33$ counts s^{-1} , $k_m = 885 \pm 5s$. D) Second derivate rate acceleration curve for primer set $mecA_{12}$ -C3. $\vec{v}_{max} = 12.16 \pm 1.65 \times 10^{-2}$ counts s^{-2} , $\vec{v}_{min} = -7.9 \pm 3.11 \times 10^{-2}$ counts s^{-2} , $t_i = 495 \pm 5s$, $t_d = 1230 \pm 5s$.

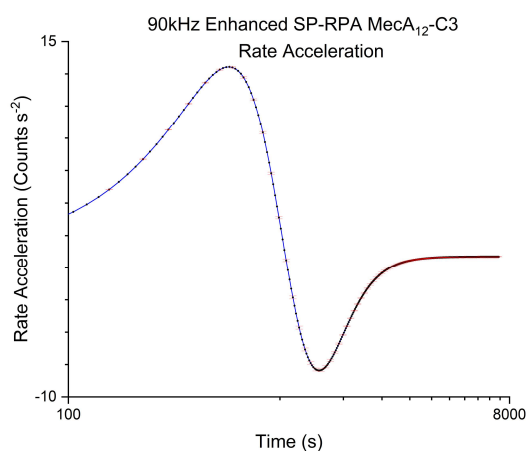
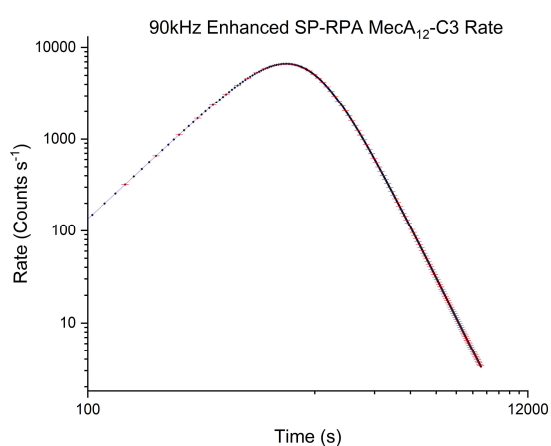
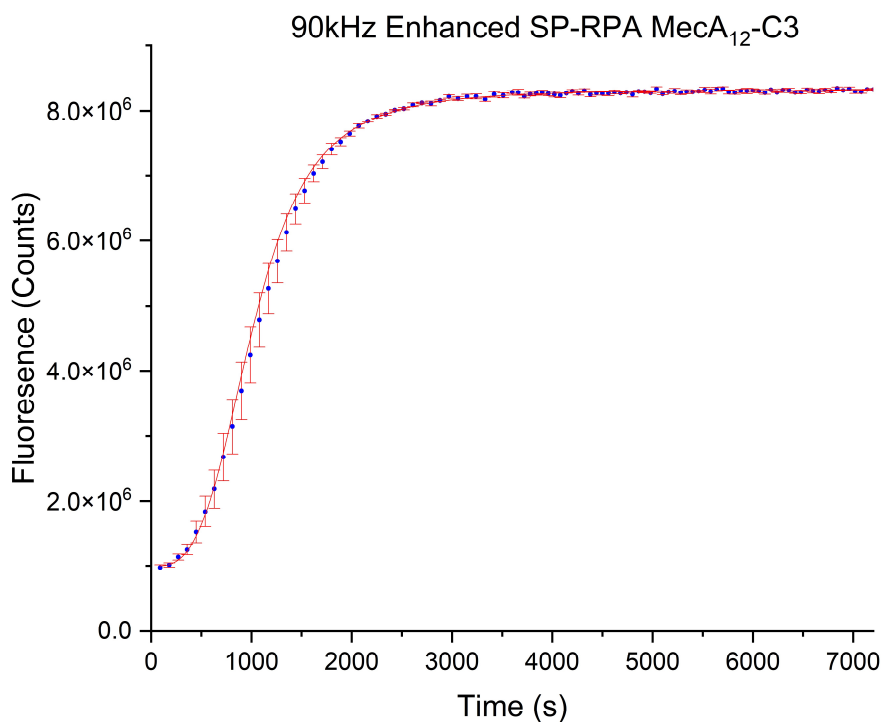


Figure 7.21. A) Processed gyromagnetically enhanced RT-SP-RPA fluorescence curve of primer set *mecA*₁₂-C3 with 10M copies *gDNA* and a 80kHz alternating magnetic field fitted using equation 1. $R^2 = 0.992$, $\Phi_i = 9.95 \times 10^5 \pm 0.26 \times 10^5$, $\varphi_m = 0.83 \times 10^6 \pm 0.23 \times 10^5$, $h = 3.6 \pm 0.082$, $f = 0.87 \pm 0.102 \times 1069 \pm 3.1s$. C) First derivate rate curve for primer set *mecA*₁₂-C3. $v_{max} = 6667 \pm 0.19 \text{ counts s}^{-1}$, $k_m = 870 \pm 5s$. D) Second derivate rate acceleration curve for primer set *mecA*₁₂-C3. $\vec{v}_{max} = 13.0 \pm 1.65 \times 10^{-2} \text{ counts s}^{-2}$, $\vec{v}_{min} = -7.8 \pm 1.31 \times 10^{-2} \text{ counts s}^{-2}$, $t_i = 495 \pm 5s$, $t_d = 1215 \pm 5s$.

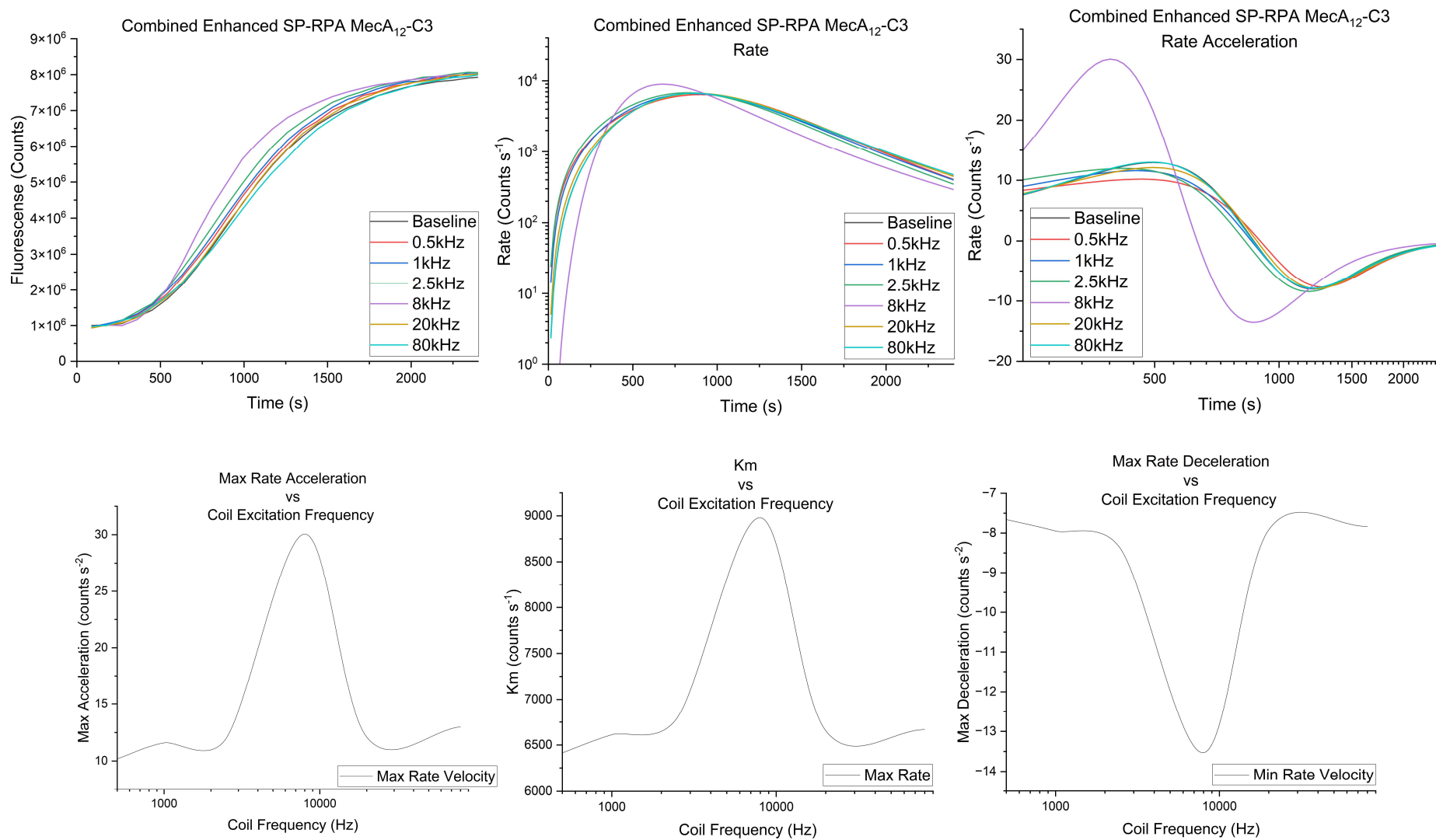


Figure 7.22. Combined processed fits of successful primer sets under RT-RPA condition (top). Key kinetic reaction constants vs coil frequency (bottom).

7.6.4 –Discussion and concluding remarks:

The presented results clearly illustrate the catalytic effect produced by the excited rotating nanoparticle have on the amplification reactions. (Fig. 7.16-7.22). Of the frequencies available to use with the deigned AC-micro coils 8 kHz, produced the largest catalytic effect. Showing an average increase in amplification efficiency of 26.7 %.

Table 7.2. Key reaction constants.

Frequency. (kHz)	Initiation Time (s)	Time to Max Sudo-Rate (s)	Time to Depletion (s)
No particles	595	870	1215
0.5	465	900	1275
1	450	855	1215
2.5	420	825	1185
8	360	690	915
20	495	885	1230
80	495	870	1215

Figure 7.23 sows the resonance frequency required to rotate the nanoparticles in this fluid matrix sits between 7-12 kHz as this is the area of highest catalytic effect. This directly corresponds to the estimated frequency range required to rotate a 22 nm particle is a fluid of this viscosity.¹⁵⁶

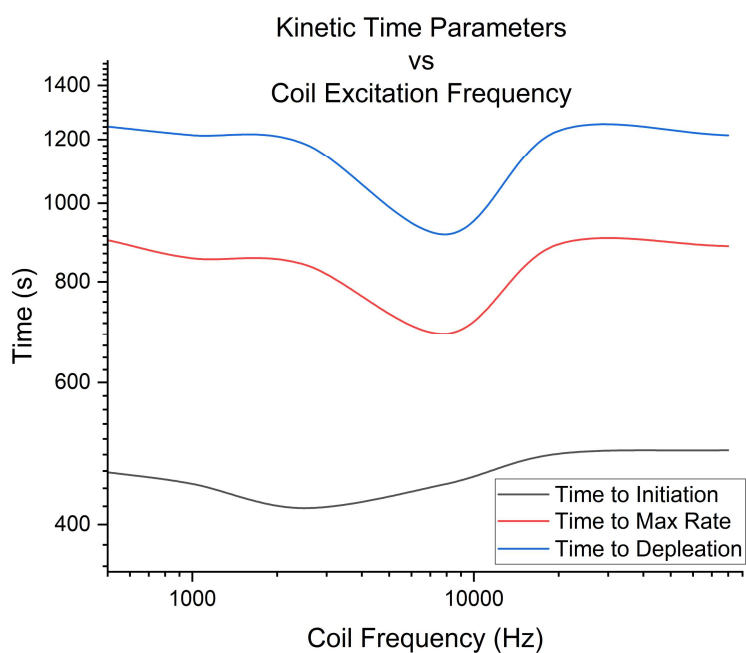


Figure 7.23. Combined processed fits of successful primer sets under RT-RPA condition.

This outstanding result is the culmination of numerous optimisation and development experiments, highlighting the immense potential of the overall system. Under the presented conditions, the time required to potentially generate detectable amplicons for the coupled LFA can be as short as 6 minutes within a solid-phase matrix. This rapid initiation can be achieved even with a target sample concentration as low as in the pM range. Furthermore, with amplification proven to work with all reaction components situated *in situ*. Thus, a fully integrated device where amplification and detection is completed *in situ* with no user interaction is one step closer.

Chapter 8

Nucleic Acid Lateral Flow Assay Development.

“PLEASE DO NOT PEE ON THESE STICKS!”

8.1 Introduction:

Chapter eight will examine the design, production, optimisation, and performance of the proposed novel multiplexed nucleic acid lateral flow assay. As discussed in *chapter 2*, the proposed system uses specifically designed short single-stranded oligonucleotide sequences as capture probes. When genes are amplified using the modified RPA reactions demonstrated thus far, the attached complementary capture sequence allows the capture of the amplified gene fragments in specific locations on the lateral or vertical flow assay. *Figure 2.13*, reproduced from *chapter 2, page 55* shows how the novel NALFA test line can only be reported if both the forward and reverse primers have been successfully “stitched” together, by an RPA reaction.

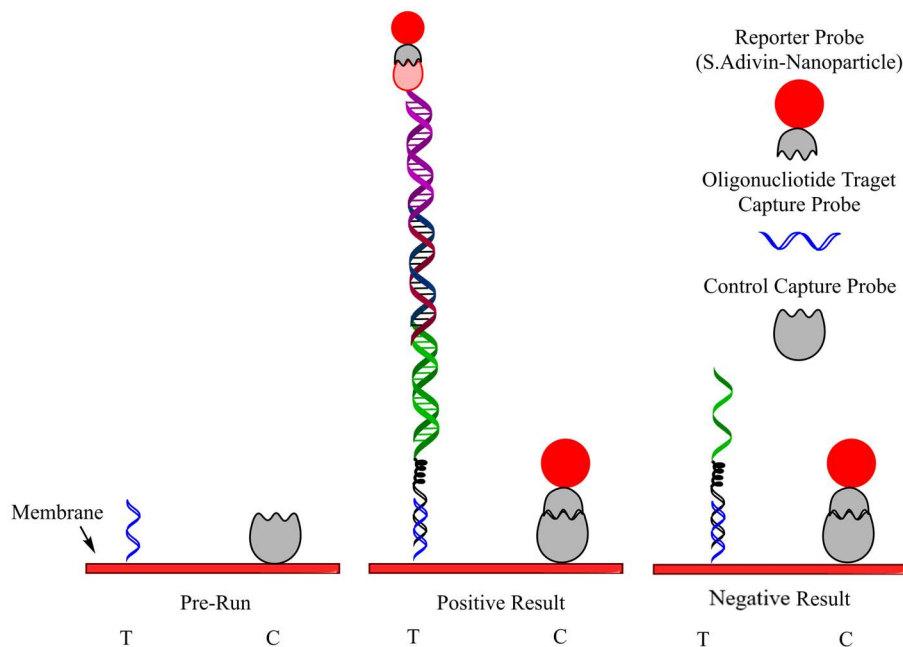


Figure 8.1. Shows how the NALFA test line can only be reported if both the forward and reverse primers have been successfully “stitched” together by an RPA reaction. Figure 2.13, reproduced from chapter 2, page 55 for clarity

Chapter 1 discusses several important factors to consider when developing any lateral flow assay, such as membrane material, pore size, and flow rate. Thus, to achieve the desired system set out in *Chapter 2*, three possible construction/probe immobilisation systems were formulated to produce the proposed multiplexed assay using the most commonly available membrane materials. An essential element to consider for developing a nucleic acid lateral flow assay is the interaction between probes - analytes and capture sequences with the surface of the test membrane. The nucleic acid bases of probes must not adhere to the membrane surface or interact with any other surface

treatment while remaining “accessible” to the flowed analytes for conjugation. All three shown assembly methodologies utilising different membrane types achieve this in distinct ways.

Method 1 utilises nitrocellulose membranes, uses a stepwise process to ensure the capture probe sequences are located correctly after the membrane is effectively blocked. Such a method should be robust, and the number of analytes detected on a single strip scalable, within the natural flow limits of the chosen membrane. However, manufacturing such a system on a small scale is difficult, mainly due to the number of steps required and the precision needed to blot the biotinylated probes within the correct location without bleed flow into other test areas of the strip. Conversely, such a system would be achievable on a larger scale with the standard reel-to-reel manufacturing methodologies already in place today. (Fig. 8.2).

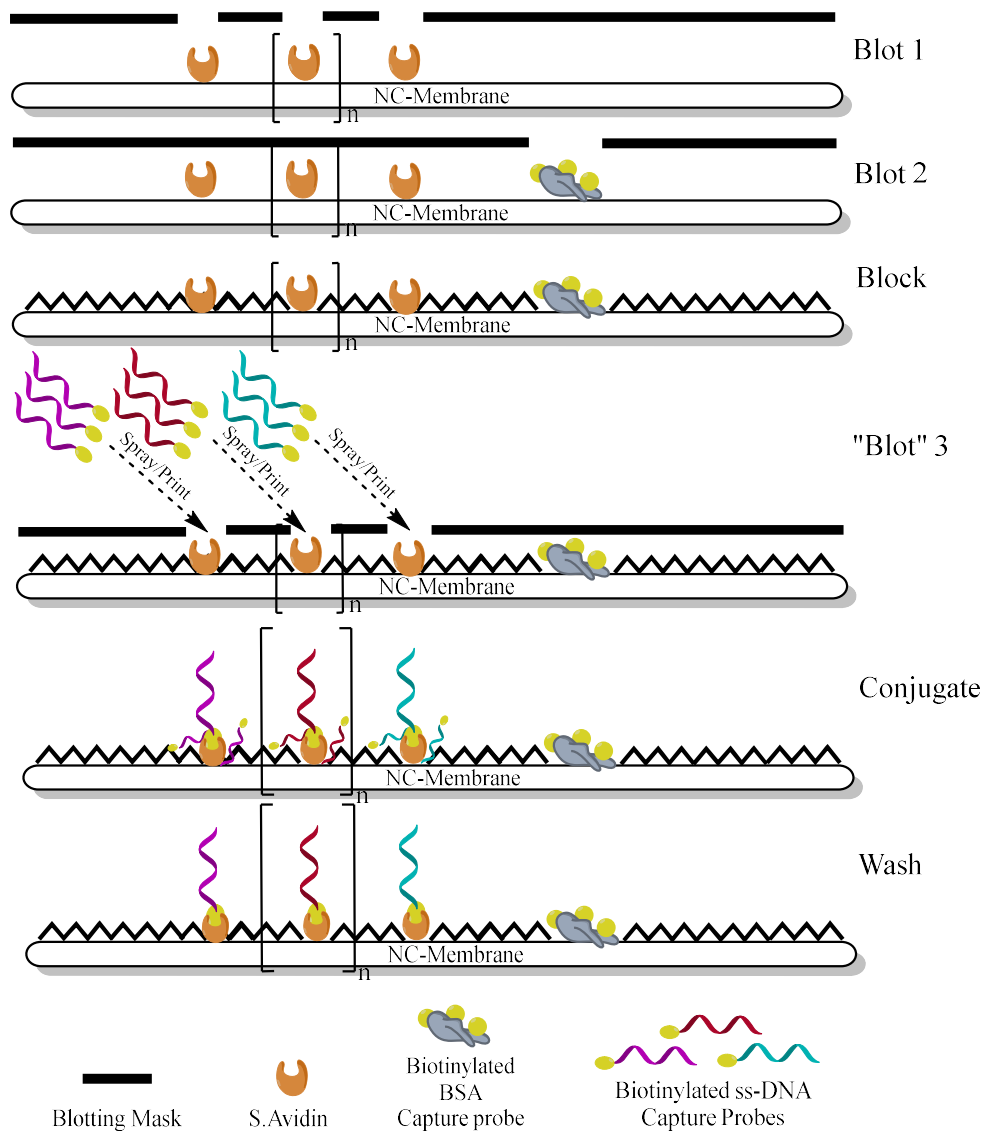


Figure 8.2. Shows the NALFA construction/probe immobilisation methodology utilising a nitrocellulose membrane.

Method 2 utilises positively charged nylon membranes, uses short polymeric guanine oligonucleotides as “clips” and effectively replaces Streptavidin to hold the capture probe in location via a polymeric cytosine tag. The membrane can be effectively blocked using only ds-DNA before precisely blotting the tagged capture probes in their respective location. One significant advantage of this approach is that the positively charged sides of the capture probe sequences and tags are repelled from the membrane surface during blotting, yielding advantageous surface structure and uniformity. Another advantage of such an approach is the lack of immunomolecular tags reducing the cost of materials and higher QC. However, such an approach comes with significant drawbacks. Firstly, the complexity of production using this stepwise manner as in method 1. Secondly, although robust, nylon membranes are expensive and particularly challenging to work with on small scales due to their charged nature. (Fig. 8.3).

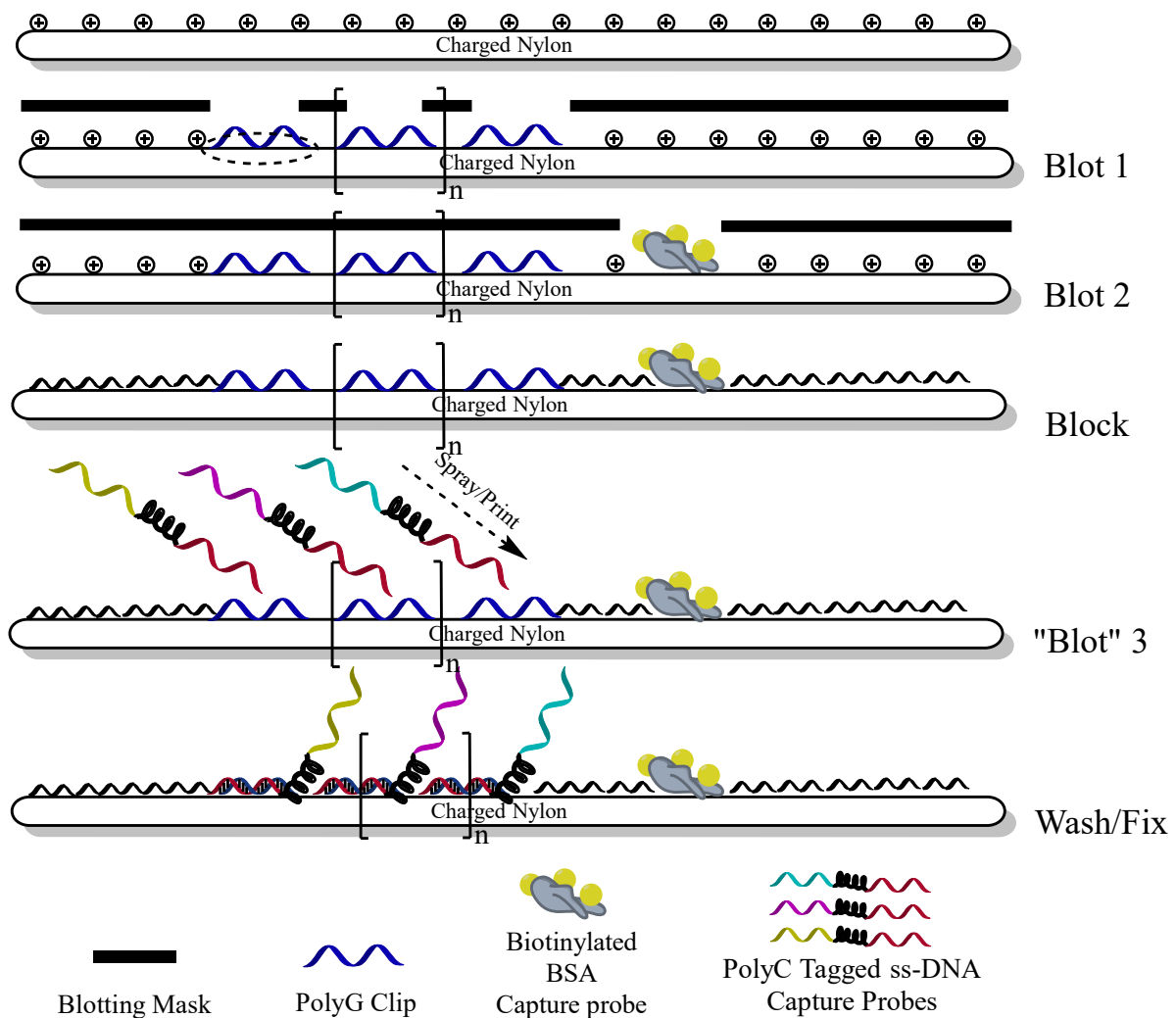


Figure 8.3. Shows the NALFA construction/probe immobilisation methodology utilising a charged nylon membrane.

Method 3 utilises a hydrophobic polyvinylidene fluoride membrane, uses C12 tagged capture probes directly blotted to the test membrane, meaning unlike methods 1 and 2, the construction is much similar to that of a traditional lateral flow device. Exploiting the hydrophilic nature of the membrane to repel the charged oligonucleotide sequences from the surface, allowing blocking of the membrane after all probe blotting. Another advantage to this approach is the lack of immunomolecular tags, reducing the cost of materials like method 2. However, PVDF membranes are particularly challenging to work with at any scale and require the use of organic solvents to blot or block. Another issue with such membranes is the poor flow performance with hydrophilic solvent mediums even when entirely blocked with a suitable reagent. Thus, such membranes would be excellent for mass production but extremely difficult to develop, especially considering the wealth of literature based on nitrocellulose membranes versus the limited extent of literature utilising such hydrophobic membranes in lateral flow applications. (Fig. 8.4)

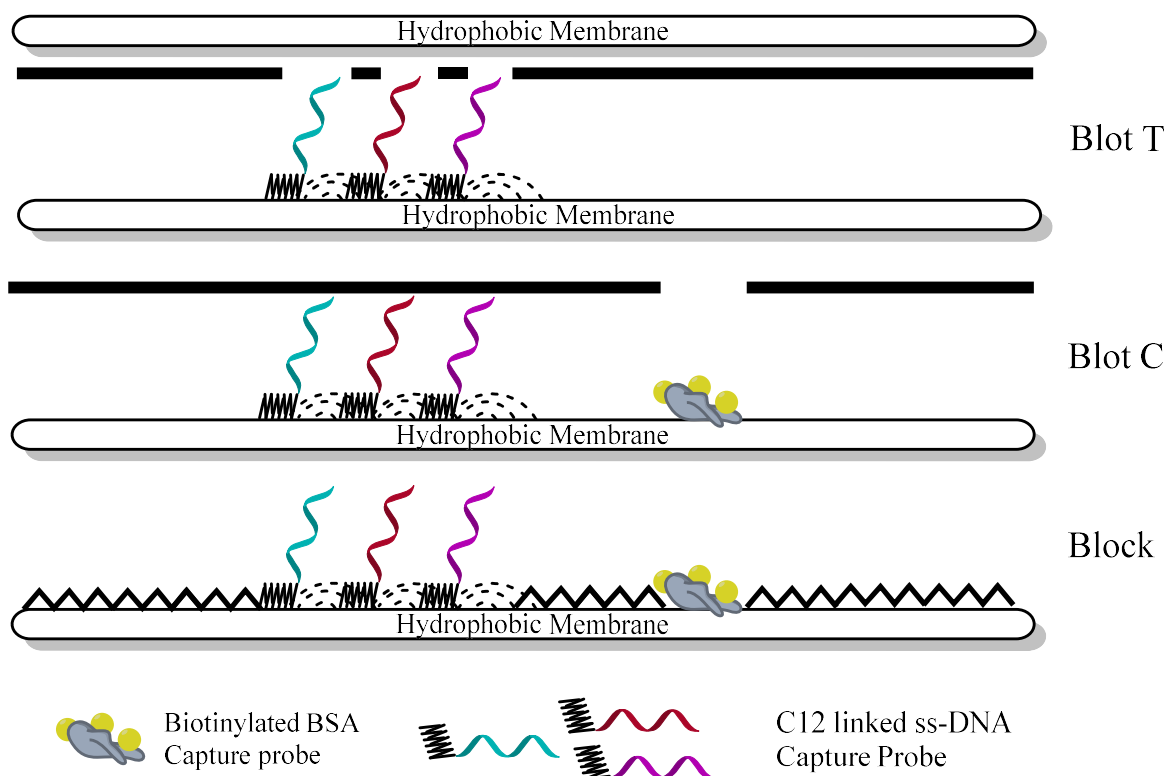


Figure 8.4. Shows the NALFA construction/probe immobilisation methodology utilising a PVDF membrane.

8.2 Membrane Blocking optimisation:

8.2.1 – Introduction to membrane blocking solution formulation.

To develop an effective lateral flow assay, correctly blocking assay materials is crucial to ensure desired surface interactions between analytes, reactants and probes with the materials used in the assay, i.e. membranes and conjugate materials. With membranes, in both cases, under or over-blocking can drastically degrade the overall performance of the system. (Fig. 8.5).

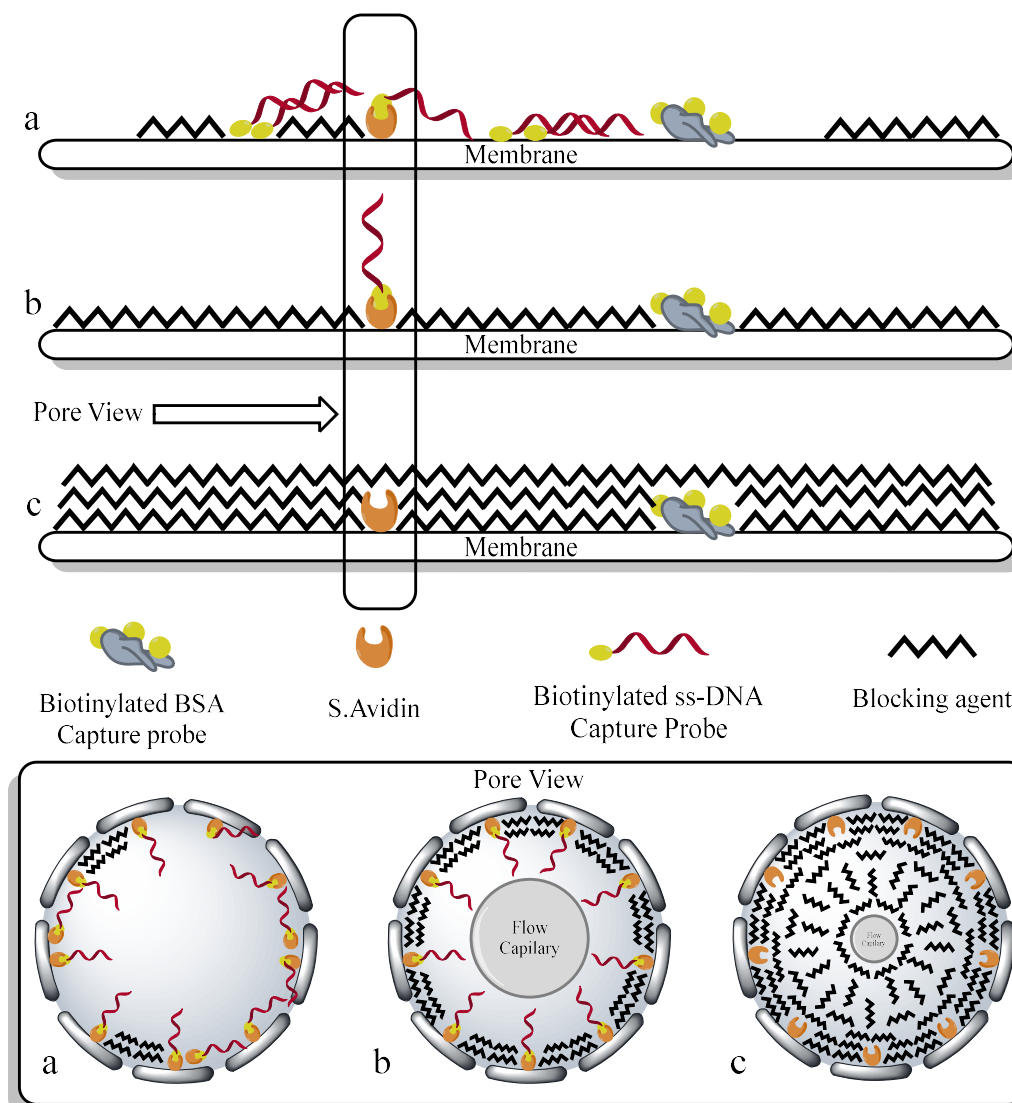


Figure 8.5. Shows graphically how under or over-applying blocking reagents can have the effect of allowing unwanted surface interactions, crowding/blocking active sites of probes or blocking membrane pores, and reducing analyte flow.

Therefore, before attempting any blotting or hybridisation experiments with any membrane, it is essential to optimise the blocking of the material first. Each material will require different blocking procedures to block the surface effectively, even within identical material types, namely the nitrocellulose membranes, due to the variability in flow rate and, by extension, pore size and effective surface area. To effectively optimise the blocking for each membrane used during the development of the NALFA, four possible blocking systems and their combinations were explored. Namely blocking using bovine serum albumen, casein, polyvinylpyrrolidone and UV-baked ds-DNA. For each membrane, titrations using each blocking system were carried out with varying concentrations of blocking agents to determine optimum conditions. Blocking performance was assessed by quantitative fluorometric measurements to determine the ss-DNA and protein adsorptivity of the blocked membrane. Additionally, the flow rate was checked using the industry standard procedure to determine that blocking had no adverse effects on membrane flow.

8.2.2 – Blocking solution development: Analyte Adsorptivity Measurement Methodology:

SS-DNA and protein adsorptivity measurements were run in triplicate and conducted at the bottom of 96 well plates. Membrane materials were backed with 0.1 mm PVC. Each well had a 6.5 mm disc of membrane material adhered to the bottom using clear resin epoxy diluted in methanol as the adhesive. Discs were cut using a 3D printed punch and die to drop the disc directly into the plate wells. Once adhered, membrane plates were activated using 250 μ L 6X SSC buffer for nitrocellulose and nylon membranes or 70 % methanol for PVDF membranes, sealed, incubated with gentle shaking for 30 mins, washed twice with 250 μ L ddH₂O and dried at 40 °C for 1 hour. Blocking solutions were made by diluting stock solutions to the appropriate concentration. BSA stock blocking solution was made by dissolving 0.4 g lyophilised BSA powder in 20 ml sterile 6X SSC buffer, pH adjusted to 7.2, then filtered using a 0.8 μ m cellulose acetate membrane. Casein stock blocking solution was made by adding 0.4 g to 8 ml ddH₂O and 500 μ L 0.1 M NaOH and sonicated for 1 hour at 50 degrees. 10 ml 12X SSC buffer was added, the solution pH adjusted to 7.8 and made up to 20ml with ddH₂O, then filtered using a 0.8 μ m cellulose acetate membrane. PVP Blocking solution was made by dissolving 0.4 g PVP-10 20 ml 6X SSC buffer and bath sonicated for 10mins at 40 degrees, pH adjusted to 7.2, then filtered using a 0.4 μ m cellulose acetate membrane. ds-DNA stock blocking solution was made by diluting 50 μ L 10 mg mL⁻¹ salmon sperm DNA solution in 25 ml 6X SSC buffer.

Blocking using BSA, Casein and PVP was carried out on the same plate for each membrane; 200 μ L of each solution was added to the respective well using dilutions of 20-2 mg mL⁻¹, plates sealed, incubated with gentle shaking for 4 hr at 40 °C, washed 3x with 200 μ L 6X SSC buffer, then rewashed 3x with 200 μ L ddH₂O. Blocking using ds-DNA was carried out on multiple membranes on a single plate.

To each well, 200 μL ds-DNA solution was added using dilutions of $20\text{-}2\text{ mg mL}^{-1}$, plates sealed and incubated with gentle shaking for 4 hr at 40°C . The ds-DNA solution was removed by pipette, and 50 μL 6X SCC buffer was added. The plate was irradiated with UV light from the top for 60s using a gel transilluminator. Each well was washed 3x with 200 μL 6X SCC buffer and 3x with 200 μL ddH₂O.

ss-DNA adsorptivity measurements were obtained by adding 15 μL 0.5 μM MecA Int 1-6 quencher-free fluorescent probe to each well, incubating for 1 hr at 37°C . Each well was washed 3x with 200 μL 6X SCC buffer and then refilled with 50 μL fresh 6X SCC buffer. Plates were immediately transferred to a ThermoScientific™ Varioskan™ LUX multimode microplate reader. Fluorescence measurements were taken using a 1s integral measuring time, with 515 ± 2 nm excitation light and fluorescence measured at 485 ± 5 nm. ss-DNA adsorptivity fluorescence was calibrated using internal standards for each membrane. Internal standards were prepared by adding 15 μL serial dilutions of MecA Int 1-6 quencher-free fluorescent probe to membrane discs and allowed to dry for 24 hrs at 20°C , and fluorescence measured identically to the test membranes. Protein adsorptivity measurements were then obtained by adding 15 μL fluorescent labelled BSA stain to each well, incubating for 1 hr at 37°C . Each well was washed 3x with 200 μL 6X SCC buffer and then refilled with 50 μL fresh 6X SCC buffer. Plates were immediately transferred to a 38°C pre-heated ThermoScientific™ Varioskan™ LUX multimode microplate reader. Fluorescence measurements were taken using a 1 s integral measuring time, with 515 ± 2 nm excitation light and fluorescence measured at 485 ± 5 nm. Protein adsorptivity fluorescence was calibrated using internal standards for each membrane. Internal standards were prepared by adding 15 μL serial dilutions of FITC-BSA solution to membrane discs and allowed to dry for 24 hrs at 20°C , and fluorescence was measured identically to the test membranes. Just as in the previous chapter the ss-DNA and protein adsorptivity curves were fitted using a standard 4-parameter Boltzmann regression function, *equation 9 (page 143)*. (*fig. 8.5*). The ideal concentration of each blocking reagent for a given membrane was then determined by finding the maxima of the second derivative of the adsorptivity curve using *equations 10-11 (page 143)*. (*fig. 8.6*).

Fluorescent labelled BSA was made by first dissolving 400 mg lyophilised BSA powder in 5 ml sterile 6X SSC buffer, pH adjusted to 7.2, then filtered using a 0.8 μm cellulose acetate membrane. 1 ml 1 mM FITC was added, and the solution pH was adjusted to 8.2 with 0.05 M NaOH, then sonicated at 37°C for 6 hours. The solution was loaded onto a PD10 desalting column and eluted in 500 μL aliquots of protease-free HPLC grade H₂O. Denaturing PAGE electrophoresis was used to identify the aliquots containing stained protein, and these aliquots were combined into a pre-weighed centrifuge tube, flash frozen in LN₂ and freeze-dried for 24 hr in a light-free chamber. 1 μM FITC-BSA solution, assuming an Mw 67 kDa, was made by dissolving 335 mg lyophilised FITC-BSA in 15 ml 6X SCC buffer.

8.2.3 Experimental Adsorptivity Results:

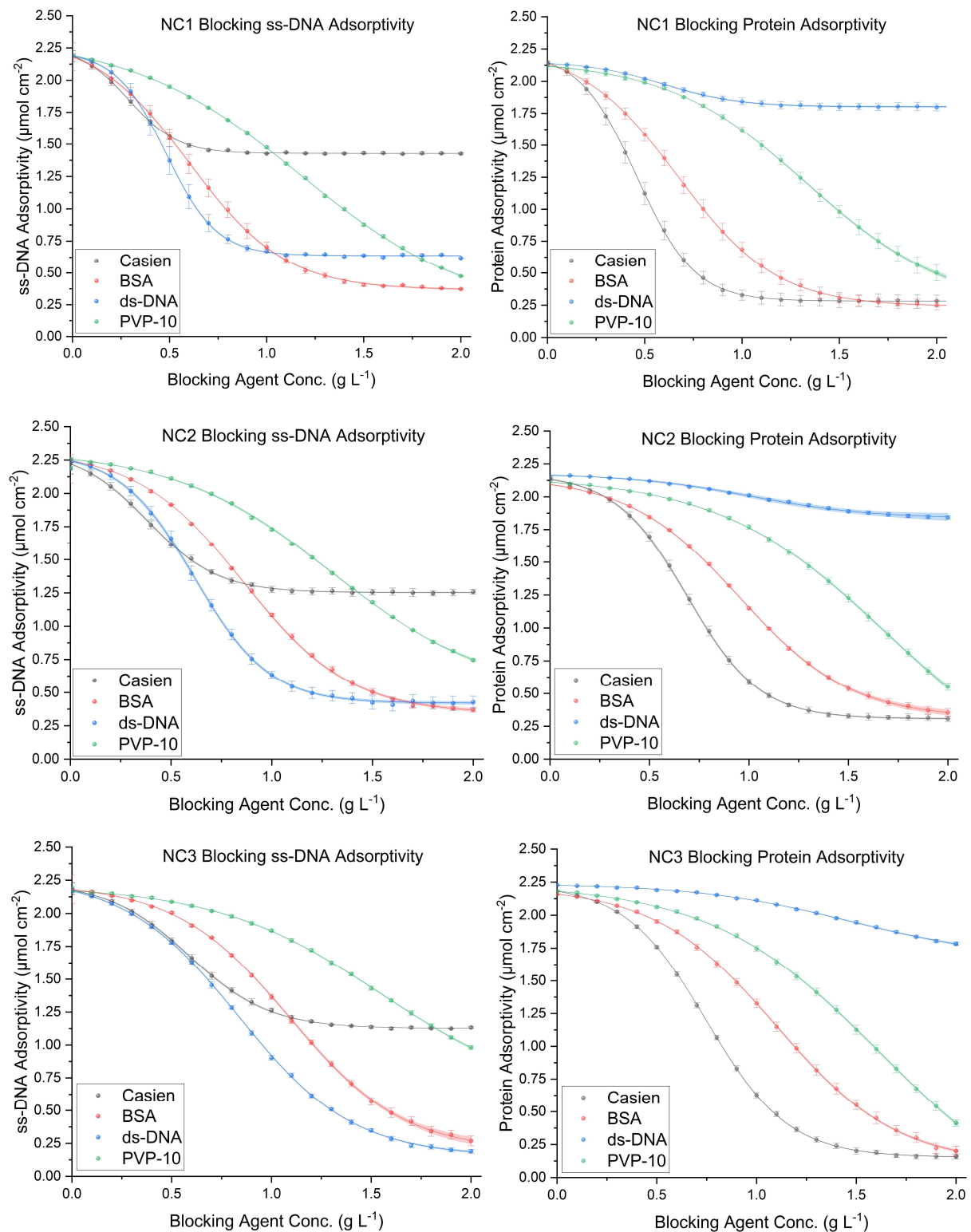


Figure 8.6. ss-DNA/protein membrane adsorptivity single reagent blocking titrations, NC1 (Millipore HF80+), NC2 (Millipore HF120+), NC3 (Millipore FF170 HP), Nylon (ThermoSci 0.45 μm Biodyne B), PVDF (Millipore Immobilon -P 0.45 μm PVDF).

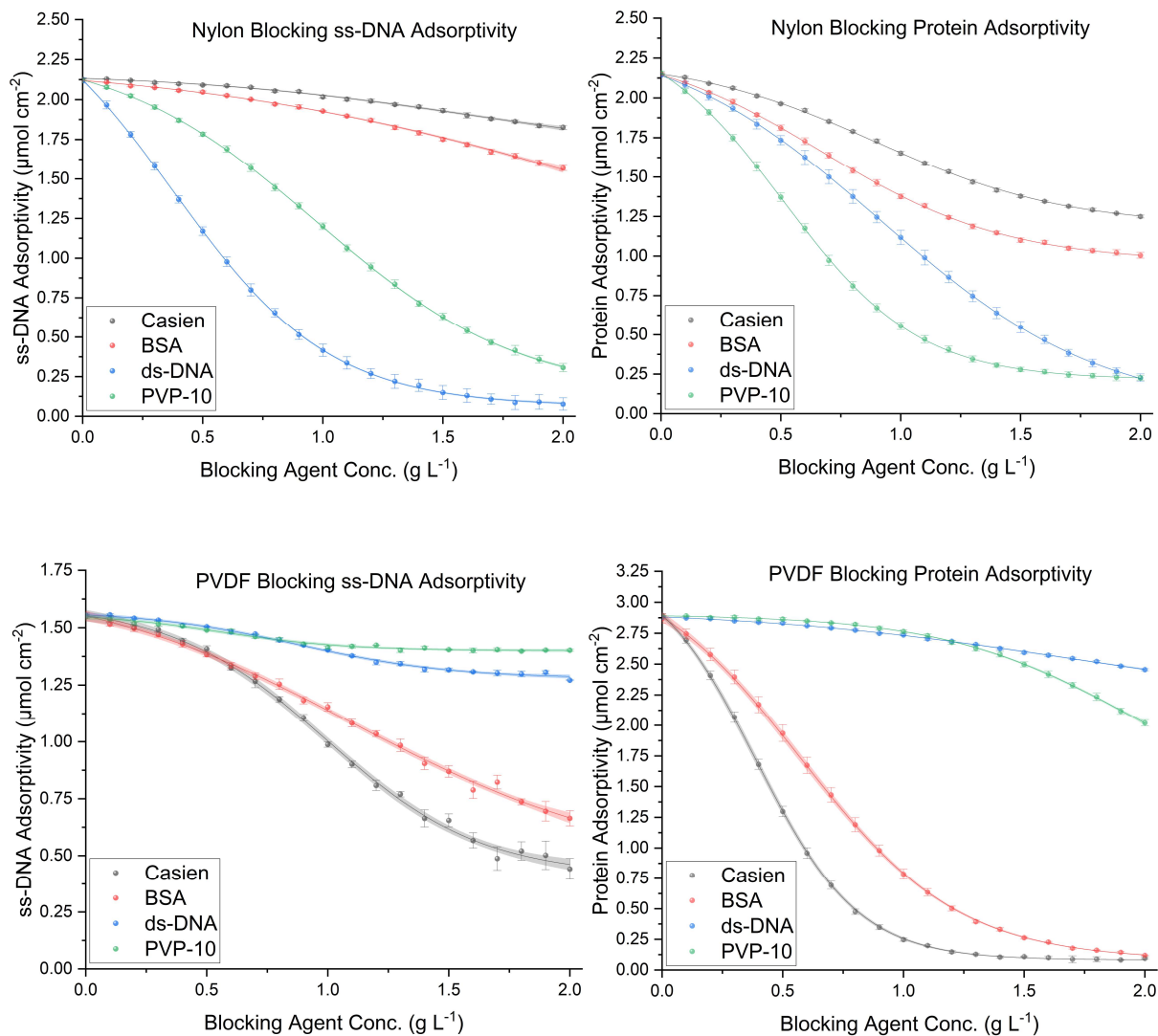


Figure 8.6. Continued ss-DNA/protein membrane adsorptivity single reagent blocking titrations, NC1 (Millipore HF80+), NC2 (Millipore HF120+), NC3 (Millipore FF170 HP), Nylon (ThermoSci 0.45 μm Biodyne B), PVDF (Millipore Immobilon -P 0.45 μm PVDF).

8.2.4 Experimental Adsorptivity Velocity Data – Ideal Blocking Reagent Concentrations:

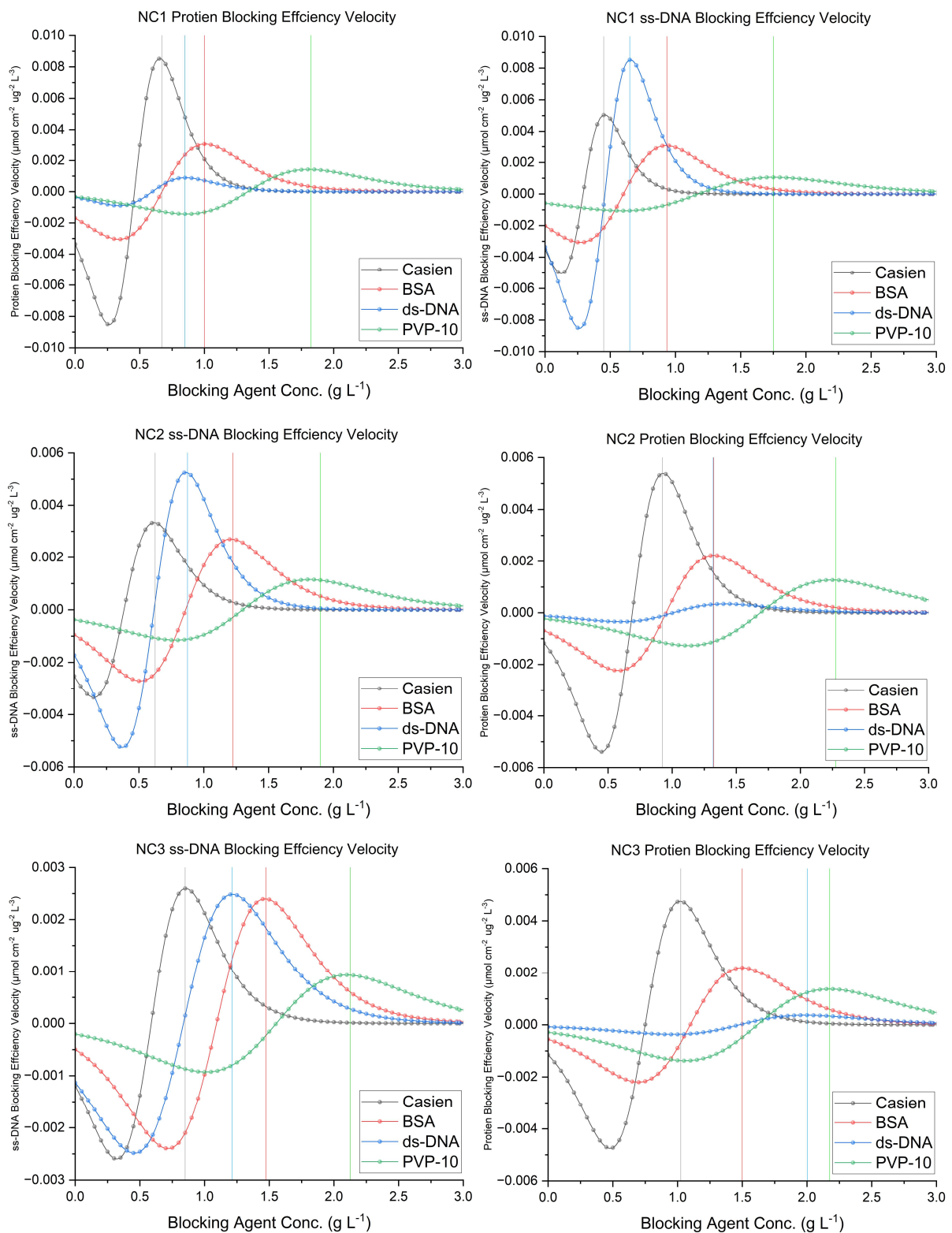


Figure 8.7. ss-DNA/protein membrane blocking efficiency velocity, NC1 (Millipore HF80+), NC2 (Millipore HF120+), NC3 (Millipore FF170 HP), Nylon (ThermoSci 0.45 µm Biodyne B), PVDF (Millipore Immobilon -P 0.45 µm PVDF).

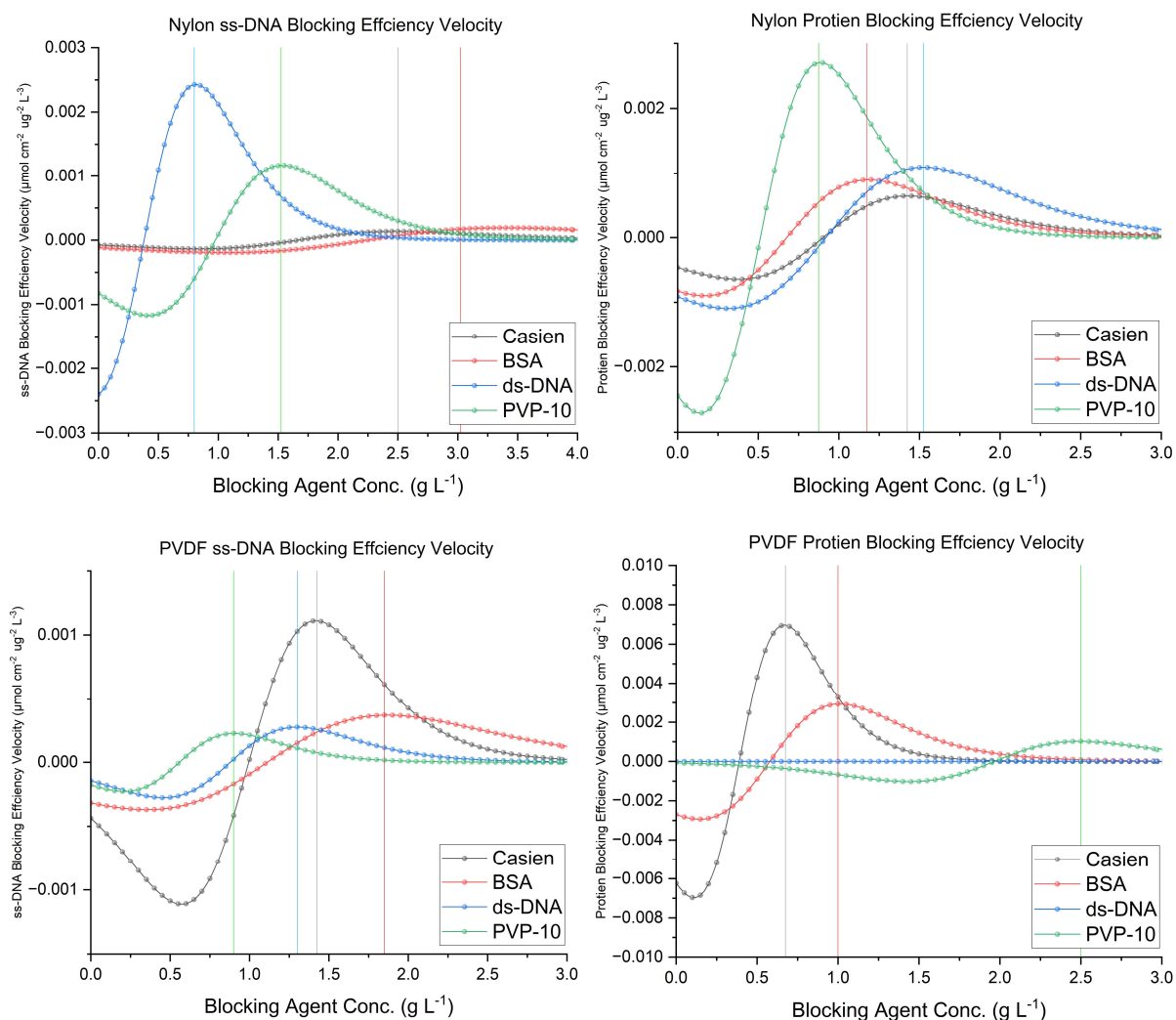


Figure 8.7. Cont. ss-DNA/protein membrane blocking efficiency velocity, NC1 (Millipore HF80+), NC2 (Millipore HF120+), NC3 (Millipore FF170 HP), Nylon (ThermoSci 0.45 µm Biodyne B), PVDF (Millipore Immobilon -P 0.45 µm PVDF).

8.2.4 Discussions and outcomes

The ideal concentration of each blocking reagent for a given membrane was then determined by finding the maxima of the second derivate of the adsorptivity curve as described by equations 10-11 (page 143). An average of the ideal concentrations of the derived DNA and protein data to formulate the final blocking solution. (Fig. 8.6-8.7, Tables 8.1-8.4).

Table 8.1. Optimal blocking agents' concentration for NC1 from fig. 8.6.

Rejected molecule	Blocking reagent	Optimal concentration (g L ⁻¹)
DNA	Casien	0.42
	BSA	0.93
	ds-DNA	0.61
	PVP-10	1.75
Protein	Casien	0.67
	BSA	0.83
	ds-DNA	1.06
	PVP-10	1.82
NC 1 Formulation	Casien	0.55
	BSA	0.88
	ds-DNA	0.84
	PVP-10	1.78

Table 8.2. Optimal blocking agents' concentration for NC2 from fig. 8.6.

Rejected molecule	Blocking reagent	Optimal concentration (g L ⁻¹)
DNA	Casien	0.62
	BSA	1.21
	ds-DNA	0.86
	PVP-10	1.9
Protein	Casien	0.91
	BSA	1.33
	ds-DNA	1.32
	PVP-10	2.27
NC 2 Formulation	Casien	0.77
	BSA	1.27
	ds-DNA	1.09
	PVP-10	2.09

Table 8.3. Optimal blocking agents' concentration for NC3 from fig. 8.6.

Rejected molecule	Blocking reagent	Optimal concentration (g L ⁻¹)
DNA	Casien	0.85
	BSA	1.47
	ds-DNA	1.21
	PVP-10	2.13
Protein	Casien	1.02
	BSA	1.5
	ds-DNA	2.01
	PVP-10	2.175
NC 3 Formulation	Casien	0.94
	BSA	1.49
	ds-DNA	1.61
	PVP-10	2.15

Table 8.4. Optimal blocking agents' concentration for Nylon from fig. 8.6.

Rejected molecule	Blocking reagent	Optimal concentration (g L ⁻¹)
DNA	Casien	2.5
	BSA	3.02
	ds-DNA	0.8
	PVP-10	1.52
Protein	Casien	1.43
	BSA	1.18
	ds-DNA	1.52
	PVP-10	0.87
Nylon Formulation	Casien	1.43
	BSA	1.18
	ds-DNA	1.16
	PVP-10	1.20

From the above data the following membrane blotting solutions were formulated and used for any membrane blotting operations for that given membrane unless stated otherwise:

- NC1 (Millipore HF80+) 1X blocking solution composed of 0.55 g L⁻¹ Casein, 0.88 g L⁻¹ BSA, 0.84 g L⁻¹ ds-DNA, 1.78 g L⁻¹ PVP-10.
- NC2 (Millipore HF120+) 1X blocking solution composed of 0.77 g L⁻¹ Casein, 1.27 g L⁻¹ BSA, 1.09 g L⁻¹ ds-DNA, 2.09 g L⁻¹ PVP-10.
- NC3 (Millipore FF170 HP) 1X blocking solution composed of 0.94 g L⁻¹ Casein, 1.49 g L⁻¹ BSA, 1.61 g L⁻¹ ds-DNA, 2.15 g L⁻¹ PVP-10.
- Nylon (ThermoSci 0.45µm Biodyne B) 1X blocking solution composed of 1.43 g L⁻¹ Casein, 1.18 g L⁻¹ BSA, 1.16 g L⁻¹ ds-DNA, 1.2 g L⁻¹ PVP-10.

The Millipore Immobilon -P 0.45 µm PVDF membrane proved challenging to work with and was difficult to block effectively against ss-DNA adsorption. During absorptivity measurements PVDF membranes when cut stretching or teared across the material. Furthermore, during drying steps, the material tended to release from the adhesive and curl. Additionally, the PVDF membrane proved significantly too adsorbent for a lateral flow application and required very high blocking reagent concentrations and blocking time. As a result, this severely affected the membrane flow making it unsuitable for lateral flowing large molecules. Furthermore, even when heavily blocked the membrane retained high affinity to ds-DNA thus the PVDF membranes were excluded from further development.

8.3 Membrane Blocking Time Optimisation:

8.3.1 Introduction:

In addition to optimising the composition of a membrane blocking solution, it is equally crucial to fine-tune the duration of the blocking soak. While allowing a membrane to soak in a blocking solution can effectively block it, an extended soaking time may also result in a decline in flow performance due to the aggregation of blocking agents, which can restrict the pores within the membrane structure. As shown previously in *figure 8.5*. This concern is particularly significant for slowly flowing membranes with small pore sizes, such as NC3.

8.3.2 Soak time titration procedures:

To determine the optimal blocking soak times for each membrane Total ss-DNA and protein adsorptivity measurements titrations were carried out. Again, these were run in triplicate and conducted at the bottom of 96 well plates. Membrane materials were backed with 0.1 mm PVC. Each well had a 6.5 mm disc of membrane material adhered to the bottom using clear resin epoxy diluted in methanol as the adhesive. Discs were cut using a 3D printed punch and die to drop the disc directly into the plate wells. Once adhered, membrane plates were activated using 250 μ L 6X SCC buffer sealed, incubated with gentle shaking for 30 mins, washed twice with 250 μ L ddH₂O and dried at 40 °C for 1 hour. Membranes were blocked using BSA, Casein, ds-DNA and PVP at ideal concentrations and carried out on the same plate for each membrane; 200 μ L of retrospective blocking solution, plates sealed, incubated with gentle shaking for 4 hr at 40°C, washed 3x with 200 μ L 6X SCC buffer, then rewashed 3x with 200 μ L ddH₂O. Plates were irradiated with UV light from the top for 60 s using a gel transilluminator. Each well was then washed 3x with 200 μ L 6X SCC buffer and 3x with 200 μ L ddH₂O and protein and ds-DNA absorptivity assessed at different time intervals. Flow rates were assessed by blocking a 5cm strip membrane using the same procedure and measuring flow rates at different soak time intervals. Flow rates were assessed using the industry standard 4 cm wick time by submersion in 1 cm of ddH₂O, flow rates were assessed in triplicate. (*Fig 8.8*)

8.3.3 Results and discussion:

From the experimental data it was evident that each membrane required significantly different blocking soaking times. It is also clear to see the drop in flow performance as the membrane becomes blocked. However, all membrane showed less than 10 % reduction in flow when fully blocked. As expected, the membranes with smaller pore sizes took the longest to block and also have their flow performance negatively impacted significantly sooner.

Optimal soaking times determined for each membrane are as follows:

- NC1 (Millipore HF80+): 1 hr 40 mins
- NC2 (Millipore HF120+): 2 hr 30 mins
- NC3 (Millipore FF170 HP) 3 hr 10 mins
- Nylon (ThermoSci 0.45 μm Biodyne B): 2 hr 50 mins

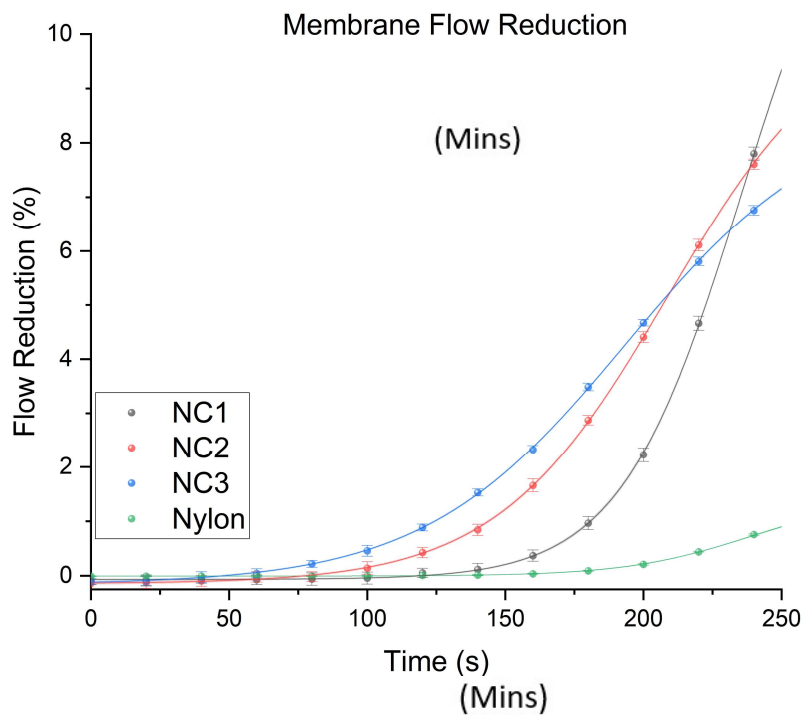
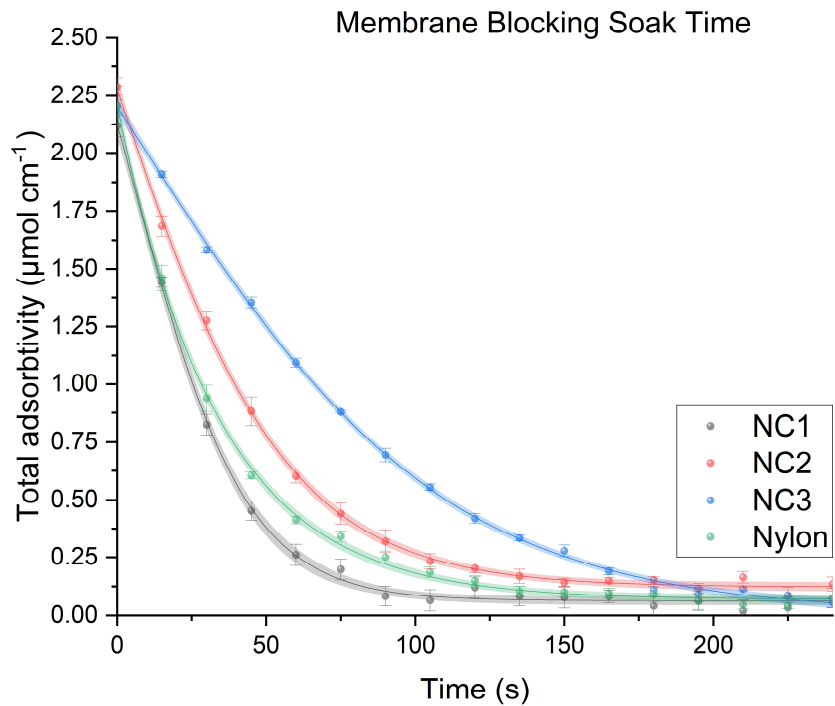


Figure 8.8. Membrane blocking time effect on total adsorbivity and capillary flow. NC1 (Millipore HF80+), NC2 (Millipore HF120+), NC3 (Millipore FF170 HP), Nylon (ThermoSci 0.45 μm Biodyne B).

8.4 Membrane Blotting Optimisation:

8.4.1 – Introduction.

To develop an effective lateral flow assay, correctly blotting the membrane is crucial to ensure maximum surface interactions between analytes, reactants, and probes. Under or over-blotting can drastically degrade the overall performance of the system. Under blotting reduces the assay LoD and visual clearness/ intensity of any test lines due to the reduced interaction sites. While over-blotting test lines can cause probe stripping via pore blockages, effectively filtering detection probes out of the flowing solution causing poor flow upstream of any blotted surface in the same way over-blocking can. Therefore, the blotting conditions must be considered and optimised to produce an effective assay for each bolted molecule, especially for nitrocellulose membranes with largely different pore structures.

8.4.2 – Optimisation Methodology:

To determine the correct capture probe loading concentrations fluorometric titrations were performed. Measurements were run in triplicate and conducted at the bottom of 96 well plates. Membrane materials were backed with 0.1 mm PVC. Each well had a 6.5 mm disc of membrane material adhered to the bottom using clear resin epoxy diluted in methanol as the adhesive. Discs were cut using a 3D printed punch and die to drop the disc directly into the plate wells. Once adhered, membrane plates were activated using 250 μ L 6X SCC buffer sealed, incubated with gentle shaking for 30mins, washed twice with 250 μ L ddH₂O and dried at 40 °C for 1 hour.

Fluorescent labelled biotinylated BSA was made by first dissolving 5 mg lyophilised biotinylated BSA powder in 1ml sterile 6X SSC buffer, pH adjusted to 7.2, then filtered using a 0.8 μ m cellulose acetate membrane. 1 ml 0.2 mM FITC was added, and the solution pH was adjusted to 8.2 with 0.05 M NaOH, then sonicated at 37 °C for 6 hours. The solution was loaded onto a low volume PD10 desalting column and eluted in 25 μ l aliquots of protease-free HPLC grade H₂O. Denaturing PAGE electrophoresis was used to identify the aliquots containing stained protein, and these aliquots were combined into a pre-weighed centrifuge tube, flash frozen in LN₂ and freeze-dried for 24 hr in a light-free chamber. Yielding 4.2 mg fluorescent labelled biotinylated BSA powder.

Blotting solutions were made by diluting stock solutions to the appropriate concentrations. Fluorescent labelled biotinylated BSA powder stock blotting solution was made by dissolving 4mg lyophilised biotinylated BSA powder and 400 mg lyophilised BSA powder in 4 ml sterile 6X TBS-SSC buffer made with 0.1 % Tween and 5 % MeOH, pH adjusted to 7.4. Streptavidin-FITC stock blotting

solution was made by dissolving 5mg lyophilised streptavidin-FTIC and 500mg lyophilised BSA powder in 5 ml sterile 6X TBS-SSC buffer made with 0.1 % Tween and 5 % MeOH, pH adjusted to 7.4. Each membrane was blotted using serial dilutions of each blotting solution to determine the optimum solution concentration. Serial dilutions were made with the addition of green loading dye to aid the application of the blotting solution to the membrane discs.

Blotting was performed by painting on the solution via nylon brush to fill the working volume of the membranes (1-1.5 μ L). Membrane discs were incubated for 4 hours at 37 $^{\circ}$ C with damp cotton wool cover the top of the plate. Membranes were then washed 3x with 200 μ L 6X SCC buffer, then rewashed 3x with 200 μ L ddH₂O. Plates were immediately transferred to a ThermoScientific™ Varioskan™ LUX multimode microplate reader. Fluorescence measurements were taken using a 1 s integral measuring time, with 515 \pm 2 nm excitation light and fluorescence measured at 485 \pm 5 nm.

8.4.3 – Results and discussion:

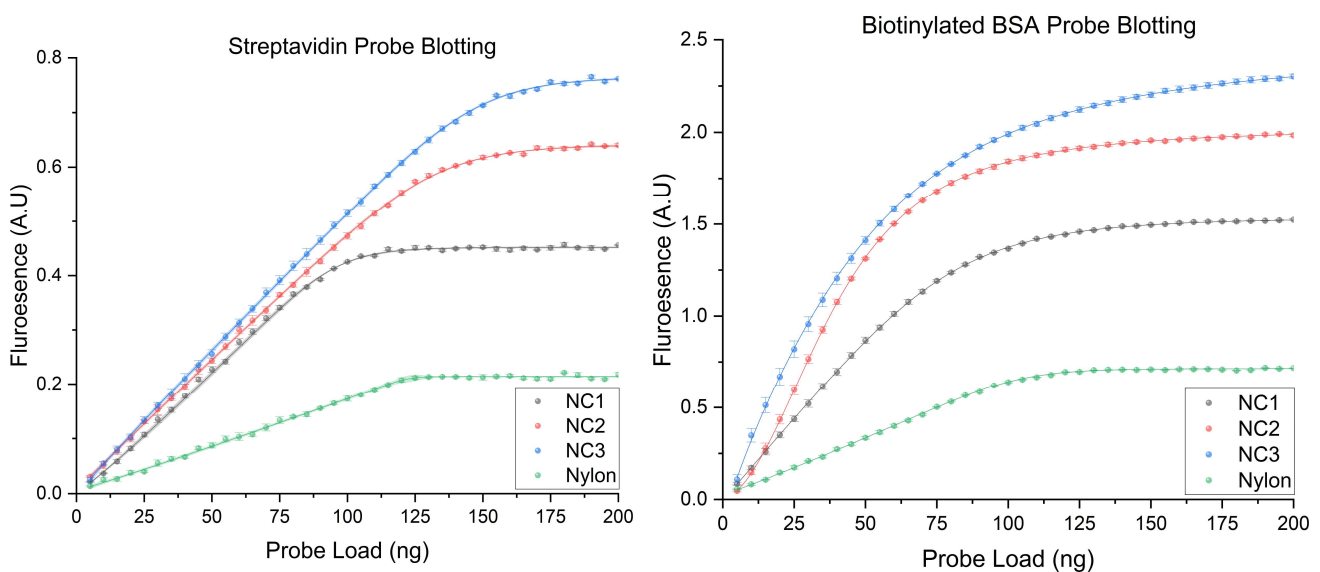


Figure 8.9. Probe blotting loading curves showing ideal blotting buffer loading. NC1 (Millipore HF80+), NC2 (Millipore HF120+), NC3 (Millipore FF170 HP), Nylon (ThermoSci 0.45 μ m Biotin B).

As expected, the membranes with the smallest pore size were able to bind significantly more capture probes due to the increased surface area. From the data above the following probe loading concentrations were determined. (Fig. 8.9)

Streptavidin:

- NC1 (*Millipore HF80+*): 100 ng ul⁻¹
- NC2 (*Millipore HF120+*): 130 ng ul⁻¹
- NC3 (*Millipore FF170 HP*) 150 ng ul⁻¹
- Nylon (*ThermoSci 0.45µm Biodyne B*): 125 ng ul⁻¹

Biotinylated BSA:

- NC1 (*Millipore HF80+*): 100 ng ul⁻¹
- NC2 (*Millipore HF120+*): 125 ng ul⁻¹
- NC3 (*Millipore FF170 HP*) 200 ng ul⁻¹
- Nylon (*ThermoSci 0.45µm Biodyne B*): 100 ng ul⁻¹

The nylon membrane was not selected for further analysis due to its inferior probe binding performance compared to nitrocellulose membranes. Furthermore, when examined the blotted nylon membranes exhibited considerable variability within single blots and between blotted batches when examined with a 534 nm laser. Consequently, no further optimisation or development of nylon membranes was pursued as they would not produce consistent test and control lines with good contrast.

8.5 Capture probe : Amplicon Hybridisation Optimisation:

8.5.1 –Introduction:

Optimisation of hybridisation conditions is crucial for the success of a NALFA assay. This involves maximising capture efficiency of the desired analyte and achieving the highest possible binding constant between the ss-DNA at the targeted location. By optimizing these hybridization conditions, the assay can be made as efficient as possible yielding the best LoD, dynamic range and selectivity. Key variables that should be controlled include buffer composition, pH, temperature, and post blotting/blocking membrane preparation. To find the initial conditions for each membrane a series of hybridisation condition titrations were performed using a synthetic truncated amplicon which comprised only of the amplicon side capture sequences, terminated with a C3 spacer. Hybridisation performance was assessed using an ethidium bromide hybridisation fluorometric assay.

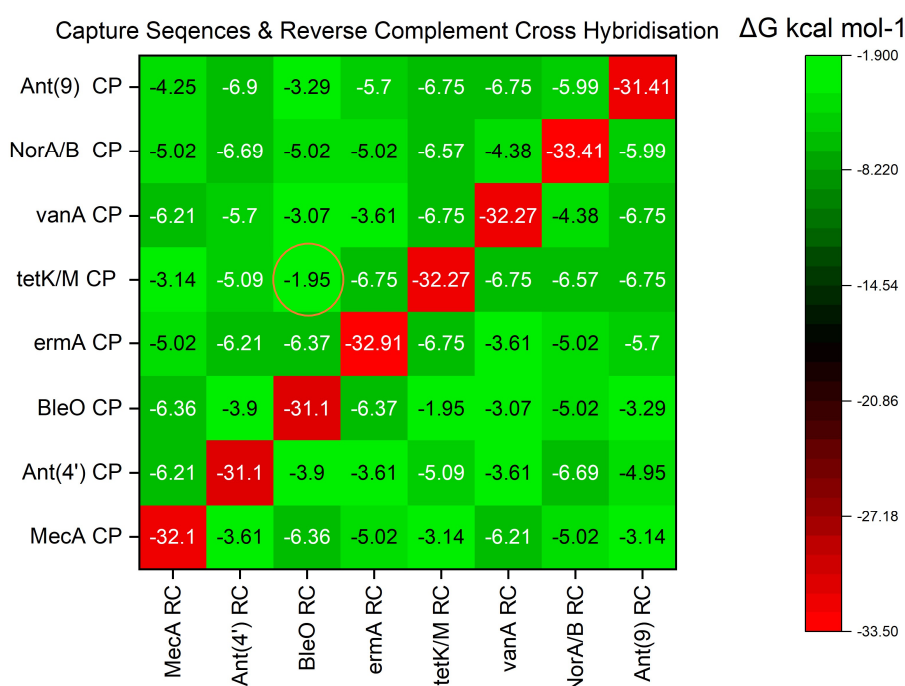


Figure 8.10 Heatmap showing calculated $-\Delta G_{\text{hybridisation}}$ between capture and reverse complement sequences. Reproduced from chapter 2, page 59.

This assay works by adding small amounts of ethidium bromide post hybridisation and measuring the fluorescence using 360nm light, with emission was measured at 620 nm. This is possible as ethidium bromide-ssDNA coil complexes have a drastically lower quantum yields to that of EtBr-dsDNA complexes with peak emission at 595 nm vs 610 nm. Therefore, for a system with

constant concentrations of ss-nucleic acids any increase in fluorescence is a direct result of hybridisation between strands. However, membranes must omit ds-DNA blocking to perform this assay, as any ds-DNA adhered to the membrane surface for blocking will drastically reduce the dynamic range of the measurement making it practically undetectable. While the addition of EtBr will affect the specific binding constants between the DNA strands, provided measurements are taken quickly and the EtBr solution is added post hybridisation with a wash step. The effects of altering hybridisation conditions on overall binding constants can still be seen, and semi-quantified by using non-complementary sets of ss-DNA sequences as references and taking a ratio of the two emissions under identical conditions. The reference values used for this experiment were obtained by using sequence pair BleO-CP and TetK/M-RC as the negative control to calculate the binding ratios. This set was chosen as they had the lowest cross hybridisation enthalpy's calculated in *Chapter 2, figure 1.15, page 59*. The conditions under study were temperature, pH, formamide concentration and ficoll concentration.

8.5.2 Fluorometric Titration Methodology:

For each condition under test hybridisation titrations were performed using fluorometric measurements run in triplicate and conducted at the bottom of 96 well plates. Membrane materials were backed with 0.1 mm PVC. Each well had a 6.5 mm disc of membrane material adhered to the bottom using clear resin epoxy diluted in methanol as the adhesive. Discs were cut using a 3D printed punch and die to drop the disc directly into the plate wells. Once adhered, membrane plates were activated using 250 μ L 6X SCC buffer sealed, incubated with gentle shaking for 30mins, washed twice with 250 μ L ddH₂O and dried at 40 °C for 1 hour.

Each membrane was blotted using the calculated streptavidin loading concentration for each membrane shown in *section 8.4*. Blotting was performed by pipetting 1 μ L of blotting solution into the centre of the membrane in 6X TBS-SSC buffer with 0.1% Tween and 5% MeOH, pH adjusted to 7.4. Membrane discs were incubated for 4 hours at 37 °C with damp cotton wool cover the top of the plate. Membranes were then washed 3x with 200 μ L 6X SCC buffer and rewashed 3x with 300 μ L 70% ethanol and dried with a stream of nitrogen.

Membranes were then blocked using BSA, Casein and PVP at calculated concentrations and soak times. 200 μ L of retrospective blocking solution with no ds-DNA was added to the membrane discs and incubated with gentle shaking for designated time at 40°C, washed 3x with 200 μ L 6X SCC buffer, then rewashed 3x with 200 μ L ddH₂O. Each well was then washed 3x with 200 μ L 6X SCC buffer, 3x with 200 μ L ddH₂O.

10 μL of biotinylated capture probe in 6x SCC buffer with 0.1 % w/v PVP-10, 0.05 % w/v SDS and 1 μM EDTA was added and left to conjugate for 10 mins at 20 $^{\circ}\text{C}$, then diluted with 100 μL 6X HPLC grade SCC buffer and left for 30 mins at 37 $^{\circ}\text{C}$. The biotinylated capture probe loading was 10 % of the calculated blotting concentration for each given membrane. Thus, giving a 1:10 dilution to allow the capture probes to be spread out from each other to prevent intermolecular interactions on the membrane.

Membranes were then washed 3 times with 100 μL of the hybridisation buffer under test to precondition for hybridisation. C3 & C12 truncated ss-DNA sequences were loaded by pipetting 10ul solution containing a 0.5 molar equivalent to blotted streptavidin : BSA 1:10 for that specific membrane and left to hybridise at varying temperatures for 1 hr at 100 % relative humidity. The membranes were then washed with 50 μL hybridisation buffer and irradiated with 255nm UV-light for 120 s at 10 mW cm^2 . 25 μL Hybridisation buffer was added followed by 5 μL EtBr-fluorometric solution (1 μL 5 mg mL^{-1} ethidium bromide, 50 mL 1X SCC) and irradiated with 255 nm UV-light for 3 s at 100 mW cm^2 , then washed 3x with 25 μL Hybridisation buffer. Membranes were excited with 360 nm light, and emission was measured at 620 nm. (Fig. 8.11).

8.5.3 Results and discussion:

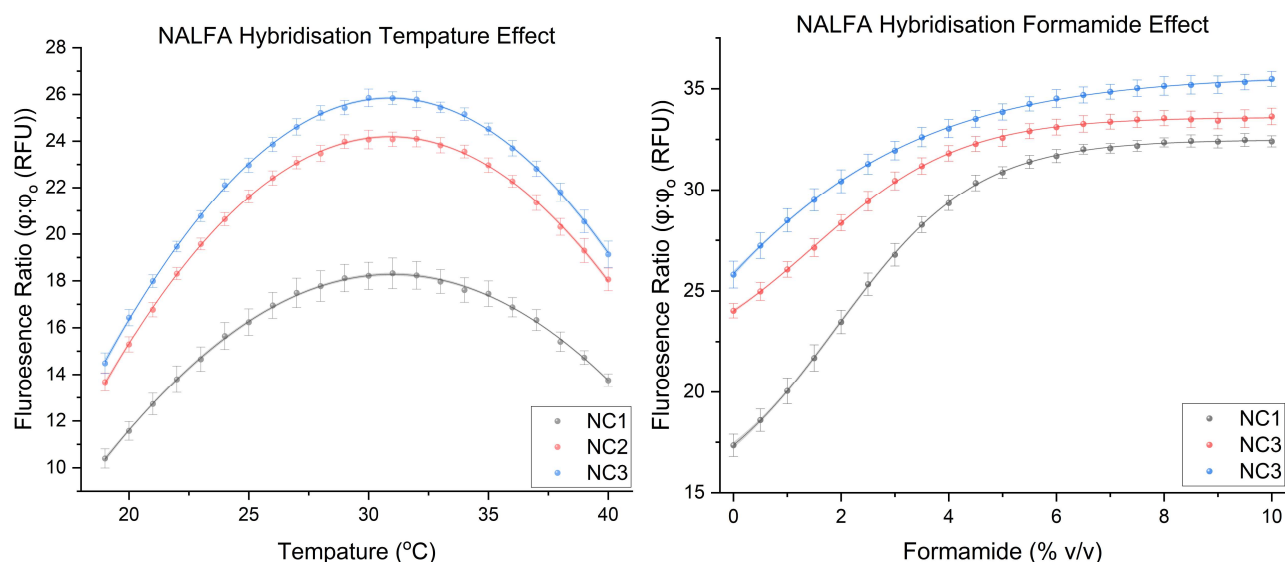


Figure 8.11. Temperature, pH, formamide concentration and ficoll concentration fluorometric hybridisation titrations. NC1 (Millipore HF80+), NC2 (Millipore HF120+), NC3 (Millipore FF170 HP), Nylon (ThermoSci 0.45 μm Biotodyne B).

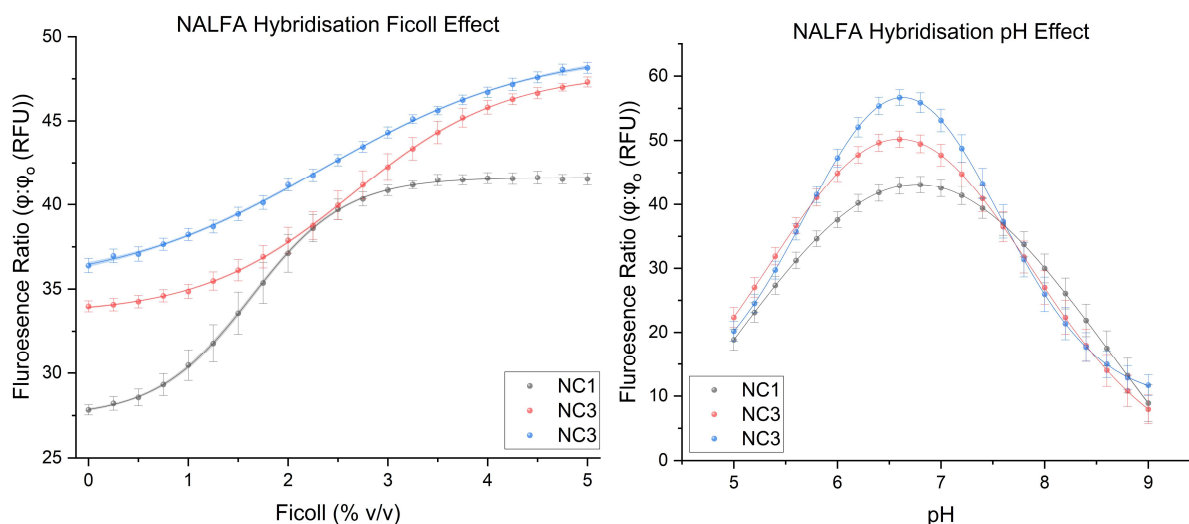


Figure 8.11. Cont. Temperature, pH, formamide concentration and ficoll concentration fluorometric hybridisation titrations. NC1 (Millipore HF80+), NC2 (Millipore HF120+), NC3 (Millipore FF170 HP), Nylon (ThermoSci 0.45 μ m Biodyne B).

The above titrations were run iteratively starting with adjusting the temperature during probe hybridisation with no additives at pH 7.4. Followed formamide additive concentration run at optimal temperature. Followed by Ficoll concentration with optimal [formamide] and temperature. Finally ending with the pH titration. In doing so you can clearly see the hybridisation ratio increase from one titration to the next. The membranes shared 3 optimal hybridisation conditions. Namely, a temperature of hybridisation of approximately 32 °C with 6.5 % formamide and a pH of approximately 6.75. Ficoll had the greatest effect on hybridisation ratio with NC1, which was expected as it has the largest pore size. Ficoll is an extremely large polymer which is used in liquid-based hybridisation assays to good effect. However, it is clear to see from the above titrations that it has a lesser effect in the confines of the smaller pore of NC2 and NC3. (Fig. 8.11). From, the data above the following hybridisation conditions for later experiments was formulated:

- NC1 (Millipore HF80+): 6x SCC buffer with 0.1% w/v PVP-10, 0.05% w/v SDS, 1 μ M EDTA, 6.5% v/v formamide, 3% v/v ficoll, at pH 6.9, 32 °C
- NC2 (Millipore HF120+): 6x SCC buffer with 0.1% w/v PVP-10, 0.05% w/v SDS, 1 μ M EDTA, 6.5% v/v formamide, 4.5% v/v ficoll, at pH 6.65, 32 °C
- NC3 (Millipore FF170 HP) 6x SCC buffer with 0.1% w/v PVP-10, 0.05% w/v SDS, 1 μ M EDTA, 6.5% v/v formamide, 5% v/v ficoll, at pH 6.75, 32 °C

8.6 - Full Membrane Lay-up and AuNP-detection:

8.6.1 - Introduction and aim:

Prior to laying up full lateral flow assays the detection system, and three candidate membranes was assessed using purified RPA amplicons and streptavidin conjugated AuNP's. Further assessed was which amplicon modification type performed best with the detection system C3 or C12 spaced primers. To do this the three membranes were tested using a hybridisation float test under their now determined ideal membrane construction and hybridisation conditions. To assess their performance the prepared membranes were floated on serial dilutions of real purified C3 and C12 amplicons allowed to hybridise, fixed, and then visualised using the AuNP reporter probes. In doing so the efficiency of the test zones capture efficiency can be assessed across membranes and amplicon types.

8.6.2 - Methodology:

RPA was run under optimised conditions in liquid phase using primer sets mecA₁₂-C₃. According to the manufacturer's instructions, mixtures were purified using Monarch® 5 µg PCR & DNA clean-up columns. The resulting products were further purified by 20 % non-denaturing TBE-DNA polyacrylamide gels run at 3 °C, 5 V cm⁻¹, in 1.25X TBE buffer for 2 hrs using the crush and soak method. Purification was done twice to ensure the purity of the assembled amplicon and eluted into a final volume of 500µL hybridisation buffer. Product concentration was quantified by EtBr fluorometric assay, purified RPA product was measured as a 10x dilution at 1.44±0.09 ng µL⁻¹, giving a total yield of 7.2 µg at a working concentration of 186 nM.

Detection membranes were activated using 6X SCC buffer sealed, incubated with gentle shaking for 30mins, washed twice with ddH₂O and dried at 40 °C for 1 hour. Each membrane was blotted, using the calculated streptavidin loading for each using the conditions detailed in the proceeding chapters; by pipetting 5ul of blotting solution into the centre of the membrane. Membrane strips were incubated for 4 hours at 37 °C at 100% RH. Membranes were then washed by submersion in 6X SCC buffer and rewashed in 70 % ethanol and dried with a stream of nitrogen. Membranes were then blocked using BSA, Casein, ds-DNA and PVP by floating on top of retrospective blocking solution and incubated with gentle shaking for designated time at 40 °C, washed by submersion in 6X SCC buffer, then rewashed 3x ddH₂O.

Membranes were soaked with 0.1 µM biotinylated MecA capture probe in 6x SCC buffer with 0.1 % w/v PVP-10, 0.05 % w/v SDS and 1 µM EDTA and left to conjugate for 10 mins at 20 °C, then floated

on 6X HPLC grade SCC buffer for 30 mins at 37 °C. Membranes were then washed 3 times by submerging in 0.5 µM d-biotin solution followed by soaking in hybridisation buffer for 10mins.

Membranes were then floated on serial dilutions of MecA₁₂-C3 & MecA₁₂-C12 amplicon in each membranes optimal hybridisation buffer determined in *section 8.4* for 20 mins at 30 °C with gentle shaking. Membranes were then drip dried and immediately submerged in 0.5 OD 20 nm streptavidin conjugated AuNP's in 0.5X hybridisation buffer for 5 mins, drip dried and irradiated with 255 nm UV-light for 3 s at 100 mW cm⁻² then bath sonicated in 0.5X hybridisation buffer for 5 s to remove excess AuNP's. (*Fig. 8.12 – 8.13*).

8.6.3 -Results and discussion:

The first and clearest observation to be made from the presented membranes shown in *figure 8.12 and 8.13*; is the performance difference between the C3 spaced and C12 spaced amplicons. While the C3 spaced amplicon produced clear and consistent test spots on each membrane; the same was not observed with the C12 spaced amplicons. Furthermore, when attempting to capture C12 spaced amplicons on NC3 no test spots could be discerned from the negative control. This experiment was repeated twice and still NC1 was unable to capture any amplicon even at the highest concentration available. NC2 and NC3 did manage to produce very faint positive test spots when soaked with C12 amplicon but the contrast was extremely poor across the concentration ranges. In contrast, the C3 spaced amplicons demonstrated exceptionally clear and well-contrasted positive test spots, with the intensity of these spots directly correlating with the concentration of C3 amplicons available for hybridization. The test-to-negative control spot contrast remained sufficient, down to the lowest tested concentration of 1 femtomolar (1 fM), for NC3, and down to 10 femtomolar (10 fM) for NC2. Notably, since the membranes were constructed identically for both C3 and C12 experiments, it is evident that there is an issue with the C12 spaced amplicons.

The most likely explanation for this issue was hypothesized to be the capture sequence becoming not remaining presentable following amplification. This hypothesis finds support in the clear kinetic evidence presented in *chapter 6*, which shows that C12 spaced primer sequences performed noticeably worse in the RPA amplification reactions. Initially, it was theorized that larger spacers might result in improved amplification and detection, as the increased spacing between functional nucleic acid sequences would reduce potential cross-interactions between the amplification and detection processes. An intriguing avenue for further optimization and research would involve repeating this experiment using piecewise synthesized model amplicons. This approach would help exclude the impact of amplification reactions on spacer lengths, allowing for a more comprehensive exploration of spacer effects.

NC3



Negative
Control

1fM

10fM

100fM

1pM

10pM

100pM

1nM

NC2



Negative
Control

1fM

10fM

100fM

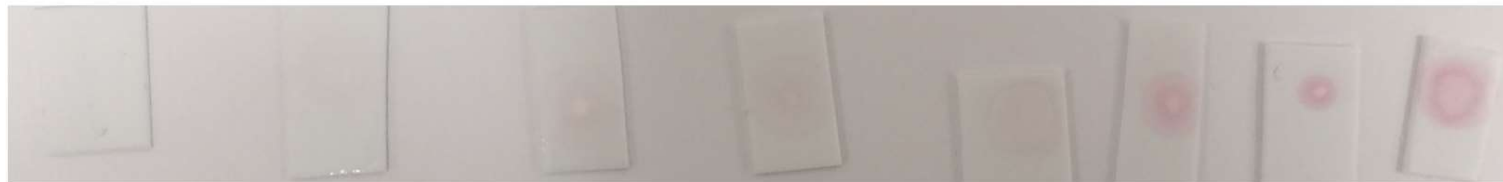
1pM

10pM

100pM

1nM

NC1



Negative
Control

1fM

10fM

100fM

1pM

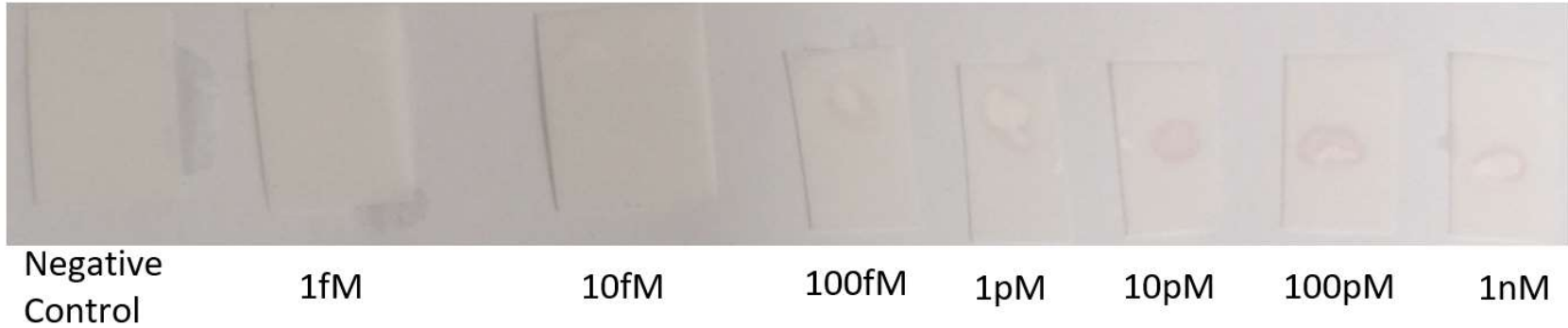
10pM

100pM

1nM

Figure 8.12. Fully optimised test membrane layouts hybridised with *MecA12-C3* amplicon, producing >1 femtomolar limit of detection. NC1 (Millipore HF80+), NC2 (Millipore HF120+), NC3 (Millipore FF170 HP).

NC3



NC2

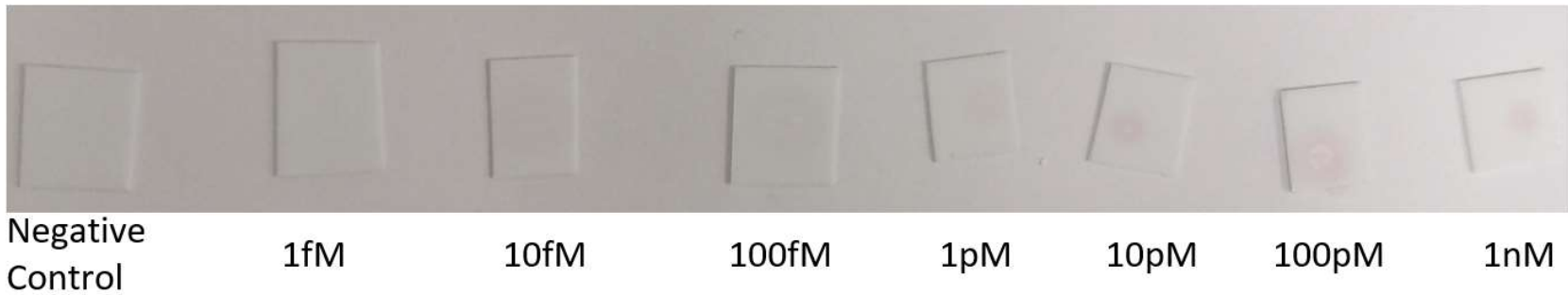


Figure 8.13. Fully optimised test membrane layouts hybridised with Meca12-C3 amplicon, producing >10pM femtomolar limit of detection. NC1 (Millipore HF80+) omitted as membranes failed to detect any concentrations below 1nM, NC2 (Millipore HF120+), NC3 (Millipore FF170 HP).

8.7 Initial full NALFA layups:

8.7.1 - Introduction and aim:

Building on the preliminary experiments detailed in this chapter, we progressed to the assembly of complete lateral flow devices with all the functional components in situ on device. These full-fledged lateral flow assays were developed using Millipore FF170 HP and Millipore HF120+ membranes. Given the number of practical hours required to construct the devices by hand, and the poor performance of NC1 in the previous section, the NC1 membrane was not further assessed. We evaluated the performance of these assays by employing 50 μ L reaction liquors from MecA₁₂-C3 RPA reactions that had undergone purification through clean-up columns.

During this assessment, we utilized the cleaned reaction liquors instead of the raw RPA reaction liquors as our test samples. The central objective of this evaluation was to determine the lateral flow device's proficiency in detecting the desired amplicons, especially when tested alongside reactions that incorporated negative controls. At this stage, our focus was primarily on assessing the system's sensitivity to the presence of the target amplicons, as opposed to evaluating its robustness against reaction impurities.

8.7.2 - Methodology:

RPA was run under enhanced solid phase conditions in solid phase matrix using the developed standard procedure and eluted manually by double tube centrifugation. Positive control reactions were run using 100k copies of MRSA reference gDNA, while negative controls were run using 1M copies K-12 *E. coli* reference DNA and 100k copies of origin unknown MSSA gDNA. Both control gDNA templates were extracted using the same described method for extracting MRSA gDNA found on *page 69*.

Lateral flow assays were constructed by first preparing membranes. Membranes were backed with 0.4mm PVC then cut using fresh razor blade per cut in approximately 0.5cm strips. Membranes were activated by submersion in 6X SCC buffer with 0.05% w/v SDS and incubated with gentle shaking for 30mins, washed twice with ddH₂O and dried at 40 °C for 1 hour. Each membrane was blotted thrice with streptavidin using a nylon brush and a 3D printed stencil. Membrane strips were incubated for 1 hour at 37 °C under 100 % RH between blots. Membranes were then washed by submersion in 6X SCC buffer and rewashed in 70% ethanol then dried with a stream of nitrogen. Membranes were then blocked by floating on top of the respective blocking solution and incubated with gentle shaking for designated time at 40 °C, washed by submersion in 6X SCC buffer, then rewashed 3x ddH₂O.

Membranes were then soaked with 0.1 μM biotinylated MecA capture probe in 6x SCC buffer with 0.1 % w/v PVP-10, 0.05 % w/v SDS and 1 μM EDTA and left to conjugate for 10 mins at 20 °C, then floated on 6X HPLC grade SCC buffer for 30 mins at 37 °C. Membranes were then washed 3 times by submerging in 0.5 μM d-biotin solution and thrice washed in ultrapure HPLC water. Membranes were allowed to dry to a dampness then flash frozen by submersion in Liquid N₂ and transferred to a freeze dryer in a light free container and dried for 24 hrs. Cellulose sample pads, glass fibre conjugate pads and wicking pads were then cut in 2 cm, 1 cm and 3 cm strips respectively and blocked using NC3 2X blocking solution by submersion at 40°C with gentle shaking for 16hrs. Pads were irradiated with UV light for 60 s using a gel transilluminator then dried at 40°C 1hr. Sample pads were then soaked in 6X SCC buffer, drip dried, submersion in Liquid N₂ and transferred to a freeze dryer in a light free container and dried for 24 hrs. Conjugate pads were then soaked 0.1 OD 20 nm streptavidin conjugated AuNP's, drip dried, submersion in Liquid N₂ and transferred to a freeze dryer in a light free container and dried for 24hrs. NALFA strips were then constructed using a 0.5cm overlap between pads in the industry standard configuration. Pad contact was insured by pressing strips in a 3D printed jig at 200 kg via a hydraulic press for 10 s. Strips were run in a reusable 3D printed housing which provided gentle pressure on pad interfaces to insure consistent wicking and flow performance.

For positive reactions liquors were eluted off the solid phases on to clean-up columns and eluted following clean up using 50 μL hybridisation buffer versus native reaction which were left unpurified. Samples were then added to the lateral flow strips and allowed to wick for 30mins. Once completed assays were drip dried and irradiated with 255nm UV-light for 3 s at 100 mW cm^{-2} then bath sonicated in 0.5X hybridisation buffer and washed in ddH₂O dried for 1 hr at 40 °C.

8.7.3 – Results and discussion:

Both of the produced test trips successfully detected the presence of mecA-C3 amplicon successful and reported in situ on both the test and control lines after approximately 10mins before fully developing after 30mins following washing. (Fig. 8.14). Negative control test lines remained clear for both the produced lateral flow strips showing the specificity of the combined RPA-LFA system. The lateral flow strips unitising NC3 significantly outperformed NC2. The likely cause of this observed result is down to membrane flow rate. In section 8.5 both NC3 and NC2 had similar performance, however of key difference between the experiments in section 8.5 and these experiments is the flow direction of the analyte. In section 8.5 the amplicons are not being flowed through the membrane and thus had ample time to hybridise to the capture probe. In this experiment it is clear to see the slower flow rate of NC3 provided more time for amplicon hybridisation yielding a significantly darker reported test line,

this is especially true when noting the control line contrasts were relatively consistent across later flow strips. (Fig. 8.14).

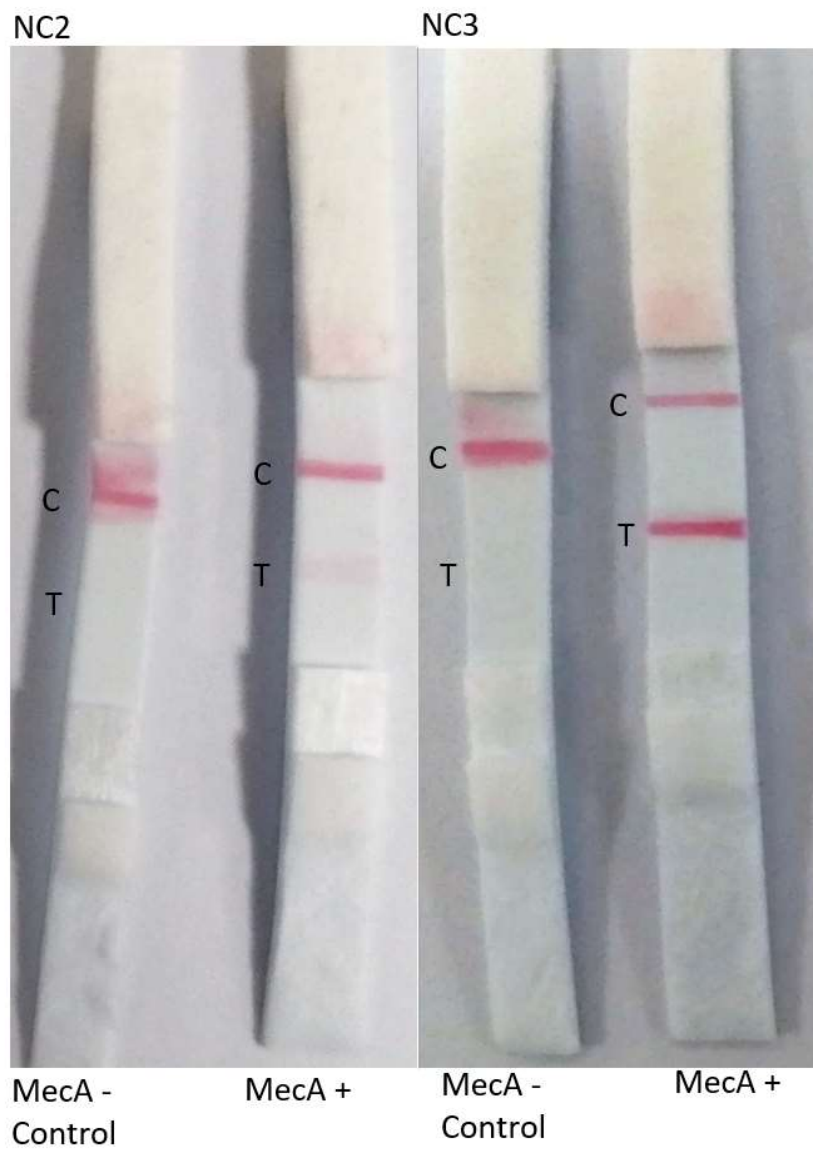


Figure 8.14. Fully optimised RPA-NALF coupled assays showing selective detection of the *MecA* gene.
NC2 (Millipore HF120+), NC3 (Millipore FF170 HP).

8.8 Final NALFA Layup:

8.8.1 - Introduction and Objective:

Following the successful demonstration of selective MecA gene detection using magnetically enhanced solid-phase RPA coupled with the novel NALF, this experiment aims to establish the Limit of Detection (LoD) for the presented system. Building upon preliminary experiments, we constructed a complete lateral flow device using the optimal procedure conditions and materials discussed earlier. To assess the system's limits of detection, these assays utilized MecA₁₂-C3 enhanced solid-phase RPA reactions with serial dilutions of MRSA gDNA as a template, going as low as 1 genomic copy.

8.8.2 - Methodology:

Lateral flow assays were developed using only Millipore FF170 HP membranes, as described in section 8.6.2. The LoD of the hybrid system was evaluated using unprocessed MecA₁₂-C3 50 µL solid particle-enhanced solid-phase RPA reaction liquors. Enhanced solid phase RPA reactions pads were cut into two equal pieces, one half was eluted centrifugally then purified using Monarch[®] 5 µg PCR & DNA clean-up columns then evaluated using 20 % non-denaturing TBE-DNA polyacrylamide gels run at 3 °C, 5 V cm⁻¹, in 1.25X TBE buffer for 2 hrs. Gels were stained by soaking in EtBr stain (0.5 µg ml⁻¹ EtBr in 1X TBE) for 5mins, rinsed and visualised using transmissive UV light. The other half of the RPA reaction eluted onto the tests strip by placing it on top of the sample pad and pressed inside the 3D printed housing, then eluted by adding 25 µL 2X hybridisation buffer and allowed to wick for 30mins. Once complete assays were drip dried and irradiated with 255nm UV-light for 3 s at 100 mW cm⁻² then bath sonicated in 0.5X hybridisation buffer and washed in ddH₂O dried for 1 hr at 40 °C. (*fig. 8.15*).

8.8.3 – Results and discussion:

The developed device exhibited outstanding performance, consistently producing distinct and well-contrasted test and control bands across all positive RPA reaction mixture samples. The Limit of Detection (LoD) for the combined system demonstrated its capability to consistently detect down to a single genomic copy when exclusively run in solid phase. However, while it remained visually discernible following thorough washing and observation under adequate lighting down to 1 genomic copy when compared to a negative control reference, the LoD in real-world conditions was approximately 20 genomic copies of MRSA DNA.

This discrepancy could likely be improved, considering the handmade nature of the present lateral flow strips, which led to variations in test and control line widths. With the implementation of modern reel-to-reel production techniques, it would be feasible to enhance the system's contrast down to the demonstrated potential of a 1 genomic copy detection region, particularly in cases where such high sensitivity is a requirement.

Furthermore, it's worth noting that the presented lateral flow device proved to be capable of detecting the presence of completed amplicons beyond the visualization limit of DNA-PAGE, highlighting its effectiveness in practical diagnostic applications.

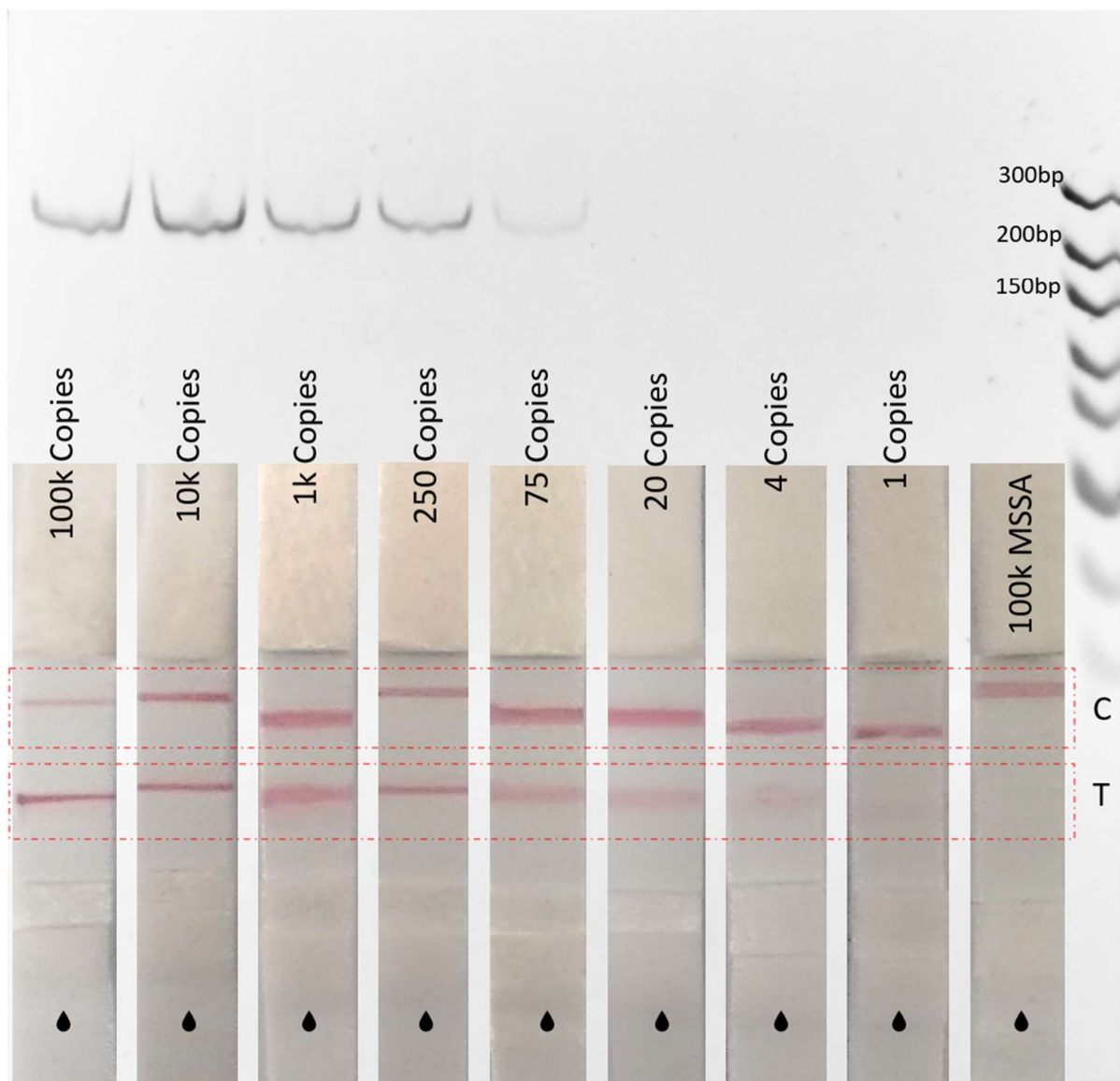


Figure 8.15. Fully optimised SP-RPA-NALF coupled assay showing LoD detection for the *MecA* gene.

References

“Nothing to see here.... Move along...”

- 1 M. Masalha, I. Borovok, R. Schreiber, Y. Aharonowitz and G. Cohen, *J Bacteriol*, 2001, **183**, 7260–7272.
- 2 A. Pantosti and M. Venditti, *European Respiratory Journal*, 2009, **34**, 1190–1196.
- 3 R. H. Deurenberg, C. Vink, S. Kalenic, A. W. Friedrich, C. A. Bruggeman and E. E. Stobberingh, *Clinical Microbiology and Infection*, 2007, **13**, 222–235.
- 4 J. W. Bigger, *The Lancet*, 1944, **244**, 497–500.
- 5 C. H. Rammelkamp and T. Maxon, *Experimental Biology and Medicine*, 1942, **51**, 386–389.
- 6 H. Grundmann, M. Aires-de-Sousa, J. Boyce and E. Tiemersma, *Lancet*, 2006, **368**, 874–885.
- 7 E. Principle, *Br Med J*, 1959, 658–662.
- 8 P. ACRED, D. M. BROWN, D. H. TURNER and D. WRIGHT, *Br J Pharmacol Chemother*, 1961, **17**, 70–81.
- 9 G. K. Daikos, P. Kourkoumelikontomichalou and A. Paradelis, *Br.Med.J.*, 1960, **2**, 1668.
- 10 A. O. Okesola, A. A. Oni and R. A. Bakare, 1999, **41**, 74–75.
- 11 E. Calderón-Jaimes, L. E. Espinosa De Los Monteros and R. Avila-Beltrán, *Salud Publica Mex*, 2002, **44**, 108–112.
- 12 G. R. Nimmo, J. M. Bell, D. Mitchell, I. B. Gosbell, J. W. Pearman and J. D. Turnidge, *Microb Drug Resist*, 2003, **9**, 155–60.
- 13 H. Bin Kim, W. B. Park, K. D. Lee, Y. J. Choi, S. W. Park, M. don Oh, E. C. Kim and K. W. Choe, *J Clin Microbiol*, 2003, **41**, 2279–2281.
- 14 A. M. Shibl, A. F. Tawfik and A. M. Khan, *J Antimicrob Chemoth*, 1994, **33**, 1255–1257.
- 15 M. B. D. J. Diekema, M. A. Pfaller, F. J. Schmitz, J. Smayevsky, J. Bell, R. N. Jones, *Infectious Diseases in Clinical Practice*, 2001, **10**, 294.
- 16 E. Meyer, D. Jonas, F. Schwab, H. Rueden, P. Gastmeier and F. D. Daschner, *Infection*, 2003, **31**, 208–15.
- 17 H. S. Sader, R. N. Jones, S. Andrade-Baiocchi and D. J. Biedenbach, *Diagn Microbiol Infect Dis*, 2002, **44**, 273–280.
- 18 ECDC, *European Centre for Disease Prevention and Control. Antimicrobial resistance surveillance in Europe 2014. Annual Report of the European Antimicrobial Resistance Surveillance Network (EARS-Net). Stockholm: ECDC; 2015*, 2015.
- 19 S. J. Peacock and G. K. Paterson, *Annu Rev Biochem*, 2015, **84**, 577–601.
- 20 P. Giesbrecht, T. Kersten, H. Maidhof and J. Wecke, *Microbiol Mol Biol Rev*, 1998, **62**, 1371–414.
- 21 D. J. Tipper and J. L. Strominger, *Proc Natl Acad Sci U S A*, 1965, **54**, 1133–1141.
- 22 C. Fuda, M. Suvorov, S. B. Vakulenko and S. Mobashery, *J Biol Chem*, 2004, **279**, 40802–6.

- 23 W. P. Lu, Y. Sun, M. D. Bauer, S. Paule, P. M. Koenigs and W. G. Kraft, *Biochemistry*, 1999, **38**, 6537–6546.
- 24 K. Graves-Woodward and R. F. Pratt, *Biochem J*, 1998, **332** (Pt 3, 755–61.
- 25 H. F. Chambers, M. J. Sachdeva and C. J. Hackbarth, *Biochem J*, 1994, **301**, 139–144.
- 26 C. Fuda, D. Heseck, M. Lee, K. I. Morio, T. Nowak and S. Mobashery, *J Am Chem Soc*, 2005, **127**, 2056–2057.
- 27 D. Lim and N. C. J. Strynadka, *Nat Struct Mol Biol*, 2002, **9**, 870–876.
- 28 L. H. Otero, A. Rojas-Altuve, L. I. Llarrull, C. Carrasco-López, M. Kumarasiri, E. Lastochkin, J. Fishovitz, M. Dawley, D. Heseck, M. Lee, J. W. Johnson, J. F. Fisher, M. Chang, S. Mobashery and J. A. Hermoso, *Proc Natl Acad Sci U S A*, 2013, **110**, 16808–13.
- 29 M. J. Struelens, *Clinical Microbiology and Infection*, 2006, **12**, 23–26.
- 30 M. C. Enright, N. P. J. Day, C. E. Davies, S. J. Peacock and B. G. Spratt, *J Clin Microbiol*, 2000, **38**, 1008–1015.
- 31 C. Pourcel, K. Hormigos, L. Onteniente, O. Sakwinska, R. H. Deurenberg and G. Vergnaud, *J Clin Microbiol*, 2009, **47**, 3121–3128.
- 32 H. M. Frenay, A. E. Bunschoten, L. M. Schouls, W. J. van Leeuwen, C. M. Vandenbroucke-Grauls, J. Verhoef and F. R. Mooi, *European Journal of Clinical Microbiology and Infectious Diseases*, 1996, **15**, 60–64.
- 33 T. Ito, K. Okuma, X. X. Ma, H. Yuzawa and K. Hiramatsu, *Drug Resistance Updates*, 2003, **6**, 41–52.
- 34 M. C. Enright, D. A. Robinson, G. Randle, E. J. Feil, H. Grundmann and B. G. Spratt, *Proc Natl Acad Sci U S A*, 2002, **99**, 7687–92.
- 35 A. L. Cohen et al. *American Society for Microbiology*, 2002, **40**, 4289–4294.
- 36 F. Vandenesch, T. Naimi, M. C. Enright, G. Lina, G. R. Nimmo, H. Heffernan, N. Liassine, M. Bes, T. Greenland, M. E. Reverdy and J. Etienne, *Emerg Infect Dis*, 2003, **9**, 978–984.
- 37 T. Ito, F. Takeuchi, K. Okuma, H. Yuzawa and K. Hiramatsu, *Society*, 2004, **48**, 2637–2651.
- 38 R. H. Deurenberg, C. Vink, G. J. Oudhuis, J. E. Mooij, C. Driessen, G. Coppens, J. Craeghs, E. De Brauwier, S. Lemmen, H. Wagenvoort, A. W. Friedrich, J. Scheres and E. E. Stobberingh, *Antimicrob Agents Chemother*, 2005, **49**, 4263–4271.
- 39 T. Ito, Y. Katayama, K. Asada, N. Mori and K. Tsutsumimoto, *Antimicrob Agents Chemother*, 2001, **45**, 1323–1336.
- 40 D. C. Oliveira and H. de Lencastre, *Antimicrob Agents Chemother*, 2002, **46**, 2155–2161.
- 41 R. Leclercq, *Clinical Infectious Diseases*, 2002, **34**, 482–492.
- 42 J. Ye, A. Kandegedara, P. Martin and B. P. Rosen, *J. Bacteriol.*, 2005, **187**, 4214–4221.
- 43 M. S. A. K. Mojumdar, *J Bacteriol*, 1988, **170**, 5522–5528.
- 44 A. Pantosti, A. Sanchini and M. Monaco, *Future Microbiol*, 2007, **2**, 323–334.

- 45 F. Lowy, *Journal of Clinical Investigation*, 2003, **111**, 1265–1273.
- 46 E. Y. W. Ng, M. Trucksis and D. C. Hooper, *Antimicrob Agents Chemother*, 1994, **38**, 1345–1355.
- 47 R. Kelmani Chandrakanth, S. Raju and S. A. Patil, *Curr Microbiol*, 2008, **56**, 558–562.
- 48 H. F. Chambers, *Infect Control Hosp Epidemiol*, 1991, **12**, 29–35.
- 49 S. Gardete and A. Tomasz, *J Clin Invest*, 2014, **124**, 2836–40.
- 50 S. Boyle-vavra, S. Boyle-vavra, B. Ereshefsky, B. Ereshefsky, C. Wang, C. Wang, R. S. Daum and R. S. Daum, *Society*, 2005, **43**, 4719–4730.
- 51 N. H. Kwon, K. T. Park, J. S. Moon, W. K. Jung, S. H. Kim, J. M. Kim, S. K. Hong, H. C. Koo, Y. S. Joo and Y. H. Park, *Journal of Antimicrobial Chemotherapy*, 2005, **56**, 624–632.
- 52 A. Shore, A. S. Rossney, C. T. Keane, M. C. Enright and D. C. Coleman, *Antimicrob Agents Chemother*, 2005, **49**, 2070–2083.
- 53 X. X. Ma, T. Ito, C. Tiensasitorn, P. Chongtrakool, S. Boyle-vavra, R. S. Daum, K. Hiramatsu and M. Jamklang, *Antimicrob Agents Chemother*, 2002, **46**, 1147–1152.
- 54 K. Hisata, K. Kuwahara-arai, M. Yamanoto, T. Ito, Y. Nakatomi, L. Cui, T. Baba, M. Terasawa, C. Sotozono, S. Kinoshita, K. Hisata, K. Kuwahara-arai, M. Yamanoto, T. Ito, Y. Nakatomi, L. Cui, T. Baba, M. Terasawa, C. Sotozono, S. Kinoshita, Y. Yamashiro and K. Hiramatsu, *J Clin Microbiol*, 2005, **43**, 3364–3372.
- 55 D. C. Oliveira, A. Tomasz and H. de Lencastre, *Microb. Drug Resist.*, 2001, **7**, 349–361.
- 56 Y. Katayama, T. Ito and K. Hiramatsu, *Society*, 2001, **45**, 1955–1963.
- 57 R. S. Daum, T. Ito, K. Hiramatsu, F. Hussain, K. Mongkolrattanothai, M. Jamklang and S. Boyle-Vavra, *J. Infect. Dis.*, 2002, **186**, 1344–1347.
- 58 K. Hiramatsu, L. Cui, M. Kuroda and T. Ito, *Trends Microbiol.*, 2001, **9**, 486–493.
- 59 P. Grieb, L. Miranda, H. Nanvan, W. Max, B. Piet and K. Anton, *J Clin Microbiol*, 1999, **37**, 2789–2792.
- 60 R. H. Deurenberg, C. Vink, S. Kalenic, A. W. Friedrich, C. A. Bruggeman and E. E. Stobberingh, .
- 61 M. K. Safo, T. P. Ko, F. N. Musayev, Q. Zhao, A. H. J. Wang and G. L. Archer, *Acta Crystallogr Sect F Struct Biol Cryst Commun*, 2006, **62**, 320–324.
- 62 S. Wu, C. Piscitelli, H. de Lencastre and A. Tomasz, *Microb Drug Resist*, 1996, **2**, 435–441.
- 63 Shang Wei Wu, H. De Lencastre and A. Tomasz, *J Bacteriol*, 2001, **183**, 2417–2424.
- 64 J. M. Musser and V. Kapur, *J Clin Microbiol*, 1992, **30**, 2058–2063.
- 65 G. L. Archer, J. A. Thanassi, D. M. Niemeyer and M. J. Pucci, *Antimicrob Agents Chemother*, 1996, **40**, 924–929.
- 66 N. Kobayashi, S. Urasawa, N. Uehara and N. Watanabe, *Antimicrob Agents Chemother*, 1999, **43**, 2780–2782.

- 67 C. L. C. Wielders, M. R. Vriens, S. Brisse, L. A. M. De Graaf-Miltenburg, A. Troelstra, A. Fleer, F. J. Schmitz, J. Verhoef and A. C. Fluit, *Lancet*, 2001, **357**, 1674–1675.
- 68 I. Couto, H. de Lencastre, E. Severina, W. Kloos, J. a Webster, R. J. Hubner, I. S. Sanches and a Tomasz, *Microb Drug Resist*, 1996, **2**, 377–91.
- 69 S. Tsubakishita, K. Kuwahara-Arai, T. Sasaki and K. Hiramatsu, *Antimicrob Agents Chemother*, 2010, **54**, 4352–4359.
- 70 G. L. French, *Clinical Microbiology and Infection*, 2009, **15**, 10–16.
- 71 R. Coello, J. Jiménez, M. García, P. Arroyo, D. Minguez, C. Fernández, F. Cruzet and C. Gaspar, *European Journal of Clinical Microbiology & Infectious Diseases*, 1994, **13**, 74–81.
- 72 M. J. Struelens, P. M. Hawkey, G. L. French, W. Witte and E. Tacconelli, *Clinical Microbiology and Infection*, 2009, **15**, 112–119.
- 73 G. H. Chapman, *THE SIGNIFICANCE OF SODIUM CHLORIDE IN STUDIES OF STAPHYLOCOCCI*, .
- 74 B. Diederer, I. Van Duijn, A. Van Belkum, P. Willemse, P. Van Keulen and J. Kluytmans, *J Clin Microbiol*, 2005, **43**, 1925–1927.
- 75 S. Malhotra-Kumar, J. C. Abrahantes, W. Sabiiti, C. Lammens, G. Vercauteren, M. Ieven, G. Molenberghs, M. Aerts and H. Goossens, *J Clin Microbiol*, 2010, **48**, 1040–1046.
- 76 O. Smithies, 2012, pp. 1–21.
- 77 D. C. Schwartz and C. R. Cantor, *Cell*, 1984, **37**, 67–75.
- 78 C. Chung, H. de Lencastre, P. Matthews, A. Tomasz, M. A. de Sousa, T. Camou, C. Cocuzza, A. Corso, I. Couto, A. Dominguez, M. Gniadkowski, R. Goering, A. Gomes, K. Kikuchi, A. Marchese, R. Mato, O. Melter, D. Oliveira, R. Palacio, R. Sá-leão, I. Santos Sanches, J. Song, P. T. Tassios and P. Villari, *Microbial Drug Resistance*, 2000, **6**, 189–198.
- 79 F. C. Tenover, R. D. Arbeit, R. V. Goering, P. A. Mickelsen, B. E. Murray, D. H. Persing and B. Swaminathan, *J Clin Microbiol*, 1995, **33**, 2233–2239.
- 80 A. Van Belkum, W. Van Leeuwen, M. E. Kaufmann, B. Cookson, F. Forey, J. Etienne, R. Goering, F. Tenover, C. Steward, F. O'Brien, W. Grubb, P. Tassios, N. Legakis, A. Morvan, N. El Solh, R. De Ryck, M. Struelens, S. Salmenlinna, J. Vuopio-Varkila, M. Kooistra, A. Talens, W. Witte and H. Verbrugh, *J Clin Microbiol*, 1998, **36**, 1653–1659.
- 81 F. C. Tenover, R. Arbeit, G. Archer, J. Biddle, S. Byrne, R. Goering, G. Hancock, G. A. Hebert, B. Hill and R. Hollis, *J. Clin. Microbiol.*, 1994, **32**, 407–415.
- 82 S. Murchan, M. E. Kaufmann, A. Deplano, M. Struelens, C. E. Zinn, V. Fusing, S. Salmenlinna, J. Vuopio-varkila, E. Solh, C. Cuny, W. Witte, P. T. Tassios, N. Legakis, A. Vindel, I. Laconcha, J. Garaizar, S. Haeggman, B. Olsson-liljequist, U. Ransjo, G. Coombes and B. Cookson, *Society*, 2003, **41**, 1574–1585.
- 83 M. C. Enright, N. P. J. Day, C. E. Davies, S. J. Peacock and B. G. Spratt, *J Clin Microbiol*, 2000, **38**, 1008–1015.
- 84 G. Wu and M. H. Zaman, *Bull World Health Organ*, 2012, **90**, 914–920.

- 85 A. van Amerongen, J. H. Wichers, L. B. J. M. Berendsen, A. J. M. Timmermans, G. D. Keizer, A. W. J. van Doorn, A. Bantjes and W. M. J. van Gelder, *J Biotechnol*, 1993, **30**, 185–195.
- 86 J. H. W. Leuvers, P. J. H. M. Thal, M. van der Waart and A. H. W. M. Schuurs, *J Immunoassay*, 1980, **1**, 77–91.
- 87 NIH, The History of the Pregnancy Test Kit - A Timeline of Pregnancy Testing, <https://history.nih.gov/exhibits/thinblueline/timeline.html>, (accessed 1 October 2016).
- 88 J. L. Vaitukaitis, G. D. Braunstein and G. T. Ross, *Am J Obstet Gynecol*, 1972, **113**, 751–758.
- 89 P. Chun, in *Lateral Flow Immunoassay*, eds. R. C. Wong and H. Y. Tse, Springer, 2009, pp. 75–93.
- 90 M. A. Mansfield, in *Lateral Flow Immunoassay*, eds. R. C. Wong and H. Y. Tse, Springer, 2009, pp. 95–113.
- 91 B. O’Farrell, in *Lateral Flow Immunoassay*, eds. R. C. Wong and H. Y. Tse, Springer, 2009, vol. 1, pp. 1–34.
- 92 Grand View Research, Point of Care Diagnostics Market Worth \$20.9 Billion By 2024, <https://www.grandviewresearch.com/press-release/global-point-of-care-diagnostics-market>, (accessed 1 October 2016).
- 93 G. A. Posthuma-Trumpie, J. Korf and A. Van Amerongen, *Anal Bioanal Chem*, 2009, **393**, 569–582.
- 94 J. Hu, S. Wang, L. Wang, F. Li, B. Pingguan-Murphy, T. J. Lu and F. Xu, *Biosens Bioelectron*, 2014, **54**, 585–597.
- 95 Y. Xu, Y. Liu, Y. Wu, X. Xia, Y. Liao and Q. Li, *Anal Chem*, 2014, **86**, 5611–5614.
- 96 P. Lie, J. Liu, Z. Fang, B. Dun and L. Zeng, *Chem. Commun. Chem. Commun*, 2012, **48**, 236–238.
- 97 J. Li and J. Macdonald, *Biosensors and Bioelectronic*, 2016, **83**, 177–192.
- 98 J. H. Cho and S. H. Paek, *Biotechnol Bioeng*, 2001, **75**, 725–732.
- 99 D. J. Carter and R. B. Cary, *Nucleic Acids Res*, , DOI:10.1093/nar/gkm269.
- 100 K. A. Edwards and A. J. Baeumner, *Anal Bioanal Chem*, 2006, **386**, 1335–1343.
- 101 J. Bogdanovic, M. Koets, I. Sander, I. Wouters, T. Meijster, D. Heederik, A. van Amerongen and G. Doekes, *J Allergy Clin Immunol*, 2006, **118**, 1157–63.
- 102 R. Verheijen, I. K. Osswald, R. Dietrich and W. Haasnoot, *Food Agric Immunol*, 2000, **12**, 31–40.
- 103 D. P. Kalogianni, S. Goura, A. J. Aletras, T. K. Christopoulos, M. G. Chanos, M. Christofidou, A. Skoutelis, P. C. Ioannou and E. Panagiotopoulos, *Anal Biochem*, 2007, **361**, 169–175.
- 104 J. a Tomlinson, M. J. Dickinson and N. Boonham, *Phytopathology*, 2010, **100**, 143–149.
- 105 T. Klewitz, F. Gessler, H. Beer, K. Pflanz and T. Scheper, *Sens Actuators B Chem*, 2006, **113**, 582–589.
- 106 B. S. Delmulle, S. M. D. G. De Saeger, L. Sibanda, I. Barna-Vetro and C. H. Van Peteghem, *J Agric Food Chem*, 2005, **53**, 3364–3368.

- 107 A. Chen and S. Yang, *Biosens Bioelectron*, 2015, **71**, 230–242.
- 108 M. Moeremans, G. Daneels and J. De Mey, *Anal Biochem*, 1985, **145**, 315–321.
- 109 D. Brada and J. Roth, *Anal Biochem*, 1984, **142**, 79–83.
- 110 G. Frens, *Nature Physical Science*, 1973, **241**, 20–22.
- 111 W. Haiss, N. T. K. Thanh, J. Aveyard and D. G. Fernig, 2015, **79**, 4215–4221.
- 112 G. Danscher, *Histochemistry*, 1984, **81**, 331–335.
- 113 G. Danscher, *Histochemistry*, 1981, **71**, 81–88.
- 114 C. S. Holgate, P. Jackson, P. N. Cowen and C. C. Bird, *J Histochem Cytochem*, 1983, **31**, 938–44.
- 115 G. A. Posthuma-Trumpie, J. H. Wichers, M. Koets, L. B. J. M. Berendsen and A. Van Amerongen, *Anal Bioanal Chem*, 2012, **402**, 593–600.
- 116 J. C. Slater, *Rev Mod Phys*, 1953, **25**, 199–210.
- 117 M. A. Reed, R. T. Bate, K. Bradshaw, W. M. Duncan, W. R. Frensley, J. W. Lee and H. D. Shih, *Journal of Vacuum Science & Technology B: Microelectronics Processing and Phenomena*, 1986, **4**, 358–360.
- 118 R. Rossetti, S. Nakahara and L. E. Brus, *J Chem Phys*, 1983, **79**, 1086–1088.
- 119 S. Fujita, J. McNabb III and A. Suzuki, *Journal of Modern Physics*, 2015, **06**, 733–748.
- 120 F. Bloch, *Zeitschrift fur Physik*, 1929, **52**, 555–600.
- 121 L. Kouwenhoven and C. Marcus, *Physics World*, 1998, **11**, 35–39.
- 122 The Royal Swedish Academy of Sciences, *QUANTUM DOTS – SEEDS OF NANOSCIENCE*, 2023.
- 123 L. B. McGown and K. Nithipatikom, *Appl Spectrosc Rev*, 2000, **35**, 353–393.
- 124 C. Zhang, Y. Zhang and S. Wang, *J Agric Food Chem*, 2006, **54**, 2502–2507.
- 125 S. Wang, Y. Quan, N. Lee and I. R. Kennedy, *J. Agric. Food Chem.*, 2006, **54**, 2491–2495.
- 126 J. Zhao Su-Ping He, W. Liu, A.-X. Deng, T.-G. Nan, B.-M. Wang, Z.-X. Zhai and Z.-H. Li, *Food Agric Immunol*, 2006, **17**, 173–181.
- 127 T. Huo, C. Peng, C. Xu and L. Liu, *Food Agric Immunol*, 2006, **17**, 183–190.
- 128 Y. M. Kim, S. W. Oh, S. Y. Jeong, D. J. Pyo and E. Y. Choi, *Environ Sci Technol*, 2003, **37**, 1899–1904.
- 129 K. Campbell, T. Fodey, J. Flint, C. Danks, M. Danaher, M. O’Keeffe, D. G. Kennedy and C. Elliott, *J Agric Food Chem*, 2007, **55**, 2497–2503.
- 130 R. E. Biagini, D. L. Sammons, P. Jerome, B. a Mackenzie, C. a F. Striley, E. John, S. a Robertson, C. P. Quinn, J. P. Smith and J. E. Snawder, *Clin Vaccine Immunol*, 2006, **13**, 541–546.
- 131 J. R. Newgard, G. C. Rouse and J. K. McVicker, *J Agric Food Chem*, 2002, **50**, 3094–3097.
- 132 W. Leung, P. Chan, F. Bosgoed, K. Lehmann, I. Renneberg, M. Lehmann and R. Renneberg, *J Immunol Methods*, 2003, **281**, 109–118.

- 133 a van Amerongen, D. van Loon, L. B. Berendsen and J. H. Wichers, *Clin Chim Acta*, 1994, **229**, 67–75.
- 134 R. Tanaka, T. Yuhi, N. Nagatani, T. Endo, K. Kerman, Y. Takamura and E. Tamiya, *Anal Bioanal Chem*, 2006, **385**, 1414–1420.
- 135 K. Henderson and J. Stewart, *Reprod Fertil Dev*, 2001, **12**, 183–189.
- 136 M. P. Laitinen and M. Vuento, *Acta Chem Scand*, 1996, **50**, 141–145.
- 137 S. Choi, E. Y. Choi, D. J. Kim, J. H. Kim, T. S. Kim and S. W. Oh, *Clinica Chimica Acta*, 2004, **339**, 147–156.
- 138 J. S. Ahn, S. Choi, S. H. Jang, H. J. Chang, J. H. Kim, K. B. Nahm, S. W. Oh and E. Y. Choi, *Clinica Chimica Acta*, 2003, **332**, 51–59.
- 139 W. Leung, C. P. Chan, M. Leung, K. Lehmann, I. Renneberg, M. Lehmann, A. Hempel, J. F. C. Glatz and R. Renneberg, *Anal Lett*, 2005, **38**, 423–439.
- 140 S. C. Lou, C. Patel, S. Ching and J. Gordon, *Clin Chem*, 1993, **39**, 619–624.
- 141 G. Rundström, A. Jonsson, O. Mårtensson, I. Mendel-Hartvig and P. Venge, *Clin Chem*, 2007, **53**, 342–348.
- 142 C. Fernández-Sánchez, C. J. McNeil, K. Rawson, O. Nilsson, H. Y. Leung and V. Gnanapragasam, *J Immunol Methods*, 2005, **307**, 1–12.
- 143 Y. Oku, K. Kamiya, H. Kamiya, Y. Shibahara, T. Ii and Y. Uesaka, *J Immunol Methods*, 2001, **258**, 73–84.
- 144 G. P. Zhang, J. Q. Guo, X. N. Wang, J. X. Yang, Y. Y. Yang, Q. M. Li, X. W. Li, R. G. Deng, Z. J. Xiao, J. F. Yang, G. X. Xing and D. Zhao, *Vet Parasitol*, 2006, **137**, 286–293.
- 145 E. Clavijo, R. Díaz, Á. Anguita, A. Pinedo, H. L. Smits and A. García, 2003, **10**, 612–615.
- 146 K. Snowden and M. Hommel, *J Immunol Methods*, 1991, **140**, 57–65.
- 147 G. C. Gussenhoven, M. A. W. G. Van Der Hoorn, M. G. A. Goris, W. J. Terpstra, R. A. Hartskeerl, B. W. Mol, C. W. Van Ingen and H. L. Smits, *J Clin Microbiol*, 1997, **35**, 92–97.
- 148 Y. Al-Yousif, J. Anderson, C. Chard-Bergstrom and S. Kapil, *Clin Diagn Lab Immunol*, 2002, **9**, 723–725.
- 149 Y. Zhu, W. He, Y. Liang, M. Xu, C. Yu, W. Hua and G. Chao, *J Immunol Methods*, 2002, **266**, 1–5.
- 150 M. Suzuki, M. Matsumoto, M. Hata, M. Takahashi and K. Sakae, *J Clin Microbiol*, 2004, **42**, 5462–5466.
- 151 C. N. Baker and F. C. Tenover, *Evaluation of Alamar Colorimetric Broth Microdilution Susceptibility Testing Method for Staphylococci and Enterococci*, 1996, vol. 34.
- 152 A. Kothari, Y. W. Wu, J. M. Chandonia, M. Charrier, L. Rajeev, A. M. Rocha, D. C. Joyner, T. C. Hazen, S. W. Singer and A. Mukhopadhyay, *mBio*, DOI:10.1128/mBio.02899-18.
- 153 D. Caruntu, G. Caruntu and C. J. O'Connor, *J Phys D Appl Phys*, 2007, **40**, 5801–5809.

- 154 G. Hemery, A. C. Keyes, E. Garaio, I. Rodrigo, J. A. Garcia, F. Plazaola, E. Garanger and O. Sandre, *Inorg Chem*, 2017, **56**, 8232–8243.
- 155 J. Chen, D. Wang, Y. Wang, Y. Xiong, S. Cheng, K. Wei, Z. Liu, F. Birnkammer and D. Gerling, *IEEE Transactions on Applied Superconductivity*, DOI:10.1109/TASC.2016.2594801.
- 156 I. M. Obaidat, V. Narayanaswamy, S. Alaabed, S. Sambasivam and C. V. V. Muralee Gopi, *Magnetochemistry*, 2019, 5.

Appendix

“What does this organ do again?”

Appendix 1. Reference gene sequences from MRSA K12 reference strains:

MecA:

5'-

ATGAAAAAGATAAAAATTGTTCCACTTATTTTAATAGTTGTAGTTGTCGGGTTTGGTATATATTTTTATGCTTCA
AAAGATAAAGAAATTAATAATACTATTGATGCAATTGAAGATAAAAATTTCAAACAAGTTTATAAAGATAGCA
GTTATATTTCTAAAAGCGATAATGGTGAAGTAGAAATGACTGAACGTCCGATAAAAAATATAAATAGTTTAGG
CGTTAAAGATAAACAATTCAGGATCGTAAAATAAAAAAGTATCTAAAAATAAAAAACGAGTAGATGCTCAA
TATAAAAATTAACAACAACTACGGTAACATTGATCGCAACGTTCAATTTAATTTTGTAAAGAAGATGGTATGTG
GAAGTTAGATTGGGATCATAGCGTCATTATCCAGGAATGCAGAAAGACCAAAGCATACATATTGAAAAATTA
AAATCAGAACGTGGTAAAAATTTAGACCGAAAACAATGTGGAATTGGCCAATACAGGAACAGCATATGAGATA
GGCATCGTCCAAAAGAATGTATCTAAAAAAGATTATAAAGCAATCGCTAAAGAACTAAGTATTTCTGAAGACT
ATATCAACAACAATGGATCAAAATTTGGGTACAAGATGATACCTTCGTTCCACTTAAAAACCGTTAAAAAAT
GGATGAATATTTAAGTGATTTGCAAAAAAATTTTATCTTACAACATAAAGAAAGAGTAAAGTAACTATCCTC
TAGAAAAAGCGACTTCACATCTATTAGGTTATGTTGGTCCCATAACTCTGAAGAATTAACAACAAGAAATAT
AAAGGCTATAAAGATGATGCAGTTATTGGTAAAAAGGGACTCGAAAAACTTTACGATAAAAAAGCTCCAACAT
GAAGATGGCTATCGTGTCACAATCGTTGACGATAATAGCAATACAATCGCACATACATTAATAGAGAAAAAGA
AAAAAGATGGCAAAGATATCAACTAATATTGATGCTAAAAGTTCAAAAGAGTATTTATAACAACATGAAAAA
TGATTATGGCTCAGGTACTGCTATCCACCTCAAACAGGTGAATATTAGCACTTGTAAAGCACACCTTCATATG
ACGTCTATCCATTTATGTATGGCATGAGTAACGAAGAATATAATAAATTAACCGAAGATAAAAAAGAACCTCT
GCTCAACAAGTTCCAGATTACAACCTCACCGGTTCAACTCAAAAAATTTAACAGCAATGATTGGGTTAAATA
ACAAAAATTAGACGATAAAACAAGTTATAAAATCGATGGTAAAGGTTGGCAAAAAGATAAATCTTGGGGTG
GTTACAACGTTACAAGATATGAAGTGGTAAATGGTAAATTCGACTTAAAACAAGCAATAGAATCATCAGATAA
CATTTTCTTGTAGAGTAGCACTCGAATTAGGCAGTAAGAAATTTGAAAAAGGCATGAAAAAAGTGGTGT
GGTGAAGATATACCAAGTATTATCCATTTTATAATGCTCAAAATTTCAACAACAATTTAGATAATGAAATATT
ATTAGCTGATTACGGTACGGACAAGGTGAAATACTGATTAACCCAGTACAGATCCTTTCAATCTATAGCGCAT
TAGAAAAATAATGGCAATATTAACGCACCTCACATTTAAAAGACACGAAAAACAAGTTTGGAAAGAAAAATAT
TATTTCAAAGAAAAATCAATCTATTAACCTGATGGTATGCAACAAGTCTAAATAAAAACACATAAAGAAGAT
ATTTATAGATCTTATGCAAACTTAATTGGCAAATCCGGTACTGCAGAACTCAAATGAAACAAGGAGAACTG
GCAGACAAATTTGGGTGGTTTATATCATATGATAAAGATAATCCAAACATGATGATGGCTATTAATGTTAAAGA
TGTACAAGATAAAGGAATGGCTAGCTACAATGCCAAAATCTCAGGTAAGTGTATGATGAGCTATATGAGAA
CGGTAATAAAAAATACGATATAGATGAATAA -3'

Ant(4'):

5'-

ATGAGAATAGTGAATGGACCAATAATAATGACTAGAGAAGAAAGAATGAAGATTGTTGATGAAATTAAGGAA
CGAATATTGGATAAATATGGGGATGATGTTAAGGCTATTGGTGTATGGCTCTCTGGTCTCAGACTGATG
GGCCCTATTCGGATATTGAGATGATGTGTGTGATGCAACAGAGGAAGCAGAGTTCAGCCATGAATGGACAA
CCGGTGAGTGGAAAGGTGGAAGTGAATTTTATAGCGAAGAGATTCTACTAGATTATGCATCTCAGGTGGAAT
CAGATTGGCCGTTACACATGGTCAATTTTTCTATTTTTGCCGATTTATGATTAGGTGGTACTTAGAGAAA
GTGTATCAAACGCTAAATCGGTAGAAGCCCAACGTTCCACGATGCGATTTGTGCCCTTATCGTAGAAGAGC
TGTTTGAATATGCAGGCAAATGGCGTAATATTCTGTGTGCAAGGACCGACAACATTTCTACCATCCTTACTGTA
CAGGTAGCAATGGCAGGTGCCATGTTGATTGGTCTGCATCATCGCATCTGTTATACGACGAGCGCTTCGGTCT
TAACTGAAGCAGTTAAGCAATCAGATCTTCTTACGGTATGACCATCTGTGCCAGTTCTGAATGTCTGGTCAA
CTTTCCGACTCTGAGAACTTCTGGAATCGCTAGAGAATTTCTGGAATGGGATTCAGGAGTGGACAGAACGAC
ACGGATATATAGTGGATGTGTCAAACGCATACCATTTTGA -3'

BleO:

5'-

GTGAGAATGTTACAGTCTATCCCGGCATTGCCAGTCGGGGATATTAAGGTTTTATTGCGATA
AACTAGGTTTCACTTTGGTTCACCATGAAGATGGATTCCGAGTTCTAATGTGTAATGAGGTTCCGGATTCATCTA
TGGGAGGCAAGTGATGAAGGCTGGCGCTCTCGTAGTAATGATTCACCGGTTTGTACAGGTGCGGAGTCGTTT
ATTGCTGGTACTGCTAGTTGCCGCATTGAAGTAGAGGGAATTGATGAATTATCAACATATTAAGCCTTTGG
GCATTTTGCACCCCAATACATCATTAAAAGATCAGTGGTGGGATGAACGAGACTTTGCAGTAATTGATCCCGA
CAACAATTTGATTAGCTTTTTTCAACAATAAAAAGCTAA -3'

ermA:

5'-

TTAGTGAAACAATTTGTAAGTATTGAAAATAGAAAGAAATTTGTTCCCTTCGATAGTTTATTAATATTAGTGACAT
TTGCATGCTTCAAAGCCTGTCCGGAATTGGTTTTAGTGAAAAGAACACGATATTCACGGTTTACCCACTTATAA
ACAAAAGATCGATACTTTTTGTAGTCCCTCTTTGAAATCAATGGTTGATGTCGTTCAAGAACAATCAATACAGA
GTCTACACTTGGCTTAGGATGAAAATATAGTGGTGGTACTTTTTGAGCATTTTTATATCCATCTCCACCATTAA
TAGTAAACCCAAAGCTCGTTGCAGATTTTGAATCTTTTCGCAAATCCCTTCTCAACGATAAGATAGCTATATTT
AGCCTGACTTTCAAAGGTAATTTCTTTGACAATATCCGTAAGTATTATAAGGAATATTACCATATATCTTATA
GTTTATATGTTTTGGGAAGGAAAATTTAGAATATCCGTTTGAATCACTTTTATTTCTCAGAGGGGTTTACCG
CTTCTTTAGTCACTTGACATAAGCCTCCATCAATTTCTATAGCAGTAAGTATCGACTCATTTTGAAGTACTCTTT
GGTAAAATGTCCTTTTCTGATCCGATTTCTATTACGTTGTCTTGTACTGATATTCGTGTGATTCATATTTCT
TTTACATGCTTTTTAGAAGTAATAAAAATTTGCGTGTCTTTAGGGTTTTTCTGGTTCAT -3'

TetK:

5'-

TTGTTTAGTTTATATAAAAAATTTAAAGGTTTGTATAGCGTTTTATTTGGCTTTGTATTCTTTCATTTTTAG
TGTATTAATGAAATGGTTTTAAATGTTTCTTACCTGATATTGCAAATCATTTAATACTACTCCTGGAATTAC
AAACTGGGTAACACTGCATATATGTTAACTTTTTCGATAGGAACAGCAGTATATGGAAAATTATCTGATTATA
TAAATATAAAAAATTTGTTAATTTGGTATTAGTTTGGCTTTGATTGCTTTTATTGGTCACA
ATCACTTTTTATTTGATTTTTGGTAGGTTAGTACAAGGAGTAGGATCTGCTGCATTCCCTTCACTGATTATGG
TGGTTGTAGCTAGAAATATTACAAGAAAAACAAGGCAAAGCCTTTGGTTTTATAGGATCAATTGTAGCTTT
AGGTGAAGGGTTAGGTCCCTTCAATAGGGGGAATAATAGCACATTATTCATTGGTCTTACCTACTTATACTTC
CTATGATTACAATAGTAACTATACCTTTTCTATTAAAGTAATGGTACCTGGTAAATCAACAAAAAATACATTA
GATATCGTAGGTATTGTTTTAATGTCTATAAGTATTATATGTTTTATGTTATTTACGACAAATTATAATTGGACT
TTTTAATACTCTTCAATCTTTTTGTGATTTTTATTAACATATTTCAAGAGTTTCTAACCTTTTATTAATCC
TAAACTAGGGAAAAACATTCCGTTTATGCTTGGTTTGTCTGGTGGGCTAATTTTTCTATAGTAGCTGGTTT
TATATCAATGGTGCCTTATATGATGAAAATTTATCATGTAAATGTAGCGACAATAGGTAATAGTGTTATTT
TTCTGGAACCATGAGTGTTATTGTTTTGGTTATTTGGTGGTTTTTATGGATAGAAAAGGATCATTATTTG
TTTTATTTAGGATCATTGTCTATCTCTATAAGTTTTTAACTATTGCATTTTTTGTGAGTTTAGTATGTGGTT
GACTACTTTTTATGTTTATTTGTTATGGGCGGATTATCTTTACTAAAACAGTTATATCAAAAATAGTATCAAG
TAGTCTTTCTGAAGAAGAAGTTGCTTCTGGAATGAGTTTCTAAATTTACAAGTTTTTATCAGAGGGAACAG
GTATAGCAATTTGAGGAGGTTTATTGCACTACAATTGATTAATCGTAAACTAGTTCTGGAATTTATAAATTATT
CTTCTGGAGTGTATAGTAATATTCTTGTAGCCATGGCTATCCTTATTTATTTATGTTGTCTTTGACGATTATTGT
ATTTAAACGTTCTGAAAAGCAGTTTGAATAG -3'

TetM:

5'-

ATGAAAAATTATTAATATTGGAGTTTTAGCTCATGTTGATGCGGGAAAACTACCTTAACAGAAAGCTTATTATA
TAACAGTGGAGCGATTACAGAATTAGGAAGCGTGGACAGAGGTACAACGAAAAAGGATAATACGCTTTTAGA
ACGTCAGAGAGGAATTACAATTCAGACGGCGATAACCTCTTTTCAGTGGAAAAATACTAAGGTGAACATCATA
GACACGCCAGGACATATGGATTTTTAGCAGAAGTATATCGTTCATTATCAGTATTAGATGGGGCAATTCTACT
GATTTCTGCAAAAAGATGGCGTACAAGCACAACTCGTATATTGTTTCATGCACCTTAGGAAAATAGGTATTCCCA
CAATCTTTTTATCAATAAGATTGACCAAAATGGAATTGATTTATCAACGGTTTATCAGGATATTAAGAGAAA
CTTTCTGCGGAAATTGTAATCAAAACAGAAGGTAGAAGTGCATCCTAATATGCGTGTAAATGAACCTTACCGAATC
TGAACAATGGGATATGGTAATAGAAGGAAATGATTACCTTTGGAGAAATATACGTCTGGGAAATATTGGA
AGCATTAGAACTCGAACAAGAGGAAAGCATAAGATTTATAAATTGTTCCCTGTTCCCTGTTTATCACGGAAGT
GCAAAAAACAATATAGGGATTGATAACCTTATAGAAGTGATTACGAATAAATTTTATTCATCAACACATCGAG
GTCAGTCTGAACTTTGCGGAAAAGTTTTCAAAATTGAGTATTCGGAAAAAGACAGCGTCTTGATATATACG
TCTTTATAGTGGCGTACTGCATTTGCGAGATCCGGTTAGAATATCGGAAAAGGAAAAAATAAAAAATTACAGAA
ATGTATACTTCAATAAATGGTGAATTATGTAAAAATCGATAAGGCTTATCCGGGAAATGTTATTTTGAGAA
TGAGTTTTGAAGTTAAATAGTGTCTTTGGAGATACAAAGCTATTGCCACAGAGAGAGAGAAATTGAAAATCCC
CTCCCTCTGCTGCAAACTGTTGAACCGAGCAAACTCAACAAAGGGAAATGTTACTTGATGCACCTTTAG
AAATCTCCGACAGTGAACCGCTTCTGCGATATTATGTGGATTCTGCGACACATGAAATCATACTTTCTTTCTTAG
GGAAAGTACAAATGGAAGTGAATTTGTCTGCTGCAAGAAAAGTATCATGTGGAGATAGAAAATAAAGAGC
CTACAGTCAATTTATATGGAAAGACCGTTAAAAAAGCAGAGTATACCATTACATCGAAGTTCCACCGAATCCT
TTCTGGGCTTCCATTGGTCTATCTGTAGCACCGCTTCCATTAGGGAGCGGAGTACAGTATGAGAGCTCGGTTT
CTCTGGATACTTAAATCAATCGTTTCAAATGCAGTTATGGAGGGGATACGCTATGGCTGTGAACAAGGATT
GTATGGTTGGAATGTGACGGACTGTAAAACTGTTTTAAGTATGGCTTATACTATAGCCCTGTTAGTACCCGAG
CAGATTTTTCGGATGCTTGCTCCTATTGTATTGGAACAAGTCTTAAAAAAGCTGGAACAGAATTGTTAGAGCC
ATATCTTAGTTTTAAAATTTATGCGCCACAGGAATATCTTTCACGAGCATACAACGATGCTCCTAAATATTGTGC
GAACATCGTAGACACTCAATTGAAAAATAATGAGGTCAATCTTAGTGGAGAAATCCCTGCTCGGTGATTCAA
GAATATCGTAGTGATTTAACTTTCTTTACAAATGGACGTAGTGTGTTTAAACAGAGTTAAAGGGTACCATGT
TACTACCGGTGAACCTGTTTGCCAGCCCCGTCTCCAATAGTCGGATAGATAAAGTACGATATATGTTCAATA
AAATAACTTAG -3'

VanA:

5'-

GATCCATACAAGGTCTGTTTGAATTGTCCGGTATCCCTTTTGTAGGCTGCGATATTCAAAGCTCAGCAATTTGT
ATGGACAAATCGTTGACATACATCGTTGCGAAAAATGCTGGGATAGCTACTCCCGCTTTTGGGTTATTAATAA
AGATGATAGGCCGGTGGCAGCTACGTTTACCTATCCTGTTTTTGTAAAGCCGGCGGTTTCCAGGCTCATCCTTCG
GTGTGAAAAAAGTCAATAGCGCGGACGAATTGGAATCGCAATCGGCAAGACAATATGACAGCAAAA
TCTTAATTGAGCAGGCTGTTTCCGGGCTGTGAGGTCCGGTTGTGCGGTATTGGGAAACAGTGCCGCGTTAGTTGT
TGGCGAGGTGGACCAATCAGGCTGCAGTACGGAATCTTTCGTATTATCAGGAAGTCGAGCCGGAAAAAGG
CTCTGAAAAACGCAATTATAACCGTTCCCGCAGACCTTTACGAGAGGAGCGAGGACGGATACAGGAAACGGC
AAAAAAAATATATAAAGCGCTCGGCTGTAGAGGTCTAGCCCGTGTGGATATGTTTTTACAAGATAACGGCCGC
ATTGTAAGTGAACGAAGTCAATACTCTGCCCCGTTTACGTCATACAGTCTGTTATCCCCGTATGATGGCCGCTGC
AGGTATTGCACTTCCC-3'

NorA:

5'-

ATTTTAATACAACGTCATCACATGCACCAATGCCGCTGACAGATGTAATGTTAAGTCTTGGTCATCTGCAAAG
GTTGTTATACATTCAACGATATCTTCTCCTTTTTCCAACACTAGTAGTATAGTATGATTACTTTTTTGCAATTTCA
TATGATCAATCCCCTTATTTTAATATGTCATTAATTATACAAATAAATGGAAAATAGTGATAATTACAAAGAAA
AAATATTGTCAAATGTAGCAATGTTGTAATACAATATAGAACTTTTTACGAATATTTAGCATGAATTGCAATC
TGTGCTGGAAAAGAAGAATAACAGCTTTAAGCATGACATGGAGAAAAAAGAGGTGAGCATATGAATAAACA
GATTTTTGTCTTATATTTTAATATTTTTCTTGATTTTTTGGTATCGGTTTAGTAATACCAGTCTTGCCTGTTTATT
TAAAAGATTTGGGATTAAGTGGTAGTATTTAGGATTAAGTCTGCTGTTTTGCGTTATCTCAAATGATTATA
TCGCCGTTTGGTGGTACGCTAGCTGACAAATTAGGGAAGAAATTAATTATATGTATAGGATTAATTTTTGTTTTC
AGTGTGAGAAATTTATGTTTGCAGTTGGCCACAATTTTTCGGTATTGATGTTATCGAGAGTGATTGGTGGTATGA
GTGCTGGTATGGTAATGCCTGGTGTGACAGGTTTAATAGCTGACATTTACCCAAGCCATCAAAAAGCAAAAAA
CTTTGGCTACATGTCAGCGATTATCAATTCGGATTCATTTTAGGACCAGGGATTGGTGGATTTATGGCAGAA
GTTTCACATCGTATGCCATTTTACTTTGCAGGAGCATTAGGTATTCTAGCATTTATAATGTCAAATGATTGATT
CACGATCCGAAAAAGTCTACGACAAGTGGTTTTCAAAAAGTTAGAGCCACAATTGCTAACGAAAAATAACTGGA
AAGTGTTTATTACACCAGTTATTTAACACTTGTATTATCGTTTGGTTTATCTGCATTTGAAACATTGTATCACT
ATACACAGCTGACAAGGTAAATTTACCTAAAGATATTTGATTGCTATTACGGGTGGCGGTATATTTGGG
GCATTTTTCAAATCTATTTCTCGATAAATTTATGAAGTATTTCTCAGAGTTAACATTTATAGCTTGGTCATTAT
TATATTCAGTTGTTGTCTTAATATTATTAGTTTTTCTAATGACTATTGGTCAATAATGTTAATCAGTTTTGTTGT
CTTCATAGGTTTTGATATGATACGACCAGCCATTACAAATTAATTTTTCTAATATTGCTGGAGAAAGGCAAGGCT
TTGCAGGCGGATTGAACTCGACATTCAGTATGGGTAAATTTATAGGTCCTTTAATCGCAGGTGCGTTATTT
GATGTACACATTGAAGCACCAATTTATATGGCTATAGGTGTTTCATTAGCAGGTGTTGTTATTGTTTTAATTGA
AAAGCAACATAGAGCAAAAATTGAAAGAACAAAATATGTAGCATAAGTATTTTGGTGTATATTGATATAAAGTA
AAGCGTAATATTATGAATGATTAGCATCGTTTTCTTATGAAATTTATTAAGAAAAATCGATGCTTTACATTTAA
AAAGATTGATTGACTAAATGTTTTACTCTTTATATTTAAATGTTATATGTAACAAAAAATGATTTTGAGTAATA
AACATGTTACAAATATTACATTTCTTTTTAAATGCAATCCACATACCTAATTCATTAACGTTAATGTGTTAAGAT
GATAAAAAATGAGTAAGGAAATGTGGGTAAGGGGAT -3'

NorB:

5'-

TCATAATTGAGTATCGTTTTGTTAGGCACAAGTAACAAAATGATAACGAATGATAATATTTCCCATACCTGCAT
TTAACATAATGCAATCATTGCACCTGTATAAATGTTTGTATATTTGATACGATTGCATATACTGCACCACTCA
ATGCGACGCCAAATGCTCCACCTAATGCAGAAGCCATTTTATAGATACCTGCAGCAACGCCTACTTTTTCTAAC
GGTGCATTTGCAATTGCTGTATCTGTTGATGGTGTAGCATATATCCCTAGTCTTAAACCAAGAATAAATAACC
TATAATACAAAAATGACATAGAATATTTCTGGCAAGAAAGTTAATGAAATGAGACATTTCTCCGACAATAAGAA
CTCCTGTTCCAATTAACATTGGTTTCTGCATCCGAGTGTGTTGAAGTAACTTTTACCAACACGAATCATAATTA
GTACCATTACTAAATAAGTGATTGATAAACTTCTGCTTGAAGTAAATGAAATATCCTAAACCTCTTTGAACAAAT
GTGTTGGCTACTATTAATGTTTCTGCAACACCAATTTAACAAAAAGTTTGAAGCTGTTGCACCTGTGTAAGCTTT
ATTTTTAAATAATTTAAAATCGATTAAGGATTTGTAGCACGTTTTCAAGAACTATAAATAAACTAAAAGATC
CAATTGCAATAGCTAATAAAGTAATAAAAAGAAGTGAGGTTACACCTAATCTGATCCTTTAGTAATTTAAATA
TTTAAACTGAGGAGCATAATGACTAAAAGAACCAGACCTTTAATGTCAAATTTATTTAGAGAAATCGATTTAGA
TTTAGTTTTAGGTGTGCCTTAATAAGAAAAGTGAATTAATGAAATTAATTTGATAGGATGAAAATCCAAC
GCCAACCTAAAAGCGTTGCAACTGCACCTCCAAAAAATGAACAAACACCAGAGCCGCCCCATGAGCCAATTGA
CCAATAACTTAAAGCGGTTGTCTATCTTTCCAATGTAATATGACTTAATAATAGACAAAGTTGCAGGCATAA
TACATGCTGCTGAAAGTCTTGAATTAATCTTCTATAATAAGTAATAAAGGAATATTTGAAATAATGATTAAT
AATGAACCTAATATATTTAAGATAATACCAATGTTGTTGAGTTAATTTCTGCCATTTTATCAGCAAGACCCT
GCTCCTACTACAAACATTCCTGAAAAATAAGCAGTTATACTAACGGCGATTTAACCGTTCCAATATCTGTATT

GAAACTATCTTCAAGTATTGGTACAACATTAACCAATGATTGTGCAAATAGCCAAAACGTTATTACACTTAGAA
CAATTCCTATTAACAACCTATTATTGCCTTCAAATGCCTCTCTTGACGGCTTTTCCAT -3'

Ant(9):

5'-

ATGAGCAATTTGATTAACGGAAAAATACCAAATCAAGCGATTCAAACATTA AAAAATCGTAAAAGATTTATTTG
GAAGTTCAATAGTTGGAGTATATCTATTTGGTTCAGCAGTAAATGGTGGTTTACGCATTAACAGCGATGTAGA
TGTTCCTAGTCGTCGTGAATCATAGTTTACCTCAATTAACCTCGAAAAAACTAACAGAAAGACTAATGACTATAT
CAGGAAAAGATTGGAAATACGGATTCTGTTAGACCACTTGAAGTTACGGTTATAAATAGGAGTGAAGTTGTCCC
TTGGCAATATCCTCCAAAAAGAGAATTTATATACGGTGAGTGGCTCAGGGGTGAATTTGAGAATGGACAAATT
CAGGAACCAAGCTATGATCCTGATTTGGCTATTGTTTTAGCACAAAGCAAGAAAGAATAGTATTTCTCTATTTGG
TCCTGATTCTTCAAGTATACTTGTCTCCGTACCTTTGACAGATATTCGAAGAGCAATTAAGGATTCTTTGCCAGA
ACTAATTGAGGGGATAAAAAGTGATGAGCGTAATGTAATTTTAACCCCTAGCTCGAATGTGGCAAACAGTGAC
TACTGGTGAAATTACCTCGAAAGATGTCGCTGCAGAATGGGCTATACCTCTTTTACCTAAAGAGCATGTAACCT
TACTGGATATAGCTAGAAAAGGCTATCGGGGAGAGTGTGATGATAAGTGGGAAGGACTATATTCAAAGGTG
AAAGCACTCGTTAAGTATATGAAAAATTCTATAGAAACTTCTCTCAATTAG-3'

Appendix 2. Sequence alignments:

The MLST alignments raw data printouts are up to 2000 pages long and are too complex to view using the NCBI alignment viewer. Therefore, to view them please do so by downloading the source alignment files hosted via the below links.

MecA:

https://drive.google.com/file/d/19iPw7JRiqetv59cyeJZPnQgNYLQpAmV0/view?usp=drive_link

Ant(4'):

https://drive.google.com/file/d/1pjuJ-7GrgSINuGZSTUJ_xNbUxiKfSmIS/view?usp=drive_link

BleO:

https://drive.google.com/file/d/171soSKVjSEA2P6HnluFRaXvLhMT0fnLI/view?usp=drive_link

ermA:

https://drive.google.com/file/d/1qr_NR6Nsn4nGPD3dSPegqBHxPpTTNKn2/view?usp=drive_link

TetK:

https://drive.google.com/file/d/1IJOJp8WRT9IVSEMna6kbr3gD9sk_82V5/view?usp=drive_link

TetM:

https://drive.google.com/file/d/1RyI9vPsGIDl88Opvwe-9uh6gllBtoidq/view?usp=drive_link

VanA:

https://drive.google.com/file/d/1gALDBxgF9aMQtDDJonC8jIA4fXqp7CT7/view?usp=drive_link

NorA:

https://drive.google.com/file/d/1seA0CrDlIO-s0xqfGu1CYQUZwK-5HOaQ/view?usp=drive_link

NorB:

https://drive.google.com/file/d/1Ae8U-u523n11axssNnRAeL_dJpaKhX2U/view?usp=drive_link

Ant(9):

https://drive.google.com/file/d/13u3zCHCBIVQkeyPIVNiInRlyobe4DK7q/view?usp=drive_link

To view these files BioEdit is available for free. Please download the software direct from the author Thomas Hall's GitHub. Many thanks to Thomas for providing this excellent and vital piece of software free of charge with an open-source license for all to use:

<https://thalljscience.github.io/>

Appendix 3. Capture probe BLASTn results:

Data set too large to present graphically. Therefore, to view them please do so by downloading the source files hosted via the below links or Search the RID on the NCBI for visualisation.

MecA:

<https://blast.ncbi.nlm.nih.gov/Blast.cgi?CMD=Get&RID=KWUDF654013>

https://drive.google.com/file/d/1yuSUwzOcGy_rA1ouRZ8q8QMZj7fhnZEG/view?usp=drive_link

Ant(4'):

<https://blast.ncbi.nlm.nih.gov/Blast.cgi?CMD=Get&RID=KWTTSKKF013>

https://drive.google.com/file/d/1jXwFvm6cGWowQSSXxQpBACDeqXfwgEQJ/view?usp=drive_link

BleO:

No hits on BLASTn of the nr database.

ermA:

<https://blast.ncbi.nlm.nih.gov/Blast.cgi?CMD=Get&RID=KWTUNABP016>

https://drive.google.com/file/d/1-Rz9WFC2o4kX5Hq2T5ti4noSaOXOvTx/view?usp=drive_link

TetK/M:

<https://blast.ncbi.nlm.nih.gov/Blast.cgi?CMD=Get&RID=KWTWEY7H016>

https://drive.google.com/file/d/1q9TQiNpSZXm0yHhNUm6G_ZlBtq1XcSS6/view?usp=drive_link

VanA:

<https://blast.ncbi.nlm.nih.gov/Blast.cgi?CMD=Get&RID=KWTX6B8Y013>

https://drive.google.com/file/d/1aOzDUyPG33bJvbHPApN79YOaXL_3pjVK/view?usp=drive_link

NorA/B:

<https://blast.ncbi.nlm.nih.gov/Blast.cgi?CMD=Get&RID=KWXTMER016>

https://drive.google.com/file/d/1qjRPP2uZiUBA04B7p2p4Lh2FDMNOI2SY/view?usp=drive_link

Ant(9):

<https://blast.ncbi.nlm.nih.gov/Blast.cgi?CMD=Get&RID=KWTY6D57013>

https://drive.google.com/file/d/1mjn5C_CexcEYtw1RQYWjJisu8uVF6Wa7/view?usp=drive_link

Appendix 4. Full list of modified primer sequences:

<https://docs.google.com/spreadsheets/d/1l->

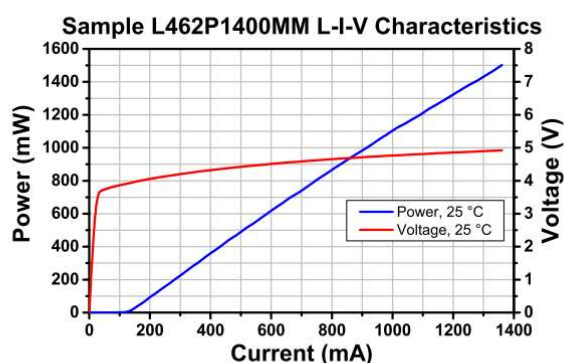
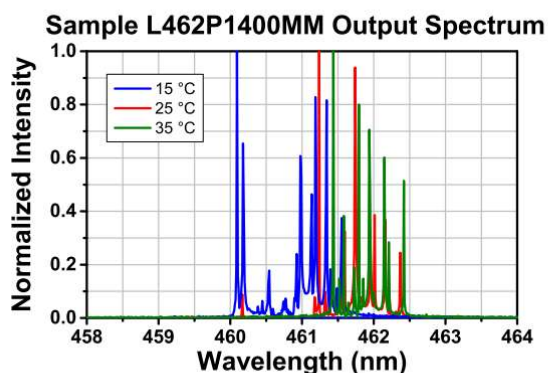
[DBvaxyc89StajKI0oIL4xqaBNgC_Ko/edit?usp=drive_link&oid=110362623677752764972&rtpof=true&sd=true](https://docs.google.com/spreadsheets/d/1l-DBvaxyc89StajKI0oIL4xqaBNgC_Ko/edit?usp=drive_link&oid=110362623677752764972&rtpof=true&sd=true)

Appendix 5. Kinetics derivations:

$$\begin{aligned}
 & \frac{d}{dt} \left[\frac{\varphi_m - \varphi_i}{\left(\frac{t}{t_0} \right)^h + 1} + \varphi_i \right] \\
 &= (\varphi_m - \varphi_i) \cdot \frac{d}{dt} \left[\frac{1}{\left(\frac{t}{t_0} \right)^h + 1} \right] + \frac{d}{dt} [\varphi_i] \\
 &= (\varphi_m - \varphi_i) (-f) \left(\frac{1}{\left(\frac{t}{t_0} \right)^h + 1} \right)^{-f-1} \cdot \frac{d}{dt} \left[\frac{1}{\left(\frac{t}{t_0} \right)^h + 1} \right] + 0 \\
 &= - \left(\frac{d}{dt} \left[\frac{1}{\left(\frac{t}{t_0} \right)^h} \right] + \frac{d}{dt} [1] \right) f \cdot (\varphi_m - \varphi_i) \left(\frac{1}{\left(\frac{t}{t_0} \right)^h + 1} \right)^{-f-1} \\
 &= - \left(\frac{d}{dt} \left[\frac{1}{\left(\frac{t}{t_0} \right)^h} \right] + \frac{d}{dt} [1] \right) f \cdot (\varphi_m - \varphi_i) \left(\frac{1}{\left(\frac{t}{t_0} \right)^h + 1} \right)^{-f-1} \\
 &= - \left((-h) \cdot \left(\frac{t}{t_0} \right)^{-h-1} \cdot \frac{d}{dt} \left[\frac{t}{t_0} \right] + 0 \right) f \cdot (\varphi_m - \varphi_i) \left(\frac{1}{\left(\frac{t}{t_0} \right)^h + 1} \right)^{-f-1} \\
 &= \frac{1}{t_0} \cdot \frac{d}{dt} [t] \cdot fh \cdot (\varphi_m - \varphi_i) \cdot \left(\frac{t}{t_0} \right)^{-h-1} \left(\frac{1}{\left(\frac{t}{t_0} \right)^h + 1} \right)^{-f-1} \\
 &= \frac{1fh \cdot (\varphi_m - \varphi_i) \cdot \left(\frac{t}{t_0} \right)^{-h-1} \left(\frac{1}{\left(\frac{t}{t_0} \right)^h + 1} \right)^{-f-1}}{t_0} \\
 &= \frac{fh \cdot (\varphi_m - \varphi_i) \cdot \left(\frac{t}{t_0} \right)^{-h-1} \left(\frac{1}{\left(\frac{t}{t_0} \right)^h + 1} \right)^{-f-1}}{t_0}
 \end{aligned}$$

Appendix 6. Laser output characteristics:

Performance Plots



The data presented here is for one particular laser diode. Slight variations in performance data will occur from device to device. The sample spectrum of the L462P1400MM laser diode was measured at 15 °C, 25 °C, and 35 °C using a Thorlabs OSA201 Spectrum Analyzer with resolution of 7.5 GHz. The L-I-V characteristics data was taken at 25 °C. Please visit our website for raw spectral data and L-I-V characteristics.

Specifications

Absolute Maximum Ratings*	
Specification	Maximum
Forward Current, CW	1700 mA
Reverse Current	85 mA
Operating Case Temperature	-0 to +50 °C
Storage Temperature	-40 to +85 °C



*Absolute Maximum Rating specifications should never be exceeded. Operating at or beyond these conditions can permanently damage the laser.

L462P1400MM Specifications					
	Symbol	Min	Typical	Max	
Center Wavelength @ P _{op}	λ_o	455 nm	462 nm	470 nm	
Output Power (CW)	P _{op}	-	1400 mW	-	
Threshold Current	I _{TH}	50 mA	140 mA	220 mA	
Operating Current @ P _{op}	I _{op}	-	1350 mA	1550 mA	
Operating Voltage @ P _{op}	V _{op}	-	5.0 V	5.6 V	
Slope Efficiency ³	η	-	1.1 W/A	-	
Modulation Bandwidth	f	1 MHz	-	-	
Beam Divergence (1/e ²) Full Angle	Parallel @ P _{op}	$\theta_{//}$	5°	14°	25°
	Perpendicular @ P _{op}	θ_{\perp}	35	44°	50°

T_{CASE} = 25 °C

Appendix 7. TIA amp datasheet:



Femtoampere Input Bias Current Electrometer Amplifier

Data Sheet

ADA4530-1

FEATURES

- Low input bias current
 - ±20 fA maximum at $T_A = 25^\circ\text{C}$ (guaranteed at production test)
 - ±20 fA maximum at $-40^\circ\text{C} < T_A < +85^\circ\text{C}$
 - ±250 fA maximum at $-40^\circ\text{C} < T_A < +125^\circ\text{C}$ (guaranteed at production test)
- Low offset voltage: 50 μV maximum over specified CMRR range
- Offset voltage drift: ±0.13 $\mu\text{V}/^\circ\text{C}$ typical, ±0.5 $\mu\text{V}/^\circ\text{C}$ maximum
- Integrated guard buffer with 100 μV maximum offset
- Low voltage noise density: 14 nV/ $\sqrt{\text{Hz}}$ at 10 kHz
- Wide bandwidth: 2 MHz unity-gain crossover
- Supply voltage: 4.5 V to 16 V (± 2.25 V to ± 8 V)
- Operating temperature: -40°C to $+125^\circ\text{C}$
- Long-term offset voltage drift (10,000 hours): 0.5 μV typical
- Temperature hysteresis: 1.5 μV typical

APPLICATIONS

- Laboratory and analytical instrumentation: spectrophotometers, chromatographs, mass spectrometers, and potentiostatic and amperostatic coulometry
- Instrumentation: picoammeters and coulombmeters
- Transimpedance amplifier (TIA) for photodiodes, ion chambers, and working electrode measurements
- High impedance buffering for chemical sensors and capacitive sensors

GENERAL DESCRIPTION

The ADA4530-1 is a femtoampere (10^{-15} A) level input bias current operational amplifier suitable for use as an electrometer that also includes an integrated guard buffer. It has an operating voltage range of 4.5 V to 16 V, enabling it to operate in conventional 5 V and 10 V single supply systems as well as ± 2.5 V and ± 5 V dual supply systems.

It provides ultralow input bias currents that are production tested at 25°C and at 125°C to ensure the device meets its performance goals in user systems. The integrated guard buffer isolates the input pins from leakage in the printed circuit board (PCB), minimizes board component count, and enables easy system design. The ADA4530-1 is available in an industry-standard surface-mount 8-lead SOIC package with a unique pinout optimized to prevent signals from coupling between the sensitive input pins, the power supplies, and the output pin while enabling easy routing of the guard ring traces.

The ADA4530-1 also offers low offset voltage, low offset drift, and low voltage and current noise needed for the types of applications that require such low leakages.

PIN CONNECTION DIAGRAM

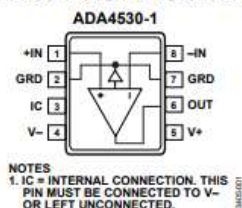


Figure 1.

To maximize the dynamic range of the system, the ADA4530-1 has a rail-to-rail output stage that can typically drive to within 30 mV of the supply rails under a 10 k Ω load.

The ADA4530-1 operates over the -40°C to $+125^\circ\text{C}$ industrial temperature range and is available in an 8-lead SOIC package.

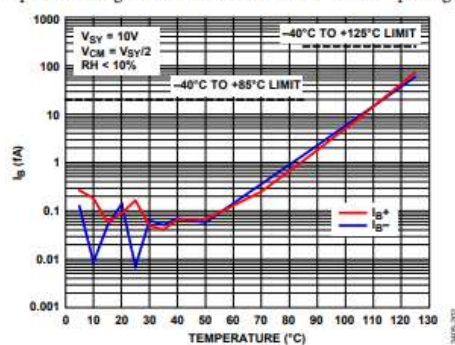


Figure 2. Input Bias Current (I_b) vs. Temperature, $V_{SY} = 10$ V

Rev. B [Document Feedback](#)
Information furnished by Analog Devices is believed to be accurate and reliable. However, no responsibility is assumed by Analog Devices for its use, nor for any infringements of patents or other rights of third parties that may result from its use. Specifications subject to change without notice. No license is granted by implication or otherwise under any patent or patent rights of Analog Devices. Trademarks and registered trademarks are the property of their respective owners.

One Technology Way, P.O. Box 9106, Norwood, MA 02062-9106, U.S.A.
Tel: 781.329.4700 ©2015–2017 Analog Devices, Inc. All rights reserved.
[Technical Support](#) www.analog.com

<https://www.analog.com/media/en/technical-documentation/data-sheets/ADA4530-1.pdf>